# Carbon Nanomaterials and Their Application for Emerging Solar Cells

Munkhbayar Batmunkh


THE UNIVERSITY of ADELAIDE

Thesis submitted for the degree of

**Doctor of Philosophy**

School of Chemical Engineering

Faculty of Engineering, Computer and Mathematical Sciences

The University of Adelaide, Australia

April 2017

# Dedication

*This thesis is dedicated to my parents J. Batmunkh and Ts. Tsetsegmaa, and also to my loving wife (Munkhjargal Bat-Erdene) and son (Khuslen Munkhbayar).*

# Table of Contents

# Declaration

I certify that this work contains no material which has been accepted for the award of any other degree or diploma in my name, in any university or other tertiary institution and, to the best of my knowledge and belief, contains no material previously published or written by another person, except where due reference has been made in the text. In addition, I certify that no part of this work will, in the future, be used in a submission in my name, for any other degree or diploma in any university or other tertiary institution without the prior approval of the University of Adelaide and where applicable, any partner institution responsible for the joint-award of this degree.

I give consent to this copy of my thesis when deposited in the University Library, being made available for loan and photocopying, subject to the provisions of the Copyright Act 1968.

The author acknowledges that copyright of published works contained within this thesis resides with the copyright holder(s) of those works.

I also give permission for the digital version of my thesis to be made available on the web, via the University's digital research repository, the Library Search and also through web search engines, unless permission has been granted by the University to restrict access for a period of time.

I acknowledge the support I have received for my research through the provision of an Australian Government Research Training Program Scholarship.

Name: Munkhbayar Batmunkh

Signed ……..…… Date…….

# Acknowledgements

It would not have been possible for me to write this doctoral thesis without the help and support of many kind people around me, to only some of whom it is possible to give particular mention here. I wish to express my sincere appreciation to those who have contributed to this thesis and supported me in one way or the other during this amazing journey.

First of all, I would like to express my deepest gratitude to Professor Joseph G. Shapter at Flinders University for being a wonderful supervisor and for enabling me to reach this milestone in my life. I attribute my success in doctoral program to his excellent scientific guidance, never-ending encouragement and willingness to share his extensive knowledge and invaluable experiences. He is also a wonderful role model both professionally and personally, and I hope to be able to follow his example.

I would also like to thank my supervisors Professor Mark J. Biggs and A/Professor Sheng Dai, who have supported me throughout this journey of doctoral study. Special thanks must be given to Professor Mark J. Biggs for his valuable guidance and excellent support in developing my extensive skills in research and scientific writing. I am truly thankful to A/Professor Sheng Dai for his endless help during my study.

Further, I would like to express my gratitude to all of our lab members and colleagues, who have made my Ph.D. study fruitful and enjoyable, at both the University of Adelaide and Flinders University. Especially, I would like to thank Dr. Cameron J. Shearer for his great assistance, invaluable advice and constructive comments for all of my work that has been carried out during my Ph.D. study. I would also like to thank my colleagues Dr. Aabhash Shrestha, Md. J. Nine, Dr. Mahnaz Dadkhah, Md. Ziaur Rahman, Leping Yu, Dr. Meisam V. kiamahalleh, Dr. Milan Mijajlovic, Dr. Cheng Hu, Dr. Lachlan Larsen, Tom Grace, Dr. Zahrah Alhalili, Jutarat Sudchanham and others for being wonderful friends and helping me succeed.

I would like to extend my sincerest thanks and appreciation to those patient souls who helped me to learn about and use many state-of-the-art facilities critical to successfully complete high quality research reported in this thesis. These people are Dr. Ashley Slattery, Dr. Christopher Gibson, Alex Sibley, Jade Taylor, David Vincent, Dr. Jing Zhao at Flinders University and Dr. Quihong Hu at the University of Adelaide.

I have had the privilege to work in the research group of Professor Joseph G. Shapter at Flinders University. The excellent research environment and world-class research facilities at both Flinders University and University of Adelaide have enabled me to collaborate with leading experts, scientists and researchers in the field on many projects including Dr. Thomas J. Macdonald (University College London), Prof. Thomas Nann (MacDiarmid Institute), Prof. Shizhang Qiao (University of Adelaide), Prof. Gao Guo (Shanghai Jiao Tong University), Prof. Colin L. Raston (Flinders University), Prof. Shashank Priya (Virginia Tech), Dr. Yun Wang (Griffith University), Dr. Pasit Pakawatpanurut (Mahidol University) and others.

I would like to acknowledge the financial support of both an International Postgraduate Research Scholarship (IPRS) and an Australian Postgraduate Award (APA) during my Ph.D. study in Australia. I must also acknowledge the use of South Australian nodes of the Australian Microscopy & Microanalysis Research Facility (AMMRF) and the Australian National Fabrication Facility (ANFF) at Flinders University.

Finally, none of this would have been possible without the strong support of two families. Words cannot express the feelings I have for both my parents and Munkhjargal Bat-Erdene's parents for their unconditional love and endless support. I am extremely lucky to have Munkhjargal Bat-Erdene as my lovely wife and Khuslen Munkhbayar as my lovely son in my life, who have been very supportive and happy to be beside me throughout these years.

# Abstract

The fact that only one–thousandth of the Sun's energy incident on the Earth is equal to the entire world's current energy needs means direct conversion of this energy into electricity–photovoltaic (PV) energy–is now a mainstream renewable energy source.

There are many types of emerging PV cells. Dye–sensitized solar cells (DSSCs) are an attractive potential source of renewable energy due to their eco–friendliness and ease of fabrication. However, in DSSCs, the rarity and high cost of some electrode materials (*e.g.* platinum) and the inefficient performance caused by slow electron transport, poor light–harvesting efficiency, and significant charge recombination present significant limitations. Over the past several years, carbon nanomaterials including carbon particles, carbon nanotubes and graphene have played important roles in addressing these issues. Although excellent progress has been made in the application of carbon materials in DSSCs, the exact role of nanocarbons in both the photoelectrode and counter electrode (CE) of DSSCs is still unclear.

Organic–inorganic halides based perovskite solar cells (PSCs) have attracted a great deal of attention due to the extremely rapid increases in efficiencies observed over the past few years. Although the efficiencies of the PCS have exceeded 20%, they do have some disadvantages such as use of expensive electrode materials, the high temperature processing required during production and poor stability when in use. In this regard, it is no surprise that carbonaceous materials would have significant role in the development of PSCs as nanocarbons have been extensively studied in various energy related applications because of their fascinating properties, low cost and abundance. Research into the potential application of carbon nanomaterials in PSC is still at an early stage and a lot remains to be explored.

This Ph.D. project focuses on the application and development of carbon nanomaterials for emerging PV devices such as DSSCs and PSCs. The following research has been included in this thesis:

1) A hybrid structure consisting of $SnO_2$ and reduced graphene oxide ($SnO_2$-RGO) was synthesized via a microwave-assisted method and has been employed as a photoanode in DSSCs, for the first time. It was found that the incorporation of RGO

into the $SnO_2$ film not only enhances the electron transfer rate of the photoanode, but it also increases the adsorption of dye molecules into the film. Both these effects greatly enhance the DSSC performance.

2) As an alternative to platinum (Pt), a hybrid electrocatalyst based on sulfur-doped graphene with $FeS_2$ microspheres (SGN-$FeS_2$) was designed and used as a CE of DSSCs. Benefiting from the high conductivity of SGN and excellent electrocatalytic activity of $FeS_2$, the bifunctional hybrid electrocatalyst based device displays an efficiency of 8.1%, which was comparable to that (8.3%) of expensive Pt CE based DSSC and also exhibits excellent stability in ambient conditions.

3) Solution processed transparent conductive graphene films are utilized, for the first time, as an alternative to traditional transparent conducting oxide (TCO) electrodes at the electron collecting layer in perovskite solar cells (PSCs). By optimising the sheet resistance ($R_s$) and transparency of the films, maximum power conversion efficiency of 0.62% was obtained. The successful incorporation of graphene structures into both compact $TiO_2$ and mesoporous $TiO_2$ layers of the PSCs was also demonstrated.

4) The influence of CNTs on the PV performance of 1D titanium dioxide nanofiber ($TiO_2$ NF) photoelectrode perovskite solar cells (PSCs) was systematically explored. It was found that in addition to the significant enhancement in the efficiency of PSCs with SWCNTs, the incorporation of SWCNTs into $TiO_2$ NFs reduced the hysteresis effect and improved the stability of the PSC devices both under light and during storage in ambient conditions.

5) Significant enhancement in the power conversion efficiency (PCE) and stability (light- and long-term storage-stability) of perovskite solar cells (PSCs) by incorporating single-walled carbon nanotubes (SWCNTs) into the nanocrystalline $TiO_2$ photoelectrode was reported. The $TiO_2$-SWCNTs photoelectrode based PSC device exhibited a PCE of up to 16.11%, while the cell fabricated without SWCNTs displayed an efficiency of 13.53%.

# List of figures

# Figures in Supporting Information

# List of schemes

# List of tables

# List of publications

This doctoral thesis is prepared based upon the "Publication" format according to the "Specifications for Thesis (2016)" of the University of Adelaide. The thesis, therefore, contains the following works that have been published or submitted for publication during the period of my Ph.D. candidature.

Peer-reviewed journal publications:

1] Munkhbayar Batmunkh, Mark J. Biggs and Joseph G. Shapter, Carbonaceous dye-sensitized solar cell photoelectrodes, *Advanced Science*, **2015**, *2*, 1400025. *Inside Front Cover - Vol 2/2015*.

2] Munkhbayar Batmunkh, Mark J. Biggs and Joseph G. Shapter, Carbon nanotubes for dye-sensitized solar cells, *Small*, **2015**, *11*, 2963-2989.

3] Munkhbayar Batmunkh, Cameron J. Shearer, Mark J. Biggs, Joseph G. Shapter, Nanocarbons for mesoscopic perovskite solar cells, *Journal of Materials Chemistry A*, **2015**, *3*, 9020-9031. *Themed collection: Perovskite Solar Cells and 2015 J Mater Chem A – Most Accessed Manuscripts*.

4] Munkhbayar Batmunkh, Munkhjargal Bat-Erdene and Joseph G. Shapter, Phosphorene and phosphorene based materials – prospects for future application, *Advanced Materials*, **2016**, *28*, 8586–8617. *ChemInform Abstract*.

5] Munkhbayar Batmunkh, Cameron J. Shearer, Mark J. Biggs and Joseph G. Shapter, Solution processed graphene structures for perovskite solar cells, *Journal of Materials Chemistry A*, **2016**, *4*, 2605-2616.

6] Munkhbayar Batmunkh, Mahnaz Dadkhah, Cameron J. Shearer, Mark J. Biggs and Joseph G. Shapter, Incorporation of graphene into $SnO_2$ photoanode for dye-sensitized solar cells, *Applied Surface Science*, **2016**, *387*, 690-697.

7] Munkhbayar Batmunkh, Mahnaz Dadkhah, Cameron J. Shearer, Mark J. Biggs and Joseph G. Shapter, Tin oxide light-scattering layer for titania photoanodes in dye-sensitized solar cells, *Energy Technology*., **2016**, *4*, 959–966.

8] Gao Guo, Leping Yu, Ajayan Vinu, Joseph. G. Shapter, Munkhbayar Batmunkh, Cameron J. Shearer, Ting Yin, Peng Huang and Daxiang Cu, Synthesis of ultra-long hierarchical ZnO whiskers in the hydrothermal system for dye-sensitised solar cells, *RSC Advances*, **2016**, *6*, 109406-109413.

9] Aabhash Shrestha, Munkhbayar Batmunkh, Cameron J. Shearer, Yanting Yu, Gunther Andersson, Joseph G. Shapter, Shizhang Qiao and Sheng Dai, Nitrogen-doped $CN_x$/CNTs hetero-electrocatalysts for highly efficient dye-sensitized solar cells, *Advanced Energy Materials*, **2017**, *7*, 1602276.

10] Leping Yu, Munkhbayar Batmunkh, Tom Grace, Mahnaz Dadkhah, Cameron J. Shearer and Joseph G. Shapter, Application of a hole transporting organic interlayer in graphene oxide/single walled carbon nanotube-silicon heterojunction solar cells, *Journal of Materials Chemistry A*, **2017**, DOI: 10.1039/C7TA01782K.

11] Jutarat Sudchanham, Munkhbayar Batmunkh, Vichai Reutrakul, Joseph G. Shapter, Colin L. Raston and Pasit Pakawatpanurut, Vortex fluidics improved morphology of $CH_3NH_3PbI_{3-x}Cl_x$ films for perovskite solar cells, *ChemistrySelect*, **2017**, *2*, 369-374. *First two authors contributed equally*.

12] Munkhbayar Batmunkh, Thomas J. Macdonald, Cameron J. Shearer, Munkhjargal Bat-Erdene, Yun Wang, Mark J. Biggs, Ivan P. Parkin, Thomas Nann, and Joseph G. Shapter, Carbon nanotubes in $TiO_2$ nanofiber photoelectrodes for high performance perovskite solar cells, *Advanced Science*, **2017**, *4*, 1600504.

13] Munkhbayar Batmunkh, Aabhash Shrestha, Gao Guo, Leping Yu, Jing Zhao, Mark J. Biggs, Cameron J. Shearer and Joseph G. Shapter, Sulfur–doped graphene with iron pyrite ($FeS_2$) as an efficient and stable electrocatalyst for iodine reduction reaction in dye–sensitized solar cells, *Solar RRL.,* **2017**, *1*, 1700011. *Back Cover: Solar RRL 3-4/2017*.

14] Munkhbayar Batmunkh, Cameron J. Shearer, Munkhjargal Bat-Erdene, Mark J. Biggs and Joseph G. Shapter, Single-walled carbon nanotubes enhance the efficiency and stability of mesoscopic perovskite solar cells, **2017**, Submitted.

Book chapter:

1] T. Grace, C. J. Shearer, D. D. Tune, L. Yu, Munkhbayar Batmunkh, M. J. Biggs, Z. ALOthman, J. G. Shapter, *Use of Carbon Nanotubes in Third Generation Solar Cells*, in 'Industrial Applications of Carbon Nanotubes: 1st Edition' edited by H. Peng, Q. Li, T. Chen. **2016**, Amsterdam, Netherlands: Elsevier.

Work that has been presented at conferences:

1] Munkhbayar Batmunkh, Cameron J. Shearer, Mark J. Biggs, Joseph G. Shapter, Solution processed graphene electrodes for perovskite solar cells, *Khureltogoot - 11th International Conferences of Young Researchers on Technology and Innovation*, Ulaanbaatar, Mongolia, 22nd October, **2015**. Paper ID: II-4. *Grant Winner and "Best Paper" Award*. (Oral presentation).

2] Munkhbayar Batmunkh, Cameron J. Shearer, Mark J. Biggs and Joe Shapter, Transparent conductive graphene electrodes for perovskite solar cells, *International Conference on Recent Progress in Graphene and 2D Materials Research*, Seoul, South Korea, 25th Sep to 29th Sep, **2016**. Paper ID: 09_1001. (Oral presentation).

3] Munkhbayar Batmunkh, Thomas J. Macdonald, Cameron J. Shearer, Munkhjargal Bat-Erdene, Yun Wang, Mark J. Biggs and Joe Shapter, High-performance perovskite solar cells based on carbon nanotubes incorporated $TiO_2$ nanofiber photoelectrodes, *Australian National Fabrication Facility (ANFF) Annual Research Showcase 2016*, Melbourne, Australia, 15th Nov to 17th Nov, **2016**. Page Number: 34. (Oral presentation).

4] Munkhbayar Batmunkh, Thomas J. Macdonald, Cameron J. Shearer, Munkhjargal Bat-Erdene, Yun Wang, Mark J. Biggs and Joe Shapter, Carbon nanotubes in $TiO_2$ nanofiber photoelectrodes for perovskite solar cells, *The Emerging Energy Technologies Summit and Exhibition 2016 (EETSE'16)*, Melbourne, Australia, 05th Nov to 07th Dec, **2016**. Poster Number: P20. *"Best Poster Award" 3rd place.* (Poster presentation).

5] Munkhbayar Batmunkh, Cameron J. Shearer, Munkhjargal Bat-Erdene, Mark J. Biggs and Joe Shapter, Efficiency and stability enhancement of perovskite solar cells using single-walled carbon nanotubes based photoelectrodes, *Conference on Optoelectronic and Microelectronic Materials and Devices (COMMAD2016),* Sydney, Australia, 12$^{th}$ Dec to 14$^{th}$ Dec, **2016**. Contribution Talk ID: 140. (Oral presentation).

# Chapter 1.

## Introduction

## 1.1. Background

The world's energy consumption has dramatically increased because of the rapidly growing global population and development of modern technologies. The U. S. Department of Energy predicts that the world's energy demands will double by 2050 and triple by 2100.[1] Today's energy requirements are principally met by burning fossil fuels. However, continued increases in fuel price must be taken into account. More importantly, potentially harmful damage to the environment, caused by this combustion process, has become a serious problem. All these issues have the potential for disastrous consequences and solutions should be pursued with a great sense of urgency. Until now, significant developments have been made in renewable energy technologies including wind power,[2] biofuels,[3] solar cells[4] and fuel cells[5]. Amongst these renewable energy technologies, solar cells, which convert sunlight directly into electricity, is a serious alternative to traditional fossil energy owing to its unlimited potential power production at reasonable cost.

Photovoltaic (PV) cells are generally classified into main three generations. In brief: (1) The first generation solar cells based on single-crystalline silicon, which make up ~90% of the commercial production at present, are estimated to deliver power with approximately 15% efficiency, but they suffer from high manufacturing, installation and material costs. (2) The second generation cells (also referred as a thin film tech) are lower cost than the traditional PV cells, but their lower performance is the main concern. (3) The third generation PV cells, which include organic solar cells, dye-sensitized solar cells (DSSCs) and perovskite solar cells (PSCs), are designed to further lower the costs of the second generation cells, by maintaining the economic and environmental aspects while increasing the performance. Of particular interests in this Ph.D. thesis are DSSCs and PSCs.

### 1.1.1. Dye-sensitized solar cells (DSSCs)

In particular, DSSCs have gained much attention because of not only the simple fabrication method, low manufacturing cost and eco-friendliness, but also their high efficiency (13%[6] for DSSCs) compared to OPVs (10.7%[7] for organic PV (OPV) cells). Because of the rapidly growing interest in this cutting-edge technology, several companies, (namely Solaronix from Switzerland, Dyesol from Australia and

Dyenamo from Sweden) have been established to contribute to DSSCs commercialization. Moreover, in 2009, G24-Power introduced the world's first commercial production of DSSCs using a roll-to-roll manufacturing process.[8]

Typically, a DSSC consists of a transparent conductive oxide (TCO) substrate, dye molecules (Ru-based organic dye) adsorbed nanocrystalline semiconducting oxide film, a platinum (Pt) counter electrode and an electrolyte containing iodide/tri-iodide ($I^-/I_3^-$) redox couple between two electrodes (Figure 1-1).[9] The working principle of DSSC can be found elsewhere.[10-12] However, this conventionally structured DSSC suffers from the following significant issues: (i) the low energy conversion efficiency caused by charge recombination (red dashes in Figure 1-1) between the injected electrons and either the oxidized dye molecules or electron-accepting species in the electrolyte, (ii) the high cost and scarcity of materials such as indium or fluoride used for TCO electrodes such as indium-doped tin oxide (ITO) and fluorine-doped tin oxide (FTO) and (iii) the expensive and rarity of platinum (Pt).

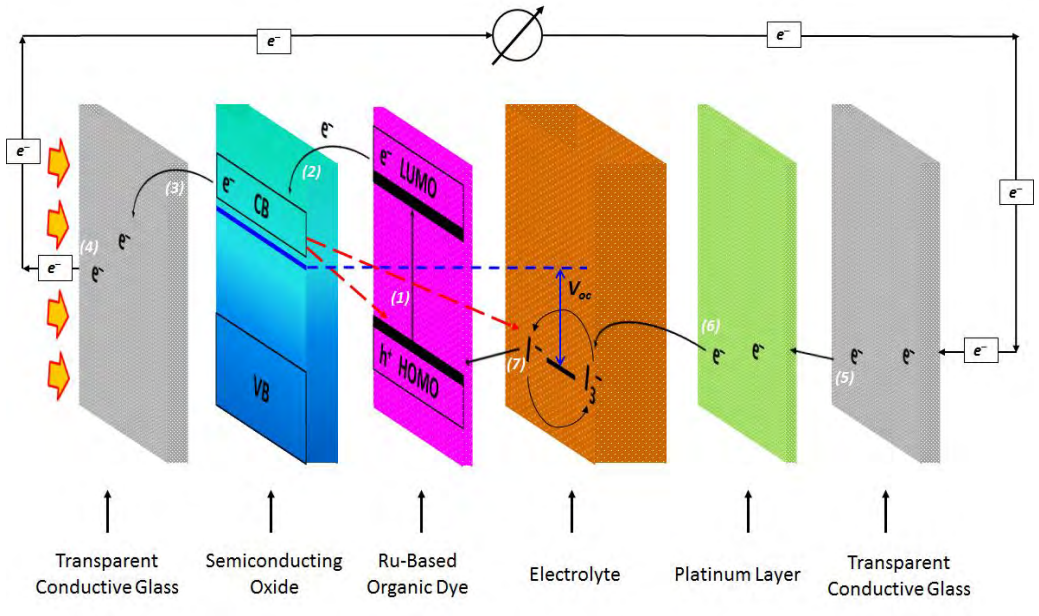


**Figure 1-1**. The structure an operational mechanism of a typical DSSC, Gold arrows represent sunlight. Reproduced with permission from ref. 9 © 2015, Wiley-VCH.

In order to improve the performance and lower the production cost of DSSCs, it is believed that nanostructured materials will play an important role. In particular,

carbon nanomaterials including carbon particles, carbon nanotubes (CNTs) and graphene have attracted great attention for use in various components of DSSCs because of their unique properties such as excellent conductivity, good transparency, high catalytic activity, low cost and abundance.[13,14]

A nanocrystalline $TiO_2$ film made up of 20 nm diameter nanoparticles is commonly used as a conventional photoanode material for DSSCs. However, the conventional $TiO_2$ nanostructured photoanodes have the following disadvantages: (i) slow electron transport caused by a large number of grain boundaries (Figure 1-2a), (ii) high rate of charge recombination between $TiO_2$-photosensitizer and $TiO_2$-electrolyte (Figure 1-2b), and (iii) significant light loss (Figure 1-2c). In order to address these bottlenecks, several attractive strategies have been developed and their advantages and disadvantages are systematically highlighted in recent reviews.[9, 13] These strategies include the use of a light scattering layer, hole-blocking layer, surface plasmonic effects, 1D materials and their composites and hierarchical structures.[15-19] Moreover, a range of alternative metal oxide semiconductors have been explored as a substitute for the $TiO_2$, including ZnO, $SnO_2$, $Nb_2O_3$ etc., owing to their suitable energy band structure and high charge mobility.[15-19] However, none of these materials have successfully replaced the $TiO_2$ due partially to the lower low surface-area-to-volume ratio of the various oxides used.[20] Therefore, further development in these metal oxide semiconductors such as $SnO_2$ based DSSCs is highly desired because they have the potential to achieve an excellent efficiency.

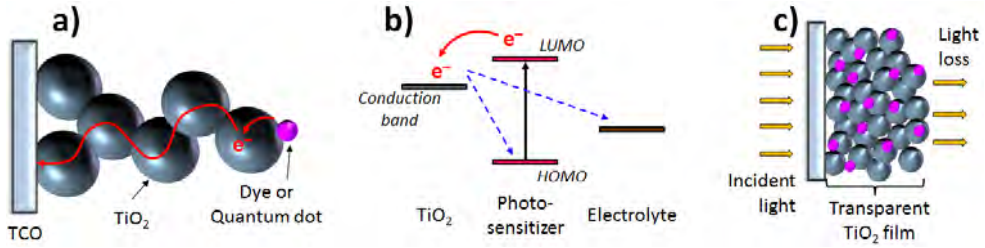


**Figure 1-2**. Schematic illustration for (a) slow electron transport caused by $TiO_2$ grain boundaries, (b) charge recombination between $TiO_2$-dye and $TiO_2$-electrolyte and (c) unabsorbed lights in the conventional $TiO_2$ photoanode of DSSCs and QDSSCs. Reproduced with permission from ref. 30 © 2016, Wiley-VCH.

In DSSCs, a Pt based electrocatalyst coated TCO electrode (counter electrode) serves an important role in reducing $I_3^-$ to $I^-$ for the regeneration of the photosensitizer. However, in addition to its high cost and scarcity, the slow dissolution of the Pt electrode in the corrosive redox electrolyte leads to deterioration of device performance. For this reason, there has been a surge of research interest in finding low-cost alternative electrocatalysts that are readily available for use and can achieve higher or comparable performance to the typical Pt.[21-25] Although excellent progress has been made in nanocarbons based counter electrode materials for DSSCs, finding cheaper and more efficient electrocatalyst materials for the iodine reduction reaction in DSSCs is still needed to further lower the manufacturing cost of this technology.

### 1.1.2. Perovskite solar cells (PSCs)

Over the past few years, the unprecedented rapid progress that has been made in the energy conversion efficiency of organometal halide light absorbers based perovskite solar cells (PSCs) have attracted increasing attention from the whole photovoltaic (PV) community. The power conversion efficiencies (PCEs) of PSCs have increased from 3.8% in 2009 to 22.1% in early-2016 (shown in Figure 1-3), making it the fastest-advancing PV technology.[26-29] The efficiencies of PSCs are now approaching that of commercially available silicon-based solar cells. With the potential of producing remarkably high PCEs with low manufacturing costs, these PV cells have become commercially attractive, in addition to their success in research sector. Since the first report published in 2009,[26] the number of publications regarding PSCs has increased very rapidly (see the inset of Figure 1-3). This extremely rapid growth in publication rate underlines the importance and emergence of perovskite based PV cells.

However, despite these advantages, they also suffer from several drawbacks namely: (i) use of expensive, rare materials, (ii) high-temperature processing of n-type $TiO_2$ layer, (iii) relatively slow electron transport between the perovskite and $TiO_2$ and (iv) a lack of long-term stability. Consequently, it is necessary to overcome these issues in order to make this novel high efficiency solar cell commercially viable.

Due to their excellent properties, low cost and abundance, it is expected that carbon nanomaterials including carbon particles, CNTs and graphene will have significant

role in the development of PSCs. It is expected that the use of carbonaceous materials will advance the PV performance of PSCs whilst maintaining low production cost. But, research into the practical use of nanocarbon materials in PSC is still at an early stage, and a lot remains to be explored.

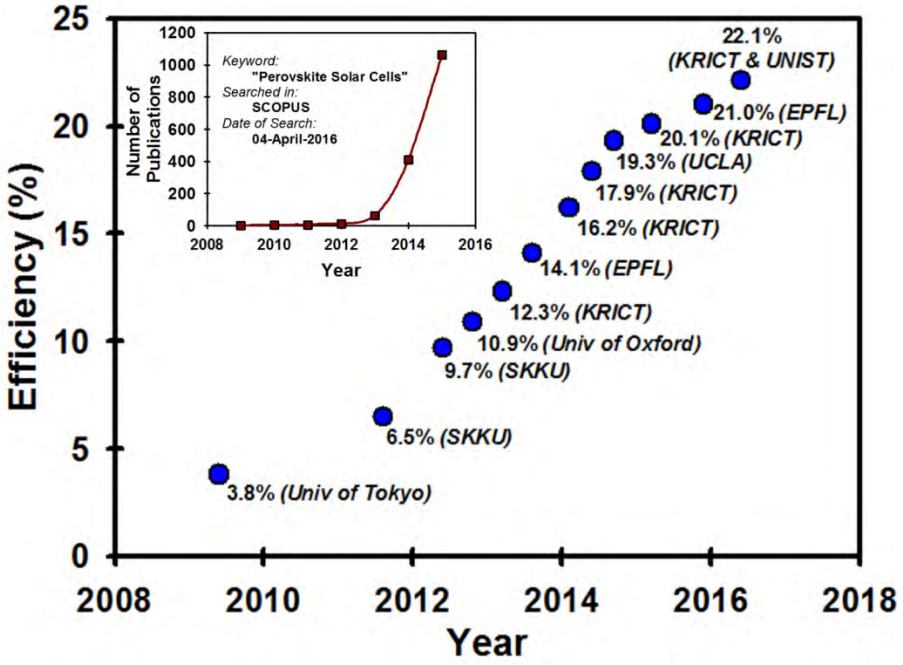


**Figure 1-3**. Efficiency records vs. year of PSCs. Abbreviations: SKKU – Sungkyunkwan University, KRICT – Korea Research Institute of Chemical Technology, EPFL – École Polytechnique Fédérale de Lausanne, UCLA – University of California, Los Angeles, and UNIST – Ulsan National Institute of Science and Technology. Inset shows the number of publications from 2009 to 2015.

Overall, this Ph.D. research project aims to address many of aforementioned issues in both DSSCs and PSCs by employing various types of carbon nanomaterials and their hybrids. In addition to addressing the issues in these two cutting-edge photovoltaic technologies, we also aim to enhance the power conversion efficiencies of the devices by using carbon nanotubes and graphene; and their derivatives.

## 1.2. Aims and Objectives

The aim of this Ph.D. thesis is to explore the applicability of carbon nanomaterials including carbon nanotubes and graphene derivatives in emerging photovoltaic devices such as dye-sensitized solar cells and perovskite solar cells. As such, the following objectives were set for this thesis:

(a) Understanding the role and mechanism of action of carbonaceous materials in dye-sensitized solar cells.

(b) Exploring the effect of reduced graphene oxide on the photovoltaic performance of $SnO_2$ photoelectrode based dye-sensitized solar cells.

(c) Developing efficient Pt-free electrocatalysts based on graphene nanosheets for use as counter electrode materials in dye-sensitized solar cells.

(d) Preparing low-temperature processable transparent conductive graphene films and exploring their feasibility as alternatives to the traditional transparent conducting oxide electrodes in perovskite solar cells.

(e) Investigating the influence of graphene and carbon nanotubes in the $TiO_2$ photoelectrode on the efficiency, light- and long-term storage stability of perovskite solar cells.

## 1.3. Thesis Outline

The outline of the thesis is described as follows:

**Chapter 1** provides an overview of the research topics studied in this Ph.D., aims, objectives and outline of the thesis.

**Chapter 2** reviews recent advancements that have been achieved in the application of carbonaceous-based materials in the photoelectrodes of DSSCs and how these advancements have improved performance.

**Chapter 3** presents a facile preparation method for hybrid structures based on morphologically controllable $SnO_2$ combined with reduced graphene oxide for use as a photoelectrode in dye-sensitized solar cells. The application of reduced graphene oxide overcomes the major shortcoming of $SnO_2$ when applied as a DSSC

photoanode, namely poor dye adsorption. In addition, owing to its suitable energy levels and excellent conductivity, reduced graphene oxide significantly improves the electron transport in the cells.

**Chapter 4** reports the development of efficient electrocatalyst material as an alternative to the conventional platinum counter electrode (CE) for dye-sensitized solar cells. This chapter compares seven different graphene based materials including, graphene oxide, graphene, I–doped graphene, P–doped graphene, B–doped graphene, N–doped graphene and S–doped graphene for use as CEs in DSSCs. By employing the best candidate (S-doped graphene) among these heteroatom doped graphene materials, the hybrid electrocatalyst based on sulfur-doped graphene with $FeS_2$ microspheres (SGN-$FeS_2$) was designed and used as a CE of DSSCs. The optimized device fabricated with this SGN-$FeS_2$ hybrid CEs exhibits an efficiency of 8.10 %, which is comparable to the Pt based cell (8.33 %).

**Chapter 5** examines the feasibility of transparent conductive graphene films as a substitute for the conventional electron collecting transparent conducting oxide electrode (TCO) in perovskite solar cells. This chapter also reports the preparation of transparent conductive graphene films from chemically derived graphene (or solution processed graphene) using a low-temperature processable technique. The chapter further demonstrates that the incorporation of graphene nanosheets into $TiO_2$ electron transporting layers can enhance the efficiency of perovskite solar cells. An efficiency of 0.62% is achieved using TCO-free perovskite solar cells.

**Chapter 6** investigates the influence of various types of carbon nanotubes on the photovoltaic performance, hysteresis behavior and stability of $TiO_2$ nanofiber photoelectrode based perovskite solar cells. This chapter also reports the preparation of one-dimensional (1D) $TiO_2$ nanofibers for use as electron transporting materials in perovskite solar cells. The best performing PSC device constructed with single-walled carbon nanotubes structures displays a PCE of 14.03%. In addition to the enhancement in the efficiency, the incorporation of SWCNTs into $TiO_2$ NFs reduces the hysteresis effect and improves the stability of the PSC devices both under light and during storage in ambient conditions (>60% humidity).

**Chapter 7** focuses on increasing the power conversion efficiency of $TiO_2$ nanoparticle photoelectrode based perovskite solar cells by introducing highly

conductive single-walled carbon nanotubes (SWCNTs) into the electron transporting layer. The perovskite solar cells fabricated with nanocomposite of $TiO_2$ nanoparticles and SWCNTs based photoelectrode shows a remarkable PCE of 16.11%. More importantly, the use of SWCNTs in the photoelectrodes reduces the anomalous hysteretic J-V behavior, while it also improves the light- and long-term storage-stability of the devices.

**Chapter 8** summarizes the research that have been carried out and reported in this thesis and highlights some important future directions in this research field.

## References


[1] M. I. Hoffert, K. Caldeira, A. K. Jain, E. F. Haites, L. D. D. Harvey, S. D. Potter, M. E. Schlesinge, S. H. Schneider, R. G. Watts, T. M. L. Wigley, D. J. Wuebbles, *Nature,* **1998,** *395,* 881-884.
[2] F. D. Gonzalez, A. Sumper, O. G. Bellmunt, R. V. Robles, *Renew Sust Energy Rev,* **2012**, *16*, 2154-2171.
[3] L. Brennan, P. Owende, *Renew Sust Energy Rev,* **2010**, *14*, 557-577.
[4] S. R. Wenham, M. A. Green, *Prog in Photovoltaics: Res and App,* **1996**, *4*, 3-33.
[5] A. Hawkes, I. Staffell, D. Brett, N. Brandon, *Energy Environ Sci,* **2009,** *2*, 729-744.
[6] S. Mathew, A. Yella, P. Gao, R. B. Baker, B. F. E. Curchod, N. A. Astani, I. Tavernelli, U. Rothl, *Nat Chem,* **2014,** *6*, 242-247.
[7] http://www.heliatek.com/newscenter/latest_news/heliatek-erzielt-mit-107-effizienz-neuen-weltrekord-fur-seine-organische-tandemzelle/?lang=en.
[8] [http://gcell.com/.
[9] M. Batmunkh, M. J. Biggs, J. G. Shapter, *Small*, **2015**, *11*, 2963–2989.
[10] M. Graetzel, *Nature*, **2001**, *414*, 338–344.
[11] M. Graetzel, *Inorganic Chem*, **2005**, *44*, 6841–6851.
[12] A. Hagfeldt, G. Boschloo, L. Sun, L. Kloo, H. Pettersson, *Chem Rev*. **2010**, *110*, 6595–6663.
[13] M. Batmunkh, M. J. Biggs, J. G. Shapter, *Adv. Sci*, **2015**, *2*, 1400025.
[14] S. Hwang, M. Batmunkh, M. J. Nine, H. Chung, H. Jeong, *ChemPhysChem*, **2015**, *16*, 53-65.
[15] Q. Zhang, E. Uchaker, S. L. Candelaria, G. Cao, *Chem. Soc. Rev,* **2013**, *42*, 3127-3171.
[16] Q. Zhang, G. Cao, *Nano Today*, **2011**, *6*, 91-109.
[17] N. Tetreault, M. Grätzel, *Energy Environ. Sci*, **2012**, *5*, 8506-8516.
[18] J. Tian, Z. Zhao, A. Kumar, R. I. Boughton, H. Liu, *Chem. Soc. Rev,* **2014**, *43*, 6920-6937.

[19] B. Roose, S. Pathak, U. Steiner, *Chem. Soc. Rev*, **2015**, *44*, 8326-8349.
[20] A. K. Chandiran, M. Abdi-Jalebi, M. K. Nazeeruddin, M. Grätzel, *ACS Nano,* **2014**, *8*, 2261-2268.
[21] S. Yun, A. Hagfeldt, T. Ma, *Adv. Mater*, **2014**, *26*, 6210-6237.
[22] M. Ye, X. Wen, M. Wang, J. Iocozzia, N. Zhang, C. Lin, Z. Lin, *Mater Today*, **2015**, *18*, 155-162.
[23] S. Thomas, T. G. Deepak, G. S. Anjusree, T. A. Arun, S. V. Naira, A. S. Nair, *J. Mater. Chem. A,* **2014**, *2*, 4474-4490.
[24] M. Wu, T. Ma, *J. Phys. Chem. C*, **2014**, *118*, 16727-16742.
[25] J. D. Roy-Mayhew, I. A. Aksay, *Chem Rev*. **2014**, *114*, 6323-6348.
[26] A. Kojima, K. Teshima, Y. Shirai, T. Miyasaka, *J. Am. Chem. Soc,* **2009**, *131*, 6050-6051.
[27] M. M. Lee, J. Teuscher, T. Miyasaka, T. N. Murakami, H. J. Snaith, *Science,* **2012**, *338*, 643-647.
[28] M. Saliba, S. Orlandi, T. Matsui, S. Aghazada, M. Cavazzini, J.-P. Correa-Baena, P. Gao, R. Scopelliti, E. Mosconi, K.-H. Dahmen, F. De Angelis, A. Abate, A. Hagfeldt, G. Pozzi, M. Grätzel, M. K. Nazeeruddin, *Nat. Energy*, **2016,** *1*, 15017.
[29] NREL, http://www.nrel.gov/ncpv/images/efficiency_chart.jpg
[30] M. Batmunkh, M. Bat-Erdene, J. G. Shapter, *Adv. Mater*, **2016**, *28*, 8586-8617.

# Chapter 2.

# Carbonaceous Dye–Sensitized Solar Cell Photoelectrodes

Munkhbayar Batmunkh,[1,2] Mark J. Biggs,[1,3]* Joseph G. Shapter,[2]*

[1] *School of Chemical Engineering, The University of Adelaide, Adelaide, South Australia 5005, Australia*

[2] *School of Chemical and Physical Sciences, Flinders University, Bedford Park, Adelaide, South Australia 5042, Australia*

[3] *School of Sciences, Loughborough University, Loughborough, Leicestershire, LE11 3TU, UK*

* Corresponding authors:

joe.shapter@flinders.edu.au; m.biggs@lboro.ac.uk

**Published:** *Advanced Science,* **2015**, *2*, 1400025

The published copy of the manuscript is attached in Appendix A.

# Statement of Authorship

| | |
|---|---|
| Title of Paper | Carbonaceous Dye-Sensitized Solar Cell Photoelectrodes |
| Publication Status | ☑ Published ☐ Accepted for Publication<br>☐ Submitted for Publication ☐ Unpublished and Unsubmitted work written in manuscript style |
| Publication Details | Munkhbayar Batmunkh, Mark J. Biggs and Joseph G. Shapter, Carbonaceous Dye-Sensitized Solar Cell Photoelectrodes, *Advanced Science.*, 2015, 2, 1400025. |

## Principal Author

| | |
|---|---|
| Name of Principal Author (Candidate) | Munkhbayar Batmunkh |
| Contribution to the Paper | Prepared the first draft of manuscript, Edited and revised the manuscript |
| Overall percentage (%) | 80% |
| Certification: | This paper reports on original research I conducted during the period of my Higher Degree by Research candidature and is not subject to any obligations or contractual agreements with a third party that would constrain its inclusion in this thesis. I am the primary author of this paper. |
| Signature | Date 30/12/2016 |

## Co-Author Contributions

By signing the Statement of Authorship, each author certifies that:

i. the candidate's stated contribution to the publication is accurate (as detailed above);

ii. permission is granted for the candidate in include the publication in the thesis; and

iii. the sum of all co-author contributions is equal to 100% less the candidate's stated contribution.

| | |
|---|---|
| Name of Co-Author | Mark J. Biggs |
| Contribution to the Paper | Supervised the development of work, Edited the manuscript, and Corresponding author. |
| Signature | Date 12/1/17 |

| | |
|---|---|
| Name of Co-Author | Joseph G. Shapter |
| Contribution to the Paper | Supervised the development of work, Edited the manuscript, and Corresponding author. |
| Signature | Date 4/1/17 |

## Abstract

High photovoltaic efficiency is one of the most important keys to the commercialization of dye sensitized solar cells (DSSCs) in the quickly growing renewable electricity generation market. The heart of the DSSC system is a wide band–gap semiconductor based photoelectrode film that helps to adsorb dye molecules and transport the injected electrons away into the external electrical circuit. However, charge recombination, poor light harvesting efficiency and slow electron transport of the nanocrystalline oxide photoelectrode film are major issues in DSSCs' performance. Recently, semiconducting composites based on carbonaceous materials (carbon nanoparticles, carbon nanotubes (CNTs) and graphene) have been shown to be promising materials for the photoelectrode of DSSCs due to their fascinating properties and low cost. After a brief introduction to development of nanocrystalline oxide based films, this review outlines advancements that have been achieved in the application of carbonaceous–based materials in the photoelectrode of DSSCs and how these advancements have improved performance. In addition, several of the unsolved issues in this research area are discussed and some important future directions are also highlighted.



**Keywords:** photovoltaic cells, dye-sensitized solar cell, photoelectrode, carbon particle, carbon nanotube, graphene


**TOC Figure**

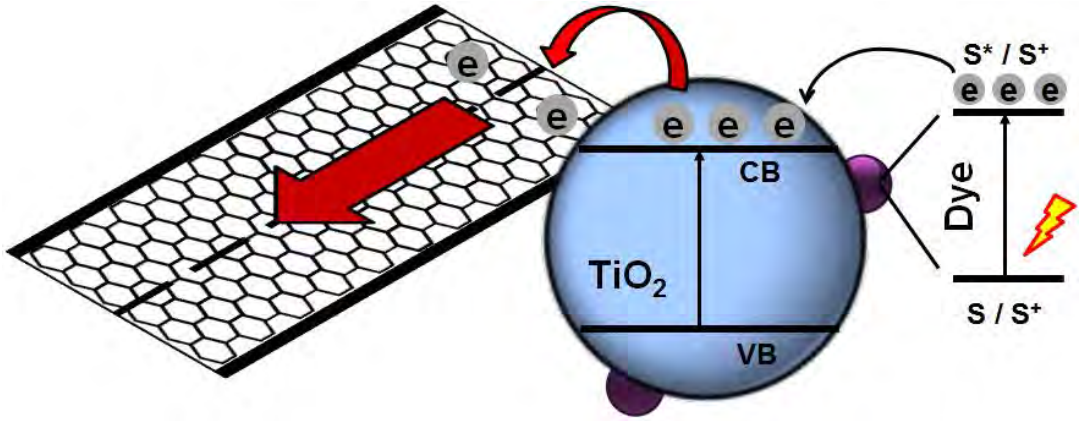

## 2.1. Introduction

The fact that only one-thousandth of the Sun's energy incident on the Earth is equal to the entire World's current energy needs[1] means direct conversion of this energy into electricity – photovoltaic (PV) energy – is now a mainstream renewable energy source.[2] PV devices, or solar cells, have undergone considerable development over the past two decades: (i) first generation silicon (Si) solar cells;[3] (ii) second generation solar cells based on semiconductor thin films;[4] and (iii) most recently, third generation solar cells represented by dye sensitized solar cells (DSSCs) and organic semiconductor solar cells.[5, 6] While the first two generations are well established, their manufacture is inherently complex and expensive.[5] The third generation cells such as DSSCs, on the other hand, are in principle far easier and cheaper to manufacture while also offering, at least in theory, greater efficiencies,[7-9] although these have yet to be realized.[10] Indeed, the highest standard configuration DSSC efficiency achieved to date is around 13%.[10]

A typical DSSC consists of a metal-oxide semiconductor electrode on which a photoactive dye is adsorbed (the photoelectrode), an electrolyte, and a counter-electrode, as shown in Figure 2-1.[11-13] Upon exposure to photons, electrons from the dye molecules are excited and injected into the metal-oxide electrode (i.e. the dye molecules are oxidized). These electrons then slowly diffuse through the metal-oxide electrode before being conducted away through a power circuit to the counter-electrode. The electrons then pass from the counter-electrode into the electrolyte (i.e. the ions of the electrolyte are reduced), which in turn diffuses to the photoelectrode where it gives up the electrons to the dye molecules that have previously lost an electron to the circuit (i.e. they are regenerated). Of particular concern in this review is the photoelectrode.

In order to gain sufficient power, the photoelectrode of a DSSC is typically mesoporous so as to balance the need to maximize the density of adsorbed dye molecules while minimizing the resistance to electrolyte diffusion to the dye molecules. The most common (and original) mesoporous photoelectrodes are composed of titania ($TiO_2$) nanoparticles of around 20 nm in diameter deposited on a conductive transparent medium such as fluoride-doped tin dioxide (FTO) glass. A variety of other nanostructured semi-conducting films have, however, also been

investigated, including those composed of zinc oxide (ZnO), tin oxide ($SnO_2$) and niobium pentoxide ($Nb_2O_5$) nanoparticles.[14-16] A significant issue with these nanostructured films is charge recombination arising from reaction between the photoexcited electrons that are slowly diffusing through them (towards the circuit) and the oxidized electrolyte species at that part of the electrode surface that happens to not be covered by dye molecules. This issue has led to some effort being focused on alternative photoelectrode materials, including those based on carbonaceous materials such as carbon particles, carbon nanotubes (CNTs) and, most recently, graphene. Therefore, review articles on carbon nanomaterials for the energy related applications are well documented.[17-28] It should be noted that since the production of this article, two other reviews of the use of graphene for DSSCs have been published.[29, 30] The most recent one is very comprehensive and spans all aspects of DSSCs,[29] while the other one briefly discussed the recent progresses of graphene based nanostructures in DSSCs.[30] Here, we pay particular attention to the use of the complete spectrum of carbon materials and briefly cover some of the graphene work in the photoelectrodes of DSSCs. Following a brief overview of nanostructured DSSC photoelectrodes, we focus on the latest advancements that have been made on the utilization of carbonaceous materials in this context.

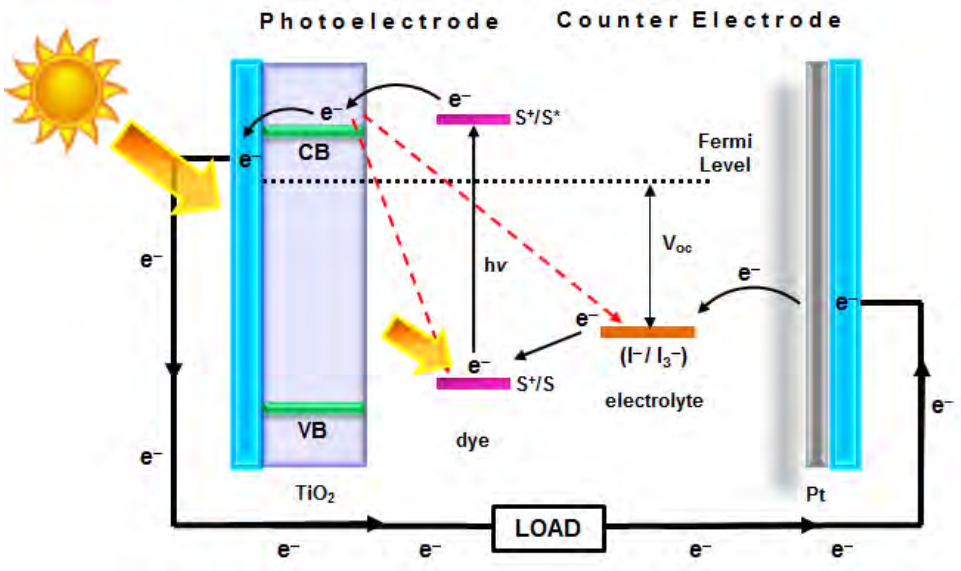


**Figure 2-1**. A schematic representation and principle of a typical DSSC with nanocrystalline $TiO_2$ photoelectrode.

## 2.2. Development of Photoelectrodes in DSSCs

### 2.2.1. Nanostructured photoelectrodes

In the early 1960s, metal oxide semiconductors with wide band–gap structures such as ZnO, $TiO_2$, and $SnO_2$ were used as photosensitizer materials.[31-33] However, one major drawback of these wide band–gaps materials is their poor response to much of the solar spectrum. In particular, they only efficiently harvest the ultraviolet (UV) light, which constitutes around 2–3% of sunlight.[34] This issue was eventually addressed by 'sensitizing' the semiconductors with dye molecules whose light absorption capacity lies in the visible region (i.e. wavelengths greater than 400 nm).[35] By adsorbing dye molecules onto the oxides in this way, electrons excited in the dye by the sunlight can be injected into the conduction band of oxides (Figure 2-2). The problem then was to adsorb a sufficient density of dye molecules to obtain the desired power – this was duly achieved by adopting thin (~10 μm) mesoporous films of metal oxide nanoparticles,[36] which possess relatively high surface area to volume ratios.

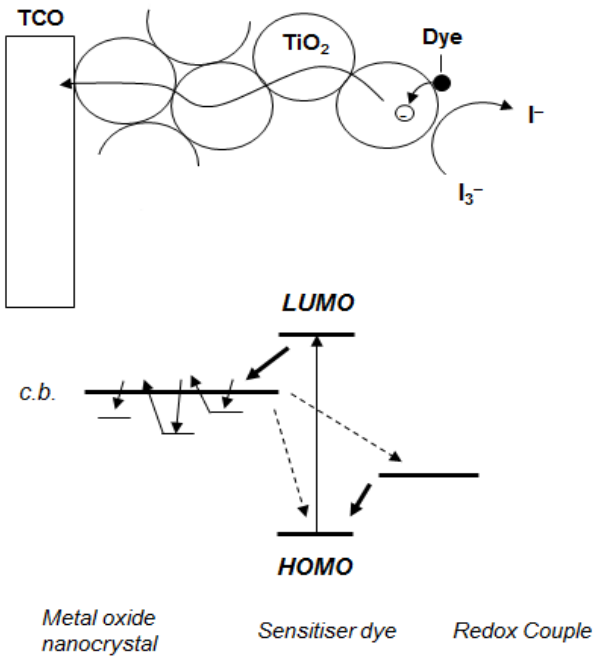


**Figure 2-2**. A schematic of electron transport in nanocrystallites based film. Electron trapping and detrapping process.[50, 51] Reproduced with permission from ref. 50 ©

2004, Elsevier. Reproduced with permission from ref. 51 © 2000, American Chemical Society.

Since the initial work of O'Regan and Graetzel, a range of n-type metal oxide semiconductors have been investigated as alternatives to the $TiO_2$ they used, including ZnO, $SnO_2$, $Nb_2O_5$ and $SrTiO_3$, all of which exhibit higher electron mobility than $TiO_2$ while still being low cost and non-toxic.[37-40] None have, however, replaced the nanostructured $TiO_2$ (Figure 2-3a) because surface area to volume ratios of these materials are lower than that of $TiO_2$.[13, 41-43] There are three primary factors that limit the performance of DSSCs fabricated based on these nanostructured semiconducting oxide materials: (i) they are poor light harvesters because their constituent nanoparticles, which are smaller than the wavelength of the light, do not scatter the light;[44-47] (ii) charge recombination is of major concern in the case of films consisting of nanocrystallites due to the fact that their size is several tens of nanometers and they are soaked in a liquid electrolyte with high ion concentration meaning they cannot support the required charge separation or facilitate a rapid electron transfer within the nanocrystallite network.[48, 49] and (iii) numerous grain boundaries between the nanoparticles and the diffusion of photo-generated electrons in the nanocrystalline films suffer from random walk of electrons caused by a series of trapping and detrapping processes (Figure 2-2).[50, 51] The electron trapping in the nanocrystalline film is a mechanism that causes significant energy loss. To date, several interesting approaches have been demonstrated to address these issues.[41, 44, 48, 52] Here, the most important of these are briefly discussed.

One means of bringing about light scattering within the photoelectrode and, hence, improved interaction with the adsorbed dye is through the use of a bilayer structure as illustrated in Figure 2-3b.[53, 54] Typically, the double layer structure consists of a layer of particles larger than the light wavelength (~400 nm in size) being layered over the traditional film of small particles (~20 nm in size).[55] This layer of larger particles backscatters the light that passes through the layer of smaller particles so as it has a further opportunity to interact with the dye molecules adsorbed within it. This bilayer approach is an effective way to enhance the optical absorption of the photoelectrode, especially at wavelengths over 700 nm where the dye is not as

efficient at absorbing light. Moreover, it is known that more than 40% of the total irradiance is absorbed in this wavelength region.[44] Although the use of bilayer structure improves light collection efficiency, the large particles also bring a decrease in surface area and, hence, power generation capacity.

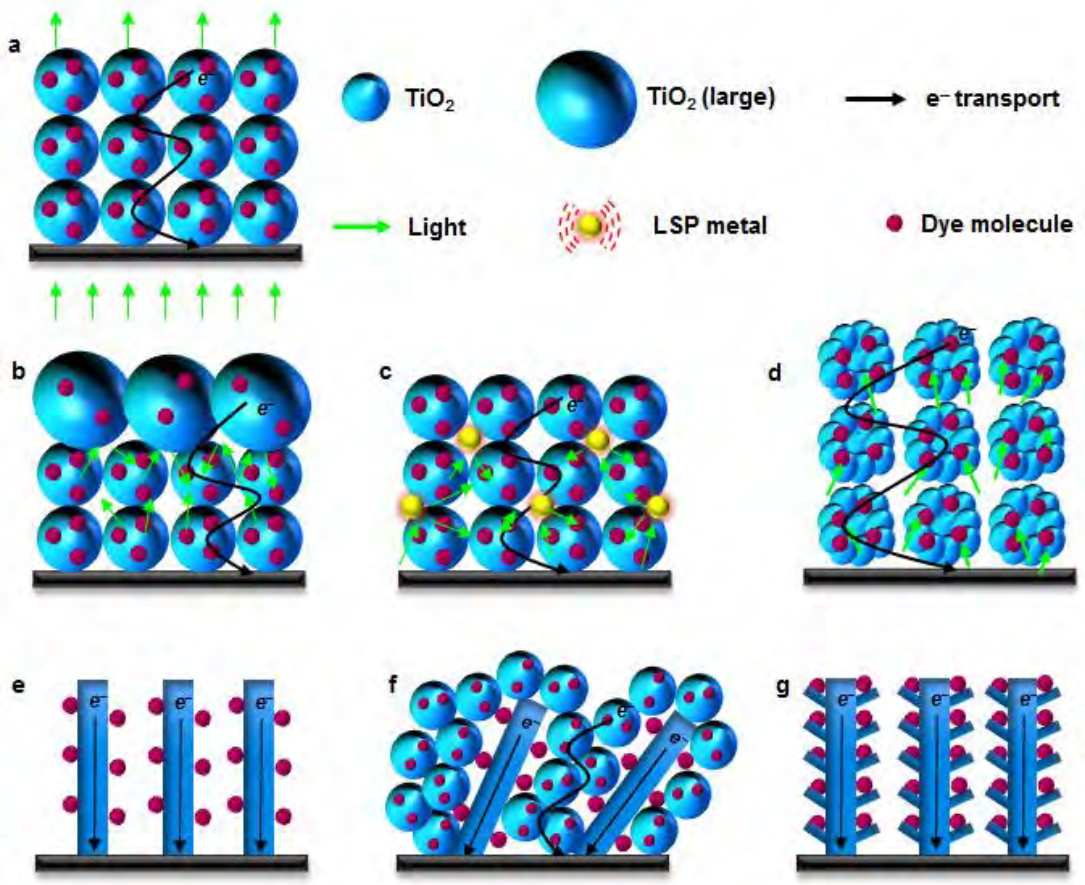


**Figure 2-3**. The structures of different photoelectrodes for DSSCs. (a) Nanocrystalline $TiO_2$ based photoelectrode film, (b) double layer structured photoelectrode film, (c) plasmon–enhanced photoelectrode film, (d) hierarchically structured nanoporous film, (e) 1D structured photoelectrode film, (f) 1D/nanoparticles hybrid structure based film and (g) hierarchically structured 1D photoelectrode.

In the past few years, localized surface plasmon resonance (LSPR) of metal nanostructures has been considered a promising way to improve DSSC performance.[56] Plasmonic noble metal nanostructures interact with light in the

visible to near-IR range through the creation of resonant surface plasmons. Several authors have seen significant improvement in the DSSC photocurrent by incorporating metal (Au, Ag) particles into semiconducting oxide nanoparticles (see Figure 2-3c).[57-61] For example, Hou et al.[57] observed a very high (2.4–fold) enhancement in the PV efficiency compared to the conventional $TiO_2$ film based DSSC due to the extension of light absorption over the wavelength range from 460–730 nm. However, the preparation method of homogeneous plasmonic nanocomposites involves a number of complex steps and high temperature & pressure, and the metal NPs are susceptible to corrosion by the electrolyte.[62, 63]

Hierarchical spherical nanostructures (HSN) such as that illustrated in Figure 2-3d have also been recently proposed as a means of simultaneously addressing the poor light harvesting efficiency of conventional DSSC films while boosting the surface area.[44, 64] By using micrometer sized aggregates of nanosized particles, HSNs enhance the scattering of light within the films while retaining the area associated with the nanoparticles.[39, 44, 65] The first study of such a bifunctional (high surface area to volume ratio and good light scattering property) structure in DSSCs was reported by Koo et al.[65] who observed the amount of adsorbed dye was about 5 times greater than for film composed of similarly micro-sized $TiO_2$ particles. This leads to an energy conversion efficiency of 10.34%.[65] Even though the HSNs remarkably improve both the light harvesting efficiency and adsorption of dye molecules into the film, the electrodes still suffer from charge recombination and slow electron transfer because they are composed of several small (20 nm) nanoparticles that cause electron trapping and detrapping.

The high rate of charge recombination and slow electron transfer in the nanocrystalline films increase the energy loss in the DSSC. In an effort to eliminate this issue, one dimensional (1D) nanostructures (see Figure 2-3e) such as nanotubes,[66, 67] nanowires,[68] nanorods,[69, 70] and nanofibers[71] have been proposed. The use of single crystal anatase $TiO_2$ nanowires resulted in a photo conversion efficiency (PCE) of ~9.3%.[68] While 1D materials lead to much more rapid transport of the electrons to the circuit, they suffer from low surface area to volume ratio due to their relatively large diameter[66] (~100 nm) and/or free space between them.[37, 52]

In order to address the low surface area to volume ratio and free space of 1D nanomaterials photoelectrode, a composite of 1D nanomaterials and nanoparticles

such as that illustrated in Figure 2-3f have been proposed.[72, 73] These composites not only ensure rapid electron transport and efficient use of space, they also enhance light scattering.[37, 48] However, the PV performance (3.1%) obtained by this strategy was not as high as expected.[74] This lower performance was, once again, attributed to the large number of grain boundaries between the 1D nanostructures and the spherical nanoparticles, leading to high electron recombination.[52]

In an effort to gain the advantages of 1D nanomaterials while avoiding the issues of poor volume utilization and excessive grain boundaries, Qu et al.[75] have developed the hierarchical structure shown in Figure 2-3g. This structure fabricated using 1D hierarchical $TiO_2$ yielded a PCE of 4.46%, far higher than that obtained from the 1D-only structure in Figure 2-3f.[75] Although 1D hierarchical $TiO_2$ may fulfil many of the requirements of the ideal photoelectrode, the performance of the corresponding DSSC is still not high enough. Moreover, the synthesis of such structured $TiO_2$ materials for the photoelectrodes uses complicated processes but still does not yield high performing devices. Very recently, due to their excellent conductivity, high electron mobility, low cost, good stability and abundance, carbonaceous materials have been considered good candidates for the photoelectrode of DSSCs. The detailed discussion of DSSCs fabricated with semiconducting composites based on the carbonaceous materials is presented in the following.

## 2.2.2. Carbonaceous photoelectrodes

### *2.2.2.1. Carbon particles*

A wide range of carbon nanomaterials have been applied in DSSCs.[76-83] Among them, carbon black is one of the most commonly used materials for the counter electrode in DSSCs owing to its good electrical conductivity, catalytic activity, low cost and availability.[76, 81] Although carbon blacks have been widely used in counter electrodes, they have been rarely used in DSSC photoelectrode.

Ting and Chao were the first to use carbon black in photoelectrodes.[84] They used 22 nm diameter carbon particles as a bridge between nanocrystalline $TiO_2$ and dye molecules in the photoelectrode of DSSCs (Figure 2-4a). The open-circuit voltage ($V_{oc}$) of the cell improved after incorporating carbon black into $TiO_2$ films. The authors hypothesized that this improvement is due to the increased energy level of

$TiO_2$ conduction band by adding carbon black (Figure 2-4b). It is well known that the $V_{oc}$ in PV cells is mainly determined by the energy difference between the conductive band of semiconducting material and the potential energy of redox couple in the electrolyte (see Figure 2-1).[13] However, the DSSC efficiency declined sharply when a high concentration of the carbon black was used. The authors suggested that this decrease in performance was due to the high loading of carbon particles in the photoelectrode films which interrupted the contact among $TiO_2$, dye and electrolyte. In addition to this explanation, too much carbon black could decrease the light absorption of the window electrode and thereby limit the photoexcitation process. Indeed, the PCE (max. 0.17%) obtained in this study was relatively low compared to the typical DSSCs because of the major replacement of each component.[84]

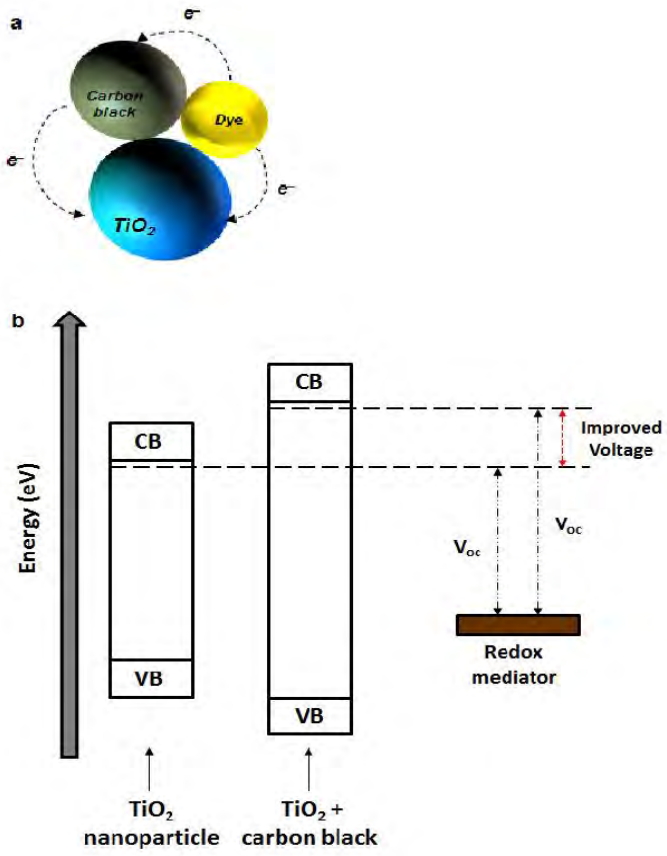


**Figure 2-4**. (a) Schema of the $TiO_2$ particle, carbon black and dye (triangular structure) and (b) a possible mechanism for the $V_{oc}$ improvement of $TiO_2$ by adding carbon black. Figures are drawn based on the discussion of ref. 84.

In order to effectively utilize the carbon particles in the photoelectrode of DSSCs, several researchers have used thermal treatment processes on the carbon powder incorporated $TiO_2$ film.[85-87] By using this method, these authors prepared highly porous structured films with improved surface area for high dye loading and light scattering ability. In Kang et al.,[85] after applying thermal treatment on carbon/$TiO_2$ electrode, a considerable improvement (max. ~31%) in the surface area of the film was observed as compared to a $TiO_2$ only film. Because of this improved surface area, they achieved a high energy conversion efficiency of 5.65% using DSSCs fabricated with 1 wt% (optimized content) carbon particles added to the $TiO_2$ film. This optimum concentration of the carbon powder in $TiO_2$ film was further confirmed by Kim et al.[86] who also prepared nanoporous carbon/$TiO_2$ films using a hydrothermal method for use as the photoelectrode in DSSCs. The efficiency of their carbon/$TiO_2$ photoelectrode based DSSC was about 3.4% which was higher than that (2.5%) of the reference device.

Yang et al.[87] synthesized spherical carbon particles with three different sizes (diameters of 250 nm, 500 nm and 700 nm) using a hydrothermal method and incorporated them into nanocrystalline $TiO_2$ films. After sintering the films at high temperature, the carbon spheres were burned out and thus holes were formed corresponding to the size of initial carbon spheres. The authors studied the influence of hole sizes made in the films on the light absorption characteristics for DSSC performance. The sequence of the light scattering ability of these films was C500 > C700 > C250 > C0. Due to the higher light scattering ability of the C500 film, a 26.5% improvement in the $J_{sc}$ (when compared to a $TiO_2$ nanocrystalline only film based device) was achieved using photoelectrodes based on the 500 nm carbon spheres. A poor $J_{sc}$ obtained by DSSCs with the large holes (700 nm) was due to the decreased amount of dye in the film. Indeed, by balancing the light absorption and dye adsorption ability of the film, the highest efficiency was 7.2% achieved by the cell fabricated with 500 nm carbon particles, while the standard cell reaches 5.6% efficiency.

Carbon fibres (CFs) are cylindrical structures with graphene layers arranged as stacked cones, cups, ribbons or plates. In the past few years, CFs have been used in the photoelectrode of DSSCs due to their good conductivity, low weight and high stability.[88, 89] Moreover, the cylindrical shape of CFs is also expected to promote

electron transport within the film.[90] Recently, Guo et al.[89] synthesized rectangular bunched $TiO_2$ nanorod (NR) arrays using a hydrothermal approach. This structure was vertically aligned on the CFs to build the photoelectrode of DSSCs. The preparation route of NRs on the CFs is shown in Figure 2-5a. This synthesis method of the CFs with $TiO_2$ NRs is called a "dissolve and grow" process. In the resulting structure (Figure 2-5b), the rectangular bunched $TiO_2$ NRs (as termed by the authors) were designed to simultaneously address the poor dye loading of a 1D structure and the light capturing ability of $TiO_2$ nanocrystalline film. Therefore, the bunched NRs/CFs structured photoelectrode exhibited an improved surface area, which enabled more dye molecules to be adsorbed. With the 3D structured photoelectrode made using the carbon fibres (Figure 2-5c), the conversion efficiency of DSSC reached 1.28%, which was ~68% higher than that of the NRs–only (see Figure 2-5d).

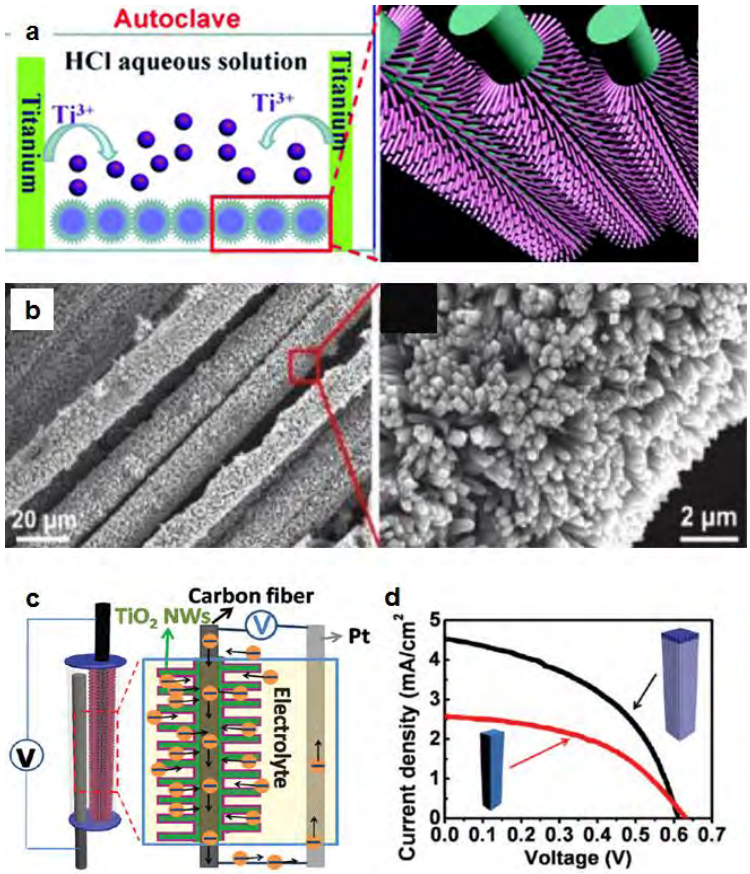


**Figure 2-5**. (a) A schematic illustration of the growth of rectangular bunched $TiO_2$ NRs on CFs, (b) SEM of 3D structure formed with $TiO_2$ NRs@CFs, (c) DSSC fabricated with 3D structured photoelectrode and (d) current density–voltage (J–V)

curves of DSSCs fabricated with the $TiO_2$ NRs and $TiO_2$ NRs@CFs.[89] Reproduced with permission from ref. 89 © 2012, American Chemical Society.

Application of carbon structures in $TiO_2$ nanocrystalline based films is a good strategy that can suppress the charge recombination using a highly conductive carbon layer. A graphitic thin film embedded (referred as carbonized) with semiconducting oxide particles was prepared for use as the photoelectrode of a DSSC.[91] In Jang et al.,[91] three different (carbon layer under, on or both under and on the film) carbonized nanocrystalline $TiO_2$ films were fabricated. By introducing graphitic carbons into the $TiO_2$, the amount of dye loading was decreased slightly due to the reduced surface area of the film. Although the adsorption of dye molecules was reduced, the embedded carbons in the $TiO_2$ film improved the electron recombination lifetimes ($\tau_r$) of DSSCs significantly because of their high conductivity. Due to this improved property of the cells, carbonized $TiO_2$ films based DSSCs achieved very high current densities (Table 2-1). It was noted by these authors that the surface area of the films in such structured device plays a minor role for the PV performance.[91] Finally, a 40.6% improvement (as compared to the reference cell) in the PV efficiency was obtained by DSSC fabricated with both parts (under and on top) carbonized $TiO_2$ thin layers.

**Table 2-1**. PV and electrochemical characteristics of four different DSSCs fabricated in the literature (Data points are collected from ref. 91).

| Photoelectrode | Dye amount, (mmol $cm^{-2}$) | $R_{ct}$ (Ω) | $\tau_r$ (ms) | $J_{sc}$ (mA $cm^{-2}$) | PCE (%) |
|---|---|---|---|---|---|
| $TiO_2$–only film | $7.19 \times 10^{-5}$ | 74.47 | 5.1 | 6.58 | 3.21 |
| Lower part carbonized film | $6.09 \times 10^{-5}$ | 64.02 | 22.1 | 6.94 | 3.71 |
| Upper part carbonized film | $5.78 \times 10^{-5}$ | 52.10 | 25.3 | 8.96 | 4.91 |
| Both parts carbonized film | $5.47 \times 10^{-5}$ | 51.84 | 29.6 | 9.35 | 5.21 |

Carbon particles can be prepared from sucrose, glucose and starch which are generated by the polymerization and aromatization of carbohydrate molecules. The carbohydrates are mostly converted into carbons using a hydrothermal method under certain conditions.[92, 93] Preparing carbons from the carbohydrates has many advantages including a lack of toxicity, a facile synthesis process, use of relatively low temperature coupled with economic viability. Due to these advantages, Jang and co-workers used a glucose–based carbon incorporated $TiO_2$ photoelectrode film (see Figure 2-6) for DSSC.[94] The $J_{sc}$ and PCE of the DSSCs containing glucose/$TiO_2$ photoelectrode were increased by 20.9% and 11.6%, respectively, as compared to those of the conventional DSSC. The improved performance by adding glucose–based carbon was proven to be due to the improved charge transport within the photoelectrode. However, the cell efficiency was significantly decreased when a high concentration of carbons were used because the presence of large amount of carbons acted as a competitor of dye molecules in light harvesting.

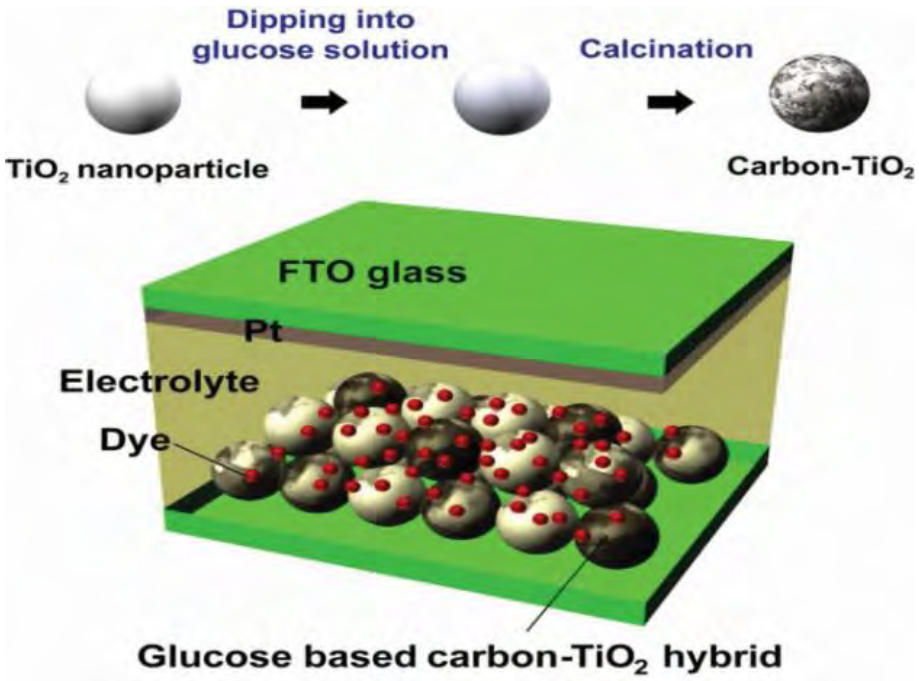


**Figure 2-6**. Configuration of DSSC fabricated with glucose–based carbon/$TiO_2$ film.[94] Reproduced with permission from ref. 94 © 2013, Wiley-VCH.

#### *2.2.2.2. Carbon nanotubes (CNTs)*

As shown by red dash arrows in Figure 2-1, charge recombination and/or back electron transfer are the most pressing problems to be solved to give an improvement in DSSC efficiency. There are mainly two possible recombination routes in DSSCs: the direct recombination of electrons from the conduction band of semiconducting $TiO_2$ to the oxidized dyes or to the electrolyte. The frequency of the electron recombination to the dye molecule is in the order of a micro to millisecond, whereas that to the electrolyte is in the range of a millisecond to second. Both these recombinations take place at the $TiO_2$/dye and $TiO_2$/electrolyte interface. It has been established that these recombinations can be suppressed by using 1D nanostructures based photoelectrodes. In this regard, as a first member of 1D structures, CNTs are very promising candidates for the DSSC photoelectrodes due to several of their extraordinary properties. Notably, CNTs not only benefit from the 1D structure that provides fast electron transport pathway, their highly conductive character also plays a critical role in DSSCs.

Because of their high charge mobility and/or excellent electrical conductivity that can decrease the charge transfer resistance ($R_{ct}$) of films, CNTs were expected to improve the performance of DSSCs. In 2004, Jang et al.[95] were the first to report using CNTs in the photoelectrode of DSSCs and they achieved a 25% increase in the $J_{sc}$ compared to the CNTs–free cell. Since this significant improvement in the DSSC performance was demonstrated by these authors using CNTs, considerable attention has been paid to the research on this topic.[96-109] For instance, Lin et al.[99] prepared bilayer structured photoelectrode films composed of multi-walled carbon nanotubes (MWCNTs)–$TiO_2$/$TiO_2$ which when used in DSSCs exhibited two times higher PV efficiency than the cell fabricated with the bare $TiO_2$ film. This improvement in the PV performance has been demonstrated to be related to the 1D CNT which supports transfer of the photo-generated charges quickly, thus suppressing charge recombination. Figure 2-7a depicts the complete attachment of $TiO_2$ to the CNT surface. The injected electrons from the excited dye molecules into the conduction band of $TiO_2$ can be transferred quickly through the CNTs conduit, as expressed in Figure 2-7b. Furthermore, Chen et al.[100] confirmed that the electrical conductivity of the bare $TiO_2$ films can be significantly improved by incorporating the CNTs structure into $TiO_2$ nanocrystalline films. Although the conductivity of the films can

be improved by incorporating higher CNTs content, the opaqueness and light absorbing properties of CNTs with high concentration ultimately decreases the incident photon-to-conversion efficiency (IPCE) of the film electrodes. Therefore, it is very important to pursue the right content of CNTs structures in $TiO_2$ films that can optimize the conductivity and light harvesting efficiency of the electrode.

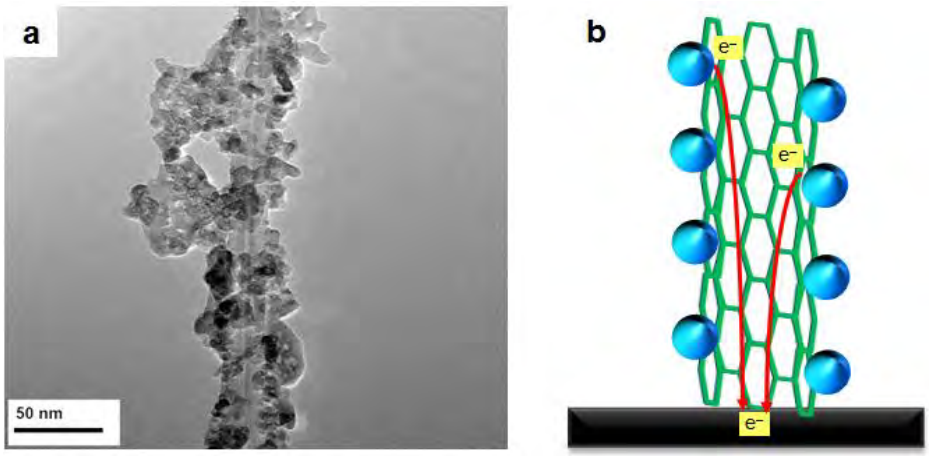


**Figure 2-7**. (a) TEM image of MWCNTs-$TiO_2$ composite,[99] Reproduced with permission from ref. 99 © 2011, Elsevier; and (b) schematic diagram for electron transfer in the CNTs-$TiO_2$ film.

In order to obtain a balance between the $R_{ct}$ and IPCE, several efforts have been undertaken with different concentrations of CNTs structures.[97, 100-104] In these studies, the optimized concentrations of CNTs in $TiO_2$ films were relatively different because the corresponding DSSCs were fabricated under different experimental conditions. A general method to prepare CNTs/$TiO_2$ photoelectrodes is as follows: CNTs are first chemically treated using acid solutions ($HNO_3$ or $H_2SO_4$) to generate functional groups such as hydroxyl (–OH), carbonyl (C=O) and carboxyl (–COOH) groups. Then, the functionalized CNTs are mixed with nanocrystalline $TiO_2$ nanoparticles, followed by a drying process under a certain temperature to prepare CNTs/$TiO_2$ pastes. Finally, the obtained paste can be either deposited on transparent conducting oxide substrates via doctor blade technique or screen printing technique. By applying this method, Yu et al.[101] prepared CNTs/$TiO_2$ based photoelectrodes with various concentrations of CNTs (0–1.0 wt%) and compared the efficiencies of the devices. As a result, a maximum conversion efficiency of 4.5% was obtained for

a DSSC with a photoelectrode with 0.2 wt% CNTs incorporated into the $TiO_2$ film. Furthermore, a similar observation has been made by Chen et al.[100] who prepared MWCNTs/$TiO_2$ composite films with CNTs concentrations of 0, 0.021, 0.043, 0.086, 0.172, 0.258, and 0.343 wt%. The DSSC made using a 0.172 wt% CNTs/$TiO_2$ based photoelectrode gave the highest efficiency of ~5.2%. On the other hand, some studies showed that to obtain the best DSSC performance the concentration of CNTs in $TiO_2$ film should be around 0.01–0.03 wt%.[102-104] These different optimized contents in these case studies are mainly due to the fact that those CNTs were not functionalized using chemical acids prior to incorporating into $TiO_2$ films. By comparing these results reported in the literatures,[97, 100-104] it can be concluded that the optimal content of the functionalized CNTs in $TiO_2$ films varies from 0.1 to 0.3 wt% depending on the acid–functionalization level.

The performance of DSSCs containing CNTs materials strongly depends on the dispersion of CNTs in a base fluid.[105, 106] It has been established that pristine CNTs are difficult to disperse in base fluids (distilled water, anhydrous ethanol, etc.), which could be due to a large aspect ratio and lack of hydrophilic groups.[110] Therefore, enhanced spatial distribution and improved dispersibility of CNTs in the solvents are the key requirements to obtain the excellent properties of CNTs. Recently, Zhang et al.[106] introduced DNA as a biological scaffold on semiconducting single–walled carbon nanotubes (s–SWCNTs) network in order to upgrade the dispersibility of CNT solution. The upgraded s–SWCNTs dispersion was then utilized to integrate the s–SWCNTs/$TiO_2$ composite for the use in photoelectrode films. In addition, they also added plasmonic metallic silver nanoparticles (AgNPs) into the s–SWCNTs/$TiO_2$ film to further improve the performance of DSSCs. The synthesis process of the s–SWCNTs/$TiO_2$/AgNPs nanocomposite is illustrated in Figure 2-8a-e. In this work,[106] the energy conversion efficiency of the DSSC increased from 4.37% to 5.32% after adding 0.15 wt% s–SWCNTs compared to the $TiO_2$–only photoelectrode system. Furthermore, the DSSC fabricated with s–SWCNTs/$TiO_2$/AgNPs photoelectrode exhibited the highest efficiency of 5.99% due to the improved electron collection and transportation by s–SWCNTs, and the enhanced light-harvesting efficiency by plasmonic AgNPs (see Figure 2-8f and g).

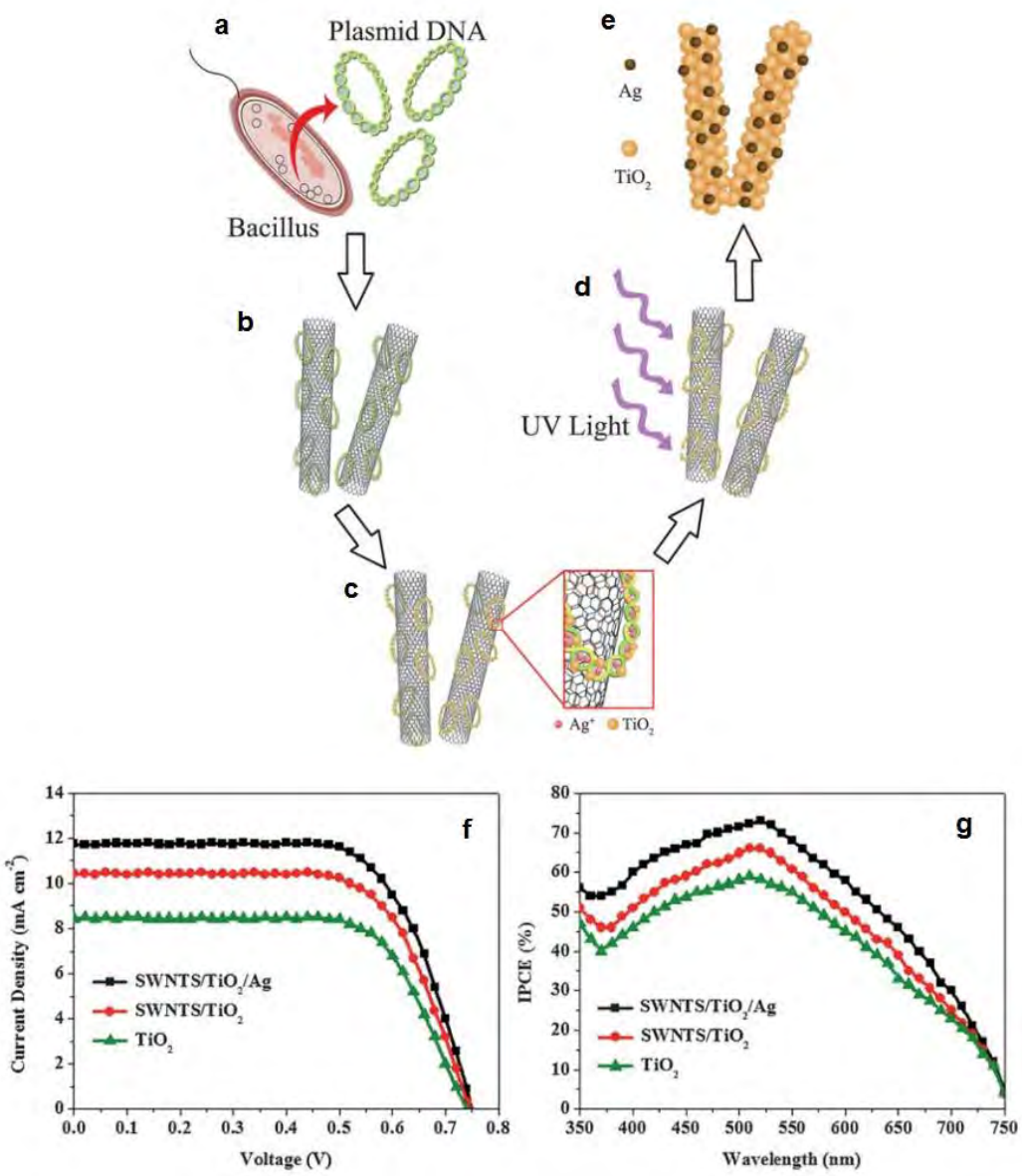


**Figure 2-8**. (a–e) Schematic illustration of the synthesis process of s-SWCNTs/$TiO_2$/Ag nanocomposite for the DSSC photoelectrode, (f) J–V curves and (g) IPCE spectra of DSSCs fabricated with $TiO_2$-only, s-SWCNTs/$TiO_2$ and s-SWCNTs/$TiO_2$/Ag photoelectrodes.[106] Reproduced with permission from ref. 106 © 2013, Royal Society of Chemistry.

Several researchers have used CNT materials in $TiO_2$ photoelectrode films to boost the PV efficiency of DSSCs.[96-109] It can be clearly seen from Figure 2-9 that the recorded efficiencies of CNTs/$TiO_2$ photoelectrodes based DSSCs vary from 4.1% to 10.6% depending on the experimental conditions and applied techniques. So far, the best efficiency of CNTs/$TiO_2$ photoelectrode based DSSC has been achieved by

Dang et al.[107] who introduced multiple genes of a virus into s–SWCNTs based aqueous solution. The prepared pastes composed of virus/s–SWCNTs/$TiO_2$ were deposited onto FTO glass substrates using a doctor blade technique. As a result, the observed $J_{sc}$, $V_{oc}$ and FF for DSSC fabricated with 0.1 wt% s–SWCNTs/$TiO_2$ composite film were 20.3 mA $cm^{-2}$, 0.78 V and 0.7, respectively, and yielded a very high energy conversion efficiency of 10.6%. Interestingly, these authors observed a 27% improvement in the $J_{sc}$ when s–SWCNTs were used; whereas the $J_{sc}$ was decreased by ~20% after adding a pure metallic SWCNTs (m–SWCNTs), as compared to only $TiO_2$ based DSSC.

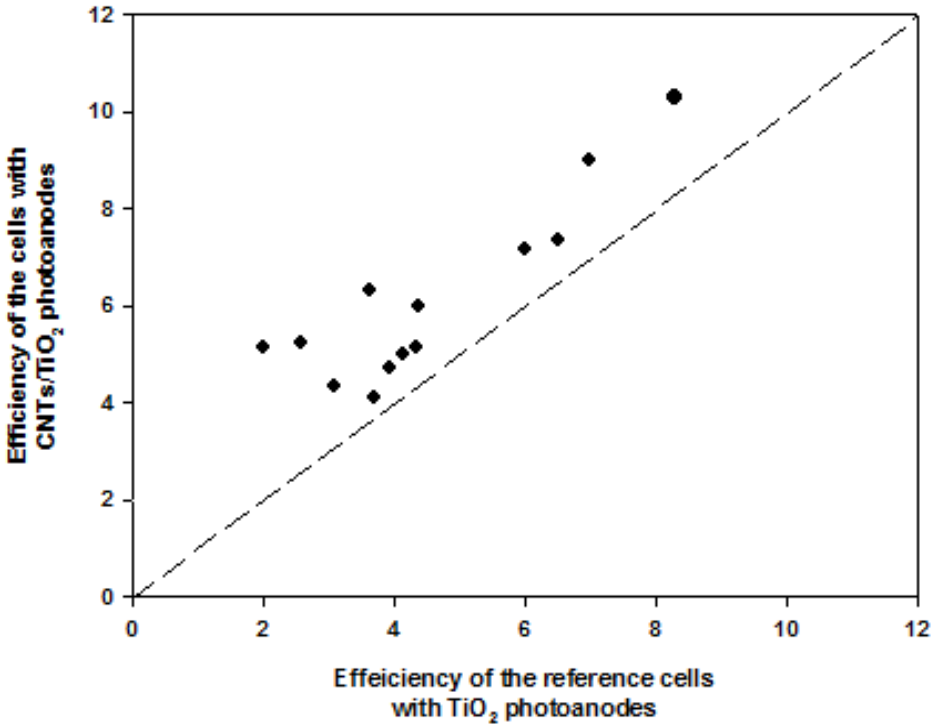


**Figure 2-9**. PV efficiencies of DSSCs fabricated with and without CNTs in the $TiO_2$ films. (Data are obtained from obtained from ref. 97-109).

Guai et al.[108] later showed a similar finding to that of Dang et al.,[107] namely that the s–SWCNTs suppress the charge recombination in DSSCs and thereby enhance the overall efficiency. The improved performance of DSSC was because of the increased electron diffusion length by s–SWCNTs, leading to higher electron collections. Notably, the s–SWCNTs possess a non-continuous band structure, while

the m–SWCNTs have zero band gap.[107] So, in the 3D networks of s–SWCNTs/$TiO_2$, the electrons, transferred from the conduction band of $TiO_2$, can be transported to the conducting oxide film without charge recombination because the higher energy barrier of s-SWCNTs compared to m-SWCNTs and this blocked the back flow of dye-injected electrons to the electrolyte (see Figure 2-10a). For the case of the m–SWCNTs, although they can transport the photoelectrons more rapidly due to higher mobility than s-SWCNTs, the charge transport was disrupted with an increased back electron transfer to the electrolyte (Figure 2-10b).

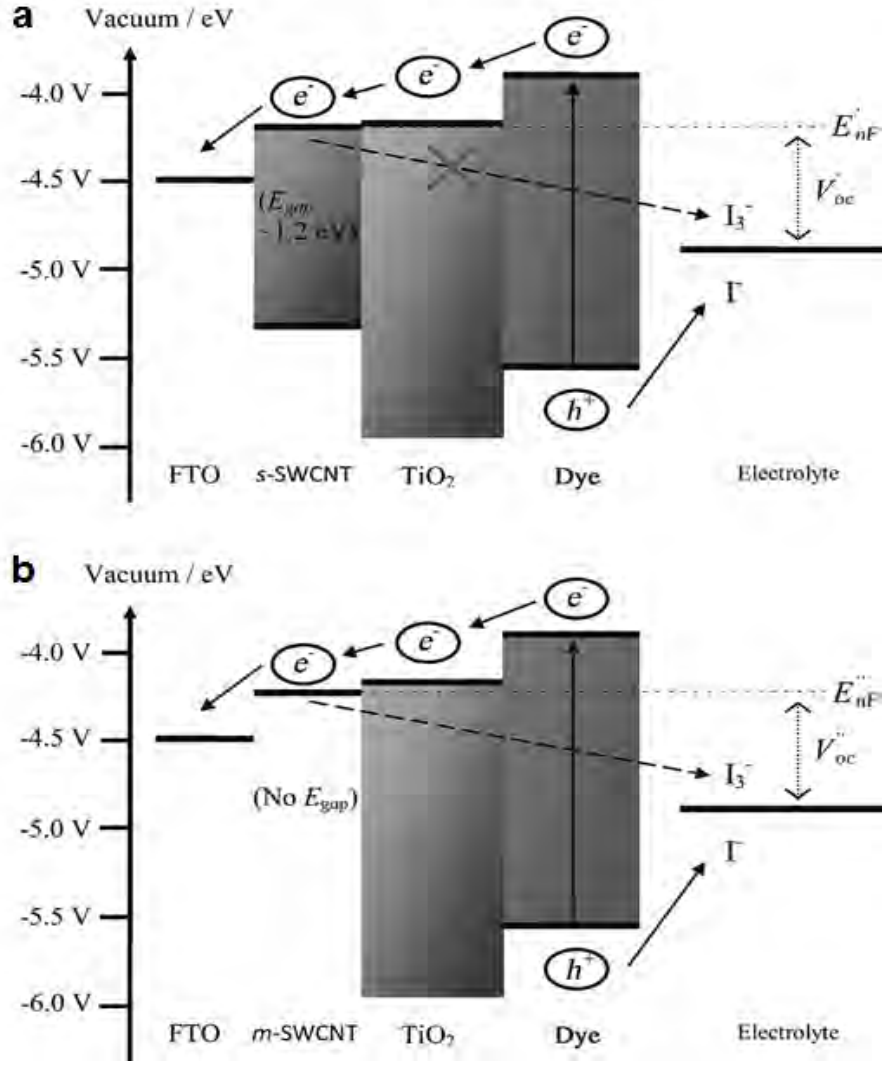


**Figure 2-10**. A schematic representation of the energy diagram of DSSCs with (a) s–SWCNTs and (b) m–SWCNTs added $TiO_2$ films.[108] Reproduced with permission from ref. 108 © 2012, Wiley-VCH.

SWCNTs can be metallic or semiconducting with band–gaps ranging from 0 to 2.0 eV depending on their diameter, level of defects or functionalization, and degree of aggregation.[111] Based on this concept, it should be possible to improve the efficiency of DSSCs by optimizing the band gap energy of s–SWCNTs. Therefore, systematically exploring the influence of different band–gap energies of s–SWCNTs on the performance of DSSCs would be of great value.

#### *2.2.2.3. Graphene*

Graphene[112] – a single layer of carbon atoms arranged in a hexagonal lattice – is a material that possesses remarkable properties including excellent conductivity, superior strength to any material ever isolated, good flexibility, high transparency and chemical resistivity.[113-117] The 2010 Nobel Prize in physics was awarded to Andre Geim and Konstantin Novoselov for their discovery of the unique properties of graphene.[112] Since then, graphene has become known the world-over as an advanced material and is quickly moving from research laboratories to industrial applications.[118] The exceptional properties of this material have pioneered recent explorations to apply graphene structures in the photoelectrode of DSSCs.[119-131] It can be clearly seen from Table 2-2 that the improved efficiencies of DSSCs with graphene materials incorporated $TiO_2$ photoelectrode films vary from 1.68% to 8.13%. These differences in the cell performances are possibly due to the utilization of different experimental conditions such as the active area of the cells, type of dyes, film preparation methods and various treatments (see Table 2-2).

Moreover, as listed in Table 2-2, the efficiencies recorded for the conventional DSSCs also vary considerably ranging from 0.32% to 5.8%, despite all the cells being made very similarly ($TiO_2$ photoelectrode film, Ruthenium based organic dye, iodolyte electrolyte and Pt counter electrode). Because of these varying performances, it is difficult to compare the improvements that have been achieved by the use of graphene structures. To better understand the real enhancement of DSSCs performance obtained by applying carbonaceous materials based films, the efficiency enhancements are calculated and plotted in Figure 2-11.

**Table 2-2**. PV characteristics of different DSSCs fabricated under various conditions. Graphene, modified Hummers method[132] and hydrazine are abbreviated as "G", "MH method" and "hyd", respectively. The abbreviation of "↑↑" and "↓" in the dye adsorption column represents the amount of adsorbed dye in the rGO/$TiO_2$ film "increased" and "decreased", respectively, as compared to $TiO_2$–only film.

| Photoelectrode film | $J_{sc}$, $mA*cm^{-2}$ | PCE, % | Area, $cm^2$ | Dye type | Deposition method | Synthesis of "G" | Treatment | "G" conc | Dye (↑↑,↓) | Ref |
|---|---|---|---|---|---|---|---|---|---|---|
| rGO/$TiO_2$<br>$TiO_2$ | 16.29<br>11.26 | 6.97<br>5.01 | 0.2 | N3 | doctor blade | MH method – hyd & thermal reduction | poly vinyl–alcohol | 0.6 wt% | – | 121 |
| rGO/$TiO_2$<br>$TiO_2$ | 6.67<br>1.95 | 1.68<br>0.32 | 0.5 | N719 | electro-phoretic | MH method – hyd reduction | molecular grafting | – | ↑↑ | 122 |
| G/G/$TiO_2$<br>$TiO_2$ | 19.47<br>15.2 | 8.13<br>5.8 | 0.25 | N719 | doctor blade | MH method – hyd & thermal reduction | 'G'+$TiCl_4$ coated FTO | – | ↓ | 123 |
| rGO/$TiO_2$<br>P25 $TiO_2$ | 13.5<br>6.2 | 7.25<br>2.85 | 0.2 | N719 | doctor blade | MH method – solvothermal reduction | ultrathin $TiO_2$ NRs | – | ↑↑ | 124 |
| rGO/$TiO_2$<br>P25 $TiO_2$ | 14.8<br>11.9 | 6.49<br>4.96 | 0.15 | Indoline | doctor blade | MH method – hyd & hydro-thermal reduction | multilayer film | – | ↑↑ | 125 |
| rGO/$TiO_2$<br>$TiO_2$ | 13.93<br>10.99 | 7.1<br>5.3 | – | N719 | doctor blade | MH method – high thermal reduction | *in situ* reduction-hydrolysis | – | ↓ | 126 |
| rGO/$TiO_2$<br>$TiO_2$ | 7.6<br>4.96 | 2.78<br>1.79 | 0.5 | N719 | doctor blade | MH method – thermal reduction | – | 0.83 wt% | ↓ | 127 |
| rGO/$TiO_2$<br>$TiO_2$ | 16.8<br>13.7 | 5.77<br>4.61 | 0.4 | N719 | doctor blade | – | pre-treated $TiO_2$ | 0.75 wt% | – | 128 |
| rGO/$TiO_2$<br>$TiO_2$ | 12.16<br>10.75 | 5.5<br>4.2 | 0.5 | N719 | screen print | MH method – solvothermal reduction | GO in ethylene glycol | 0.75 wt% | – | 129 |
| G/$TiO_2$<br>$TiO_2$ | 19.92<br>18.83 | 6.86<br>5.98 | – | N719 | spin coating | – | Addition surfactant | 1.0 wt% | ↑↑ | 130 |
| rGO/$TiO_2$<br>$TiO_2$ | 18.2<br>16.4 | 6.06<br>5.09 | 0.16 | D9 | doctor blade & spray coat | MH method – hyd & thermal reduction | rGO was coated on $TiO_2$ film | – | ↓ | 131 |

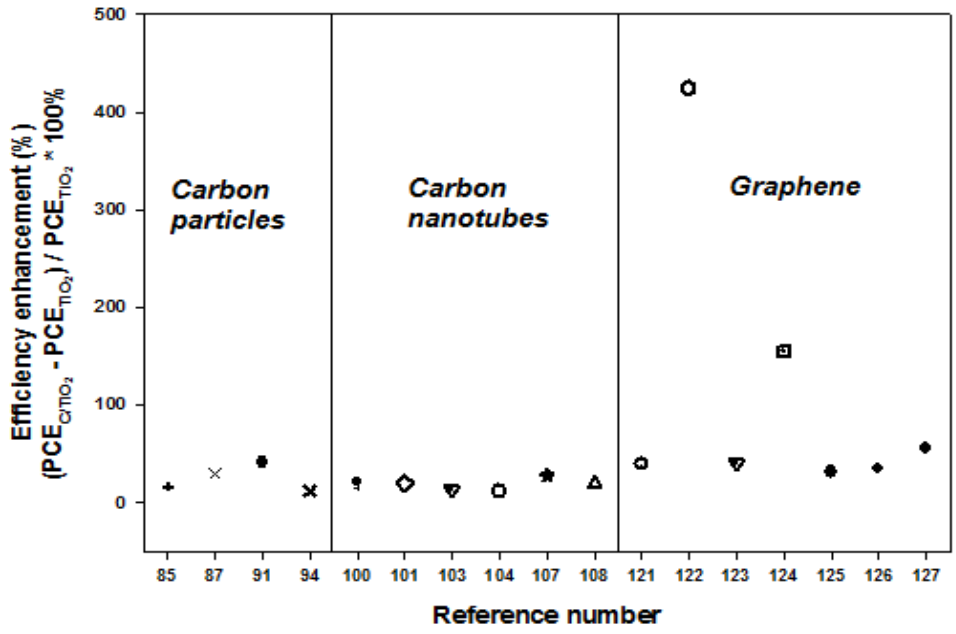


**Figure 2-11**. Efficiency enhancements of the DSSCs with carbon particles, CNTs and graphene incorporated $TiO_2$ films. (Data points are adopted from ref. 85, 87, 91, 94, 100, 101, 103, 104, 107, 108 and 121-127).

Figure 2-11 shows the efficiency enhancements (%) of various DSSCs fabricated using carbon particles, CNTs and graphene incorporated $TiO_2$ photoelectrode films. One can simply observe from Figure 2-11 that the average enhanced efficiencies obtained by graphene/$TiO_2$ photoelectrode based DSSCs are higher than those achieved by DSSCs with carbon particles and CNTs based $TiO_2$ films. There are several reasons that can be given to explain this observation that graphene improves the performance of cells more compared to other carbonaceous materials.

The reasons can be listed as follows: (i) For the case of CNTs, although they can improve the efficiency of DSSCs, their poorer interconnection with the spherical $TiO_2$ nanoparticles (as compared to the graphene) would limit the overall performance of DSSCs due to some charge transfer barrier and possibility of recombination (see Figure 2-12a). In contrast, graphene is a large single sheet that can significantly contact $TiO_2$ nanocrystallites, thus, it would significantly suppress the charge recombination (see Figure 2-12b).

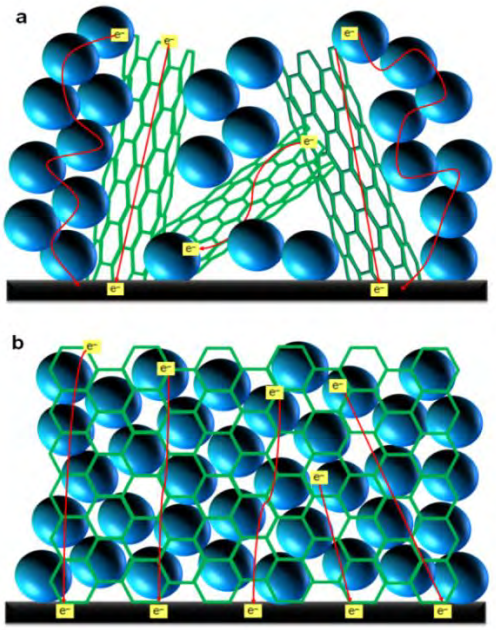


**Figure 2-12**. Schematic representation of (a) CNTs/$TiO_2$ and (b) graphene/$TiO_2$ films, demonstrating that in graphene/$TiO_2$ composite, the $TiO_2$ particles can anchor in the graphene better.

(ii) The work function of graphene (–4.42 eV)[122] lies between the conduction band of $TiO_2$ (–4.4 eV)[13] and FTO substrate (–4.7 eV)[13]. Owing to this suitable energy level, photo-generated electrons transfer stepwise from the $TiO_2$ to FTO without an energy barrier (see Figure 2-13). Here, graphene can act as a bridge between $TiO_2$ and FTO.

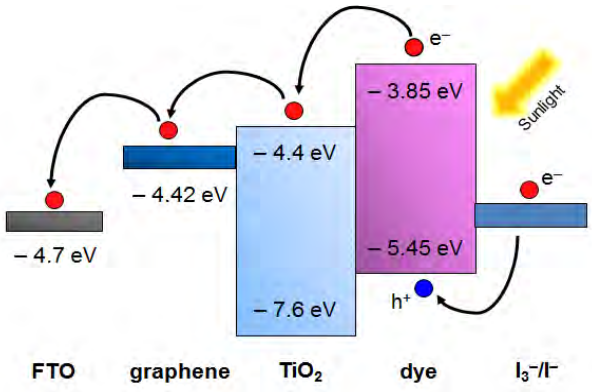


**Figure 2-13**. Schematic diagram of the energy level for graphene/$TiO_2$ film based DSSC.

(iii) The very high conductivity of graphene can accelerate the electron transport process and reduces the rate of charge recombination (see Figure 2-14). Because of these advantages, graphene materials have been believed to be perfect candidates for the photoelectrode of DSSCs.

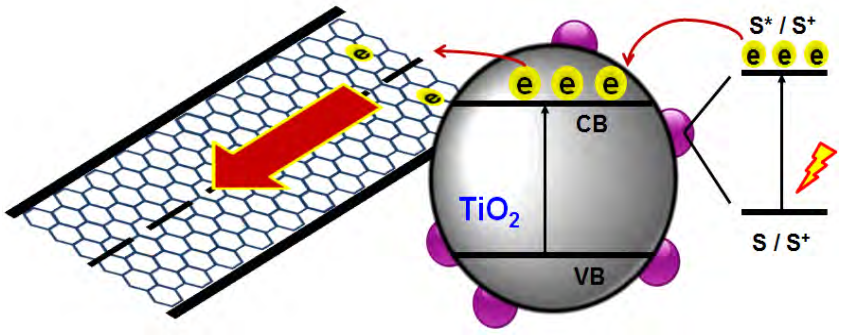


**Figure 2-14**. A mechanism for the enhanced electron transfer in graphene/$TiO_2$.

To the best of our knowledge, the first study incorporating graphene materials in a $TiO_2$ photoelectrode was reported by Kim et al.[120], who used a reduced graphene oxide/$TiO_2$ nanoparticles composite as interfacial layer between the FTO and nanocrystalline $TiO_2$ film. By applying this reduced graphene oxide/$TiO_2$ blocking layer, they obtained an energy conversion efficiency of 5.26% which was slightly higher than that (4.89%) of the reference cell. Based on this low improvement in the DSSC performance (only 7.56%), it seems that the common $TiCl_4$ treatment ($TiO_2$ blocking layer) is a more effective method than using this reduced graphene oxide/$TiO_2$ blocking layer. Although the enhancement in the DSSC efficiency achieved using graphene materials as blocking layer was relatively low in this work,[120] the idea has inspired many studies to further advance this topic.

Tang et al.[122] prepared graphene/$TiO_2$ nanocomposite based photoelectrodes for highly efficient DSSCs using a molecular grafting method on titanium (IV) butoxide and graphene sheet. Because of the presence of oxygen containing functional groups on graphene, organic titanium molecules could be grafted on the functionalized graphene sheets by chemisorption. By adjusting the reduction level of graphene oxide, a good interconnection of $TiO_2$ particles to the graphene sheets was achieved

producing a highly conductive film. As a result, when the optimized amount of graphene was incorporated into $TiO_2$ nanoparticles based film, the cell obtained five times higher efficiency than the bare $TiO_2$ based one. These authors showed that this significant improvement in the DSSC performance was due to the increased adsorption of dye molecules in the graphene/$TiO_2$ film as compared to the $TiO_2$–only film. Several other studies have showed that the presence of graphene in the nanocrystalline films improves the dye loading.[124, 125, 130] The reason for this improvement in the dye loading was explained by these authors as follows: the high surface area to volume ratio of graphene provides more anchoring sites for $TiO_2$ which enable the loading of a high amount of dye molecules. In contrast, it can be seen from Table 2-2 that in some studies,[123, 126, 127, 131] the dye loading in the $TiO_2$ nanocrystallites film decreased after adding the graphene structures. Recently, Chen et al.[126] showed that the amount of adsorbed dye in the graphene incorporated $TiO_2$ film was measured to be $7.6 \times 10^{-9}$ mol $cm^{-2}$, which was lower than that ($1.0 \times 10^{-8}$ mol $cm^{-2}$) of the film with only $TiO_2$ nanoparticles. Furthermore, some other authors also suggested that the incorporation of graphene in $TiO_2$ based film does not significantly increase the dye adsorption into the film, despite the fact that graphene with a high surface area to volume ratio was used.[123, 127, 131] Based on this argument, it can be concluded that the high surface area to volume ratio of graphene does not completely explain the mechanism of the dye adsorption characteristic. Therefore, the kinetics of dye adsorption in graphene based films is still unclear, with some studies showing contrary results. For this reason, a deeper understanding and reasonable explanation of dye adsorption onto graphene incorporated films needs to be provided based on the careful investigations. For example, it would be reasonable to explore the amount of oxygen containing functional groups on graphene surface for the adsorption of dye molecules. Graphene is mostly synthesized by a chemical oxidation (Hummers method),[132] followed by a chemical (by hydrazine) or a thermal reduction process. The chemically oxidized graphene involves various functional groups such as –OH, C=O and –COOH. On the other hand, it has been reported that the functionalized graphene (graphene oxide) is capable of hydrogen bonding and π–π stacking with other organic dye molecules.[43, 133, 134] This may mean graphene with a high number of functional groups may adsorb more dye molecules onto their surface. On the other hand, the pristine graphene has a higher electrical conductivity than the functionalized graphene. Therefore, if the functional

groups on graphene play an important role in the dye loading, further investigation will be required to determine a balance between the conductivity and the dye adsorption ability of graphene oxide by optimizing the oxidation or reduction level.

It is obvious that a high concentration of graphene significantly reduces the $R_{ct}$ of DSSCs that improves the electron transport rate, whereas this downgrades the transparency of films and thereby decreases the light harvesting efficiency of the photoelectrode. Therefore, advanced work was needed to find an optimal graphene content that benefits for both the charge recombination and light harvesting efficiency. Yang et al.[121] synthesized graphene/$TiO_2$ composites by varying the content (0–8.5 wt%) of graphene in the DSSC photoelectrodes. They found that the optimal content of reduced graphene oxide in the $TiO_2$ film is ~0.6 wt% which is the best for cell performance. Furthermore, many studies have explored the influence of graphene content on the DSSC performance.[127-129] It can be clearly seen from Table 2-2 that loading ranging from 0.6 to 0.83 wt% of reduced graphene oxide incorporated in the $TiO_2$ photoelectrode films achieved the highest efficiency in the majority of studies.

Due to the π–π interactions and/or hydrophobic surface of graphene layers, pristine graphene is insoluble in conventional solvents such as water and anhydrous ethanol, which is a major barrier to its successful utilization. Several noteworthy approaches have been developed to overcome this issue.[135, 136] Yen and co–workers improved the dispersion stability of graphene in an ethanol solution using MWCNTs as a spacer between graphene layers (see Figure 2-15a) and they used the graphene/MWCNTs materials in the DSSC photoelectrodes.[136] This 3D structured photoelectrode composed of graphene/MWCNTs/$TiO_2$ nanocomposites exhibited an efficiency of 6.11%, which was significantly higher than that (4.54%) obtained by the $TiO_2$–only cell, as shown in Figure 2-15b. The improved performance was proven to be due to the improved dispersibility of graphene and MWCNTs in ethanol solution.

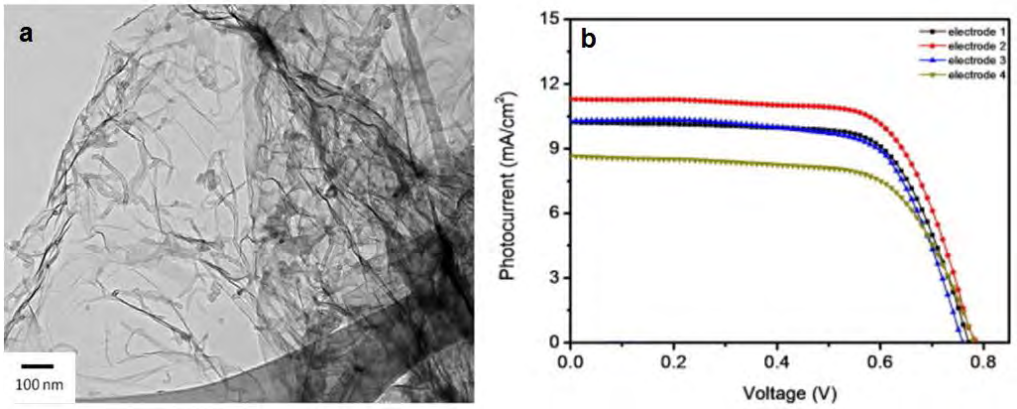


**Figure 2-15**. (a) TEM image of MWCNTs/graphene composite and (b) J–V curves of DSSCs based on acid functionalized-MWCNTs (electrode 1), MWCNTs/graphene composite (electrode 2), graphene (electrode 3) and $TiO_2$-only (electrode 4) photoelectrodes.[136] Reproduced with permission from ref. 136 © 2011, Elsevier.

## 2.3. Conclusion and Future Directions

In this review, we discussed the advanced research on the use of carbon materials in the photoelectrodes of DSSCs because the activity in this research field has been rapidly growing in the past few years. A brief overview of novel nanostructured materials based photoelectrodes is also provided. Based on the results of extensive research, it can be concluded that CNTs and graphene are very promising materials for high performance photoelectrodes for DSSCs due to their fascinating properties. Although significant achievements have been made in this cutting-edge research, several challenges must be addressed to build up high–performance devices based on CNTs and graphene. Further optimizations of carbonaceous photoelectrodes in DSSCs are still required.

It was found that vertically aligned CNTs are promising counter electrode materials to achieve highly efficient Pt–free DSSCs due to its improved electrical conductivity and electrocatalytic activity.[77, 137, 138] It is reasonable to expect improved performance of DSSCs by applying vertically grown CNTs structure with the $TiO_2$ photoelectrode films.

S–SWCNTs can significantly enhance the efficiency of DSSCs because of their non-continuous band structure, whereas the m–SWCNTs reduce the cell performance. Therefore, the band gap of s–SWCNTs can be tuned by controlling their defect or

functionalization level, diameter and aggregation degree etc. In this regard, exploring the influence of different band structures of s–SWCNTs on the cell performance will be an important research direction for further development of DSSCs. Similarly, chemically functionalizing graphene is an established method to open the band gap of graphene and is critical to the improvements in the cell characteristics. The band structure of graphene oxide or reduced graphene oxide can be tuned by the level of functionalization.[139, 140] The electronic band structure of the functionalized graphene should be considered in the future studies of graphene materials based DSSCs.

Since the dye adsorption kinetics on graphene structures based DSSCs are not fully understood, the underlying fundamental driving forces of dye interactions should be explored in depth. According to the literature,[43, 133, 134] it seems reasonable that the reactive sites (functional groups) on graphene surfaces and edges would play a major roles in dye interactions and this will need to be investigated to better understand the dye loading characteristics. If the functional groups on graphene play a critical role in the dye adsorption, further optimization of the oxidation or reduction level of graphene may be required to achieve the highest possible performance of DSSCs.

Dye lifetime is also another critical limiting factor in DSSCs.[29] The presence of carbonaceous materials with high conductivity may help extend dye lifetimes. The use of thin films of carbonaceous material would allow the selective filtering of certain regions of the spectrum which will extend dye lifetimes.[141, 142] For example, chirally sorted CNTs of particular types could be applied on the incident light side of the photoelectrode to absorb UV-light while letting visible light pass for adsorption by the dye. The lack of UV- light reaching the dye will enhance the active lifetime of the photoelectrode.

Furthermore, chirally sorting of the CNTs would allow the precise tuning of electronic energy levels in the electrode. This has the potential to improve performance but it will also provide avenues to investigate the exact role of CNTs in the hybrid photoelectrodes. The current understanding of the semiconducting photoelectrodes with carbonaceous structures in DSSCs is somewhat limited in terms of the exact roles of each component. Therefore, future investigations to elucidate the exact role of the various carbon materials (especially CNTs and graphene) in the photoelectrode of DSSCs will be of great value.

Some workers have also explored the effect of different types of nanotubes in the counter electrode of DSSCs.[143, 144] While this review highlighted the differences between SWCNTs and MWCNTs, there seem to have been little work with double-walled CNTs (DWCNTs). Interestingly, there is considerable work showing that DWCNTs can often provide enhanced conductivity while still providing very similar structural properties of SWCNTs.[143, 145, 146] The use of DWCNTs in photoelectrodes is a clear research opportunity that is still to be extensively explored.

Chemical doping has been shown to be an effective method to enhance the conductivity of CNTs and graphene.[147-149] In this regard, the use of chemically doped CNTs and graphene in the photoelectrode of DSSCs would be a valuable research direction. Additionally the use of these nanomaterials offers the exciting opportunity of nanostructuring the photoelectrode. For example, a layered structure would allow the selective, efficient harvesting of different portions of the solar spectrum as the light passed through the electrode. This affords the opportunity to make use of very high adsorbing dyes for narrow wavelength regions and this stack of high absorbers could be more efficient that the broad spectrum absorbers currently in use.

It has been shown in polymer based solar cells that beyond the electronic properties of the donor/acceptor system where functionalized CNTs are involved, the morphology also plays a key role in PV applications.[150] For instance, the addition of functionalized CNTs to a PEDOT: PSS lowered the overall performance, but did increase the current. These changes were attributed to the nano-morphology of the system. Recent work has demonstrated the key importance of the nanostructure of the active layer and indeed suggests light trapping in this layer could be a powerful approach to improve performance. The best structure is difficult to predict due to the competing influences of light trapping and charge conduction.[151]

Alignment within a CNT film has been demonstrated recently and offers the opportunity to both increase light transmission and film conductivity.[152] These films offer a smooth substrate which might also be of benefit in a layered structure where direct contact between a high loading of dye molecules and the conducting element of the electrode will be possible but the current alignment approaches using highly toxic chemicals will need to be improved before this approach can be considered a serious alternative for wide scale use.

It has been demonstrated that carbon materials exhibit excellent electrocatalytic activity for the reduction of liquid electrolyte.[22, 29, 80] However, the use of too high a concentration of the carbonaceous materials in the photoelectrode brings significant charge recombination at the interface of carbons and electrolyte by reducing tri-iodide to iodide. Therefore, the electrocatalytic activity of carbonaceous materials should be taken into account when they are used in the photoelectrode. Graphene is known not to be penetrable by gases so a film of graphene on the photoelectrode may offer an ability to control molecular diffusion while still allowing efficient charge transport. Such diffusion control might extend the lifetime of the electrolyte. This work would likely require the construction of a complex hybrid electrode perhaps using CNTs to enhance conductivity or tune electronic states while using graphene to control levels of reactivity at the critical interfaces.

We believe that the carbonaceous material will bring an important breakthrough when they are used in the photoelectrode of solid state DSSCs.

In addition, we note that review article on the application of carbon nanomaterials in perovskite solar cells is provided in the introduction of this Thesis, which links to the future chapters of this Thesis.

## Acknowledgements

The support of the Australian Research Council Discovery Program (DP130101714) is gratefully acknowledged. Munkhbayar Batmunkh acknowledges International Postgraduate Research Scholarship (IPRS) and Australian Postgraduate Award (APA) for their financial support during his study in Australia.

## References

[1] N. S. Lewis. *Science*. **2007**, 315, 798-801.
[2] L. Wang, H. Liu, R. M. Konik, J. A. Misewich, S. S. Wong. *Chem. Soc. Rev,* **2013**, 42, 8134-8156.
[3] D. M. Chapin, C. S. Fuller, G. L. Pearson. *J. Appl. Phys,* **1954**, 25, 676-677.
[4] M. Bosi, C. Pelosi. *Prog in Photovoltaics: Res and App,* **2007**, 15, 51-68.

[5] T. W. Hamann, R. A. Jensen, A. B. F. Martinson, H. Van Ryswyk, J. T. Hupp. *Energy Environ Sci,* **2008**, 1, 66-78.
[6] D. Wöhrle, D. Meissner. *Adv. Mater,* **1991**, 3, 129-138.
[7] M. A. Green. *Springer-Verlag: Berlin*. **2003**, Heidelberg.
[8] J. Zhao, A. Wang, M. A. Green. *Prog in Photovoltaics: Res and App,* **1999**, 7, 471-474.
[9] H. S. Jung, J.-K. Lee. *J. Phys. Chem. Lett*, **2013**, 4, 1682-1693.
[10] S. Mathew, A. Yella, P. Gao, R. Humphry-Baker, F. E. CurchodBasile, N. Ashari-Astani, I. Tavernelli, U. Rothlisberger, K. NazeeruddinMd, M. Grätzel. *Nat Chem,* **2014**, 6, 242-247.
[11] M. Gratzel. *Nature*, **2001**, 414, 338-344.
[12] M. Grätzel. *Inorganic Chem,* **2005**, 44, 6841-6851.
[13] A. Hagfeldt, G. Boschloo, L. Sun, L. Kloo, H. Pettersson. *Chem Rev,* **2010**, 110, 6595-6663.
[14] F. Xu, L. Sun. *Energy Environ Sci,* **2011**, 4, 818-841.
[15] J. Xu, Z. Chen, J. A. Zapien, C.-S. Lee, W. Zhang. *Adv. Mater,* **2014**, 26, 5337-5367.
[16] J. S. Bendall, L. Etgar, S. C. Tan, N. Cai, P. Wang, S. M. Zakeeruddin, M. Gratzel, M. E. Welland. *Energy Environ Sci,* **2011**, 4, 2903-2908.
[17] P. V. Kamat. *J. Phys. Chem. Lett,* **2009**, 1, 520-527.
[18] P. V. Kamat. *J. Phys. Chem. Lett,* **2011**, 2, 242-251.
[19] J. Tuček, K. C. Kemp, K. S. Kim, R. Zbořil. *ACS Nano*. **2014**, 8, 7571-7612.
[20] R. L. D. Whitby. *ACS Nano*, **2014**, 8, 9733-9754.
[21] Z. Y. Yin, J. X. Zhu, Q. Y. He, X. H. Cao, C. L. Tan, H. Y. Chen, Q. Y. Yan, H. Zhang. *Adv. Energy Mater,* **2014**, 4, 1300574.
[22] S. Yun, A. Hagfeldt, T. Ma. *Adv. Mater,* **2014**, 26, 6210-6237.
[23] C. J. Shearer, A. Cherevan, D. Eder. *Adv. Mater,* **2014**, 26, 2295-2318.
[24] L. J. Brennan, M. T. Byrne, M. Bari, Y. K. Gun'ko. *Adv. Energy Mater,* **2011**, 1, 472-485.
[25] D. Wei, J. Kivioja. *Nanoscale*, **2013**, 5, 10108-10126.
[26] S. Hwang, M. Batmunkh, M. J. Nine, H. Chung, H. Jeong. *ChemPhysChem*, **2015**, 16, 53-65.
[27] D. Golberg, Y. Bando, Y. Huang, T. Terao, M. Mitome, C. Tang, C. Zhi. *ACS Nano*, **2010**, 4, 2979-2993.
[28] R. D. Costa, F. Lodermeyer, R. Casillas, D. M. Guldi. *Energy Environ Sci,* **2014**, 7, 1281-1296.
[29] J. D. Roy-Mayhew, I. A. Aksay. *Chem Rev,* **2014**, 114, 6323-6348.
[30] L. Kavan, J.-H. Yum, M. Graetzel. *Phys Stat Solid b,* **2013**, 250, 2643-2648.
[31] H. J. Danzmann, K. Hauffe, B. Bunsen. *Phys. Chem. Chem. Phys,* **1975**, 79, 438-453.
[32] S. Anderson, E. C. Constable, M. P. Dare-Edwards, J. B. Goodenough, A. Hamnett, K. R. Seddon, R. D. Wright. *Nature*, **1979**, 280, 571-573.
[33] A. Hamnett, M. P. Dare-Edwards, R. D. Wright, K. R. Seddon, J. B. Goodenough. *J. Phys. Chem,* **1979**, 83, 3280-3290.

[34] G. R. Torres, T. Lindgren, J. Lu, C.-G. Granqvist, S.-E. Lindquist. *J. Phys. Chem. B,* **2004**, 108, 5995-6003.
[35] M. Matsumura, Y. Nomura, H. Tsubomura. *Bull. Chem. Soc. Jap,* **1977**, 50, 2533-2537.
[36] B. O'Regan, M. Gratzel. *Nature*, **1991**, 353, 737-740.
[37] P. Poudel, Q. Qiao. *Nanoscale*, **2012**, 4, 2826-2838.
[38] F. Lenzmann, J. Krueger, S. Burnside, K. Brooks, M. Grätzel, D. Gal, S. Rühle, D. Cahen. *J. Phys. Chem. B,* **2001**, 105, 6347-6352.
[39] Q. Zhang, T. P. Chou, B. Russo, S. A. Jenekhe, G. Cao. *Angew. Chem. Int. Ed,* **2008**, 47, 2402-2406.
[40] S. Burnside, J.-E. Moser, K. Brooks, M. Grätzel, D. Cahen. *J. Phys. Chem. B,* **1999**, 103, 9328-9332.
[41] Q. Zhang, C. S. Dandeneau, X. Zhou, G. Cao. *Adv. Mater,* **2009**, 21, 4087-4108.
[42] Ü. Özgür, Y. I. Alivov, C. Liu, A. Teke, M. A. Reshchikov, S. Doğan, V. Avrutin, S.-J. Cho, H. Morkoç. *J. Appl. Phys,* **2005**, 98, -.
[43] A. K. Chandiran, M. Abdi-Jalebi, M. K. Nazeeruddin, M. Grätzel. *ACS Nano*, **2014**, 8, 2261-2268.
[44] Q. Zhang, K. Park, J. Xi, D. Myers, G. Cao. *Adv. Energy Mater,* **2011**, 1, 988-1001.
[45] Y. Qiu, W. Chen, S. Yang. *Angew. Chem. Int. Ed,* **2010**, 49, 3675-3679.
[46] B. Munkhbayar, M. Dorjderem, D. Sarangerel, B. Ochirkhuyag. *Nanosci. Nanotechnol. Lett,* **2013**, 5, 741-749.
[47] W.-Q. Wu, Y.-F. Xu, H.-S. Rao, C.-Y. Su, D.-B. Kuang. *Nanoscale*, **2013**, 5, 4362-4369.
[48] Q. Zhang, G. Cao. *Nano Today*, **2011**, 6, 91-109.
[49] A. Hagfeldt, M. Grätzel. *Acc. Chem. Res,* **2000**, 33, 269-277.
[50] J. Nelson, R. E. Chandler. *Coordin. Chem. Rev,* **2004**, 248, 1181-1194.
[51] J. van de Lagemaat, N. G. Park, A. J. Frank. *J. Phys. Chem. B,* **2000**, 104, 2044-2052.
[52] J. Maçaira, L. Andrade, A. Mendes. *Renew Sust Energy Rev,* **2013**, 27, 334-349.
[53] J. Ferber, J. Luther. *Sol. Energy. Mater. Sol. Cell,* **1998**, 54, 265-275.
[54] H. Yu, Y. Bai, X. Zong, F. Tang, G. Q. M. Lu, L. Wang. *Chem. Comm,* **2012**, 48, 7386-7388.
[55] S. Ito, T. N. Murakami, P. Comte, P. Liska, C. Grätzel, M. K. Nazeeruddin, M. Grätzel. *Thin Solid Films,* **2008**, 516, 4613-4619.
[56] H. A. Atwater, A. Polman. *Nat Mater*, **2010**, 9, 205-213.
[57] W. Hou, P. Pavaskar, Z. Liu, J. Theiss, M. Aykol, S. B. Cronin. *Energy Environ Sci,* **2011**, 4, 4650-4655.
[58] S. D. Standridge, G. C. Schatz, J. T. Hupp. *J. Am. Chem. Soc,* **2009**, 131, 8407-8409.
[59] J. Qi, X. Dang, P. T. Hammond, A. M. Belcher. *ACS Nano*, **2011**, 5, 7108-7116.
[60] X. Dang, J. Qi, M. T. Klug, P.-Y. Chen, D. S. Yun, N. X. Fang, P. T. Hammond, A. M. Belcher. *Nano Lett,* **2013**, 13, 637-642.
[61] H. Choi, W. T. Chen, P. V. Kamat. *ACS Nano,* **2012**, 6, 4418-4427.

[62] M. Ihara, K. Tanaka, K. Sakaki, I. Honma, K. Yamada. *J. Phys. Chem. B,* **1997**, 101, 5153-5157.
[63] C. Hägglund, M. Zäch, G. Petersson, B. Kasemo. *Appl. Phys. Lett,* **2008**, 92, 053110.
[64] F. Zhu, D. Wu, Q. Li, H. Dong, J. Li, K. Jiang, D. Xu. *RSC Adv,* **2012**, 2, 11629-11637.
[65] H. J. Koo, Y. J. Kim, Y. H. Lee, W. I. Lee, K. Kim, N. G. Park. *Adv. Mater,* **2008**, 20, 195-199.
[66] P. Roy, D. Kim, K. Lee, E. Spiecker, P. Schmuki. *Nanoscale*, **2010**, 2, 45-59.
[67] A. Vomiero, V. Galstyan, A. Braga, I. Concina, M. Brisotto, E. Bontempi, G. Sberveglieri. *Energy Environ Sci,* **2011**, 4, 3408-3413.
[68] M. Adachi, Y. Murata, J. Takao, J. Jiu, M. Sakamoto, F. Wang. *J. Am. Chem. Soc,* **2004**, 126, 14943-14949.
[69] M. Wang, J. Bai, F. Le Formal, S.-J. Moon, L. Cevey-Ha, R. Humphry-Baker, C. Grätzel, S. M. Zakeeruddin, M. Grätzel. *J. Phys. Chem. C,* **2012**, 116, 3266-3273.
[70] B. Liu, E. S. Aydil. *J. Am. Chem. Soc,* **2009**, 131, 3985-3990.
[71] W. Zhang, R. Zhu, L. Ke, X. Liu, B. Liu, S. Ramakrishna. *Small*, **2010**, 6, 2176-2182.
[72] C.-H. Ku, J.-J. Wu. *Appl. Phys. Lett,* **2007**, 91, 093117.
[73] P. Joshi, L. Zhang, D. Davoux, Z. Zhu, D. Galipeau, H. Fong, Q. Qiao. *Energy Environ Sci,* **2010**, 3, 1507-1510.
[74] P. Zhong, W. Que, J. Zhang, Q. Jia, W. Wang, Y. Liao, X. Hu. *J. Alloys. Comp,* **2011**, 509, 7808-7813.
[75] J. Qu, G. R. Li, X. P. Gao. *Energy Environ Sci,* **2010**, 3, 2003-2009.
[76] A. Kay, M. Grätzel. *Sol. Energy. Mater. Sol. Cell,* **1996**, 44, 99-117.
[77] E. Ramasamy, W. J. Lee, D. Y. Lee, J. S. Song. *Electrochem. Comm,* **2008**, 10, 1087-1089.
[78] J. D. Roy-Mayhew, D. J. Bozym, C. Punckt, I. A. Aksay. *ACS Nano*, **2010**, 4, 6203-6211.
[79] B. Munkhbayar, M. J. Nine, J. Jeoun, M. Ji, H. Jeong, H. Chung. *J. Power Sources,* **2013**, 230, 207-217.
[80] H. Wang, Y. H. Hu. *Energy Environ Sci,* **2012**, 5, 8182-8188.
[81] G. R. Li, F. Wang, J. Song, F. Y. Xiong, X. P. Gao. *Electrochem. Acta,* **2012**, 65, 216-220.
[82] B. Munkhbayar, S. Hwang, J. Kim, K. Bae, M. Ji, H. Chung, H. Jeong. *Electrochem. Acta,* **2012**, 80, 100-107.
[83] E. Bi, H. Chen, X. Yang, W. Peng, M. Gratzel, L. Han. *Energy Environ Sci,* **2014**, 7, 2637-2641.
[84] C.-C. Ting, W.-S. Chao. *Appl. Energy,* **2010**, 87, 2500-2505.
[85] S. H. Kang, J.-Y. Kim, Y.-K. Kim, Y.-E. Sung. *J. Photochem. Photobiol. A,* **2007**, 186, 234-241.
[86] D. Y. Kim, J. Kim, J. Kim, A. Y. Kim, G. Lee, M. Kang. *J. Ind. Eng. Chem,* **2012**, 18, 1-5.

[87] G. Yang, J. Zhang, P. Wang, Q. Sun, J. Zheng, Y. Zhu. *Curr. Appl. Phys,* **2011**, 11, 376-381.
[88] X. Cai, S. Hou, H. Wu, Z. Lv, Y. Fu, D. Wang, C. Zhang, H. Kafafy, Z. Chu, D. Zou. *Phys. Chem. Chem. Phys,* **2012**, 14, 125-130.
[89] W. Guo, C. Xu, X. Wang, S. Wang, C. Pan, C. Lin, Z. L. Wang. *J. Am. Chem. Soc,* **2012**, 134, 4437-4441.
[90] E. C. Landis, K. L. Klein, A. Liao, E. Pop, D. K. Hensley, A. V. Melechko, R. J. Hamers. *Chem. Mater,* **2010**, 22, 2357-2366.
[91] Y. H. Jang, X. Xin, M. Byun, Y. J. Jang, Z. Lin, D. H. Kim. *Nano Lett,* **2011**, 12, 479-485.
[92] X. Sun, Y. Li. *Angew. Chem. Int. Ed,* **2004**, 43, 597-601.
[93] L.-W. Zhang, H.-B. Fu, Y.-F. Zhu. *Adv. Funct. Mater,* **2008**, 18, 2180-2189.
[94] Y. J. Jang, Y. H. Jang, D. H. Kim. *Part. Part. Syst. Char,* **2013**, 30, 1030-1033.
[95] S.-R. Jang, R. Vittal, K.-J. Kim. *Langmuir,* **2004**, 20, 9807-9810.
[96] P. Brown, K. Takechi, P. V. Kamat. *J. Phys. Chem. C,* **2008**, 112, 4776-4782.
[97] K.-M. Lee, C.-W. Hu, H.-W. Chen, K.-C. Ho. *Sol. Energy. Mater. Sol. Cell,* **2008**, 92, 1628-1633.
[98] S. Zhang, H. Niu, Y. Lan, C. Cheng, J. Xu, X. Wang. *J. Phys. Chem. C,* **2011**, 115, 22025-22034.
[99] W.-J. Lin, C.-T. Hsu, Y.-C. Tsai. *J. Coll. Interf. Sci,* **2011**, 358, 562-566.
[100] J. Chen, B. Li, J. Zheng, J. Zhao, Z. Zhu. *J. Phys. Chem. C,* **2012**, 116, 14848-14856.
[101] J. Yu, J. Fan, B. Cheng. *J. Power Sources,* **2011**, 196, 7891-7898.
[102] K. T. Dembele, G. S. Selopal, C. Soldano, R. Nechache, J. C. Rimada, I. Concina, G. Sberveglieri, F. Rosei, A. Vomiero. *J. Phys. Chem. C,* **2013**, 117, 14510-14517.
[103] A. M. Bakhshayesh, M. R. Mohammadi, N. Masihi, M. H. Akhlaghi. *J. Nanopart. Res,* **2013**, 15, 1-10.
[104] K. T. Dembele, R. Nechache, L. Nikolova, A. Vomiero, C. Santato, S. Licoccia, F. Rosei. *J. Power Sources,* **2013**, 233, 93-97.
[105] S. Sun, L. Gao, Y. Liu. *Thin Solid Films,* **2011**, 519, 2273-2279.
[106] X. Zhang, J. Liu, S. Li, X. Tan, J. Zhang, M. Yu, M. Zhao. *J. Mater. Chem. A,* **2013**, 1, 11070-11077.
[107] X. Dang, H. Yi, M.-H. Ham, J. Qi, D. S. Yun, R. Ladewski, M. S. Strano, P. T. Hammond, A. M. Belcher. *Nat Nano,* **2011**, 6, 377-384.
[108] G. H. Guai, Y. Li, C. M. Ng, C. M. Li, M. B. Chan-Park. *ChemPhysChem,* **2012**, 13, 2566-2572.
[109] J. Y. Ahn, J. H. Kim, K. J. Moon, S. D. Park, S. H. Kim. *Nanoscale,* **2013**, 5, 6842-6850.
[110] B. Munkhbayar, M. J. Nine, J. Jeoun, M. Bat-Erdene, H. Chung, H. Jeong. *Powder Technol,* **2013**, 234, 132-140.
[111] J. W. G. Wilder, L. C. Venema, A. G. Rinzler, R. E. Smalley, C. Dekker. *Nature,* **1998**, 391, 59-62.

[112] K. S. Novoselov, A. K. Geim, S. V. Morozov, D. Jiang, Y. Zhang, S. V. Dubonos, I. V. Grigorieva, A. A. Firsov. *Science,* **2004**, 306, 666-669.
[113] K. S. Novoselov, A. K. Geim, S. V. Morozov, D. Jiang, M. I. Katsnelson, I. V. Grigorieva, S. V. Dubonos, A. A. Firsov. *Nature,* **2005**, 438, 197-200.
[114] A. K. Geim, K. S. Novoselov. *Nat Mater,* **2007**, 6, 183-191.
[115] R. R. Nair, P. Blake, A. N. Grigorenko, K. S. Novoselov, T. J. Booth, T. Stauber, N. M. R. Peres, A. K. Geim. *Science,* **2008**, 320, 1308.
[116] C. Lee, X. Wei, J. W. Kysar, J. Hone. *Science,* **2008**, 321, 385-388.
[117] X. Du, I. Skachko, A. Barker, E. Y. Andrei. *Nat Nano,* **2008**, 3, 491-495.
[118] A. Zurutuza, C. Marinelli. *Nat Nano,* **2014**, 9, 730-734.
[119] Y. H. Ng, I. V. Lightcap, K. Goodwin, M. Matsumura, P. V. Kamat. *J. Phys. Chem. Lett,* **2010**, 1, 2222-2227.
[120] S. R. Kim, M. K. Parvez, M. Chhowalla. *Chem. Phys. Lett,* **2009**, 483, 124-127.
[121] N. Yang, J. Zhai, D. Wang, Y. Chen, L. Jiang. *ACS Nano,* **2010**, 4, 887-894.
[122] Y.-B. Tang, C.-S. Lee, J. Xu, Z.-T. Liu, Z.-H. Chen, Z. He, Y.-L. Cao, G. Yuan, H. Song, L. Chen, L. Luo, H.-M. Cheng, W.-J. Zhang, I. Bello, S.-T. Lee. *ACS Nano,* **2010**, 4, 3482-3488.
[123] T. Chen, W. Hu, J. Song, G. H. Guai, C. M. Li. *Adv. Funct. Mater,* **2012**, 22, 5245-5250.
[124] Z. He, G. Guai, J. Liu, C. Guo, J. S. Chye Loo, C. M. Li, T. T. Y. Tan. *Nanoscale,* **2011**, 3, 4613-4616.
[125] B. Tang, G. Hu. *J. Power Sources,* **2012**, 220, 95-102.
[126] L. Chen, Y. Zhou, W. Tu, Z. Li, C. Bao, H. Dai, T. Yu, J. Liu, Z. Zou. *Nanoscale,* **2013**, 5, 3481-3485.
[127] H. Wang, S. L. Leonard, Y. H. Hu. *Ind. Eng. Chem. Res,* **2012**, 51, 10613-10620.
[128] J. Fan, S. Liu, J. Yu. *J. Mater. Chem,* **2012**, 22, 17027-17036.
[129] W. Shu, Y. Liu, Z. Peng, K. Chen, C. Zhang, W. Chen. *J. Alloys. Comp,* **2013**, 563, 229-233.
[130] T.-H. Tsai, S.-C. Chiou, S.-M. Chen. *Int. J. Electrochem. Sci,* **2011**, 6, 3333-3343.
[131] J. Song, Z. Yin, Z. Yang, P. Amaladass, S. Wu, J. Ye, Y. Zhao, W.-Q. Deng, H. Zhang, X.-W. Liu. *Chem. A. Euro. J,* **2011**, 17, 10832-10837.
[132] W. S. Hummers, R. E. Offeman. *J. Am. Chem. Soc,* **1958**, 80, 1339-1339.
[133] J. Xu, L. Wang, Y. Zhu. *Langmuir,* **2012**, 28, 8418-8425.
[134] T.-T. Meng, Z.-B. Zheng, K.-Z. Wang. *Langmuir,* **2013**, 29, 14314-14320.
[135] M. Myekhlai, B. Munkhbayar, T. Lee, M. R. Tanshen, H. Chung, H. Jeong. *RSC Adv,* **2014**, 4, 2431-2436.
[136] M.-Y. Yen, M.-C. Hsiao, S.-H. Liao, P.-I. Liu, H.-M. Tsai, C.-C. M. Ma, N.-W. Pu, M.-D. Ger. *Carbon,* **2011**, 49, 3597-3606.
[137] K. S. Lee, W. J. Lee, N.-G. Park, S. O. Kim, J. H. Park. *Chem. Comm,* **2011**, 47, 4264-4266.

[138] M. Wu, X. Lin, Y. Wang, L. Wang, W. Guo, D. Qi, X. Peng, A. Hagfeldt, M. Grätzel, T. Ma. *J. Am. Chem. Soc,* **2012**, 134, 3419-3428.
[139] Q. Tang, Z. Zhou, Z. Chen. *Nanoscale,* **2013**, 5, 4541-4583.
[140] J.-A. Yan, L. Xian, M. Y. Chou. *Phys. Rev. Lett,* **2009**, 103, 086802.
[141] D. D. Tune, J. G. Shapter. *Energy Environ Sci,* **2013**, 6, 2572-2577.
[142] M. A. Bissett, J. G. Shapter. *J. Phys. Chem. C,* **2010**, 114, 6778-6783.
[143] D. Zhang, X. Li, S. Chen, Z. Sun, X. Jiang Yin, S. Huang. *Microchim Acta,* **2011**, 174, 73-79.
[144] M. Xiaoguang, C. Swee Jen, F. Benhu, O. Jianyong. *Nanotechnology,* **2010**, 21, 395202.
[145] D. W. Zhang, X. D. Li, S. Chen, F. Tao, Z. Sun, X. J. Yin, S. M. Huang. *J Solid State Electrochem,* **2010**, 14, 1541-1546.
[146] K. E. Moore, B. S. Flavel, C. J. Shearer, A. V. Ellis, J. G. Shapter. *Electrochem. Comm,* **2011**, 13, 1190-1193.
[147] F. Schedin, A. K. Geim, S. V. Morozov, E. W. Hill, P. Blake, M. I. Katsnelson, K. S. Novoselov. *Nat Mater,* **2007**, 6, 652-655.
[148] R. S. Lee, H. J. Kim, J. E. Fischer, A. Thess, R. E. Smalley. *Nature,* **1997**, 388, 255-257.
[149] S. Z. Butler, S. M. Hollen, L. Cao, Y. Cui, J. A. Gupta, H. R. Gutiérrez, T. F. Heinz, S. S. Hong, J. Huang, A. F. Ismach, E. Johnston-Halperin, M. Kuno, V. V. Plashnitsa, R. D. Robinson, R. S. Ruoff, S. Salahuddin, J. Shan, L. Shi, M. G. Spencer, M. Terrones, W. Windl, J. E. Goldberger. *ACS Nano,* **2013**, 7, 2898-2926.
[150] N. Chehata, A. Ltaief, R. Bkakri, A. Bouazizi, E. Beyou. *Mater. Lett,* **2014**, 121, 227-230.
[151] B.-C. Chen, Y.-S. Cheng, C. Gau, Y.-C. Lee. *Thin Solid Films,* **2014**, 564, 384-389.
[152] D. S. Hecht, L. Hu, G. Irvin. *Adv. Mater,* **2011**, 23, 1482-1513.

# Chapter 3.

# Incorporation of Graphene into $SnO_2$ Photoanode for Dye-Sensitized Solar Cells

Munkhbayar Batmunkh,[1,2] Mahnaz Dadkhah,[2] Cameron J. Shearer,[2] Mark J. Biggs,[1,3] Joseph G. Shapter,[2]*

[1] *School of Chemical Engineering, The University of Adelaide, Adelaide, South Australia 5005, Australia*

[2] *School of Chemical and Physical Sciences, Flinders University, Bedford Park, Adelaide, South Australia 5042, Australia*

[3] *School of Sciences, Loughborough University, Loughborough, Leicestershire, LE11 3TU, UK*

* Corresponding authors:

joe.shapter@flinders.edu.au

**Published:** *Applied Surface Science,* **2016**, *387*, 690-697

The published copy of the manuscript is attached in Appendix B.

# Statement of Authorship

| | |
|---|---|
| Title of Paper | Incorporation of graphene into $SnO_2$ photoanode for dye-sensitized solar cells |
| Publication Status | ☑ Published ☐ Accepted for Publication<br>☐ Submitted for Publication ☐ Unpublished and Unsubmitted w ork w ritten in manuscript style |
| Publication Details | Munkhbayar Batmunkh, Mahnaz Dadkhah, Cameron J. Shearer, Mark J. Biggs and Joseph G. Shapter, Incorporation of graphene into $SnO_2$ photoanode for dye-sensitized solar cells, *Applied Surface Science.*, **2016**, *387*, 690-697. |

## Principal Author

| | |
|---|---|
| Name of Principal Author (Candidate) | Munkhbayar Batmunkh |
| Contribution to the Paper | Conducted the experimental works, performed analysis on all samples, interpreted data and wrote manuscript. |
| Overall percentage (%) | 75% |
| Certification: | This paper reports on original research I conducted during the period of my Higher Degree by Research candidature and is not subject to any obligations or contractual agreements with a third party that would constrain its inclusion in this thesis. I am the primary author of this paper. |
| Signature | Date 16/09/2016 |

## Co-Author Contributions

By signing the Statement of Authorship, each author certifies that:

i. the candidate's stated contribution to the publication is accurate (as detailed above);

ii. permission is granted for the candidate in include the publication in the thesis; and

iii. the sum of all co-author contributions is equal to 100% less the candidate's stated contribution.

| | |
|---|---|
| Name of Co-Author | Mahnaz Dadkhah |
| Contribution to the Paper | Prepared samples, Performed analysis on some samples, |
| Signature | Date 16/09/2016 |

| | |
|---|---|
| Name of Co-Author | Cameron J. Shearer |
| Contribution to the Paper | Interpreted some data, and Edited the manuscript |
| Signature | Date 16/9/2016 |

| Name of Co-Author | Mark J. Biggs |
|---|---|
| Contribution to the Paper | Co-advised the development of work, and manuscript evaluation. |
| Signature | Date 12/1/17 |

| Name of Co-Author | Joseph G. Shapter |
|---|---|
| Contribution to the Paper | Supervised development of work, Edited the manuscript, and Corresponding author. |
| Signature | Date 4/1/18 |

## Abstract

In dye-sensitized solar cell (DSSC) photoanodes, tin dioxide ($SnO_2$) structures are a promising alternative semiconducting oxide to the conventional titania ($TiO_2$), but they suffer from poor photovoltaic (PV) efficiency caused by insufficient dye adsorption and low energy of the conduction band. A hybrid structure consisting of $SnO_2$ and reduced graphene oxide ($SnO_2$–RGO) was synthesized *via* a microwave-assisted method and has been employed as a photoanode in DSSCs. Incorporation of RGO into the $SnO_2$ photoanode enhanced the power conversion efficiency of DSSC device by 91.5%, as compared to the device assembled without RGO. This efficiency improvement can be attributed to increased dye loading, enhanced electron transfer and addition of suitable energy levels in the photoanode. Finally, the use of RGO addresses the major shortcoming of $SnO_2$ when employed as a DSSC photoanode, namely poor dye adsorption and slow electron transfer rate.



**Keywords:** Photovoltaic, dye-sensitized solar cells, photoanodes, tin oxide, graphene


**TOC Figure**

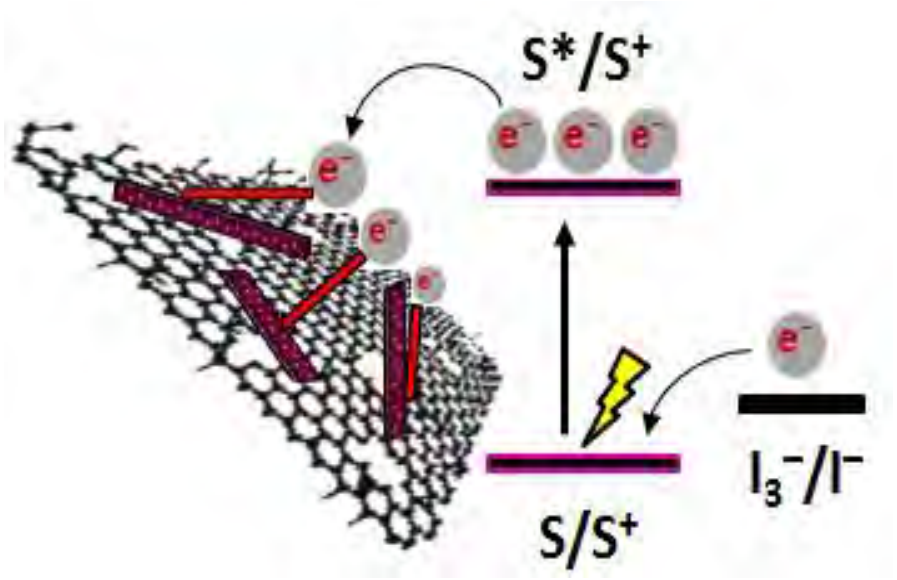

## 3.1. Introduction

One of the mature developments in new energy production approaches is the dye-sensitized solar cell (DSSC).[1] For a broad perspective of the field, there are several good reviews available.[2-4] A typical DSSC photoanode is made using a transparent conducting oxide (TCO) substrate, wide band gap oxide semiconductor and dye sensitizer. A nanocrystalline $TiO_2$ semiconductor is mostly used as the semiconductor due to its unique properties.[5] Despite the high power conversion efficiencies (PCEs) achieved by devices fabricated with $TiO_2$ photoanodes,[6-8] the intrinsic low carrier mobility of $TiO_2$ is a matter of great concern.[9, 10] This issue has led many researchers to probe the development of alternative photoanode materials.

Among many alternative semiconductors, $SnO_2$ has been the subject of numerous investigations.[11-13] This is partially due to the fact that $SnO_2$ has a higher electron mobility than $TiO_2$.[14, 15] Since the first use of $SnO_2$ in DSSCs, significant developments have been made in the $SnO_2$ photoanodes.[11, 13] These developments include morphology control, doping with various species, surface modification, and hybrid structures with other oxide semiconductors.[16-18] Despite the considerable effort to improve $SnO_2$ based photoanodes, a major challenge for $SnO_2$ based DSSCs is still their low performance caused by poor dye adsorption capability.[19] Additionally, the $SnO_2$ photoanode based DSSCs suffer from a low open circuit voltage ($V_{oc}$) value due to the intrinsically low energy of the conduction band of $SnO_2$.[20] Therefore, addressing these issues is of great importance for the development of $SnO_2$ based photovoltaic (PV) cells. Moreover, although $SnO_2$ possesses higher electron mobility than $TiO_2$, further improvement in the electron transport in $SnO_2$ photoanode would be of great value to maximize the efficiency.

Due to their excellent conductivity, carbon nanotubes (CNTs) and graphene can act to improve electron transport and reduce the charge recombination which results from sluggish charge transport of semiconducting oxide based photoanodes; thus significantly enhancing the PCE of PV cells.[21-26] Over the past few years, researchers have incorporated graphene derivatives into various $TiO_2$ structures and shown remarkable efficiency enhancement.[27-30] However, until now, there has been no report on the use of graphene structures in $SnO_2$ photoanodes for DSSCs. Moreover, the kinetics of dye adsorption and performance enhancement for

carbonaceous photoanodes is still unclear, with some studies suggesting contrary results.[21, 28, 29, 31, 32] Therefore, exploring the effect of graphene or reduced graphene oxide (RGO) in $SnO_2$ photoanode based DSSCs would be valuable.

Herein we report a facile preparation of hybrid structures based on morphologically controllable $SnO_2$ combined with RGO for use as a photoanode in DSSCs. To the best of our knowledge, this work is the first effort involving the application of a graphene structure in $SnO_2$ photoanode based DSSCs. We found that the incorporation of RGO into the $SnO_2$ film not only enhances the electron transfer rate of the photoanode, it also increases the adsorption of dye molecules into the film, thus greatly improving DSSC performance.

## 3.2. Experimental

### 3.2.1. Materials

All chemicals were purchased from Sigma-Aldrich and used without further purification, unless otherwise stated. Tin (II) chloride dihydrate ($SnCl_2 \cdot 2H_2O$) powder (>99% purity, Merck) was used as a starting material. Flourine-doped tin oxide (FTO) coated glass electrode with a sheet resistance ($R_s$) of ~12 Ω/□ (TCO30-8), Ruthenizer 535-bisTBA (N719 dye), iodide/tri-iodide electrolyte (Iodolyte Z-50), DuPont Surlyn® (Meltonix 1170-60) and Platinum catalyst (Platisol T) were obtained from Solaronix, Switzerland.

### 3.2.2. Preparation of graphene oxide

Graphite oxide was prepared from natural graphite using the approach from Marcano et al.[33] Briefly, a 9:1 (v:v) mixture of sulfuric acid (95-98% $H_2SO_4$) and phosphoric acid (85% $H_3PO_4$) (240:27 mL) was kept in the cold room (3-5$^oC$) until it was added to a mixture of graphite flakes (2 g) and potassium permanganate (99% $KMnO_4$) (12 g). The oxidation process of graphite was carried out by stirring the mixture at ~50$^oC$ for 12 h. Upon completion, the reaction was cooled down to room temperature and poured onto ice (approximately 300 mL) with 30% hydrogen peroxide ($H_2O_2$) (2 mL). The mixture was then washed with distilled (DI) water, 30% hydrochloric acid (HCl) and ethanol (x 2 times). For each sequential wash, the product was centrifuged

at 4400 rpm for 3 h and the supernatant decanted away. The light brown sample obtained was then vacuum-dried overnight at room temperature. Then the as-prepared graphite oxide was exfoliated in water (1 mg $mL^{-1}$) by bath ultrasonication (Elma, Germany) for 60 min to obtain homogenous graphene oxide (GO) dispersion.

### 3.2.3. Synthesis of $SnO_2$-RGO hybrid

The $SnO_2$-RGO hybrid was prepared using a facile microwave-assisted method.[34] In a typical process, six glass beakers containing 90 mL DI water and different amounts of GO (0 mg, 2 mg, 4.5 mg, 7 mg, 12 mg and 50 mg) were ultrasonicated for 2h. Meanwhile, 1.5 g of $SnCl_2 \cdot 2H_2O$ powder was added into 200 mL of 0.02M HCl solution. Then the previously prepared GO dispersions were added into the $SnCl_2 \cdot 2H_2O$ solutions, followed by stirring for 30 min. The as-obtained mixtures were then reacted using a microwave technique (StartSYNTH Microwave Synthesis Labstation, Milestone s.r.l) for 5 min under 600 W power. The temperature was adjusted to 90$^oC$ during the microwave treatment. After cooling to room temperature, the obtained precipitates were centrifuged at 2000 rpm for 10 min and washed several times with DI water, followed by drying overnight at 80$^oC$ in an oven to obtain $SnO_2$-RGO powders. Finally, six samples of different RGO content (0 wt%, 0.2 wt%, 0.45 wt%, 0.7 wt%, 1.2 wt% and 4.75 wt% in the hybrid) were prepared and have been used for DSSC fabrication. It should be noted that the amount of $SnO_2$ in these samples was not changed. For the calculation of the RGO concentration in the hybrid, it was assumed that the conversion of $SnCl_2 \cdot 2H_2O$ to $SnO_2$ is 100% based on the lack of Cl peak observed in various hybrid characterizations.

### 3.2.4. Device fabrication

Firstly, viscous $SnO_2$ and $SnO_2$-RGO pastes were prepared from the previously prepared six samples according to the established procedures described in the literature.[35] FTO coated glass substrates were cleaned by a detergent (Pyroneg), followed by washing with Milli-Q water, acetone and ethanol under ultrasonication for 10 min each and subsequently dried with a nitrogen gas. The cleaned FTO glass substrates were immersed in a 40 mM $TiCl_4$ aqueous solution at 70$^oC$ for 30 min. Then the $TiCl_4$ treated FTO electrodes were coated with the $SnO_2$ and $SnO_2$-RGO

pastes by a doctor blade technique to prepare the photoanodes. All photoanode films were obtained by applying two layers of adhesive scotch tape (Magic™ Tape, 3M) on the FTO electrode, which gives a film thickness of ~15 μm.[36] It is well established that a photoanode thickness of 12-16 μm is the optimum condition to achieve high DSSC performance.[36-38] After the deposition of $SnO_2$ and $SnO_2$-RGO pastes onto the FTO substrates, the photoanode films were gradually heated under an air flow at 125°C for 5 min, 325°C for 5 min, at 375°C for 15 min and at 450°C for 30 min, followed by cooling to room temperature. Then the films were again soaked in 40 mM $TiCl_4$ solution at 70°C for 30 min, followed by sintering at 450°C for 30 min. After cooling to ~50°C, the prepared films were immersed into 0.5 mM N719 dye in an ethanol solution for 20 h at 40°C. Then, the dye adsorbed photoanodes were washed with ethanol to remove non-adsorbed dye from the films.

In the meantime, the platinum (Pt) catalyst was coated onto FTO substrates from Pt precursor (Solaronix) by a brush-painting method to prepare the counter electrodes. The dye-adsorbed photoanodes and Pt counter electrodes were assembled into a sealed sandwich-type cell, with a 60 μm thick hot-melt sealing Surlyn between each layer. The electrolyte solution, Iodolyte Z-50 (Solaronix), was introduced into the cell via a vacuum-filling method through an injection hole on the counter electrode side. Finally, the hole was sealed with scotch tape.

### 3.2.5. Characterization

Scanning electron microscopy (SEM) images were obtained using an Inspect F50 SEM (FEI) with accelerating voltage of 10 kV. Energy dispersive X-ray spectroscopy (EDX) analysis was completed on the same system with Team EDS Octane Pro (EDAX) attachment. Elemental compositions of the samples were analyzed at binding energy ranging from 0 eV to 1200 eV using a X-ray photoelectron spectrometer (XPS), Leybold Heraeus LHS-10 with a SPECS XR-50 dual anode source operating at 250W. A Mg-Kα source, which has energy of 1253.6 eV, was used for the XPS analysis. X-ray diffraction (XRD) patterns were carried out on a powder X-ray diffractometer at 40 kV and 15 mA in the range of $2\theta$ = 3–80° using Cu Kα radiation (Model Miniflex 600, Rigaku, Japan). Attenuated Total Reflection-Fourier Transform Infrared Spectroscopy (ATR-FTIR) spectra were

acquired over a wavenumber range of 4000-500 $cm^{-1}$ in transmission mode using a Frontier FTIR spectrometer (Perkin Elmer, USA) with a germanium crystal. Raman spectroscopy was carried out on LabRAM HR Evolution spectrometer (Horiba Jobin Yvon, Japan). Raman spectra were collected using a 532 nm laser (mpc 3000) as the excitation source. A 50x objective was used with a confocal hole size of 100 μm. Auger spectromicroscope "PHI 710 scanning auger nanoprobe" operating at base vacuum below 1 x $10^{-9}$ Torr was used to analyse the elemental analysis of the samples. Sputtering samples for the analysis was performed using ultra high purity Argon. Data was collected using an electron beam of 10 kV, 10nA.

To determine the adsorbed amount of dye molecules in the $SnO_2$ and $SnO_2$-RGO films, the dye in the films was dissolved in 0.1 M NaOH aqueous solution and then measured by a Varian Cary 50G UV-vis Spectrophotometer at wavelengths ranging from 300 to 1000 nm. Sheet resistivities were determined on a microscope slide substrate coated with $SnO_2$-only and/or $SnO_2$-RGO hybrid using a four point probe technique (KeithLink Technology Co., Ltd. Taiwan). The photocurrent–voltage (J–V) characteristics were investigated using a Keithley 2400 SMU instrument and recorded using a custom LabView Virtual Instrument program. A standard silicon test cell with NIST-traceable certification was used to calibrate the power density as 100 mW $cm^{-2}$ at the sample plane of the collimated xenon-arc light source, which was passed through an AM 1.5G filter. The active area of each device was 0.25 $cm^2$. The J-V curves were measured in the air through the reverse-scan direction from 1 V to -1 V. Incident-photon-to-current conversion efficiency (IPCE) measurements as a function of wavelength ranging from 400 nm to 800 nm were taken by passing chopped light from a Xenon source through a monochromator and onto the devices.

## 3.3. Results and Discussion

The preparation of $SnO_2$–RGO hybrid is shown in Scheme 3-1. Firstly, $SnCl_2 \cdot 2H_2O$ powder (Figure S3-1) was mixed with GO (Figure 3-1a) in aqueous hydrochloric acid (HCl, 0.02 M) to form a homogenous solution, which was stirred and reacted using a microwave technique. During this process, GO was reduced and is termed "RGO". Then, the resulting product was centrifuged and dried to obtain a $SnO_2$-RGO

hybrid. For comparison, the same process was carried out in the absence of GO to produce only $SnO_2$.[36]

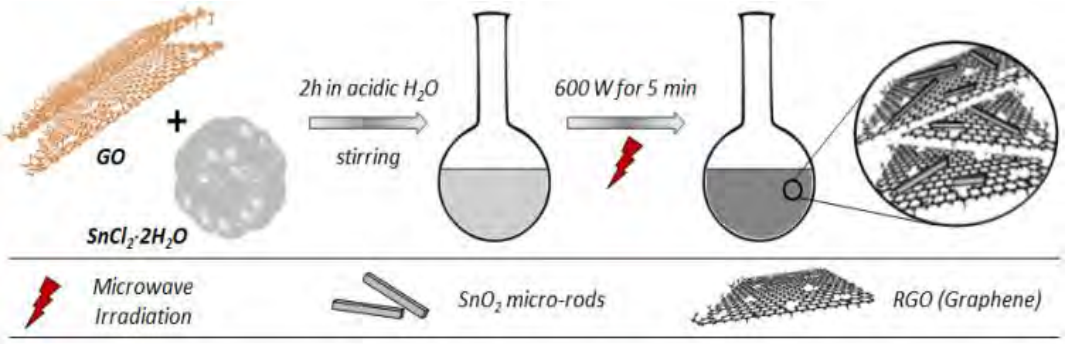


**Scheme 3-1**. Synthetic procedure of $SnO_2$–RGO hybrid structure.

The SEM image in Figure 3-1b shows that the synthesized $SnO_2$ is a 1 dimensional (1D) microstructure with a rod-like shape. It is worth noting that 1D structures can provide fast electron transport pathway.[39] Figure 3-1c depicts the SEM image of the $SnO_2$-RGO hybrid, which demonstrates clear differences compared to GO (Figure 3-1a) and $SnO_2$-only. It can be seen that the $SnO_2$ micro-rods were well mixed and wrapped in the RGO flakes, as expected, to form the hybrid material. As shown in Figure 3-1d and e, during the microwave-assisted synthesis, small $SnO_2$ nanoparticles were also formed on both $SnO_2$ rods and RGO flakes which are expected to be beneficial for dye adsorption.

Figure 3-2a shows the XRD patterns of GO, $SnO_2$-only and $SnO_2$-RGO hybrid. GO displays an intense peak at around $2\theta$ = 10.9°, which corresponds to the (002) reflection of the stacked GO nanosheets.[40] It can be observed that the $SnO_2$-only sample shows broad and weak peaks ((110), (101), (200), (211) and (112)), which can be indexed to a tetragonal-structured $SnO_2$ with poor crystallinity.[41] It is well known that after the reduction process, the diffraction peak of the GO shifts to around $2\theta$ = 24.5°. This peak at $2\theta$ = 24.5° cannot be observed in the XRD pattern of the hybrid because this peak will be overlapped by the $SnO_2$ peak (110). Another noticeable feature in the XRD pattern of $SnO_2$-RGO is that the $SnO_2$ in the hybrid shows narrow and strong peaks, which can be assigned to a tetragonal structure (JCPDS card no. 41-1445), indicating an improved crystallinity of $SnO_2$ and larger

average crystal size.[42] This improvement in the crystallinity is often observed in nanocarbon-metal oxide materials and is attributed to a heat-sink effect in which the nanocarbon facilitates crystallization via heat transfer.[43] Moreover, in the hybrid synthesis, GO may played an important role in producing highly crystalline hybrid SnO2-RGO due to e.g. heterogeneous nucleation.

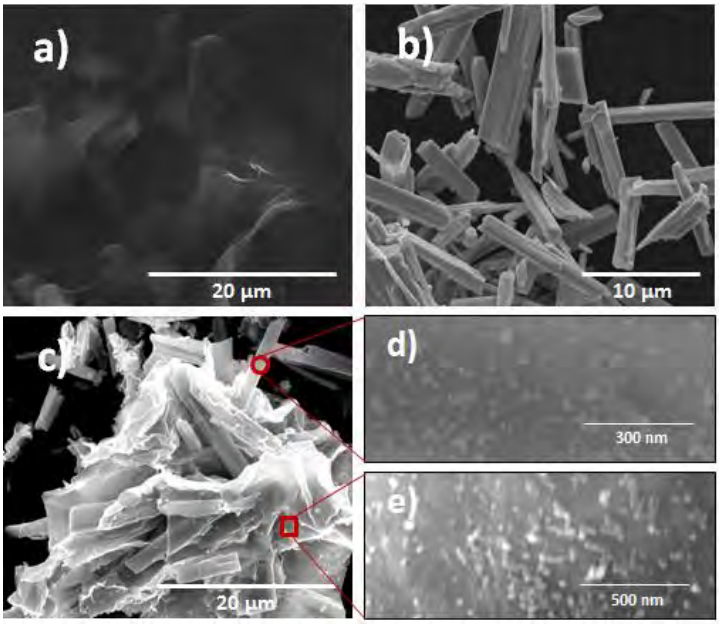


**Figure 3-1**. SEM images of (a) GO, (b) $SnO_2$ micro-rod and (c) $SnO_2$-RGO hybrid. High resolution SEM images of (d) $SnO_2$ micro-rod and (e) RGO sheet in the hybrid showing that small $SnO_2$ nanoparticles are formed on $SnO_2$ and RGO surface.

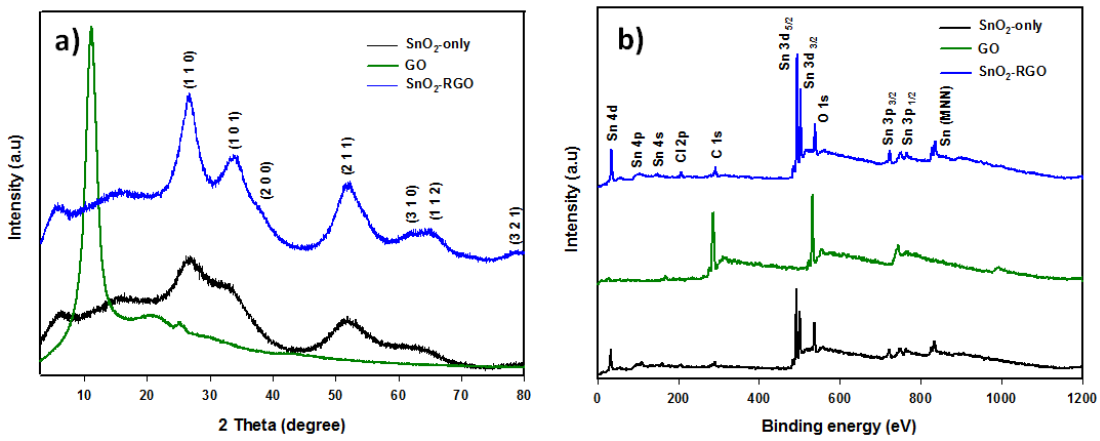


**Figure 3-2**. (a) XRD patterns and (b) XPS survey spectra of the samples.

The results of the XRD analysis were further confirmed by characterizing the samples using XPS (Figure 3-2b), ATR-FTIR (Figure 3-3a) and Raman spectroscopy (Figure 3-3b). It can be clearly observed from the Raman spectra of the $SnO_2$-RGO hybrid (Figure 3-3b) that the $I_D/I_G$ ratio of RGO increased compared to that (1.08) of the GO (0.88). This increase in the $I_D/I_G$ ratio can be attributed to the defects caused during reduction of GO.[27] Moreover, it should be noted that in the XPS survey spectra, negligible Cl peaks (Cl 2p) can be found in the $SnO_2$-based samples, which, if present, could be attributed to the unreacted $Cl^-$ of $SnCl_2 \cdot 2H_2O$. Additionally, Auger and EDX elemental analysis were carried out on selected areas of the SEM images of the $SnO_2$-RGO hybrid and reveal very small amounts of chlorine remaining in the sample (see Figure S3-2). The results from Auger and EDX spectroscopies were in good agreement with the XPS and may explain the improved crystallinity of the $SnO_2$-RGO hybrid.

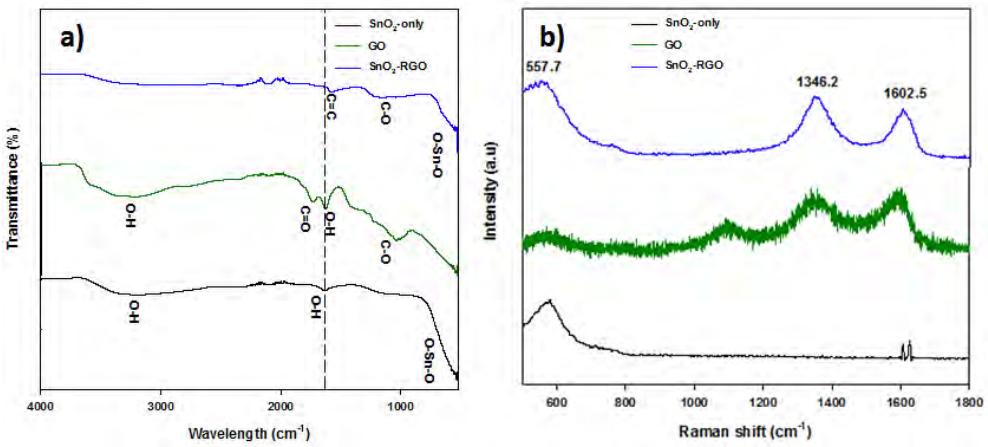


**Figure 3-3**. (a) ATR-FTIR and (b) Raman spectra of $SnO_2$-only, GO and $SnO_2$-RGO hybrid materials. Long dash line in ATR-FTIR spectra proves that "–OH" is different from the "C=C" in the hybrid.

To study the influence of RGO on the efficiency of PV cells, DSSCs were fabricated using six photoanodes of different RGO content in the hybrid and were evaluated using simulated AM1.5 sunlight with an output power of 100 mW $cm^{-2}$. Notably, for the fabrication of DSSCs, the photoanodes were immersed in a $TiCl_4$ aqueous solution before they were soaked in the dye solution. This process is a commonly followed strategy to deposit a thin layer of $TiO_2$ over $SnO_2$ ($SnO_2$-RGO in our case)

which can improve the $V_{oc}$ of the $SnO_2$-based DSSCs.[18, 44-46] Therefore, the photoanodes were denoted as "$TiO_2$-$SnO_2$-RGO (X)", where the value of X indicates the weight concentration (wt%) of RGO in the hybrid. For example, the photoanode film prepared with 0.2 wt% RGO is denoted "$TiO_2$-$SnO_2$-RGO (0.2)".

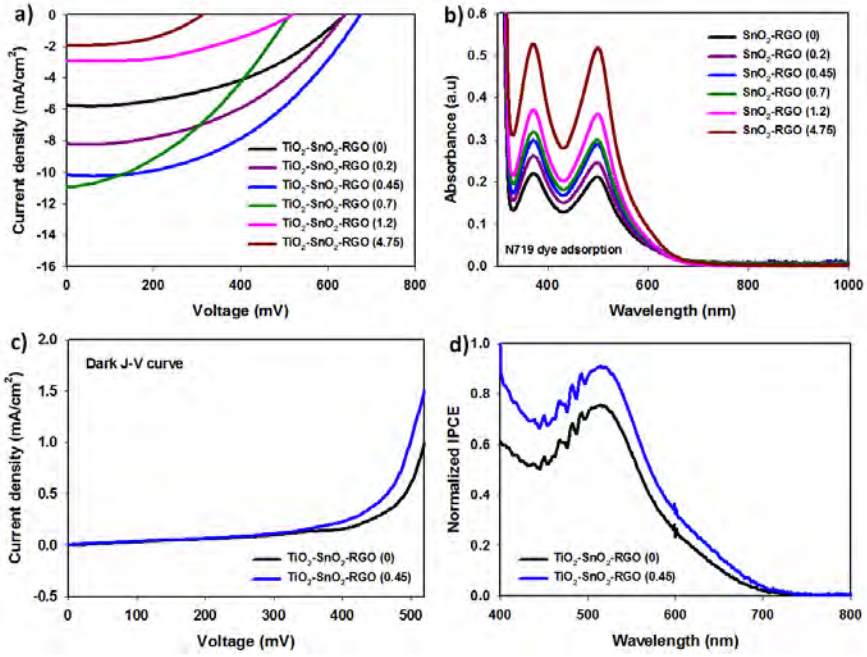


**Figure 3-4**. (a) J–V curves of DSSCs assembled with different RGO content in the $TiO_2$-$SnO_2$ photoanode. (b) UV-vis spectra of N719 dye molecules desorbed from $SnO_2$ films with different amount of RGO using 0.1 M NaOH solution. (c) J–V curves of DSSCs fabricated without and with RGO in the $SnO_2$ photoanodes measured under the dark state. (d) Normalized IPCE value of DSSCs fabricated based on $TiO_2$-$SnO_2$ photoanodes with (0.45 wt%) and without RGO.

The photocurrent density–voltage (*J–V*) characteristics of the DSSCs assembled with these photoanodes are shown in Figure 3-4a and the corresponding PV parameters have been summarized in Table 3-1. The control DSSC device ($TiO_2$-$SnO_2$-RGO (0)) fabricated based on $SnO_2$ photoanode without RGO showed an average PCE (η) of 1.28 ± 0.52% with a short–circuit current ($J_{sc}$) value of 4.78 ± 0.95 mA $cm^{-2}$ and $V_{oc}$ of 0.64 ± 0.01V which are typical values for such cells.[12, 18]

**Table 3-1**. PV parameters of the DSSCs fabricated based on $SnO_2$ photoanodes with different RGO content. Average values and the standard deviations of the DSSCs are shown based on at least three cells for each device. Parameters of the best cells are highlighted in **bold**.

| Device | RGO, wt% | $J_{sc}$, (mA $cm^{-2}$) | $V_{oc}$, (V) | FF | η (%) |
|---|---|---|---|---|---|
| $TiO_2$-$SnO_2$-RGO (0) | 0 | **5.735**; 4.78 ± 0.95 | **0.64**; 0.64 ± 0.01 | **0.45**; 0.43 ± 0.04 | **1.65**; 1.28 ± 0.52 |
| $TiO_2$-$SnO_2$-RGO (0.2) | 0.2 | **8.196**; 8.20 ± 0.15 | **0.64**; 0.63 ± 0.01 | **0.45**; 0.44 ± 0.01 | **2.36**; 2.27 ± 0.07 |
| $TiO_2$-$SnO_2$-RGO (0.45) | 0.45 | **10.185**; 9.41 ± 1.00 | **0.67**; 0.67 ± 0.01 | **0.46**; 0.46 ± 0.01 | **3.16**; 2.94 ± 0.24 |
| $TiO_2$-$SnO_2$-RGO (0.7) | 0.7 | **10.954**; 10.23 ± 0.88 | **0.52**; 0.50 ± 0.02 | **0.39**; 0.41 ± 0.04 | **2.15**; 2.08 ± 0.17 |
| $TiO_2$-$SnO_2$-RGO (1.2) | 1.2 | **2.914**; 2.91 ± 0.03 | **0.52**; 0.51 ± 0.01 | **0.45**; 0.44 ± 0.01 | **0.68**; 0.66 ± 0.03 |
| $TiO_2$-$SnO_2$-RGO (4.75) | 4.75 | **1.984**; 1.74 ± 0.26 | **0.31**; 0.27 ± 0.05 | **0.46**; 0.43 ± 0.04 | **0.29**; 0.22 ± 0.08 |

It can be seen from Table 3-1 that from $TiO_2$-$SnO_2$-RGO (0) to $TiO_2$-$SnO_2$-RGO (0.7) (increasing RGO content), the $J_{sc}$ value increases from 4.78 ± 0.95 to 10.23 ± 0.88 mA $cm^{-2}$. We hypothesize that this increase in the $J_{sc}$ is due to the improved dye loading into the film and enhanced electron transfer within the photoanode.[22, 27, 28] In order to confirm our hypothesis, we fabricated $SnO_2$ films (Figure S3-3) with different RGO content and investigated the dye adsorption capability of the films. No treatment with $TiCl_4$ solution was done to allow the effect of RGO in the $SnO_2$ film on the extent of dye adsorption to be probed without any interference. As shown in Figure S3-3, the films after dye adsorption and also the solutions after subsequent desorption of the dye molecules using NaOH show that the dye adsorption of the $SnO_2$ films was significantly improved by incorporating RGO. Moreover, UV-vis spectra in Figure 3-4b show the absorbance of dye desorbed from the films and shows that dye adsorption increases with increasing RGO concentration in the hybrid. This improvement in the dye adsorption is most likely due to a better

matching of the molecular nature of the N719 dye and the chemical nature of the hybrid. N719 has both polar groups and aromatic regions. Since our RGO was derived from GO, some functional groups (–OH, –COOH etc.) would remain on the surface of RGO due to the partial reduction and these would interact with the polar groups on N719. These functional groups may be playing an important role in the dye adsorption.[21] $SnO_2$ would also interact with these polar groups. The introduction of the RGO provides some aromatic nature to the hybrid and one can speculate that this will create polar and aromatic regions in close proximity and will further enhance dye adsorption. Additionally the high-surface area of RGO may contribute to the adsorption of the dye.[28] Interestingly, the dye adsorption of the film with the highest RGO content (4.75 wt%) is starting to saturate, indicating that adding more RGO into the film would likely not lead to significant further increases in dye adsorption (see Figure S3-4).

To determine the mechanism for the improved $J_{sc}$ value, the resistivity ($R_s$) of the $TiCl_4$ treated $SnO_2$ film without and with 0.45 wt% RGO was measured using a four point probe. The same film thickness on a glass substrate was obtained using the doctor blade method (see experimental details). The film without RGO shows a $R_s$ of 4.51 x $10^6$ Ω/□, while the RGO incorporated film exhibits a comparatively low $R_s$ (1.81 x $10^6$ Ω/□) (see Table S3-1). The decrease in the $R_s$ (nearly 3-fold) of the film with RGO is due to the fact that the high conductivity of the RGO in the hybrid reduces the interfacial resistance between $SnO_2$. In addition, the measured series resistance ($R_{series}$) of the $TiO_2$-$SnO_2$-RGO (0.45) based DSSC was 97.9 Ω, which was ~1.7-fold lower than that of the control cell. It should be noted that the $R_{series}$ of the devices were calculated from the J-V measurement of the DSSCs. On the basis of these results, it is clear that the presence of RGO accelerated electron transport process within the photoanode and suppressed the charge recombination of the cells; thus significantly enhancing the $\eta$.

However, although $TiO_2$-$SnO_2$-RGO (0.7) based cell showed the highest $J_{sc}$ (10.95 mA $cm^{-2}$), the measured average η (2.08 ± 0.17%) was not the best observed, despite the films having high dye adsorption. When the RGO concentration in the hybrid further increased to 1.2 wt% and 4.75 wt%, a significant drop in the $J_{sc}$ value and $V_{oc}$ was observed for the $TiO_2$-$SnO_2$-RGO (1.2) and $TiO_2$-$SnO_2$-RGO (4.75) based DSSCs, thus resulting in very poor efficiencies. We attribute this $\eta$ decrease of the

DSSCs with higher RGO loading to (i) opacity of the film (see films before dye adsorption in Figure S3-3) reducing light absorption and (ii) high catalytic property of RGO, which has been shown to limit the continuous electron transfer at the photoanode.[2, 21, 47]

It is well established that though carbon materials can facilitate electron transport in DSSCs, the catalytic activity of carbon materials toward reduction of the electrolyte causes significant charge recombination at the interface of the photoanode and electrolyte (since this reaction should only occur at the cathode) if too high concentration of carbon is used.[2] Figure 3-4c shows the dark J–V characteristics of DSSCs fabricated without and with RGO in the $SnO_2$ photoanodes. It is known that the magnitude and onset of the dark current indicates the level of charge recombination between the electrons from the dye excitation process and the $I_3^-$ ions in the electrolyte.[48] It can be seen that the dark current onset shifted to a lower potential after adding a small amount of RGO into the $SnO_2$ photoanodes. This is known to be due to the increased charge recombination rate of the DSSCs caused by the reaction between the RGO and electrolyte. Therefore, at a given voltage, the dark current increased when the RGO was added into the $SnO_2$ photoanode of DSSC. Our finding is in line with similar report of adding carbon powders into $TiO_2$ photoanodes.[48]

Indeed, the highest η (3.16%) with an average η of 2.94 ± 0.24% was achieved for the device based on $TiO_2$-$SnO_2$-RGO (0.45). In the $TiO_2$-$SnO_2$-RGO based DSSC, the $TiO_2$ can act as a barrier layer reducing the contact of RGO with the electrolyte and therefore reducing the likelihood of RGO catalyzing recombination at the photoanode. Taking into account the $TiO_2$ deposition process (dip coating) which is unlikely to achieve 100 % coverage, we speculate that with higher RGO content the net amount of RGO in contact with the electrolyte will increase accordingly. Moreover, we fabricated $SnO_2$ and $SnO_2$-RGO photoanodes based DSSCs without $TiCl_4$ treatment and their PV results have been plotted in Figure S3-5a. The efficiencies of these DSSCs were ~2-fold lower than those of the devices fabricated with $TiCl_4$ treatment, confirming that the use of $TiCl_4$ treatment is a vital method to enhance the cell performance in $SnO_2$ photoanode DSSCs.

It can be seen from Table 3-1 that all parameters of DSSC fabricated with $SnO_2$ photoanodes increased after incorporating 0.45 wt% RGO. The calculated $\eta$

enhancement of $TiO_2$-$SnO_2$-RGO (0.45) photoanode based device was impressive (91.5%) as compared to the control cell especially in light of the fact that a very small amount of RGO is required to realise these large improvements in efficiency. This photoanode ($TiO_2$-$SnO_2$-RGO (0.45)) was chosen for further investigation to fully understand the role of RGO in the DSSC.

IPCE spectra offer important information on the light harvesting efficiency which is mainly determined by the absorption of light by the dye molecules at the photoanode and electron transport processes. The IPCE spectra of the DSSCs with and without RGO in the photoanode are illustrated in Figure 3-4d. It should be noted that the IPCE spectra of the DSSCs were characterized after the devices were aged for approximately 10 days. The IPCE of the $TiO_2$-$SnO_2$-RGO (0.45) photoanode based device is higher than that of the control DSSC over the entire wavelength region. The lack of wavelength dependence indicates that the addition of RGO into the $SnO_2$ photoanode improves the DSSC performance without altering the internal mechanism, likely by enhancing electron transfer rate and increasing dye adsorption onto the photoanode.

As discussed earlier, RGO in the hybrid ensures rapid electron transport process (Figure 3-5a) and significantly enhances the $J_{sc}$ value of the DSSC. Importantly, it can be expected that incorporation of RGO in the $SnO_2$ photoanode would improve the DSSC performance owing to presence of suitable energy levels. Figure 3-5b shows an energy level diagram for the $TiCl_4$ treated $SnO_2$ photoanode with RGO. Since a thin $TiO_2$ layer was deposited on the FTO and on the $SnO_2$ or $SnO_2$-RGO layers by $TiCl_4$ treatment, it is reasonable to include the energy level of $TiO_2$ in this diagram. The red arrow in Figure 3-5b represents the fact that the electron transfer from the conduction band of $SnO_2$ to that of $TiO_2$ is not possible due to their mismatching band energy levels. As the $TiO_2$ coverage on the FTO is incomplete (not 100%), both $SnO_2$ and $TiO_2$ are in contact with the FTO and hence electron transfer from both the $SnO_2$ and $TiO_2$ to the FTO is still feasible. The results from Figure S3-6 and Figure S3-7 show that despite the fact that the $TiO_2$ on the FTO is very thin, it does make a contribution to the current and voltage of the cell and as such is important to show. Since the energy level of RGO (-4.40 eV) lies between the conduction band of $TiO_2$ (-4.26 eV) and $SnO_2$ (-4.56 eV), the electrons can be rapidly transferred stepwise from the $TiO_2$ to the $SnO_2$ conduction band (see Figure

3-5b).[18, 28] Here RGO can act as a bridge between $TiO_2$ and $SnO_2$. This effective electron transfer would likely reduce the charge recombination of the cell, thus improves the performance.

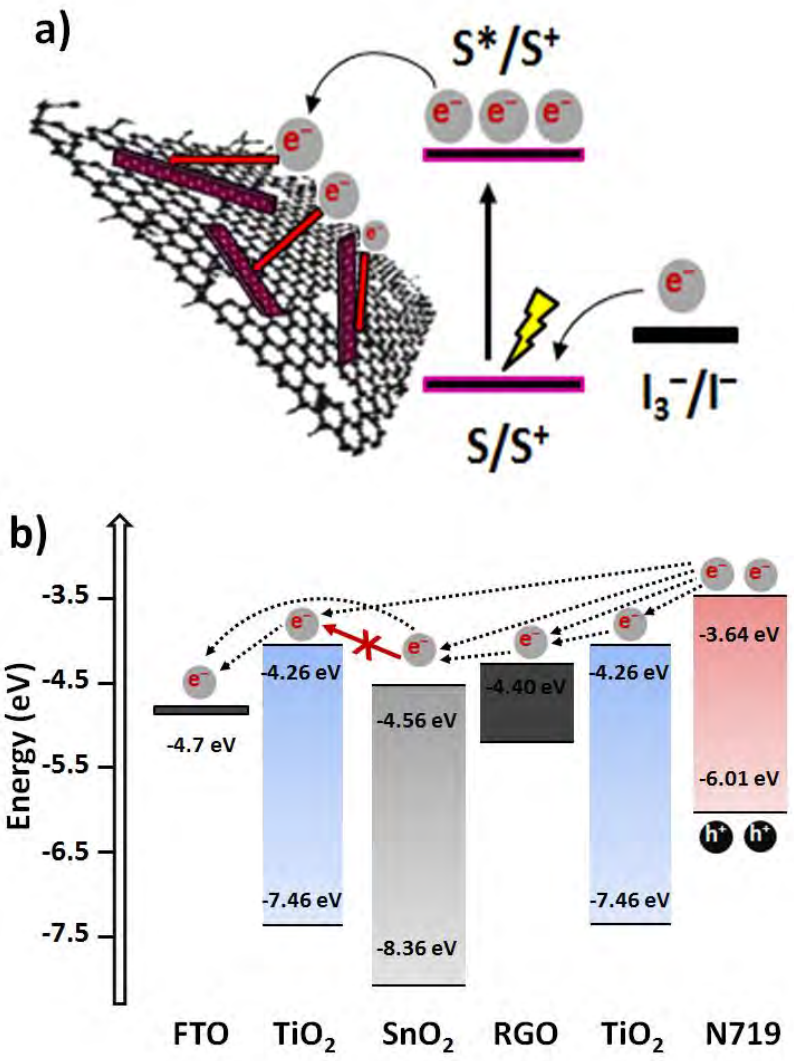


**Figure 3-5**. (a) A possible mechanism for the enhanced electron transfer in $SnO_2$-RGO hybrid. (b) Energy diagram for the $TiCl_4$ treated $SnO_2$ photoanode with RGO.

**Table 3-2**. PV parameters of the DSSCs fabricated based on various $SnO_2$ photoanode structures and our best performing cell ($TiO_2$-$SnO_2$-RGO (0.45).

| Structure | Ref. | $J_{sc}$, (mA $cm^{-2}$) | $V_{oc}$, (V) | FF | η (%) |
|---|---|---|---|---|---|
| This study | - | 10.18 | 0.67 | 0.46 | 3.16 |
| $SnO_2$ nanoparticles | [49] | 7.63 | 0.35 | 0.43 | 1.14 |
| $SnO_2$ nanoparticles | [44] | 4.90 | 0.40 | 0.51 | 1.00 |
| $SnO_2$ nanoparticles | [50] | 7.90 | 0.47 | 0.55 | 2.03 |
| $SnO_2$ nanofibers | [51] | 7.04 | 0.51 | 0.38 | 1.34 |
| $SnO_2$ multiporous NFs | [12] | 10.0 | 0.44 | 0.45 | 2.00 |
| $SnO_2$ nanoflowers | [52] | 7.30 | 0.70 | 0.60 | 3.00 |
| $SnO_2$ NWs + NPs | [53] | 9.90 | 0.53 | 0.49 | 2.53 |
| $SnO_2$ spheres (hierarchical) | [54] | 12.3 | 0.52 | 0.58 | 3.70 |

Finally, the PV parameters of our best-performing cells have been compared with values reported in the literature for other DSSCs with $SnO_2$ based photoanodes. Table 3-2 summarizes the PV parameters such as $J_{sc}$, $V_{oc}$, FF and η of DSSC devices fabricated with various $SnO_2$ structures based photoanodes and our best performing cells. It can be observed from Table 3-2 that the efficiency observed for our DSSCs fabricated with $SnO_2$-RGO photoanode is comparable or higher than those achieved by other 1D and 3D $SnO_2$ structured photoanode films. Therefore, this indicates that the incorporation of graphene structures into $SnO_2$ photoanode is an effective strategy to achieve high efficiency DSSCs.

## 3.4. Conclusion

In summary, the successful application of RGO structures in 1D $SnO_2$ micro-rod based photoanodes for DSSCs has been demonstrated. Herein we show that the application of RGO overcomes the major shortcoming of $SnO_2$ when applied as a DSSC photoanode, namely poor dye adsorption. In addition, owing to its suitable energy levels and excellent conductivity, RGO significantly improved the electron transport rate in the cells. Importantly, PCE ($\eta$) of the DSSC was significantly improved to 3.16% by incorporating a very small amount of RGO into the

photoanode, demonstrating a ~91.5% enhancement in the efficiency when compared to $SnO_2$-only photoanode based DSSC (1.65%).

## Acknowledgements

The support of the Australian Research Council Discovery Program (DP130101714) is gratefully acknowledged. Munkhbayar Batmunkh acknowledges International Postgraduate Research Scholarship (IPRS) and Australian Postgraduate Award (APA) for their financial support during his study in Australia. We acknowledge the use of South Australian node of the Australian Microscopy & Microanalysis Research Facility (AMMRF) at Flinders University.

## References

[1] G. Hashmi, K. Miettunen, T. Peltola, J. Halme, I. Asghar, K. Aitola, M. Toivola, P. Lund, *Renew Sust Energy Rev,* **2011**, 15, 3717.
[2] M. Batmunkh, M. J. Biggs, J. G. Shapter, *Small*, **2015**, 11, 2963.
[3] F. Bella, C. Gerbaldi, C. Barolo, M. Gratzel, *Chem. Soc. Rev*, **2015**, 44, 3431.
[4] J. Wu, Z. Lan, J. Lin, M. Huang, Y. Huang, L. Fan, G. Luo, *Chem Rev*, **2015**, 115, 2136.
[5] Y. Hao, E. Gabrielsson, P. W. Lohse, W. Yang, E. M. J. Johansson, A. Hagfeldt, L. Sun, G. Boschloo, *Adv. Sci*, **2015**, 2, 1500174.
[6] L. Han, A. Islam, H. Chen, C. Malapaka, B. Chiranjeevi, S. Zhang, X. Yang, M. Yanagida, *Energy Environ Sci,* **2012**, 5, 6057.
[7] S. Mathew, A. Yella, P. Gao, R. Humphry-Baker, F. E. CurchodBasile, N. Ashari-Astani, I. Tavernelli, U. Rothlisberger, K. NazeeruddinMd, M. Grätzel, *Nat Chem*, **2014**, 6, 242.
[8] S. G. Hashmi, M. Ozkan, J. Halme, K. D. Misic, S. M. Zakeeruddin, J. Paltakari, M. Grätzel, P. D. Lund, *Nano Energy*, **2015**, 17, 206.
[9] A. K. Chandiran, M. Abdi-Jalebi, M. K. Nazeeruddin, M. Grätzel, *ACS Nano,* **2014**, 8, 2261.
[10] J. Fan, Z. Li, W. Zhou, Y. Miao, Y. Zhang, J. Hu, G. Shao, *Appl. Surf. Sci,* **2014**, 319, 75.
[11] S. Ferrere, A. Zaban, B. A. Gregg, *J. Phys. Chem. B,* **1997**, 101, 4490.
[12] Q. Wali, A. Fakharuddin, I. Ahmed, M. H. Ab Rahim, J. Ismail, R. Jose, *J. Mater. Chem. A,* **2014**, 2, 17427.
[13] Q. Wali, A. Fakharuddin, R. Jose, *J. Power Sources*, **2015**, 293, 1039.
[14] I. Concina, A. Vomiero, *Small,* **2015**, 11, 1744.

[15] E. Ramasamy, J. Lee, *J. Phys. Chem. C,* **2010**, 114, 22032.
[16] S. Gubbala, V. Chakrapani, V. Kumar, M. K. Sunkara, *Adv. Funct. Mater,* **2008**, 18, 2411.
[17] J. Gong, H. Qiao, S. Sigdel, H. Elbohy, N. Adhikari, Z. Zhou, K. Sumathy, Q. Wei, Q. Qiao, *AIP Adv,* **2015**, 5, 067134.
[18] A. Thapa, J. Zai, H. Elbohy, P. Poudel, N. Adhikari, X. Qian, Q. Qiao, *Nano Res,* **2014**, 7, 1154.
[19] C.-L. Wang, J.-Y. Liao, Y. Zhao, A. Manthiram, *Chem. Comm,* **2015**, 51, 2848.
[20] A. Birkel, Y.-G. Lee, D. Koll, X. V. Meerbeek, S. Frank, M. J. Choi, Y. S. Kang, K. Char, W. Tremel, *Energy Environ Sci,* **2012**, 5, 5392.
[21] M. Batmunkh, M. J. Biggs, J. G. Shapter, *Adv. Sci,* **2015**, 2, 1400025.
[22] J. D. Roy-Mayhew, I. A. Aksay, *Chem Rev,* **2014**, 114, 6323.
[23] M. Batmunkh, C. J. Shearer, M. J. Biggs, J. G. Shapter, J. Mater. Chem. A, **2015**, 3, 9020.
[24] A. Kongkanand, R. Martínez Domínguez, P. V. Kamat, *Nano Lett,* **2007**, 7, 676.
[25] S.-B. Kim, J.-Y. Park, C.-S. Kim, K. Okuyama, S.-E. Lee, H.-D. Jang, T.-O. Kim, *J. Phys. Chem. C,* **2015**, 119, 16552.
[26] A. Sacco, S. Porro, A. Lamberti, M. Gerosa, M. Castellino, A. Chiodoni, S. Bianco, *Electrochim. Acta,* **2014**, 131, 154.
[27] Z. He, G. Guai, J. Liu, C. Guo, J. S. Chye Loo, C. M. Li, T. T. Y. Tan, *Nanoscale,* **2011**, 3, 4613.
[28] Y.-B. Tang, C.-S. Lee, J. Xu, Z.-T. Liu, Z.-H. Chen, Z. He, Y.-L. Cao, G. Yuan, H. Song, L. Chen, L. Luo, H.-M. Cheng, W.-J. Zhang, I. Bello, S.-T. Lee, *ACS Nano,* **2010**, 4, 3482.
[29] T. Chen, W. Hu, J. Song, G. H. Guai, C. M. Li, *Adv. Funct. Mater,* **2012**, 22, 5245.
[30] Y. H. Ng, I. V. Lightcap, K. Goodwin, M. Matsumura, P. V. Kamat, *J. Phys. Chem. Lett,* **2010**, 1, 2222.
[31] P. Brown, K. Takechi, P. V. Kamat, *J. Phys. Chem. C,* **2008**, 112, 4776.
[32] K. T. Dembele, G. S. Selopal, C. Soldano, R. Nechache, J. C. Rimada, I. Concina, G. Sberveglieri, F. Rosei, A. Vomiero, *J. Phys. Chem. C,* **2013**, 117, 14510.
[33] D. C. Marcano, D. V. Kosynkin, J. M. Berlin, A. Sinitskii, Z. Sun, A. Slesarev, L. B. Alemany, W. Lu, J. M. Tour, *ACS Nano,* **2010**, 4, 4806.
[34] L. Yin, D. Chen, X. Cui, L. Ge, J. Yang, L. Yu, B. Zhang, R. Zhang, G. Shao, *Nanoscale,* **2014**, 6, 13690.
[35] Y. Xiong, D. He, Y. Jin, P. J. Cameron, K. J. Edler, *J. Phys. Chem. C,* **2015**, 119, 22552.
[36] M. Batmunkh, M. Dadkhah, C. J. Shearer, M. J. Biggs, J. G. Shapter, *Energy Technology,* **2016**, *4*, 959–966.
[37] L. Yang, W. W.-F. Leung, *Adv. Mater,* **2013**, 25, 1792.
[38] S. Ito, T. N. Murakami, P. Comte, P. Liska, C. Grätzel, M. K. Nazeeruddin, M. Grätzel, *Thin Solid Films,* **2008**, 516, 4613.

[39] P. Poudel, Q. Qiao, *Nanoscale,* **2012**, 4, 2826.
[40] Y.-T. Xu, Y. Guo, H. Jiang, X.-B. Xie, B. Zhao, P.-L. Zhu, X.-Z. Fu, R. Sun, C.-P. Wong, *Energy Technology,* **2015**, 3, 488.
[41] M. Dadkhah, M. Salavati-Niasari, *Electrochim. Acta,* **2014**, 129, 62.
[42] A. L. Patterson, *Phys Rev,* **1939**, 56, 978.
[43] Z. Ren, E. Kim, S. W. Pattinson, K. S. Subrahmanyam, C. N. R. Rao, A. K. Cheetham, D. Eder, *Chem. Sci,* **2012**, 3, 209.
[44] J. Qian, P. Liu, Y. Xiao, Y. Jiang, Y. Cao, X. Ai, H. Yang, *Adv. Mater,* **2009**, 21, 3663.
[45] M.-S. Wu, Z.-Z. Ceng, C.-Y. Chen, *Electrochim. Acta,* **2016**, 191, 256.
[46] Q. Yi, S. Cong, H. Wang, Y. Wang, X. Dai, J. Zhao, Y. Sun, Y. Lou, G. Zou, *Appl. Surf. Sci,* **2015**, 356, 587.
[47] J. Chen, B. Li, J. Zheng, J. Zhao, Z. Zhu, *J. Phys. Chem. C,* **2012**, 116, 14848.
[48] S. H. Kang, J.-Y. Kim, Y.-K. Kim, Y.-E. Sung, *J. Photochem. Photobiol. A,* **2007**, 186, 234.
[49] M.-H. Kim, Y.-U. Kwon, *J. Phys. Chem. C,* **2011**, 115, 23120.
[50] Y. Duan, J. Zheng, N. Fu, Y. Fang, T. Liu, Q. Zhang, X. Zhou, Y. Lin, F. Pan, *J. Mater. Chem. A,* **2015**, 3, 3066.
[51] C. Gao, X. Li, X. Zhu, L. Chen, Z. Zhang, Y. Wang, Z. Zhang, H. Duan, E. Xie, *J. Power Sources,* **2014**, 264, 15.
[52] E. N. Kumar, R. Jose, P. S. Archana, C. Vijila, M. M. Yusoff, S. Ramakrishna, *Energy Environ Sci,* **2012**, 5, 5401.
[53] T. Krishnamoorthy, M. Z. Tang, A. Verma, A. S. Nair, D. Pliszka, S. G. Mhaisalkar, S. Ramakrishna, *J. Mater. Chem,* **2012**, 22, 2166.
[54] J. T. Park, C. S. Lee, J. H. Kim, *RSC Adv,* **2014**, 4, 31452.

# Supporting Information for

# Incorporation of Graphene into $SnO_2$ Photoanode for Dye-Sensitized Solar Cells

Munkhbayar Batmunkh,[1,2] Mahnaz Dadkhah,[2] Cameron J. Shearer,[2] Mark J. Biggs,[1,3] and Joseph G. Shapter,[2]*

[1] *School of Chemical Engineering, The University of Adelaide, Adelaide, South Australia 5005, Australia*

[2] *School of Chemical and Physical Sciences, Flinders University, Bedford Park, Adelaide, South Australia 5042, Australia*

[3] *School of Sciences, Loughborough University, Loughborough, Leicestershire, LE11 3TU, UK*

* Corresponding authors:

joe.shapter@flinders.edu.au

**Published:** *Applied Surface Science,* **2016**, *387*, 690-697

The published copy of the manuscript is attached in Appendix B.

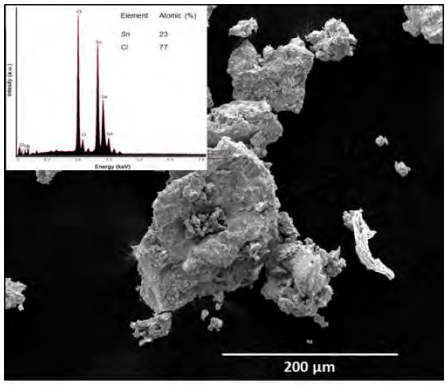


**Figure S3-1**. SEM image and EDX elemental analysis (inset) of $SnCl_2 \cdot 2H_2O$ sample (used as the starting material).

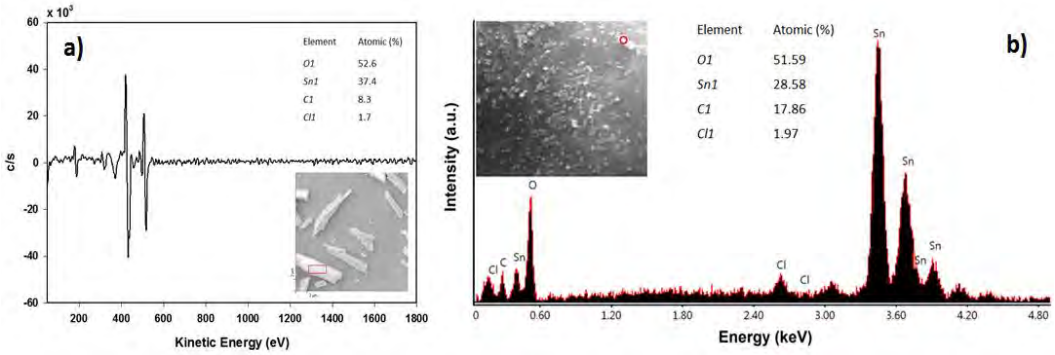


**Figure S3-2**. (a) Auger and (b) EDX elemental analysis on the selected area (highlighted by red rectangle in (a) and circle in (b)) of the corresponding SEM images of $SnO_2$-RGO hybrid, as shown in the inset in b).

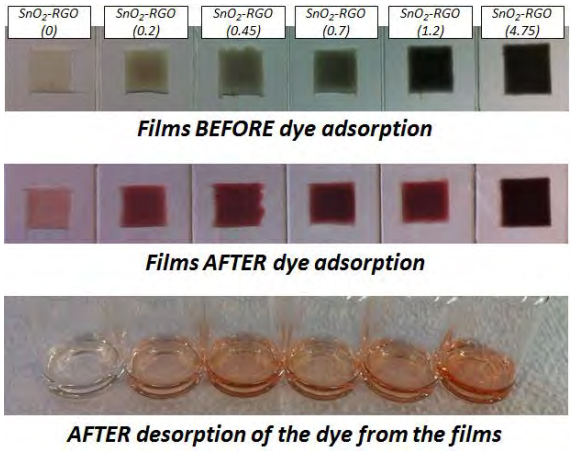


**Figure S3-3**. Dye adsorption capability of the films ($SnO_2$-RGO (X)) with different RGO content. In $SnO_2$-RGO (X), the value of X indicates the weight concentration

(wt%) of RGO in the hybrid. For instance, the concentration of RGO in the $SnO_2$-RGO (0.45) was 0.45 wt%.

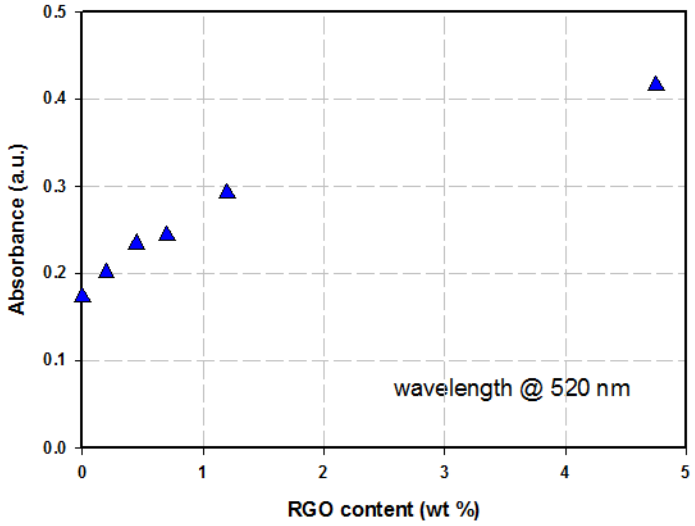


**Figure S3-4**. The absorbance of these solutions at a wavelength of 520 nm.

Figure S3-5a shows the J–V curves of DSSCs assembled with different RGO in the $SnO_2$ photoanodes (without any $TiCl_4$ treatment on the photoanode).The overall trend in the efficiency changes (increased after adding an appropriate amount of RGO into the $SnO_2$ and decreased at too high concentration of RGO in the photoanodes) of DSSCs without and with $TiCl_4$ treatment was very similar, demonstrating that adding RGO into $SnO_2$ photoanode can enhance the PV efficiency, regardless of additional $TiCl_4$ treatment. A possible energy diagram for $SnO_2$-RGO photoanode based DSSC is shown in Figure S3-5b. In this device structure, RGO enhances the electron transport rate and can also act as a bridge between dye and $SnO_2$. Notably, the efficiency of our $SnO_2$-only based DSSC was within the range (ranging from 0.6% to 1.0%) of previously reported values.[1-3]

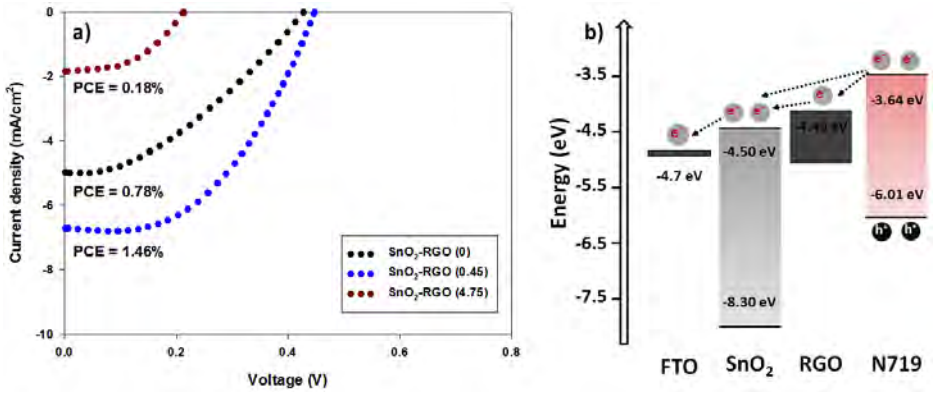


**Figure S3-5**. (a) J–V curves of DSSCs fabricated with different RGO content in the $SnO_2$ photoanode without the $TiO_2$ blocking layer and (b) an energy level diagram for the $SnO_2$-RGO photoanode without any $TiO_2$ blocking layer.

It should be noted that $TiO_2$ was formed on the FTO by $TiCl_4$ treatment. However, it is well established that the $TiO_2$ does not completely cover FTO which makes electron transfer process possible between $SnO_2$ and FTO.[4–7] In order to prove that the coverage of $TiO_2$ during from $TiCl_4$ treatment on FTO is not 100%, DSSCs with a structure FTO/$TiO_2$/$SnO_2$/dye/electrolyte/Pt/FTO (without the second $TiCl_4$ treatment) were fabricated and their J-V characteristics are illustrated in Figure S3-6a. It is reasonable to expect that the DSSC fabricated with such structure cannot work if the $TiO_2$ completely (100%) covered the FTO because the conduction band of $TiO_2$ (-4.25 eV) is higher than that of $SnO_2$ (-4.56 eV) and thus energy transfer from the $SnO_2$ to the FTO through $TiO_2$ layer would not be feasible (see Figure S3-6b). Interestingly, the fabricated DSSC exhibited a good efficiency (1.17%) with increased $V_{oc}$ value, as compared to $SnO_2$ photoanode based DSSC without any blocking layer $TiCl_4$ treatment. Cells with the $TiO_2$ blocking layer only and $SnO_2$–free photoanode give a very poor performance (see Figure S3-7). The improvement in efficiency for the cell of Figure S3-6 compared to the cell without graphene of Figure S3-5 means that while the $TiO_2$ on the FTO must play a small role in the cell, the $SnO_2$ must also be in direct contact with the FTO and able to transfer electrons. This clearly shows the thin $TiO_2$ layer does not cover the FTO completely and electron transfer from both oxides must occur. The incomplete coverage of $TiO_2$ on the FTO means the majority of the photovoltaic performance is from the $SnO_2$ layer.

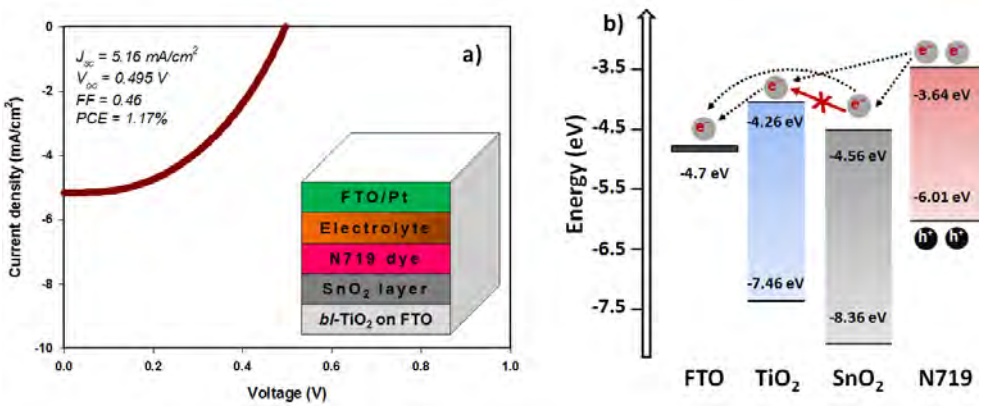


**Figure S3-6**. (a) J–V curves of DSSC device assembled with the photoanode structure of FTO/thin $TiO_2$/$SnO_2$/dye (without second $TiCl_4$ treatment). Inset shows the device structure. (b) A possible energy level diagram for this DSSC photoanode.

In addition, DSSCs based on only $TiCl_4$ treated FTO as a photoanode were fabricated and their performance is depicted in Figure S3-7. For this experiment, the cleaned FTO was immersed in a 40 mM $TiCl_4$ aqueous solution at 70$^o$C for 30 min, followed by drying with $N_2$ gas and annealing at 450$^o$C for 30 min. After cooling to room temperature, a second $TiCl_4$ treatment was performed in a same manner. Finally the film was sintered at 450$^o$C for 30 min and then exposed the dye solution as before. As a result, the fabricated cell showed high $V_{oc}$ value, but its PCE was very poor (0.13%). This result is reasonable since the $V_{oc}$ parameter is determined by the energy level difference between the conduction band of semiconducting photoanode material ($TiO_2$ here in this device) and the potential energy of the electrolyte. The very low $J_{sc}$ value of this cell is due to the insufficient dye-loading into the photoanode film as only a very thin $TiO_2$ and low surface area layer is formed on the FTO. A poor fill factor value could also be associated with the incomplete coverage of $TiO_2$ on the FTO. These results again show that the $SnO_2$ is the main active element of these photoanodes.

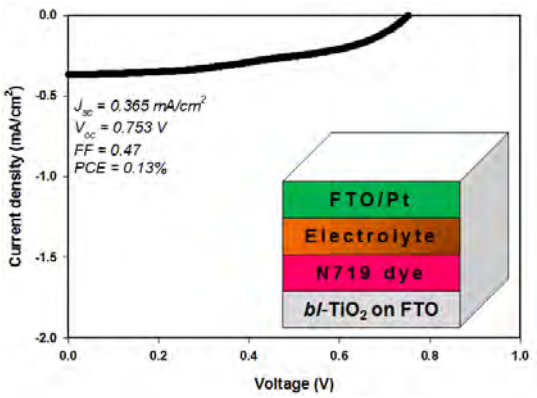


**Figure S3-7**. J–V curves of DSSC fabricated with thin $TiO_2$ layers on FTO as a photoanode. Notably, $TiO_2$ layers were formed on the FTO by 2 times $TiCl_4$ treatment as was done for the normal device. Inset shows the device structure.

**Table S3-1**. Electrical parameters of $SnO_2$ photoanode without and with RGO and their DSSCs.

| Sample | Sheet resistance, $R_s$ (Ω/□) | Series resistance, $R_{series}$ (Ω) | Shunt resistance, $R_{shunt}$ (Ω) |
|---|---|---|---|
| $TiO_2$-$SnO_2$-RGO (0) | 4.51 x $10^6$ | 167.0 | 1600 |
| $TiO_2$-$SnO_2$-RGO (0.45) | 1.81 x $10^6$ | 97.9 | 1920 |

# References


[1] E. Ramasamy, J. Lee, *J. Phys. Chem. C,* **2010**, 114, 22032–22037.

[2] F. Gu, W. Huang, S. Wang, X. Cheng, Y. Hu, G. Li*, J Power Sources,* **2014**, 268, 922-927.

[3] E. N. Kumar, R. Jose, P. S. Archana, C. Vijila, M. M. Yusoff, S. Ramakrishna, *Energy Environ. Sci,* **2012**, 5, 5401-5407.

[4] Z. Du, H. Zhang, H. Bao, X. Zhong, *J. Mater. Chem. A,* **2014**, 2, 13033-13040.

[5] S. Yang, Y. Hou, B. Zhang, X. H. Yang, W. Q. Fang, H. J. Zhao, H. G. Yang, *J. Mater. Chem. A,* **2013**, 1, 1374-1379.

[6] S.-K. Kim, M.-K. Son, S. Park, M.-S. Jeong, D. Savariraj, K. Prabakar, H.-J. Kim, *Phys. Status. Solid. A,* **2014**, 211, 1839-1843.

[7] H. Choi, C. Nahm, J. Kim, J. Moon, S. Nam, D.-R. Jung, B. Park, *Current. Appl. Phys,* **2012**, 12, 737-741.

# Chapter 4.

# Sulfur-Doped Graphene with Iron Pyrite ($FeS_2$) as an Efficient and Stable Electrocatalyst for Iodine Reduction Reaction in Dye–Sensitized Solar Cells

Munkhbayar Batmunkh,[1,2] Aabhash Shrestha,[1] Gao Guo,[3] Leping Yu,[2] Jing Zhao,[2] Mark J. Biggs,[1,4] Cameron J. Shearer,[2] Joseph G. Shapter,[2]*

[1] *School of Chemical Engineering, The University of Adelaide, Adelaide, South Australia 5005, Australia*

[2] *School of Chemical and Physical Sciences, Flinders University, Bedford Park, Adelaide, South Australia 5042, Australia*

[3] *School of Electronic Information and Electrical Engineering, Shanghai Jiao Tong University, 800 Dongchuan Road, Shanghai 200240, China*

[4] *School of Sciences, Loughborough University, Loughborough, Leicestershire, LE11 3TU, UK*

* Corresponding authors:

joe.shapter@flinders.edu.au

**Published:** *SOLAR RRL,* **2017**, *1*, 1700011

The published copy of the manuscript is attached in Appendix C.

# Statement of Authorship

| | |
|---|---|
| Title of Paper | Sulfur–doped graphene with iron pyrite ($FeS_2$) as an efficient and stable electrocatalyst for Iodine reduction reaction in dye–sensitized solar cells |
| Publication Status | ☑ Published ☐ Accepted for Publication<br>☑ Submitted for Publication ☐ Unpublished and Unsubmitted work written in manuscript style |
| Publication Details | Munkhbayar Batmunkh, Aabhash Shrestha, Gao Guo, Leping Yu, Jing Zhao, Mark. J. Biggs, Cameron J. Shearer and Joseph G. Shapter, 2016, *Submitted.*<br>Solar RRL. 2017, 1, 1700011. |

## Principal Author

| | |
|---|---|
| Name of Principal Author (Candidate) | Munkhbayar Batmunkh |
| Contribution to the Paper | Conducted the experimental works, performed analysis on all samples, interpreted data and wrote manuscript. |
| Overall percentage (%) | 75% |
| Certification: | This paper reports on original research I conducted during the period of my Higher Degree by Research candidature and is not subject to any obligations or contractual agreements with a third party that would constrain its inclusion in this thesis. I am the primary author of this paper. |
| Signature | Date 30/12/2016 |

## Co-Author Contributions

By signing the Statement of Authorship, each author certifies that:

i. the candidate's stated contribution to the publication is accurate (as detailed above);
ii. permission is granted for the candidate in include the publication in the thesis; and
iii. the sum of all co-author contributions is equal to 100% less the candidate's stated contribution.

| | |
|---|---|
| Name of Co-Author | Dr. Aabhash Shrestha |
| Contribution to the Paper | Sample preparation, Edited the manuscript |
| Signature | Date 31st Dec 2016 |

| | |
|---|---|
| Name of Co-Author | Prof. Gao Guo |
| Contribution to the Paper | Sample preparation and some characterizations |
| Signature | Date 4 Jan 2017 |

| Name of Co-Author | Leping Yu |
|---|---|
| Contribution to the Paper | Conducted some experimental works, Edited the manuscript |
| Signature | Date 04/01/2017 |

| Name of Co-Author | Dr. Jing Zhao |
|---|---|
| Contribution to the Paper | Sample preparation |
| Signature | Date 02/01/2017 |

| Name of Co-Author | Prof. Mark J. Biggs |
|---|---|
| Contribution to the Paper | Co-advised the development of work, and manuscript evaluation. |
| Signature | Date 12/1/17 |

| Name of Co-Author | Dr. Cameron J. Shearer |
|---|---|
| Contribution to the Paper | Sample characterization, edited the manuscript, and manuscript evaluation. |
| Signature | Date 4/1/17 |

| Name of Co-Author | Prof. Joseph G. Shapter |
|---|---|
| Contribution to the Paper | Supervised development of work, Edited the manuscript, manuscript evaluation and Corresponding author. |
| Signature | Date 4/1/17 |

## Abstract

As an alternative to platinum (Pt), hybrid electrocatalysts based on sulfur–doped graphene with $FeS_2$ microspheres (SGN–$FeS_2$) were used as a counter electrode (CE) in dye–sensitized solar cells (DSSCs). Benefiting from the high conductivity of SGN and excellent electrocatalytic activity of the $FeS_2$, the bifunctional hybrid electrocatalyst based device displays a power conversion efficiency (PCE) of 8.1%, which is comparable to that (8.3%) of traditional Pt CE based DSSC, while also exhibiting excellent stability in ambient conditions. These characteristics, in addition to its low-cost and facile preparation, make the SGN–$FeS_2$ hybrid an ideal CE material for DSSCs.



**Keywords:** Counter electrode, dye-sensitized solar cells, doping, graphene, iron disulfide


**TOC Figure**

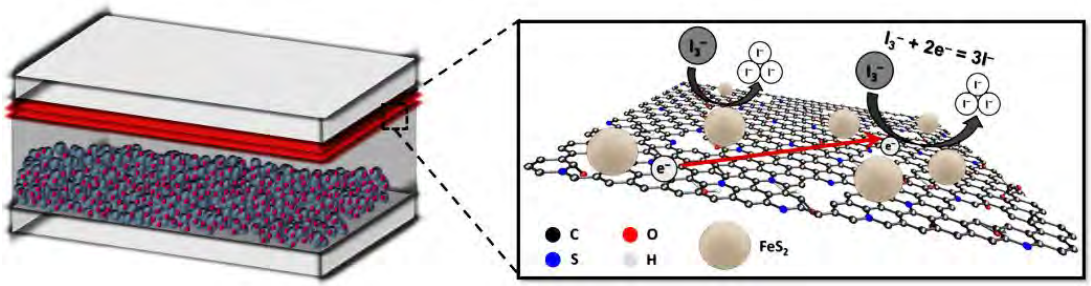

## 4.1. Introduction

Dye–sensitized solar cells (DSSCs) have attracted tremendous interest from the photovoltaic (PV) community owing to the potential they offer in terms of low manufacturing cost, high power conversion efficiency (PCE), and excellent stability.[1, 2] A typical DSSC consists of organic dye–sensitizers adsorbed onto a porous $TiO_2$ photoelectrode, an iodide/triiodide ($I^-/I_3^-$) redox electrolyte and a platinum (Pt) coated counter electrode (CE).[3] In this device structure, the Pt coated CE serves an essential role in reducing $I_3^-$ to $I^-$ (called the iodine reduction reaction, IRR). However, Pt is an expensive and relatively rare material, which limits its use in the large–scale commercialization of DSSCs.[4]

Over the past two decades, the development of alternative electrocatalysts that are low–cost and can exhibit higher or comparable performance to the conventional Pt has been the subject of intense research.[5, 6] The ideal CE materials for DSSCs should possess not only high electrical conductivity, but also excellent catalytic activity.[7] A wide range of alternative materials have been explored as electrocatalysts for IRR in DSSCs.[7-12] Graphene nanosheets doped with heteroatoms such as sulfur (S),[13] nitrogen (N),[14] boron (B),[15] phosphorous (P)[16] show great promise as the catalyst for the IRR in DSSCs owing to their high surface area and good conductivity. These alternative electrocatalysts based DSSCs have already showed excellent efficiencies that are comparable to or high than that of the corresponding control Pt CEs based devices. Among the different doping atoms, S–doped graphene (SGN) has to date yielded the most efficient electrocatalyst for IRR (also found in our preliminary investigation, see supporting information (SI)).[13, 17] This is in part due to the sulfur "S" atoms being efficient electrocatalytic active sites for the IRR.[18] This good performance is also linked to the SGN possessing enhanced electrical conductivity and improved surface area compared to un-doped graphene,[19, 20] which helps improve the charge transfer process in DSSCs. Despite these advantages, the performance of devices fabricated with SGN only based CEs are still lower than that of the Pt based CEs cells because the electrocatalytic activity of single SGN for IRR is inferior to that of Pt.

Recently, iron pyrite ($FeS_2$), a narrow band–gap semiconductor, has been shown to be a promising candidate for use as a CE material in DSSCs owing to its abundance

in nature, non–toxicity, low–cost as well as outstanding electrocatalytic activity.[21-23] Although $FeS_2$ has shown some promise as a CE material in DSSCs, its relatively low conductivity limits the further improvement of the device performances. Therefore combining the excellent catalytic activity of $FeS_2$ with the high conductivity of SGN would be a promising strategy to produce highly efficient electrocatalyst material for DSSC.

In this work, we report the preparation of Pt–free hybrid electrocatalysts, consisting of SGN nanosheets wrapped $FeS_2$, for use as CE materials in DSSCs. The DSSC device fabricated with this hybrid electrocatalyst yields a PCE of 8.1%, which was comparable to that (8.3%) of the cell using Pt. Electrochemical measurements in combination with electrical conductivity analysis reveal that this remarkable PV performance of DSSC originates from the synergistic effect of this hybrid electrocatalyst, in which $FeS_2$ provides excellent electrocatalytic activity for the IRR, while SGN facilitates the electron–transfer process (Scheme 4-1).

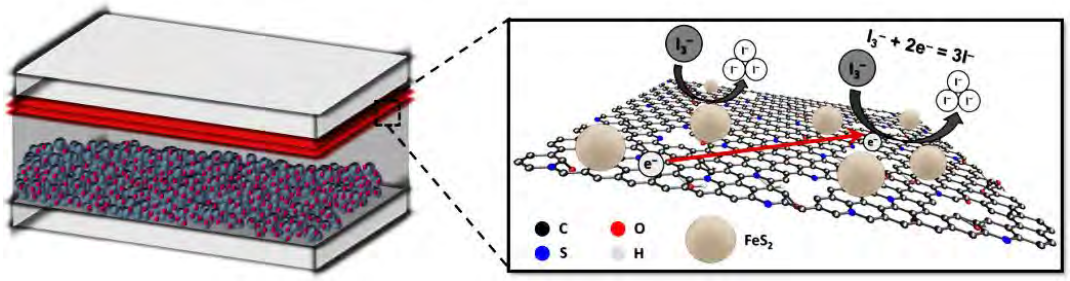


**Scheme 4-1**. Schematic illustration of DSSC device fabricated with SGN–$FeS_2$ electrocatalyst as a CE material. Note: $FeS_2$ spheres used in this scheme are from the scanning electron microscopy (SEM) images of the synthesized $FeS_2$.

## 4.2. Results and Discussion

In order to compare the doping effect of different heteroatoms on graphene in terms of their ability to catalyze the IRR in DSSC system, five individual nonmetallic elements (I, P, B, N, S) were selected and species containing each element were used to prepare single atom–doped GN materials. All the doped GN materials including I–doped GN (IGN), P–doped GN (PGN), B–doped GN (BGN), N–doped GN (NGN) and S–doped GN (SGN) were prepared from graphene oxide (GO) by using different

precursors under the same experimental conditions (details can be found in the SI, Table S4-1). These heteroatom–doped graphene electrocatalysts were then used as CE materials in DSSCs. We found that due to its good electrocatalytic activity and high conductivity, the SGN nanosheets based device showed the best PCE as compared to DSSCs with CEs made using the other heteroatom–doped GN materials (see Figure S4-1). The successful doping of sulfur atoms onto the GN nanosheets was confirmed using X–ray photoelectron spectroscopy (XPS) (Figure S4-2a and b). The morphology of the SGN nanosheets examined by scanning electron microscopy (SEM) is depicted in Figure S4-2c. Although the SGN materials exhibited the highest electrocatalytic activity and lowest charge–transfer resistance ($R_{ct}$) as compared the other doped GN nanosheets (see Table S4-2), the PCE of the DSSCs fabricated with this material was still unsatisfactory. Therefore, further work was needed to improve the performance of this single SGN electrolcatalyst.

Recent studies have demonstrated that $FeS_2$ is very promising material for DSSC application because of its excellent electrocatalytic activity.[21, 23] In this work, $FeS_2$ spheres (Figure S4-2d) were synthesized using a hydrothermal method (see experimental details in the SI).[24] In addition to XPS (see Figure S4-2e and f for detail), X–ray diffraction (XRD) analysis was used to evaluate the composition of the prepared $FeS_2$ sample. The majority of the XRD diffraction peaks in Figure 4-1a can be readily indexed to a cubic lattice of pyrite $FeS_2$ and is in good agreement with the previously published literature.[23, 25] Moreover, based on the XRD pattern, we note that some other components such as oxidized Fe and sulfur were present in the sample.

The SGN–$FeS_2$ hybrid electrocatalyst was prepared by mixing and sonicating the previously prepared SGN (Figure S4-2c) and $FeS_2$ spheres (Figure S4-2d) in an ethanol dispersion. The XRD patterns of the samples are illustrated in Figure 4-1a. The XRD of the SGN sample shows a pronounced broad peak at around $2\theta = 26°$ and a weak peak at $\approx 2\theta = 43.2°$ corresponding to the (002) and (100) diffraction planes, respectively.[14, 26] When analyzing the SGN–$FeS_2$ (40 wt % $FeS_2$) hybrid sample, XRD diffraction peaks corresponding to both SGN and $FeS_2$ throughout the sample were observed. However, the intensity of the diffraction peaks for $FeS_2$ in the hybrid was very low. This is not unexpected as the 60:40 weight ratio of SGN:$FeS_2$ corresponds to an atomic ratio on the order of 15:1 meaning the intensity of the X-

ray scattering from the carbon material, even with the lower scattering probability from the lighter element, will be much greater than the scattering from the lower amount of $FeS_2$.

The morphology of the as–prepared hybrid catalyst was examined by SEM. The SEM image in Figure 4-1b shows that the $FeS_2$ particles are wrapped by several layers of transparent silk–like SGN nanosheets. It can also be seen from Figure 4-1c that the $FeS_2$ particles are well distributed in the SGN nanosheets. Energy dispersive X–ray spectroscopy (EDX) elemental mapping was acquired to further investigate the distribution of different species in this hybrid electrocatalyst (Figure 4-1d). EDX elemental mapping confirmed that C, O, Fe and S were uniformly distributed in the SGN–$FeS_2$ hybrid sample (Figure 4-1e).

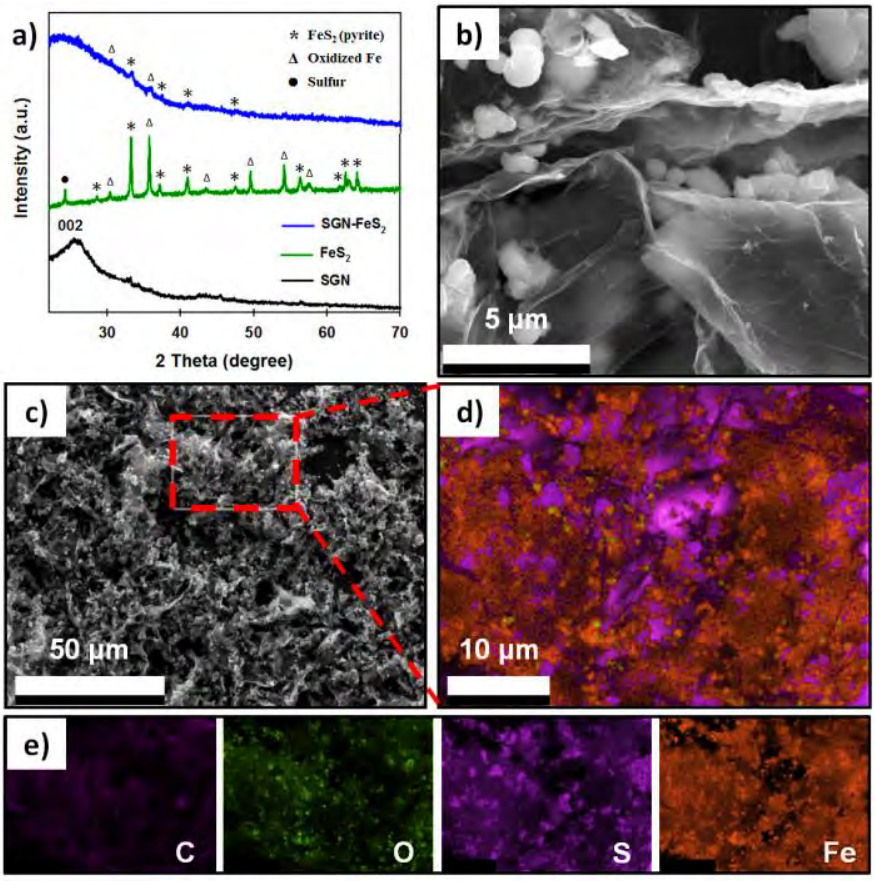


**Figure 4-1**. (a) XRD patterns of SGN, $FeS_2$ and SGN–$FeS_2$ hybrid samples. (b) High and (c) low resolution SEM image of SGN–$FeS_2$ hybrid. The red box in the inset is the selected area for EDX elemental mapping. SEM–EDX elemental mapping of (d) overlay image and (e) elemental C, O, S and Fe in the SGN–$FeS_2$ hybrid sample.

To evaluate the electrocatalytic activity of CEs based on SGN, $FeS_2$, SGN–$FeS_2$ hybrid and Pt for the IRR in the DSSC system, cyclic voltammetry (CV) measurements were carried out with a three–electrode system and recorded at the same scan rate of 50 mV $s^{-1}$. In Figure 4-2a, two pairs of oxidation and reduction peaks (Ox–A/Red–A (left) and Ox–B/Red–B (right)) are clearly observed for all samples, which can be attributed to the oxidation and reduction reactions of $I^-/I_3^-$ and $I_3^-/I_2$, respectively.[27] Since the main role of the CE in DSSCs is to catalyze the reduction of $I_3^-$ to $I^-$, which corresponds to the lower voltage pair of peaks (Ox–A and Red–A) in the CV curves, the characteristics of these peaks were the main focus of our investigation. The peak separation between the anodic and cathodic peaks ($E_{pp}$) and the peak current density are the main parameters needed to evaluate the electrocatalytic activity of CE materials.[28] In general, an ideal material for IRR – one with the highest electrocatalytic activity – should exhibit the lowest $E_{pp}$ value, while achieving the highest peak current density. As shown in Figure 4-2a, the SGN–$FeS_2$ hybrid electrode displayed an $E_{pp}$ value of 0.279 V, which was lower than that of the SGN (0.285 V) and Pt (0.345 V) (Table 4-1). We note that the $E_{pp}$ value of our Pt is consistent with recent studies.[14, 23, 27, 29, 30] Interestingly, the $FeS_2$ electrode showed an $E_{pp}$ value of as low as 0.161 V owing to its known excellent electrocatalytic activity,[21, 23] but its current density from the CV measurement was very low. To determine the mechanism for this low current density value of the $FeS_2$, we explored the sheet resistance ($R_{sheet}$) of the thin films based on our samples using a four point probe and their results are summarized in Table 4-1. We confirm that a very high $R_{sheet}$ ($1.50 \pm 0.09 \times 10_6$ Ω/□) of the $FeS_2$ is responsible for its low current density. Because of its improved electrical conductivity (see Table 4-1), the SGN–$FeS_2$ hybrid electrocatalyst based electrode exhibited a high peak current density. Higher peak current density and lower $E_{pp}$ values (see Figure 4-2a) suggest that the SGN–$FeS_2$ hybrid electrocatalyst possess excellent electrochemical activity for the IRR, which is even comparable and/or superior to that of Pt electrode. Moreover, it can be observed from Figure S4-3 that our SGN–$FeS_2$ hybrid is electrochemically stable in tri–iodide electrolyte system.

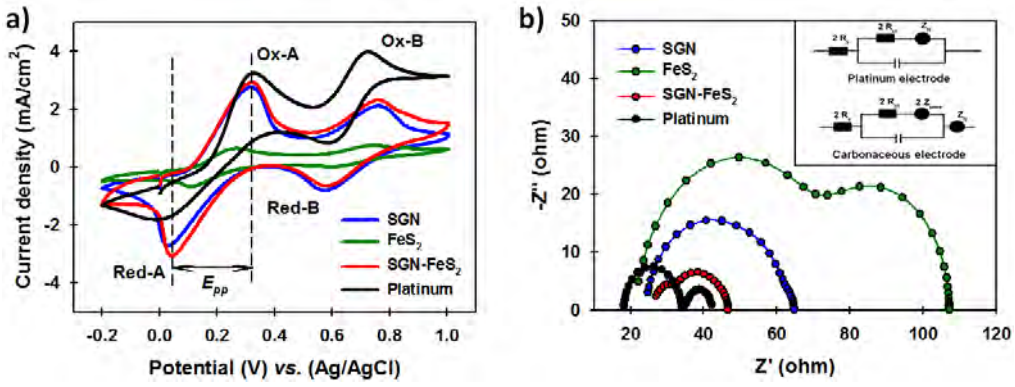


**Figure 4-2**. (a) Cyclic voltammograms (CV) of SGN, $FeS_2$, SGN–$FeS_2$ hybrid and Pt electrodes in acetonitrile solution containing 10 mM LiI, 1 mM $I_2$, and 0.1 mM $LiClO_4$ at a scan rate of 50 mV $s^{-1}$. (b) Nyquist plots of symmetric sandwich cells structure fabricated with different CE materials on FTO electrodes. Inset shows the equivalent circuit diagrams for the control Pt and other electrodes for EIS analysis.

**Table 4-1**. Detailed PV parameters of the DSSC devices fabricated based on different CE materials. Average values and the error bars are calculated based on five cells and samples. Parameters of the best cells are highlighted in bold. $E_{pp}$: peak-to-peak voltage separation was calculated from the CV measurements. $R_{ct}$: charge-transfer resistances were obtained from the EIS analysis by fitting the measured EIS data to a modelled equivalent circuit diagram. $R_{sheet}$: sheet resistances were measured using a four–point probe technique.

| Samples | $J_{sc}$, (mA cm$^{-2}$) | $V_{oc}$, (V) | FF | PCE, (%) | $E_{pp}$, (V) | $R_{ct}$, (Ω) | $R_{sheet}$, (Ω/□) |
|---|---|---|---|---|---|---|---|
| SGN | **15.96**; 15.86 ± 0.33 | **0.77**; 0.77 ± 0.01 | **0.55**; 0.52 ± 0.02 | **6.79**; 6.36 ± 0.32 | 0.285 | 22.3 | 2.37 ± 0.54 x $10^3$ |
| $FeS_2$ | **15.94**; 15.86 ± 0.37 | **0.73**; 0.74 ± 0.01 | **0.47**; 0.46 ± 0.02 | **5.51**; 5.43 ± 0.09 | 0.161 | 39.8 | 1.50 ± 0.09 x $10^6$ |
| SGN–$FeS_2$ | **16.43**; 16.51 ± 0.26 | **0.82**; 0.80 ± 0.02 | **0.60**; 0.59 ± 0.02 | **8.10**; 7.82 ± 0.26 | 0.279 | 11.2 | 4.52 ± 0.15 x $10^3$ |
| Platinum | **16.96**; 16.77 ± 0.47 | **0.81**; 0.81 ± 0.00 | **0.60**; 0.60 ± 0.01 | **8.33**; 8.13 ± 0.21 | 0.345 | 14.2 | – |

Electrochemical impedance spectroscopy (EIS) is another important technique to understand the capacity of CE materials to catalyze the IRR in DSSCs. EIS were recorded for the dummy cells consisting of a symmetrical sandwich structure (electrode/$I^-/I_3^-$ electrolyte/electrode) with SGN, $FeS_2$, SGN–$FeS_2$ hybrid and Pt as electrodes. The Nyquist plots shown in Figure 4-2b are obtained by fitting the measured EIS data to a modelled equivalent circuit diagram. Typical modelled equivalent circuit diagrams used for Pt and carbon based CEs are illustrated in the inset of Figure 4-2b. A typical Nyquist plot for CE materials for the IRR consists of two semi-circles.[28, 29, 31] The lower Z′ semicircle is attributed to the $R_{ct}$, which originates from the interface between CEs and electrolyte; whereas the higher Z′ semicircle is related to ionic diffusion impedance ($Z_N$) of the redox couples in the electrolyte.[29] Since $R_{ct}$ directly reflects to the performance of the electrocatalyst materials, the measured $R_{ct}$ values of the SGN, $FeS_2$, SGN–$FeS_2$ hybrid and Pt cells are listed in Table 4-1. Due the combination of excellent conductivity and high catalytic activity, the SGN–$FeS_2$ hybrid electrocatalyst exhibited the smallest $R_{ct}$ value (11.2 Ω), which was even slightly lower than that of Pt (14.2 Ω) and significantly lower than the values for SGN (22.3 Ω) and $FeS_2$ (39.8 Ω). The EIS results were in good agreement with the CV results. Overall, the electrochemical characterization (CV and EIS analysis) clearly indicate that our SGN–$FeS_2$ electrocatalyst could be used as a promising alternative CE to catalyze the IRR in DSSCs. Therefore, as compared to the Pt CE based devices, we expected to achieve comparable or even higher PV performance of DSSCs using this hybrid electrocatalyst based CEs.

As mentioned earlier, good CE materials should have both high catalytic activity and excellent electrical conductivity to efficiently catalyze the redox reaction and rapidly transfer the electrons in DSSCs.[7] Since our findings from the electrochemical and electrical characterization suggest that the SGN possesses excellent conductivity and $FeS_2$ has high catalytic activity, the amount (loadings) of SGN or $FeS_2$ in the hybrid would play an important role for the DSSC performance. There is clearly an optimum concentration of SGN or $FeS_2$ in the hybrid. Therefore, based on DSSC efficiencies, we optimized the concentration of the SGN or $FeS_2$ in the hybrid CEs for DSSCs and found that 60 wt% SGN and 40 wt% $FeS_2$ in the hybrid are the optimum loadings (see Figure 4-3a).

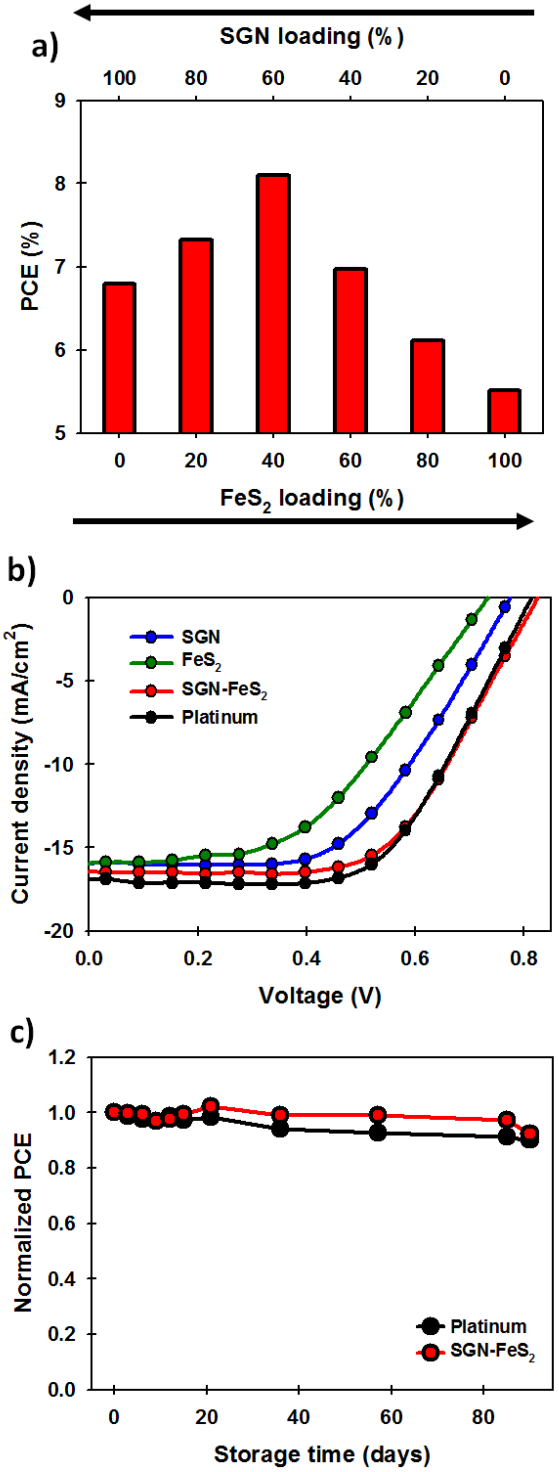


**Figure 4-3**. (a) Influence of SGN and $FeS_2$ loadings in the hybrid on the efficiency of the DSSCs. (b) J–V curves of best performing DSSCs fabricated with different CEs. (c) Normalized PCE of DSSCs fabricated with SGN–$FeS_2$ and Pt as a function of long-term storage time in ambient conditions.

Furthermore, DSSC devices were fabricated using the four electrocatalysts, namely SGN, $FeS_2$, SGN–$FeS_2$ and Pt as CE materials. The photocurrent density–voltage (J–V) characteristics of the DSSCs fabricated with these CEs are illustrated in Figure 4-3b and the corresponding PV parameters have been summarized in Table 4-1. The control DSSC fabricated with the conventional Pt CE showed a PCE of as high as 8.33% with a short–circuit current ($J_{sc}$) of 16.96 mA $cm^{-2}$, open–circuit voltage ($V_{oc}$) of 0.81 V and fill factor (FF) of 0.60. As expected, the PCEs of single SGN–only (6.79%) and $FeS_2$–only (5.51%) based DSSCs are significantly lower than the conventional Pt CE based devices. The lower PCE of the DSSCs with SGN–only, as compared to the Pt based cells, is mainly due to the lack of electrocatalytic activity, while the poor conductivity of $FeS_2$ is responsible for its poor PV efficiency. By coupling both excellent conductivity of SGN and high catalytic activity of $FeS_2$, the cell fabricated with the SGN–$FeS_2$ hybrid based CE showed a notable enhancement in the PCE as compared to the efficiencies of single SGN–only and $FeS_2$–only based DSSCs. In particular, the measured $J_{sc}$, $V_{oc}$, and FF values for this hybrid CE based DSSC were 16.43 mA $cm^{-2}$, 0.82 V, and 0.60, respectively, and a PCE of 8.10% was achieved. The results of PV performances were in line with our electrochemical characterization (CV and EIS). More importantly, this impressive PCE (8.10%) achieved by the SGN–$FeS_2$ hybrid electrocatalyst based DSSC was comparable to that (8.33%) of the expensive Pt electrocatalyst based device.

The stability of PV devices is one of the most critical factors for their potential commercialization on an industrial scale. For the storage–stability test, the unencapsulated DSSC devices fabricated with SGN–$FeS_2$ and Pt CEs were kept in ambient conditions for 90 days. Normalized PCEs of these two devices are plotted in Figure 4-3c. It can be seen from Figure 4-3c that the SGN–$FeS_2$ hybrid CE based DSSC showed excellent storage–stability (more than 90% of initial PCE after 90 days of storage was retained), which was comparable to the stability of the cell with Pt CE. This excellent stability of our SGN–$FeS_2$ hybrid based DSSC confirms the good electrochemical stability explored using CV measurements (see Figure S4-3) of this electrocatalyst.

## 4.3. Conclusion

In summary, in this work, a series of heteroatom (I, P, B, N, S)–doped graphene materials have been prepared and employed as CE materials to catalyze the IRR in DSSCs. We found based on the electrochemical characterization and PV analysis that the elemental S–doping on graphene is the most effective in improving the electrocatalytic activity among other types of doping atoms. Furthermore, we prepared highly efficient hybrid electrocatalysts by incorporating the excellent conductivity of SGN and high catalytic activity of $FeS_2$ for use in DSSCs. A device fabricated with this hybrid electrocatalyst based CE exhibited not only an excellent storage–stability, but also displayed a high PCE of 8.10%, which is comparable to that of Pt CE based DSSCs. The combination of high electrocatalytic activity, good electrical conductivity, outstanding electrochemical stability and impressive device performance of the SGN–$FeS_2$ hybrid electrocatalyst makes this material an ideal candidate for highly efficient and stable DSSCs.

## Acknowledgements

The support of the Australian Research Council Discovery Program (DP130101714, DP150101354 and DP160101301) is gratefully acknowledged. Munkhbayar Batmunkh acknowledges International Postgraduate Research Scholarship (IPRS) and Australian Postgraduate Award (APA) for their financial support during his study in Australia.We acknowledge the use of South Australian nodes of the Australian Microscopy & Microanalysis Research Facility (AMMRF) and the Australian National Fabrication Facility (ANFF) at Flinders University. The authors would also like to thank Jade Taylor and Yanting Yin of School of Chemical and Physical Sciences at Flinders University for their help with the XPS analysis.

## References

[1] S. Zhang, X. Yang, Y. Numata, L. Han, *Energy Environ. Sci.* **2013**, *6*, 1443.
[2] M. Batmunkh, M. J. Biggs, J. G. Shapter, *Adv. Sci.* **2015**, *2*, 1400025.
[3] M. Ye, X. Wen, M. Wang, J. Iocozzia, N. Zhang, C. Lin, Z. Lin, *Mater. Today.* **2015**, *18*, 155.

[4] S. Hwang, M. Batmunkh, M. J. Nine, H. Chung, H. Jeong, *ChemPhysChem.* **2015**, *16*, 53.
[5] J. Briscoe, S. Dunn, *Adv. Mater.* **2016**, *28*, 3802.
[6] M. Janani, P. Srikrishnarka, S. V. Nair, A. S. Nair, *J. Mater. Chem. A.* **2015**, *3*, 17914.
[7] H. Wang, Y. H. Hu, *Energy Environ. Sci.* **2012**, *5*, 8182.
[8] S. Thomas, T. G. Deepak, G. S. Anjusree, T. A. Arun, S. V. Nair, A. S. Nair, *J. Mater. Chem. A.* **2014**, *2*, 4474.
[9] M. Batmunkh, M. J. Biggs, J. G. Shapter, *Small.* **2015**, *11*, 2963.
[10] S. Yun, A. Hagfeldt, T. Ma, *Adv. Mater.* **2014**, *26*, 6210.
[11] J. Zhang, M. Yu, S. Li, Y. Meng, X. Wu, J. Liu, *J. Power Sources.* **2016**, *334*, 44.
[12] H. Wang, K. Sun, F. Tao, D. J. Stacchiola, Y. H. Hu, *Angew. Chem. Int. Ed.* **2013**, *52*, 9210.
[13] Q. Luo, F. Hao, S. Wang, H. Shen, L. Zhao, J. Li, M. Grätzel, H. Lin, *J. Phys. Chem. C.* **2014**, *118*, 17010.
[14] X. Meng, C. Yu, X. Song, Y. Liu, S. Liang, Z. Liu, C. Hao, J. Qiu, *Adv. Energy Mater.* **2015**, *5*, 1500180.
[15] H. Fang, C. Yu, T. Ma, J. Qiu, *Chem. Commun.* **2014**, *50*, 3328.
[16] Z. Wang, P. Li, Y. Chen, J. He, J. Liu, W. Zhang, Y. Li, *J. Power Sources.* **2014**, *263*, 246.
[17] A. G. Kannan, J. Zhao, S. G. Jo, Y. S. Kang, D.-W. Kim, *J. Mater. Chem. A.* **2014**, *2*, 12232.
[18] D. Yu, E. Nagelli, F. Du, L. Dai, *J. Phys. Chem. Lett.* **2010**, *1*, 2165.
[19] Z. Yang, Z. Yao, G. Li, G. Fang, H. Nie, Z. Liu, X. Zhou, X. a. Chen, S. Huang, *ACS Nano.* **2012**, *6*, 205.
[20] Y. Jiao, Y. Zheng, M. Jaroniec, S. Z. Qiao, *J. Am. Chem. Soc.* **2014**, *136*, 4394.
[21] Y.-C. Wang, D.-Y. Wang, Y.-T. Jiang, H.-A. Chen, C.-C. Chen, K.-C. Ho, H.-L. Chou, C.-W. Chen, *Angew. Chem. Int. Ed.* **2013**, *52*, 6694.
[22] Q.-H. Huang, T. Ling, S.-Z. Qiao, X.-W. Du, *J. Mater. Chem. A.* **2013**, *1*, 11828.
[23] S. Shukla, N. H. Loc, P. P. Boix, T. M. Koh, R. R. Prabhakar, H. K. Mulmudi, J. Zhang, S. Chen, C. F. Ng, C. H. A. Huan, N. Mathews, T. Sritharan, Q. Xiong, *ACS Nano.* **2014**, *8*, 10597.
[24] M. Zhang, B. Chen, H. Tang, G. Tang, C. Li, L. Chen, H. Zhang, Q. Zhang, *RSC Adv.* **2015**, *5*, 1417.
[25] H. Xue, D. Y. W. Yu, J. Qing, X. Yang, J. Xu, Z. Li, M. Sun, W. Kang, Y. Tang, C.-S. Lee, *J. Mater. Chem. A.* **2015**, *3*, 7945.
[26] L. Mei, H. Zhao, B. Lu, *Adv. Sci.* **2015**, *2*, 1500116.
[27] A. Shrestha, M. Batmunkh, C. J. Shearer, Y. Yin, G. G. Andersson, J. G. Shapter, S. Qiao, S. Dai, *Adv. Energy Mater* **2017**, *7*, 1602276.
[28] X. Cui, J. Xiao, Y. Wu, P. Du, R. Si, H. Yang, H. Tian, J. Li, W.-H. Zhang, D. Deng, X. Bao, *Angew. Chem. Int. Ed.* **2016**, *55*, 6708.

[29] E. Bi, H. Chen, X. Yang, W. Peng, M. Gratzel, L. Han, *Energy Environ. Sci.* **2014**, *7*, 2637.
[30] Y. Duan, Q. Tang, J. Liu, B. He, L. Yu, *Angew. Chem. Int. Ed.* **2014**, *53*, 14569.
[31] Y. Xue, J. Liu, H. Chen, R. Wang, D. Li, J. Qu, L. Dai, *Angew. Chem. Int. Ed.* **2012**, *51*, 12124.

# Supporting Information for

# Sulfur-Doped Graphene with Iron Pyrite ($FeS_2$) as an Efficient and Stable Electrocatalyst for Iodine Reduction Reaction in Dye–Sensitized Solar Cells

Munkhbayar Batmunkh,[1,2] Aabhash Shrestha,[1] Gao Guo,[3] Leping Yu,[2] Jing Zhao,[2] Mark J. Biggs,[1,4] Cameron J. Shearer,[2] Joseph G. Shapter,[2]*

[1] *School of Chemical Engineering, The University of Adelaide, Adelaide, South Australia 5005, Australia*

[2] *School of Chemical and Physical Sciences, Flinders University, Bedford Park, Adelaide, South Australia 5042, Australia*

[3] *School of Electronic Information and Electrical Engineering, Shanghai Jiao Tong University, 800 Dongchuan Road, Shanghai 200240, China*

[4] *School of Sciences, Loughborough University, Loughborough, Leicestershire, LE11 3TU, UK*

* Corresponding authors:

joe.shapter@flinders.edu.au

**Published:** *SOLAR RRL,* **2017**, *1*, 1700011

The published copy of the manuscript is attached in Appendix C.

## Experimental Section

*Materials:*

Unless otherwise specified, all chemicals used in this work were obtained from Sigma–Aldrich. Sodium hydroxide (NaOH) (purity >98%) and sulfur (S) (purity >98%) powders were purchased from Chem–Supply Pty Ltd. Ruthenizer 535–bisTBA (N719 dye), iodide/tri–iodide electrolyte (Iodolyte Z–50), DuPont Surlyn® (Meltonix 1170–60) and Platinum (Pt) catalyst (Platisol T) were purchased from Solaronix, Switzerland. A fluorine–doped tin oxide (FTO) coated glass electrodes with a sheet resistance ($R_s$) of ~8 Ω/□ (TEC8), transparent $TiO_2$ paste (18NR–T), reflector $TiO_2$ paste (WER2–O) were purchased from Dyesol, Australia.

*Preparation of graphene oxide (GO):*

Graphene oxide (GO) was prepared *via* the oxidation and exfoliation of natural graphite according to an improved Hummers method reported by Marcano et al.[1] In brief, a 9:1 (*v:v*) mixture of sulfuric acid (95–98% $H_2SO_4$) and phosphoric acid (85% $H_3PO_4$) (240:27 mL) was kept in the cold (3–5$^oC$) until it was added to a mixture of graphite flakes (2 g) and potassium permanganate (99% $KMnO_4$) (12 g). The oxidation process of graphite was carried out by stirring the mixture at ~50 $^oC$ for 12 h. Then, the reaction was cooled down to room temperature and poured onto ice (300 mL) with 30% hydrogen peroxide ($H_2O_2$) (2 mL). The mixture was then washed with distilled (DI) water, 30% hydrochloric acid (HCl) and ethanol (x 2 times). For each sequential wash, the product was centrifuged at 4400 rpm for 3 h and the supernatant decanted away. The light brown sample obtained was dispersed and exfoliated in an aqueous solution, and then freeze–dried to obtain GO powder.

*Preparation of heteroatom–doped graphene:*

Different heteroatoms (I, P, B, N, S)–doped graphene were prepared by the carbonization of the mixture of GO and dopant precursor in a programmable tube furnace under $N_2$ atmosphere using a previously established method.[2] Typically, 100 mg of GO and 500 mg of precursor (see Table S4-1 for the types of dopant precursors) were ground in a ceramic mortar to form the mixture powder of GO and

precursor. The mixture was then poured into a crucible and carbonized at 900 $^{o}$C for 3 h with a heating rate of 5 $^{o}$C min$^{-1}$. The calcination process includes five steps: 1) purge the tube furnace with $N_2$ gas at room temperature for 30 min, 2) increase the temperature to 120 $^{o}$C, 3) Hold at 120 $^{o}$C for 2 hr to remove moisture in the GO, 4) Increase the temperature to 900 $^{o}$C, 5) Hold at 900 $^{o}$C for 3 hrs, followed by cooling down to room temperature. The heating ramp for all heating and/or calcining processes was 5 $^{o}$C min$^{-1}$.

*Preparation of $FeS_2$ particles:*

The $FeS_2$ partciles were synthesized using a hydrothermal method according to a previously reported method with slight modifications.[3] In a typical experiment, Polyvinylpyrrolidone (PVP) and poly (ethylene glycol) (PEG–6000) (1.5 : 1 weight ratio) were dissolved in 10 mL DI water and stirred for 15 min to obtain a completely dissolved transparent solution. 2.2 g $FeCl_2 \cdot 4H_2O$ was then added into the above solution, followed by gradual addition of 10 mL NaOH solution (0.5 M) with stirring. Then, 0.2 g S powder was also added into the solution, followed by stirring and sonication three times. After obtaining a well dissolved precursor solution, the sample was transferred into a hydrothermal reactor and heated to 200 $^{o}$C for 12 h. After the reaction, the obtained sample was filtered, washed with DI water and ethanol, and dried for further use.

*Preparation of pastes and counter electrodes:*

Viscous pastes based on different electrocatalysts including GO, GN, IGN, PGN, BGN, NGN, SGN, $FeS_2$ and SGN–$FeS_2$ hybrid were prepared according to the established procedures described in the literature without any modification.[4] For the preparation of hybrid pastes, the concentrations of SGN or $FeS_2$ in the hybrid were varied from 0 to 100 wt% with an interval of 20 wt% (*e.g.* weight ratio of 100% : 0%, 80% : 20%, 60% : 40%, 40% : 60%, 20% : 80%, and 0% : 100%,). The as–prepared pastes were sonicated for 5 min before use and then coated onto the cleaned FTO electrodes via a doctor blade technique. The FTO glass was cleaned with a detergent followed by washing with Milli–Q water, acetone and ethanol under ultrasonication for 10 min each before use. After the paste deposition onto the FTO

electrodes, the films were dried in an oven at 90 $^{o}$C for 5–10 min and annealed at 420 $^{o}$C for 30 min under the protection of Argon gas. In the meantime, for comparison, Pt CEs were prepared by coating Pt precursor onto FTO substrates using a brush–painting method, followed by platinizing at 450 $^{o}$C for 20 min. Finally, the prepared counter electrodes (CEs) were cooled to room temperature.

*Device fabrication:*

The N719 dye–sensitized solar cell devices were fabricated as reported elsewhere.[5] Briefly, the cleaned FTO glass electrodes were first immersed into a 40 mM aqueous $TiCl_4$ solution at 70 $^{o}$C for 30 min, and rinsed with water and ethanol. Then, ~10 μm thick transparent $TiO_2$ layers (Dyesol 18NR–T, 20 nm in diameter) were deposited on the FTO electrodes by a doctor blading technique. The transparent $TiO_2$ films were gradually heated under an air flow at 125 $^{o}$C for 5 min, 325 $^{o}$C for 5 min, at 375 $^{o}$C for 15 min and at 450 $^{o}$C for 30 min, followed by cooling to room temperature. Then, ~6 μm thick reflector $TiO_2$ layers (Dyesol WER2–O, 150–250 nm in diameter) were coated on the transparent $TiO_2$ layers. The photoelectrodes coated with transparent and reflector $TiO_2$ layers were sintered at 500 $^{o}$C for 1 h. After sintering, the photoelectrodes were immersed in aqueous $TiCl_4$ (40 mM) solution at 70 $^{o}$C for 30 min, followed by final annealing at 500 $^{o}$C for 1 h. After cooling to ~50 $^{o}$C, the prepared $TiO_2$ films were immersed into 0.5 mM N719 dye in an ethanol solution for 20 h at room temperature. The dye adsorbed photoelectrodes and previously prepared CEs were assembled into a sealed sandwich–type cell, with a 60 μm thick hot–melt sealing Surlyn between each layer. The electrolyte solution, Iodolyte Z–50 (Solaronix), was introduced into the cell via a vacuum–filling method through an injection hole on the CE side. Finally, the hole was sealed with scotch tape.

*Characterization and measurements:*

Scanning electron microscopy (SEM) images were obtained using an Inspect F50 SEM (FEI) with accelerating voltage of 20 kV. Energy dispersive X–ray spectroscopy (EDX) elemental mapping analysis was completed on the same system with a Team EDS Octane Pro (EDAX) attachment. X–ray diffraction (XRD) patterns were carried out on a powder X–ray diffractometer at 40 kV and 15 mA in the range

of $2\theta$ = 10–80° using Cu K$\alpha$ radiation (Model Miniflex 600, Rigaku, Japan). X–ray photoelectron spectroscopy (XPS) using a Leybold Heraeus LHS–10 with a SPECS XR–50 dual anode source operating at 250W was carried out at binding energy ranging from 0 eV to 1200 eV. The Mg–Kα source, which has energy of 1253.6 eV, was used for the XPS analysis. Curve fitting of the XPS spectra was done using peak fitting software "CASA XPS". High resolution XPS spectra were collected with a step size of 0.1 eV and the presented spectra are an average of 5 collections. The XPS spectra were referenced to the carbon 1s peak at 284.5 eV.

Both cyclic voltammetry (CV) and electrochemical impedance spectroscopy (EIS) measurements were performed using an electrochemical analysis workstation (Autolab Nova Potentiostat). The CV was carried out in a three electrode system with different CE materials as the working electrode, a platinum wire as the CE, and $Ag/Ag^+$ electrode as the reference electrode, at a scan rate of 50 mV $s^{-1}$. For the preparation of the working electrode, 15 μL ink of each sample was dropped on the mirror polished glassy carbon electrodes. The electrodes were dipped in an anhydrous acetonitrile solution containing 10 mM LiI, 1 mM $I_2$, and 0.1 mM $LiClO_4$. EIS measurements were carried out by scanning the symmetric cells with the structure of CE/electrolyte/CE. The resultant EIS spectra were analyzed by means of the Z–view software.

Sheet resistance measurements were performed on the SGN, $FeS_2$ and SGN–$FeS_2$ hybrid coated microscope slides using a four point probe technique (KeithLink Technology Co., Ltd. Taiwan).

The photocurrent–voltage (*J–V*) characteristics were analyzed using a Keithley 2400 SMU instrument and recorded using a custom LabView Virtual Instrument program. A standard silicon test cell with NIST-traceable certification was used to calibrate the power density as 100 mW $cm^{-2}$ at the sample plane of the collimated a 150W xenon–arc light source (Newport), which was passed through an AM 1.5G filter. The active area of the fabricated devices was 0.19 $cm^2$.

**Table S4-1**. Experimental conditions and parameters for the preparation of different heteroatoms doped graphene electrocatalysts. For the preparation of all samples, graphene oxide ((GO), prepared from natural graphite using improved synthesis method) was used as a starting material. The weight ratio of GO : precursor was 1 : 5 for all samples.

| Samples | Doping Precursor | Annealing Temperature | Annealing Time | Gas |
|---|---|---|---|---|
| Graphene Oxide | - | - | - | - |
| Graphene | - | 900°C | 3 h | $N_2$ |
| I-doped Graphene | Iodine ($I_2$) | 900°C | 3 h | $N_2$ |
| P-doped Graphene | Triphenylphosphine ($C_{18}H_{15}P$) | 900°C | 3 h | $N_2$ |
| B-doped Graphene | Boric Acid ($H_3BO_3$) | 900°C | 3 h | $N_2$ |
| N-doped Graphene | Melamine ($C_3H_6N_6$) | 900°C | 3 h | $N_2$ |
| S-doped Graphene | Diphenylsulfide ($C_{12}H_{10}S_2$) | 900°C | 3 h | $N_2$ |

Five individual nonmetallic elements (I, P, B, N, S) were introduced onto GN nanosheets to obtain single atom-doped GN materials. These materials (IGN, PGN, BGN, NGN and SGN) were prepared from GO by using different types of precursors under the same experimental conditions (see Table S4-1). GO was prepared via the oxidation of natural graphite according to an improved Hummers method.[1]

The prepared heteroatom–doped GN materials were used to fabricate DSSC devices. It should be noted that the thickness of mesoporous $TiO_2$ layer in these DSSCs was ~9–10 μm achieved by using 1 layer of 3M scotch tape. This thin $TiO_2$ layer resulted in slightly lower short-circuit current ($J_{sc}$) value (see Figure S4-1 and Table S4-2) and was intentionally used in order to compare these various types of doped graphene CEs for DSSCs.

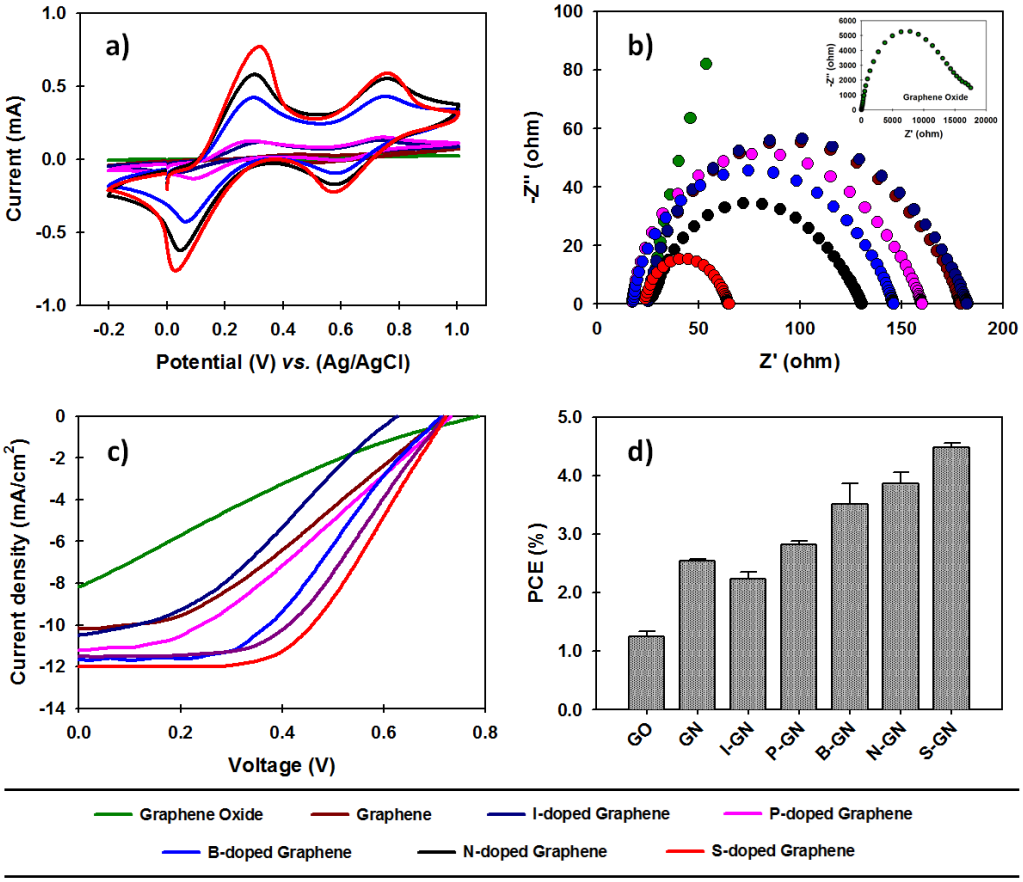


**Figure S4-1**. (a) Cyclic voltammograms (CV) and (b) electrochemical impedance spectra (EIS) of various heteroatoms doped graphene (GN) electrodes for IRR. Inset shows the EIS of graphene oxide (GO). (c) Photocurrent-voltage (J–V) curves and (d) PCE comparison of DSSC devices fabricated with different heteroatoms doped graphene based counter electrodes (CEs). Note: These devices were fabricated based on only ~9–10 µm $TiO_2$ mesoporous layer (without light scattering layer).

High-resolution X-ray photoelectron spectroscopy (XPS) spectra for the C 1s and S 2p regions of the SGN sample are shown in Figure S4-2a and b, respectively. The C 1s peak for the SGN material was observed at ~284.5 eV, which is consistent with graphene $sp^2$ carbon in the samples.[6,7] Moreover, there are some minor shoulder contributions to the XPS signals at binding energies of 285.0–288.0 eV, which can be assigned to sulfur- and/or oxygen-bound carbon atoms on the surface of SGN nanosheets.[8] Another broad peak at binding energies of 287.0–290.0 eV is assigned to the C=O and O–C=O chemical environments, which is in agreement with previous literature.[9] The broad signals at 290.0–292.0 eV correspond to the $\pi$–$\pi^*$ shake-up

peak. The main peaks in the S 2p for the XPS spectra of SGN material are at binding energies of around 163.7 eV and 164.9 eV can be attributed to the spin-orbit splitting of S atoms doped onto the graphene layers, *e.g.* S dominated in the graphene via the formation of the sulfide bridges. This result is in very good agreement with the literature.[10,11]

**Table S4-2**. Photovoltaic (PV) parameters of different heteroatoms doped graphene CEs based DSSCs. Note: These devices were fabricated based on only ~9–10 μm $TiO_2$ mesoporous layer (without light scattering layer). The average values and standard deviations are calculated based on at least three devices. Parameters of the best cells are highlighted in bold. The charge transfer resistances ($R_{ct}$) were calculated by fitting the electrochemical impedance spectra (EIS) of dummy cells with a symmetric sandwich-like structure fabricated with different CE materials.

| Samples | $J_{sc}$ (mA $cm^{-2}$) | $V_{oc}$ (V) | FF | PCE (%) | $R_{ct}$ (Ω) |
|---|---|---|---|---|---|
| Graphene Oxide | **8.158**; 8.49 ± 0.76 | **0.786**; 0.76 ± 0.03 | **0.21**; 0.19 ± 0.02 | **1.34**; 1.25 ± 0.09 | 3100 |
| Graphene | **10.154**; 9.96 ± 0.28 | **0.719**; 0.73 ± 0.02 | **0.35**; 0.35 ± 0.00 | **2.58**; 2.54 ± 0.04 | 92.4 |
| I-doped Graphene | **10.487**; 10.79 ± 0.43 | **0.629**; 0.61 ± 0.02 | **0.35**; 0.34 ± 0.01 | **2.32**; 2.24 ± 0.11 | 94.2 |
| P-doped Graphene | **11.168**; 11.06 ± 0.11 | **0.733**; 0.73 ± 0.01 | **0.35**; 0.35 ± 0.00 | **2.88**; 2.83 ± 0.05 | 83.3 |
| B-doped Graphene | **11.622**; 11.32 ± 0.42 | **0.714**; 0.71 ± 0.01 | **0.45**; 0.44 ± 0.02 | **3.75**; 3.51 ± 0.35 | 70.9 |
| N-doped Graphene | **11.493**; 11.55 ± 0.07 | **0.721**; 0.71 ± 0.01 | **0.49**; 0.47 ± 0.02 | **4.09**; 3.87 ± 0.19 | 44.0 |
| S-doped Graphene | **11.970**; 11.92 ± 0.09 | **0.723**; 0.72 ± 0.01 | **0.53**; 0.53 ± 0.01 | **4.60**; 4.49 ± 0.07 | 22.3 |

The Fe 2p and S 2p spectra are illustrated in Figure S4-2e and f, respectively. In Figure S4-2e, there are two predominant peaks at binding energies of around 707 eV (Fe $2p_{3/2}$) and 720.0 eV (Fe $2p_{1/2}$), which are consistent with the binding energies of Fe in the Fe(II)–S bond.[12] Furthermore, in Figure S4-2f, the $2p_{3/2}$ and S $2p_{1/2}$ peaks at around 163 eV and 164.2 eV, respectively are also consistent with the sulfur binding energy in the $FeS_2$.[13]

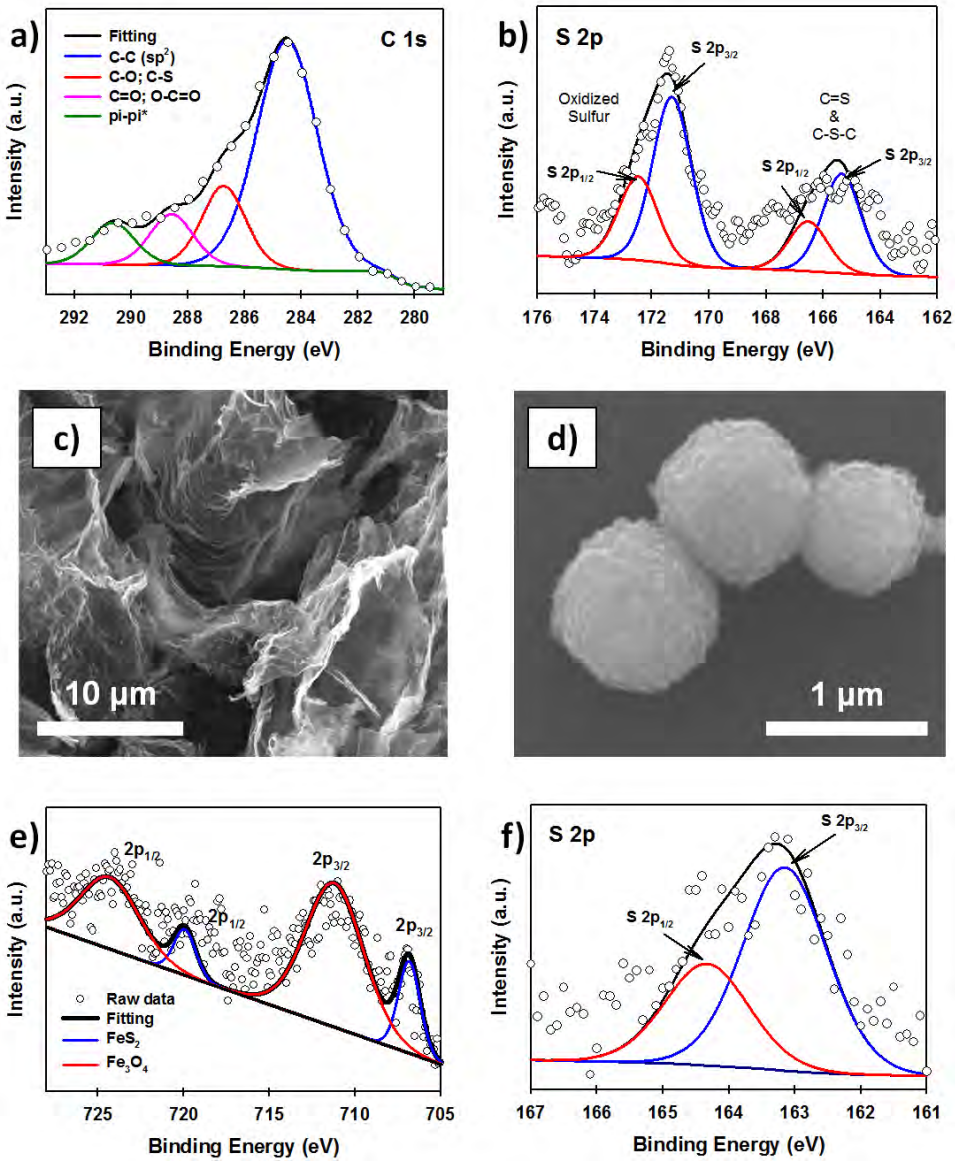


**Figure S4-2**. (a) C 1s and (b) S 2p XPS spectra of SGN sample. SEM image of (c) SGN nanosheets and (d) $FeS_2$ spheres. (e) Fe 2p and (f) S 2p XPS spectra of the as–prepared $FeS_2$.

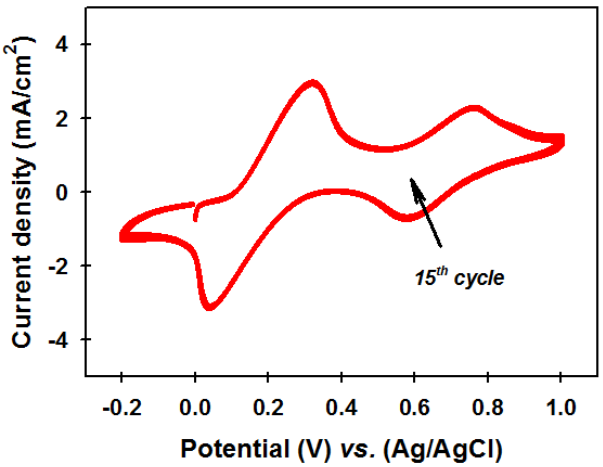


**Figure S4-3**. Electrochemical stability of SGN–$FeS_2$ hybrid electrocatalyst tested by measuring CV for 15 cycles.

## References


[1] D. C. Marcano, D. V. Kosynkin, J. M. Berlin, A. Sinitskii, Z. Sun, A. Slesarev, L. B. Alemany, W. Lu, J. M. Tour, *ACS Nano.* **2010**, *4*, 4806.

[2] Y. Jiao, Y. Zheng, M. Jaroniec, S. Z. Qiao, *J. Am. Chem. Soc.* **2014**, *136*, 4394.

[3] M. Zhang, B. Chen, H. Tang, G. Tang, C. Li, L. Chen, H. Zhang, Q. Zhang, *RSC Adv.* **2015**, *5*, 1417.

[4] J. D. Roy-Mayhew, G. Boschloo, A. Hagfeldt, I. A. Aksay, *ACS Appl. Mater. Interfaces.* **2012**, *4*, 2794.

[5] M. Batmunkh, M. Dadkhah, C. J. Shearer, M. J. Biggs, J. G. Shapter, *Energy Technol.* **2016**, *4*, 959.

[6] W. Li, Z. Zhang, Y. Tang, H. Bian, T.-W. Ng, W. Zhang, C.-S. Lee, *Adv. Sci.* **2016**, *3*, 1500276.

[7] S. Chen, J. Duan, J. Ran, S.-Z. Qiao, *Adv. Sci.* **2015**, *2*, 1400015.

[8] Q. Xu, P. Pu, J. Zhao, C. Dong, C. Gao, Y. Chen, J. Chen, Y. Liu, H. Zhou, *J. Mater. Chem. A.* **2015**, *3*, 542.

[9] J. Balamurugan, T. D. Thanh, N. H. Kim, J. H. Lee, *Adv. Mater. Interf.* **2016**, *3*, 1500348.

[10] J. Wang, R. Ma, Z. Zhou, G. Liu, Q. Liu, *Sci. Rep.* **2015**, *5*, 9304.

[11] Q. Luo, F. Hao, S. Wang, H. Shen, L. Zhao, J. Li, M. Grätzel, H. Lin, *J. Phys. Chem. C.* **2014**, *118*, 17010.

[12] P. Bonnissel-Gissinger, M. Alnot, J.-J. Ehrhardt, P. Behra, *Environ. Sci. Technol.* **1998**, *32*, 2839.

[13] X. Wen, X. Wei, L. Yang, P. K. Shen, *J. Mater. Chem. A.* **2015**, *3*, 2090.

# Chapter 5.

# Solution Processed Graphene Structures for Perovskite Solar Cells

Munkhbayar Batmunkh,[1,2] Cameron J. Shearer,[2] Mark J. Biggs,[1,3] Joseph G. Shapter,[2]*

[1] *School of Chemical Engineering, The University of Adelaide, Adelaide, South Australia 5005, Australia*

[2] *School of Chemical and Physical Sciences, Flinders University, Bedford Park, Adelaide, South Australia 5042, Australia*

[3] *School of Sciences, Loughborough University, Loughborough, Leicestershire, LE11 3TU, UK*

* Corresponding authors:

joe.shapter@flinders.edu.au

**Published:** *Journal of Materials Chemistry A*, **2016**, *4*, 2605-2616

The published copy of the manuscript is attached in Appendix D.

# Statement of Authorship

| | |
|---|---|
| Title of Paper | Solution processed graphene structures for perovskite solar cells |
| Publication Status | ☑ Published ☐ Accepted for Publication<br>☐ Submitted for Publication ☐ Unpublished and Unsubmitted w ork w ritten in manuscript style |
| Publication Details | Munkhbayar Batmunkh, Cameron J. Shearer, Mark. J. Biggs, and Joseph G. Shapter, *Journal of Materials Chemistry A*, **2016**, *4*, 2605-2616. |

## Principal Author

| | |
|---|---|
| Name of Principal Author (Candidate) | Munkhbayar Batmunkh |
| Contribution to the Paper | Conducted the experimental works, performed analysis on all samples, interpreted data and wrote manuscript. |
| Overall percentage (%) | 75% |
| Certification: | This paper reports on original research I conducted during the period of my Higher Degree by Research candidature and is not subject to any obligations or contractual agreements with a third party that would constrain its inclusion in this thesis. I am the primary author of this paper. |
| Signature | Date 30/12/2016 |

## Co-Author Contributions

By signing the Statement of Authorship, each author certifies that:

i. the candidate's stated contribution to the publication is accurate (as detailed above);

ii. permission is granted for the candidate in include the publication in the thesis; and

iii. the sum of all co-author contributions is equal to 100% less the candidate's stated contribution.

| | |
|---|---|
| Name of Co-Author | Dr. Cameron J. Shearer |
| Contribution to the Paper | Sample characterization, edited the manuscript, and manuscript evaluation. |
| Signature | Date 4/1/17 |

| | |
|---|---|
| Name of Co-Author | Prof. Mark J. Biggs |
| Contribution to the Paper | Co-advised the development of work, and manuscript evaluation. |
| Signature | Date 12/1/17 |

| | | | |
|---|---|---|---|
| *Name of Co-Author* | Prof. Joseph G. Shapter | | |
| *Contribution to the Paper* | Supervised development of work, Edited the manuscript, manuscript evaluation and Corresponding author. | | |
| *Signature* | | Date | 4/1/16 |

# Abstract

Organometallic trihalide perovskite light absorber based solar cells have drawn increasing attention because of their recent rapid increase in power conversion efficiency (PCE). These photovoltaic cells have relied significantly on transparent conducting oxide (TCO) electrodes which are costly and brittle. Herein, solution processed transparent conductive graphene films (TCGFs) are utilized, for the first time, as an alternative to traditional TCO electrodes as the electron collecting layer in perovskite solar cells (PSCs). By investigating and optimizing the trade-off between transparency and sheet resistance ($R_s$) of the graphene films, a PCE of 0.62% is achieved. This PCE is further improved to 0.81% by incorporating graphene structures into both compact and mesoporous $TiO_2$ layers of the solar cell. We anticipate that the present study will lead to further work to develop graphene-based transparent conductive electrodes for future solar cell devices.



**Keywords:** Perovskite solar cells, photoelectrode, transparent conductive film, graphene, nanocomposite


**TOC Figure**

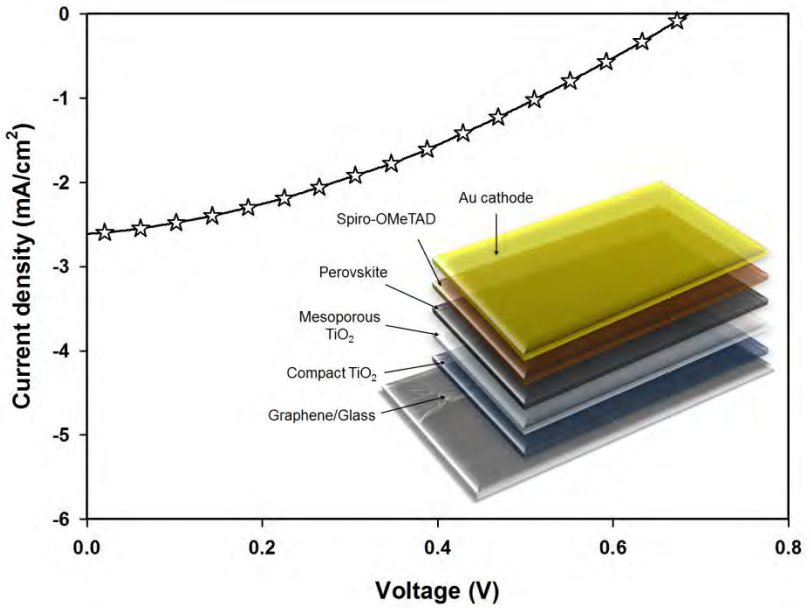

## 5.1. Introduction

Photovoltaic (PV) cells are devices that convert sunlight directly into electrical power and have great potential to meet society's continuously increasing energy demands with negligible environmental impact.[1] The current PV market is mainly dominated by crystalline silicon (1st generation) and compound semiconductor (2nd generation) based solar cells, which can produce energy with a power conversion efficiency (PCE) that is highest of all solar cell technologies.[2, 3] These commercially available solar devices are, however, produced using complex, high-cost manufacturing processes. Recently reported solar cells based on hybrid organometallic halide perovskites are considered the most promising alternatives to the more established solar cell technologies because of their relatively high PCE, and simpler, cheaper fabrication processes.[4-7]

Organic–inorganic halide structures (such as $CH_3NH_3PbX_3$ (X = Cl, I or Br)), called perovskite materials, have been known for several decades and have recently attracted much attention from the PV community owing to some key exceptional properties.[8] These properties include the ability to absorb significant levels of incident light across a wide part of the solar spectrum, and the ability to effectively carry the photoelectrons created from the incident light away into a circuit.[9] The PCE of perovskite solar cells (PSCs) has rapidly increased from less than 4% to more than 20% in only 6 years,[10-13] making the efficiency comparable with current commercial technologies.[12, 13]

A typical PSC is composed of a transparent conducting oxide (TCO) (indium-doped and/or fluorine-doped tin oxide (ITO or FTO)) electrode, a thin compact hole blocking ($TiO_2$) layer, a perovskite layer with or without a porous metal oxide scaffold layer, a hole transporting layer (HTL) and a metal contact (Au or Ag).[11, 14, 15] In such a device structure, the TCO electrode plays a vital role in collecting electrons from the semiconducting $TiO_2$ and transferring them to the external circuit. However, limited resources of the materials used in typical TCO electrodes and consequent high cost are major issues.[16] Additionally, their brittle nature and high structural defects are a major concern for PSC technologies where ease of transportation, handling and installation are important.[17] Therefore, the replacement of TCO electrodes with cheaper and robust alternatives is desirable.

Graphene has attracted considerable interest for potential applications in various optoelectronic devices due to its properties including excellent conductivity, low cost and high flexibility.[18, 19] Moreover, compared to ITO and FTO, graphene has several advantages such as abundance, high transparency in the near-infrared region and high stability in the presence of acid or base.[16, 20] These unique properties suggest graphene films could be a possible replacement for TCO electrodes. To date, two main processes have been developed for the fabrication of graphene films.[21] The first is based on chemical vapor deposition (CVD) of graphene using a metal sheet catalyst (Cu or Ni), followed by transfer printing to target substrates. However, CVD is expensive and its operation is complicated while it also requires high temperatures (>750$^{o}$C). Alternatively, solution processed graphene has been considered a promising future electrode material because it can be deposited on large-area flexible substrates and is compatible with roll-to-roll manufacturing techniques.[22] Based on these advantages, solution processed graphene films have been used as transparent electrodes for inorganic-organic hybrid solar cells,[23, 24] organic photovoltaic cells,[25, 26] and dye-sensitized solar cells (DSSCs)[27]. In addition, CVD processed-graphene based transparent conductive films have very recently been employed as hole collecting electrodes in PSCs even though they are costly and difficult to produce.[28, 29] However, until now, there has been no effort in the application of graphene based transparent and conductive films to replace traditional TCO electrodes in PSCs despite recent reviews[30, 31] and a computational study[32] suggesting some promise.

In the work reported here, transparent conductive graphene films (TCGFs) prepared from low-temperature processed and chemically derived graphene (or solution processed graphene, Scheme 5-1) have been employed as a substitute for the electron collecting TCO electrode to test their feasibility in PSCs. Furthermore, the incorporation of graphene structures into semiconducting oxide scaffolds has been shown to be a promising strategy to enhance the efficiency in DSSCs.[33] After optimizing sheet resistance ($R_s$) and light transmittance for PSC performance, we further improved the PCE by employing graphene into both compact and mesoporous $TiO_2$ layers of the devices.

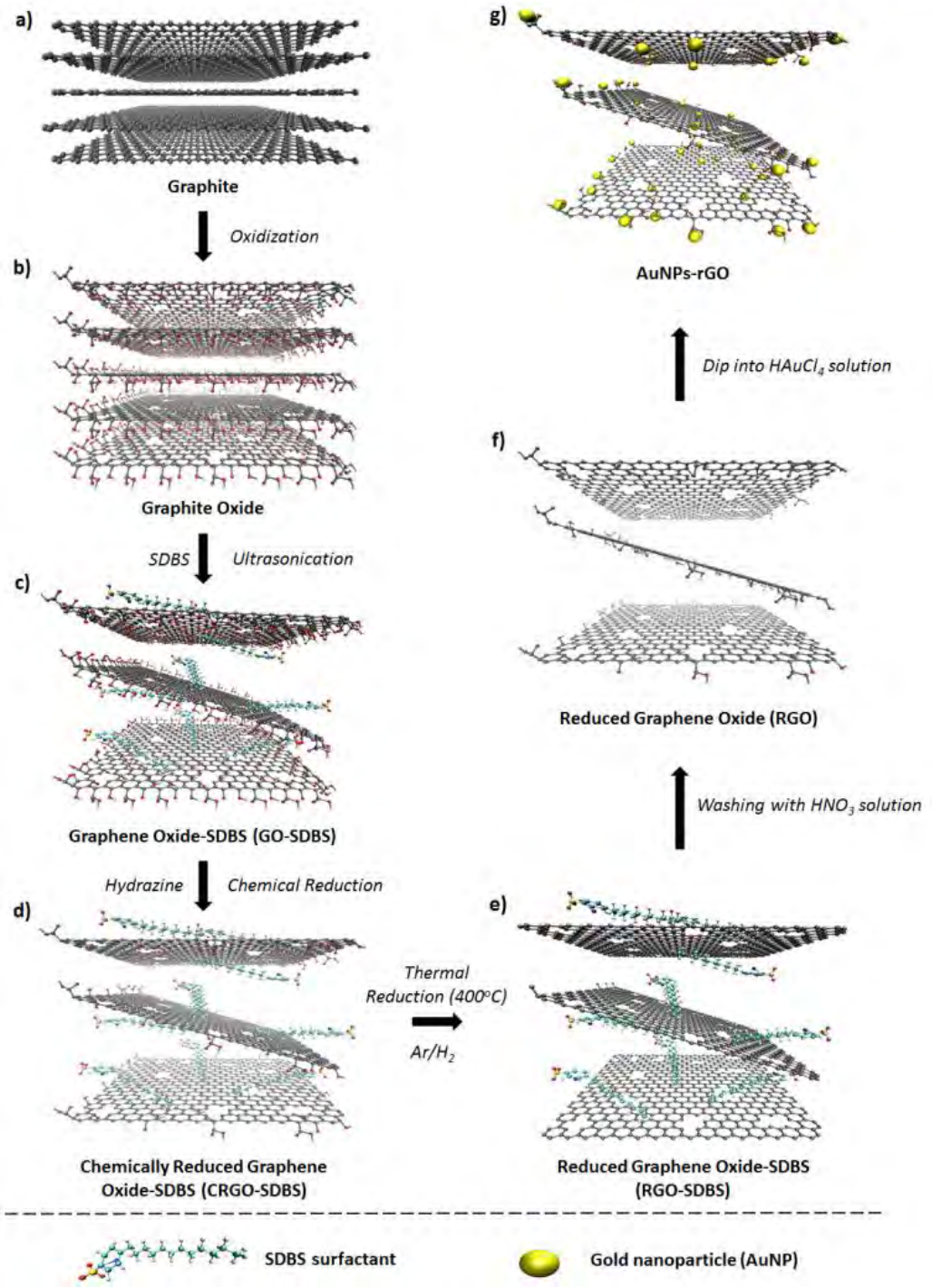


**Scheme 5-1**. Schematic of the preparation procedure of graphene films.

## 5.2. Results and Discussion

### 5.2.1. Preparation and characterization of graphene films

Graphite oxide was synthesized from natural graphite by an improved Hummers method followed by exfoliation to produce graphene oxide (GO) sheets (Scheme

5-1a-c).[34] A detailed description of the process is given in the experimental section. The prepared GO is known to be electrically non-conductive and the removal of its functional groups is necessary to obtain conductive graphene-based materials.[17] In general, GO can be reduced by using chemical agents such as hydrazine or sodium borohydride.[35] However, the insolubility of the GO after such chemical reduction limits its further application. In order to tackle this limitation, we added sodium dodecylbenzene sulfonate (SDBS) surfactant into the graphite oxide solution before the exfoliation step (Scheme 5-1c).[36, 37]

In a typical experiment, large-area GO with or without SDBS surfactant was produced by the exfoliation of the previously prepared graphite oxide solution (Scheme 5-1c). It should be noted that the prepared GO aqueous dispersion was very stable without any precipitation for several months, which is known to be due to the presence of hydrophilic groups (e.g., hydroxyl, epoxy, or carboxyl) on the surface of graphene.[21] Subsequently, the chemical reduction of GO aqueous solution was carried out with hydrazine solution in the presence of SDBS. For comparison, the same procedure was also performed in the absence of SDBS. Chemically reduced graphene oxide (CRGO-only) without surfactant disperses poorly in aqueous conditions because of its hydrophobic surface after the removal of oxygen containing functional groups during the reduction process.[23] Subsequently, strong π-π interaction between CRGO flakes leads to agglomeration and poor dispersion (inset of Figure 5-1a). The atomic force microscopy (AFM) image in Figure 5-1a shows that the CRGO-only flakes without SDBS are aggregated or stacked on each other and their lateral size was measured to be smaller than 1 μm, which is consistent with the results reported in the literature.[38, 39] In contrast, the SDBS supported CRGO (Scheme 5-1d, termed "CRGO-SDBS") showed dramatically improved dispersion in aqueous solution. As illustrated in the inset of Figure 5-1b, no precipitate was observed and the solution was stable for several months. More importantly, the flake size of the CRGO-SDBS (Figure 5-1b) was significantly larger than that of CRGO-only (Figure 5-1a).[40] It is known that sonication and conventional chemical reduction steps of GO create many structural defects and decrease the flake size and increase the degree of $sp^3$ hybridization.[21] Interestingly, in this study, the SDBS acts to prevent CRGO from fracturing during ultrasonication resulting in large-size graphene sheets. The large-sized graphene structures should, in principle, exhibit

lower $R_s$ when used in transparent conductive films because the larger flakes will have less charge scattering related to charge hopping through sheet-sheet contacts in the film.[41, 42]

Structural information for these samples was obtained using Raman spectroscopy. It is well known that the intensity ratio ($I_D/I_G$) is usually used to determine the level of defects.[43] Raman spectra (see Figure S5-1) shows that the $I_D/I_G$ value of the CRGO-SDBS is lower than that of the CRGO without surfactant, confirming that the chemical (hydrazine) reduction of GO in the presence of SDBS creates less defects on the CRGO compared to the number produced without any surfactant present. Although the use of SDBS during the chemical reduction process has the additional advantage of preventing defect production in the CRGO and providing large graphene sheets, the presence of residual SDBS surfactant may degrade the electrical properties of the graphene films because of its highly insulating nature.[36] Therefore, removing SDBS surfactant from the prepared films is of great importance for maximizing the electrical conductivity of the films. In addition, it is well known that the chemical reduction with hydrazine alone is not sufficient to fully reduce the oxygen containing functional groups from the graphene layers.[44]

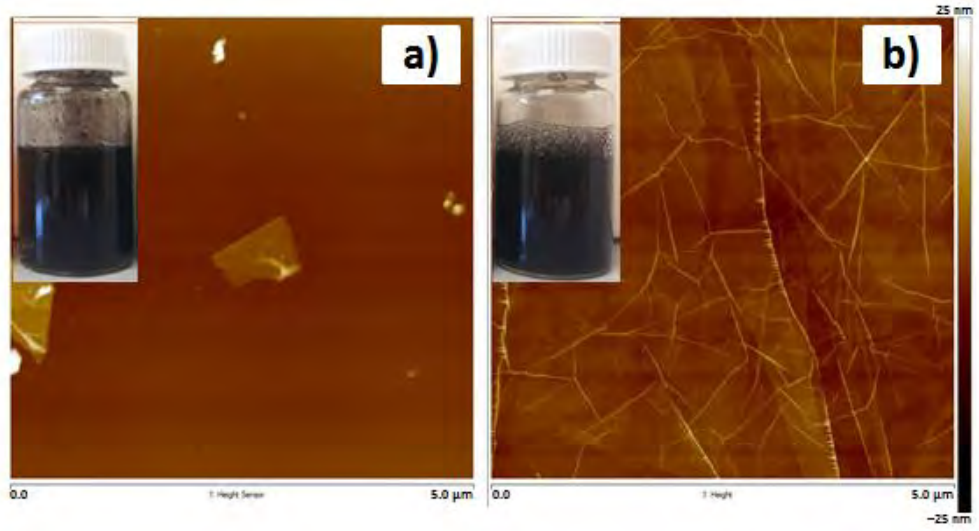


**Figure 5-1**. AFM images (5 x 5 µm$^2$) of chemically reduced graphene oxide (CRGO) (a) without and (b) with SDBS. Insets show digital photographs of the corresponding samples in an aqueous 1 mg mL$^{-1}$ solution.

In order to improve the quality of graphene structures, the films were prepared from the CRGO-SDBS solution using a vacuum-filtration and transfer technique,[44] and have been thermally annealed at a temperature of 400$^{o}$C under the protection of an Ar and $H_2$ gas flow. Interestingly, we observed that the filtration time for the CRGO-SDBS solution was longer than that for the CRGO-only samples. We attribute this phenomenon to the size of the graphene sheets with the larger CRGO-SDBS sheets blocking the filter paper pores faster. After the thermal annealing of CRGO-SDBS film, the resultant product (Scheme 5-1e) is denoted "RGO-SDBS".

The extent of reduction of the prepared samples was studied by Attenuated total reflection-Fourier transform infrared spectroscopy (ATR-FTIR) and X-ray photoelectron spectroscopy (XPS). ATR-FTIR spectra of GO, CRGO-only, CRGO-SDBS and RGO-SDBS are presented in Figure 5-2a. All the observed peaks can be ascribed to O–H stretching mode, C=O carboxyl or carbonyl stretching vibration, C=C stretching, O–H deformations in the C–OH groups, C–OH stretching and C–O stretching vibrations in C–O–C in epoxide from GO.[34] After chemical reduction, the peak intensities of the oxygen containing functional groups in both CRGO-only and CRGO-SDBS become very weak compared to that of GO, but not completely gone, indicating that only partial reduction of GO was obtained using hydrazine monohydrate solution (Scheme 5-1d). However, the CRGO-SDBS exhibits new prominent characteristic peaks at 2960 $cm^{-1}$, 2928 $cm^{-1}$ and 2870 $cm^{-1}$ which correspond to C–H vibrations in SDBS. These absorption peaks in the CRGO-SDBS sample indicates that the SDBS is adsorbed on the CRGO.[40] After thermal annealing, the majority of peaks associated with the oxygen containing functional groups in CRGO-SDBS became very weak, confirming the successful reduction of the GO by the combination of chemical and thermal processes (Scheme 5-1e, confirmed by curve fitting of C1s peaks in XPS spectra shown in Figure S5-2). However, the absorption peaks due to the presence of SDBS remain unchanged after annealing at 400$^{o}$C for 1 h. This result suggests that the insulating SDBS was not removed by the low-temperature thermal treatment.

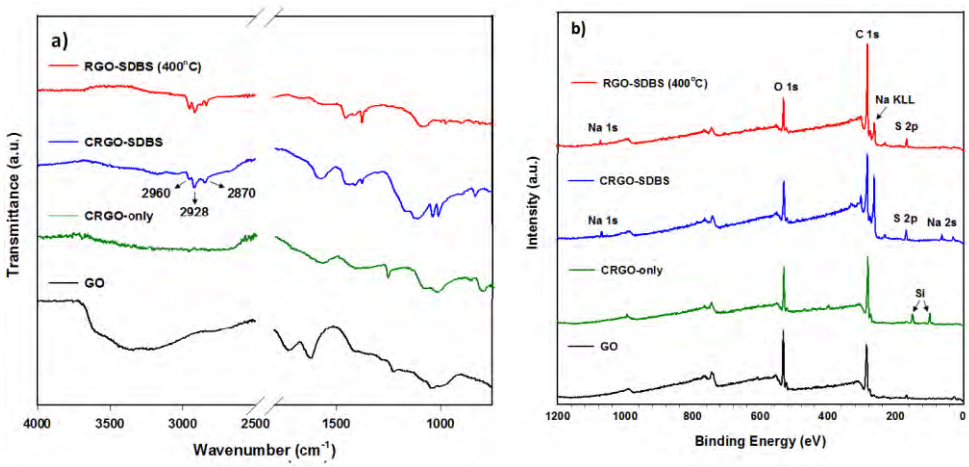


**Figure 5-2**. (a) ATR-FTIR and (b) XPS survey spectra of GO, CRGO-only, with SDBS and thermally reduced CRGO-SDBS (RGO-SDBS).

XPS survey spectra of CRGO-SDBS and RGO-SDBS (Figure 5-2b) show responses (in addition to 283.5 eV (C 1s) and 530.5 eV (O 1s)) at binding energies of around 166 eV (S 2p), 262 eV (Na KLL) and 1059.5 eV (Na 1s), further illustrating that the SDBS remains on the CRGO structure after annealing at 400°C. Nevertheless, it should be noted that the peak intensities of both ATR-FTIR and XPS for CRGO-SDBS structure decreased slightly after annealing at 400°C. Another noticeable feature from the XPS survey spectra in Figure 5-2b is that the appearance of Si 2s and Si 2p peaks at around 99.0 eV and 149.5 eV, respectively for the CRGO without SDBS. These Si peaks can be explained by the poor solubility of the CRGO solution. Due to the large aggregation of CRGO in the solvent, the CRGO sample did not completely cover the silicon substrate. Additionally, the thermal stability of SDBS was investigated using thermo-gravimetric analysis (TGA) (see Figure S5-3). Our finding from TGA analysis was in good agreement with the ATR-FTIR and XPS and suggests that the thermal annealing at 400°C cannot remove the residual surfactants from the graphene. Therefore, further treatment is required to completely remove the SDBS.

According to previous studies,[45-48] the application of concentrated acid solution can be an effective way to completely remove the residual SDBS surfactant and other organic contaminants from the graphene films. Therefore, we used concentrated nitric acid ($HNO_3$, 68%) solution (Scheme 5-1f). It is widely accepted that the use of $HNO_3$ has the advantage of not only eliminating the insulating surfactant, it also

enhances the electrical properties of carbon films by an oxidative doping effect.[49, 50] In addition to these effects, chemical $HNO_3$ treatment can also cause some weak edge defects with oxygen containing functional groups (see Scheme 5-1f, termed as "RGO"),[45, 51, 52] which could be very useful for further treatment to maximize the film performance. In order to produce high-performance graphene films, we also introduced metallic gold nanoparticles (AuNPs) onto our RGO by dipping $HNO_3$-functionalized RGO films into $HAuCl_4$ solution (Scheme 5-1g, called "AuNPs-RGO"). The removal of SDBS and the deposition of AuNPs of the RGO films were characterized by using XPS, scanning electron microscopy (SEM) and Energy-dispersive X-ray spectroscopy (EDX).

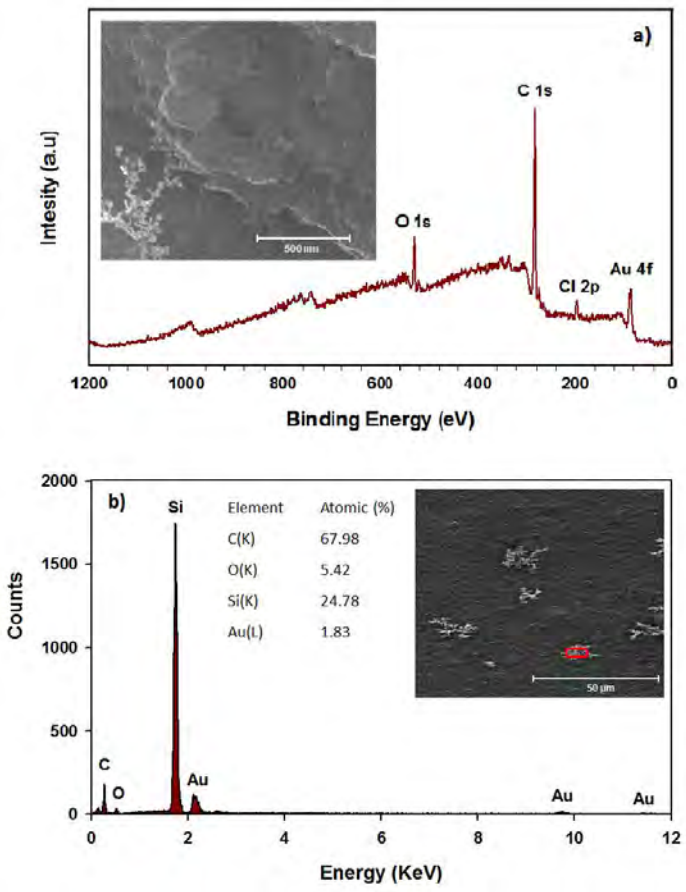


**Figure 5-3**. (a) XPS survey spectra (inset: SEM image of AuNPs-RGO) and (b) EDX analysis (red box in the inset is the selected area for analysis) of RGO-SDBS film after $HNO_3$ and $HAuCl_4$ treatments.

Figure 5-3a shows that the peaks of RGO-SDBS sample at binding energy of 166 eV (S 2p), 262 eV (Na KLL) and 1059.5 eV (Na 1s) have disappeared after treatment with $HNO_3$ and $HAuCl_4$ solutions, indicating the successful removal of the surfactant from the RGO. Additionally, in Figure 5-3a, the appearance of two new prominent peaks at around 83.5 eV (Au 4f) and 200 eV (Cl 2p) indicates the successful AuNPs deposition and some residual $HAuCl_x$. Moreover, the SEM image (inset of Figure 5-3a) clearly shows that the AuNPs were formed on the RGO after dipping the partially functionalized RGO film (Scheme 5-1f) into $HAuCl_4$ solution. It is worth noting that the deposition of AuNPs on the RGO was achieved without the assistance of any reducing agents due to the $HNO_3$ post-treatment. Therefore the edge defects (OH–, COOH– etc.) in RGO introduced by $HNO_3$ treatment play an important role in reducing $Au^{3+}$ to $Au^0$.[52, 53] Moreover, the EDX elemental analysis (Figure 5-3b) was carried out on the selected area of SEM image of the prepared sample and further confirms the removal of residual SDBS from the RGO and the formation of AuNPs on the RGO films.

### 5.2.2. Optical and electrical properties of the graphene films

An ideal PV device – one with the highest PCE – is achieved by having the lowest sheet resistance of the TCF, $R_s$, while achieving the highest transparency. Thin graphene films can exhibit high optical transparency, but they suffer from relatively high $R_s$. The $R_s$ can be reduced by making the graphene films thicker, but this leads to an increase in the film opacity. There is clearly an optimum film thickness. We sought this thickness by changing the volume of filtered CRGO-SDBS solution. Figure 5-4a illustrates the $R_s$ of graphene films prepared from four different structures plotted as a function of filtration volume. These graphene structures are (a) CRGO–SDBS films (Scheme 5-1d), (b) RGO–SDBS films (Scheme 5-1e), (c) RGO films (Scheme 5-1f, $HNO_3$-treated), and (d) AuNPs-RGO films (Scheme 5-1g). Additionally, the wavelength-dependent optical transparencies of each film with different thicknesses and their corresponding $R_s$ values are shown in Figure S5-4. It can be seen from Figure S5-4a that the transparency of the films decreased with increasing filtered volume of the RGO solution. As shown in Figure 5-4a, the $R_s$ of our CRGO-SDBS films were in the range from 2 MΩ/□ to 12 MΩ/□ depending on the thickness. Interestingly, these $R_s$ values are found to be slightly lower than that of

previously reported chemically reduced GO films,[44, 54, 55] despite our films containing insulating SDBS. We attribute this better performance of our CRGO-SDBS films to the production of large-size graphene sheets.[40] Although our CRGO-SDBS films showed lower $R_s$ compared to other studies, such $R_s$ values are still too high for satisfactory solar devices.

As also demonstrated in Figure 5-4a, the $R_s$ of CRGO-SDBS film decreased by more than 2 orders of magnitude for a given thickness after the thermal treatment. This improvement in the electrical properties is known to be due to the better graphitization, deoxygenation and cross-linking of the graphene sheets.[27, 39] However, the thermal reduction of the CRGO-SDBS film reduced the transparency by 4-5 % (Figure S5-4b). The darkening of the films after thermal annealing is due to the restoration of the π–electron system in the graphene structure and some impurities from the re-deposition of carbonaceous material which desorbs during thermal treatment and then adsorbs on both sides of the substrate.[55] Although residual insulating SDBS is still present in the film after thermal treatment, we were able to achieve a $R_s$ of as low as 8.5 kΩ/□ using this film such as that shown in Scheme 5-1e. Therefore, the removal of the SDBS surfactants with $HNO_3$ was expected to improve the performance of our films.

As expected, the $R_s$ of the RGO-SDBS films were significantly reduced (by more than 2-fold) after treating with concentrated $HNO_3$ (see Figure 5-4a). This dramatic improvement in the electrical properties is most likely due to the removal of any remaining SDBS from the film. Another possible reason behind the enhanced conductivity is the chemical doping effect of $HNO_3$ on graphene films.[17, 49, 56] In particular, the $R_s$ value of the RGO-SDBS films was reduced from 8.5 kΩ/□ to 3.74 kΩ/□ at the same thickness after treating with $HNO_3$ solution. More importantly, the $HNO_3$ treatment not only enhanced the electrical conductivity of the films, it also increased the transparency by around 5% for any given thickness (Figure S5-4c). The increase in the transparency of the films after washing with $HNO_3$ could be ascribed to the removal of remaining impurities of the films, particularly on the underside of the glass.

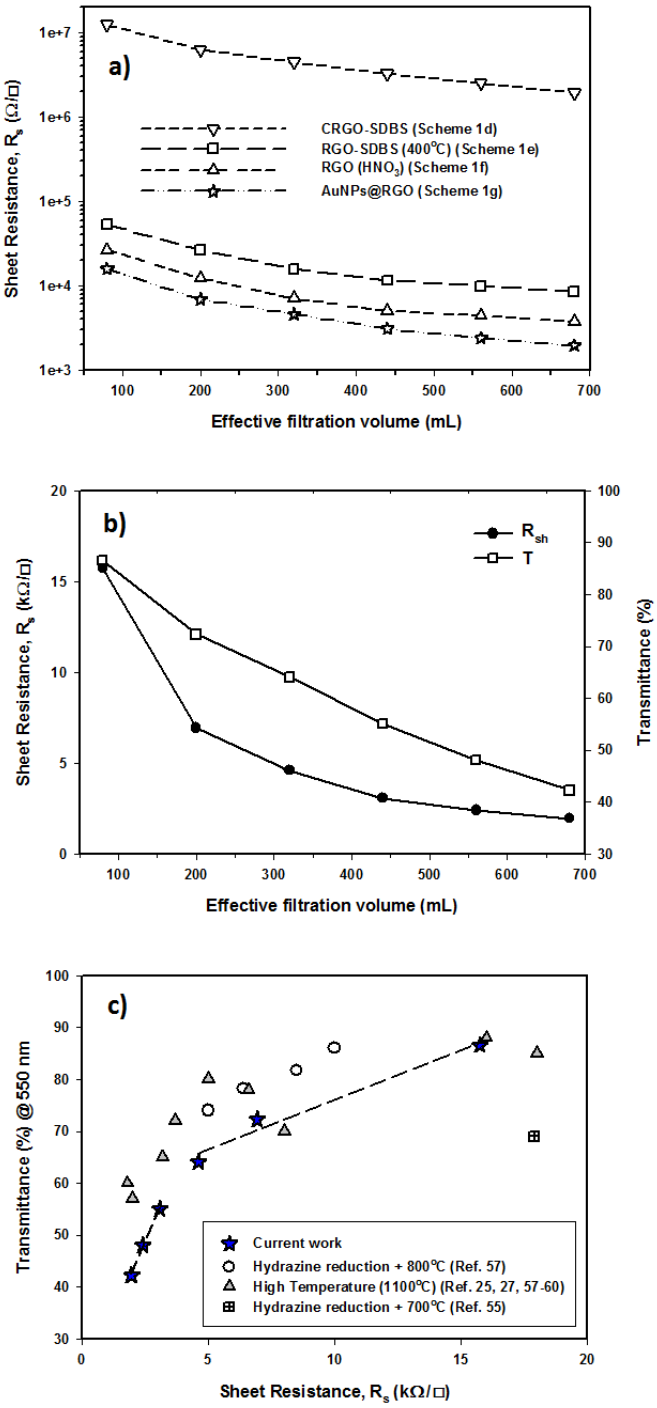


**Figure 5-4**. (a) $R_s$ vs. thickness of the graphene films prepared from four different structures; (b) $R_s$ and transmittance (at $\lambda$ = 550 nm) of selected TCGFs with different thicknesses; (c) comparison of $R_s$ as a function of transmittance (at $\lambda$ = 550 nm) between our AuNPs-RGO films and other studies. Dash lines show the two regions of differing resistance for the graphene films and the threshold transmittance and corresponding $R_s$.

After depositing the AuNPs on RGO films, the $R_s$ and transmittance of the dried films were measured. Figure 5-4a shows that the $R_s$ of RGO films decreased by about 1.8 times after introducing AuNPs onto the films, while no degradation in transmittance was observed (Figure S5-4d) compared to the $HNO_3$-treated RGO films. The improved conductivity could be due to the fact that the AuNPs deposited on RGO created bridges between adjacent sheets, both in-plane and out-of-plane. A low electrical conductivity of graphene film mainly arises from the high inter-sheet contact resistance (deriving from charge hopping) between the edges of graphene sheets.[41] In our AuNPs deposited RGO films, the AuNPs play a vital role in conjugating adjacent graphene sheets and subsequently reducing the overall $R_s$ of the film.

The correlation of $R_s$ and transmittance at $\lambda$ = 550 nm of our AuNPs-RGO films to their volume of filtered solution is depicted in Figure 5-4b. Through the systematic treatments, we obtained an $R_s$ of as low as 1.96 kΩ/□ for the thick graphene film with transmittance of 42.3%. In contrast, a high optical transparency of 86.6% was achieved for the thin film, but its $R_s$ is 15.7 kΩ/□. It should be noted that our $R_s$ values are comparable to previous reports of solution processed graphene films produced by using hydrazine reduction and high-temperature annealing processes (800-1100$^o$C) (Figure 5-4c).[25, 27, 55, 57-61] Therefore, these TCGFs exhibit great potential for use as transparent electrodes in PV devices. The films based on AuNPs-RGO structures such as that illustrated in Scheme 5-1g have been chosen for the fabrication of PSC devices. Moreover, we calculated a figure of merit ($\sigma_{DC}/\sigma_{OP}$) for these TCGFs (Table 5-1) and the film with $R_s$ = 3.08 kΩ/□ at T = 55% showed a high figure of merit (0.176). This $\sigma_{DC}/\sigma_{OP}$ value was higher than that of thinner films, which is expected to correlate with high performance of solar cells.

### 5.2.3. Fabrication and characterization of PV devices

#### *5.2.3.1. Transparent graphene electrodes based PSCs*

To investigate the suitability of our TCGFs as transparent electrodes in PV devices, $CH_3NH_3PbI_{3-x}Cl_x$ perovskite sensitizer based solar cells were fabricated on the graphene films. The layered structure of the device is displayed in Figure 5-5a. In our devices, a thin $TiO_2$ compact layer was used as blocking layer to suppress the

possible charge recombination between the graphene anode and the hole transporting material (HTM). Spiro–OMeTAD (HTM) was used as electron blocking layer between the perovskite sensitizer and Au cathode. Mesoporous $TiO_2$ and $CH_3NH_3PbI_{3-x}Cl_x$ perovskite were employed as electron transporting layer and photosensitizer, respectively. In order to investigate the balance between transparency and $R_s$ of the graphene films, six PSC devices (device 1–6) were built on the TCGFs with different thicknesses (see Figure 5-4b for properties). Digital photographs of the graphene films are also shown in Figure 5-5a. The device number depends on the transparency and $R_s$ of the films. For example, the film with highest transparency and highest $R_s$ based cell is denoted 'device 1' while the TCGF with lowest transparency and lowest $R_s$ based PSC is denoted 'device 6'.

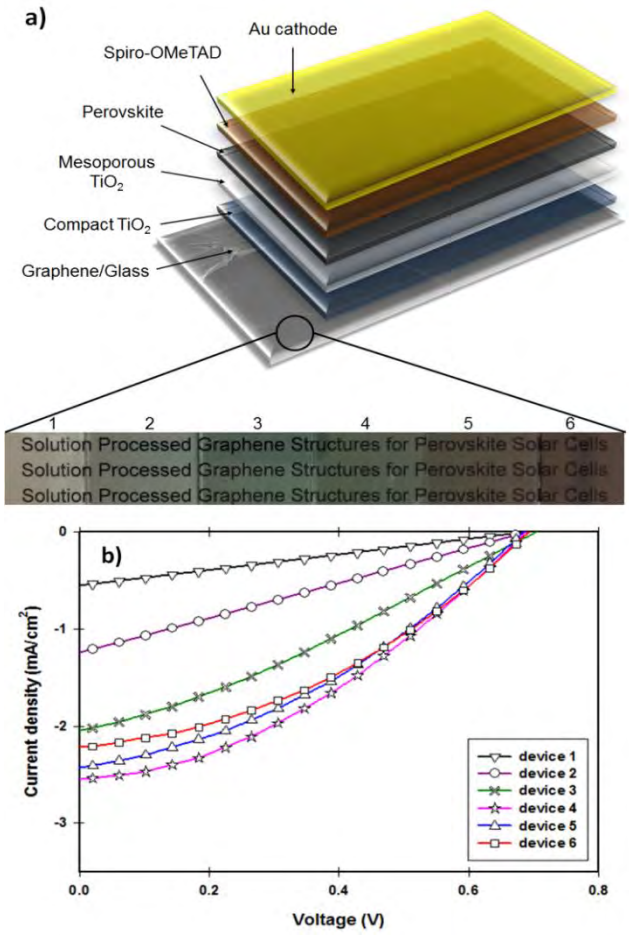


**Figure 5-5**. (a) Device structure, (b) photocurrent density–voltage (J–V) curve of the fabricated solar cells with transparent graphene electrodes. PSC devices with 0.075 $cm^2$ active area were illuminated under AM 1.5G simulated sunlight (100 mW $cm^{-2}$).

**Table 5-1**. PV parameters and PCE ($\eta$) of TCO-free PSCs with graphene films. Results for champion cells shown.

| Device | $R_s$@T | $\sigma_{DC}/\sigma_{OP}$ | $J_{sc}$ (mA $cm^{-2}$) | $V_{oc}$ (V) | FF | $\eta$ (%) |
|---|---|---|---|---|---|---|
| 1. (80 mL) | 15.7kΩ/□ @86.6% | 0.161 | 0.56 | 0.692 | 0.25 | 0.1 |
| 2. (200 mL) | 6.93kΩ/□ @72.3% | 0.154 | 1.25 | 0.695 | 0.26 | 0.23 |
| 3. (320 mL) | 4.61kΩ/□ @64.1% | 0.164 | 2.02 | 0.700 | 0.29 | 0.41 |
| 4. (440 mL) | 3.08kΩ/□ @55.0% | 0.176 | 2.55 | 0.690 | 0.35 | 0.62 |
| 5. (560 mL) | 2.41kΩ/□ @48.0% | 0.176 | 2.43 | 0.690 | 0.36 | 0.60 |
| 6. (680 mL) | 1.96kΩ/□ @42.3% | 0.177 | 2.21 | 0.694 | 0.37 | 0.57 |

The photocurrent density–voltage (J–V) characteristics of the PSCs fabricated with different TCGFs are shown in Figure 5-5b and the corresponding PV parameters such as open-circuit voltage ($V_{oc}$), short-circuit current density ($J_{sc}$), fill factor (FF) and PCE have been summarized in Table 5-1. The measured $V_{oc}$ values of all devices are essentially constant at 0.695 ± 0.05 V, indicating that the thickness of graphene films does not influence this parameter. This is reasonable since the $V_{oc}$ parameter is mainly determined by the energy level difference between the conduction band of electron transporting material and the potential energy of the HTM. In contrast, significant changes in the $J_{sc}$ and FF were observed. Because of its comparatively high $R_s$, device 1 showed the lowest $J_{sc}$ (0.56 mA $cm^{-2}$) and FF (0.25) values, despite the transparency of graphene film being quite high. Interestingly, the FF value of our PSCs continuously increased from device 1 to device 6, likely to be due to the improvement in the $R_s$ of the graphene films. Therefore the maximum FF value (0.37) was achieved for the device 6 which is made of our most-conductive graphene film with lowest transparency. However, the measured $J_{sc}$ value (2.21 mA $cm^{-2}$) of

the device 6 was not the highest observed. Unlike the FF parameter, no continuous increase was observed for the $J_{sc}$ value of our devices when the thickness of graphene films increases. In particular, from device 1 to device 4 (an increase in the thickness of graphene films), the $J_{sc}$ increases from 0.56 to 2.55 mA $cm^{-2}$ owing to the reduction of $R_s$. However, when the transmittance of the film drops below 55%, $J_{sc}$ of the cells decreases (device 5 & 6) despite the films having reduced $R_s$. This decrease in $J_{sc}$ is due to the absorption of incident light by the TCGF before it reaches the active perovskite layer. Indeed, the optimum PV parameters for the TCGFs-based PSC were achieved for the graphene film with 3.08 kΩ/□@55.0%T. The observed $J_{sc}$, $V_{oc}$ and FF values for this PSC (device 4) were 2.55 mA $cm^{-2}$, 0.69 V and 0.35, respectively, yielding an energy conversion efficiency of 0.62%.

For comparison, an FTO electrode based PSC device was also fabricated under the same conditions as devices 1-6 and its J–V curve is plotted in Figure S5-5. The FTO based device exhibited a $J_{sc}$ of 17.49 mA $cm^{-2}$, $V_{oc}$ of 0.71 V and FF of 0.63, yielding a PCE of 7.82%. It is obvious that the PCE of our graphene film-based PSCs is significantly lower to that of the control cell based on FTO. The major issues for our TCGFs based devices are relatively low $J_{sc}$ and lower FF values as compared to the cell based on FTO. This might be due to the high $R_s$ and poor optical transmittance of our graphene films. Although the PCE (0.62%) of our graphene electrode based device is far from that of the PSC fabricated with FTO, this efficiency value is higher than that achieved for previously published inorganic-organic hybrid solar cell,[24] or DSSC,[27] in which graphene films act as the electron collection electrode. It should also be noted that the $V_{oc}$ value (0.71 V) and PCE achieved using our typical FTO based PSC is lower than recently reported values for standard cells using typical ITO or FTO transparent conducting electrodes.[62-64] The perovskite precursor and deposition process we have used were chosen for their simplicity in deposition and under the conditions we followed typically yield PCEs of 7-9% with low $V_{oc}$ (0.7 V-0.8 V),[65-67] which are consistent with our results using the standard transparent conducting electrodes. More importantly, here in this work, we demonstrate the feasibility of solution processed graphene films as alternatives to the traditional TCO electrodes in the state-of-the-art PSCs. We anticipate that significant improvement in the PCE can be made for this class of PV devices by

enhancing the performance of the graphene films and/or using other solar cell architectures.

#### *5.2.3.2. Effect of graphene structures in the $TiO_2$ layers*

The use of carbonaceous materials in the semiconducting oxide scaffolds has previously led to great enhancement in the efficiency of DSSCs.[68, 69] Therefore, in this work, we introduce this concept of incorporating graphene structures into the electron transporting $TiO_2$ layers of the mesoscopic PSCs to further improve the efficiency of our graphene electrode based device. The TCGF, which was previously used for the device 4 and gave the best PCE, was chosen for the fabrication of the graphene incorporated $TiO_2$ photoanode-based PSCs. In the fabricated device, the graphene structures were incorporated into the compact $TiO_2$ only, the mesoporous $TiO_2$ only and both the compact and mesoporous $TiO_2$ layers. The incorporated graphene was prepared by mixing GO (0.6 and 0.2 % w/w in blocking layer and mesoporous layer, respectively) with the $TiO_2$ precursors prior to deposition. The GO is then thermally reduced in situ when sintering the $TiO_2$ layers at 500$^{o}$C in an Ar atmosphere.

The J–V characteristics and device structures of the TCGFs based PSCs with and without graphene in the semiconducting oxide layers are illustrated in Figure 5-6. The PV performances of these PSC devices have been summarized in Table 5-2. For comparison, the J–V curve and the corresponding energy level diagram of device 4 (TCGF based PSC without graphene in the semiconducting layer) is also plotted in Figure 5-6a and Figure 5-6a′, respectively. Since the work function of RGO is close to that of FTO, and lower than the conduction band of $TiO_2$,[25] it is reasonable to expect that the injected electrons at the $TiO_2$ conduction band can be transferred to the graphene electrode without any barrier. Changes to the work function of gold chloride doped graphene have previously been shown to be minimal after thermal annealing, as has been done in this work.[70]

On the other hand, the application of graphene in the semiconducting oxide layers should principally increase the efficiency of this class of solar cells due to enhanced charge transport.[71] However, as shown in Figure 5-6b, no significant improvement in the PV parameters for the PSC was observed after incorporating graphene into the

mesoporous $TiO_2$ layer only (Structure 2). We hypothesize that these unchanged PV parameters are associated with the energy level alignments of $TiO_2$ and graphene. In fact, the injected electrons from the excited perovskite and/or mesoporous $TiO_2$ into the graphene cannot be transferred to the conduction band of the compact $TiO_2$ (Figure 5-6b′) which results in incomplete electron transport within the networks.

Furthermore, the addition of graphene into the compact $TiO_2$ layer of device (Structure 3) exhibited some enhancement in the $J_{sc}$ and FF parameters and displayed a PCE of 0.75%, as illustrated in Figure 5-6c. These increased $J_{sc}$ and FF values could be due to the suitable energy levels of graphene in the cell. The energy levels of graphene in the compact $TiO_2$ layer can be ideal for this class of PSC (Structure 3) as its work function sits between the $TiO_2$ and graphene anode and so that the electrons transfer stepwise from the perovskite to the graphene anode without an energy barrier (see Figure 5-6c′). Here, graphene, which was incorporated into the compact $TiO_2$ layer, acts as a bridge between $TiO_2$ and graphene anode. In the energy diagram, it is reasonable to assume that the work function of RGO (graphene anode; used as a transparent conductive film in the PSC) is higher than that of the graphene used in the semiconducting oxide layers because the extent of reduction in the electrode is relatively high.

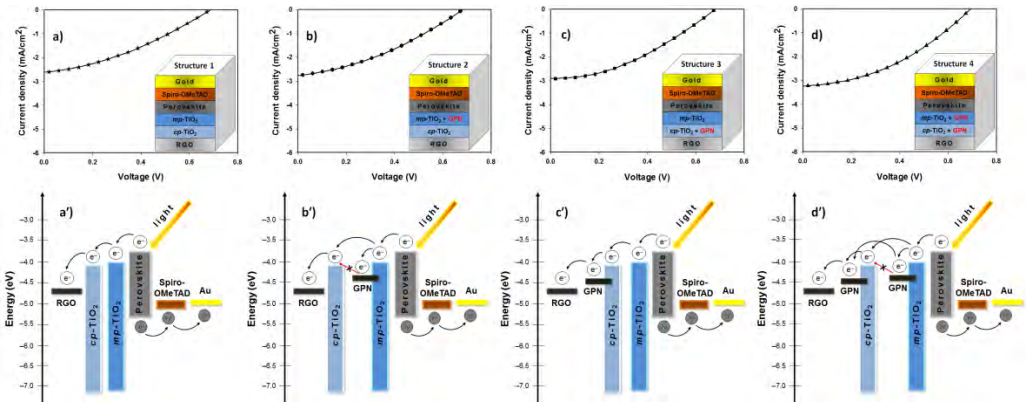


**Figure 5-6**. J–V curves (top) and the corresponding energy level diagrams (bottom) of TCGF film based PSCs with and without graphene in the semiconducting oxide layers. The device structures are shown in the insets. The word abbreviations are as follows: RGO – reduced graphene oxide; graphene – GPN; mp-$TiO_2$ – mesoporous $TiO_2$; cp-$TiO_2$ – compact $TiO_2$.

**Table 5-2**. Summary of the PV performance of PSCs (Structure 1-4, shown in Figure 5-6) with RGO incorporated in different segments. Average values and the standard deviation (at least three cells for each structure) of the PSCs are shown. Parameters of the best cells are also highlighted in **bold**.

| Device | $J_{sc}$ (mA $cm^{-2}$) | $V_{oc}$ (V) | FF | η (%) |
|---|---|---|---|---|
| Structure 1 | **2.55**; 2.55 ± 0.03 | **0.690**; 0.689 ± 0.001 | **0.35**; 0.35 ± 0.01 | **0.62**; 0.62 ± 0.00 |
| Structure 2 | **2.77**; 2.75 ± 0.02 | **0.684**; 0.686 ± 0.002 | **0.36**; 0.36 ± 0.00 | **0.66**; 0.65 ± 0.01 |
| Structure 3 | **2.90**; 2.85 ± 0.05 | **0.690**; 0.695 ± 0.005 | **0.38**; 0.38 ± 0.00 | **0.75**; 0.74 ± 0.01 |
| Structure 4 | **3.05**; 2.94 ± 0.11 | **0.687**; 0.689 ± 0.002 | **0.38**; 0.38 ± 0.01 | **0.81**; 0.79 ± 0.02 |

Structure 4 showed a promising improvement in the energy conversion efficiency (0.81%) (Figure 5-6d). In particular, the $J_{sc}$ and FF values of Structure 4 increased to 3.04 mA $cm^{-2}$ and 0.38, respectively, after incorporating graphene structures into both the compact $TiO_2$ and mesoporous $TiO_2$ layers. The improvement in these parameters ($J_{sc}$ and FF) can be ascribed to the fact that the conductive graphene in the cells enhances the charge transport rate and suppresses the charge recombination. Moreover, it is reasonable to expect that the presence of graphene in both the compact and mesoporous $TiO_2$ layers provides a thermodynamically favorable energy transfer path and potentially offers an extra graphene to graphene conduction path both of which enable successful charge collection and hence higher PCE (see Figure 5-6d′). A detailed investigation on the effect of carbonaceous materials in the $TiO_2$ photoanodes of PSCs is ongoing research in our group.

The external quantum efficiency (EQE) is an important parameter for evaluating the performance of solar cells. PSC devices (Structure 4 in Figure 5-6) with TCGF and also graphene in mesoporous and compact $TiO_2$ were chosen for EQE analysis. For comparison, the EQE characteristic of the conventional PSC fabricated on FTO electrode without graphene was also investigated. Figure 5-7 compares the EQE spectra obtained. Both cells show a broad EQE peak across the visible region, typical for PSCs.[66] The cell fabricated with graphene (Structure 4 in Figure 5-6) shows a

similar shape to the FTO-electrode based PSC (see Figure 5-7 inset) but much lower EQE value, showing that the difference is wavelength independent which indicates that the use of graphene film did not alter the internal mechanism of the PSC. The lower EQE value of TCGF based cell is expected when considering the low PCE obtained, as discussed previously. Moreover, the stability of these two PSCs, namely FTO-based and TCGF-based, was investigated for 60 h and the results are plotted in Figure S5-6. The degradation rate of TCGF based cell was very similar to that of a FTO-based device.

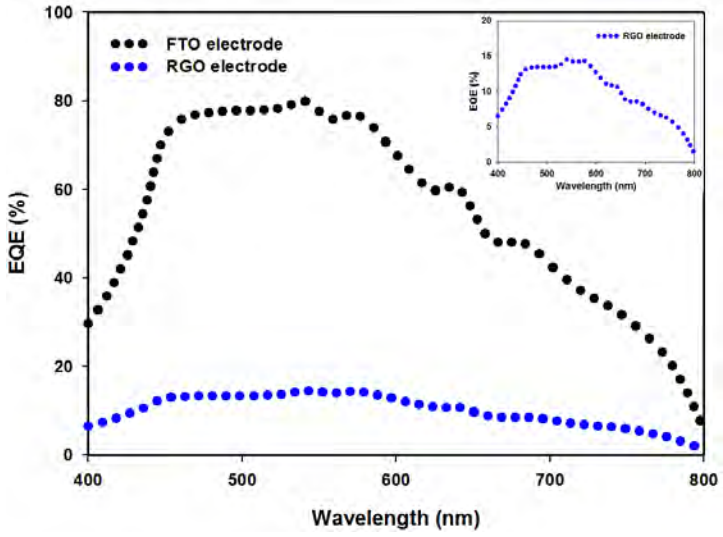


**Figure 5-7**. EQE spectra of FTO electrode (black dots) and TCGF (blue dots, Structure 4 (as termed in Figure 5-6 and Table 5-2)) based PSCs. Inset shows the expanded EQE spectrum of RGO electrode based PSC.

The initial reported PCE of PSCs was relatively low but has increased rapidly in just a few years. It is anticipated that PCE of TCGF in PSCs will show a similar rapid improvement as they have in other solar cell architectures.[19] A promising result is that the observed $V_{oc}$ for all devices fabricated with TCGF films were similar to that of FTO electrodes based cells, indicating that the energy bands of graphene are suitable for application in PSCs, supporting theoretical predictions.[32] Therefore, our results demonstrate that the use of graphene films as the electron transporting transparent conducting electrode in the PSCs is viable. The two key areas for research are the improvement in $R_s$ with high transmittance and the creation of

flexible PSCs using TCGFs. Further modification of the reduction of GO to increase flake size could produce graphene films with better performance for PSCs without increasing manufacturing cost.

## 5.3. Conclusion

Herein, we demonstrate the feasibility of transparent conductive graphene films (TCGFs) formed by solution processing as alternatives to the conventional transparent conducting oxide (TCO) electrodes in PSC devices. The TCGFs were prepared by using a low-temperature annealing process as well as chemical post-treatments. By using an optimal balance of $R_s$ and transparency of the graphene films, a maximum PCE of 0.62% was obtained. By incorporating graphene structures into both compact $TiO_2$ and mesoporous $TiO_2$ layers of the PSCs, the PCE was further improved to 0.81%. Further PCE enhancement is expected in this class of solar cells by applying high-quality graphene films with improved electrical conductivity and high transparency. Finally, we anticipate that the current work will open new avenues for the development of graphene materials in perovskite based solar cells.

## 5.4. Experimental

### 5.4.1. Materials

Unless otherwise specified, all chemicals were purchased from Sigma-Aldrich and used without further purification. Methylammonium iodide ($CH_3NH_3I$), $TiO_2$ paste (18NR-T) and tris(1-(pyridin-2-yl)-1H-pyrazol)cobalt(III)tris(hexafluorophosphate) (FK102 Co (III) PF6) salt were purchased from Dyesol. (2,2′,7,7′-tetrakis-(*N,N*-di-*p*-methoxyphenylamine)-9,9′-spirobifluorene) (Spiro-OMeTAD) was obtained from Solaronix.

### 5.4.2. Preparation of graphene films

Graphite oxide was prepared via the oxidation of natural graphite according to an improved Hummers method.[34] In brief, a 9:1 (v:v) mixture of concentrated sulfuric

acid (95-98% $H_2SO_4$) and phosphoric acid (85% $H_3PO_4$) (240:27 mL) was kept in the cold room (3-5$^oC$) until it was added to a mixture of graphite flakes (2 g) and potassium permanganate (99% $KMnO_4$) (12 g). Then the oxidation process was carried out by stirring at 50$^oC$ for 12 h. Upon completion, the reaction was cooled down to room temperature and poured onto ice (approximately 300 mL) with 30% hydrogen peroxide ($H_2O_2$) (2 mL). The mixture was then washed with distilled (DI) water, 30% hydrochloric acid (HCl) and ethanol (2 times). For each sequential wash, the product was centrifuged at 4400 rpm for 3 h and the supernatant decanted away. The light brown sample obtained was then vacuum-dried overnight at room temperature.

The as-prepared graphite oxide was exfoliated in water (1 mg $mL^{-1}$) by bath ultrasonication (Elma, Germany) for 40 min in the presence of SDBS (1 wt% in the solution). The obtained homogenous dispersion was named "GO–SDBS solution". The GO-SDBS colloidal dispersion (10 mL) was chemically reduced by hydrazine monohydrate solution (40 µL, 64-65% $N_2H_4 \cdot H_2O$) and ammonium hydroxide solution (120 µL, 30% $NH_3 \cdot H_2O$).[44] The chemical reduction was performed in an oil bath at 100°C overnight. The resultant solution (named "CRGO-SDBS") was then diluted with DI water to obtain the final concentration of CRGO-SDBS (0.16 mg $L^{-1}$). The diluted solution was further used to prepare the transparent films. For comparison, the chemical reduction of GO was performed in the absence of SDBS and the resultant solution was named CRGO-only.

The glass substrates (25 mm × 25 mm) were cleaned by detergent (Pyroneg) followed by washing with acetone, ethanol and Milli-Q water under ultrasonication for 10 min each and subsequently dried with a stream of nitrogen gas. The cleaned glass substrates were pretreated with 3-aminopropyl-triethoxysilane (APTES) (3% in toluene) to improve the surface functionalities of the substrates.[24, 39, 56] Transparent graphene films were prepared on mixed cellulose ester (MCE) membranes (0.45 µm HAWP, Millipore) through the vacuum filtration of CRGO-SDBS solution.[44] The transparency of the films was controlled by varying the effective filtration volume of solutions. The filtered films (CRGO-SDBS/MCE membrane) were subsequently pressed against the APTES-modified glass surface with the graphene side in contact with the substrate. The substrates were then firmly clamped in place at room temperature for 2 days to completely adhere the CRGO-SDBS film to the substrate.

The MCE membranes were dissolved in an acetone bath to leave CRGO-SDBS film on the substrate. The obtained CRGO-SDBS films were then rinsed with methanol and dried by blowing nitrogen. To further improve the electrical conductivity of the films, the as-produced CRGO-SDBS films were thermally reduced in a tube furnace at low temperature (400$^{o}$C) for 1 h. The annealing and cooling processes were performed under the protection of an Ar and $H_2$ (20:1) atmosphere. The obtained films are named "RGO-SDBS". To remove the residual SDBS surfactants from the films, the RGO-SDBS films were then immersed in concentrated nitric acid ($HNO_3$, 68%) solution for 3 h and rinsed thoroughly with DI water, and dried at 100$^{o}$C for 1 h in a hot oven. After the application of the $HNO_3$-treatment, the samples are called "RGO films". The AuNPs were then deposited onto the RGO films by dynamic spin coating of 0.5 mM $HAuCl_4$ in nitromethane, and finally dried completely at 200$^{o}$C overnight. The prepared films are named "AuNPs–RGO films" and have been used to fabricate the PSC devices.

### 5.4.3. Fabrication of PSC devices

PSC devices with the structure of graphene anode/compact $TiO_2$/mesoporous $TiO_2$/$CH_3NH_3PbI_{3-x}Cl_x$/Spiro-OMeTAD/Au were fabricated according to the following procedure. The fabrication process of PSCs has been reported elsewhere.[12,14] A thin compact $TiO_2$ layer was spin-coated onto the previously prepared graphene film and/or cleaned FTO electrode (~12 Ω/□, Solaronix TCO30-8) substrate at a rotation speed of 2000 rpm for 20 s using 0.2 M titanium diisopropoxide bis(acetylacetonate) (75 wt% in isopropanol, Aldrich) in 1-butanol solution, followed by heating at 125$^{o}$C for 5 min. The same process was repeated twice with the above solution, followed by drying at 125$^{o}$C for 5 min and sintering at 500$^{o}$C for 1h. For the preparation of the graphene incorporated compact $TiO_2$ layer, GO-ethanol solution (1 mg mL$^{-1}$) was added into the titanium diisopropoxide bis(acetylacetonate) in 1-butanol solution. The concentration of the GO in the composite was calculated to be 0.6 wt%. After cooling to room temperature, a thick mesoporous $TiO_2$ layer was deposited onto the compact $TiO_2$ layer by spin coating a solution of $TiO_2$ paste (Dyesol 18NR-T) in a 2:7 weight ratio to ethanol at 4000 rpm for 30 s. After drying at 125°C for 5 min, the films were sintered at 500°C for 1 h. The mesoporous $TiO_2$ deposited films were then immersed in 40 mM aqueous $TiCl_4$

(Aldrich) solution at 70°C for 30 min, which was again annealed at 500°C for 30 min. Similarly, to prepare the graphene/mesoporous $TiO_2$ layer, the GO-ethanol solution was also added into the diluted $TiO_2$ paste solution and the concentration of the GO in the composite was controlled to be 0.2 wt%. The GO in the compact and/or mesoporous $TiO_2$ layers can simply be converted to graphene during the annealing processes. Moreover, during the deposition of the compact and mesoporous layers on the transparent electrodes, Parafilm® M seal was rolled onto one side of the TCGFs to protect the graphene anode contact. After the completion of all annealing processes at 500°C, conductive adhesive tape was carefully applied onto the graphene anode to serve as electrical contact. Notably, we measured the $R_s$ of the graphene films before and after annealing at 500°C for 1h as this thermal annealing process was done after the deposition of $TiO_2$ layers and no significant changes in the $R_s$ were observed. Particularly, the $R_s$ of $HNO_3$ and $HAuCl_4$ treated RGO films before and after thermal treatment at 500°C were measured to be 4.08 ± 0.04 kΩ/□ and 4.21 ± 0.12 kΩ/□, respectively. It should also be noted that for the fabrication of PSC devices with graphene structures, the thermal annealing processes at more than 400°C were carried out under the protection of Ar to protect graphene from the mild oxidation.

For the preparation of $CH_3NH_3PbI_{3-x}Cl_x$ perovskite, a 1:3 molar ratio of $PbCl_2$:$CH_3NH_3I$ was mixed in anhydrous N, N-Dimethylformamide (DMF) solution (99.8% Aldrich), with the concentration of 0.73M and 2.2M, respectively. The mixture was stirred at room temperature for at least 6 h before spin coating (100 µL of the solution) onto the mesoporous layers at 2500 rpm for 30s in air and then heated at 100°C for 1 h. The deposition process of the perovskite was carried out in controlled humidity under 35%.

The HTM (120 µL of the prepared solution) was then deposited onto the perovskite layer by spin coating at 4000 rpm for 30 s in a nitrogen-filled glovebox. The HTM was prepared by dissolving 72.3 mg Spiro-OMeTAD, 28.8 µl 4-*tert*-butylpyridine (tBP), 17.5 µL of a stock solution of 520 mg $mL^{-1}$ lithium bis(trifluoromethylsulphonyl)imide (Li-TFSI) in acetonitrile and 29 µL of a stock solution of 300 mg $mL^{-1}$ FK102 Co(III) PF6 salt in acetonitrile, in 1 mL chlorobenzene. Finally, 60 nm gold electrodes were deposited on top of devices by

thermal evaporation at a rate of 1 Å $s^{-1}$ under a high vacuum (~$10^{-6}$ bar) through a shadow mask.

### 5.4.4. Measurement and characterization

AFM images were acquired in air using a Bruker Dimension FastScan AFM with Nanoscope V controller, operating in tapping mode. Silicon cantilevers (MikroMasch) with a fundamental resonance frequency of between 300 and 400 kHz were used. Images were obtained using a scan rate of 1 Hz with the set point, amplitude, and feedback control parameters optimized manually for each sample. The images presented have been flattened using NanoScope Analysis v1.4 software. SEM images were obtained using an Inspect F50 SEM (FEI) with accelerating voltage of 20 kV. EDX analysis was completed on the same system with Team EDS Octane Pro (EDAX) attachment. ATR-FTIR spectra were acquired over a wavenumber range of 4000-650 $cm^{-1}$ in transmission mode using a Frontier FTIR spectrometer (Perkin Elmer, USA) with a germanium crystal. The elemental compositions of the samples were characterized at binding energy ranging from 0 eV to 1200 eV using a XPS, Leybold Heraeus LHS-10 with a SPECS XR-50 dual anode source operating at 250W. The Mg-Kα source, which has energy of 1253.6 eV, was used for the XPS analysis. Curve fitting of the C1s in XPS spectra was done using peak fitting software "Fityk".[72] High resolution XPS of the C1s were collected with a step size of 0.1 eV and the presented spectra are an average of 5 collections. Raman spectroscopy was performed on LabRAM HR Evolution spectrometer (Horiba Jobin Yvon, Japan). Raman spectra were collected using a 532 nm laser (mpc 3000) as the excitation source. A 50x objective was used with a confocal hole size of 100 μm. Thermal decomposition of SDBS was performed using a thermal gravimetric analyser (TA Instruments TGA 2950 Thermogravimetric Analyzer, USA) under a flow of nitrogen at a rate of at 20.0 mL $min^{-1}$. The transmittances of the films on glass slides were determined using a Varian Cary 50G UV-vis Spectrophotometer at wavelengths ranging from 400 to 1000 nm. Sheet resistance measurements were performed on the same films using a four point probe technique (KeithLink Technology Co., Ltd. Taiwan). The J–V curves were measured using a Keithley 2400 SMU instrument and recorded using a custom LabView Virtual Instrument program. A standard silicon test cell with NIST-traceable certification was used to

calibrate the power density as 100 mW $cm^{-2}$ at the sample plane of the collimated xenon-arc light source, which was passed through an AM 1.5G filter. The active area of each device was 0.075 $cm^2$. The J-V curves were obtained in air in reverse-scan direction from 1 V to -1 V. EQE measurements as a function of wavelength ranging from 400 nm to 800 nm were taken by passing chopped light from a Xenon source through a monochromator and onto the devices.

## Acknowledgements

The support of the Australian Research Council Discovery Program (DP130101714) is gratefully acknowledged. Munkhbayar Batmunkh acknowledges International Postgraduate Research Scholarship (IPRS) and Australian Postgraduate Award (APA) for their financial support during his study in Australia. We acknowledge the use of South Australian node of the Australian Microscopy & Microanalysis Research Facility (AMMRF) at Flinders University. The authors would also like to thank Meisam V. Kiamahalleh of School of Chemical Engineering at the University of Adelaide for graphic design.

## References

[1] S. Chu, A. Majumdar, *Nature,* **2012**, 488, 294.
[2] T. Saga, *NPG. Asia. Mater,* **2010**, 2, 96.
[3] M. Bosi, C. Pelosi, *Prog in Photovoltaics: Res and App,* **2007**, 15, 51.
[4] N.-G. Park, *J. Phys. Chem. Lett,* **2013**, 4, 2423.
[5] G. Hodes, *Science,* **2013**, 342, 317.
[6] P. Docampo, S. Guldin, T. Leijtens, N. K. Noel, U. Steiner, H. J. Snaith, *Adv. Mater,* **2014**, 26, 4013.
[7] M. A. Green, A. Ho-Baillie, H. J. Snaith, *Nat Photon,* **2014**, 8, 506.
[8] M. M. Lee, J. Teuscher, T. Miyasaka, T. N. Murakami, H. J. Snaith, *Science,* **2012**, 338, 643.
[9] G. Xing, N. Mathews, S. Sun, S. S. Lim, Y. M. Lam, M. Grätzel, S. Mhaisalkar, T. C. Sum, *Science,* **2013**, 342, 344.
[10] A. Kojima, K. Teshima, Y. Shirai, T. Miyasaka, *J. Am. Chem. Soc,* **2009**, 131, 6050.
[11] J. Burschka, N. Pellet, S.-J. Moon, R. Humphry-Baker, P. Gao, M. K. Nazeeruddin, M. Gratzel, *Nature,* **2013**, 499, 316.

[12] H. Zhou, Q. Chen, G. Li, S. Luo, T.-b. Song, H.-S. Duan, Z. Hong, J. You, Y. Liu, Y. Yang, *Science,* **2014**, 345, 542.
[13] W. S. Yang, J. H. Noh, N. J. Jeon, Y. C. Kim, S. Ryu, J. Seo, S. I. Seok, *Science*, **2015**, 348, 1234-1237.
[14] G. E. Eperon, V. M. Burlakov, P. Docampo, A. Goriely, H. J. Snaith, *Adv. Funct. Mater,* **2014**, 24, 151.
[15] X. Chen, S. Yang, Y. C. Zheng, Y. Chen, Y. Hou, X. H. Yang, H. G. Yang, *Adv. Sci,* **2015**, 2, 1500105.
[16] X. Huang, Z. Zeng, Z. Fan, J. Liu, H. Zhang, *Adv. Mater,* **2012**, 24, 5979.
[17] D. S. Hecht, L. Hu, G. Irvin, *Adv. Mater,* **2011**, 23, 1482.
[18] F. Bonaccorso, Z. Sun, T. Hasan, A. C. Ferrari, *Nat Photon,* **2010**, 4, 611.
[19] Z. Yin, J. Zhu, Q. He, X. Cao, C. Tan, H. Chen, Q. Yan, H. Zhang, *Adv. Energy Mater,* **2014**, 4, 1300574.
[20] H. Chang, H. Wu, *Adv. Funct. Mater,* **2013**, 23, 1984.
[21] Y. Zhu, S. Murali, W. Cai, X. Li, J. W. Suk, J. R. Potts, R. S. Ruoff, *Adv. Mater*, **2010**, 22, 3906.
[22] M. Hösel, D. Angmo, R. R. Søndergaard, G. A. dos Reis Benatto, J. E. Carlé, M. Jørgensen, F. C. Krebs, *Adv. Sci,* **2014**, 1, 1400002.
[23] Q. Su, S. Pang, V. Alijani, C. Li, X. Feng, K. Müllen, *Adv. Mater,* **2009**, 21, 3191.
[24] Z. Yin, S. Wu, X. Zhou, X. Huang, Q. Zhang, F. Boey, H. Zhang, *Small,* **2010**, 6, 307.
[25] Z. Yin, S. Sun, T. Salim, S. Wu, X. Huang, Q. He, Y. M. Lam, H. Zhang, *ACS Nano,* **2010**, 4, 5263.
[26] E. Kymakis, K. Savva, M. M. Stylianakis, C. Fotakis, E. Stratakis, *Adv. Funct. Mater,* **2013**, 23, 2742.
[27] X. Wang, L. Zhi, K. Müllen, *Nano Lett,* **2008**, 8, 323.
[28] P. You, Z. Liu, Q. Tai, S. Liu, F. Yan, *Adv. Mater,* **2015**, 27, 3632.
[29] F. Lang, M. A. Gluba, S. Albrecht, J. Rappich, L. Korte, B. Rech, N. H. Nickel, *J. Phys. Chem. Lett,* **2015**, 6, 2745.
[30] Z. Liu, S. P. Lau, F. Yan, *Chem. Soc. Rev,* **2015**, 44, 5638.
[31] M. Batmunkh, C. J. Shearer, M. J. Biggs, J. G. Shapter, *J. Mater. Chem. A,* **2015**, 3, 9020.
[32] G. Volonakis, F. Giustino, *J. Phys. Chem. Lett,* **2015**, 6, 2496.
[33] N. Yang, J. Zhai, D. Wang, Y. Chen, L. Jiang, *ACS Nano,* **2010**, 4, 887.
[34] D. C. Marcano, D. V. Kosynkin, J. M. Berlin, A. Sinitskii, Z. Sun, A. Slesarev, L. B. Alemany, W. Lu, J. M. Tour, *ACS Nano,* **2010**, 4, 4806.
[35] O. C. Compton, S. T. Nguyen, *Small,* **2010**, 6, 711.
[36] M. Lotya, Y. Hernandez, P. J. King, R. J. Smith, V. Nicolosi, L. S. Karlsson, F. M. Blighe, S. De, Z. Wang, I. T. McGovern, G. S. Duesberg, J. N. Coleman, *J. Am. Chem. Soc,* **2009**, 131, 3611.
[37] H. Chang, L. Tang, Y. Wang, J. Jiang, J. Li, *Anal. Chem,* **2010**, 82, 2341.
[38] M. J. Fernández-Merino, L. Guardia, J. I. Paredes, S. Villar-Rodil, P. Solís-Fernández, A. Martínez-Alonso, J. M. D. Tascón, *J. Phys. Chem. C,* **2010**, 114, 6426.

[39] S. J. Wang, Y. Geng, Q. Zheng, J.-K. Kim, *Carbon,* **2010**, 48, 1815.
[40] H. Chang, G. Wang, A. Yang, X. Tao, X. Liu, Y. Shen, Z. Zheng, *Adv. Funct. Mater,* **2010**, 20, 2893.
[41] Q. Zheng, Z. Li, J. Yang, J.-K. Kim, *Prog. Mater. Sci,* **2014**, 64, 200.
[42] C. J. Shearer, A. Cherevan, D. Eder, *Adv. Mater,* **2014**, 26, 2295.
[43] A. C. Ferrari, D. M. Basko, *Nat Nanotechnol,* **2013**, 8, 235.
[44] G. Eda, G. Fanchini, M. Chhowalla, *Nat Nanotechnol,* **2008**, 3, 270.
[45] M. S. Kang, K. T. Kim, J. U. Lee, W. H. Jo, *J. Mater. Chem. C,* **2013**, 1, 1870.
[46] H.-Z. Geng, K. K. Kim, K. P. So, Y. S. Lee, Y. Chang, Y. H. Lee, *J. Am. Chem. Soc,* **2007**, 129, 7758.
[47] A. K. K. Kyaw, H. Tantang, T. Wu, L. Ke, C. Peh, Z. H. Huang, X. T. Zeng, H. V. Demir, Q. Zhang, X. W. Sun, *Appl. Phys. Lett,* **2011**, 99, 021107.
[48] S. Kim, J. Yim, X. Wang, D. D. C. Bradley, S. Lee, J. C. deMello, *Adv. Funct. Mater,* **2010**, 20, 2310.
[49] A. Kasry, M. A. Kuroda, G. J. Martyna, G. S. Tulevski, A. A. Bol, *ACS Nano,* **2010**, 4, 3839.
[50] L. J. Larsen, C. J. Shearer, A. V. Ellis, J. G. Shapter, *RSC Adv,* **2015**, 5, 38851.
[51] R. Jackson, B. Domercq, R. Jain, B. Kippelen, S. Graham, *Adv. Funct. Mater,* **2008**, 18, 2548.
[52] Q. W. Li, Y. Li, X. F. Zhang, S. B. Chikkannanavar, Y. H. Zhao, A. M. Dangelewicz, L. X. Zheng, S. K. Doorn, Q. X. Jia, D. E. Peterson, P. N. Arendt, Y. T. Zhu, *Adv. Mater,* **2007**, 19, 3358.
[53] B.-S. Kong, J. Geng, H.-T. Jung, *Chem. Comm,* **2009**, 2174.
[54] H. A. Becerril, J. Mao, Z. Liu, R. M. Stoltenberg, Z. Bao, Y. Chen, *ACS Nano,* **2008**, 2, 463.
[55] Y. Xu, G. Long, L. Huang, Y. Huang, X. Wan, Y. Ma, Y. Chen, *Carbon,* **2010**, 48, 3308.
[56] Q. B. Zheng, M. M. Gudarzi, S. J. Wang, Y. Geng, Z. Li, J.-K. Kim, *Carbon,* **2011**, 49, 2905.
[57] J. Geng, L. Liu, S. B. Yang, S.-C. Youn, D. W. Kim, J.-S. Lee, J.-K. Choi, H.-T. Jung, *J. Phys. Chem. C,* **2010**, 114, 14433.
[58] L. Zhao, L. Zhao, Y. Xu, T. Qiu, L. Zhi, G. Shi, *Electrochim. Acta,* **2009**, 55, 491.
[59] J. Wu, H. A. Becerril, Z. Bao, Z. Liu, Y. Chen, P. Peumans, *Appl. Phys. Lett,* **2008**, 92, 263302.
[60] X. Wang, L. Zhi, N. Tsao, Ž. Tomović, J. Li, K. Müllen, *Angew. Chem. Int. Ed,* **2008**, 47, 2990.
[61] J. H. Noh, S. H. Im, J. H. Heo, T. N. Mandal, S. I. Seok, *Nano Lett,* **2013**, 13, 1764.
[62] H.-S. Ko, J.-W. Lee, N.-G. Park, *J. Mater. Chem. A,* **2015**, 3, 8808.
[63] Y. Liu, Q. Chen, H.-S. Duan, H. Zhou, Y. Yang, H. Chen, S. Luo, T.-B. Song, L. Dou, Z. Hong, Y. Yang, *J. Mater. Chem. A,* **2015**, 3, 11940.

[64] P. Qin, M. Paulose, M. I. Dar, T. Moehl, N. Arora, P. Gao, O. K. Varghese, M. Grätzel, M. K. Nazeeruddin, *Small,* **2015**, 11, 5533-5539..
[65] F. Di Giacomo, V. Zardetto, A. D'Epifanio, S. Pescetelli, F. Matteocci, S. Razza, A. Di Carlo, S. Licoccia, W. M. M. Kessels, M. Creatore, T. M. Brown, *Adv. Energy Mater,* **2015**, 5, 1401808.
[66] Y. Shi, Y. Xing, Y. Li, Q. Dong, K. Wang, Y. Du, X. Bai, S. Wang, Z. Chen, T. Ma, *J. Phys. Chem. C,* **2015**, 119, 15868.
[67] M. Lyu, J.-H. Yun, R. Ahmed, D. Elkington, Q. Wang, M. Zhang, H. Wang, P. Dastoor, L. Wang, *J. Coll. Interf. Sci,* **2015**, 453, 9.
[68] M. Batmunkh, M. J. Biggs, J. G. Shapter, *Adv. Sci,* **2015**, 2, 1400025.
[69] M. Batmunkh, M. J. Biggs, J. G. Shapter, *Small,* **2015**, 11, 2963.
[70] K. C. Kwon, B. J. Kim, J.-L. Lee, S. Y. Kim, *J. Mater. Chem. C,* **2013**, 1, 2463.
[71] J. T.-W. Wang, J. M. Ball, E. M. Barea, A. Abate, J. A. Alexander-Webber, J. Huang, M. Saliba, I. Mora-Sero, J. Bisquert, H. J. Snaith, R. J. Nicholas, *Nano Lett,* **2014**, 14, 724.
[72] M. Wojdyr, *J. Appl. Crystal,* **2010**, 43, 1126.

# Supporting Information for

# Solution Processed Graphene Structures for Perovskite Solar Cells

Munkhbayar Batmunkh,[1,2] Cameron J. Shearer,[2] Mark J. Biggs,[1,3] Joseph G. Shapter,[2]*

[1] *School of Chemical Engineering, The University of Adelaide, Adelaide, South Australia 5005, Australia*

[2] *School of Chemical and Physical Sciences, Flinders University, Bedford Park, Adelaide, South Australia 5042, Australia*

[3] *School of Sciences, Loughborough University, Loughborough, Leicestershire, LE11 3TU, UK*

* Corresponding authors:

joe.shapter@flinders.edu.au

**Published:** *Journal of Materials Chemistry A*, **2016**, *4*, 2605-2616

The published copy of the manuscript is attached in Appendix D.

Figure S5-1 shows the Raman spectra of graphene oxide (GO), chemically reduced graphene oxide (CRGO) without and with SDBS surfactant and reveals two typical peaks at 1350 $cm^{-1}$ (D band) and 1592 $cm^{-1}$ (G band). It is well known that the D and G bands indicate the structural defects and $sp^2$ hybridization in carbon materials, respectively. As can be seen from Figure S5-1, the D band of CRGO is slightly broad and its intensity is relatively high compared to that of CRGO-SDBS, indicating more defects exist in the CRGO. Moreover, the intensity ratio ($I_D/I_G$) is usually used to determine the defects quantity.[1] Some defects ($I_D/I_G$=0.91) in the GO are expected and is known to be due to the strong oxidization process of graphite.[2] Indeed, the $I_D/I_G$ value of the CRGO-SDBS is 1.04, which is lower than that ($I_D/I_G$=1.23) of CRGO produced without SDBS. This value confirms that the chemical (hydrazine) reduction on GO in the presence of SDBS surfactant creates less defect on the CRGO.

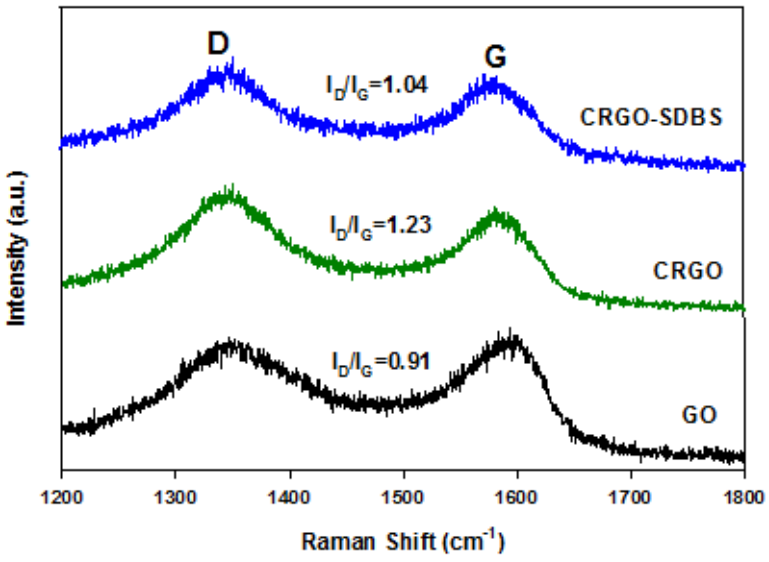


**Figure S5-1**. Raman spectra of GO, CRGO without and with SDBS surfactant.

Figure S5-2 illustrates curve fitting of the C1s peak in the X-ray photoelectron spectroscopy (XPS) spectra of the samples, namely GO, CRGO-SDBS and RGO-SDBS. The GO spectra can be fit to three individual components, namely the C-C at 284.8 eV, the C-O at 286 eV and the C=O and/or the COO at 287.5 eV. With chemical and thermal reduction the relative area of the C-C peak increased from 24

% for GO to 93 % and 81 %. This result agrees with the ATR-FTIR which showed that oxygen containing functional groups are removed with reduction. The shape of the C1s spectra may be broadened by the presence of SDBS.

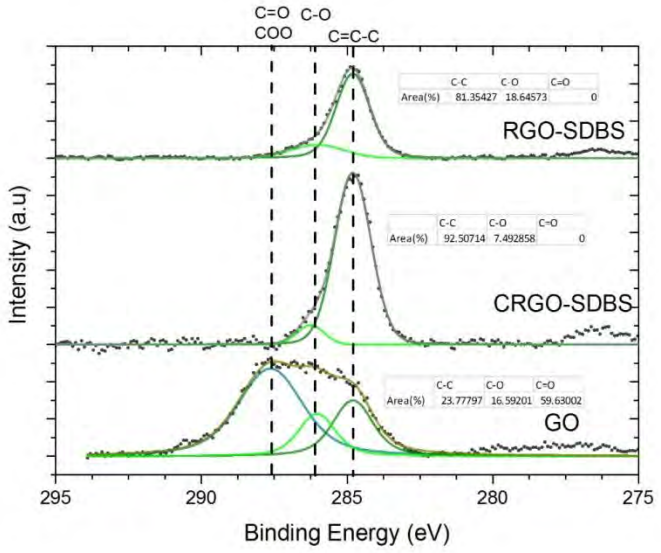


**Figure S5-2**. Curve fitting of the C1s peak in the XPS spectra of GO, CRGO-SDBS and RGO-SDBS samples.

The thermal stability of SDBS surfactant was studied using thermo-gravimetric analysis (TGA) by (i) heating at 400°C and (ii) heating to 800$^{o}$C at a rate of 20$^{o}$C min$^{-1}$ under an inert gas atmosphere. As shown in Figure S5-3, very little weight loss was observed for SDBS during heating at a temperature of 400$^{o}$C for over 1h. This small change in the weight loss of SDBS is in very good agreement with our finding from ATR-FTIR and XPS where slight decrease in the peak intensities was observed. Notably, the main mass loss of SDBS surfactant occurs after annealing at a high temperature (> 500$^{o}$C). However, our aim in this study was to use low-temperature based thermal process because high temperature annealing is undesired for the future development of flexible solar cells. Although the thermal treatment at 400$^{o}$C didn't remove the SDBS from the RGO film, the annealing process largely reduced the oxygen containing functional groups and significant improvement in the electrical conductivity of the films can be expected.

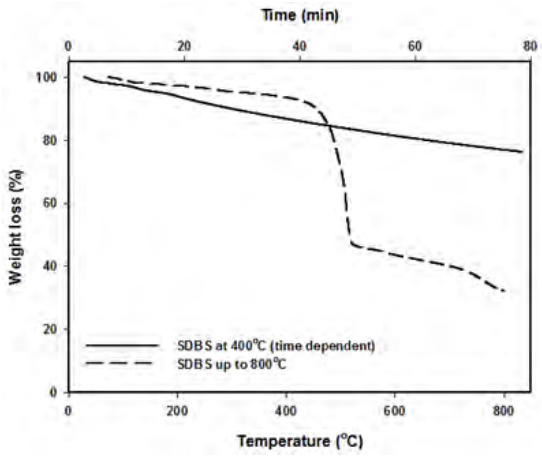


**Figure S5-3**. TGA analysis of SDBS surfactant.

Several changes in the optical transmittance of the films have been observed in each treatment. Figure S5-4 depicts the light transmittance at wavelength ranging from 400–1000 nm and sheet resistance ($R_s$) of the graphene films. Scheme 5-1d-g represents the schematic illustration of these films and is shown in Scheme 5-1.

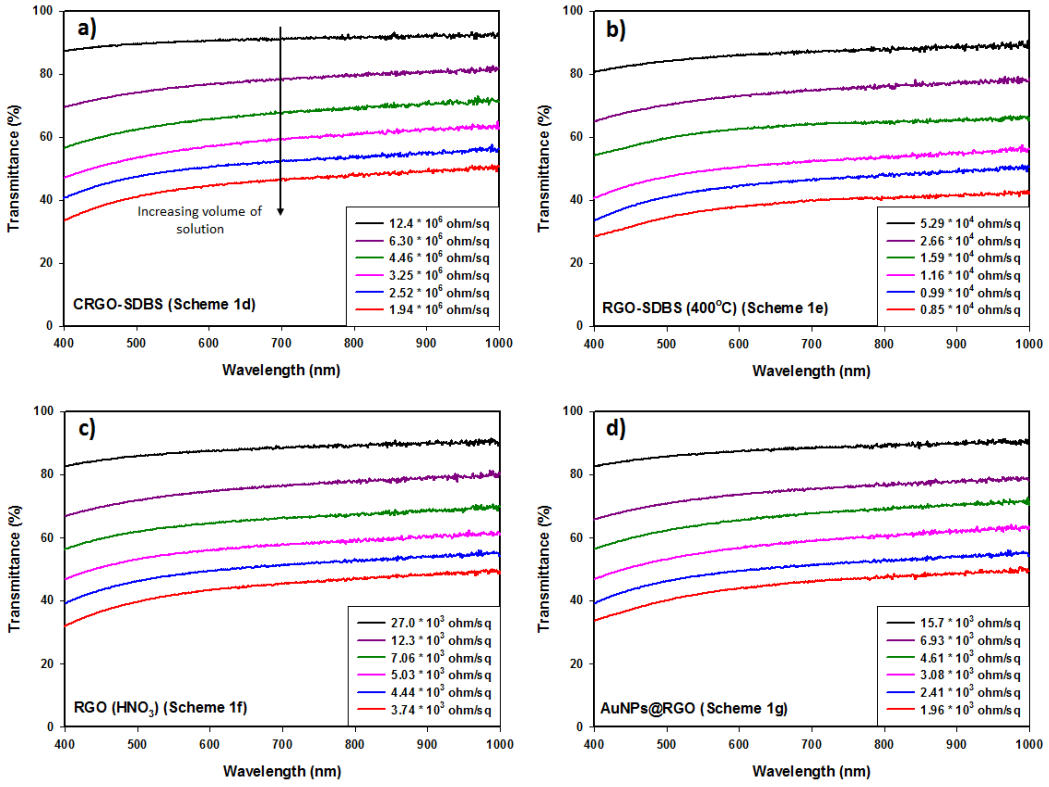


**Figure S5-4**. Optical and electrical characteristics of (a) CRGO-SDBS, (b) RGO-SDBS (400°C), (c) RGO ($HNO_3$-treated) and (d) AuNPs-RGO films.

A conventional PSC based on FTO electrode was also fabricated and its *J-V* characteristics are shown in Figure S5-5. The structure of the device is also illustrated in the inset of Figure S5-5. The FTO electrode based device exhibited $J_{sc}$ of 17.49 mA $cm^{-2}$, $V_{oc}$ of 0.71 V and *FF* of 0.63 and yielding a PCE of 7.82%.

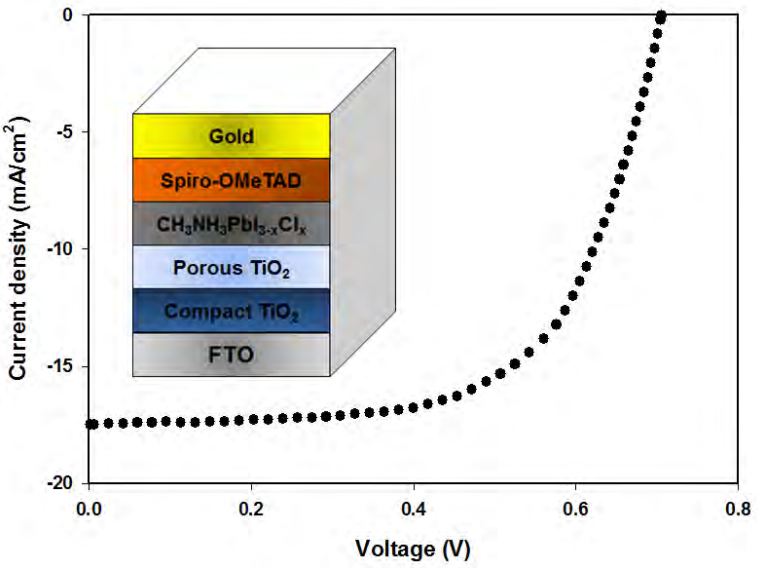


**Figure S5-5**. J–V curve of FTO-based PSC. The device structure is shown in the inset.

The stability of PSCs fabricated with FTO-electrode and TCGF electrode was studied for 60 h. After the fabrication of the cells under controlled humidity (< 35%), the cells were stored in ambient conditions (in air and uncontrolled humidity) in the dark for the stability test. The J–V characteristics of the cells were measured in every 12 h. No encapsulation was done for the devices. It can be observed from Figure S5-6 that the degradation rate of TCGF based cell was very similar to that of a FTO-based device. This indicates that the use of TCGF did not alter the internal decay mechanism of the PSC.

Section analysis of the AFM images reveals thickness of GO and CRGO-SDBS steps to be in the range of 1-5 nm. This value is typical for such samples when prepared by drop casting. The presented images have identical z-scale.

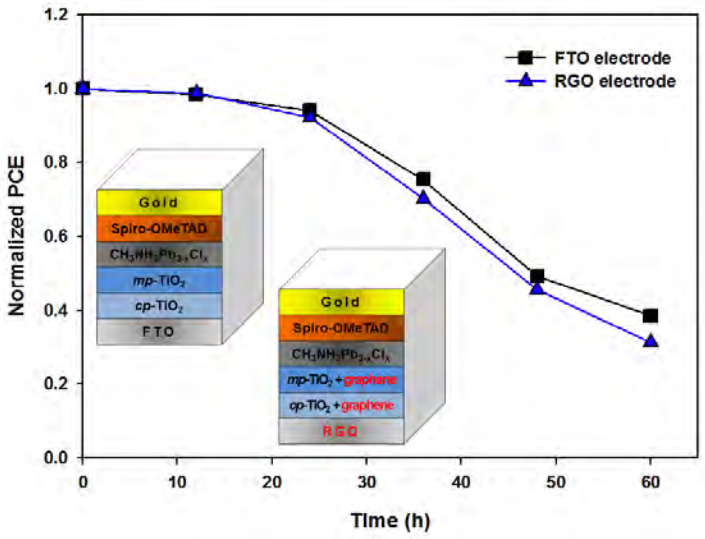


**Figure S5-6**. Stability of the PSCs fabricated based on FTO-electrode and TCGF (RGO electrode). The device structures are shown in the insets. Initial PCE for FTO-based and TCGF-based cell was 7.41% and 0.77%, respectively.

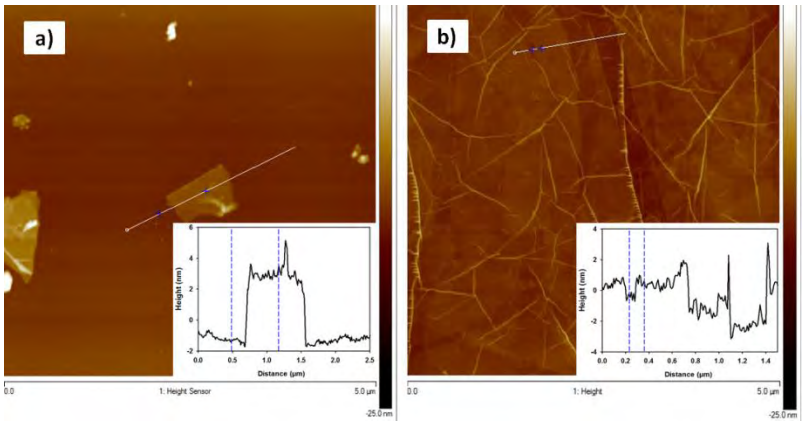


**Figure S5-7**. AFM image of CRGO (a) without and with (b) SDBS surfactant. Insets show the thickness measurement using a line profile.

## References

[1] A. C. Ferrari, D. M. Basko *Nat Nanotechnol,* **2013,** 8, 235-246.
[2] Y. Zhu, S. Murali, W. Cai, X. Li, J. W. Suk, J. R. Potts, R. S. Ruoff *Adv. Mater,* **2010,** 22, 3906-3924.

# Chapter 6.

# Carbon Nanotubes in $TiO_2$ Nanofiber Photoelectrodes for High Performance Perovskite Solar Cells

Munkhbayar Batmunkh,[1,2] Thomas J. Macdonald,[3] Cameron J. Shearer,[2] Munkhjargal Bat-Erdene,[2] Yun Wang,[4] Mark J. Biggs,[1,5] Ivan P. Parkin,[3] Thomas Nann,[6] and Joseph G. Shapter,[2]*

[1] *School of Chemical Engineering, The University of Adelaide, Adelaide, South Australia 5005, Australia*

[2] *School of Chemical and Physical Sciences, Flinders University, Bedford Park, Adelaide, South Australia 5042, Australia*

[3] *Department of Chemistry, University College London, London, UK*

[4] *Centre for Clean Environment and Energy, Griffith School of Environment, Gold Coast Campus, Griffith University, Queensland 4222, Australia*

[5] *School of Sciences, Loughborough University, Loughborough, Leicestershire, LE11 3TU, UK*

[6] *MacDiarmid Institute for Advanced Materials and Nanotechnology, School of Chemical and Physical Sciences, Victoria University of Wellington, Wellington, New Zealand*

* Corresponding authors: joe.shapter@flinders.edu.au

**Published:** *Advanced Science*, **2017**, *4*, 1600504

The published copy of the manuscript is attached in Appendix E.

# Statement of Authorship

| | |
|---|---|
| Title of Paper | Carbon Nanotubes in $TiO_2$ Nanofiber Photoelectrodes for High Performance Perovskite Solar Cells |
| Publication Status | ☑ Published ☑ Accepted for Publication<br>☐ Submitted for Publication ☐ Unpublished and Unsubmitted work written in manuscript style |
| Publication Details | Munkhbayar Batmunkh, Thomas J. Macdonald, Cameron J. Shearer, Munkhjargal Bat-Erdene, Yun Wang, Mark J. Biggs, Ivan P. Parkin, Thomas Nann, and Joseph G. Shapter, *Advanced Science*, 2017, *4*, 1600504. |

## Principal Author

| | |
|---|---|
| Name of Principal Author (Candidate) | Munkhbayar Batmunkh |
| Contribution to the Paper | Conducted the experimental works, performed analysis on all samples, interpreted data and wrote manuscript. |
| Overall percentage (%) | 75% |
| Certification: | This paper reports on original research I conducted during the period of my Higher Degree by Research candidature and is not subject to any obligations or contractual agreements with a third party that would constrain its inclusion in this thesis. I am the primary author of this paper. |
| Signature | Date 30/12/2016 |

## Co-Author Contributions

By signing the Statement of Authorship, each author certifies that:

i. the candidate's stated contribution to the publication is accurate (as detailed above);

ii. permission is granted for the candidate to include the publication in the thesis; and

iii. the sum of all co-author contributions is equal to 100% less the candidate's stated contribution.

| | |
|---|---|
| Name of Co-Author | Dr. Thomas J. Macdonald |
| Contribution to the Paper | Sample preparation, Sample characterizations, Edited the manuscript and manuscript evaluation. |
| Signature | Date 05/01/2017 |

| | |
|---|---|
| Name of Co-Author | Dr. Cameron J. Shearer |
| Contribution to the Paper | Sample characterization, edited the manuscript, and manuscript evaluation. |
| Signature | Date 4/1/17 |

| Name of Co-Author | Munkhjargal Bat-Erdene |
|---|---|
| Contribution to the Paper | Conducted some experimental works |
| Signature | Date 04/01/2017 |

| Name of Co-Author | Dr. Yun Wang |
|---|---|
| Contribution to the Paper | Conducted the computational calculation. Edited the manuscript |
| Signature | Date 04/01/2017 |

| Name of Co-Author | Prof. Mark J. Biggs |
|---|---|
| Contribution to the Paper | Co-advised the development of work, and manuscript evaluation. |
| Signature | Date 12/1/17 |

| Name of Co-Author | Prof. Ivan P. Parkin, |
|---|---|
| Contribution to the Paper | Sample characterization, edited the manuscript, and manuscript evaluation. |
| Signature | Date 05/01/2017 |

| Name of Co-Author | Prof. Thomas Nann |
|---|---|
| Contribution to the Paper | Co-advised the development of work, Edited the manuscript, and manuscript evaluation. |
| Signature | Date 9/1/17 |

| Name of Co-Author | Prof. Joseph G. Shapter |
|---|---|
| Contribution to the Paper | Supervised development of work, Edited the manuscript, manuscript evaluation and Corresponding author. |
| Signature | Date 4/1/18 |

# Abstract

One dimensional (1D) semiconducting oxides are unique structures that have been widely used for photovoltaic (PV) devices due to their capability to provide a direct pathway for charge transport. In addition, carbon nanotubes (CNTs) have played multifunctional roles in a range of PV cells because of their fascinating properties. Herein, the influence of CNTs on the PV performance of 1D titanium dioxide nanofiber ($TiO_2$ NF) photoelectrode perovskite solar cells (PSCs) is systematically explored. Among the different types of CNTs, single-walled CNTs (SWCNTs) incorporated in the $TiO_2$ NF photoelectrode PSCs showed a significant enhancement (~40%) in the power conversion efficiency (PCE) as compared to the control cell fabricated with $TiO_2$ NFs-only. Highly conductive SWCNTs incorporated in $TiO_2$ NFs provided a fast electron transfer within the photoelectrode, resulting in an increase in the short-circuit current ($J_{sc}$) value. On the basis of our theoretical calculations, the improved open-circuit voltage ($V_{oc}$) of the cells can be attributed to a shift in energy level of the photoelectrodes after the introduction of SWCNTs. Furthermore, we found that the incorporation of SWCNTs into $TiO_2$ NFs reduces the hysteresis effect and improves the stability of the PSC devices both under light and during storage in ambient conditions (>60% humidity). In this study, the best performing device constructed with SWCNT structures achieved a PCE of 14.03%.



**Keywords:** Photovoltaic, perovskite solar cells, photoelectrodes, $TiO_2$ nanofibers, carbon nanotubes


**TOC Figure**

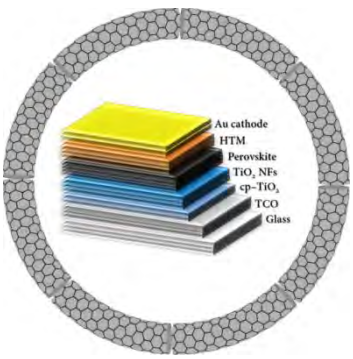

## 6.1. Introduction

High performance photovoltaic (PV) cells that can convert the sun's energy directly into electricity through the PV effect are promising clean and renewable energy technologies and have great potential to address current energy related issues.[1] Organolead halide ($CH_3NH_3PbX_3$, X = I, Cl or Br) implemented solar cells (known as perovskite solar cells (PSCs)) have received significant attention from both scientific and industrial communities and have become one of the most popular topics in scientific research in recent times.[2, 3] This increasing popularity of PSCs is due to the unprecedented rapid progress that has been made in their power conversion efficiencies (PCEs) over a short period of time.[4, 5] Since 2009, the PCEs of PSCs have increased from 3.8% to 22.1%, making them the fastest-advancing PV technology.[6-10] Recent successful fabrication of flexible and large-area PSC devices shows great promise for the commercialization of this cutting-edge technology.[11-16]

The most commonly explored PSC architecture consists of a transparent conducting oxide (TCO) coated glass substrate, a compact titanium dioxide ($TiO_2$) layer, mesoporous nanocrystalline $TiO_2$ layer, perovskite layer, hole transporting layer and metal contact.[5, 17-21] The working principle of this class of PSCs can be expressed as follows: upon illumination, the perovskite is excited, producing an electron-hole pair. Then the electrons are injected into the conduction band of the n-type semiconducting oxide (generally $TiO_2$), while the holes are transported to the p-type hole transporting materials (HTMs). Finally, the electrons and holes are collected at conductive electrodes such as TCO-based anodes and metal cathodes, respectively.[22] Fast charge-transfer processes in PSCs are of particular importance to maximize the device performance. The measured values for the injection times of electrons and holes in PSCs are 0.4 ns and 0.6 ns, respectively.[23] However, these values are three orders of magnitude longer than the hot carrier cooling time (~0.4 ps), which leads to carrier trapping and a significant loss of the photon energy due to thermalization.[23] Moreover, a large number of grain boundaries in the nanocrystalline films leads to rapid charge recombination, resulting in reduced device performance. These issues have led to some recent efforts focused on developing strategies to enhance the charge transport properties in PSCs.

One promising strategy is to use a one dimensional (1D) nanostructure as a substitute for the nanoparticles in the photoelectrode to suppress the charge recombination and provide a direct pathway along the long axis of 1D nanostructures for electron transport.[24-28] In addition, the electron transport rate in 1D nanostructures such as nanofibers, nanowires, nanocolumns and nanorods have been considered to be several orders of magnitude faster than that of nanoparticles.[29-32] This is achieved by reducing the scattering of free electrons from the grain boundaries of the interconnected nanoparticles.[33] On the other hand, the incorporation of highly conductive carbon nanomaterials such as graphene and carbon nanotubes (CNTs) has also been proven as an effective method to facilitate the charge transport and extend the electron lifetime, thereby enhancing the efficiency of PV devices.[22, 34-37] Although graphene and its derivatives have been successfully utilized for improving the performance of PSCs,[38-43] there has been no effort in the application of CNTs for use in PSC photoelectrodes. It should be noted that due to their unique structure and outstanding properties including excellent conductivity and high optical transparency, CNTs have exhibited promising results when they are used as a HTM and cathode in PSCs.[44-49] Moreover, CNTs are promising candidates for fabricating flexible fiber-shaped PSCs.[50-53] Therefore, integrating highly conductive CNTs into 1D structured $TiO_2$ for use in the photoelectrode of PSCs is an alternative approach to provide an ultrafast electron transport pathway to enhance device performance.

In the work presented here, the influence of CNTs on the performance of PSCs fabricated with 1D $TiO_2$ nanofibers (NFs) is systematically examined. By using an optimal amount of single-walled CNT nanostructures (SWCNTs) in the $TiO_2$ NFs, a significant enhancement (~40%) in the device performance is achieved as compared to the control cell fabricated without CNTs. Further PCE enhancement is obtained by incorporating SWCNTs into both compact and mesoporous $TiO_2$ layers of the PSCs. Based on our experimental and theoretical analysis, we attribute the performance enhancement of PSCs obtained by employing SWCNTs to the introduction of suitable energy levels and reduced charge recombination due to the increased charge transport of the photoelectrodes. More importantly, PSCs fabricated with SWCNT-$TiO_2$ NFs exhibited reduced hysteresis and improved stability both under light and during storage under humid conditions with respect to the control devices without SWCNTs. We also demonstrate in this study that SWCNTs can be used as an

efficient HTM in PSCs. While previous work has shown $TiO_2$ NF-based PSCs can achieve PCE values of up to 9.8 %,[25] and 13.4 % for atomic layer deposited nanorods,[54] in this work, our best performing PSC achieved a PCE of 14.03%.

## 6.2. Results and Discussion

In order to fabricate PSCs with the device architecture displayed in Figure 6-1a, $TiO_2$ NFs were first prepared using an electrospinning method. $CH_3NH_3PbI_3$ was used as a light absorbing perovskite material. A detailed description of the synthesis process can be found in the experimental section. Low and high resolution scanning electron microscopy (SEM) images of the prepared $TiO_2$ NFs are shown in Figure 6-1b and c, respectively. The $TiO_2$ NFs were several micrometres in length, while their diameter varied within a few hundreds of nanometres. In addition to the relatively uniform morphology, the prepared $TiO_2$ NFs films showed an excellent porous network which can be beneficial for perovskite absorber loading (see Figure S6-1a-d, Supporting Information). The anatase phase of the $TiO_2$ NFs on FTO was confirmed by X-ray diffraction as compared to the reference values (9853-ICSD)[55] and can be seen in Figure S6-1e. In our devices (Figure 6-1d), $TiO_2$ NFs were used as electron transporting layer (ETL).

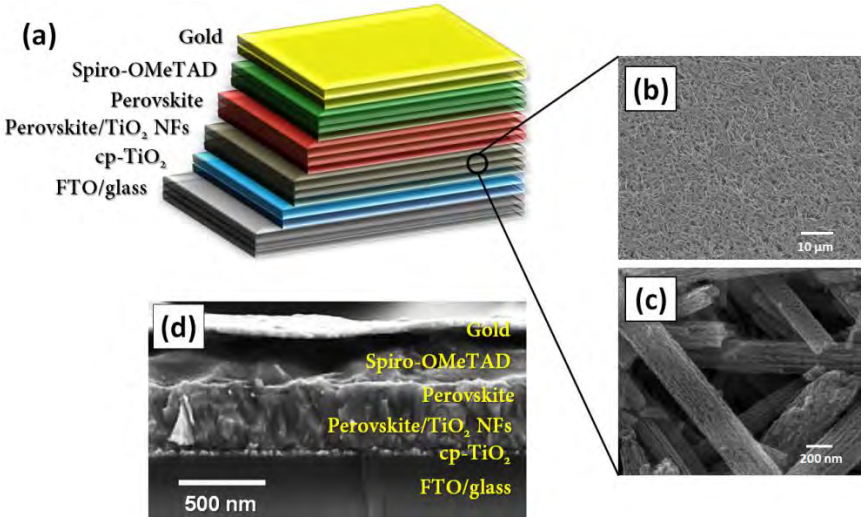


**Figure 6-1**. (a) Schematic illustration of $TiO_2$ NFs photoelectrode based PSC. (b) Low and (c) high resolution SEM image of $TiO_2$ NFs. (d) Cross sectional SEM image of representative $TiO_2$ NFs (400 nm thickness) photoelectrode based PSC.

The thickness of ETLs in the PSCs has a critical influence on the device performance.[10, 56] To investigate the effect of the thickness of $TiO_2$ NFs films on the cell efficiency, five PSC devices were fabricated based on the $TiO_2$ NF photoelectrodes with different thicknesses. The thickness of the $TiO_2$ NF layer was controlled by dilution of the $TiO_2$ NF paste. The diluted $TiO_2$ solutions were spin coated onto the compact $TiO_2$ (cp-$TiO_2$) using identical conditions. Cross sectional SEM images of $TiO_2$ NF films with different thicknesses (~285 nm to ~2200 nm) are depicted in Figure S6-2a–e. For comparison, a planar PSC device was fabricated without the $TiO_2$ NF layer (Figure S6-2f and Figure S6-3).

The PV characteristics of the fabricated devices were studied under an air mass (AM) 1.5 illumination at 100 mW $cm^{-2}$. The photocurrent density–voltage (J–V) characteristics of the PSCs fabricated with different $TiO_2$ NF thicknesses are displayed in Figure 6-2a and the corresponding PV parameters such as short-circuit current ($J_{sc}$), open-circuit voltage ($V_{oc}$), fill factor (FF) and PCE have been summarized in Table S6-1 (Supporting Information). As an optimal thickness of $TiO_2$ NFs, the PSCs fabricated with ~400 nm $TiO_2$ NFs exhibited the highest PCE (average efficiency of 8.21 ± 0.46%). The observed $J_{sc}$, $V_{oc}$ and FF values for the best device based on ~400 nm $TiO_2$ NF photoelectrode PSCs were 15.91 mA $cm^{-2}$, 0.87 V and 0.62, respectively, yielding a PCE of 8.56%.

As shown in Figure 6-2a and Table S6-1, both $J_{sc}$ and $V_{oc}$ values of PSCs continuously decreased with the higher $TiO_2$ NF film thicknesses (from ~400 nm to ~2200 nm), resulting in lower cell efficiencies. Increasing the film thickness, which in turn lowers the PCE, is believed to be a result of the high charge recombination rate within the $TiO_2$ NFs based devices.[10, 25, 57] In contrast, the devices fabricated without $TiO_2$ NFs (called planar PSCs) or with thin $TiO_2$ NF layers (~285 nm) showed high $V_{oc}$, but their PCEs were low due to the decreased $J_{sc}$ and FF values. This higher $V_{oc}$ value of planar devices can be associated with the lower probability of charge recombination as compared to the porous structured PSCs. These results are very consistent with recent studies on $CH_3NH_3PbI_3$ based planar PSC devices.[25, 58, 59] Considering the PCEs of the devices, the $TiO_2$ NF (~400 nm) film was chosen for further investigations and device fabrication.

To understand the effect of CNT type on the performance of PSCs, three different types of CNTs, namely double-walled CNTs (DWCNTs), multi-walled CNTs (MWCNTs) and single-walled CNTs (SWCNTs) were incorporated into the $TiO_2$ NF photoelectrodes based PSCs under the same experimental conditions. The J–V curves of these devices are plotted in Figure 6-2b. The concentration of CNTs in the $TiO_2$ NF-CNT hybrid was 0.02 wt%. The average PCEs of these PSCs were calculated based on five identical devices (see Table S6-2). It can be seen from Figure 6-2b and Table S6-2 that the incorporation of CNTs, regardless of their type increases the $J_{sc}$ value compared to the $TiO_2$ NF-only photoelectrodes, which can be associated with the high conductivity of CNTs.[36] In particular, the use of the SWCNTs in $TiO_2$ NFs photoelectrodes was shown to considerably enhance the PCE of PSCs by improving the $J_{sc}$ and $V_{oc}$ values despite the fact that a very small amount of SWCNTs was added and no optimization was undertaken at this point. Indeed, the addition of SWCNTs (0.02 wt%) into the $TiO_2$ NFs photoelectrodes of PSCs increased the PCE from 8.56% to 9.91%. We hypothesize that this PCE enhancement is due to the excellent conductivity and mixture of metallic and semiconducting behaviour of SWCNTs. Therefore, the SWCNTs were chosen for further optimization of the devices to maximize the cell performance.

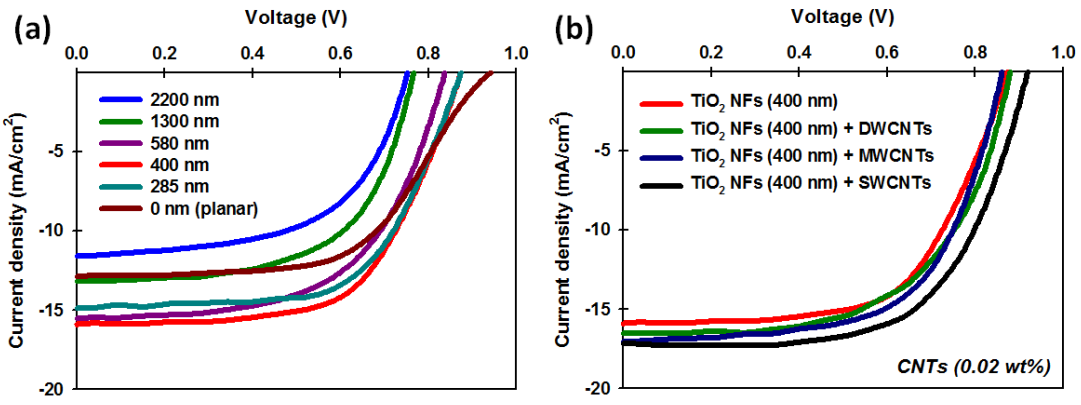


**Figure 6-2**. J–V curves of PSCs fabricated based on (a) different thicknesses of $TiO_2$ NF films and (b) various types of CNTs incorporated $TiO_2$ NF photoelectrodes. For the fabrication of $TiO_2$ NF-CNT photoelectrodes ~400 nm $TiO_2$ NFs was chosen.

Figure 6-3a displays the SEM image of SWCNTs incorporated $TiO_2$ NFs. SWCNTs a few nanometers in diameter (highlighted by yellow arrows in Figure 6-3a) are observed and wrapped around the $TiO_2$ NFs, indicating successful integration of the SWCNTs into the $TiO_2$ NFs. It is worth noting that 1D $TiO_2$ NFs can provide a direct electron transport pathway.[24] More importantly, in such hybrid structure ($TiO_2$ NFs-SWCNTs), the SWCNTs are expected to provide an extremely fast electron transport pathway with excellent conductivity (see Figure 6-3b).

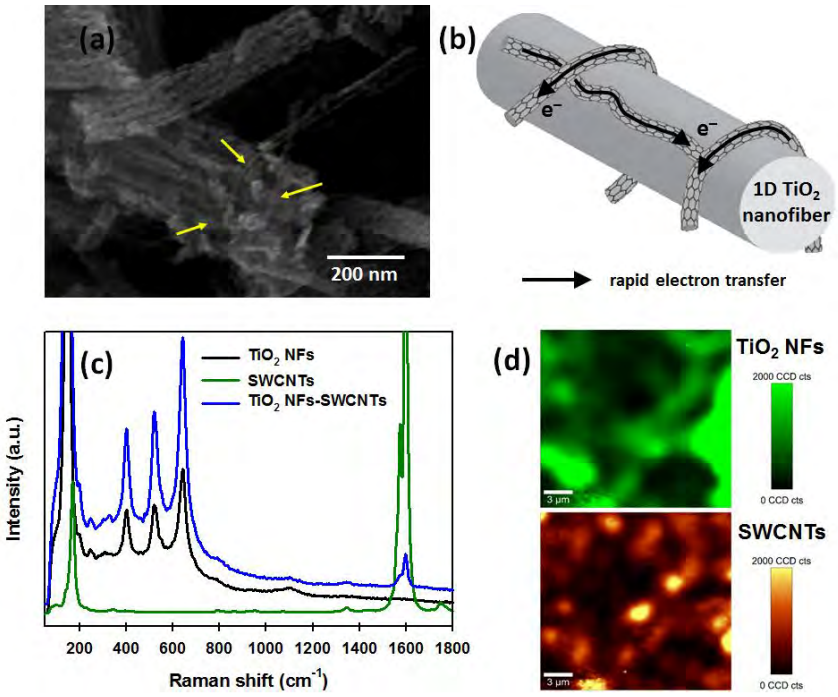


**Figure 6-3**. (a) SEM image and (b) schematic illustration of $TiO_2$ NF-SWCNT hybrid. (c) Raman spectra of $TiO_2$ NFs, SWCNTs and $TiO_2$ NFs-SWCNTs. (d) Raman mapping image of $TiO_2$ NFs (top, green) and SWCNTs (bottom, orange) in the hybrid sample. In both images, the "bright" regions represent the presence of the materials.

To further confirm the presence of SWCNTs in the hybrid, the samples were characterized using Raman microspectroscopy. Figure 6-3c shows the Raman spectra of $TiO_2$ NFs, SWCNTs and their hybrid structures. For the pure $TiO_2$ NFs, four strong peaks at around 149, 397, 512 and 639 $cm^{-1}$, which correspond to the $E_{g(1)}$, $B_{1g(1)}$, $A_{1g + B1g(2)}$ and $E_{g(2)}$ modes of anatase $TiO_2$, respectively were observed.[41] On

the other hand, the SWCNTs showed two typical Raman feature peaks at around 1346 and 1587 $cm^{-1}$ which can be assigned to the "*D*" band (the disordered mode) and "*G*" band (tangential mode), in addition to the radial breathing mode (RBM) peak at around 172 $cm^{-1}$.[44] For $TiO_2$ NFs-SWCNTs hybrid, all the Raman bands of both $TiO_2$ NFs and SWCNTs were observed, further confirming the successful incorporation of SWCNTs into the $TiO_2$ NF system. Moreover, confocal Raman spectral mapping was carried out on a selected area of the $TiO_2$ NFs-SWCNTs hybrid. Notably, the obtained maps in Figure 6-3d confirm the co-existence of $TiO_2$ NFs and SWCNTs throughout the imaged area indicating a relatively homogenous distribution of SWCNTs within the porous film.

**Table 6-1**. PV parameters of best performing PSC devices fabricated based on $TiO_2$ NF photoelectrodes with different SWCNTs loadings (extracted from the J–V characteristics reported in Figure 6-4). The average PCEs were calculated based on at least five devices. PV parameters of the best devices are highlighted in **bold**.

| Device | $J_{sc}$ (mA $cm^{-2}$) | $V_{oc}$ (V) | FF | PCE (%) |
|---|---|---|---|---|
| $TiO_2$ NFs-only | **15.91**; 15.44 ± 0.54 | **0.87**; 0.87 ± 0.01 | **0.62**; 0.61 ± 0.01 | **8.56**; 8.21 ± 0.46 |
| 0.02 wt% SWCNTs | **17.20**; 17.11 ± 0.20 | **0.93**; 0.92 ± 0.01 | **0.62**; 0.61 ± 0.01 | **9.91**; 9.69 ± 0.23 |
| 0.05 wt% SWCNTs | **19.34**; 19.04 ± 0.43 | **0.93**; 0.93 ± 0.00 | **0.61**; 0.61 ± 0.00 | **11.05**; 10.81 ± 0.34 |
| 0.10 wt% SWCNTs | **20.68**; 20.26 ± 0.37 | **0.94**; 0.94 ± 0.01 | **0.62**; 0.62 ± 0.01 | **12.03**; 11.51 ± 0.40 |
| 0.20 wt% SWCNTs | **19.24**; 19.16 ± 0.31 | **0.92**; 0.91 ± 0.01 | **0.60**; 0.59 ± 0.01 | **10.54**; 10.16 ± 0.32 |
| 0.40 wt% SWCNTs | **17.56**; 17.43 ± 0.37 | **0.90**; 0.89 ± 0.01 | **0.62**; 0.60 ± 0.02 | **9.80**; 9.40 ± 0.39 |

In order to optimize the devices, five PSCs were fabricated using different SWCNT content in the $TiO_2$ NF photoelectrodes and their performances were compared with $TiO_2$ NF-only photoelectrodes control cells. Figure 6-4 shows the typical J–V curves

of the $TiO_2$ NF-SWCNT hybrid photoelectrodes based PSC devices. The corresponding PV parameters of these devices have been summarized in Table 6-1. Starting from the control devices constructed based on $TiO_2$ NF-only photoelectrodes, the $J_{sc}$ and $V_{oc}$ are 15.91 mA $cm^{-2}$ and 0.87 V, respectively. With increasing SWCNT loading in the $TiO_2$ NF photoelectrodes, both the $J_{sc}$ and $V_{oc}$ values of the PSCs increased up to 20.68 mA $cm^{-2}$ and 0.94 V, respectively, peaking at 0.10 wt%, followed by a decrease with further increases in SWCNTs content. The increase in the $J_{sc}$ of the cells is probably due to the improved conductivity the films (see Figure S6-4) that can accelerate the electron transport process within the photoelectrode of PSCs. However, when the concentration of SWCNTs in the hybrid further increases to 0.20 wt% and 0.40 wt%, both $J_{sc}$ and $V_{oc}$ values of the devices decreased despite the films having reduced sheet resistance ($R_s$).

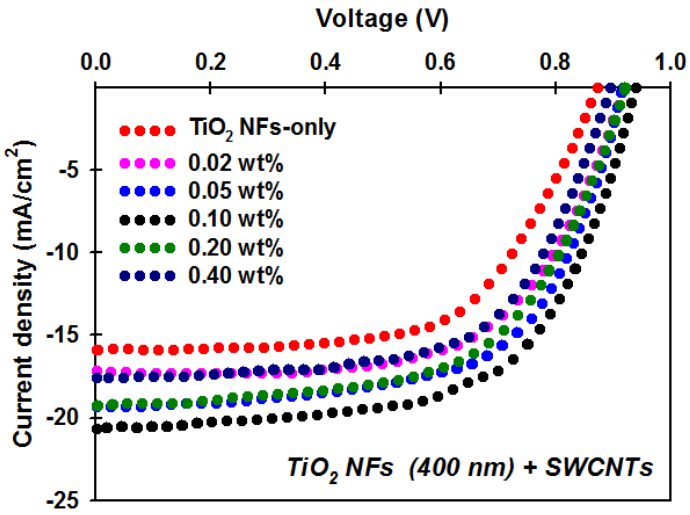


**Figure 6-4**. J–V curves of best performing PSC devices fabricated with different SWCNTs contents in the $TiO_2$ NF photoelectrodes. The performance of the cells were measured under AM 1.5G illumination at 100 mW $cm^{-2}$.

A series of detailed investigations have been carried out to understand the origin of the decrease in PV performance at higher SWCNT loadings. We measured the optical transmittance of the $TiO_2$ NF films (on a glass slide) with different SWCNT loadings (Figure S6-5a). A low optical transmittance of photoelectrode could elucidate the decreased $J_{sc}$ value of the cells due to the less light being incident upon

the perovskite layer. However, not surprisingly given the small amounts of CNTs being added, the changes in the film transmittance by adding SWCNTs into the $TiO_2$ NFs were very small. For example, for the 0.20 wt% SWCNTs incorporated $TiO_2$ NF film, the reduction of the transmittance was only ~4% as compared to that of the $TiO_2$ NFs-only film. Therefore, the decreased $J_{sc}$ of the device after adding 0.20 wt% and 0.40 wt% SWCNTs into the $TiO_2$ NF photoelectrodes cannot be explained solely by the slightly reduced transmittance of the films. As with all other work that has incorporated nanocarbons in solar cells, we observed that there is an optimal loading which gives the maximum efficiency. At loading above the optimal, it is likely that the decreased PV performance is due to the fact that the CNTs provide extra junctions or sites where recombination of charge carriers is possible. It has been found that nanocarbons including CNTs are suitable candidates to replace the conventional HTMs in PSCs and/or improving the device efficiency owing to their fascinating properties.[44-48, 60] In order to confirm our hypothesis, we used SWCNTs as a HTM for the $TiO_2$ NF-only photoelectrode based PSCs. For comparison, PSC devices with and without conventional HTM (Spiro-OMeTAD) were fabricated and compared (Figure S6-5). It is not surprising that the HTM-free device (Perovskite/Au) exhibited a very poor PCE (3.65%), while Spiro-OMeTAD (typical HTM) based PSC was able to achieve an average PCE of 8.21%. The poor performance of HTM-free PSC is known to be due to the significant charge recombination caused by direct contact between the perovskite and gold electrode.[44] Interestingly, when SWCNTs are used as a HTM in PSCs by inserting them between the perovskite and gold electrode, the fabricated device showed an improved PCE (6.01%) compared to the device without HTM, demonstrating that SWCNTs can act as an efficient HTL for PSCs. It is known that CNTs are ambipolar and can conduct both holes and electrons.[61] This ability in PSCs is confirmed in these experiments. Thus, in the $TiO_2$ NF-SWCNTs based electrode, it is very likely that the presence of larger amounts of SWCNTs will prolong the lifetime of the hole charge carriers and this will lead to increased recombination rates in the ETL. This likely explains the decreased $J_{sc}$ and $V_{oc}$ values of the PSC devices after adding high concentrations of SWCNTs into the $TiO_2$ NFs photoelectrodes.

As can be seen from Figure 6-4 and Table 6-1, the PSC devices fabricated based on the 0.10 wt% SWCNTs incorporated $TiO_2$ NFs photoelectrodes showed the highest

PCE of 12.04% with an average efficiency of 11.51 ± 0.40%, whereas the control cells without SWCNTs displayed an average PCE of 8.21 ± 0.46%. The calculated PCE enhancement of PSCs loaded with 0.10 wt% SWCNTs (in comparison to the efficiency of the control cell) was 40.6%. In addition, the reproducibility of both control and SWCNTs incorporated devices was high and this is evident from the small standard deviation in the PV efficiency (Figure S6-6). This result confirms that the incorporation of SWCNTs in the $TiO_2$ NFs photolectrodes does not alter the reproducibility of the devices. Indeed, the increased $J_{sc}$ and $V_{oc}$ values were the major contributions to this efficiency enhancement. Therefore, the devices loaded with 0.10 wt% SWCNTs and the control cells were chosen for further investigation to fully understand the role of SWCNTs in the PSCs.

To confirm the enhancement of the $J_{sc}$, the incident-photon-to-current conversion efficiency (IPCE) spectra of the PSCs fabricated with and without SWCNTs (0.10 wt%) in the photoelectrodes were recorded and their results are plotted in Figure 6-5a. Clearly, the IPCE value of $TiO_2$ NF photoelectrodes containing SWCNTs is higher than that of the control cell without SWCNTs. The integrated photocurrent density of the $TiO_2$ NFs-only and $TiO_2$ NFs-SWCNTs photoelectrodes based PSCs was 15.20 mA $cm^{-2}$ and 19.50 mA $cm^{-2}$, respectively, which are in agreement with the measured $J_{sc}$ from the J-V characteristics of the devices. The improved current is evident over the entire wavelength region, indicative of enhanced electron collection in the PSC loaded with SWCNTs. The improved $J_{sc}$ value of the $TiO_2$ NF-SWCNT photoelectrodes was further examined using electrochemical impedance spectroscopy (EIS).

EIS measurement of full PSC devices in the dark can be used to distinguish the charge transfer at the perovskite/HTM/cathode interface and the charge recombination at the ETL ($TiO_2$)/perovskite interface.[62] EIS of the PSCs fabricated with and without SWCNTs in the $TiO_2$ NFs photoelectrodes was measured at a bias of 0.3 V in the dark and the extracted data with a simplified circuit model are illustrated in Figure 6-5b. In general, the high frequency arc is associated with the diffusion of holes through the HTM, while the lower frequency arc is related to the recombination resistance, $R_{rec}$, mainly due to the charge recombination between the electron transporting material and HTM.[62, 63] Clearly, the diameter of the semicircle at the lower frequency of SWCNTs incorporated $TiO_2$ NFs photoelectrode based

PSC is larger than that of $TiO_2$ NFs-only device, indicating higher $R_{rec}$ (87.0 kΩ) for SWCNTs employed device as compared to the control device (58.3 kΩ). The high $R_{rec}$ indicates an efficient blocking for possible recombination. This result clearly demonstrates that the SWCNTs significantly reduced the charge recombination and increased the charge transfer within the cell as expected.

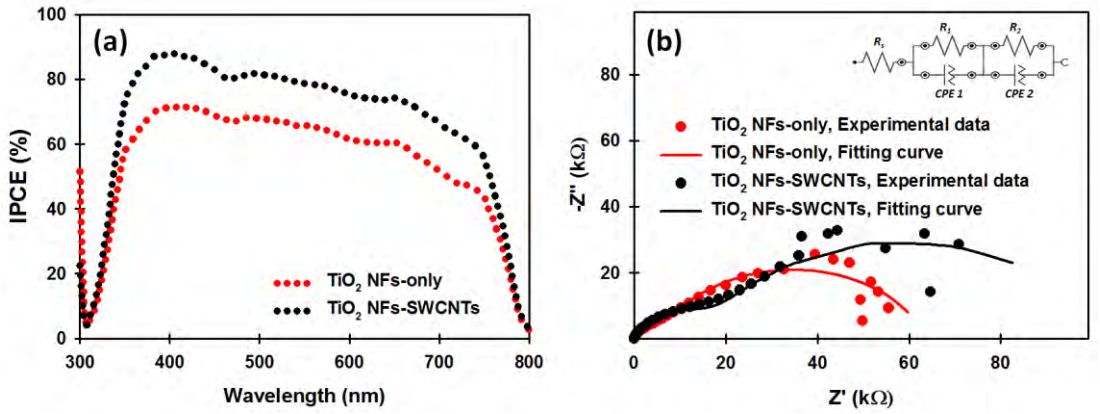


**Figure 6-5**. (a) IPCE and (b) EIS spectra of PSC fabricated with and without SWCNTs (0.10 wt%) in the $TiO_2$ NFs photoelectrode.

To further investigate the effect of SWCNTs on the charge transfer process of $TiO_2$ NF photoelectrodes based PSCs, dark J-V measurements were carried out (see Figure S6-7). The dark J-V measurement can provide important information about the recombination process in the devices.[42] From the dark J-V measurement, an ideality factor of each device can be calculated, and notably, low values of ideality factor represents less charge recombination. The ideality factor of the $TiO_2$ NFs-SWCNTs photoelectrode based PSC device was 1.82 which was lower than that (2.41) of the control PSC, proving that the incorporation of SWCNTs in the $TiO_2$ NFs significantly suppresses the recombination process in the devices.

It should be noted that the previous studies have shown decreased and/or unchanged $V_{oc}$ values of PSC devices after the incorporation of various nanocarbon materials into the ETLs.[39, 40, 42] Interestingly, our study demonstrates that the addition of a small amount of SWCNTs into the ETL leads to a considerable enhancement in the $V_{oc}$. In order to explain why the $V_{oc}$ value increased after adding SWCNTs into the $TiO_2$ NFs, we investigated the interactions between SWCNTs and anatase $TiO_2$ (101)

surface using a computational method method based on the first principles density functional theory (DFT). In theory, the $V_{oc}$ of PSCs is the difference between the conduction band minimum (CBM) of the $TiO_2$ and the potential energy of the HTM. Based on the DFT results, the CBM level is 0.58 V vs. SHE (see Figure 6-6a). After the adsorption of SWCNT, the analysis of density of states (DOS) demonstrates that the system changes from a semiconductor to a metallic material (see Figure 6-6b), which supports that the improved electronic conductivity observed in EIS measurements. Moreover, the theoretical $V_{oc}$ can be calculated based on the difference between the work function of metallic SWCNT-$TiO_2$ and the potential energy of the HTM. The theoretical results reveal that the work function of SWCNT-$TiO_2$ is 0.35 V vs SHE, which is 0.23 V higher than the CBM level of $TiO_2$. Since the redox potential of the HTM is a constant, the theoretical $V_{oc}$ can, therefore, be enhanced by 0.23 V, which matches the experimental observations.

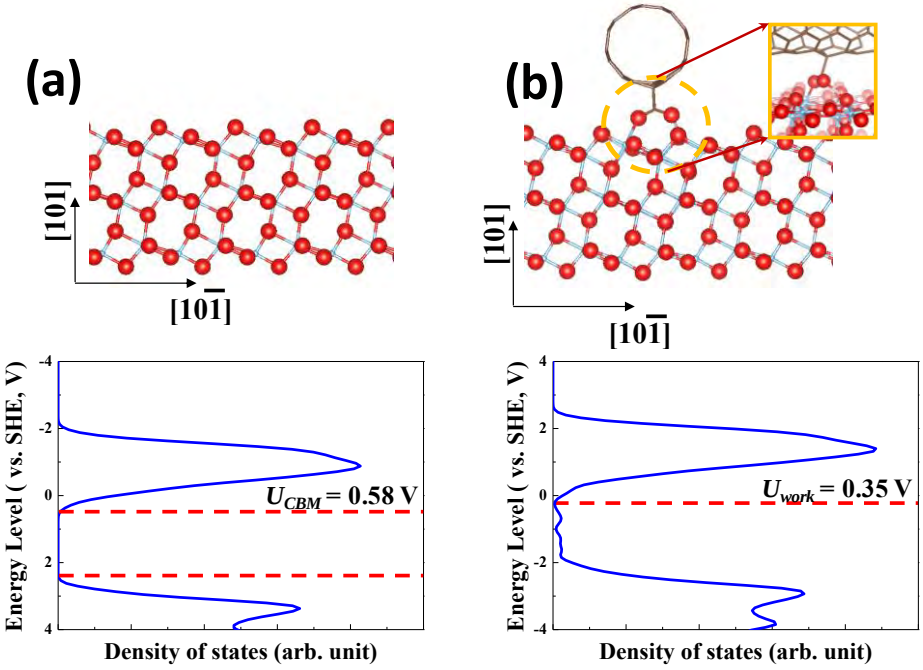


**Figure 6-6**. (a) Atomic structure of pure anatase $TiO_2$ (101) surface (upper panel) and its DOS plot vs the SHE in V (lower panel). (b) Atomic structure of SWCNT-anatase $TiO_2$ (101) surface (upper panel) and its DOS plot vs the SHE in V (lower panel). Inset in (b) is the atomic structure at the interface between the SWCNT and $TiO_2$ (101). Blue, Ti; red, O; brown, C; pink, H.

One of the critical challenges in PSCs is hysteretic J−V behaviour. In general, the hysteresis effect in PSCs is observed from the forward scan (FS, from $J_{sc}$ to $V_{oc}$) and reverse scan (RS, from $V_{oc}$ to $J_{sc}$) of a J–V measurement.[64] Here, we studied the hysteresis behaviour of our PSCs fabricated with and without SWCNTs in the $TiO_2$ NFs photoelectrodes (see Figure 6-7). As illustrated in Figure 6-7a, the $TiO_2$ NF-only based device exhibited a large hysteresis and distortion in the J–V curves. Such hysteresis behaviour causes an underestimation of the real J–V curves in the FS and overestimation in the RS. Interestingly, it can be seen from Figure 6-7b and Table S6-3 that the incorporation of SWCNTs into the photoelectrodes reduces the hysteresis behaviour of the cells. The exact mechanism of hysteresis phenomenon in PSCs is not well established, however several explanations have been suggested based on both experimental and theoretical investigations.[64] It has been suggested that an anomalous hysteresis in PSCs can be attributed to the charge recombination at the interface between perovskite and charge transporting layer.[42, 65] Clearly, SWCNTs suppressed the charge recombination in the PSC photoelectrodes and this may contribute to the reduced J–V curve hysteresis.

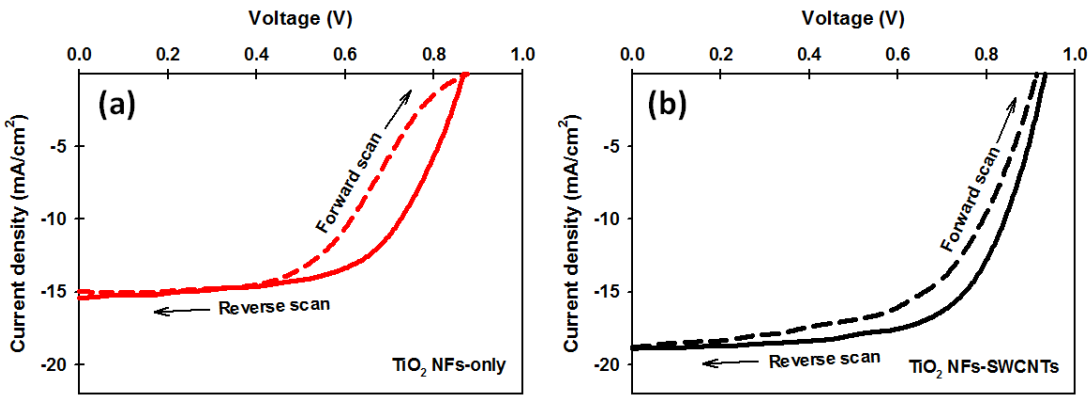


**Figure 6-7**. J–V curves measured at FS and RS for the (a) $TiO_2$ NFs-only and (b) $TiO_2$ NFs-SWCNTs photoelectrodes based PSCs. Detailed PV parameters are given in Table S6-3.

The stability of PSCs is an important factor for their potential commercialization on an industrial scale. The long-term storage stability of the PSC devices fabricated with and without SWCNTs in the $TiO_2$ NF photoelectrodes was investigated over 12 days

(288 h). For the long-term storage stability test, the unencapsulated cells were stored in the dark and kept in ambient conditions (normal laboratory) at a relative humidity of at least 60%. Normalized PCEs of these 2 devices are plotted in Figure 6-8a and detailed PV parameters ($J_{sc}$, $V_{oc}$, FF and PCE) are also shown in Figure S6-8a. It can be seen from Figure 6-8a that the PCE of the control PSC without SWCNTs in the photoelectrode dropped by ~90% after 288 h, while the $TiO_2$ NF-SWCNT photoelectrodes exhibited ~66% degradation after the same period. Similar phenomena were also observed in several recent reports using graphene derivatives in the $TiO_2$ photoelectrodes of PSCs.[42, 43] It is now accepted that in a humid environment, water molecules cause the decomposition of perovskite and results in severe morphological changes (such as pinholes, small grains and coarse surface).[66] Such morphological features are detrimental to the direct electron transfer between perovskite and $TiO_2$. The presence of SWCNTs in the $TiO_2$ photoelectrodes provides better connectivity with the perovskite, and hence provides extra charge carrying pathways, which may mitigate the changes in the perovskite structure. Undoubtedly this extends the electron lifetime in the cell helping to maintain efficiency over longer times.

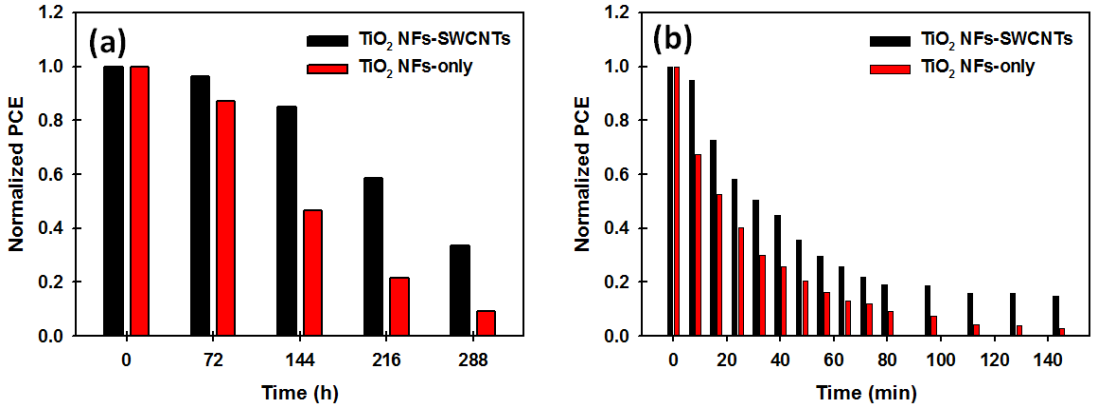


**Figure 6-8**. (a) Normalized PCE of PSCs fabricated with and without SWCNTs in the $TiO_2$ NF photoelectrodes as a function of long-term storage time. The unencapsulated cells were kept in the dark in ambient conditions at a relative humidity of at least 60%. (b) Normalized PCE of the devices with and without SWCNTs in the $TiO_2$ NF photoelectrodes as a function of time exposed to continuous light illumination (100 mW $cm^{-2}$, xenon lamp) for 144 min.

In addition to the long-term storage stability in ambient conditions, the light-stability of the PSCs with and without SWCNTs was explored. This was achieved by exposing PSCs to continuous light illumination (100 mW $cm^{-2}$, xenon lamp) for 144 min. The data were collected in the reverse scan direction every 8 min in an ambient atmosphere. Detailed PV parameters are also shown in Figure S6-8b. It can be clearly observed from Figure 6-8b that the device fabricated with $TiO_2$ NF-SWCNTs photoelectrodes showed better stability than the control cell based on $TiO_2$ NFs-only photoelectrode. This improved light-stability of the device with SWCNTs in the photoelectrode may be attributed to the high thermal conductivity of SWCNTs. The highly conductive SWCNTs are expected to effectively remove the heat during cell operation (during light soaking) which will likely help stability of the devices during operation.

It has been well established that the use of nanocarbons in the compact $TiO_2$ (cp–$TiO_2$) layer of PSCs is an effective strategy to enhance the performance of PSC devices.[38, 40] Therefore, in this work, we also explored the influence of SWCNTs in the cp–$TiO_2$ layer on the efficiency of $TiO_2$ NFs-only photoelectrode based PSCs. As compared to the control device without any SWCNTs (Figure S6-9a), SWCNTs incorporated cp-$TiO_2$ layer based $TiO_2$ NFs photoelectrode based device exhibited a clear enhancement in the efficiency (see Figure S6-9b and Table S6-4). We postulate that this improvement in the efficiency of PSCs is due to the enhanced electron transport rate and thermodynamically favourable energy transfer path within the photoelectrode.[40] Furthermore, in order to maximize our device performance, we fabricated PSC devices with SWCNTs in both cp-$TiO_2$ layer and $TiO_2$ NF layer. The layered structure and PV characteristics of the device are illustrated in Figure 6-9. The observed $J_{sc}$, $V_{oc}$ and FF values for this device were 21.42 mA $cm^{-2}$, 0.98 V and 0.67, respectively, yielding a PCE of 14.03%. It should be pointed out that while this enhanced PCE is not over the 20% and higher being reported for the best cells,[8] the considerable improvement in PCE using CNTs in combination with a 1D nanomaterial does point to a promising research direction where other materials could be used for these systems, and as such, the improved PCE observed is an important result.

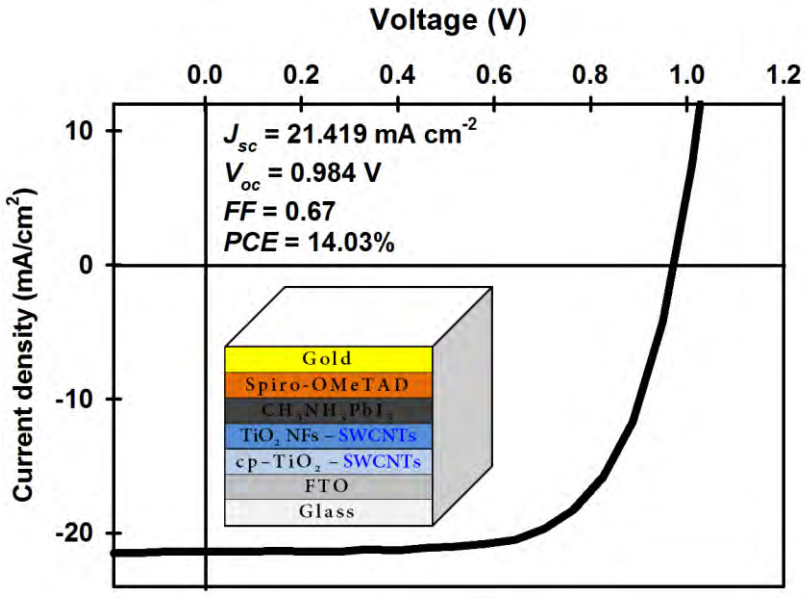


**Figure 6-9**. J–V curve of the best performing device in this study. Inset shows the device structure and detailed PV parameters.

It should be noted that the $V_{oc}$ values of our devices were slightly lower than those reported in other studies,[24, 25] despite optimization. It was found that the aperture masking of the PSCs during the J–V analysis has some influence on the $V_{oc}$ of the devices, which leads to an underestimation and/or overestimation of cell performance.[67] We note that the aperture mask with an area of 0.081 cm$^2$ was used for all J–V measurements in this work to provide an accurate comparison of PSC devices, while the active area (overlapped area of FTO electrode and gold electrode) of the devices was 0.14 cm$^2$. In order to understand the effect of the aperture mask on the PV parameters of our devices, the control device based on $TiO_2$ NFs-only photoelectrodes and the best performing PSC (device structure shown in the inset of Figure 6-9) were fabricated and their J–V characteristics are analysed with and without an aperture mask. It can be observed from Figure S6-10 that the $V_{oc}$ values of PSCs were increased by ~53 mV when measurement is carried out without an aperture mask, but no changes were observed in the $J_{sc}$ and FF values. For example, the $V_{oc}$ of the $TiO_2$ NF-only PSCs (control cell) increased from 0.87 V to 0.93 V when J–V characteristics are measured without a mask, and yielding an improved PCE (9.1%). These improved values ($V_{oc}$ and PCE) are comparable and similar to those reported in the literature,[24, 25] suggesting that in our study, the $V_{oc}$ values

measured with aperture mask were slightly underestimated and would be higher if no mask was applied during the J–V analysis.

## 6.3. Conclusion

In this work, we have demonstrated the successful incorporation of highly conductive CNTs into 1D $TiO_2$ NF photoelectrodes for highly efficient PSCs. We found that the use of SWCNTs is the most effective material among three different types of CNTs to obtain high PCEs from the devices. In comparison to the control device fabricated without CNTs, a significant enhancement (~40%) in the cell efficiency is achieved by incorporating an optimized amount of SWCNTs into the $TiO_2$ NF PSCs. The improved $J_{sc}$ and $V_{oc}$ values are the main contributions to this efficiency enhancement. The increased $J_{sc}$ is due to the fact that hybrid structure of $TiO_2$ NF-SWCNT provided a fast electron transport pathway with excellent conductivity and thus suppressed the charge recombination rate in the PSCs. Our theoretical calculation revealed that the energy levels of the photoelectrode are changed by introducing SWCNTs into the $TiO_2$ NFs, and resulted in an increase in the $V_{oc}$. Interestingly, we found that the use of SWCNTs in the $TiO_2$ NFs photoelectrode reduced the hysteresis behaviour and improved the stability of the PSC devices both during operation under light and for long term storage in humid conditions. Importantly, our best performing PSC device fabricated with SWCNTs in both cp–$TiO_2$ and $TiO_2$ NFs layers achieved a PCE of 14.03%. Therefore, we believe that this work will open new research avenues for the development of nanocarbon and nanofiber materials in PSCs.

## 6.4. Experimental Section

### 6.4.1. Materials

Unless otherwise stated, all chemicals and reagents were purchased from Sigma-Aldrich. A fluorine-doped tin oxide (FTO) coated glass electrode, methylammonium iodide ($CH_3NH_3I$), tris(1-(pyridin-2-yl)-1*H*-pyrazol) cobalt(III) tris (hexafluoro phosphate) (FK102 Co(III) PF6) salt were obtained from Dyesol. (2,2′,7,7′-tetrakis-(*N,N*-di-*p*-methoxyphenylamine)-9,9′-spirobifluorene) (Spiro-OMeTAD) was

purchased from Solaronix. Arc-discharge SWCNTs (P3-SWNT) were purchased from Carbon Solution Inc., Riverside, CA, USA, while both DWCNTs (<5 nm in diameter) and MWCNTs (<10 nm in diameter) with a purity of 90% and a length of 5–15 μm were obtained from Shenzhen Nanotech Port Co., Ltd, China.

### 6.4.2. Materials preparation

$TiO_2$ NFs were prepared by electrospinning a sol-gel solution consisting of titanium (IV) n-butoxide (TIB, 5.0 g), poly(vinyl pyrrolidone) (PVP, 1.0 g), and glacial acidic acid (1 mL) in an ethanol (10 mL). A detailed description of the $TiO_2$ NFs synthesis process can be found in the literature.[37] The obtained $TiO_2$ NFs were further used to prepare a viscous paste according to the established procedure.[37] The concentration of the $TiO_2$ NFs in the paste was calculated to be ~15.14 wt%. To optimize the thickness of the $TiO_2$ NFs layer in the photoelectrodes, the prepared viscous paste was diluted with various amounts of ethanol for various times, followed by spin coating at 2500 rpm for 30 s. Various dilution ratios of $TiO_2$ NFs paste and ethanol were used, 1:1, 1:2, 1:4, 1:6 and 1:8 (weight ratio), to prepare films with thicknesses of 2200 nm, 1300 nm, 580 nm, 400 nm and 280 nm, respectively. On the basis of PV performance obtained using these diluted solutions, the dilution ratio of 1:6 (paste/ethanol) was chosen.

In order to prepare the stock solution of CNTs, an aqueous Triton X-100 solution with 1 vol% concentration was first prepared. Then, CNTs (10 mg) were dispersed in the previously prepared Triton X-100 solution (10 mL) using an ultrasonication (bath) for 1 h. The concentration of the CNTs stock solution was 1 mg $mL^{-1}$. For the preparation of $TiO_2$ NFs-CNTs hybrid based solutions, the desired concentration (wt%) of CNTs in the hybrid was obtained by adding an appropriate volume of the CNTs stock solution into 3.50 g of the diluted $TiO_2$ NFs dispersion.

### 6.4.3. Device fabrication

Firstly, FTO-coated glass substrates were etched using 2M HCl and Zn powder, followed by sequential cleaning with a detergent (Pyroneg) and washing with acetone, ethanol, and Milli-Q water under ultrasonication for 10 min each. After drying the cleaned FTO electrodes with a stream of nitrogen gas, a thin compact

layer of $TiO_2$ was deposited onto the FTO substrate by spin coating 0.15 M and 0.25 M titanium diisopropoxide bis(acetylacetonate) (75 wt% in isopropanol, Aldrich) in 1-butanol solution. After each spin coating, the films were dried by heating at 150 $^oC$ for 15 min in air. For the fabrication of our best performing PSC (the device structure is shown in the inset of Figure 6-9), SWCNTs were added into the titanium diisopropoxide bis(acetylacetonate) in 1-butanol solution to prepare the precursor for the compact layer. The concentration of the SWCNTs in the composite was 0.02 wt%. Then, a thick ETL was deposited onto the compact layer to prepare the photoelectrode by spin coating a solution of $TiO_2$ NFs-only and/or $TiO_2$ NFs-CNTs at 2500 rpm for 30 s. The films were heated gradually under an air flow at 125 $^oC$ for 5 min, 325 $^oC$ for 5 min, 375 $^oC$ for 15 min, and 450 $^oC$ for 1 h, followed by cooling to room temperature. The photoelectrode films were immersed in 40 mM $TiCl_4$ aqueous solution at 70$^oC$ for 30 min and dried with nitrogen gas, which was again annealed at 450 $^oC$ for 1 h. After cooling to ~120 $^oC$, the films were transferred into a nitrogen-filled glove box.

The perovskite precursor solution was prepared by dissolving a stoichiometric amount (1:1 molar ratio) of $PbI_2$ (0.507 g) and $CH_3NH_3I$ (0.175 g) in an anhydrous dimethylsulfoxide (DMSO, 1 mL). The perovskite layer was deposited onto the photoelectrode films by spin coating as described in the literature.[68] The spin coating recipe includes two steps, first 1000 rpm for 10 s with a ramp of 250 rpm $s^{-1}$, then 5000 rpm for 30 s with a ramp of 2000 rpm $s^{-1}$. ~12 s before the end of the spin-coating program, anhydrous chlorobenzene (120 µL) was gently dropped on the spinning substrate. The films were then heated at 95 $^oC$ for 1h in the glovebox.

After drying the perovskite coated films completely, the HTM (70 µL) was deposited onto the perovskite layer by spin coating at 4000 rpm for 20 s. The HTM was prepared by dissolving 28.9 mg Spiro-OMeTAD, 11.5 µL 4-*tert*-butylpyridine (tBP), 7.0 µL of a stock solution of 520 mg $mL^{-1}$ lithium bis (trifluoromethylsulphonyl) imide (Li-TFSI) in acetonitrile and 9.0 µL of a stock solution of 100 mg $mL^{-1}$ FK102 Co(III) PF6 salt in acetonitrile, in 400 µL chlorobenzene. For the fabrication of SWCNTs–HTM based device, dispersion of SWCNTs in chlorobenzene (1 mg $mL^{-1}$) was spin coated onto the perovskite layer at 4000 rpm for 20 s. After the HTMs deposition, the films were stored overnight in a dry air desiccator. Finally, 50 nm

gold electrodes were thermally evaporated at a rate of 1 Å $s^{-1}$ under a high vacuum through a shadow mask.

### 6.4.4. Characterization

Top-view and cross-sectional SEM images were obtained using an Inspect F50 SEM (FEI) with accelerating voltage of 20 kV. X-ray diffraction (XRD) of $TiO_2$ NF films on FTO was carried out using a Bruker D8 diffractometer with Cu Kα source and parallel beam optics equipped with a PSD LynxEye silicon strip detector. The incident beam was kept at an angle of 1° and the angular range of diffraction patterns were collected at $10° < 2\theta < 66°$ with a step size of 0.05° at 2 s/step. The anatase phase of $TiO_2$ was confirmed by comparing the patterns from the Inorganic Crystal Structure Database (ICSD). Raman confocal spectroscopy and spectral mapping were completed using a Witec Alpha 300RS with a 40 x objective and 532 nm laser excitation. Raman single spectra were acquired with integration times of 5 s and 3 accumulations. The Raman spectral image was obtained by collecting a series of 100 x 100 single spectra (0.2 s integration per spectrum) over an area of 20 x 20 μm. The optical transmittances of the films on glass slides were analysed using a Varian Cary 50G UV-vis spectrophotometer at wavelengths ranging from 400 to 1000 nm. Sheet resistance measurements were performed on the same films using a four point probe technique (KeithLink Technology Co., Ltd. Taiwan). The electrochemical impedance spectroscopy was measured with an Autolab PGSTAT128N on the photoelectrodes using a half cell configuration in 0.1 M NaCl. Analysis was completed in the dark with 0 V bias with 10 mV modulation over the frequency range of 100000 – 0.1 Hz.

The photocurrent–voltage (*J–V*) characteristics were analysed using a Keithley 2400 SMU instrument and recorded using a custom LabView Virtual Instrument program. A standard silicon test cell with NIST-traceable certification was used to calibrate the power density as 100 mW $cm^{-2}$ at the sample plane of the collimated a 150W xenon-arc light source (Newport), which was passed through an AM 1.5G filter. The scan rate and delay time are 200 mV $s^{-1}$ and 30 ms, respectively. The active area of the fabricated devices was 0.14 $cm^2$. The devices were masked with an aperture mask (with area of 0.081 $cm^2$) and tested in air atmosphere. The incident-photon-to-current

conversion efficiency (IPCE) spectra as a function of wavelength ranging from 300 nm to 800 nm were taken by passing chopped light from a xenon source through a monochromator and onto the devices. The light intensity of the illumination source was adjusted using a photodiode detector (silicon calibrated detector, Newport).

### 6.4.5. Computational detail

All density functional theory (DFT) computations were performed with the Vienna *ab initio* simulation package (VASP, version 5.4.1) using the projector-augmented wave (PAW) method.[69, 70] Electron-ion interactions were described using standard PAW potentials with valence configurations of $3s^2 3p^6 4s^2 3d^2$ for Ti (Ti_sv_GW), $2s^2 2p^2$ for C (C_GW_new), $2s^2 2p^4$ for O (O_GW_new), and $1s^1$ for H (H_GW). A plane-wave basis set was employed to expand the smooth part of wave functions with a cut-off kinetic energy of 520 eV. The electron-electron exchange and correlation interactions were parameterized by Perdew-Burke-Ernzerhhof (PBE),[71] a form of the general gradient approximation (GGA), was used throughout.

To simulate the interaction between the SWCNT and anatase $TiO_2$, the anatase $TiO_2$ (101) surface was employed since it is the most stable.[72] For structural relaxations of the anatase (101) surfaces, a 12-layer slab for the (2×2) surface cell with 144 atoms was enclosed in a supercell with sufficiently large vacuum regions of 15 Å to ensure the periodic images to be well separated. During the geometry optimizations, all atoms were allowed to relax until the Hellmann-Feynman forces were smaller than 0.001 eV $Å^{-1}$. The convergence criterion for the electronic self-consistent loop was set to $10^{-5}$ eV. We performed Brillouin-zone integrations using a gamma-centered (1 × 3 × 1) k-point grid. The corresponding k-mesh densities and the cut-off kinetic energy have been justified in our previous studies.[73, 74] Since P3-SWCNT used in this study have 3-6% carboxylic acid groups, the adsorption of SWCNT was investigated through the interaction between on carboxylic acid group with the Ti and O atoms in the (101) surface. The detailed atomic structure at the interface of SWCNT and $TiO_2$ can be found in Figure 6b. The energy level vs the SHE is calculated according to the Equation:

$$U \text{ (vs SHE, V)} = (E_{vac} - E_b - E_{SHE})/e$$

where $E_{vac}$, $E_b$ and $E_{SHE}$ are vacuum energy, the energy of electronic bands, and the absolute energy of standard hydrogen electrode (SHE, which is 4.44 eV), respectively. And the *e* represents the electron charge here.

## Acknowledgements

Munkhbayar Batmunkh acknowledges International Postgraduate Research Scholarship (IPRS) and Australian Postgraduate Award (APA) for their financial support during his study in Australia. Dr. Thomas J. Macdonald and Prof. Ivan P. Parkin acknowledge the Engineering and Physical Sciences Research Council (EPSRC) for their financial support (EP/L015862/1).

We acknowledge the use of South Australian nodes of the Australian Microscopy & Microanalysis Research Facility (AMMRF) and the Australian National Fabrication Facility (ANFF) at Flinders University. All theoretical research was undertaken on the supercomputer of National Computational Infrastructure (NCI) in Canberra, Australia, which is supported by the Australian Commonwealth Government.

## References

[1] A. Polman, M. Knight, E. C. Garnett, B. Ehrler, W. C. Sinke, *Science,* **2016**, 352, 307.

[2] http://www.sciencemag.org/news/2013/12/sciences-top-10-breakthroughs-**2013**, Science's Top 10 Breakthroughs of 2013. Accessed on Dec 2016.

[3] http://www.nature.com/news/365-days-nature-s-10-1.14367, 365 days: Nature's 10. Accessed on Dec 2016.

[4] X. Tong, F. Lin, J. Wu, Z. M. Wang, *Adv. Sci,* **2016**, 3, 1500201.

[5] T. Salim, S. Sun, Y. Abe, A. Krishna, A. C. Grimsdale, Y. M. Lam, *J. Mater. Chem. A,* **2015**, 3, 8943.

[6] A. Kojima, K. Teshima, Y. Shirai, T. Miyasaka, *J. Am. Chem. Soc,* **2009**, 131, 6050.

[7] M. M. Lee, J. Teuscher, T. Miyasaka, T. N. Murakami, H. J. Snaith, *Science,* **2012**, 338, 643.

[8] M. Saliba, S. Orlandi, T. Matsui, S. Aghazada, M. Cavazzini, J.-P. Correa-Baena, P. Gao, R. Scopelliti, E. Mosconi, K.-H. Dahmen, F. De Angelis, A. Abate, A. Hagfeldt, G. Pozzi, M. Graetzel, M. K. Nazeeruddin, *Nat Energy,* **2016**, 1, 15017.

[9] http://www.nrel.gov/ncpv/images/efficiency_chart.jpg, *Best Research-Cell Efficiencies (NREL)* **2016**, Visited on 01st June,
[10] H.-S. Kim, C.-R. Lee, J.-H. Im, K.-B. Lee, T. Moehl, A. Marchioro, S.-J. Moon, R. Humphry-Baker, J.-H. Yum, J. E. Moser, M. Grätzel, N.-G. Park, *Sci. Reports,* **2012**, 2, 591.
[11] F. Di Giacomo, V. Zardetto, A. D'Epifanio, S. Pescetelli, F. Matteocci, S. Razza, A. Di Carlo, S. Licoccia, W. M. M. Kessels, M. Creatore, T. M. Brown, *Adv. Energy Mater,* **2015**, 5, 1401808.
[12] F. Matteocci, L. Cinà, F. Di Giacomo, S. Razza, A. L. Palma, A. Guidobaldi, A. D'Epifanio, S. Licoccia, T. M. Brown, A. Reale, A. Di Carlo, *Prog in Photovoltaics: Res and App,* **2016**, 24, 436.
[13] S. Razza, F. Di Giacomo, F. Matteocci, L. Cinà, A. L. Palma, S. Casaluci, P. Cameron, A. D'Epifanio, S. Licoccia, A. Reale, T. M. Brown, A. Di Carlo, *J. Power. Sources,* **2015**, 277, 286.
[14] B. J. Kim, D. H. Kim, Y.-Y. Lee, H.-W. Shin, G. S. Han, J. S. Hong, K. Mahmood, T. K. Ahn, Y.-C. Joo, K. S. Hong, N.-G. Park, S. Lee, H. S. Jung, *Energy Environ Sci,* **2015**, 8, 916.
[15] A. Fakharuddin, F. Di Giacomo, A. L. Palma, F. Matteocci, I. Ahmed, S. Razza, A. D'Epifanio, S. Licoccia, J. Ismail, A. Di Carlo, T. M. Brown, R. Jose, *ACS Nano,* **2015**, 9, 8420.
[16] K. Hwang, Y.-S. Jung, Y.-J. Heo, F. H. Scholes, S. E. Watkins, J. Subbiah, D. J. Jones, D.-Y. Kim, D. Vak, *Adv. Mater,* **2015**, 27, 1241.
[17] P. P. Boix, K. Nonomura, N. Mathews, S. G. Mhaisalkar, *Mater Today,* **2014**, 17, 16.
[18] M. A. Green, A. Ho-Baillie, H. J. Snaith, *Nat Photon,* **2014**, 8, 506.
[19] H. S. Jung, N.-G. Park, *Small,* **2015**, 11, 10.
[20] S. D. Sung, D. P. Ojha, J. S. You, J. Lee, J. Kim, W. I. Lee, *Nanoscale,* **2015**, 7, 8898.
[21] C. Yi, X. Li, J. Luo, S. M. Zakeeruddin, M. Grätzel, *Adv. Mater,* **2016**, 28, 2964.
[22] M. Batmunkh, C. J. Shearer, M. J. Biggs, J. G. Shapter, *J. Mater. Chem A,* **2015**, 3, 9020.
[23] G. Xing, N. Mathews, S. Sun, S. S. Lim, Y. M. Lam, M. Grätzel, S. Mhaisalkar, T. C. Sum, *Science,* **2013**, 342, 344.
[24] H.-S. Kim, J.-W. Lee, N. Yantara, P. P. Boix, S. A. Kulkarni, S. Mhaisalkar, M. Grätzel, N.-G. Park, *Nano Lett,* **2013**, 13, 2412.
[25] S. Dharani, H. K. Mulmudi, N. Yantara, P. T. Thu Trang, N. G. Park, M. Graetzel, S. Mhaisalkar, N. Mathews, P. P. Boix, *Nanoscale,* **2014**, 6, 1675.
[26] O. A. Jaramillo-Quintero, M. Solis de la Fuente, R. S. Sanchez, I. B. Recalde, E. J. Juarez-Perez, M. E. Rincon, I. Mora-Sero, *Nanoscale,* **2016**, 8, 6271.
[27] H. Sun, J. Deng, L. Qiu, X. Fang, H. Peng, *Energy Environ Sci,* **2015**, 8, 1139.
[28] T. Macdonald, J. Xu, S. Elmas, Y. Mange, W. Skinner, H. Xu, T. Nann, *Nanomaterials,* **2014**, 4, 256.

[29] L. Yang, W. W.-F. Leung, *Adv. Mater,* **2011**, 23, 4559.
[30] F. J. Ramos, M. Oliva-Ramirez, M. K. Nazeeruddin, M. Gratzel, A. R. Gonzalez-Elipe, S. Ahmad, *J. Mater. Chem. A,* **2015**, 3, 13291.
[31] L. Yang, W. W.-F. Leung, *Adv. Mater,* **2013**, 25, 1792.
[32] G. S. Han, H. S. Chung, D. H. Kim, B. J. Kim, J.-W. Lee, N.-G. Park, I. S. Cho, J.-K. Lee, S. Lee, H. S. Jung, *Nanoscale,* **2015**, 7, 15284.
[33] G. K. Mor, K. Shankar, M. Paulose, O. K. Varghese, C. A. Grimes, *Nano Lett,* **2006**, 6, 215.
[34] A. Abrusci, S. D. Stranks, P. Docampo, H.-L. Yip, A. K. Y. Jen, H. J. Snaith, *Nano Lett,* **2013**, 13, 3124.
[35] M. Batmunkh, M. J. Biggs, J. G. Shapter, *Adv. Sci,* **2015**, 2, 1400025.
[36] M. Batmunkh, M. J. Biggs, J. G. Shapter, *Small,* **2015**, 11, 2963.
[37] T. J. Macdonald, D. D. Tune, M. R. Dewi, C. T. Gibson, J. G. Shapter, T. Nann, *ChemSusChem,* **2015**, 8, 3396.
[38] J. T.-W. Wang, J. M. Ball, E. M. Barea, A. Abate, J. A. Alexander-Webber, J. Huang, M. Saliba, I. Mora-Sero, J. Bisquert, H. J. Snaith, R. J. Nicholas, *Nano Lett,* **2014**, 14, 724.
[39] Z. Zhu, J. Ma, Z. Wang, C. Mu, Z. Fan, L. Du, Y. Bai, L. Fan, H. Yan, D. L. Phillips, S. Yang, *J. Am. Chem. Soc,* **2014**, 136, 3760.
[40] M. Batmunkh, C. J. Shearer, M. J. Biggs, J. G. Shapter, *J. Mater. Chem. A,* **2016**, 4, 2605.
[41] G. S. Han, Y. H. Song, Y. U. Jin, J.-W. Lee, N.-G. Park, B. K. Kang, J.-K. Lee, I. S. Cho, D. H. Yoon, H. S. Jung, *ACS Appl. Mater. Interf,* **2015**, 7, 23521.
[42] A. Agresti, S. Pescetelli, L. Cinà, D. Konios, G. Kakavelakis, E. Kymakis, A. D. Carlo, *Adv. Funct. Mater,* **2016**, 26, 2686.
[43] M. M. Tavakoli, R. Tavakoli, Z. Nourbakhsh, A. Waleed, U. S. Virk, Z. Fan, *Adv. Mater. Interf,* **2016**, 3, 1500790.
[44] K. Aitola, K. Sveinbjornsson, J.-P. Correa-Baena, A. Kaskela, A. Abate, Y. Tian, E. M. J. Johansson, M. Gratzel, E. I. Kauppinen, A. Hagfeldt, G. Boschloo, *Energy Environ Sci,* **2016**, 9, 461.
[45] Z. Li, P. P. Boix, G. Xing, K. Fu, S. A. Kulkarni, S. K. Batabyal, W. Xu, A. Cao, T. C. Sum, N. Mathews, L. H. Wong, *Nanoscale,* **2016**, 8, 6352.
[46] X. Wang, Z. Li, W. Xu, S. A. Kulkarni, S. K. Batabyal, S. Zhang, A. Cao, L. H. Wong, *Nano Energy,* **2015**, 11, 728.
[47] S. N. Habisreutinger, T. Leijtens, G. E. Eperon, S. D. Stranks, R. J. Nicholas, H. J. Snaith, *Nano Lett,* **2014**, 14, 5561.
[48] Z. Li, S. A. Kulkarni, P. P. Boix, E. Shi, A. Cao, K. Fu, S. K. Batabyal, J. Zhang, Q. Xiong, L. H. Wong, N. Mathews, S. G. Mhaisalkar, *ACS Nano,* **2014**, 8, 6797.
[49] R. Ihly, A.-M. Dowgiallo, M. Yang, P. Schulz, N. J. Stanton, O. G. Reid, A. J. Ferguson, K. Zhu, J. J. Berry, J. L. Blackburn, *Energy Environ Sci,* **2016**, 9, 1439.
[50] L. Qiu, J. Deng, X. Lu, Z. Yang, H. Peng, *Angew. Chem. Int. Ed,* **2014**, 53, 10425.

[51] S. He, L. Qiu, X. Fang, G. Guan, P. Chen, Z. Zhang, H. Peng, *J. Mater. Chem. A,* **2015**, 3, 9406.
[52] J. Deng, L. Qiu, X. Lu, Z. Yang, G. Guan, Z. Zhang, H. Peng, *J. Mater. Chem. A,* **2015**, 3, 21070.
[53] L. Qiu, S. He, J. Yang, J. Deng, H. Peng, *Small,* **2016**, 12, 2419.
[54] S. S. Mali, C. S. Shim, H. K. Park, J. Heo, P. S. Patil, C. K. Hong, *Chem. Mater,* **2015**, 27, 1541.
[55] M. Horn, C. F. Schwerdtfeger, E. P. Meagher, *Zeitschrift für Kristallographie* **2010**, 136, 273.
[56] H.-S. Kim, N.-G. Park, *J. Phys. Chem. Lett,* **2014**, 5, 2927.
[57] J. H. Heo, S. H. Im, J. H. Noh, T. N. Mandal, C.-S. Lim, J. A. Chang, Y. H. Lee, H.-j. Kim, A. Sarkar, K. NazeeruddinMd, M. Gratzel, S. I. Seok, *Nat Photon*, **2013**, 7, 486.
[58] Y. H. Lee, J. Luo, M.-K. Son, P. Gao, K. T. Cho, J. Seo, S. M. Zakeeruddin, M. Grätzel, M. K. Nazeeruddin, *Adv. Mater,* **2016**, 28, 3966.
[59] Y. Shi, Y. Xing, Y. Li, Q. Dong, K. Wang, Y. Du, X. Bai, S. Wang, Z. Chen, T. Ma, *J. Phys. Chem. C,* **2015**, 119, 15868.
[60] M. Cai, V. T. Tiong, T. Hreid, J. Bell, H. Wang, *J. Mater. Chem. A,* **2015**, 3, 2784.
[61] R. Martel, V. Derycke, C. Lavoie, J. Appenzeller, K. K. Chan, J. Tersoff, P. Avouris, *Phys. Rev. Lett,* **2001**, 87, 256805.
[62] D. S. Lee, W. Kim, B. G. Cha, J. Kwon, S. J. Kim, M. Kim, J. Kim, D. H. Wang, J. H. Park, *ACS Appl. Mater. Interf,* **2016**, 8, 449.
[63] G. Niu, W. Li, F. Meng, L. Wang, H. Dong, Y. Qiu, *J. Mater. Chem. A,* **2014**, 2, 705.
[64] B. Chen, M. Yang, S. Priya, K. Zhu, *J. Phys. Chem. Lett,* **2016**, 7, 905.
[65] S. V. Reenen, M. Kemerink, H. J. Snaith, *J. Phys. Chem. Lett,* **2015**, 6, 3808.
[66] W. Huang, J. S. Manser, P. V. Kamat, S. Ptasinska, *Chem. Mater,* **2016**, 28, 303.
[67] X. Xu, J. Shi, H. Wu, Y. Yang, J. Xiao, Y. Luo, D. Li, Q. Meng, *J. Renew. Sust. Energy,* **2015**, 7, 043104.
[68] K. Rakstys, A. Abate, M. I. Dar, P. Gao, V. Jankauskas, G. Jacopin, E. Kamarauskas, S. Kazim, S. Ahmad, M. Grätzel, M. K. Nazeeruddin, *J. Am. Chem. Soc,* **2015**, 137, 16172.
[69] G. Kresse, D. Joubert, *Phys. Rev. B,* **1999**, 59, 1758.
[70] G. Kresse, J. Furthmüller, *Computation. Mater. Sci,* **1996**, 6, 15.
[71] J. P. Perdew, K. Burke, M. Ernzerhof, *Phys. Rev. Lett,* **1996**, 77, 3865.
[72] Y. Wang, H. Zhang, Y. Han, P. Liu, X. Yao, H. Zhao, *Chem. Comm,* **2011**, 47, 2829.
[73] P. Liu, Y. Wang, H. Zhang, T. An, H. Yang, Z. Tang, W. Cai, H. Zhao, *Small,* **2012**, 8, 3664.
[74] Y. Wang, T. Sun, D. Yang, H. Liu, H. Zhang, X. Yao, H. Zhao, *Phys. Chem. Chem. Phys,* **2012**, 14, 2333.

# Supporting Information for

# Carbon Nanotubes in $TiO_2$ Nanofiber Photoelectrodes for High Performance Perovskite Solar Cells

Munkhbayar Batmunkh,[1,2] Thomas J. Macdonald,[3] Cameron J. Shearer,[2] Munkhjargal Bat-Erdene,[2] Yun Wang,[4] Mark J. Biggs,[1,5] Ivan P. Parkin,[3] Thomas Nann,[6] and Joseph G. Shapter,[2]*

[1] *School of Chemical Engineering, The University of Adelaide, Adelaide, South Australia 5005, Australia*

[2] *School of Chemical and Physical Sciences, Flinders University, Bedford Park, Adelaide, South Australia 5042, Australia*

[3] *Department of Chemistry, University College London, London, UK*

[4] *Centre for Clean Environment and Energy, Griffith School of Environment, Gold Coast Campus, Griffith University, Queensland 4222, Australia*

[5] *School of Sciences, Loughborough University, Loughborough, Leicestershire, LE11 3TU, UK*

[6] *MacDiarmid Institute for Advanced Materials and Nanotechnology, School of Chemical and Physical Sciences, Victoria University of Wellington, Wellington, New Zealand*

* Corresponding authors: joe.shapter@flinders.edu.au

**Published:** *Advanced Science*, **2017**, *4*, 1600504

The published copy of the manuscript is attached in Appendix E.

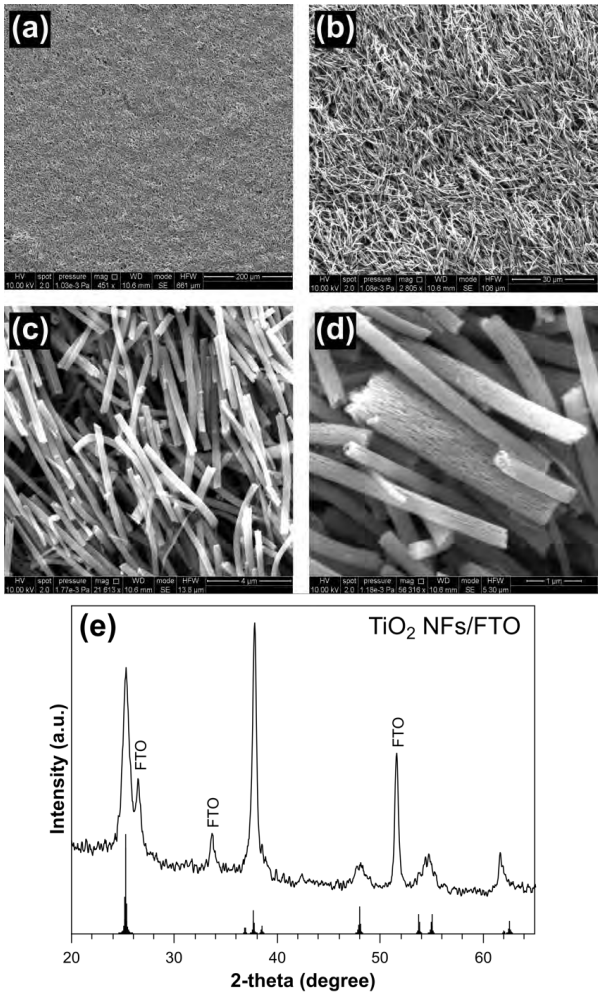


**Figure S6-1**. (a-d) SEM images of the electrospun $TiO_2$ NFs. (e) XRD pattern of $TiO_2$ NFs on FTO confirming the anatase phase with reference to 9853-ICSD.

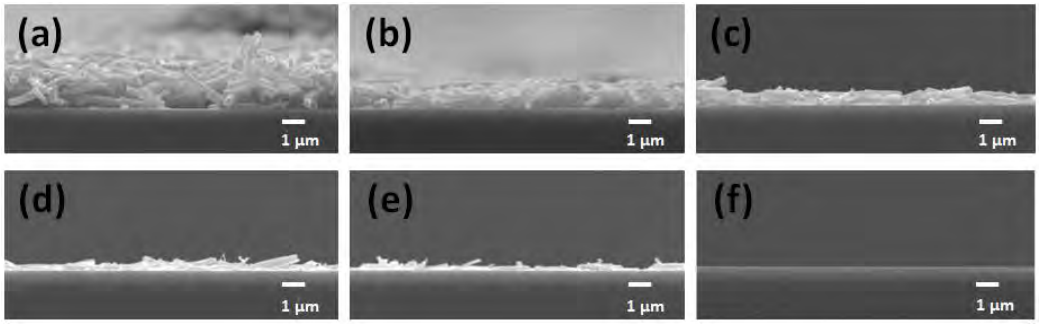


**Figure S6-2**. Cross sectional SEM images of $TiO_2$ NF photoelectrodes with the thickness of (a) ~2200 nm, (b) ~1300 nm, (c) ~580 nm, (d) ~400 nm, (e) ~285 nm and (f) 0 nm (planar).

**Table S6-1**. PV parameters of best performing PSCs fabricated with different $TiO_2$ NF thicknesses based photoelectrodes (extracted from the J–V characteristics reported in Figure 6-2a). The thicknesses of $TiO_2$ NF films for the fabrication of PSC devices are illustrated in Figure S6-2. The average PCEs of the cells were calculated based on at least five identical devices.

| $TiO_2$ NFs thickness | $J_{sc}$ (mA $cm^{-2}$) | $V_{oc}$ (V) | FF | PCE (%) | Average PCE (%) |
|---|---|---|---|---|---|
| 2200 nm | 11.58 | 0.75 | 0.58 | 5.01 | 4.77 ± 0.27 |
| 1300 nm | 13.19 | 0.77 | 0.61 | 6.13 | 5.50 ± 0.47 |
| 580 nm | 15.55 | 0.84 | 0.58 | 7.54 | 7.21 ± 0.36 |
| 400 nm | 15.91 | 0.87 | 0.62 | 8.56 | 8.21 ± 0.46 |
| 285 nm | 14.86 | 0.87 | 0.62 | 8.07 | 7.74 ± 0.44 |
| 0 nm (planar) | 12.87 | 0.94 | 0.58 | 7.02 | 6.70 ± 0.44 |

**Table S6-2**. PV parameters of best performing PSC devices fabricated with different types of CNTs incorporated $TiO_2$ NF photoelectrodes (extracted from the J–V characteristics reported in Figure 6-2b). ~400 nm $TiO_2$ NF films were chosen for these cells. The concentration of CNTs in the $TiO_2$ NF-CNT hybrid was 0.02 wt%. The average PCEs were calculated based on at least five identical devices.

| Device | $J_{sc}$ (mA $cm^{-2}$) | $V_{oc}$, (V) | FF | PCE, (%) | Average, PCE (%) |
|---|---|---|---|---|---|
| $TiO_2$ NFs-only | 15.91 | 0.87 | 0.62 | 8.56 | 8.21 ± 0.46 |
| $TiO_2$ NFs-DWCNTs | 16.71 | 0.88 | 0.62 | 9.04 | 8.81 ± 0.20 |
| $TiO_2$ NFs-MWCNTs | 17.07 | 0.86 | 0.62 | 9.08 | 8.97 ± 0.15 |
| $TiO_2$ NFs-SWCNTs | 17.20 | 0.93 | 0.62 | 9.91 | 9.69 ± 0.23 |

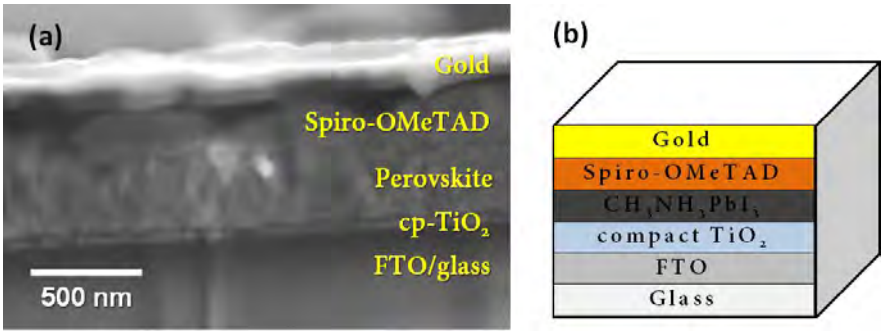


**Figure S6-3**. (a) Cross sectional SEM image and (b) schematic illustration of the planar PSC device structure.

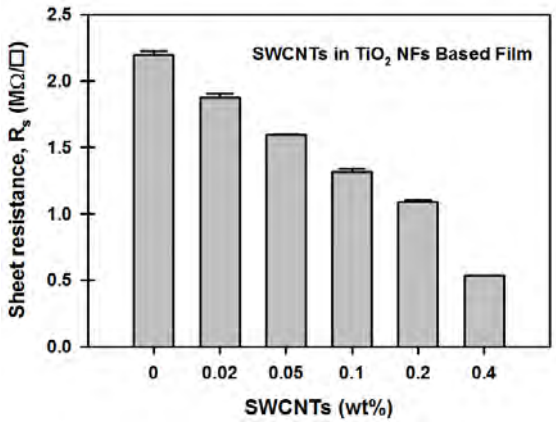


**Figure S6-4**. $R_s$ of the $TiO_2$ NF films with various SWCNT loadings. Error bars are calculated from five different measurements.

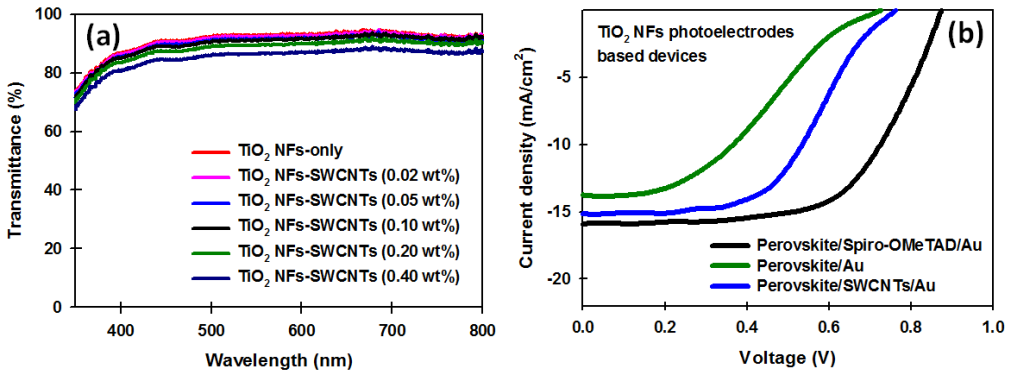


**Figure S6-5**. (a) Optical transmittance of the $TiO_2$ NF based films with different concentrations of SWCNTs. (b) J–V curves of $TiO_2$ NF-only photoelectrodes based PSCs with different hole transporting materials (HTMs).

The measurement of sheet resistance ($R_s$) of the $TiO_2$ NF-SWCNT thin films (on glass substrate) was carried out using a four point probe to investigate the mechanism of enhancement in the $J_{sc}$ value of the devices. As shown in Figure S6-4, the $R_s$ of $TiO_2$ NF films decreased gradually with increasing concentration of SWCNTs. This decrease in the $R_s$ of the films is attributed to the high conductivity of SWCNTs that decreases the interfacial resistance between $TiO_2$ NFs.

**Table S6-3**. PV parameters of PSCs with and without SWCNTs in the photoelectrodes measured at forward and reverse J–V scans.

| Device | Scan direction | $J_{sc}$ (mA $cm^{-2}$) | $V_{oc}$ (V) | FF | PCE (%) |
|---|---|---|---|---|---|
| $TiO_2$ NFs-only | Forward | 14.96 | 0.87 | 0.52 | 6.78 |
| | Reverse | 15.38 | 0.87 | 0.61 | 8.16 |
| $TiO_2$ NFs-SWCNTs | Forward | 18.76 | 0.92 | 0.57 | 9.86 |
| | Reverse | 18.89 | 0.93 | 0.64 | 11.44 |

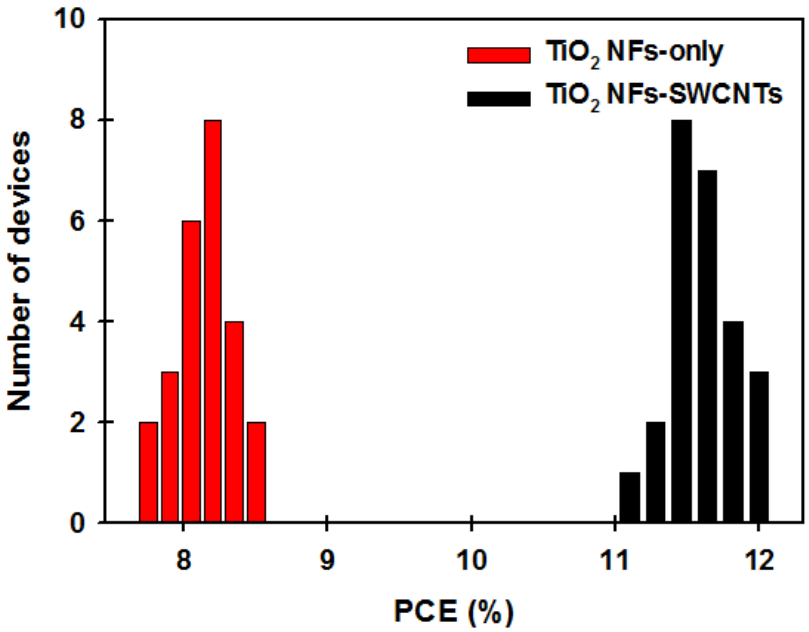


**Figure S6-6**. Histograms of PCE for the $TiO_2$ NFs-only and $TiO_2$ NF-SWCNT PSCs (measurement of 25 cells for each device structure).

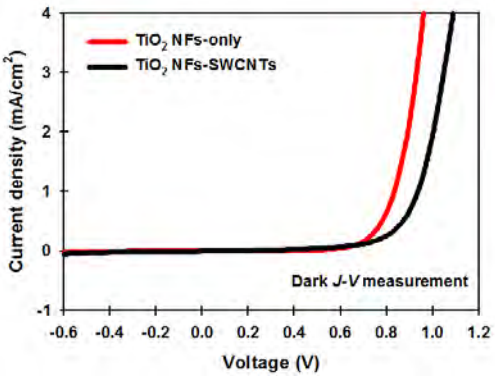


**Figure S6-7**. Dark J-V curves of PSCs fabricated based on $TiO_2$ NFs-only and $TiO_2$ NFs-SWCNTs photoelectrodes.

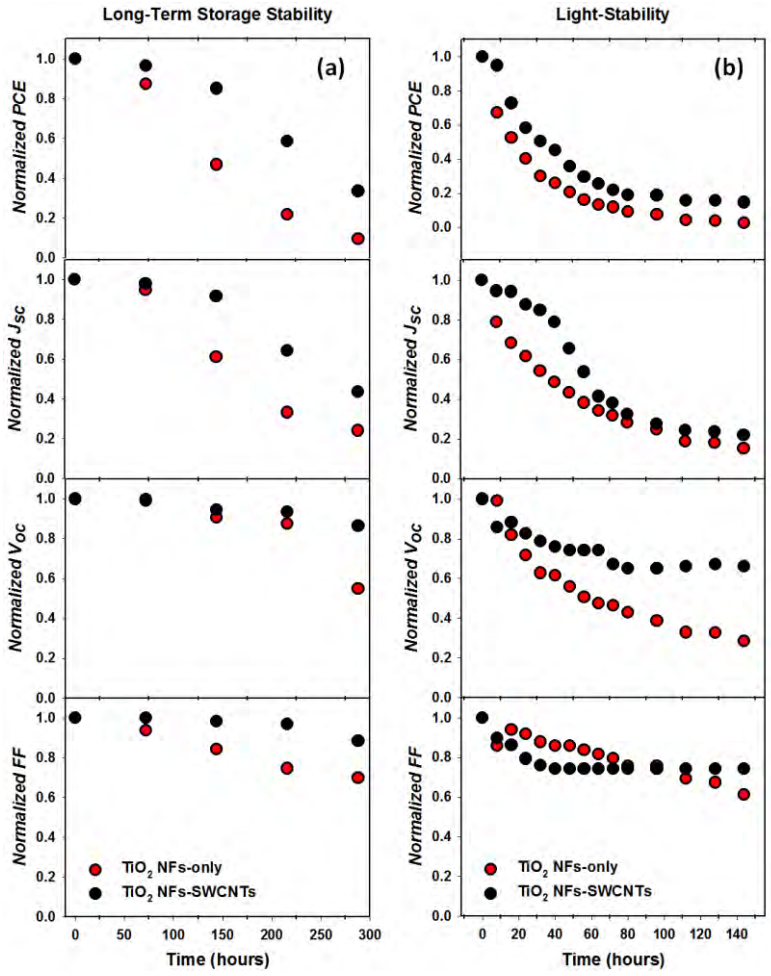


**Figure S6-8**. (a) Long-term storage- and (b) light-stability of the PSCs fabricated with and without SWCNTs in the $TiO_2$ NF photoelectrodes. In Y-axis (normalized PV parameters), $PCE_{(in)}$, $J_{sc(in)}$, $V_{oc(in)}$ and $FF_{(in)}$ represents the initial (0 hr) PV values of the devices.

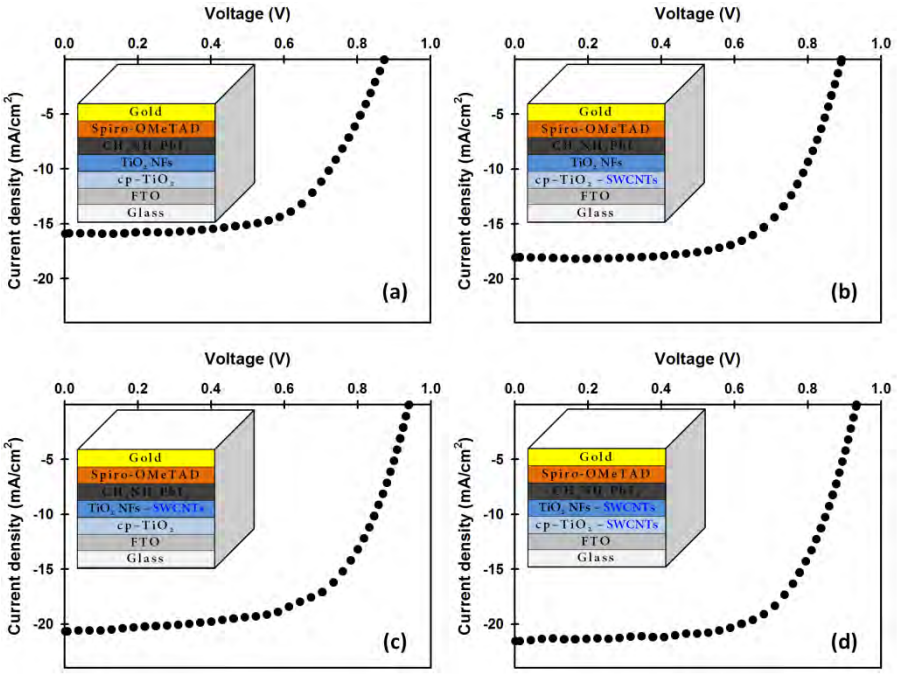


**Figure S6-9**. J–V curves of PSCs based on (a) compact (cp)-$TiO_2$ and $TiO_2$ NFs-only photoeletrode without any SWCNTs, (b) SWCNTs incorporated cp-$TiO_2$ layer and $TiO_2$ NFs-only photoelectrode, (c) cp-$TiO_2$ layer and SWCNTs incorporated $TiO_2$ NFs photoelectrode, and (d) SWCNTs incorporated into both cp-$TiO_2$ and $TiO_2$ NFs photoelectrode. An aperture mask was used during the J–V test.

**Table S6-4**. Detailed PV parameters of PSCs based on (Structure A) cp-$TiO_2$ and $TiO_2$ NFs-only photoeletrode without any SWCNTs, (Structure B) SWCNTs incorporated cp-$TiO_2$ layer and $TiO_2$ NFs-only photoelectrode, (Structure C) cp-$TiO_2$ layer and SWCNTs incorporated $TiO_2$ NFs photoelectrode, and (Structure D) SWCNTs incorporated into both cp-$TiO_2$ and $TiO_2$ NFs photoelectrode. The device structures are shown in the inset of Figure S6-9.

| Device | $J_{sc}$ (mA $cm^{-2}$) | $V_{oc}$ (V) | FF | PCE (%) | Average PCE (%) |
|---|---|---|---|---|---|
| Structure A | 15.91 | 0.87 | 0.62 | 8.56 | 8.21 ± 0.46 |
| Structure B | 18.02 | 0.89 | 0.64 | 10.38 | 9.88 ± 0.43 |
| Structure C | 20.68 | 0.94 | 0.62 | 12.03 | 11.51 ± 0.40 |
| Structure D | 21.51 | 0.93 | 0.65 | 13.04 | 12.75 ± 0.43 |

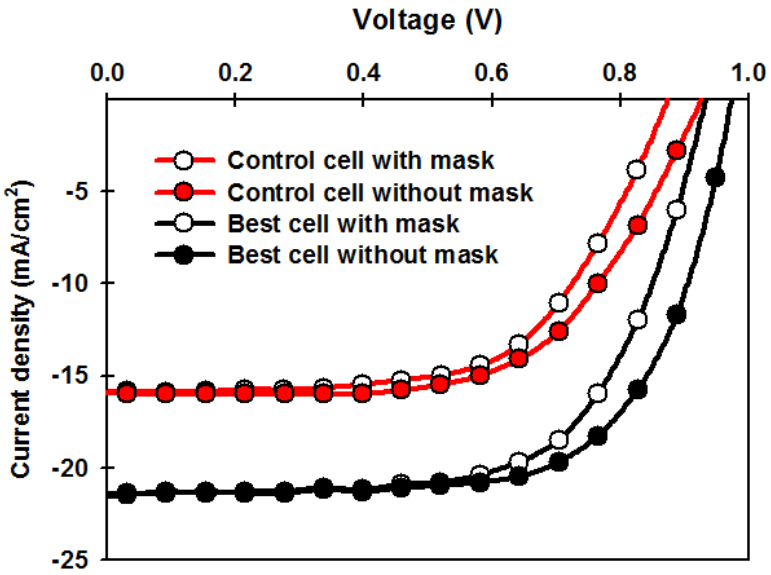


**Figure S6-10**. Effect of aperture masking on the J–V measurement of the PSC devices. The control cell is fabricated with the device structure shown in Figure 6-1a (without any SWCNT), while the best cell is made of structure such as that illustrated in the inset of Figure 6-9. The overlapped area of FTO electrode (anode) and gold electrode (cathode) was 0.14 $cm^2$. The aperture mask with an area of 0.081 $cm^2$ was used for the measurement with mask.

# Chapter 7.

# Single-Walled Carbon Nanotubes Enhance the Efficiency and Stability of Nanocrystalline $TiO_2$ Photoelectrode Based Perovskite Solar Cells

Munkhbayar Batmunkh,[1,2] Cameron J. Shearer,[2] Munkhjargal Bat–Erdene,[2] Mark J. Biggs,[1,3] Joseph G. Shapter,[2]*

[1] *School of Chemical Engineering, The University of Adelaide, Adelaide, South Australia 5005, Australia*

[2] *School of Chemical and Physical Sciences, Flinders University, Bedford Park, Adelaide, South Australia 5042, Australia*

[3] *School of Sciences, Loughborough University, Loughborough, Leicestershire, LE11 3TU, UK*

* Corresponding authors:

joe.shapter@flinders.edu.au

*Submitted Manuscript*

# Statement of Authorship

| | |
|---|---|
| Title of Paper | Single-walled carbon nanotubes enhance the efficiency and stability of nanocrystalline $TiO_2$ photoelectrode based perovskite solar cells |
| Publication Status | ☐ Published ☐ Accepted for Publication<br>☑ Submitted for Publication ☐ Unpublished and Unsubmitted w ork w ritten in manuscript style |
| Publication Details | Munkhbayar Batmunkh, Cameron J. Shearer, Munkhjargal Bat-Erdene, Mark J. Biggs, and Joseph G. Shapter, **2016**, *Submitted*. |

## Principal Author

| | |
|---|---|
| Name of Principal Author (Candidate) | Munkhbayar Batmunkh |
| Contribution to the Paper | Conducted the experimental works, performed analysis on all samples, interpreted data and wrote manuscript. |
| Overall percentage (%) | 75% |
| Certification: | This paper reports on original research I conducted during the period of my Higher Degree by Research candidature and is not subject to any obligations or contractual agreements with a third party that would constrain its inclusion in this thesis. I am the primary author of this paper. |
| Signature | Date 30/12/2016 |

## Co-Author Contributions

By signing the Statement of Authorship, each author certifies that:

i. the candidate's stated contribution to the publication is accurate (as detailed above);
ii. permission is granted for the candidate in include the publication in the thesis; and
iii. the sum of all co-author contributions is equal to 100% less the candidate's stated contribution.

| | |
|---|---|
| Name of Co-Author | Dr. Cameron J. Shearer |
| Contribution to the Paper | Sample characterization, edited the manuscript, and manuscript evaluation. |
| Signature | Date 4/1/17 |

| | |
|---|---|
| Name of Co-Author | Munkhjargal Bat-Erdene |
| Contribution to the Paper | Conducted some experimental works |
| Signature | Date 4/01/2017 |

| Name of Co-Author | Prof. Mark J. Biggs |
|---|---|
| Contribution to the Paper | Co-advised the development of work, and manuscript evaluation. |
| Signature | Date 12/1/17 |

| Name of Co-Author | Prof. Joseph G. Shapter |
|---|---|
| Contribution to the Paper | Supervised development of work, Edited the manuscript, manuscript evaluation and Corresponding author. |
| Signature | Date 4/1/18 |

## Abstract

Carbon nanotubes are 1D nanocarbons with excellent properties and have been extensively used in various electronic and optoelectronic device applications including solar cells. Herein, we report a significant enhancement in the efficiency and stability of perovskite solar cells (PSCs) by employing single-walled carbon nanotubes (SWCNTs) in the mesoporous photoelectrode. It was found that SWCNTs provide both rapid electron transfer and advantageously shifts the conduction band minimum of the $TiO_2$ photoelectrode and thus enhances all photovoltaic parameters of PSCs. The $TiO_2$-SWCNTs photoelectrode based PSC device exhibited a power conversion efficiency (PCE) of up to 16.11%, while the device fabricated without SWCNTs displayed an efficiency of 13.53%. More importantly, we found that the SWCNTs in the $TiO_2$ nanoparticles ($TiO_2$ NPs) based photoelectrode suppress the hysteresis behavior and significantly enhance both the light and long-term storage-stability of the PSC devices. The present work provides important guidance for future investigations in utilizing carbonaceous materials for solar cells.



**Keywords**: Photovoltaic, perovskite solar cells, photoelectrode, mesoporous $TiO_2$, carbon nanotubes


**TOC Figure**

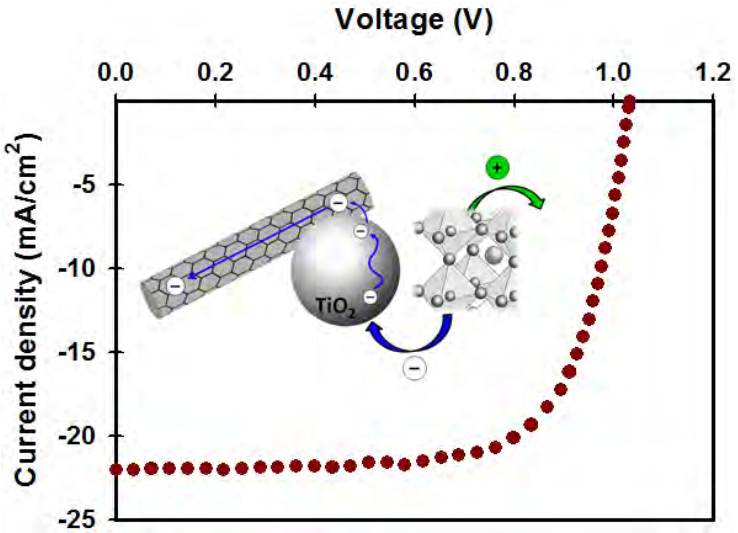

## 7.1. Introduction

Since the pioneering work on organometal halide perovskite ($ABX_3$, A = organic cation, B = metal cation, and X = halide) based photovoltaic (PV) cells was reported in 2009,[1] perovskite solar cells (PSCs) have attracted significant attention and are now sitting in the spotlight as a promising technology for renewable energy production.[2-4] This emerging PV system, in comparison to traditional silicon solar cells, promises to be less expensive, lighter, more flexible and portable.[5-9] More importantly, the power conversion efficiency (PCE) of these PV devices has reached a certified value of 22.1% and is approaching that of the conventional silicon solar cells.[10-12]

High PCEs have been mainly achieved using mesoscopic structured PSCs.[11, 13, 14] The heart of the mesoscopic PSC system is a semiconducting oxide electron transporting material (ETM) that collects photo-generated electrons from the perovskite light absorber and injects them into an external circuit. Typically, nanocrystalline $TiO_2$ particles are used as the ETM.[15, 16] However, the electron transport in the disordered $TiO_2$ nanocrystallite network involves a random transit path and numerous grain boundaries increasing the rate of charge recombination and thus limiting device efficiency.[17-19] Therefore, designing photoelectrodes with improved charge transport pathways is expected to enhance the efficiency of PSCs.

A variety of strategies have been developed to improve the electron transport properties of PSC photoelectrodes.[20-23] In particular, graphene and its derivatives for use in the photoelectrodes of PSCs have recently attracted increasing attention due to graphene's availability, high conductivity and suitable energy levels.[19, 24, 25] Although PSCs based on photoelectrodes with various graphene derivatives incorporated have shown enhancement in the performance compared to their control devices, the obtained efficiencies are still limited probably due to the structural defects of the graphene sheets created during the production process. In this regard, carbon nanotubes (CNTs), particularly single-walled (SWCNTs), are expected to exhibit significant enhancement in the PCE of PSCs because of their unique structure and excellent properties. It is worth noting that in dye-sensitized solar cell (DSSC) systems, CNTs have been shown to be more effective in enhancing the PCE than

other carbon materials.[26, 27] Despite this great promise, there has been no effort focused on employing CNTs in nanocrystalline $TiO_2$ photoelectrodes for PSCs.

Herein we introduce SWCNTs into the nanocrystalline $TiO_2$ porous layers to fabricate PSC devices illustrated in Scheme 7-1. The incorporation of SWCNTs into the PSC photoelectrodes was found to be far more effective than the other types of nanocarbon materials including graphene and its derivatives. By finding an optimal loading of SWCNTs, the PSC device fabricated based on $TiO_2$ NPs-SWCNTs hybrid photoelectrode achieved a maximum PCE of 16.11%, which was significantly higher than that (13.53%) of the $TiO_2$ NPs based control cells. In addition to this impressive PCE, we found that the use of SWCNTs in the nanocrystalline $TiO_2$ photoelectrodes reduces the anomalous hysteresis behavior and considerably enhances the light- and long-term storage-stability of the PSC devices.

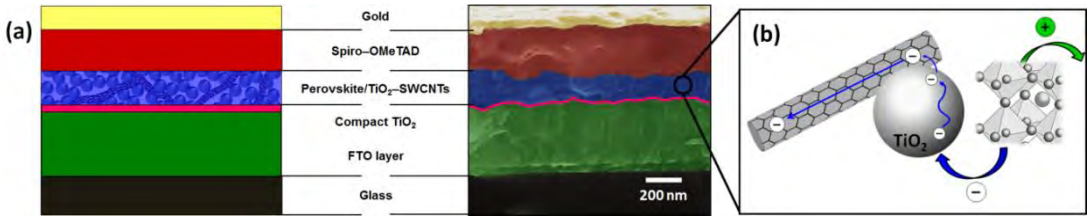


**Scheme 7-1**. (a) Schematic representation (left) and cross sectional SEM image (right) of the $TiO_2$ NPs-SWCNTs photoelectrode based PSC device. (b) Schematic illustration of the improved charge transport process in the $TiO_2$ NPs-SWCNTs nanocomposite.

## 7.2. Results and Discussion

SWCNTs were incorporated into the $TiO_2$ photoelectrode by mixing an aqueous solution of SWCNTs with the $TiO_2$ paste prior to deposition (scanning electron microscopy (SEM) images of starting materials are provided in Figure S7-1, supporting information (SI)). Figure 7-1a shows the top view SEM image of the prepared $TiO_2$ NPs-SWCNTs nanocomposites. It is difficult to directly observe the well dispersed SWCNTs within the $TiO_2$ NP matrix. Given the low loading of the SWCNTs (0.10 % w/w), this was expected. Raman spectral microscopy was used to determine SWCNT homogeneity in the film.

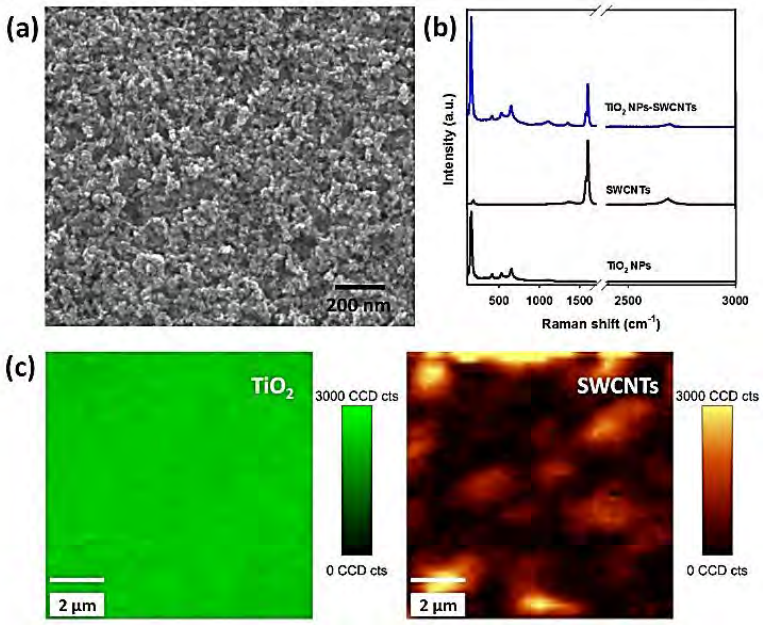


**Figure 7-1**. (a) Top-view SEM image of $TiO_2$ NPs-SWCNT nanocomposite. (b) Raman spectra of $TiO_2$ NPs, SWCNTs and their nanocomposite. (c) Raman spectral mapping the same area (20 x 20 mm) showing distribution of $TiO_2$ NPs (top, green) and SWCNTs (bottom, orange) in the composite. The colour scale represents the sum of the anatase $TiO_2$ and CNT related signal, respectively.

Raman spectroscopy is an important tool for analysing carbon nanomaterials and has frequently been used to confirm the presence of nanocarbons in composites or hybrids.[24, 26, 28] Therefore, Raman spectra of the samples were collected and are plotted in Figure 7-1b to further confirm the existence of SWCNTs in the nanocomposite. The Raman peaks located at around 150, 398, 518 and 641 $cm^{-1}$ correspond to the typical modes of the anatase $TiO_2$.[24] The SWCNT spectra showed the feature peaks at 1357 and 1597 $cm^{-1}$, which can be assigned to the disorder-induced "D" band and the "G" band, in addition to the typical radial breathing mode (RBM) and "G'" band peaks. When analysing the composite film (blue series, Figure 7-1b) Raman signals corresponding to both $TiO_2$ NPs and CNTs throughout the sample were observed. Confocal Raman spectral microscopy maps of the $TiO_2$ NPs-SWCNTs nanocomposites shown in Figure 7-1c illustrate the distribution of SWCNTs throughout the $TiO_2$ NP matrix, confirming that the existence of both $TiO_2$ and SWCNTs in the sample.

After confirming the presence of SWCNTs throughout the $TiO_2$ NP film, the SWCNT content was varied to determine optimal content to maximize PSC PCE. Five photoelectrodes of different SWCNT concentrations in the composite were used from 0 wt% to 0.50 wt% to fabricate PSCs such as the representative cell illustrated in Figure S7-2. Our PSCs were fabricated based on $CH_3NH_3PbI_3$ which was deposited on $TiO_2$ NPs films with and without SWCNTs. The PV characteristics of these PSCs were evaluated using simulated AM1.5 sunlight with an output power of 100 mW $cm^{-2}$ and are shown in Figure S7-3. Detailed PV parameters of PSC devices with different SWCNT loadings have been summarized in Figure 7-2 and Table 7-1.

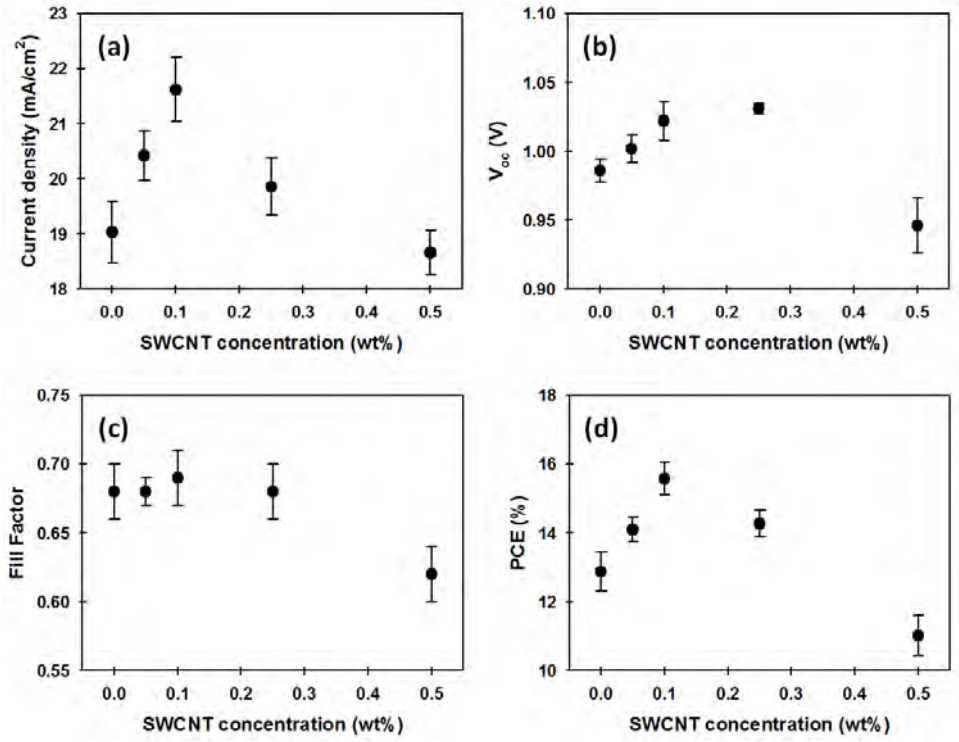


**Figure 7-2**. Plots of (a) $J_{sc}$, (b) $V_{oc}$, (c) FF and (d) PCE of the PSCs as a function of SWCNT concentration in the $TiO_2$ films.

Starting from the control PSCs fabricated based on $TiO_2$ NPs-only photoelectrodes, the average short-circuit current ($J_{sc}$), open-circuit voltage ($V_{oc}$) and fill factor ($FF$) are 19.03 mA $cm^{-2}$, 0.986 V and 0.68, respectively. With increasing SWCNT loading in the $TiO_2$ NPs photoelectrodes, both the $J_{sc}$ and $V_{oc}$ values of the devices increased to 21.62 mA $cm^{-2}$ and 1.022 V, respectively, peaking at 0.10 wt%, followed by a

decrease with further increases in the concentration of SWCNTs. The changes in the $J_{sc}$ values can be traced to the conductivity of the CNTs and their ambipolar nature. The improved current must result from the improved conductivity of the films initially however the addition of large amounts of CNTs introduces many junctions which will act as recombination points. These two competing factors will see a peaked dependence of current as a function of CNT loading completely in line with other observations. It is important to note that CNTs can also transport holes which will increase their lifetime in the photoelectrode and this will, at higher CNT loadings, lead to increased recombination lowering the observed current. The increase in recombination rate in the photoelectrode at high loadings is also clear in the decrease in the *FF* at the highest loadings. There are some changes in the $V_{oc}$ with loading. Importantly, for the lower SWCNTs loadings, the $V_{oc}$ is higher than that observed for the electrode without the SWCNT which will be explained later. At the very highest loadings, the $V_{oc}$ is lower than that without SWCNT likely due to increased conduction pathways that are not part of the core circuit producing current.

**Table 7-1**. PV parameters of PSCs fabricated based on $TiO_2$ NP photoelectrodes with different SWCNTs loadings.

| Device | $J_{sc}$ (mA $cm^{-2}$) | $V_{oc}$ (V) | FF | PCE (%) |
|---|---|---|---|---|
| $TiO_2$ NPs-only | **19.49**; 19.03 ± 0.56 | **0.988**; 0.986 ± 0.008 | **0.70**; 0.68 ± 0.02 | **13.53**; 12.88 ± 0.56 |
| 0.05 wt% SWCNTs | **20.87**; 20.42 ± 0.45 | **1.010**; 1.002 ± 0.010 | **0.69**; 0.68 ± 0.01 | **14.50**; 14.10 ± 0.35 |
| 0.10 wt% SWCNTs | **21.96**; 21.62 ± 0.58 | **1.041**; 1.022 ± 0.014 | **0.70**; 0.69 ± 0.02 | **16.11**; 15.58 ± 0.47 |
| 0.25 wt% SWCNTs | **20.43**; 19.86 ± 0.52 | **1.035**; 1.031 ± 0.004 | **0.70**; 0.68 ± 0.02 | **14.72**; 14.27 ± 0.39 |
| 0.50 wt% SWCNTs | **18.98**; 18.66 ± 0.41 | **0.956**; 0.946 ± 0.020 | **0.64**; 0.62 ± 0.02 | **11.64**; 11.02 ± 0.59 |

The average efficiency of the cells increased from 12.88% (without SWCNTs) to a maximum average of 15.58% (0.10 wt%), followed by a decrease at higher (0.25 and

0.50 wt%) SWCNT content. The optimum PV parameters for the PSCs were achieved for the 0.10 wt% SWCNTs incorporated $TiO_2$ NP photoelectrode. The measured short-circuit current ($J_{sc}$), open-circuit voltage ($V_{oc}$) and fill factor (FF) values for the best performing $TiO_2$ NPs-SWCNTs photoelectrode based device were 21.96 mA $cm^{-2}$, 1.041V and 0.70, respectively, yielding a PCE of 16.11%, which was significantly higher than that (13.53%) of the best control PSCs fabricated without SWCNTs in the photoelectrodes (Figure 7-3a). Notably, this efficiency (16.11%) achieved using our SWCNTs incorporated $TiO_2$ NP photoelectrode is higher than other reported values of the PSC devices based on photoelectrodes with carbonaceous content.[19, 23-25, 29, 30] Moreover, the reproducibility of PSCs based on both $TiO_2$ NPs-only (control) and $TiO_2$ NPs-SWCNTs photoelectrodes is displayed in Figure 7-3b, indicating that the performances of these highly efficient PSCs are highly reproducible. This result confirms that the addition of SWCNTs in the photolectrodes does not alter the reproducibility of the PSC devices.

Of the major factors affecting PCE (FF, $V_{oc}$, $J_{sc}$), the incorporation of SWCNTs increases $V_{oc}$ and $J_{sc}$ but does not alter FF (see Figure 7-2). It is important to note that although the incorporation of carbon nanomaterials such as graphene and its derivatives into the PSC photoelectrodes was found to improve the cell efficiency in previous studies, the $V_{oc}$s in these studies have remained unchanged or decreased.[19, 25] In contrast, in the present work, the $V_{oc}$ values of the nanocrystalline $TiO_2$ photoelectrode based PSC devices increased by ~50 mV after adding SWCNTs. Density functional theory calculations have shown that SWCNT interaction with $TiO_2$ (101) raises the conduction band minimum (CBM) in comparison to the $TiO_2$ semiconductor.[31] The $V_{oc}$ in PSC devices is determined by the energy difference between the CBM of the ETM and the valence band maximum of the hole transporting material (HTM).[32] This theoretical study supports our experimental observation of SWCNT incorporation into the $TiO_2$ photoelectrode increasing the $V_{oc}$ of PSCs. It should be noted that despite this theoretical explanation, a considerable drop in the PV parameters of the PSCs was observed for the 0.50 wt% SWCNTs incorporated $TiO_2$ photoelectrode. This is probably due to the fact that the SWCNTs are acting as a hole transporting material, which leads to a possible charge recombination within the device.[22]

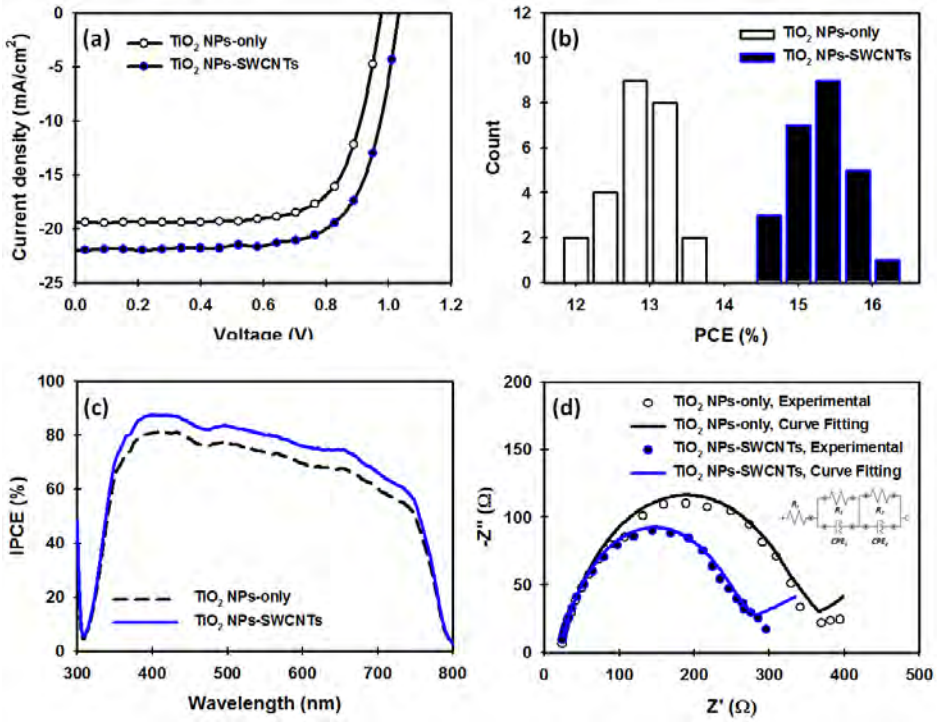


**Figure 7-3**. (a) J–V curves of the best performing PSCs fabricated with and without SWCNTs (0.10 wt%) in the photoelectrodes measured under 100 mW $cm^{-2}$ (AM 1.5G) illumination. (b) Histogram of the PCE of devices based on $TiO_2$ NPs-only and $TiO_2$ NPs-SWCNTs photoelectrodes. (c) IPCE spectra and (d) Nyquist plots of EIS measurements of the devices measured under illumination at 0.3 V bias ($V_{oc}$).

With theoretical support to explain the observed increase in $V_{oc}$ after adding SWCNTs, we sought further experimental evidence to explain the increased $J_{sc}$. Incident-photon-to-current conversion efficiencies (IPCEs) of the devices were measured. Figure 7-3c displays the IPCE spectra of $TiO_2$ NPs-only and $TiO_2$ NPs-SWCNTs photoelectrodes based PSCs. The device with SWCNT shows a clear improvement in IPCE across the entire wavelength range (from around 350 nm to 760 nm). Since the $J_{sc}$ of the device can be determined from the IPCE spectra, the higher IPCE value with SWCNTs was expected. The integrated $J_{sc}$ values from the IPCE spectra for the PSCs fabricated with $TiO_2$ NPs-only and $TiO_2$ NPs-SWCNTs films were 17.30 and 19.20 mA $cm^{-2}$, respectively, which are in agreement (within ±10% error) with the measured $J_{sc}$ from the J-V characteristics of the devices. More importantly, the $J_{sc}$ difference (1.90 mA $cm^{-2}$) obtained from the IPCE spectra of $TiO_2$ NPs-only based device and $TiO_2$ NPs-SWCNTs based cell was very close to that (2.30 mA $cm^{-2}$) calculated from the J-V characteristics, confirming the

relationship of the J–V curves to the IPCE spectra. The wavelength independent improvement of IPCE suggests the SWCNT are passively improving charge transfer.

Electrochemical impedance spectroscopy (EIS) was performed to investigate the interfacial charge transfer properties of the devices. The EIS measurements were carried out at an applied bias of 0.3V under illumination at 35 mW $cm^{-2}$ in ambient atmosphere. Figure 7-3d shows the Nyquist plots derived from the results of EIS spectra of $TiO_2$ NPs-only and $TiO_2$ NPs-SWCNTs photoelectrode based PSC devices, in which two RC arcs were observed. It is well established that the first arc at the higher frequency (R1) is attributed to the charge-transfer resistance ($R_{ct}$), while the second arc at the lower frequency (R2) is related to the recombination resistances of the fabricated PSC devices. The SWCNTs employed PSC device exhibited lower charge-transfer resistance ($R_{ct}$, 320 Ω) as compared to the control cell (376 Ω), indicating improved electron transport properties. The combination of IPCE and EIS suggest the enhanced $J_{sc}$ by incorporating SWCNT results from improved electron transfer through the photoelectrode. This improvement in the electron transport properties is expected to suppress the charge recombination of the PSCs.

To further investigate the reduction of the charge recombination rate at the PSC photoelectrodes in the presence of SWCNTs, dark J-V measurements of the devices were carried out to study the diode properties (Figure 7-4a). From the dark J-V measurement, ideality factor and saturation-current ($J_{sat}$) values were obtained for both the $TiO_2$ NPs-only and $TiO_2$ NPs-SWCNTs photoelectrodes based PSC devices. As shown in Table S7-1, the $J_{sat}$ values of the PSCs fabricated with SWCNTs in the photoelectrodes (1.05 (± 0.38) x $10^{-10}$ mA $cm^{-2}$) were nearly five times lower than that (5.47 (± 0.21) x $10^{-10}$ mA $cm^{-2}$) of the $TiO_2$ NPs-only based cells. Interestingly, the average ideality factor of $TiO_2$ NPs-SWCNTs photoelectrodes based PSCs is approximately 1.31 ± 0.14, while the control devices showed average ideality factor of 1.46 ± 0.14. We note that the ideality factors of our devices were considerably lower than those reported in a recent study using graphene derivatives incorporated mesoporous $TiO_2$ NPs films based PSCs.[25] A lower $J_{sat}$ value and an ideality value closer to 1 both indicate less charge recombination from reverse current and charge trapping is occurring in the diode.[25, 28, 33, 34] Moreover, the measurement of sheet resistance ($R_s$) of the thin films (on glass substrates) was carried out using a four point probe to explore the mechanism of $J_{sc}$ enhancement of the devices. The $R_s$ of

the $TiO_2$ films with SWCNTs was 1.86 ± 0.01 x $10^6$ Ω, which was nearly 2.5 times lower than that (4.51 ± 0.005 x $10^6$ Ω) of the $TiO_2$ NPs-only films. This reduction in the $R_s$ of the films is due to the high conductivity of SWCNTs that decreases the interfacial resistance between $TiO_2$ NPs.

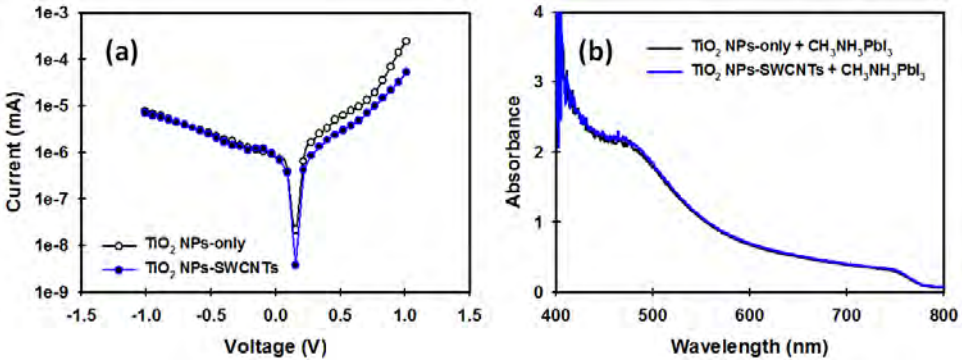


**Figure 7-4**. (a) Representative J–V curves of the PSCs fabricated with and without SWCNTs in the $TiO_2$ NPs measured in dark condition. (b) UV-vis absorption spectra of the $TiO_2$ NPs-only and $TiO_2$ NPs-SWCNTs films coated with perovskite layer.

These results indicate that the SWCNTs incorporated $TiO_2$ NPs photoelectrodes based PSCs have reduced charge recombination as compared to the $TiO_2$ NPs-only based devices. In addition, the device fabricated with SWCNTs exhibited reduced series resistance ($R_{series}$, Table S7-1) (77.3 ± 7.96 Ω for the cells with SWCNTs and 111 ± 10.5 Ω for the devices without SWCNTs), which further confirms the $R_{ct}$ of the cells obtained from the EIS analysis. Moreover, we note that no difference in light absorption including the intensity of the perovskite films was observed after adding 0.10 wt% SWCNTs into the $TiO_2$ NPs films (Figure 7-4b). This indicates that the use of small amount of SWCNTs does not change the perovskite crystallization.

Widespread commercial application of PSC will not become a reality without significant improvement to stability and reduction of J-V hysteresis. We have compared the hysteresis behavior and stability of PSCs with and without SWCNTs.

Anomalous hysteresis behavior observed during the J-V analysis of PSCs limits their stabilized power output under working conditions and causes serious issues for the device stability and PCE accuracy.[35] J-V curves of the devices (at least 3 cells for each device structure) measured were recorded using different scan directions

(reverse and forward) and the representative results are plotted in Figure 7-5a and b. Detailed PV parameters have been summarized in Table 7-2. To provide a reasonable comparison, the PCE difference (known as the difference factor)[36] of the PSCs was calculated according to the following equation.

$$PCE_{difference} = \frac{PCE_{reverse} - PCE_{forward}}{PCE_{reverse}} \quad \text{Eq. (1)}$$

From the Eq. (1), a high PCE difference means the cells show large hysteresis and distortion. For the control cell without SWCNTs, the calculated average PCE difference was 19.22 ± 1.63%, which was considerably higher than that (12.36 ± 2.43%) of the $TiO_2$ NPs-SWCNTs photoelectrode based PSC device. Therefore, it is clear that the use of SWCNTs in the nanostructured photoelectrodes significantly reduced the hysteresis behavior of the PSCs. Although the fundamental mechanism of hysteretic J-V behavior in the PSC devices is not well understood, recent theoretical and experimental studies put forward several explanations. It has been reported that an anomalous hysteresis in PSCs arises from the trap-assisted charge recombination at the interface between perovskite and ETM.[25, 37] Therefore, the reduced hysteresis of our PSC devices fabricated with $TiO_2$ NPs-SWCNTs photoelectrodes may be explained by the decreased recombination at the perovskite and ETM interfaces.

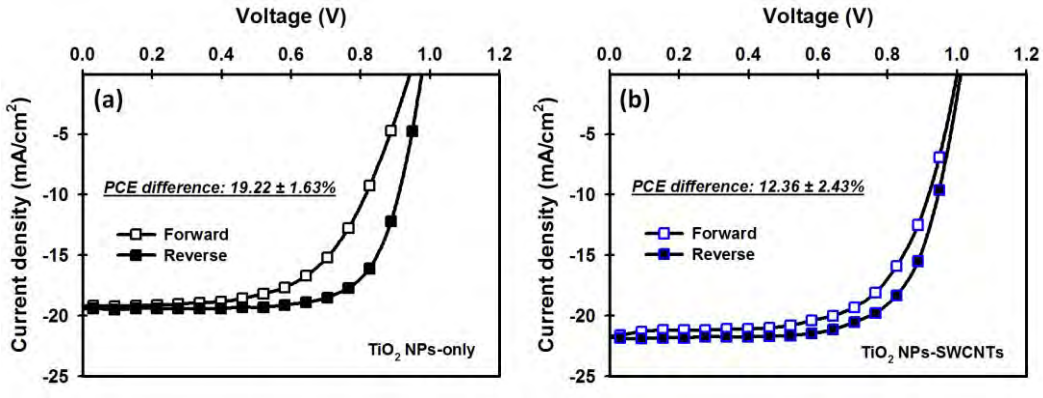


**Figure 7-5**. Representative J–V curves of the (a) $TiO_2$ NPs-only and (b) $TiO_2$ NPs-SWCNTs photoelectrode based PSCs measured with reverse and forward scans. PCE differences are calculated using Eq. 1. Scan rate: 200 mV $s^{-1}$.

**Table 7-2**. PV parameters of the PSCs fabricated with and without SWCNTs in the photoelectrodes measured reverse and forward scan directions. The average values and standard deviations are calculated based on at least 3 devices.

| | $TiO_2$ NPs-only | | $TiO_2$ NPs-SWCNTs | |
|---|---|---|---|---|
| | Forward | Reverse | Forward | Reverse |
| $J_{sc}$ (mA $cm^{-2}$) | 19.05 ± 0.57 | 19.03 ± 0.56 | 21.52 ± 0.35 | 21.62 ± 0.58 |
| $V_{oc}$ (V) | 0.939 ± 0.013 | 0.986 ± 0.008 | 0.978 ± 0.017 | 1.022 ± 0.014 |
| FF | 0.58 ± 0.02 | 0.68 ± 0.02 | 0.64 ± 0.01 | 0.69 ± 0.02 |
| PCE (%) | 10.46 ± 0.29 | 12.88 ± 0.56 | 13.62 ± 0.25 | 15.58 ± 0.47 |
| PCE difference | 19.22 ± 1.63% | | 12.36 ± 2.43% | |

Solar cell stability and lifetime is one of the most significant road blocks toward commercialization of PSCs in the quickly growing renewable electricity generation market. Here we investigated both the light- and long-term storage-stability of the PSCs with and without SWCNTs in the photoelectrodes (Figure 7-6).

The light-stability of the unencapsulated PSCs fabricated with $TiO_2$ NPs-only and $TiO_2$ NPs-SWCNTs photoelectrodes, shown in Figure 7-6a, was evaluated and tested by exposing cells to continuous light illumination (100 mW $cm^{-2}$, xenon lamp) under ambient conditions. It can be seen that the devices employing SWCNTs exhibited better stability than the $TiO_2$ NPs-only photoelectrode based devices. For instance, the $J_{sc}$ value of the control devices degraded by 41% after 40 min, whereas the cells fabricated with SWCNTs only degraded by ~26% of their initial $J_{sc}$. In our study, the PCE degradation of the devices under prolonged light soaking is mainly due to the photocurrent reduction, which is in good agreement with recent comprehensive investigations of PSC stability by Snaith's group.[38, 39] It was reported that upon exposure of the $TiO_2$ to light, the holes in valence band recombine with adsorbed molecular oxygen, causing desorption and leaving positively charged deep trap sites in the $TiO_2$ surface. These deep trap sites then act as sinks for electrons, with recombination of the trapped electrons occurring directly with the holes in the perovskite or HTM.[39] In this regard, the SWCNTs with their excellent conductivity may suppress this recombination process by providing an alternative charge transport path and thus improving the device stability.

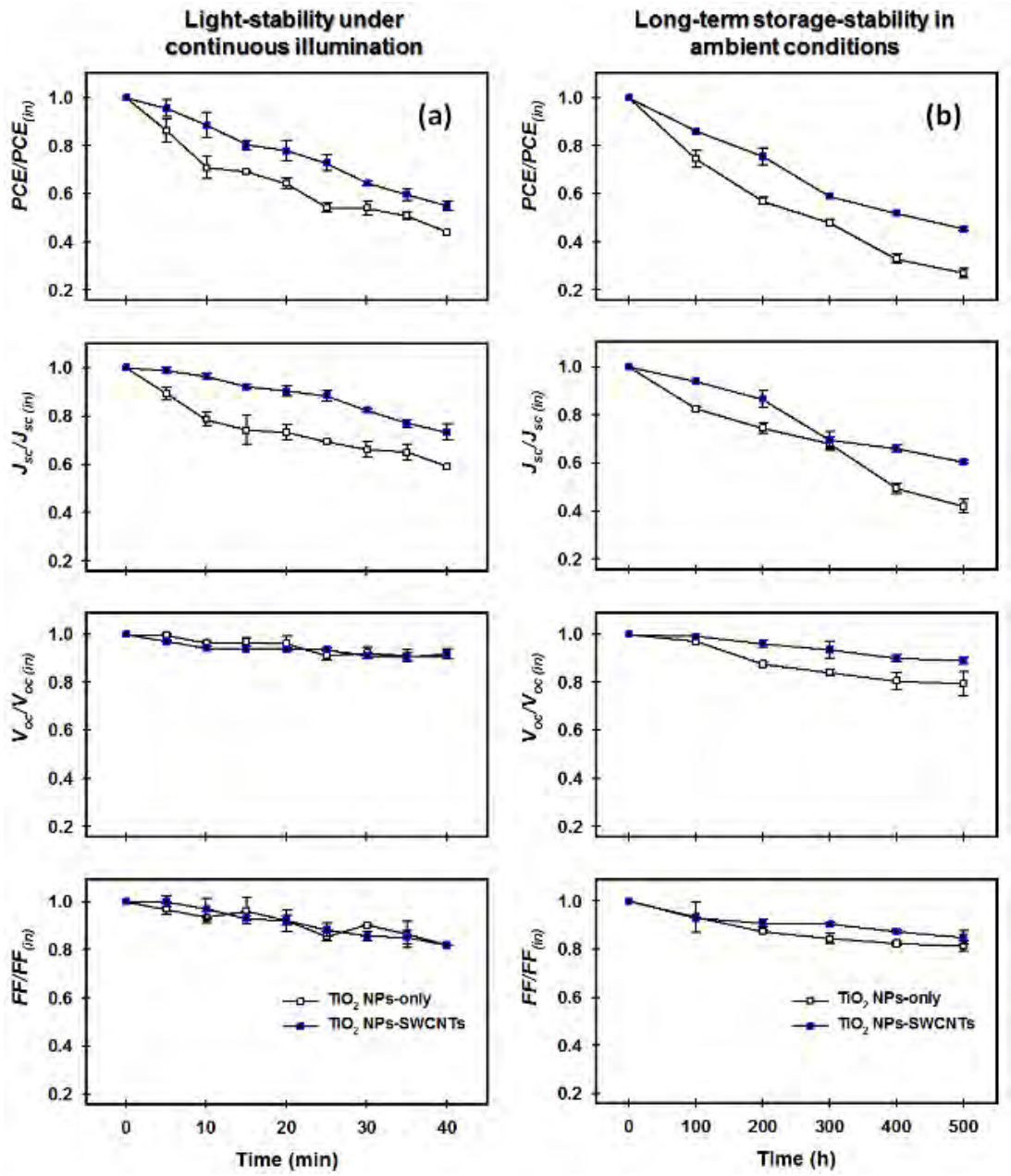


**Figure 7-6**. (a) Light and (b) long-term storage-stability of the devices fabricated with and without SWCNTs in the photoelectrodes. For the light-stability test, the cells were exposed to continuous light illumination (100 mW $cm^{-2}$) in ambient conditions and the data were obtained in reverse scan direction at every 5 min. For the cell storage-stability in ambient environment, the fabricated devices were kept in the dark in ambient conditions for 500 h. The devices were not encapsulated for the stability test. In Y-axis (normalized PV parameters), $PCE_{(in)}$, $J_{sc(in)}$, $V_{oc(in)}$ and $FF_{(in)}$ represents the initial (0 hr) PV values of the devices.

Additionally it is well known that SWCNTs adsorb molecular oxygen very strongly.[40] As such, it is very likely that in the structure reported here the SWCNTs will be a sink for some of the molecular oxygen adsorbed on $TiO_2$ and hence decrease the production of the detrimental deep trap sites. Additionally, the high thermal conductivities of SWCNTs will more effectively remove heat during operation (during light soaking) which will also help stability.

Figure 7-6b illustrates the normalized PV parameters ($J_{sc}$, $V_{oc}$, FF and PCE) of the PSC devices fabricated with and without SWCNTs in the photoelectrodes over 500 h (3 weeks). For the stability test, the unencapsulated devices were stored in the dark in ambient conditions at a relative humidity of >60% and were tested every 100 hours. While both devices degraded, the device with SWCNTs exhibited improved stability. In particular, the devices based on $TiO_2$ NPs-SWCNTs photoelectrodes preserved 45.5% of the initial PCE after aging for 500 h under humid environment, whereas the PSC fabricated without SWCNTs retained only 27% of its initial performance. In order to confirm this stability improvement in the PSC performance with SWCNTs in the photoelectrode, dark J-V characteristics and EIS analysis of unencapsulated aged (~250 h stored in ambient conditions) devices with and without SWCNTs were investigated. It was observed from the dark J-V measurements that the ideality factor of the $TiO_2$ NPs-SWCNTs photoelectrode based PSC is 1.94 which was lower than that (2.23) of the control cell. In addition, the $J_{sat}$ values of the PSCs fabricated with and without SWCNTs photoelectrodes were 1.51 x $10^{-7}$ mA $cm^{-2}$ and 1.37 x $10^{-6}$ mA $cm^{-2}$, respectively. The $J_{sat}$ difference between $TiO_2$ NPs-only and $TiO_2$ NPs-SWCNTs films based 250 h-aged PSCs was nearly an order of magitude, while the difference in their fresh devices was around 5 times. This clearly confirms that the SWCNTs not only enhance the PV performances of the PSCs, but they also improve the stability of the devices in ambient conditions. This finding was further confirmed by EIS analysis of the aged PSCs. As shown in Figure S7-5, the SWCNTs employed PSC device showed a reduced $R_{ct}$ and an increased recombination resistance. In the aged devices, the $R_{ct}$ difference between the PSCs fabricated with and without SWCNTs was around 120 Ω, while the previously measured $R_{ct}$ difference for the freshly prepared PSC devices was only ~60 Ω (for both cases, SWCNTs based cells have lower $R_{ct}$). The higher difference in the $R_{ct}$ of the PSCs with and without SWCNTs after aging is indicative of improved stability of the device with SWCNTs

in the photoelectrodes. Moreover, much higher SWCNT loading (0.50 wt%) in the $TiO_2$ NPs film exhibited significantly enhanced cell stability under the same condition (RH >60%) (see Figure S7-4), which further confirms that the use of SWCNTs in the nanocrystalline $TiO_2$ NPs photoelectrodes improves the long-term storage-stability of the PSC devices. We attribute this storage-stability enhancement of the SWCNTs incorporated devices to the wettability of the photoelectrode film (see Figure S7-6). Clearly, the hydrophilic nature (Figure S7-6a) of the $TiO_2$ NPs-only film could lead to significant absorption of moisture in a humid environment before the deposition of perovskite. The absorbed moisture further gradually degrades the perovskite films and thus reduces the device performance over a period of time. Since SWCNTs have greater hydrophobicity than the $TiO_2$ NPs (Figure S7-6b), the partial coverage of SWCNTs on $TiO_2$ NPs may decrease or slow moisture absorption resulting in an enhanced stability in humid environment. In addition, recently, Huang et al.[41] reported that the polar nature of the water molecules causes the decomposition of perovskite structures and results in severe morphological changes (formation of pinholes and coarsening of the crystalline surface) in humid conditions. It was revealed based on SEM analysis that densely packed large perovskite grains change into relatively small grains after long-term storage under ambient conditions. Such morphological features such as pinholes, small grains and coarse surface would be detrimental to the direct charge transfer between perovskite and $TiO_2$. The $TiO_2$/SWCNT interface provides better connectivity with the perovskite and hence provides extra charge carrying pathways which will somewhat mitigate the changes in the perovskite structure. Ultimately this should extend the electron lifetime in the device helping maintain performance over longer time.

Although this study clearly demonstrates that the application of SWCNTs in the PSC photoelectrodes play significant role in improving the device stability, the exact mechanism of stability improvement still remains to be explored in the future with experimental and theoretical investigations. We anticipate that further improvement in the device performance will be achieved by using chirality specific SWCNTs as it allows the precise tuning of electronic energy levels in the electrode.

## 7.3. Conclusion

In summary, we have produced a nanocomposite material comprising nanocrystalline $TiO_2$ NPs and conductive SWCNTs to prepare photoelectrodes for highly efficient PSCs. We found that the incorporation of SWCNTs into the nanocrystalline $TiO_2$ photoelectrodes significantly improves the electron transfer process and reduces the charge recombination rate, and thus results in the enhancement of $J_{sc}$. In addition, the $V_{oc}$ value of the PSCs was found to increase after introducing SWCNTs into the PSC photoelectrode due to the suitable band energy alignment. As a result, a remarkable PCE of 16.11% was achieved using the nanocomposite photoelectrode based PSC device. Importantly, we found that the use of SWCNTs in the PSC photoelectrodes reduces the anomalous hysteretic J-V behavior, while it also improves the light- and long-term storage-stability of the devices. Finally, our work provides clear guidance for future studies in incorporating nanocarbon materials in PV devices.

## 7.4. Experimental Section

### 7.4.1. Materials

All chemicals and reagents were purchased from Sigma-Aldrich, unless otherwise specified. (2,2′,7,7′-tetrakis-(*N,N*-di-*p*-methoxyphenylamine)-9,9′-spirobifluorene) (Spiro-OMeTAD) was obtained from Solaronix, Switzerland. A fluorine-doped tin oxide (FTO) coated glass electrode, transparent titania ($TiO_2$) paste (18NR-T), methylammonium iodide ($CH_3NH_3I$), tris(1-(pyridin-2-yl)-1*H*-pyrazol) cobalt(III)tris(hexafluorophosphate) (FK102 Co(III) PF6) salt were purchased from Dyesol, Australia. Arc-discharge SWCNTs (P3-SWNT) were purchased from Carbon Solution Inc., Riverside, CA, USA.

### 7.4.2. Preparation of $TiO_2$ NPs-SWCNTs nanocomposite

The stock solution (aqueous) of SWCNTs with 1 mg $mL^{-1}$ concentration was prepared according to the previous reported method.[28] Briefly, SWCNTs (10 mg, P3-SWNT) were bath sonicated for 1 h in aqueous Triton-X 100 (10 mL, 1% v/v). On the other hand, the commercially available $TiO_2$ paste (Dyesol, 18NR-T) was diluted in ethanol (1:5.5 w/w). In order to prepare the $TiO_2$ NPs-SWCNTs, an

appropriate volume of the CNTs stock solution was added into the diluted $TiO_2$ dispersion. The concentration of SWCNTs in the nanocomposite was adjusted by changing the volume of CNT solution.

### 7.4.3. Device fabrication

FTO-coated glass substrates were first etched using 2M HCl and Zn powder. Then the etched FTO substrates were cleaned with a detergent (Pyroneg) and washed with acetone, ethanol, and DI water using an ultrasonication for 10 min each. A 50 nm $TiO_2$ compact layer was deposited onto the FTO substrate via spin coating 0.15 M titanium diisopropoxide bis(acetylacetonate) (75 wt% in isopropanol, Aldrich) in 1-butanol solution twice. The spin coating was carried out for 25 s at 2000 rpm with a ramp of 1000 rpm $s^{-1}$. After each spin coating, the electrodes were dried by heating at 150 $^{o}$C for 15 min in air. Upon cooling to room temperature, the mesoporous $TiO_2$ layer without and/or with SWCNTs was deposited onto the compact $TiO_2$ film by spin coating the previously prepared (diluted) $TiO_2$ solution with different amounts of SWCNTs for 25 s at 4000 rpm with a ramp of 2000 rpm $s^{-1}$. The photoelectrodes were then heated gradually in air at 125 $^{o}$C for 5 min, 325 $^{o}$C for 5 min, 375 $^{o}$C for 15 min, and 450 $^{o}$C for 1 h. After cooling to room temperature, the films were immersed in a 20 mM aqueous $TiCl_4$ solution at 90$^{o}$C for 15 min and the resulting films were again annealed at 450 $^{o}$C for 1 h. After cooling to ~120 $^{o}$C, the films were transferred into a nitrogen-filled glove box for the deposition of perovskite layer, hole transport layer (HTL) and Au electrode.

$PbI_2$ (0.507 g) and $CH_3NH_3I$ (0.175 g) were mixed in anhydrous dimethylsulfoxide (DMSO, 1 mL) to prepare the perovskite precursor solution. The deposition of the perovskite layer was performed according to a previously established spin coating method.[42, 43] The spin coating recipe includes two steps, first 1000 rpm for 10 s with a ramp of 250 rpm $s^{-1}$, then 5000 rpm for 30 s with a ramp of 2000 rpm $s^{-1}$. ~12 s before the end of the spin-coating program, anhydrous chlorobenzene (120 µL) was gently dropped on the centre of spinning substrate. The films were then heated at 100 $^{o}$C for 1h in a glovebox.

After drying the perovskite coated films overnight in the glove box, the HTM (50 µL) was deposited onto the perovskite layer by spin coating for 20 s at 4000 rpm

with a ramp of 2000 rpm $s^{-1}$. The HTM was prepared by dissolving 28.9 mg Spiro-OMeTAD, 11.5 µL 4-*tert*-butylpyridine (tBP), 7.0 µL of a stock solution of 520 mg $mL^{-1}$ lithium bis(trifluoromethylsulphonyl)imide (Li-TFSI) in acetonitrile and 9.0 µL of a stock solution of 100 mg $mL^{-1}$ FK102 Co(III) PF6 salt in acetonitrile, in 400 µL chlorobenzene. After the HTM deposition, the films were stored overnight in a dry air desiccator. Finally, 50 nm gold electrodes were thermally evaporated (Angstrom Engineering Covap) at a rate of 1 Å $s^{-1}$ under high vacuum through a shadow mask.

### 7.4.4. Measurement and characterization

SEM images were obtained using an Inspect F50 SEM (FEI) with accelerating voltage of 20 kV. Raman confocal spectroscopy and spectral mapping were completed using a Witec Alpha 300RS with a 40 x objective and 532 nm laser excitation. Raman single spectra were acquired with integration times of 5 s and 3 accumulations. The Raman spectral image was obtained by collecting a series of 100 x 100 single spectra (0.5 s integration per spectrum) over an area of 20 x 20 µm. Electrochemical impedance spectroscopy (EIS) was carried out with an Autolab PGSTAT128N on the fabricated PSC devices. Analysis was completed under light at 0.3 V bias with 10 mV modulation over the frequency range of 100000 – 0.1 Hz. Measurements were taken under illumination from an optic fibre light source (Dolan-Jenner Fiber-Lite 190-1) at ~35 mW $cm^{-2}$, which was measured with a light meter (Newport Power Meter, model 1815-C). Sheet resistance measurements were performed on the same films using a four point probe technique (KeithLink Technology Co., Ltd. Taiwan).

The photocurrent–voltage (*J–V*) characteristics were analysed using a Keithley 2400 SMU instrument and recorded using a custom LabView Virtual Instrument program. A standard silicon test cell with NIST-traceable certification was used to calibrate the power density at 100 mW $cm^{-2}$ at the sample plane of the collimated a 150W xenon-arc light source (Newport), which was passed through an AM 1.5G filter. The scan rate and delay time are 200 mV $s^{-1}$ and 30 ms, respectively. The active area of the fabricated devices was 0.09 $cm^2$. The devices were masked with a non-reflective mask of 0.1 $cm^2$ and were tested in an air atmosphere without encapsulation. No device preconditioning, such as prolonged light soaking, forward voltage biasing, or

equilibration time was used. The IPCE spectra ranging from 300 nm to 800 nm were taken by passing chopped light from a xenon source through a monochromator and onto the devices. The light intensity of the illumination source was adjusted using a photodiode detector (silicon calibrated detector, Newport).

## Acknowledgements

Munkhbayar Batmunkh acknowledges International Postgraduate Research Scholarship (IPRS) and Australian Postgraduate Award (APA) for financial support during his study in Australia. The support of the Australian Research Council Discovery Program (DP130101714) is gratefully acknowledged. We acknowledge the use of South Australian node of the Australian Microscopy & Microanalysis Research Facility (AMMRF) at Flinders University. The authors also acknowledge the Australian National Fabrication Facility (ANFF).

## References

[1] A. Kojima, K. Teshima, Y. Shirai, T. Miyasaka, *J. Am. Chem. Soc.* **2009**, *131*, 6050.
[2] C. Zuo, H. J. Bolink, H. Han, J. Huang, D. Cahen, L. Ding, *Adv. Sci.* **2016**, *3*, 1500324.
[3] H. S. Jung, N.-G. Park, *Small,* **2015**, *11*, 10.
[4] S. Kazim, M. K. Nazeeruddin, M. Grätzel, S. Ahmad, *Angew. Chem. Int. Ed.* **2014**, *53*, 2812.
[5] X. Tong, F. Lin, J. Wu, Z. M. Wang, *Adv. Sci.* **2016**, *3*, 1500201.
[6] P. Docampo, S. Guldin, T. Leijtens, N. K. Noel, U. Steiner, H. J. Snaith, *Adv. Mater.* **2014**, *26*, 4013.
[7] L. Qiu, J. Deng, X. Lu, Z. Yang, H. Peng, *Angew. Chem. Int. Ed.* **2014**, *53*, 10425.
[8] L. Qiu, S. He, J. Yang, J. Deng, H. Peng, *Small.* **2016**, *12*, 2419.
[9] Z. Wei, H. Chen, K. Yan, S. Yang, *Angew. Chem. Int. Ed.* **2014**, *53*, 13239.
[10] H. Zhou, Q. Chen, G. Li, S. Luo, T.-b. Song, H.-S. Duan, Z. Hong, J. You, Y. Liu, Y. Yang, *Science.* **2014**, *345*, 542.
[11] M. Saliba, S. Orlandi, T. Matsui, S. Aghazada, M. Cavazzini, J.-P. Correa-Baena, P. Gao, R. Scopelliti, E. Mosconi, K.-H. Dahmen, F. De Angelis, A. Abate, A. Hagfeldt, G. Pozzi, M. Graetzel, M. K. Nazeeruddin, *Nat Energy.* **2016**, *1*, 15017.

[12] http://www.nrel.gov/ncpv/images/efficiency_chart.jpg, Best Research-Cell Efficiencies (NREL), ***2016***, Visited on 06th June.
[13] N. J. Jeon, J. H. Noh, Y. C. Kim, W. S. Yang, S. Ryu, S. I. Seok, *Nat Mater.* **2014**, *13*, 897.
[14] A. Molina-Ontoria, I. Zimmermann, I. Garcia-Benito, P. Gratia, C. Roldán-Carmona, S. Aghazada, M. Graetzel, M. K. Nazeeruddin, N. Martín, *Angew. Chem. Int. Ed.* **2016**, *55*, 6270.
[15] X. Li, M. Tschumi, H. Han, S. S. Babkair, R. A. Alzubaydi, A. A. Ansari, S. S. Habib, M. K. Nazeeruddin, S. M. Zakeeruddin, M. Grätzel, *Energy Technology*. **2015**, *3*, 551.
[16] A. Matas Adams, J. M. Marin-Beloqui, G. Stoica, E. Palomares, *J. Mater. Chem. A.* **2015**, *3*, 22154.
[17] G. Xing, N. Mathews, S. Sun, S. S. Lim, Y. M. Lam, M. Grätzel, S. Mhaisalkar, T. C. Sum, *Science.* **2013**, *342*, 344.
[18] M. Batmunkh, M. J. Biggs, J. G. Shapter, *Adv. Sci.* **2015**, *2*, 1400025.
[19] Z. Zhu, J. Ma, Z. Wang, C. Mu, Z. Fan, L. Du, Y. Bai, L. Fan, H. Yan, D. L. Phillips, S. Yang, *J. Am. Chem. Soc.* **2014**, *136*, 3760.
[20] M. Saliba, W. Zhang, V. M. Burlakov, S. D. Stranks, Y. Sun, J. M. Ball, M. B. Johnston, A. Goriely, U. Wiesner, H. J. Snaith, *Adv. Funct. Mater.* **2015**, *25*, 5038.
[21] G. Yang, H. Tao, P. Qin, W. Ke, G. Fang, *J. Mater. Chem. A.* **2016**, *4*, 3970.
[22] M. Batmunkh, C. J. Shearer, M. J. Biggs, J. G. Shapter, *J. Mater. Chem. A.* **2015**, *3*, 9020.
[23] J. T.-W. Wang, J. M. Ball, E. M. Barea, A. Abate, J. A. Alexander-Webber, J. Huang, M. Saliba, I. Mora-Sero, J. Bisquert, H. J. Snaith, R. J. Nicholas, *Nano Lett.* **2014**, *14*, 724.
[24] G. S. Han, Y. H. Song, Y. U. Jin, J.-W. Lee, N.-G. Park, B. K. Kang, J.-K. Lee, I. S. Cho, D. H. Yoon, H. S. Jung, *ACS Appl. Mater. Interfaces.* **2015**, *7*, 23521.
[25] A. Agresti, S. Pescetelli, L. Cinà, D. Konios, G. Kakavelakis, E. Kymakis, A. D. Carlo, *Adv. Funct. Mater.* **2016**, *26*, 2686.
[26] X. Dang, H. Yi, M.-H. Ham, J. Qi, D. S. Yun, R. Ladewski, M. S. Strano, P. T. Hammond, A. M. Belcher, *Nat Nano.* **2011**, *6*, 377.
[27] M. Batmunkh, M. J. Biggs, J. G. Shapter, *Small.* **2015**, *11*, 2963.
[28] T. J. Macdonald, D. D. Tune, M. R. Dewi, C. T. Gibson, J. G. Shapter, T. Nann, *ChemSusChem.* **2015**, *8*, 3396.
[29] M. M. Tavakoli, R. Tavakoli, Z. Nourbakhsh, A. Waleed, U. S. Virk, Z. Fan, *Adv. Mater. Interfaces.* **2016**, *3*, 1500790.
[30] A. Abrusci, S. D. Stranks, P. Docampo, H.-L. Yip, A. K. Y. Jen, H. J. Snaith, *Nano Lett.* **2013**, *13*, 3124.
[31] M. Batmunkh, T. J. Macdonald, C. J. Shearer, M. Bat-Erdene, Y. Wang, M. J. Biggs, I. P. Parkin, T. Nann, J. G. Shapter, *Submitted Manuscript.* **2016**,
[32] F. Giordano, A. Abate, J. P. Correa Baena, M. Saliba, T. Matsui, S. H. Im, S. M. Zakeeruddin, M. K. Nazeeruddin, A. Hagfeldt, M. Graetzel, *Nat Commun.* **2016**, *7*, 10379.

[33] A. Cuevas, *Energy Procedia.* **2014**, *55*, 53.
[34] W. Shockley, W. T. Read, *Phys Rev.* **1952**, *87*, 835.
[35] B. Chen, M. Yang, S. Priya, K. Zhu, *J. Phys. Chem. Lett.* **2016**, *7*, 905.
[36] Z. Wei, H. Chen, K. Yan, X. Zheng, S. Yang, *J. Mater. Chem. A.* **2015**, *3*, 24226.
[37] S. van Reenen, M. Kemerink, H. J. Snaith, *J. Phys. Chem. Lett.* **2015**, *6*, 3808.
[38] T. Leijtens, G. E. Eperon, S. Pathak, A. Abate, M. M. Lee, H. J. Snaith, *Nat Commun.* **2013**, *4*, 2885.
[39] K. Wojciechowski, T. Leijtens, S. Siprova, C. Schlueter, M. T. Hörantner, J. T.-W. Wang, C.-Z. Li, A. K. Y. Jen, T.-L. Lee, H. J. Snaith, *J. Phys. Chem. Lett.* **2015**, *6*, 2399.
[40] P. G. Collins, K. Bradley, M. Ishigami, A. Zettl, *Science.* **2000**, *287*, 1801.
[41] W. Huang, J. S. Manser, P. V. Kamat, S. Ptasinska, *Chem. Mater.* **2016**, *28*, 303.
[42] M. Xiao, F. Huang, W. Huang, Y. Dkhissi, Y. Zhu, J. Etheridge, A. Gray-Weale, U. Bach, Y.-B. Cheng, L. Spiccia, *Angew. Chem. Int. Ed.* **2014**, *126*, 10056.
[43] K. Rakstys, A. Abate, M. I. Dar, P. Gao, V. Jankauskas, G. Jacopin, E. Kamarauskas, S. Kazim, S. Ahmad, M. Grätzel, M. K. Nazeeruddin, *J. Am. Chem. Soc.* **2015**, *137*, 16172.

# Supporting Information for

# Single-Walled Carbon Nanotubes Enhance the Efficiency and Stability of Nanocrystalline $TiO_2$ Photoelectrode Based Perovskite Solar Cells

Munkhbayar Batmunkh,[1,2] Cameron J. Shearer,[2] Munkhjargal Bat–Erdene,[2] Mark J. Biggs,[1,3] Joseph G. Shapter,[2]*

[1] *School of Chemical Engineering, The University of Adelaide, Adelaide, South Australia 5005, Australia*

[2] *School of Chemical and Physical Sciences, Flinders University, Bedford Park, Adelaide, South Australia 5042, Australia*

[3] *School of Sciences, Loughborough University, Loughborough, Leicestershire, LE11 3TU, UK*

* Corresponding authors:

joe.shapter@flinders.edu.au

*Submitted Manuscript*

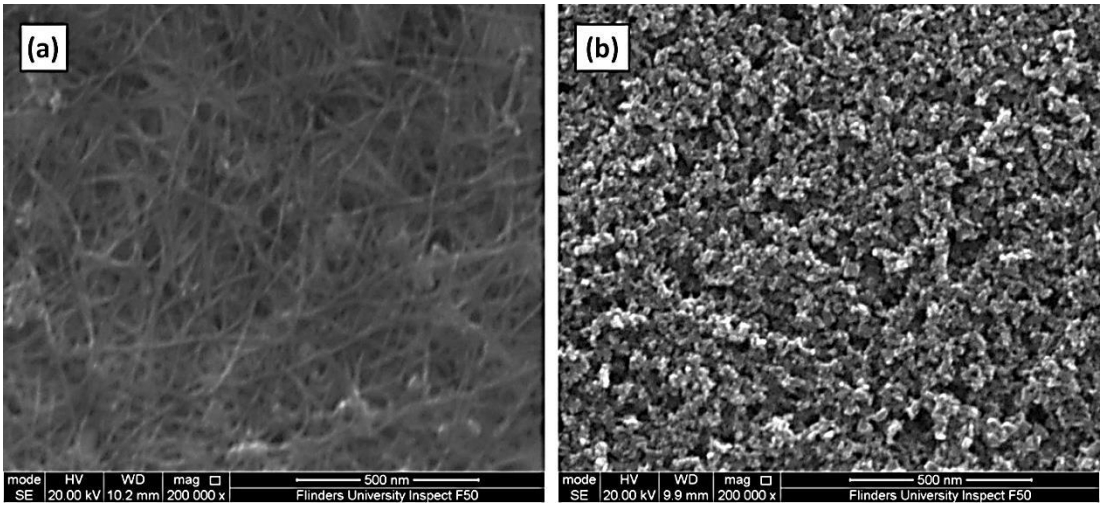


**Figure S7-1**. SEM image of (a) SWCNTs and (b) $TiO_2$ NPs based film.

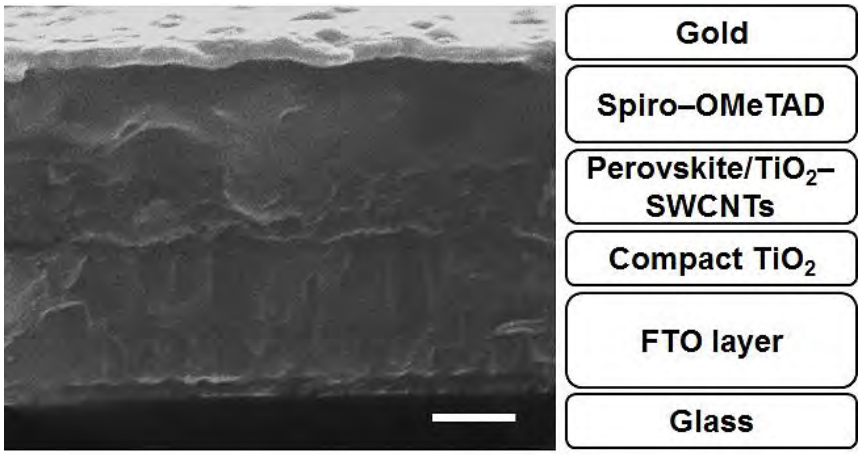


**Figure S7-2**. Cross sectional SEM image of the $TiO_2$ NPs-SWCNTs photoelectrode based PSC.

**Table S7-1**. Diode characteristics for PSCs fabricated with $TiO_2$ NPs-only and $TiO_2$ NPs-SWCNTs based photoelectrodes.

| Device | $J_{sat}$ (mA $cm^{-2}$) | Ideality Factor | $R_{shunt}$ (kΩ) | $R_{series}$ (Ω) |
|---|---|---|---|---|
| $TiO_2$ NPs-only | 5.47 (± 0.21) x $10^{-10}$ | 1.46 ± 0.14 | 13.8 ± 3.7 | 111 ± 10.5 |
| $TiO_2$ NPs-SWCNTs | 1.05 (± 0.38) x $10^{-10}$ | 1.31 ± 0.14 | 23.0 ± 5.2 | 77.3 ± 7.96 |

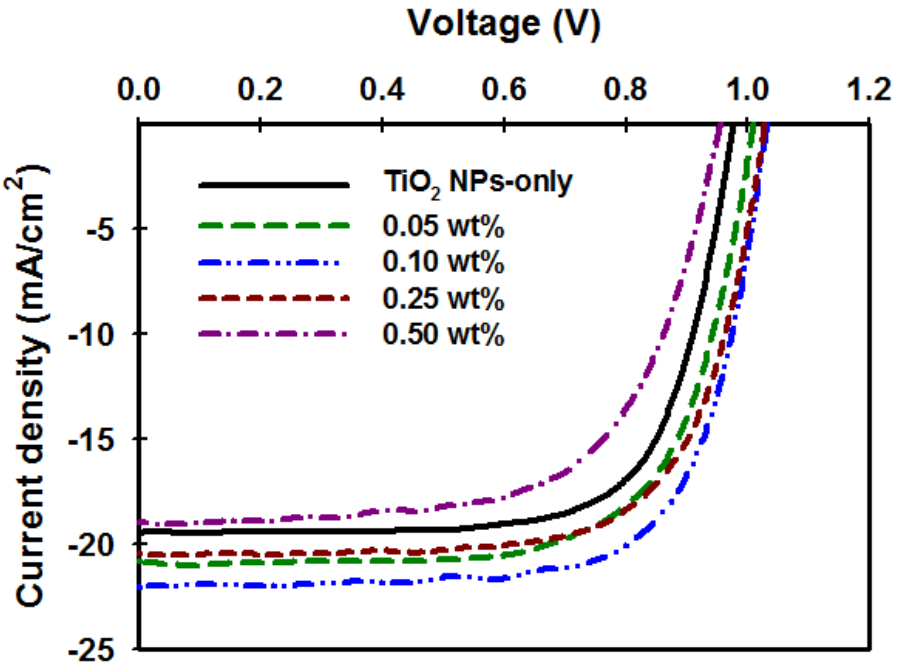


**Figure S7-3**. J–V curves of best-performing PSCs fabricated based on $TiO_2$ NP photoelectrodes with different SWCNT content.

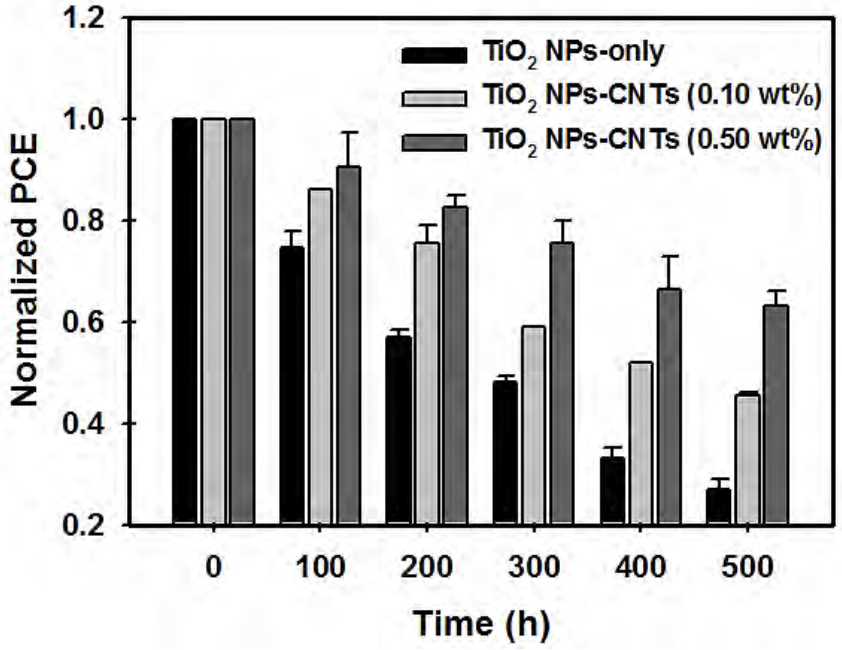


**Figure S7-4**. Moisture-stability of the PSCs fabricated based on $TiO_2$ NPs photoelectrodes employing different SWCNT concentrations (0 wt%, 0.10 wt% and 0.50 wt%). Standard deviations are calculated based on at least 3 devices.

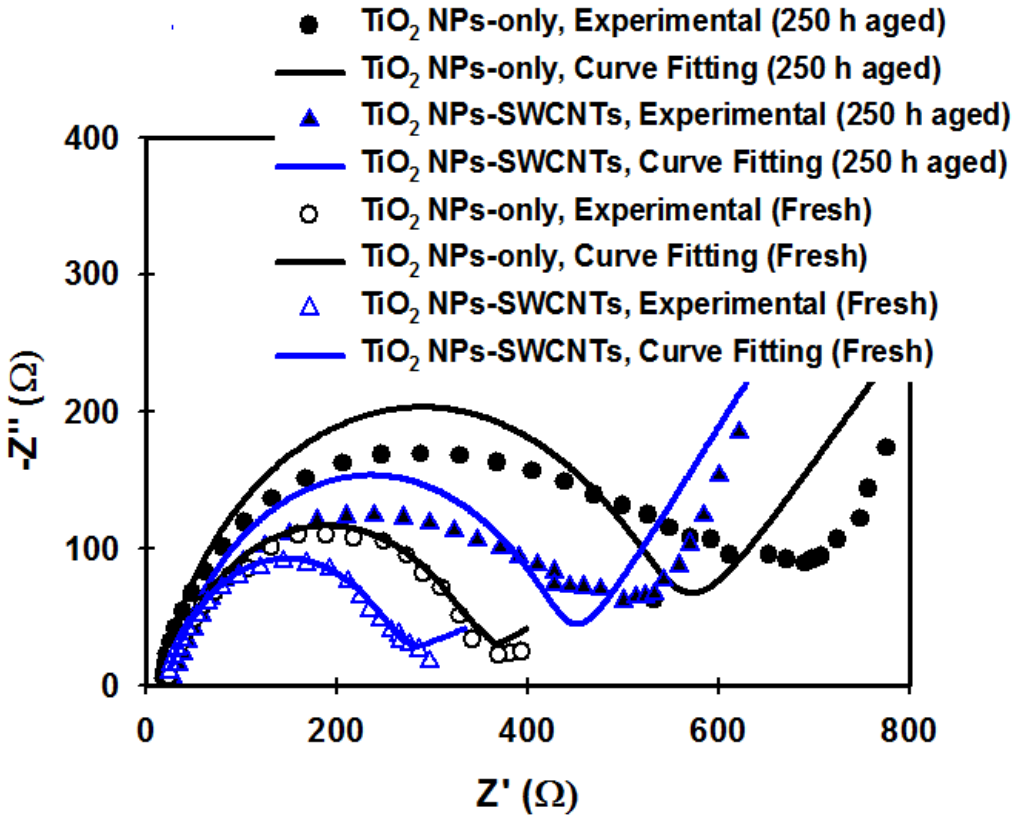


**Figure S7-5**. Nyquist plots of EIS measurements of the fresh and aged devices measured under illumination at 0.3 V bias ($V_{oc}$). The unencapsulated devices were aged for around 250 h in ambient conditions.

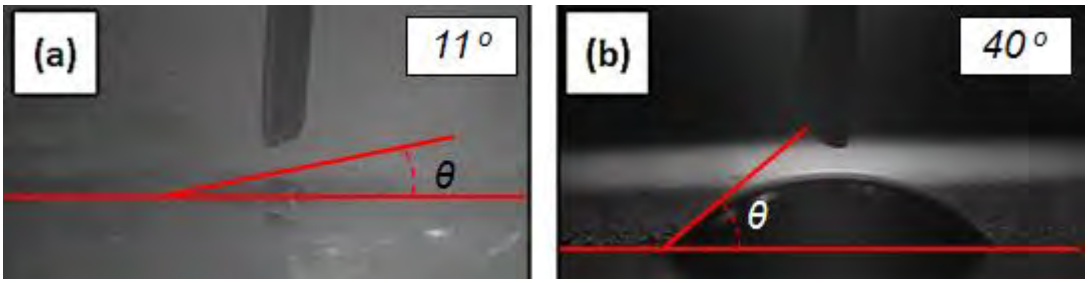


**Figure S7-6**. Wettability test of (a) $TiO_2$ NPs-only film and (b) SWCNTs film.

# Chapter 8.

## Conclusion

## 8.1. Conclusions

High photovoltaic efficiency, excellent stability and low manufacturing cost are the main key factors to the commercialization of dye sensitized solar cells (DSSCs) and perovskite solar cells (PSCs) in the quickly growing renewable electricity generation market.[1] The properties of carbon nanomaterials such as carbon nanoparticles, carbon nanotubes (CNTs) and graphene have been shown to play important roles in achieving high efficiency, improving light and long-term stability and reducing the production cost of both DSSCs and PSCs.[2, 3] However, the progress of carbonaceous photoelectrodes based DSSCs is lacking due to the limited and unclear understanding of the exact role of carbon materials in the devices. Moreover, the development of alternative electrocatalysts that are low–cost and can exhibit higher or comparable performance to the conventional platinum (Pt) counter electrode (CE) in DSSCs is highly desired. On the other hand, research into the potential application of carbon nanomaterials in the state-of-the-art PSCs is still in its initial stages. As such, this Ph.D. thesis was focused on the utilization of carbon nanomaterials in different components of DSSCs and PSCs. The main objectives of this Ph.D. project were to investigate the effect of CNTs and graphene derivatives based photoelectrode and counter electrode (CE) on the efficiency and stability of DSSCs and PSCs.

In this Ph.D. thesis, in order to provide a detailed understanding of the role of carbon nnaomaterials in DSSC photoelectrodes, recent advances that have been made in the use of carbon nanomaterials in the photoelectrode of DSSCs were reviewed and outlined. Then the influence of reduced graphene oxide on the dye adsorption kinetic and efficiency of $SnO_2$ photoelectrode based DSSCs was experimentally investigated. The development of efficient electrocatalyst material as an alternative to the conventional Pt for DSSCs was also reported. Next, the suitability of transparent conductive graphene films as a substitute for the conventional electron collecting transparent conducting oxide electrode (TCO) in perovskite solar cells was examined. The influence of various types of CNTs and graphene derivatives on the photovoltaic efficiency, hysteresis behavior and stability of $TiO_2$ photoelectrodes based perovskite solar cells was comprehensively and systematically explored. The main conclusions drawn from the results presented in chapters 2-7 can be summarized as follows:

**Chapter 2** discussed the advanced research on the use of carbon materials in the photoelectrodes of DSSCs because the activity in this research field has been rapidly growing in the past few years. A brief overview of novel nanostructured material based photoelectrodes is also provided. Based on the results and findings of extensive research, it can be concluded that carbon nanotubes (CNTs) and graphene are very promising materials for high performance photoelectrodes for DSSCs.

**Chapter 3** presented the successful application of reduced graphene oxide (RGO) structures in 1D $SnO_2$ micro-rod based photoanodes for DSSCs. We found that the use of RGO overcomes the major shortcoming of $SnO_2$ when applied as a DSSC photoanode, namely poor dye adsorption. In addition, owing to its suitable energy levels and excellent conductivity, RGO significantly enhanced the electron transport rate in the cells. As compared to the control device, a ~91.5% enhancement in the efficiency was achieved by employing RGO in the $SnO_2$ photoanode for DSSCs.

**Chapter 4** compared a series of heteroatom (I, P, B, N, S)–doped graphene electrocatalysts as CE materials for the iodine reduction reaction (IRR) in DSSCs. We found based on the electrochemical characterization and photovoltaic (PV) analysis that the S–doping on graphene is the most effective in improving the electrocatalytic activity among the other types of doping. Furthermore, we prepared highly efficient hybrid electrocatalysts by incorporating the excellent conductivity of S–doped graphene and high catalytic activity of $FeS_2$ for use in DSSCs. The combination of high electrocatalytic activity, good electrical conductivity, and outstanding electrochemical stability led to impressive device performance (8.10%) of the S–doped graphene and $FeS_2$ hybrid electrocatalyst making this material an ideal candidate for highly efficient and stable DSSCs.

**Chapter 5** demonstrated the applicability of transparent conductive graphene films (TCGFs) formed by solution processable techniques as alternatives to the conventional transparent conducting oxide (TCO) electrodes in perovskite solar cells (PSCs). A maximum efficiency of 0.62% was achieved. Furthermore, by incorporating graphene structures into both compact $TiO_2$ and mesoporous $TiO_2$ layers of the PSCs, the efficiency was further improved to 0.81%. We anticipate that this work will open new avenues for the development of graphene materials in perovskite based solar cells.

**Chapter 6** reported the successful incorporation of highly conductive carbon nanotubes (CNTs) into one-dimensional $TiO_2$ nanofiber (1D $TiO_2$ NF) photoelectrodes for highly efficient PSCs. We found that the use of single-walled CNTs (SWCNTs) is the most effective material among the three different types of CNTs to achieve high efficiencies from the devices. As compared to the $TiO_2$ NF-only photoelectrode based device, a significant enhancement (~40%) in the cell efficiency is achieved by incorporating an optimized amount of SWCNTs into the $TiO_2$ NF PSCs. We also found that the use of SWCNTs in the $TiO_2$ NFs photoelectrode reduces the hysteresis behaviour and improves the stability of the PSCs. More importantly, our best performing device fabricated with SWCNTs in both cp–$TiO_2$ and $TiO_2$ NFs layers achieved a PCE of 14.03%.

**Chapter 7** explored the production of a nanocomposite material comprising nanocrystalline $TiO_2$ NPs and conductive SWCNTs to prepare photoelectrodes for highly efficient PSCs. We found that the use of SWCNTs in the nanocrystalline $TiO_2$ photoelectrodes significantly improves the electron transfer process and reduces the charge recombination rate in PSCs. As a result, a remarkable power conversion efficiency of 16.11% was obtained using the nanocomposite photoelectrode based device. We also found that the incorporation of SWCNTs in the PSC photoelectrodes reduces the anomalous hysteretic *J-V* behaviour, while it also helps to improve the light- and long-term storage-stability of the devices.

## 8.2. Future Directions and Recommendations

### 8.2.1. Nanocarbons in dye-sensitized solar cells (DSSCs)

Although significant achievements have been made in this cutting-edge research (carbon nanomaterials based DSSCs), several challenges must be addressed to build up high–performance devices based on CNTs and graphene. Further optimizations of carbonaceous materials in DSSCs are still required.

(1) The application of CNTs and graphene in semiconducting $TiO_2$ layer for DSSCs is an effective strategy to improve DSSC performance. It has been suggested that the improvement in the efficiency of CNTs/$TiO_2$ and/or graphene/$TiO_2$ photoelectrodes based DSSCs is due to the increased electron transport, enhanced light harvesting

efficiency and/or high dye loading. However, it was found that the dye adsorption mechanism of CNTs and graphene materials based $TiO_2$ films is very unclear, with some studies showing conflicting results. A clear understanding of the dye adsorption would be of great value. Our hypothesis was that the functional groups on CNTs and graphene play an important role in dye loading of the electrodes. If so, further optimization on the dye adsorption and conductivity of CNTs and graphene should be determined by adjusting the extent of functionalization.

Semiconducting (s-SWCNTs) in the semiconducting $TiO_2$ layer can enhance the efficiency of DSSCs. The conductivity of s-SWCNTs can be controlled by the amount of functionalization. Additionally, investigating the effect of the band structures of s–SWCNTs on the performance of DSSCs would be very valuable.

(2) It was found that vertically aligned CNTs are promising counter electrode materials to achieve highly efficient Pt–free DSSCs due to its improved electrical conductivity and electrocatalytic activity.[4-6] It is reasonable to expect improved performance of DSSCs by applying vertically grown CNTs structure with the $TiO_2$ photoelectrode films.

(3) Chemically functionalizing graphene is an established method to open the band gap of graphene and is critical to improvements in the cell characteristics. The band structure of graphene oxide or reduced graphene oxide can be tuned by the extent of functionalization.[8, 9] The electronic band structure of the functionalized graphene should be considered in the future studies of graphene materials based DSSCs.

(4) Since the dye adsorption kinetics on graphene structures based DSSCs are not fully understood, the underlying fundamental driving forces of dye interactions should be explored in depth. According to the literature,[10-12] it seems reasonable that the reactive sites (functional groups) on graphene surfaces and edges would play a major roles in dye interactions and this will need to be investigated to better understand the dye loading characteristics. If the functional groups on graphene play a critical role in the dye adsorption, further optimization of the oxidation or reduction level of graphene may be required to achieve the highest possible performance of DSSCs.

(5) It has been demonstrated that carbon materials exhibit excellent electrocatalytic activity for the reduction of liquid electrolyte.[13-15] However, the use of too high

concentration of the carbonaceous materials in the photoelectrode brings significant charge recombination at the interface of carbons and electrolyte by reducing tri-iodide to iodide. Therefore, the electrocatalytic activity of carbonaceous materials should be taken into account when they are used in the photoelectrode. Graphene is known not to be penetrable by gases so a film of graphene on the photoelectrode may offer an ability to control molecular diffusion while still allowing efficient charge transport. Such diffusion control might extend the lifetime of the electrolyte. This work would likely require the construction of a complex hybrid electrode perhaps using CNTs to enhance conductivity or tune electronic states while using graphene to control levels of reactivity at the critical interfaces. We believe that the carbonaceous material will bring an important breakthrough when they are used in the photoelectrode of solid state DSSCs.

(6) Since chemical doping is a powerful method to improve the CNTs properties including conductivity and catalytic activity,[16-18] the application of various chemical dopants as well as dual doping for CNTs presents an important opportunity to further improve Pt-free counter electrodes for DSSCs.

Since hybrid materials based on CNTs exhibit unique electrocatalytic properties and high electrical conductivity, further improvement in the DSSC performance can be expected via the incorporation of CNTs with other materials (especially transition metallic compounds (TMCs)) to fabricate effective hybrid electrodes.

### 8.2.2. Nanocarbons in perovskite solar cells (PSCs)

Although excellent achievements have been made in the use of carbon materials in PSCs, this cutting-edge research field is still in its initial stages. Therefore, we expect that the following points will be carefully investigated in the future efforts of using nanocarbons in PSCs.

(1) Carbon nanomaterials have been proven to be ideal candidates to replace the precious metal in the cathode of PSCs. Nanocarbon films exhibit the added advantage that they can replace both the metal electrode and hole transporting materials (HTMs). We believe that further improvement in this class of solar cells could be made by upgrading the CNT properties. For instance, the use of pure metallic CNTs would bring critical improvements in the performance of PSCs.

Although carbon black and CNTs have been utilized as the PSC cathode, the use of graphene materials in this application is lacking despite graphene possessing higher electrical conductivity than the other forms of carbon. Therefore, reports on using highly conductive graphene as the conductive cathode of PSCs would be worthwhile. Moreover, chemically doped CNTs and graphene should exhibit very high charge transfer rates. So, applying chemically doped CNTs and graphene in the counter electrode of PSCs would be promising way to improve cell performance. Furthermore, we anticipate that composite materials based on carbon nanostructures (especially CNTs and graphene) will provide remarkable improvement in the performance of PSCs when they are used in the counter electrode.

(2) It was found that the carbon materials play a critical role in improving the stability of PSCs. Therefore, additional treatments on CNTs and/or other types of carbon structures would bring significant enhancement. In addition to this, incorporating functionalised CNT structures with other polymers would be an important research direction for the long-term stability of PSCs especially in the hole-transporting layer.

(3) Inserting graphene quantum dots (GQDs) between the perovskite and $TiO_2$ layers of PSCs was found to be effective method to improve the efficiency of PSCs although the exact mechanism of this improvement is unclear. Therefore, it is clear that further improvements will be possible by adjusting the band gap of GQDs to optimise electron injection and transfer to the anode.

(4) Application of graphene in the $TiO_2$ blocking layer exhibited significant improvement in the cell performance. On the other hand, it is well known that chemical doping is an effective approach to enhance the conductivity of graphene. Based on this concept, improved performance by using chemically doped graphene in the $TiO_2$ electron collection layers is very likely. In addition, graphene and CNT based composite materials exhibit unique electrical, chemical and physical properties as well as excellent synergetic effect. For this reason, the use of CNTs/graphene composite in the $TiO_2$ blocking layer of PSCs would be very valuable for high-performance device.

(5) There is still valuable and important work to be done by exploring the incorporation of carbon materials and other novel materials such as phosphorene [19]

and $MoS_2$ [20] for the state-of-the-art PSCs. This research would have the potential to further improve the efficiency of the PSC system and provide a new research avenue.

## References


[1] M. Batmunkh, M. J. Biggs, J. G. Shapter, *Adv. Sci*, **2015**, *2*, 1400025.

[2] M. Batmunkh, M. J. Biggs, J. G. Shapter, *Small*, **2015**, *11*, 2963–2989.

[3] M. Batmunkh, C. J. Shearer, M. J. Biggs, J. G. Shapter, *J. Mater. Chem. A,* **2015**, 3, 9020.

[4] E. Ramasamy, W. J. Lee, D. Y. Lee, J. S. Song *Electrochem. Comm,* **2008**, 10, 1087-1089.

[5] K. S. Lee, W. J. Lee, N.-G. Park, S. O. Kim, J. H. Park *Chem. Comm,* **2011**, 47, 4264-4266.

[6] M. Wu, X. Lin, Y. Wang, L. Wang, W. Guo, D. Qi, X. Peng, A. Hagfeldt, M. Grätzel, [7] T. Ma. *J. Am. Chem. Soc,* **2012**, 134, 3419-3428.

[8] Q. Tang, Z. Zhou, Z. Chen. *Nanoscale,* **2013**, 5, 4541-4583.

[9] J.-A. Yan, L. Xian, M. Y. Chou. *Phys. Rev. Lett,* **2009**, 103, 086802.

[10] A. K. Chandiran, M. Abdi-Jalebi, M. K. Nazeeruddin, M. Grätzel. *ACS Nano,* **2014**, 8, 2261-2268.

[11] J. Xu, L. Wang, Y. Zhu. *Langmuir*, **2012**, 28, 8418-8425.

[12] T.-T. Meng, Z.-B. Zheng, K.-Z. Wang. *Langmuir,* **2013**, 29, 14314-14320.

[13] S. Yun, A. Hagfeldt, T. Ma. *Adv. Mater,*. **2014**, 26, 6210-6237.

[14] J. D. Roy-Mayhew, I. A. Aksay. *Chem. Rev,* **2014**, 114, 6323-6348.

[15] H. Wang, Y. H. Hu. *Energy. Environ Sci,* **2012**, 5, 8182-8188.

[16] D. M. Sun, C. Liu, W. C. Ren, H. M. Cheng, *Small,* **2013,** 9, 1188-1205.

[17] W. J. Lee, U. N. Maiti, J. M. Lee, J. Lim, T. H. Han, S. O. Kim, *Chem. Comm,* **2014,** 50, 6818-6830.

[18] U. N. Maiti, W. J. Lee, J. M. Lee, Y. Oh, J. Y. Kim, J. E. Kim, J. Shim, T. H. Han, S. O. Kim, *Adv. Mater,* **2014,** 26, 40-67.

[19] M. Batmunkh, M. Bat-Erdene, J. G. Shapter, *Adv. Mater*, **2016**, *28*, 8586-8617.

[20] X. Zhang, Z. Lai, C. Tan, H. Zhang, *Angew. Chem. Int. Ed,* **2016**, 55, 8816-8838.

# Appendix A

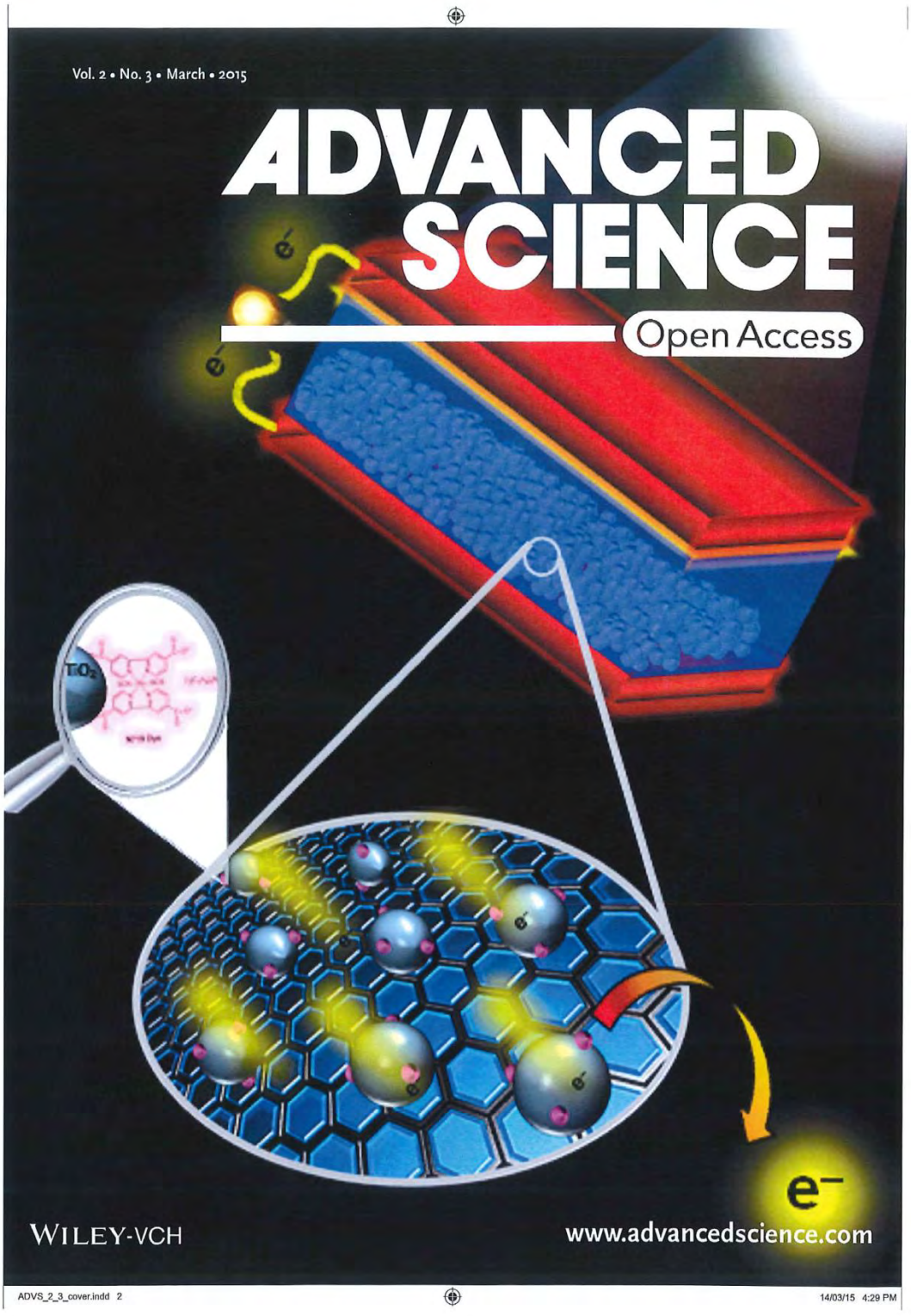
Vol. 2 • No. 3 • March • 2015
ADVANCED SCIENCE
Open Access
e⁻
e⁻
TiO₂
e⁻
e⁻
e⁻
e⁻
e⁻
WILEY-VCH
www.advancedscience.com
ADVS_2_3_cover.indd 2
14/03/15 4:29 PM

ADVANCED SCIENCE
Open Access
www.advancedscience.com



# Carbonaceous Dye-Sensitized Solar Cell Photoelectrodes

*Munkhbayar Batmunkh, Mark J. Biggs,* and Joseph G. Shapter**

**High photovoltaic efficiency is one of the most important keys to the commercialization of dye sensitized solar cells (DSSCs) in the quickly growing renewable electricity generation market. The heart of the DSSC system is a wide bandgap semiconductor based photoelectrode film that helps to adsorb dye molecules and transport the injected electrons away into the electrical circuit. However, charge recombination, poor light harvesting efficiency and slow electron transport of the nanocrystalline oxide photoelectrode film are major issues in the DSSC's performance. Recently, semiconducting composites based on carbonaceous materials (carbon nanoparticles, carbon nanotubes (CNTs), and graphene) have been shown to be promising materials for the photoelectrode of DSSCs due to their fascinating properties and low cost. After a brief introduction to development of nanocrystalline oxide based films, this Review outlines advancements that have been achieved in the application of carbonaceous-based materials in the photoelectrode of DSSCs and how these advancements have improved performance. In addition, several of the unsolved issues in this research area are discussed and some important future directions are also highlighted.**

## 1. Introduction

The fact that only one-thousandth of the Sun's energy incident on the Earth is equal to the entire world's current energy needs[1] means direct conversion of this energy into electricity—photovoltaic (PV) energy—is now a mainstream renewable energy source.[2] PV devices, or solar cells, have undergone considerable development over the past two decades: i) first generation silicon (Si) solar cells;[3] ii) second generation solar cells based on semiconductor thin films;[4] and iii) most recently, third generation solar cells represented by dye sensitized solar cells (DSSCs) and organic semiconductor solar cells.[5,6] While the first two generations are well established, their manufacture is inherently complex and expensive.[5] The third generation cells such as DSSCs, on the other hand, are in principle far easier and cheaper to manufacture while also offering, at least in theory, greater efficiencies,[7–9] although these have yet to be realized. Indeed, the highest standard configuration DSSC efficiency achieved to date is around 13%.[10]

A typical DSSC consists of a metal-oxide semiconductor electrode on which a photoactive dye is adsorbed (the photoelectrode), an electrolyte, and a counter-electrode, as shown in **Figure 1**.[11–13] Upon exposure to photons, electrons from the dye molecules are excited and injected into the metal-oxide electrode (i.e., the dye molecules are oxidized). These electrons then slowly diffuse through the metal-oxide electrode before being conducted away through a power circuit to the counter-electrode. The electrons then pass from the counter-electrode into the electrolyte (i.e., the ions of the electrolyte are reduced), which in turn diffuses to the photoelectrode where it gives up the electrons to the dye molecules that have previously lost an electron to the circuit (i.e., they are regenerated). Of particular concern in this report is the photoelectrode.

In order to gain sufficient power, the photoelectrode of a DSSC is typically mesoporous so as to balance the need to maximize the density of adsorbed dye molecules while minimizing the resistance to electrolyte diffusion to the dye molecules. The most common (and original) mesoporous photoelectrodes are composed of Titania ($TiO_2$) nanoparticles of around 20 nm in diameter deposited on a conductive transparent medium such as fluoride-doped tin dioxide (FTO) glass. A variety of other nanostructured semi-conducting films have, however, also been investigated, including those composed of zinc oxide (ZnO), tin oxide ($SnO_2$) and niobium pentoxide ($Nb_2O_5$) nanoparticles.[14–16] A significant issue with these nanostructured films is charge recombination arising from reaction between the photoexcited electrons that are slowly diffusing through them (towards the circuit) and the oxidized electrolyte species at that part of the electrode surface that happens to not be covered by dye molecules. This issue has led to some effort being focused on alternative photoelectrode materials, including those based on carbonaceous materials such as carbon particles, carbon nanotubes (CNTs) and, most recently, graphene. Therefore, review articles on carbon nanomaterials for the energy related applications are well documented.[17–28] It should be noted

M. Batmunkh, Prof. M. J. Biggs
School of Chemical Engineering
The University of Adelaide
Adelaide, South Australia 5005, Australia
E-mail: m.biggs@lboro.ac.uk
M. Batmunkh, Prof. J. G. Shapter
School of Chemical and Physical Sciences
Flinders University
Bedford Park, Adelaide, South Australia 5042, Australia
E-mail: joe.shapter@flinders.edu.au
Prof. M. J. Biggs
School of Science
Loughborough University
Loughborough, Leicestershire LE11 3TU, UK



DOI: 10.1002/advs.201400025

that since the production of this article, two other reviews of the use of graphene for DSSCs have been published.[29,30] The most recent one is very comprehensive and spans all aspects of DSSCs,[29] while the other one briefly discussed the recent progresses of graphene based nanostructures in DSSCs.[30] Here, we pay particular attention to the use of the complete spectrum of carbon materials and briefly cover some of the graphene work in the photoelectrodes of DSSCs. Following a brief overview of nanostructured DSSC photoelectrodes, we focus on the latest advancements that have been made on the utilization of carbonaceous materials in this context.

## 2. Development of Photoelectrodes in DSSCs

### 2.1. Nanostructured Photoelectrodes

In the early 1960s, metal oxide semiconductors with wide bandgap structures such as ZnO, $TiO_2$, and $SnO_2$ were used as photosensitizer materials.[31–33] However, one major drawback of these wide bandgaps materials is their poor response to much of the solar spectrum. In particular, they only efficiently harvest the ultraviolet (UV) light, which constitutes around 2–3% of sunlight.[34] This issue was eventually addressed by 'sensitizing' the semiconductors with dye molecules whose light absorption capacity lies in the visible region (i.e., wavelengths greater than 400 nm).[35] By adsorbing dye molecules onto the oxides in this way, electrons excited in the dye by the sunlight can be injected into the conduction band of oxides (**Figure 2**). The problem then was to adsorb a sufficient density of dye molecules to obtain the desired power – this was duly achieved by adopting thin (ca. 10 μm) mesoporous films of metal oxide nanoparticles,[36] which possess relatively high surface area to volume ratios.

Since the initial work of O'Regan and Graetzel, a range of n-type metal oxide semiconductors have been investigated as alternatives to the $TiO_2$ they used, including ZnO, $SnO_2$, $Nb_2O_5$ and $SrTiO_3$, all of which exhibit higher electron mobility than $TiO_2$ while still being low cost and non-toxic.[37–40] None have, however, replaced the nanostructured $TiO_2$ (**Figure 3a**) because surface area to volume ratios of these materials are lower than that of $TiO_2$.[13,41–43] There are three primary factors that limit the performance of DSSCs fabricated based on these nanostructured semiconducting oxide materials: i) they are poor light harvesters because their constituent nanoparticles, which are smaller than the wavelength of the light, do not scatter the light;[44–47] ii) recombination is of major concern in the case of films consisting of nanocrystallites due to the fact that their size is several tens of nanometers and they are soaked in a liquid electrolyte with high ion concentration meaning they cannot support the required charge separation or facilitate a rapid electron transfer within the nanocrystallite network;[48,49] and iii) numerous grain boundaries between the nanoparticles and the diffusion of photo-generated electrons in the nanocrystalline films suffer from random walk of electrons caused by a series of trapping and detrapping processes (Figure 2).[50,51] The electron trapping in the nanocrystalline film is a mechanism that causes significant energy loss. To date, several interesting approaches have been demonstrated to address these issues.[41,44,48,52] Here, the most important of these are briefly discussed.

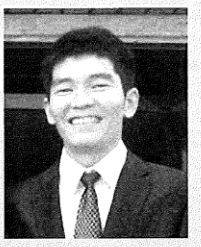

**Munkhbayar Batmunkh** (referred to as B. Munkhbayar) is currently a Ph.D. candidate (Australian Government and University sponsored student) at School of Chemical Engineering in The University of Adelaide, Australia. He is also a visiting researcher at School of Chemical and Physical Sciences in the Flinders University of South Australia. He obtained his B.Sc. in chemistry from the National University of Mongolia, Mongolia, in 2010. Then, he completed his Master of Engineering degree at Gyeongsang National University, South Korea, in 2012. His research interests involve the modification and characterization of carbon nanotubes and graphene structures for use in dye-sensitized solar cells perovskite solar cells.

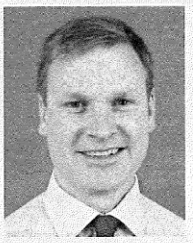

**Mark J. Biggs**, who received his Ph.D. in chemical engineering in 1996 from the University of Adelaide, Australia, is the Professor of Interfacial Science and Engineering and Dean of Science at Loughborough University, UK. He is also a visiting professor at the University of Adelaide, where he was until recently Professor of Chemical Engineering and Head of the School of Chemical Engineering. Before this, he held positions in chemical engineering at the University of Edinburgh and Surrey University, both in the UK. His research interests are focused on understanding and exploiting interfacial phenomena, with particular interest in carbon-based materials.

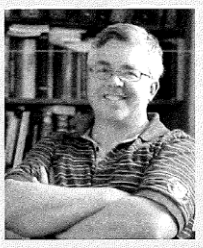

**Joseph G. Shapter** obtained his Ph.D. from the University of Toronto in 1990 working on the detection of small molecules and the determination of their energies. From 1990 to 1996, he worked at the University of Western Ontario, London, Ontario. Since 1996, he has been at Flinders University and is now Professor of Nanotechnology and Dean of the School of Chemical and Physical Sciences. He was the founding Director of the Centre of Expertise in Energetic Materials (CEEM) and is currently the Director of the South Australian node of the Australian Microscopy and Microanalysis Facility (AMMRF). His research interests lie in the use of carbon nanotubes for various applications, including the production of novel photovoltaic systems.

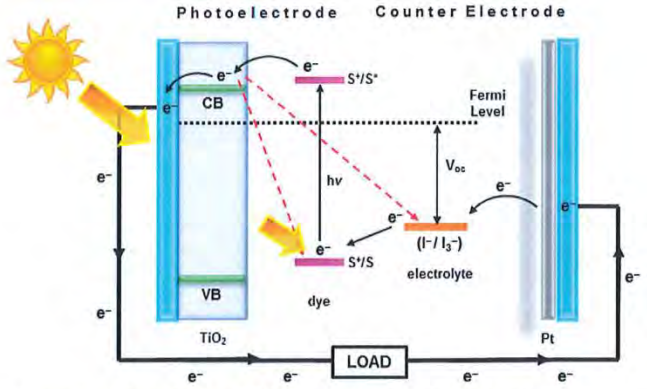


Figure 1. A schematic representation and principle of a typical DSSC with nanocrystalline $TiO_2$ photoelectrode.

One means of bringing about light scattering within the photoelectrode and, hence, improved interaction with the adsorbed dye is through the use of a bilayer structure as illustrated in Figure 3b.[53,54] Typically, the double layer structure consists of a layer of particles larger than the light wavelength (ca. 400 nm in size) being layered over the traditional film of small particles (ca. 20 nm in size).[55] This layer of larger particles backscatters the light that passes through the layer of smaller particles so as it has a further opportunity to interact with the dye molecules adsorbed within it. This bilayer approach is an effective way to enhance the optical absorption of the photoelectrode, especially at wavelengths over 700 nm where the dye is not as efficient at absorbing light. Moreover, it is known that more than 40% of the total irradiance is absorbed in this wavelength region.[44] Although the use of bilayer structure improves light collection efficiency, the large particles also bring a decrease in surface area and, hence, power generation capacity.

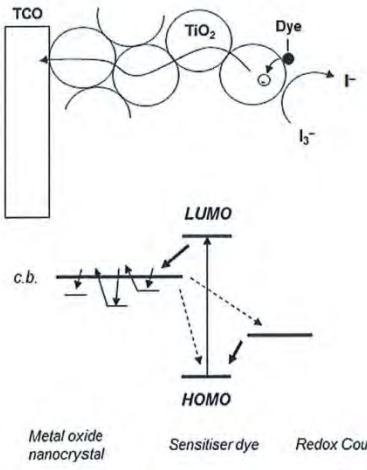


Figure 2. A schematic of electron transport in nanocrystallites based film. Electron trapping and detrapping process.[50,51] Reproduced with permission.[50] Copyright 2004, Elsevier. Reproduced with permission.[51] Copyright 2000, American Chemical Society.

In the past few years, localized surface plasmon resonance (LSPR) of metal nanostructures has been considered a promising way to improve DSSC performance.[56] Plasmonic noble metal nanostructures interact with light in the visible to near-IR range through the creation of resonant surface plasmons. Several authors have seen significant improvement in the DSSC photocurrent by incorporating metal (Au, Ag) particles into semiconducting oxide nanoparticles (see Figure 3c).[57–61] For example, Hou et al.[57] observed a very high (2.4-fold) enhancement in the PV efficiency compared to the conventional $TiO_2$ film based DSSC due to the extension of light absorption over the wavelength range from 460–730 nm. However, the preparation method of homogeneous plasmonic nanocomposites involves a number of complex steps and high temperature & pressure, and the metal NPs are susceptible to corrosion by the electrolyte.[62,63]

Hierarchical spherical nanostructures (HSN) such as that illustrated in Figure 3d have also been recently proposed as a means of simultaneously addressing the poor light harvesting efficiency of conventional DSSC films while boosting the surface area.[44,64] By using micrometer-sized aggregates of nanosized particles, HSNs enhance the scattering of light within the films while retaining the area associated with the nanoparticles.[39,44,65] The first study of such a bifunctional (high surface area to volume ratio and good light scattering property) structure in DSSCs was reported by Koo et al.[65] who observed the amount of adsorbed dye was about 5 times greater than for film composed of similarly micro-sized $TiO_2$ particles. This

  

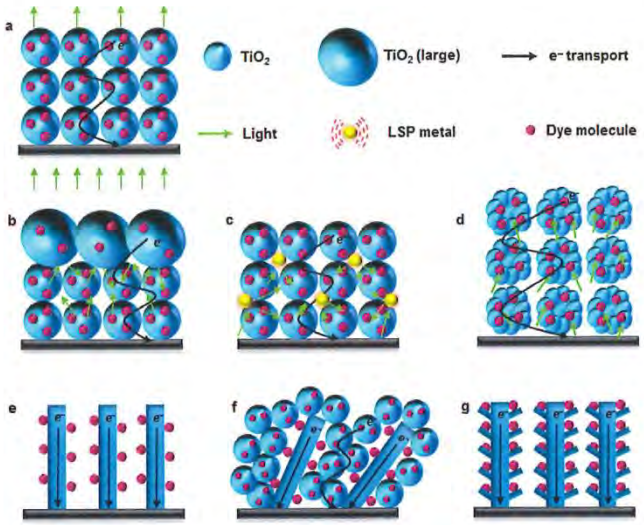


**Figure 3.** The structures of different photoelectrodes for DSSCs. a) Nanocrystalline $TiO_2$ based photoelectrode film, b) double layer structured photoelectrode film, c) plasmon-enhanced photoelectrode film, d) hierarchically structured nanoporous film, e) 1D structured photoelectrode film, f) 1D/nanoparticles hybrid structure based film, and g) hierarchically structured 1D photoelectrode.

leads to an energy conversion efficiency of 10.34%.[65] Even though the HSNs remarkably improve both the light harvesting efficiency and adsorption of dye molecules into the film, the electrodes still suffer from charge recombination and slow electron transfer because they are composed of several small (20 nm) nanoparticles that cause electron trapping and detrapping.

The high rate of charge recombination and slow electron transfer in the nanocrystalline films increase the energy loss in the DSSC. In an effort to eliminate this issue, one dimensional (1D) nanostructures (see Figure 3e) such as nanotubes,[66,67] nanowires,[68] nanorods,[69,70] and nanofibers[71] have been proposed. The use of single crystal anatase $TiO_2$ nanowires resulted in a photo conversion efficiency (PCE) of ca. 9.3%.[68] While 1D materials lead to much more rapid transport of the electrons to the circuit, they suffer from low surface area to volume ratio due to their relatively large diameter[66] (ca. 100 nm) and/or free space between them.[37,52]

In order to address the low surface area to volume ratio and free space of 1D nanomaterials photoelectrode, a composite of 1D nanomaterials and nanoparticles such as that illustrated in Figure 3f have been proposed.[72,73] These composites not only ensure rapid electron transport and efficient use of space, they also enhance light scattering.[37,48] However, the PV performance (3.1%) obtained by this strategy was not as high as expected.[74] This lower performance was, once again, attributed to the large number of grain boundaries between the 1D nanostructures and the spherical nanoparticles, leading to high electron recombination.[52]

In an effort to gain the advantages of 1D nanomaterials while avoiding the issues of poor volume utilization and excessive grain boundaries, Qu et al.[75] have developed the hierarchical structure shown in Figure 3g.[75] This structure fabricated using 1D hierarchical $TiO_2$ yielded a PCE of 4.46%, far higher than that obtained from the 1D-only structure in Figure 3f. Although 1D hierarchical $TiO_2$ may fulfil many of the requirements of the ideal photoelectrode, the performance of the corresponding DSSC is still not high enough. Moreover, the synthesis of such structured $TiO_2$ materials for the photoelectrodes uses complicated processes but still does not yield high performance. Very recently, due to their excellent conductivity, high electron mobility, low cost, good stability and abundance, carbonaceous materials have been considered good candidates for the photoelectrode of DSSCs. The detailed discussion of DSSCs fabricated with semiconducting composites based on the carbonaceous materials is presented in the following.

### 2.2. Carbonaceous Photoelectrodes

#### *2.2.1. Carbon Particles*

A wide range of carbon nanomaterials have been utilized in DSSC application.[76–83] Among them, carbon black is one of the most commonly used materials for the counter electrode of DSSCs owing to its good electrical conductivity, catalytic activity, low cost and availability.[76,81] Although carbon blacks have been

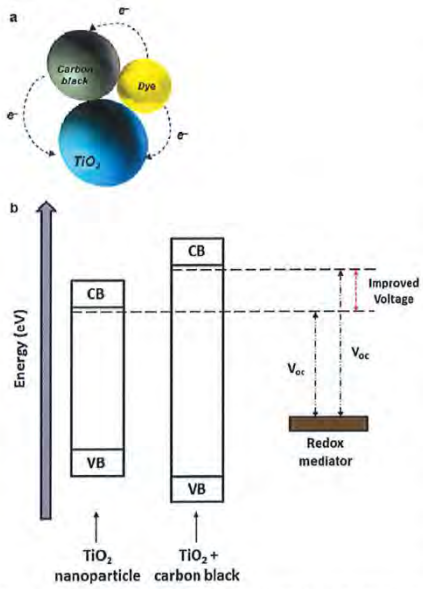


**Figure 4.** a) Schema of the $TiO_2$ particle, carbon black and dye (triangular structure) and b) a possible mechanism for the $V_{oc}$ improvement of $TiO_2$ by adding carbon black. Figures are drawn based on the discussion of ref. [84].

widely used in counter electrodes, they have been rarely used in DSSC photoelectrode.

Ting and Chao were the first to use carbon black in photoelectrodes.[84] They used 22 nm diameter carbon particles as a bridge between nanocrystalline $TiO_2$ and dye molecules in the photoelectrode of DSSCs (**Figure 4**a). The open-circuit voltage ($V_{oc}$) of the cell improved after incorporating carbon black into $TiO_2$ films. The authors hypothesized that this improvement is due to the increased energy level of $TiO_2$ conduction band by adding carbon black (Figure 4b). It is well known that the $V_{oc}$ in PV cells is mainly determined by the energy difference between the conductive band of semiconducting material and the potential energy of redox couple in the electrolyte (see Figure 1).[13] However, the DSSC efficiency declined sharply when a high concentration of the carbon black is used. The authors suggested that this decrease in performance was due to the high loading of carbon particles in the photoelectrode films which interrupted the contact among $TiO_2$, dye and electrolyte. In addition to this explanation, too much carbon black could decrease the light absorption of the window electrode and thereby limit the photoexcitation process. Indeed, the PCE (max. 0.17%) obtained in this study was relatively low as compared to the typical DSSCs because of the major replacement of each component.[84]

In order to effectively utilize the carbon particles in the photoelectrode of DSSCs, several researchers have used thermal treatment processes on the carbon powder incorporated $TiO_2$ film.[85–87] By using this method, these authors prepared highly porous structured films with improved surface area for high dye loading and light scattering ability. In Kang et al,[85] after applying thermal treatment on carbon/$TiO_2$ electrode, a considerable improvement (max. ca. 31%) in the surface area of the film was observed as compared to a $TiO_2$ only film. Because of this improved surface area, they achieved a high energy conversion efficiency of 5.65% using DSSCs fabricated with 1 wt% (optimized content) carbon particles added to the $TiO_2$ film. This optimum concentration of the carbon powder in $TiO_2$ film was further confirmed by Kim et al.[86] who also prepared nanoporous carbon/$TiO_2$ films using a hydrothermal method for use as the photoelectrode in DSSCs. The efficiency of their carbon/$TiO_2$ photoelectrode based DSSC was about 3.4% which was higher than that (2.5%) of the reference device.

Yang et al.[87] synthesized spherical carbon particles with three different sizes (diameters of 250 nm, 500 nm, and 700 nm) using a hydrothermal method and incorporated them into nanocrystalline $TiO_2$ films. After sintering the films at high temperature, the carbon spheres were burned out and thus holes were formed corresponding to the size of initial carbon spheres. The authors studied the influence of hole sizes made in the films on the light absorption characteristics for DSSC performance. The sequence of the light scattering ability of these films was C500 > C700 > C250 > C0. Due to the higher light scattering ability of the C500 film, a 26.5% improvement in the $J_{sc}$ (when compared to a $TiO_2$ nanocrystalline only film based device) was achieved using photoelectrodes based on the 500 nm carbon spheres. A poor $J_{sc}$ obtained by DSSCs with the large holes (700 nm) was due to the decreased amount of dye in the film. Indeed, by balancing the light absorption and dye adsorption ability of the film, the highest efficiency was 7.2% achieved by the cell fabricated with 500 nm carbon particles, while the standard cell reaches 5.6% efficiency.

Carbon fibres (CFs) are cylindrical structures with graphene layers arranged as stacked cones, cups, ribbons or plates. In the past few years, CFs have been used in the photoelectrode of DSSCs due to their good conductivity, low weight and high stability.[88,89] Moreover, the cylindrical shape of CFs is also expected to promote the electron transport within the film.[90] Recently, Guo et al.[89] synthesized rectangular bunched $TiO_2$ nanorod (NR) arrays using a hydrothermal approach. This structure was vertically aligned on the CFs to build the photoelectrode of DSSCs. The preparation route of NRs on the CFs is shown in **Figure 5**a. This synthesis method of the CFs with $TiO_2$ NRs is called a "dissolve and grow" process. In the resulting structure (Figure 5b), the rectangular bunched $TiO_2$ NRs (as termed by the authors) were designed to simultaneously address the poor dye loading of a 1D structure and the light capturing ability of $TiO_2$ nanocrystalline film. Therefore, the bunched NRs/CFs structured photoelectrode exhibited an improved surface area, which enabled more dye molecules to be adsorbed. With the 3D structured photoelectrode made using the carbon fibres (Figure 5c), the conversion efficiency of DSSC reached 1.28%, which was ca. 68% higher than that of the NRs-only (see Figure 5d).

  

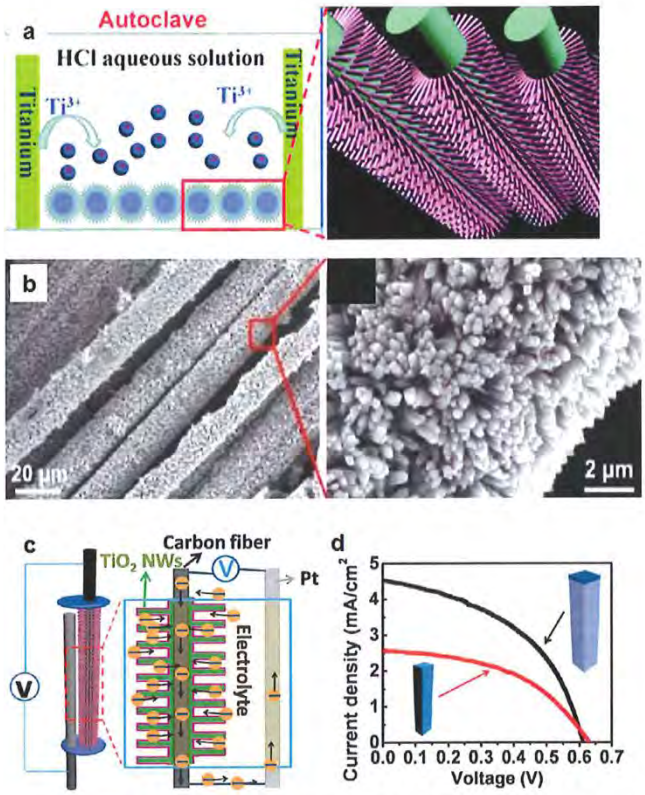


**Figure 5.** a) A schematic illustration of the growth of rectangular bunched $TiO_2$ NRs on CFs, b) SEM of 3D structure formed with $TiO_2$ NRs@CFs, c) DSSC fabricated with 3D structured photoelectrode, and d) current density–voltage (J–V) curves of DSSCs fabricated with the $TiO_2$ NRs and $TiO_2$ NRs@CFs.[89] Reproduced with permission.[89] Copyright 2012, American Chemical Society.

Application of carbon structures in $TiO_2$ nanocrystalline based films is a good strategy that can suppress the charge recombination using a highly conductive carbon layer. A graphitic thin film embedded (referred as carbonized) with semiconducting oxide particles was prepared for use as the photoelectrode of a DSSC.[91] In Jang et al,[91] three different (carbon layer under, on or both under and on the film) carbonized nanocrystalline $TiO_2$ films were fabricated. By introducing graphitic carbons into the $TiO_2$, the amount of dye loading was decreased slightly due to the reduced surface area of the film. Although the adsorption of dye molecules was reduced, the embedded carbons in the $TiO_2$ film improved the electron recombination lifetimes ($\tau_r$) of DSSCs significantly because of their high conductivity. Due to this improved property of the cells, carbonized $TiO_2$ films based DSSCs achieved very high current densities (Table 1). It was noted by these authors that the surface area of the films in such structured device plays a minor role for the PV performance.[91] Finally, a 40.6% improvement (as compared to the reference cell) in the PV efficiency was obtained by DSSC fabricated with both parts (under and on top) carbonized $TiO_2$ thin layers.

Carbon particles can be prepared from sucrose, glucose and starch which are generated by the polymerization and aromatization of carbohydrate molecules. The carbohydrates are mostly converted into carbons using a hydrothermal method under certain conditions.[92,93] Preparing carbons from the carbohydrates has many advantages including a lack of toxicity, a facile synthesis process, use of relatively low temperature coupled with economic viability. Due to these advantages, Jang and co-workers used a glucose-based carbon incorporated $TiO_2$

**Table 1.** PV and electrochemical characteristics of four different DSSCs fabricated in the literature.

| Photoelectrode | Dye amount, (mmol*cm$^{-2}$) | $R_{ct}$ (Ω) | τr (ms) | Jsc (mA*cm$^{-2}$) | PCE (%) |
|---|---|---|---|---|---|
| $TiO_2$–only film | $7.19 \times 10^{-5}$ | 74.47 | 5.1 | 6.58 | 3.21 |
| Lower part carbonized film | $6.09 \times 10^{-5}$ | 64.02 | 22.1 | 6.94 | 3.71 |
| Upper part carbonized film | $5.78 \times 10^{-5}$ | 52.10 | 25.3 | 8.96 | 4.91 |
| Both parts carbonized film | $5.47 \times 10^{-5}$ | 51.84 | 29.6 | 9.35 | 5.21 |

Data points are collected from ref. [91].

photoelectrode film (see **Figure 6**) for DSSC.[94] The $J_{sc}$ and PCE of the DSSCs containing glucose/$TiO_2$ photoelectrode were increased by 20.9% and 11.6%, respectively, as compared to those of the conventional DSSC. The improved performance by adding glucose-based carbon was proven to be due to the improved charge transport within the photoelectrode. However, the cell efficiency was significantly decreased when a high concentration of carbons were used because the presence of large amount of carbons acted as a competitor of dye molecules in light harvesting.

### 2.2.2. Carbon Nanotubes (CNTs)

As shown by red dash arrows in Figure 1, charge recombination and/or back electron transfer are the most pressing problems for the improvement in DSSC efficiency. There are mainly two possible recombination routes in DSSCs: the direct recombination of electrons from the conduction band of semiconducting $TiO_2$ to the oxidized dyes or to the electrolyte. The frequency of the electron recombination to the dye molecule is in the order of a micro to millisecond, whereas that to the electrolyte is in the range of a millisecond to second. Both these recombinations take place at the $TiO_2$/dye and $TiO_2$/electrolyte interface. It has been established that these recombinations can be suppressed by using 1D nanostructures based photoelectrodes. In this regard, as a first member of 1D structures, CNTs are very promising candidates for the DSSC photoelectrodes due to several of their extraordinary properties. Notably, CNTs not only benefit from the 1D structure that provides fast electron transport pathway, their highly conductive character also plays a critical role in DSSCs.

Because of their high charge mobility and/or excellent electrical conductivity that can decrease the charge transfer resistance ($R_{ct}$) of films, CNTs were expected to improve the performance of DSSCs. In 2004, Jang et al.[95] were the first to report using CNTs in the photoelectrode of DSSCs and they achieved a 25% increase in the $J_{sc}$ compared to the CNTs–free cell. Since this significant improvement in the DSSC performance was demonstrated by these authors using CNTs, considerable attention has been paid to the research on this topic.[96–109] For instance, Lin et al.[99] prepared bilayer structured photoelectrode films composed of multi-walled carbon nanotubes (MWCNTs)–$TiO_2$/$TiO_2$ which when used in DSSCs exhibited two times higher PV efficiency than the cell fabricated with the bare $TiO_2$ film. This improvement in the PV performance has been demonstrated to be related to the 1D CNT which supports transfer of the photo-generated charges quickly, thus suppressing charge recombination. **Figure 7**a depicts the complete attachment of $TiO_2$ to the CNT surface. The injected electrons from the excited dye molecules into the conduction band of $TiO_2$ can be transferred quickly through the CNTs conduit, as expressed in Figure 7b. Furthermore, Chen et al.[100] confirmed that the electrical conductivity of the bare $TiO_2$ films can be significantly improved by incorporating the CNTs structure into $TiO_2$ nanocrystalline films. Although the conductivity of the films can be improved by incorporating higher CNTs content, the opaqueness and light absorbing properties of CNTs with high concentration ultimately decreases the incident

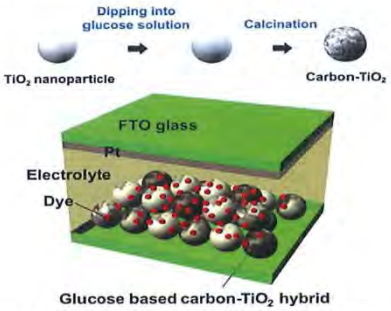


**Figure 6.** Configuration of DSSC fabricated with glucose–based carbon/$TiO_2$ film.[94] Reproduced with permission.[94]

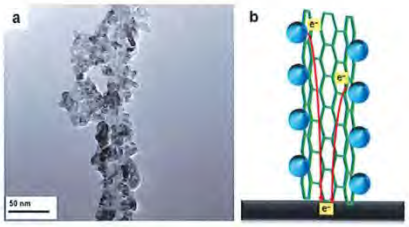


**Figure 7.** a) TEM image of MWCNTs-$TiO_2$ composite,[99] and b) schematic diagram for electron transfer in the CNTs-$TiO_2$ film. Part (a) reproduced with permission.[99] Copyright 2011, Elsevier.

  

photon-to-conversion efficiency (IPCE) of the film electrodes. Therefore, it is very important to pursue the right content of CNTs structures in $TiO_2$ films that can optimize the conductivity and light harvesting efficiency of the electrode.

In order to obtain a balance between the $R_{ct}$ and IPCE, several efforts have been undertaken with different concentrations of CNTs structures.[97,100–104] In these studies, the optimized concentrations of CNTs in $TiO_2$ films were relatively different because the corresponding DSSCs were fabricated under different experimental conditions. A general method to prepare CNTs/$TiO_2$ photoelectrodes is as follows: CNTs are first chemically treated using acid solutions ($HNO_3$ or $H_2SO_4$) to generate functional groups such as hydroxyl (–OH), carbonyl (C=O) and carboxyl (–COOH) groups. Then, the functionalized CNTs are mixed with nanocrystalline $TiO_2$ nanoparticles, followed by a drying process under certain temperature to prepare CNTs/$TiO_2$ pastes. Finally, the obtained paste can be either deposited on transparent conducting oxide substrates via doctor blade technique or screen printing technique. By applying this method, Yu et al.[101] prepared CNTs/$TiO_2$ based photoelectrodes with various concentrations of CNTs (0–1.0 wt%) and compared the efficiencies of the devices. As a result, a maximum conversion efficiency of 4.5% was obtained for a DSSC with a photoelectrode with 0.2 wt% CNTs incorporated into the $TiO_2$ film. Furthermore, a similar observation has been made by Chen et al.[100] who prepared MWCNTs/$TiO_2$ composite films with CNTs concentrations of 0, 0.021, 0.043, 0.086, 0.172, 0.258, and 0.343 wt%. The DSSC made using a 0.172 wt% CNTs/$TiO_2$ based photoelectrode gave the highest efficiency of ca. 5.2%. On the other hand, some studies showed that to obtain the best DSSC performance the concentration of CNTs in $TiO_2$ film should be around 0.01–0.03 wt%.[102–104] These different optimized contents in these case studies are mainly due to the fact that those CNTs were not functionalized using chemical acids prior to incorporating into $TiO_2$ films. By comparing these results reported in the literatures,[97,100–104] it can be concluded that the optimal content of the functionalized CNTs in $TiO_2$ films varies from 0.1 to 0.3 wt% depending on the acid–functionalization level.

The performance of DSSCs containing CNTs materials strongly depends on the dispersion of CNTs in a base fluid.[105,106] It has been established that pristine CNTs are difficult to disperse in base fluids (distilled water, anhydrous ethanol, etc.), which could be due to a large aspect ratio and lack of hydrophilic groups.[110] Therefore, enhanced spatial distribution and improved dispersibility of CNTs in the solvents are the key requirements to obtain the excellent properties of CNTs. Recently, Zhang et al.[106] introduced DNA as a biological scaffold on semiconducting single-walled carbon nanotubes (s-SWCNTs) network in order to upgrade the dispersibility of CNT solution. The upgraded s-SWCNTs dispersion was then utilized to integrate the s-SWCNTs/$TiO_2$ composite for the use in photoelectrode films. In addition, they also added plasmonic metallic silver nanoparticles (AgNPs) into the s–SWCNTs/$TiO_2$ film to further improve the performance of DSSCs. The synthesis process of the s-SWCNTs/$TiO_2$/AgNPs nanocomposite is illustrated in **Figure 8**a–e. In this work,[106] the energy conversion efficiency of the DSSC increased from 4.37% to 5.32% after adding 0.15 wt% s-SWCNTs compared to the $TiO_2$-only photoelectrode system. Furthermore, the DSSC fabricated with s-SWCNTs/$TiO_2$/AgNPs photoelectrode exhibited the highest efficiency of 5.99% due to the improved electron collection and transportation by s-SWCNTs, and the enhanced light-harvesting efficiency by plasmonic AgNPs (see Figure 8f and 8g).

Several researchers have used CNT materials in $TiO_2$ photoelectrode films to boost the PV efficiency of DSSCs.[96–109] It can be clearly seen from **Figure 9** that the recorded efficiencies of CNTs/$TiO_2$ photoelectrodes based DSSCs vary from 4.1% to 10.6% depending on the experimental conditions and applied techniques. So far, the best efficiency of CNTs/$TiO_2$ photoelectrode based DSSC has been achieved by Dang et al.[107] who introduced multiple genes of a virus into s-SWCNTs based aqueous solution. The prepared pastes composed of virus/s-SWCNTs/$TiO_2$ were deposited onto FTO glass substrates using a doctor blade technique. As a result, the observed $J_{sc}$, $V_{oc}$ and FF for DSSC fabricated with 0.1 wt% s-SWCNTs/$TiO_2$ composite film were 20.3 mA $cm^{-2}$, 0.78 V and 0.7, respectively, and yielded a very high energy conversion efficiency of 10.6%. Interestingly, these authors observed a 27% improvement in the $J_{sc}$ when s-SWCNTs were used; whereas the $J_{sc}$ was decreased by ca. 20% after adding a pure metallic SWCNTs (m-SWCNTs), as compared to only $TiO_2$ based DSSC.

Guai et al.[108] later showed a similar finding to that of Dang et al[107] namely that the s-SWCNTs suppress the charge recombination in DSSCs and thereby enhance the overall efficiency. The improved performance of DSSC was because of the increased electron diffusion length by s-SWCNTs, leading to higher electron collections. Notably, the s-SWCNTs possess a non-continuous band structure, while the m-SWCNTs have zero bandgap.[107] So, in the 3D networks of s-SWCNTs/$TiO_2$, the electrons, transferred from the conduction band of $TiO_2$, can be transported to the conducting oxide film without charge recombination because the higher energy barrier of s-SWCNTs compared to m-SWCNTs blocked the back flow of dye-injected electrons to the electrolyte (see **Figure 10**a). For the case of the m-SWCNTs, although they can transport the photoelectrons more rapidly due to higher mobility than s-SWCNTs, the charge transport was disrupted with an increased back electron transfer to the electrolyte (Figure 10b).

SWCNTs can be metallic or semiconducting with bandgaps ranging from 0 to 2.0 eV depending on their diameter, level of defects or functionalization, and degree of aggregation.[111] Based on this concept, it should be possible to improve the efficiency of DSSCs by optimizing the bandgap energy of s-SWCNTs. Therefore, systematically exploring the influence of different bandgap energies of s-SWCNTs on the performance of DSSCs would be of great value.

#### 2.2.3. Graphene

Graphene[112]—a single layer of carbon atoms arranged in a hexagonal lattice—is a material that possesses remarkable properties including excellent conductivity, superior strength to any material ever isolated, good flexibility, high transparency and chemical resistivity.[113–117] The 2010 Nobel Prize in physics was awarded to Andre Geim and Konstantin Novoselov for their

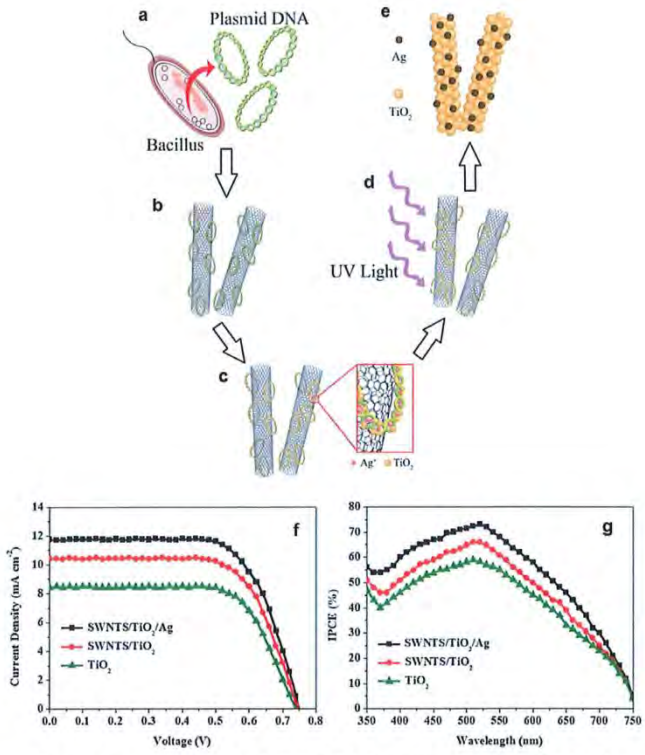


**Figure 8.** a–e) Schematic illustration of the synthesis process of s-SWCNTs/$TiO_2$/Ag nanocomposite for the DSSC photoelectrode, f) J–V curves and g) IPCE spectra of DSSCs fabricated with $TiO_2$-only, s-SWCNTs/$TiO_2$ and s-SWCNTs/$TiO_2$/Ag photoelectrodes.[106] Reproduced with permission.[106] Copyright 2013, Royal Society of Chemistry.

discovery of the unique properties of graphene.[112] Since then, graphene has become known the world-over as an advanced material and is quickly moving from the research laboratories to the industrial applications.[118] The exceptional properties of this material have pioneered recent explorations to apply graphene structures in the photoelectrode of DSSCs.[119–131] It can be clearly seen from **Table 2** that the improved efficiencies of DSSCs with graphene materials incorporated $TiO_2$ photoelectrode films vary from 1.68% to 8.13%. These differences in the cell performances are possibly due to the utilization of different experimental conditions such as the active area of the cells, type of dyes, film preparation methods and various treatments (see Table 2).

Moreover, as listed in Table 2, the efficiencies recorded for the conventional DSSCs also vary considerably ranging from 0.32% to 5.8%, despite all the cells being made very similarly ($TiO_2$ photoelectrode film, Ruthenium based organic dye, iodolyte electrolyte and Pt counter electrode). Because of these varying performances, it is difficult to compare the improvements that have been achieved by the use of graphene structures. To better understand the real enhancement of DSSCs performance obtained by applying carbonaceous materials based films, the efficiency enhancements are calculated and plotted in **Figure 11**.

Figure 11 shows the efficiency enhancements (%) of various DSSCs fabricated using carbon particles, CNTs and graphene incorporated $TiO_2$ photoelectrode films. One can simply observe from Figure 11 that the average enhanced efficiencies obtained by graphene/$TiO_2$ photoelectrode based DSSCs is higher than those achieved by DSSCs with carbon particles and CNTs based $TiO_2$ films. There are several reasons that can be given to explain this observation that graphene improves the performance of cells more compared to other carbonaceous materials.

  

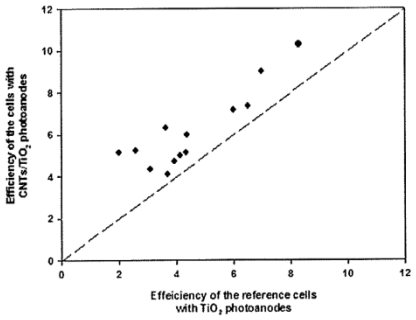


**Figure 9.** PV efficiencies of DSSCs fabricated with and without CNTs in the $TiO_2$ films. Data obtained from refs. [97–109].

The reasons can be listed as follows: i) For the case of CNTs, although they can improve the efficiency of DSSCs, their poorer interconnection with the spherical $TiO_2$ nanoparticles (as compared to the graphene) would limit the overall performance of DSSCs due to some charge transfer barrier and possibility of recombination (see **Figure 12a**). In contrast, graphene is a large single sheet that can significantly contact $TiO_2$ nanocrystallites, thus, it would significantly suppress the charge recombination (see Figure 12b).

ii) The work function of graphene (–4.42 eV)[122] lies between the conduction band of $TiO_2$ (–4.4 eV)[13] and FTO substrate (–4.7 eV).[13] Owing to this suitable energy level, photo-generated electrons transfer stepwise from the $TiO_2$ to FTO without an energy barrier (see **Figure 13**). Here, graphene can act as a bridge between $TiO_2$ and FTO.

iii) The very high conductivity of graphene can accelerate the electron transporting process and reduces the rate of charge recombination (see **Figure 14**). Because of these advantages, graphene materials have been believed to be perfect candidates for the photoelectrode of DSSCs.

To the best of our knowledge, the first study incorporating graphene materials in a $TiO_2$ photoelectrode was reported by Kim et al.,[120] who used a reduced graphene oxide/$TiO_2$ nanoparticles composite as interfacial layer between the FTO and nanocrystalline $TiO_2$ film. By applying this reduced graphene oxide/$TiO_2$ blocking layer, they obtained an energy conversion efficiency of 5.26% which was slightly higher than that (4.89%) of the reference cell. Based on this low improvement in the DSSC performance (only 7.56%), it seems that the common $TiCl_4$ treatment ($TiO_2$ blocking layer) is a more effective method than using this reduced graphene oxide/$TiO_2$ blocking layer. Although the enhancement in the DSSC efficiency achieved using graphene materials as blocking layer was relatively low in this work,[120] the idea has inspired many studies to further advance this topic.

Tang et al.[122] prepared graphene/$TiO_2$ nanocomposite based photoelectrodes for highly efficient DSSCs using a molecular grafting method on titanium (IV) butoxide and graphene sheet. Because of the presence of oxygen containing functional groups on graphene, organic titanium molecules could be grafted on the functionalized graphene sheets by chemisorption. By adjusting the reduction level of graphene oxide, a good interconnection of $TiO_2$ particles to the graphene sheets was achieved producing a highly conductive film. As a result, when the optimized amount of graphene was incorporated into $TiO_2$ nanoparticles based film, the cell obtained five times higher efficiency than the bare $TiO_2$-based one. These authors showed that this significant improvement in the DSSC performance was due to the increased adsorption of dye molecules in the graphene/$TiO_2$ film as compared to the $TiO_2$-only film. Several other studies have showed that the presence of graphene in the nanocrystalline films improves the dye loading.[124,125,130] The reason for this improvement in the dye loading was explained by these authors as follows: the high surface area to volume ratio of graphene provides more anchoring sites for $TiO_2$ which enable the loading of a high amount of dye molecules. In contrast, it can be seen from Table 2 that in some studies,[123,126,127,131] the dye loading in the $TiO_2$ nanocrystallites film decreased after adding the graphene structures. Recently, Chen et al.[126] showed that the amount of adsorbed dye in the graphene incorporated $TiO_2$ film was measured to be $7.6 \times 10^{-9}$ mol cm$^{-2}$, which was lower than that ($1.0 \times 10^{-8}$ mol cm$^{-2}$) of the film with only $TiO_2$ nanoparticles. Furthermore, some other authors also suggested that the incorporation of graphene in $TiO_2$ based film does not significantly increase the dye adsorption into the film, despite the fact that graphene with a high surface area to volume ratio was

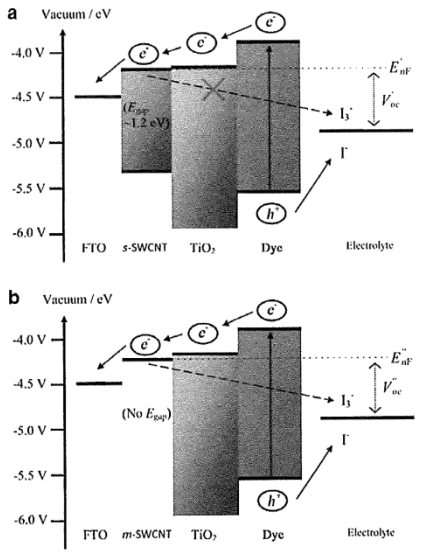


**Figure 10.** A schematic representation of the energy diagram of DSSCs with a) s-SWCNTs and b) m-SWCNTs added $TiO_2$ films.[108] Reproduced with permission.[108]

**Table 2.** PV characteristics of different DSSCs fabricated under various conditions. Graphene, modified Hummers method[132] and hydrazine are abbreviated as "G", "MH method" and "hyd", respectively. The abbreviation of "↑↑" and "↓" in the dye adsorption column represents the amount of adsorbed dye in the rGO/$TiO_2$ film "increased" and "decreased", respectively, as compared to $TiO_2$-only film.

| Photoelectrode film | $J_{sc}$, $mA*cm^{-2}$ | PCE,% | Cell area, $cm^2$ | Dye type | Deposition method | Synthesis method of "G" | Treatment | "G" conc | Dye loading | Ref |
|---|---|---|---|---|---|---|---|---|---|---|
| rGO/$TiO_2$ | 16.29 | 6.97 | 0.2 | N3 | doctor blade | MH method – hyd & thermal reduction | poly vinyl–alcohol | 0.6 wt% | – | [121] |
| $TiO_2$ | 11.26 | 5.01 | | | | | | | | |
| rGO/$TiO_2$ | 6.67 | 1.68 | 0.5 | N719 | electro-phoretic | MH method – hyd reduction | molecular grafting | – | ↑↑ | [122] |
| $TiO_2$ | 1.95 | 0.32 | | | | | | | | |
| G/G/$TiO_2$ | 19.47 | 8.13 | 0.25 | N719 | doctor blade | MH method – hyd and thermal reduction | 'G'+$TiCl_4$ coated FTO | – | ↓ | [123] |
| $TiO_2$ | 15.2 | 5.8 | | | | | | | | |
| rGO/$TiO_2$ | 13.5 | 7.25 | 0.2 | N719 | doctor blade | MH method – solvothermal reduction | ultrathin $TiO_2$ NRs | – | ↑↑ | [124] |
| P25 $TiO_2$ | 6.2 | 2.85 | | | | | | | | |
| rGO/$TiO_2$ | 14.8 | 6.49 | 0.15 | Indoline | doctor blade | MH method – hyd and hydro-thermal reduction | multilayer film | – | ↑↑ | [125] |
| P25 $TiO_2$ | 11.9 | 4.96 | | | | | | | | |
| rGO/$TiO_2$ | 13.93 | 7.1 | – | N719 | doctor blade | MH method – | in situ reduction-hydrolysis | – | ↓ | [126] |
| $TiO_2$ | 10.99 | 5.3 | | | | high thermal reduction | | | | |
| rGO/$TiO_2$ | 7.6 | 2.78 | 0.5 × 1.0 | N719 | doctor blade | MH method – thermal reduction | – | 0.83 wt% | ↓ | [127] |
| $TiO_2$ | 4.96 | 1.79 | | | | | | | | |
| rGO/$TiO_2$ | 16.8 | 5.77 | 0.4 | N719 | doctor blade | – | pre-treated $TiO_2$ | 0.75 wt% | – | [128] |
| $TiO_2$ | 13.7 | 4.61 | | | | | | | | |
| rGO/$TiO_2$ | 12.16 | 5.5 | 0.5 | N719 | screen print | MH method – solvothermal reduction | GO in ethylene glycol | 0.75 wt% | – | [129] |
| $TiO_2$ | 10.75 | 4.2 | | | | | | | | |
| G/$TiO_2$ | 19.92 | 6.86 | – | N719 | spin coating | – | Addition surfactant | 1.0 wt% | ↑↑ | [130] |
| $TiO_2$ | 18.83 | 5.98 | | | | | | | | |
| rGO/$TiO_2$ | 18.2 | 6.06 | 0.16 | D9 | doctor blade and spray coat | MH method – hyd and thermal reduction | rGO was coated on $TiO_2$ film | – | ↓ | [131] |
| $TiO_2$ | 16.4 | 5.09 | | | | | | | | |

used.[123,127,131] Based on this argument, it can be concluded that the high surface area to volume ratio of graphene does not completely explain the mechanism of the dye adsorption characteristic. Therefore, the kinetics of dye adsorption in graphene based films is still unclear, with some studies showing contrary results. For this reason, a deeper understanding and reasonable explanation of dye adsorption onto graphene incorporated films needs to be provided based on the careful investigations. For example, it would be reasonable to explore the amount of oxygen containing functional groups on graphene surface for the adsorption of dye molecules. Graphene is mostly synthesized by a chemical oxidation (Hummers method,[132] followed by a chemical (by hydrazine) or a thermal reduction process. The chemically oxidized graphene involves various functional groups such as –OH, C=O, and –COOH. On the other hand, it has been reported that the functionalized graphene (graphene oxide) is capable of hydrogen bonding and $\pi$–$\pi$ stacking with other organic dye molecules.[43,133,134] This may mean graphene with a high number of functional groups may adsorb more dye molecules onto their surface. On the other hand, the pristine graphene has a higher electrical conductivity than the functionalized graphene. Therefore, if the functional groups on graphene play an important role in the dye loading, further investigation will be required to determine a balance between the

  

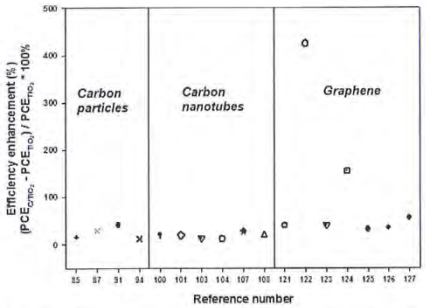


**Figure 11.** Efficiency enhancements of the DSSCs with carbon particles, CNTs and graphene incorporated $TiO_2$ films. Data points are adopted from refs. [85,87,91,94,100,101,103,104,107,108,121–127].

conductivity and the dye adsorption ability of graphene oxide by optimizing the oxidation or reduction level.

It is obvious that a high concentration of graphene significantly reduces the $R_{ct}$ of DSSCs that improves the electron transport rate, whereas this downgrades the transparency of films and thereby decreases the light harvesting efficiency of the photoelectrode. Therefore, advanced work was needed to find an optimal graphene content that benefits for both the charge recombination and light harvesting efficiency. Yang et al.[121] synthesized graphene/$TiO_2$ composites by varying the content (0–8.5 wt%) of graphene in the DSSC photoelectrodes.

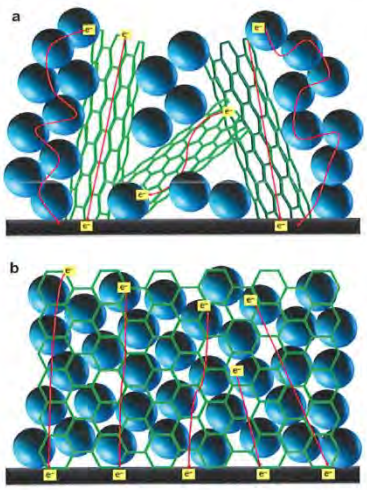


**Figure 12.** Schematic representation of a) CNTs/$TiO_2$ and b) graphene/$TiO_2$ films.

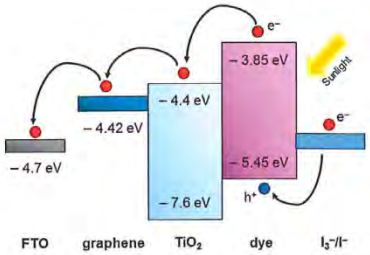


**Figure 13.** Schematic diagram of the energy level for graphene/$TiO_2$ film based DSSC.

They found that the optimal content of reduced graphene oxide in the $TiO_2$ film is ca. 0.6 wt% which is the best for cell performance. Furthermore, many studies have explored the influence of graphene content on the DSSC performance.[127–129] It can be clearly seen from Table 2 that loading ranging from 0.6 to 0.83 wt% of reduced graphene oxide incorporated in the $TiO_2$ photoelectrode films achieved the highest efficiency in the majority of studies.

Due to the $\pi$–$\pi$ interactions and/or hydrophobic surface of graphene layers, pristine graphene is insoluble in conventional solvents such as water and anhydrous ethanol, which is a major barrier to its successful utilization. Several noteworthy approaches have been developed to overcome this issue.[135,136] Yen and co-workers improved the dispersion stability of graphene in an ethanol solution using MWCNTs as a spacer between graphene layers (see **Figure 15**a) and they used the graphene/MWCNTs materials in the DSSC photoelectrodes.[136] This 3D structured photoelectrode composed of graphene/MWCNTs/$TiO_2$ nanocomposites exhibited an efficiency of 6.11%, which was significantly higher than that (4.54%) obtained by the $TiO_2$-only cell, as shown in Figure 15b. The improved performance was proven to be due to the improved dispersibility of graphene and MWCNTs in ethanol solution.

## 3. Conclusion and Future Directions

In this Review, we discussed the advanced research on the use of carbon materials in the photoelectrodes of DSSCs because the activity in this research field has been rapidly growing in the past few years. A brief overview of novel nanostructured materials based photoelectrodes is also provided. Based on the results and findings of extensive research, it can be concluded

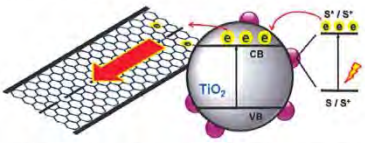


**Figure 14.** A mechanism for the enhanced electron transfer in graphene/$TiO_2$.

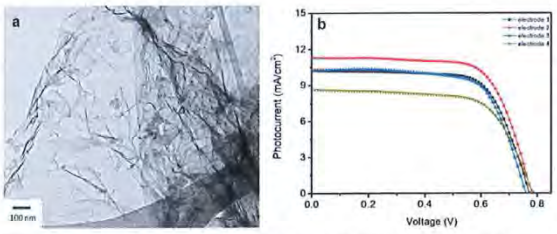


**Figure 15.** a) TEM image of MWCNTs/graphene composite and b) J–V curves of DSSCs based on acid functionalized-MWCNTs (electrode 1), MWCNTs/graphene composite (electrode 2), graphene (electrode 3) and $TiO_2$-only (electrode 4) photoelectrodes.[136] Reproduced with permission.[136] Copyright 2011, Elsevier.

that CNTs and graphene are very promising materials for high performance photoelectrodes for DSSCs due to their fascinating properties. Although significant achievements have been made in this cutting-edge research, several challenges must be addressed to build up high-performance devices based on CNTs and graphene. Further optimizations of carbonaceous photoelectrodes in DSSCs are still required.

It was found that vertically aligned CNTs are promising counter electrode materials to achieve highly efficient Pt–free DSSCs due to its improved electrical conductivity and electrocatalytic activity.[77,137,138] It is reasonable to expect improved performance of DSSCs by applying vertically grown CNTs structure with the $TiO_2$ photoelectrode films.

s-SWCNTs can significantly enhance the efficiency of DSSCs because of their non-continuous band structure, whereas the m-SWCNTs reduce the cell performance. Therefore, the bandgap of s-SWCNTs can be tuned by controlling their defect or functionalization level, diameter and aggregation degree etc. In this regard, exploring the influence of different band structures of s-SWCNTs on the cell performance will be an important research direction for further development of DSSCs. Similarly, chemically functionalizing graphene is an established method to open the bandgap of graphene and is critical to the improvements in the cell characteristics. The band structure of graphene oxide or reduced graphene oxide can be tuned by the level of functionalization.[139,140] The electronic band structure of the functionalized graphene should be considered in the future studies of graphene materials based DSSCs.

Since the dye adsorption kinetics on graphene structures based DSSCs are not fully understood, the underlying fundamental driving forces of dye interactions should be explored in depth. According to the literature,[43,133,134] it seems reasonable that the reactive sites (functional groups) on graphene surfaces and edges would play a major roles in dye interactrions and this will need to be investigated to better understand the dye loading characteristics. If the functional groups on graphene play a critical role in the dye adsorption, further optimization of the oxidation or reduction level of graphene may be required to achieve the highest possible performance of DSSCs.

Dye lifetime is also another critical limiting factor in DSSCs.[29] The presence of carbonaceous materials with high conductivity may help extend dye lifetimes. The use of thin films of carbonaceous material would allow the selective filtering of certain regions of the spectrum which will extend dye lifetimes.[141,142] For example, chirally sorted CNTs of particular types could be applied on the incident light side of the photoelectrode to absorb UV-light while letting visible light pass for adsorption by the dye. The lack of UV-light reaching the dye will enhance the active lifetime of the photoelectrode.

Furthermore, chirally sorting of the CNTs would allow the precise tuning of electronic energy levels in the electrode. This has the potential to improve performance but it will also provide avenues to investigate the exact role of CNTs in the hydrid photoelectrodes. The current understanding of the semiconducting photoelectrodes with carbonaceous structures in DSSCs is somewhat limited in terms of the exact roles of each component. Therefore, future investigations to elucidate the exact role of the various carbon materials (especially CNTs and graphene) in the photoelectrode of DSSCs will be of great value.

Some workers have also explored the effect of different types of nanotubes in the counter electrode of DSSCs.[143,144] While this review highlighted the differences between SWCNTs and MWCNTs, there seem to have been little work with double-walled CNTs (DWCNTs). Interestingly, there is considerable work showing that DWCNTs can often provide enhanced conductivity while still providing very similar structural properties of SWCNTs.[143,145,146] The use of DWCNTs in photoelectrodes is a clear research opportunity that is still to be extensively explored.

Chemical doping has been shown to be an effective method to enhance the conductivity of CNTs and graphene.[147–149] In this regard, the use of chemically doped CNTs and graphene in the photoelectrode of DSSCs would be a valuable research direction. Additionally the use of these nanomaterials offers the exciting opportunity of nanostructuring the photoelectrode. For example, a layered structure would allow the selective, efficient harvesting of different portions of the solar spectrum as the light passed through the electrode. This affords the opportunity to make use of very high adsorbing dyes for narrow wavelength regions and this stack of high absorbers could be more efficient that the broad spectrum absorbers currently in use.

It has been shown in polymer based solar cells that beyond the electronic properties of the donor/acceptor system where functionalized CNTs are involved, the morphology also plays a key role in PV applications.[150] For instance, the addition of functionalized CNTs to a PEDOT:PSS lowered the overall performance, but did increase the current. These changes were attributed to the nano-morphology of the system. Recent work has demonstrated the key importance of the nanostructure of the active layer and indeed suggests light trapping in this layer could be a powerful approach to improve performance. The best structure is difficult to predict due to the competing influences of light trapping and charge conduction.[151]

Alignment within a CNT film has been demonstrated recently and offers the opportunity to both increase light transmission and film conductivity.[152] These films offer a smooth

  

substrate which might also be of benefit in a layered structure where direct contact between a high loading of dye molecules and the conducting element of the electrode will be possible but the current alignment approaches using highly toxic chemicals will need to be improved before this approach can be considered a serious alternative for wide scale use.

It has been demonstrated that carbon materials exhibit excellent electrocatalytic activity for the reduction of liquid electrolyte.[22,29,80] However, the use of too high concentration of the carbonaceous materials in the photoelectrode brings significant charge recombination at the interface of carbons and electrolyte by reducing tri-iodide to iodide. Therefore, the electrocatalytic activity of carbonaceous materials should be taken into account when they are used in the photoelectrode. Graphene is known not to be penetrable by gases so a film of graphene on the photoelectrode may offer an ability to control molecular diffusion while still allowing efficient charge transport. Such diffusion control might extend the lifetime of the electrolyte. This work would likely require the construction of a complex hybrid electrode perhaps using CNTs to enhance conductivity or tune electronic states while using graphene to control levels of reactivity at the critical interfaces.

We believe that the carbonaceous material will bring an important breakthrough when they are used in the photoelectrode of solid state DSSCs.

## Acknowledgements

The support of the Australian Research Council Discovery Program (DP130101714) is gratefully acknowledged. Munkhbayar Batmunkh acknowledges International Postgraduate Research Scholarship (IPRS) and Australian Postgraduate Award (APA) for their financial support during his study in Australia.
Note: The article type was changed from a Progress Report to a Review after initial online publication. Two mentions of Progress Report were changed to Review in the text. A duplicated word was deleted in the caption for Figure 9. These changes were implemented on March 12, 2015. Otherwise, the content of the article has not been changed.

Received: December 18, 2014
Published online: February 18, 2015

[1] N. S. Lewis, *Science* **2007**, *315*, 798.
[2] L. Wang, H. Liu, R. M. Konik, J. A. Misewich, S. S. Wong, *Chem. Soc. Rev.* **2013**, *42*, 8134.
[3] D. M. Chapin, C. S. Fuller, G. L. Pearson, *J. Appl. Phys.* **1954**, *25*, 676.
[4] M. Bosi, C. Pelosi, *Prog. Photovoltaics* **2007**, *15*, 51.
[5] T. W. Hamann, R. A. Jensen, A. B. F. Martinson, H. Van Ryswyk, J. T. Hupp, *Energy Environ. Sci.* **2008**, *1*, 66.
[6] D. Wöhrle, D. Meissner, *Adv. Mater.* **1991**, *3*, 129.
[7] G. Conibeer, *Mater. Today* **2007**, *10*, 42.
[8] J. Zhao, A. Wang, M. A. Green, *Prog. Photovoltaics: Res. Appl.* **1999**, *7*, 471.
[9] H. S. Jung, J.-K. Lee, *J. Phys. Chem. Lett.* **2013**, *4*, 1682.
[10] S. Mathew, A. Yella, P. Gao, R. Humphry-Baker, B. F. E. Curchod, N. Ashari-Astani, I. Tavernelli, U. Rothlisberger, Md. K. Nazeeruddin, M. Grätzel, *Nat. Chem.* **2014**, *6*, 242.
[11] M. Gratzel, *Nature* **2001**, *414*, 338.
[12] M. Grätzel, *Inorg. Chem.* **2005**, *44*, 6841.
[13] A. Hagfeldt, G. Boschloo, L. Sun, L. Kloo, H. Pettersson, *Chem. Rev.* **2010**, *110*, 6595.
[14] F. Xu, L. Sun, *Energy Environ. Sci.* **2011**, *4*, 818.
[15] J. Xu, Z. Chen, J. A. Zapien, C.-S. Lee, W. Zhang, *Adv. Mater.* **2014**, *26*, 5337.
[16] J. S. Bendall, L. Etgar, S. C. Tan, N. Cai, P. Wang, S. M. Zakeeruddin, M. Gratzel, M. E. Welland, *Energy Environ. Sci.* **2011**, *4*, 2903.
[17] P. V. Kamat, *J. Phys. Chem. Let.* **2009**, *1*, 520.
[18] P. V. Kamat, *J. Phys. Chem. Lett.* **2011**, *2*, 242.
[19] J. Tuček, K. C. Kemp, K. S. Kim, R. Zbořil, *ACS Nano* **2014**, *8*, 7571.
[20] R. L. D. Whitby, *ACS Nano* **2014**, *8*, 9733.
[21] Z. Yin, J. Zhu, Q. He, X. Cao, C. Tan, H. Chen, Q. Yan, H. Zhang, *Adv. Energy Mater.* **2014**, *4*, 201300574.
[22] S. Yun, A. Hagfeldt, T. Ma, *Adv. Mater.* **2014**, *26*, 6210.
[23] C. J. Shearer, A. Cherevan, D. Eder, *Adv. Mater.* **2014**, *26*, 2295.
[24] L. J. Brennan, M. T. Byrne, M. Bari, Y. K. Gun'ko, *Adv. Energy Mater.* **2011**, *1*, 472.
[25] N. Mahmood, Y. Hou, *Adv. Sci.* **2014**, *1*, 201400012.
[26] S. Hwang, M. Batmunkh, M. J. Nine, H. Chung, H. Jeong, *ChemPhysChem* **2015**, *16*, 53.
[27] D. Golberg, Y. Bando, Y. Huang, T. Terao, M. Mitome, C. Tang, C. Zhi, *ACS Nano* **2010**, *4*, 2979.
[28] R. D. Costa, F. Lodermeyer, R. Casillas, D. M. Guldi, *Energy Environ. Sci.* **2014**, *7*, 1281.
[29] J. D. Roy-Mayhew, I. A. Aksay, *Chem. Rev.* **2014**, *114*, 6323.
[30] L. Kavan, J.-H. Yum, M. Graetzel, *Phys. Stat. Solidi B* **2013**, *250*, 2643.
[31] K. Hauffe, H. J. Danzmann, H. Pusch, J. Range, H. Volz, *J. Electrochem. Soc.* **1970**, *117*, 993.
[32] S. Anderson, E. C. Constable, M. P. Dare-Edwards, J. B. Goodenough, A. Hamnett, K. R. Seddon, R. D. Wright, *Nature* **1979**, *280*, 571.
[33] A. Hamnett, M. P. Dare-Edwards, R. D. Wright, K. R. Seddon, J. B. Goodenough, *J. Phys. Chem.* **1979**, *83*, 3280.
[34] G. R. Torres, T. Lindgren, J. Lu, C.-G. Granqvist, S.-E. Lindquist, *J. Phys. Chem. B* **2004**, *108*, 5995.
[35] M. Matsumura, Y. Nomura, H. Tsubomura, *Bull. Chem. Soc. Jpn.* **1977**, *50*, 2533.
[36] B. O'Regan, M. Gratzel, *Nature* **1991**, *353*, 737.
[37] P. Poudel, Q. Qiao, *Nanoscale* **2012**, *4*, 2826.
[38] F. Lenzmann, J. Krueger, S. Burnside, K. Brooks, M. Grätzel, D. Gal, S. Rühle, D. Cahen, *J. Phys. Chem. B* **2001**, *105*, 6347.
[39] Q. Zhang, T. P. Chou, B. Russo, S. A. Jenekhe, G. Cao, *Angew. Chem. Int. Edn.* **2008**, *47*, 2402.
[40] S. Burnside, J.-E. Moser, K. Brooks, M. Grätzel, D. Cahen, *J. Phys. Chem. B* **1999**, *103*, 9328.
[41] Q. Zhang, C. S. Dandeneau, X. Zhou, G. Cao, *Adv. Mater.* **2009**, *21*, 4087.
[42] Ü. Özgür, Y. I. Alivov, C. Liu, A. Teke, M. A. Reshchikov, S. Doğan, V. Avrutin, S.-J. Cho, H. Morkoç, *J. Appl. Phys.* **2005**, *98*, 041301.
[43] A. K. Chandiran, M. Abdi-Jalebi, M. K. Nazeeruddin, M. Grätzel, *ACS Nano* **2014**, *8*, 2261.
[44] Q. Zhang, K. Park, J. Xi, D. Myers, G. Cao, *Adv. Energy Mater.* **2011**, *1*, 988.
[45] Y. Qiu, W. Chen, S. Yang, *Angew. Chem. Int. Edn.* **2010**, *49*, 3675.
[46] B. Munkhbayar, M. Dorjderem, D. Sarangerel, B. Ochirkhuyag, *Nanosci. Nanotechnol. Lett.* **2013**, *5*, 741.
[47] W.-Q. Wu, Y.-F. Xu, H.-S. Rao, C.-Y. Su, D.-B. Kuang, *Nanoscale* **2013**, *5*, 4362.
[48] Q. Zhang, G. Cao, *Nano Today* **2011**, *6*, 91.
[49] A. Hagfeldt, M. Grätzel, *Acc. Chem. Res.* **2000**, *33*, 269.
[50] J. Nelson, R. E. Chandler, *Coord. Chem. Rev.* **2004**, *248*, 1181.
[51] J. van de Lagemaat, N. G. Park, A. J. Frank, *J. Phys. Chem. B.* **2000**, *104*, 2044.

[52] J. Maçaira, L. Andrade, A. Mendes, *Renewable Sustainable Energy Rev.* **2013**, *27*, 334.
[53] J. Ferber, J. Luther, *Sol. Energy Mater. Sol. Cells* **1998**, *54*, 265.
[54] H. Yu, Y. Bai, X. Zong, F. Tang, G. Q. M. Lu, L. Wang, *Chem. Commun.* **2012**, *48*, 7386.
[55] S. Ito, T. N. Murakami, P. Comte, P. Liska, C. Grätzel, M. K. Nazeeruddin, M. Grätzel, *Thin Solid Films* **2008**, *516*, 4613.
[56] H. A. Atwater, A. Polman, *Nat. Mater.* **2010**, *9*, 205.
[57] W. Hou, P. Pavaskar, Z. Liu, J. Theiss, M. Aykol, S. B. Cronin, *Energy Environ. Sci.* **2011**, *4*, 4650.
[58] S. D. Standridge, G. C. Schatz, J. T. Hupp, *J. Am. Chem. Soc.* **2009**, *131*, 8407.
[59] J. Qi, X. Dang, P. T. Hammond, A. M. Belcher, *ACS Nano* **2011**, *5*, 7108.
[60] X. Dang, J. Qi, M. T. Klug, P.-Y. Chen, D. S. Yun, N. X. Fang, P. T. Hammond, A. M. Belcher, *Nano Lett.* **2013**, *13*, 637.
[61] H. Choi, W. T. Chen, P. V. Kamat, *ACS Nano* **2012**, *6*, 4418.
[62] M. Ihara, K. Tanaka, K. Sakaki, I. Honma, K. Yamada, *J. Phys. Chem. B* **1997**, *101*, 5153.
[63] C. Hägglund, M. Zäch, G. Petersson, B. Kasemo, *Appl. Phys. Lett.* **2008**, *92*, 053110.
[64] F. Zhu, D. Wu, Q. Li, H. Dong, J. Li, K. Jiang, D. Xu, *RSC Adv.* **2012**, *2*, 11629.
[65] H. J. Koo, Y. J. Kim, Y. H. Lee, W. I. Lee, K. Kim, N. G. Park, *Adv. Mater.* **2008**, *20*, 195.
[66] P. Roy, D. Kim, K. Lee, E. Spiecker, P. Schmuki, *Nanoscale.* **2010**, *2*, 45.
[67] A. Vomiero, V. Galstyan, A. Braga, I. Concina, M. Brisotto, E. Bontempi, G. Sberveglieri, *Energy Environ. Sci.* **2011**, *4*, 3408.
[68] M. Adachi, Y. Murata, J. Takao, J. Jiu, M. Sakamoto, F. Wang, *J. Am. Chem. Soc.* **2004**, *126*, 14943.
[69] M. Wang, J. Bai, F. Le Formal, S.-J. Moon, L. Cevey-Ha, R. Humphry-Baker, C. Grätzel, S. M. Zakeeruddin, M. Grätzel, *J. Phys. Chem. C* **2012**, *116*, 3266.
[70] B. Liu, E. S. Aydil, *J. Am. Chem. Soc.* **2009**, *131*, 3985.
[71] W. Zhang, R. Zhu, L. Ke, X. Liu, B. Liu, S. Ramakrishna, *Small* **2010**, *6*, 2176.
[72] C.-H. Ku, J.-J. Wu, *Appl. Phys. Lett.* **2007**, *91*, 093117.
[73] P. Joshi, L. Zhang, D. Davoux, Z. Zhu, D. Galipeau, H. Fong, Q. Qiao, *Energy Environ. Sci.* **2010**, *3*, 1507.
[74] P. Zhong, W. Que, J. Zhang, Q. Jia, W. Wang, Y. Liao, X. Hu, *J. Alloys Compounds* **2011**, *509*, 7808.
[75] J. Qu, G. R. Li, X. P. Gao, *Energy Environ. Sci.* **2010**, *3*, 2003.
[76] A. Kay, M. Grätzel, *Sol. Energy Mater. Sol. Cells* **1996**, *44*, 99.
[77] E. Ramasamy, W. J. Lee, D. Y. Lee, J. S. Song, *Electrochem. Commun.* **2008**, *10*, 1087.
[78] J. D. Roy-Mayhew, D. J. Bozym, C. Punckt, I. A. Aksay, *ACS Nano.* **2010**, *4*, 6203.
[79] B. Munkhbayar, M. J. Nine, J. Jeoun, M. Ji, H. Jeong, H. Chung, *J. Power Sources* **2013**, *230*, 207.
[80] H. Wang, Y. H. Hu, *Energy Environ. Sci.* **2012**, *5*, 8182.
[81] G. R. Li, F. Wang, J. Song, F. Y. Xiong, X. P. Gao, *Electrochim. Acta* **2012**, *65*, 216.
[82] B. Munkhbayar, S. Hwang, J. Kim, K. Bae, M. Ji, H. Chung, H. Jeong, *Electrochim. Acta* **2012**, *80*, 100.
[83] E. Bi, H. Chen, X. Yang, W. Peng, M. Gratzel, L. Han, *Energy Environ. Sci.* **2014**, *7*, 2637.
[84] C.-C. Ting, W.-S. Chao, *Appl. Energy* **2010**, *87*, 2500.
[85] S. H. Kang, J.-Y. Kim, Y.-K. Kim, Y.-E. Sung, *J. Photochem. Photobiol. A: Chem.* **2007**, *186*, 234.
[86] D. Y. Kim, J. Kim, J. Kim, A. Y. Kim, G. Lee, M. Kang, *J. Indust. Eng. Chem.* **2012**, *18*, 1.
[87] G. Yang, J. Zhang, P. Wang, Q. Sun, J. Zheng, Y. Zhu, *Curr. Appl. Phys.* **2011**, *11*, 376.
[88] X. Cai, S. Hou, H. Wu, Z. Lv, Y. Fu, D. Wang, C. Zhang, H. Kafafy, Z. Chu, D. Zou, *Phys. Chem. Chem. Phys.* **2012**, *14*, 125.
[89] W. Guo, C. Xu, X. Wang, S. Wang, C. Pan, C. Lin, Z. L. Wang, *J. Am. Chem. Soc.* **2012**, *134*, 4437.
[90] E. C. Landis, K. L. Klein, A. Liao, E. Pop, D. K. Hensley, A. V. Melechko, R. J. Hamers, *Chem. Mater.* **2010**, *22*, 2357.
[91] Y. H. Jang, X. Xin, M. Byun, Y. J. Jang, Z. Lin, D. H. Kim, *Nano Lett.* **2011**, *12*, 479.
[92] X. Sun, Y. Li, *Angew. Chem. Int. Edn.* **2004**, *43*, 597.
[93] L.-W. Zhang, H.-B. Fu, Y.-F. Zhu, *Adv. Funct. Mater.* **2008**, *18*, 2180.
[94] Y. J. Jang, Y. H. Jang, D. H. Kim, *Part. Part. Syst. Charact.* **2013**, *30*, 1030.
[95] S.-R. Jang, R. Vittal, K.-J. Kim, *Langmuir.* **2004**, *20*, 9807.
[96] P. Brown, K. Takechi, P. V. Kamat, *J. Phys. Chem. C.* **2008**, *112*, 4776.
[97] K.-M. Lee, C.-W. Hu, H.-W. Chen, K.-C. Ho, *Sol. Energy Mater. Sol. Cells* **2008**, *92*, 1628.
[98] S. Zhang, H. Niu, Y. Lan, C. Cheng, J. Xu, X. Wang, *J. Phys. Chem. C* **2011**, *115*, 22025.
[99] W.-J. Lin, C.-T. Hsu, Y.-C. Tsai, *J. Colloid Interface Sci.* **2011**, *358*, 562.
[100] J. Chen, B. Li, J. Zheng, J. Zhao, Z. Zhu, *J. Phys. Chem. C* **2012**, *116*, 14848.
[101] J. Yu, J. Fan, B. Cheng, *J. Power Sources* **2011**, *196*, 7891.
[102] K. T. Dembele, G. S. Selopal, C. Soldano, R. Nechache, J. C. Rimada, I. Concina, G. Sberveglieri, F. Rosei, A. Vomiero, *J. Phys. Chem. C* **2013**, *117*, 14510.
[103] A. M. Bakhshayesh, M. R. Mohammadi, N. Masihi, M. H. Akhlaghi, *J. Nanopart. Res.* **2013**, *15*, 1.
[104] K. T. Dembele, R. Nechache, L. Nikolova, A. Vomiero, C. Santato, S. Licoccia, F. Rosei, *J. Power Sources* **2013**, *233*, 93.
[105] S. Sun, L. Gao, Y. Liu, *Thin Solid Films* **2011**, *519*, 2273.
[106] X. Zhang, J. Liu, S. Li, X. Tan, J. Zhang, M. Yu, M. Zhao, *J. Mater. Chem. A* **2013**, *1*, 11070.
[107] X. Dang, H. Yi, M.-H. Ham, J. Qi, D. S. Yun, R. Ladewski, M. S. Strano, P. T. Hammond, A. M. Belcher, *Nat. Nanotechnol.* **2011**, *6*, 377.
[108] G. H. Guai, Y. Li, C. M. Ng, C. M. Li, M. B. Chan-Park, *ChemPhysChem* **2012**, *13*, 2566.
[109] J. Y. Ahn, J. H. Kim, K. J. Moon, S. D. Park, S. H. Kim, *Nanoscale* **2013**, *5*, 6842.
[110] B. Munkhbayar, M. J. Nine, J. Jeoun, M. Bat-Erdene, H. Chung, H. Jeong, *Powder Technol.* **2013**, *234*, 132.
[111] J. W. G. Wilder, L. C. Venema, A. G. Rinzler, R. E. Smalley, C. Dekker, *Nature* **1998**, *391*, 59.
[112] K. S. Novoselov, A. K. Geim, S. V. Morozov, D. Jiang, Y. Zhang, S. V. Dubonos, I. V. Grigorieva, A. A. Firsov, *Science* **2004**, *306*, 666.
[113] K. S. Novoselov, A. K. Geim, S. V. Morozov, D. Jiang, M. I. Katsnelson, I. V. Grigorieva, S. V. Dubonos, A. A. Firsov, *Nature* **2005**, *438*, 197.
[114] A. K. Geim, K. S. Novoselov, *Nat. Mater.* **2007**, *6*, 183.
[115] R. R. Nair, P. Blake, A. N. Grigorenko, K. S. Novoselov, T. J. Booth, T. Stauber, N. M. R. Peres, A. K. Geim, *Science* **2008**, *320*, 1308.
[116] C. Lee, X. Wei, J. W. Kysar, J. Hone, *Science* **2008**, *321*, 385.
[117] X. Du, I. Skachko, A. Barker, E. Y. Andrei, *Nat. Nanotechnol.* **2008**, *3*, 491.
[118] A. Zurutuza, C. Marinelli, *Nat. Nanotechnol.* **2014**, *9*, 730.
[119] Y. H. Ng, I. V. Lightcap, K. Goodwin, M. Matsumura, P. V. Kamat, *J. Phys. Chem. Lett.* **2010**, *1*, 2222.
[120] S. R. Kim, M. K. Parvez, M. Chhowalla, *Chem. Phys. Lett.* **2009**, *483*, 124.
[121] N. Yang, J. Zhai, D. Wang, Y. Chen, L. Jiang, *ACS Nano* **2010**, *4*, 887.
[122] Y.-B. Tang, C.-S. Lee, J. Xu, Z.-T. Liu, Z.-H. Chen, Z. He, Y.-L. Cao, G. Yuan, H. Song, L. Chen, L. Luo, H.-M. Cheng, W.-J. Zhang, I. Bello, S.-T. Lee, *ACS Nano* **2010**, *4*, 3482.
[123] T. Chen, W. Hu, J. Song, G. H. Guai, C. M. Li, *Adv. Funct. Mater.* **2012**, *22*, 5245.

  

[124] Z. He, G. Guai, J. Liu, C. Guo, J. S. Chye Loo, C. M. Li, T. T. Y. Tan, *Nanoscale* **2011**, *3*, 4613.
[125] B. Tang, G. Hu, *J. Power Sources* **2012**, *220*, 95.
[126] L. Chen, Y. Zhou, W. Tu, Z. Li, C. Bao, H. Dai, T. Yu, J. Liu, Z. Zou, *Nanoscale* **2013**, *5*, 3481.
[127] H. Wang, S. L. Leonard, Y. H. Hu, *Ind. Eng. Chem. Rev.* **2012**, *51*, 10613.
[128] J. Fan, S. Liu, J. Yu, *J. Mater. Chem.* **2012**, *22*, 17027.
[129] W. Shu, Y. Liu, Z. Peng, K. Chen, C. Zhang, W. Chen, *J. Alloys Compounds* **2013**, *563*, 229.
[130] T.-H. Tsai, S.-C. Chiou, S.-M. Chen, *Int. J. Electrochem. Sci.* **2011**, *6*, 3333.
[131] J. Song, Z. Yin, Z. Yang, P. Amaladass, S. Wu, J. Ye, Y. Zhao, W.-Q. Deng, H. Zhang, X.-W. Liu, *Chem. – Eur. J.* **2011**, *17*, 10832.
[132] W. S. Hummers, R. E. Offeman, *J. Am. Chem. Soc.* **1958**, *80*, 1339.
[133] J. Xu, L. Wang, Y. Zhu, *Langmuir* **2012**, *28*, 8418.
[134] T.-T. Meng, Z.-B. Zheng, K.-Z. Wang, *Langmuir* **2013**, *29*, 14314.
[135] M. Myekhlai, B. Munkhbayar, T. Lee, M. R. Tanshen, H. Chung, H. Jeong, *RSC Adv.* **2014**, *4*, 2495.
[136] M.-Y. Yen, M.-C. Hsiao, S.-H. Liao, P.-I. Liu, H.-M. Tsai, C.-C. M. Ma, N.-W. Pu, M.-D. Ger, *Carbon* **2011**, *49*, 3597.
[137] K. S. Lee, W. J. Lee, N.-G. Park, S. O. Kim, J. H. Park, *Chem. Commun.* **2011**, *47*, 4264.
[138] M. Wu, X. Lin, Y. Wang, L. Wang, W. Guo, D. Qi, X. Peng, A. Hagfeldt, M. Grätzel, T. Ma, *J. Am. Chem. Soc.* **2012**, *134*, 3419.
[139] Q. Tang, Z. Zhou, Z. Chen, *Nanoscale* **2013**, *5*, 4541.
[140] J.-A. Yan, L. Xian, M. Y. Chou, *Phys. Rev. Lett.* **2009**, *103*, 086802.
[141] D. D. Tune, J. G. Shapter, *Energy Environ. Sci.* **2013**, *6*, 2572.
[142] M. A. Bissett, J. G. Shapter, *J. Phys. Chem.* **2010**, *114*, 6778.
[143] D. Zhang, X. Li, S. Chen, Z. Sun, X. Jiang Yin, S. Huang, *Microchim Acta.* **2011**, *174*, 73.
[144] M. Xiaoguang, C. Swee Jen, F. Benhu, O. Jianyong, *Nanotechnology* **2010**, *21*, 395202.
[145] D. W. Zhang, X. D. Li, S. Chen, F. Tao, Z. Sun, X. J. Yin, S. M. Huang, *J. Solid State Electrochem.* **2010**, *14*, 1541.
[146] K. E. Moore, B. S. Flavel, C. J. Shearer, A. V. Ellis, J. G. Shapter, *Electrochem. Commun.* **2011**, *13*, 1190.
[147] F. Schedin, A. K. Geim, S. V. Morozov, E. W. Hill, P. Blake, M. I. Katsnelson, K. S. Novoselov, *Nat. Mater.* **2007**, *6*, 652.
[148] R. S. Lee, H. J. Kim, J. E. Fischer, A. Thess, R. E. Smalley, *Nature* **1997**, *388*, 255.
[149] S. Z. Butler, S. M. Hollen, L. Cao, Y. Cui, J. A. Gupta, H. R. Gutiérrez, T. F. Heinz, S. S. Hong, J. Huang, A. F. Ismach, E. Johnston-Halperin, M. Kuno, V. V. Plashnitsa, R. D. Robinson, R. S. Ruoff, S. Salahuddin, J. Shan, L. Shi, M. G. Spencer, M. Terrones, W. Windl, J. E. Goldberger, *ACS Nano* **2013**, *7*, 2898.
[150] N. Chehata, A. Ltaief, R. Bkakri, A. Bouazizi, E. Beyou, *Mater. Lett.* **2014**, *121*, 227.
[151] B.-C. Chen, Y.-S. Cheng, C. Gau, Y.-C. Lee, *Thin Solid Films* **2014**, *564*, 384.
[152] D. S. Hecht, L. Hu, G. Irvin, *Adv. Mater.* **2011**, *23*, 1482.

# Appendix B

Applied Surface Science 387 (2016) 690–697

Contents lists available at ScienceDirect

Applied Surface Science

journal homepage: www.elsevier.com/locate/apsusc

# Incorporation of graphene into $SnO_2$ photoanodes for dye-sensitized solar cells

Munkhbayar Batmunkh[a,b,1], Mahnaz Dadkhah[b,1], Cameron J. Shearer[b], Mark J. Biggs[a,c], Joseph G. Shapter[b,*]

[a] School of Chemical Engineering, The University of Adelaide, Adelaide, South Australia 5005, Australia
[b] Centre for Nanoscale Science and Technology, School of Chemical and Physical Sciences, Flinders University, Bedford Park, Adelaide, South Australia 5042, Australia
[c] School of Science, Loughborough University, Loughborough, Leicestershire LE11 3TU, UK

ARTICLE INFO

*Article history:*
Received 21 April 2016
Received in revised form 6 June 2016
Accepted 24 June 2016
Available online 29 June 2016

*Keywords:*
Photovoltaic
Dye-sensitized solar cells
Photoanodes
Tin dioxide
Graphene

ABSTRACT

In dye-sensitized solar cell (DSSC) photoanodes, tin dioxide ($SnO_2$) structures present a promising alternative semiconducting oxide to the conventional titania ($TiO_2$), but they suffer from poor photovoltaic (PV) efficiency caused by insufficient dye adsorption and low energy value of the conduction band. A hybrid structure consisting of $SnO_2$ and reduced graphene oxide ($SnO_2$-RGO) was synthesized via a microwave-assisted method and has been employed as a photoanode in DSSCs. Incorporation of RGO into the $SnO_2$ photoanode enhanced the power conversion efficiency of DSSC device by 91.5%, as compared to the device assembled without RGO. This efficiency improvement can be attributed to increased dye loading, enhanced electron transfer and addition of suitable energy levels in the photoanode. Finally, the use of RGO addresses the major shortcoming of $SnO_2$ when employed as a DSSC photoanode, namely poor dye adsorption and slow electron transfer rate.



## 1. Introduction

One of the mature developments in new energy production approaches is the dye-sensitized solar cell (DSSC) [1]. For a broad perspective of the field, there are several good reviews available [2–4]. A typical DSSC photoanode is made using a transparent conducting oxide (TCO) substrate, wide band gap oxide semiconductor and dye sensitizer. A nanocrystalline $TiO_2$ semiconductor is mostly used as the semiconductor due to its unique properties [5]. Despite the high power conversion efficiencies (PCEs) achieved by devices fabricated with $TiO_2$ photoanodes [6–8], the intrinsic low carrier mobility of $TiO_2$ is a matter of great concern [9,10]. This issue has led many researchers to probe the development of alternative photoanode materials.

Among many alternative semiconductors, $SnO_2$ has been the subject of numerous investigations [11–13]. This is partially due to the fact that $SnO_2$ has a higher electron mobility than $TiO_2$ [14,15]. Since the first use of $SnO_2$ in DSSCs, significant developments have been made in the $SnO_2$ photoanodes [11,13]. These developments include morphology control, doping with various species, surface modification, and hybrid structures with other oxide semiconductors [16–18]. Despite the considerable effort to improve $SnO_2$ based photoanodes, a major challenge for $SnO_2$ based DSSCs is still their low performance caused by poor dye adsorption capability [19]. Additionally, the $SnO_2$ photoanode based DSSCs suffer from a low open circuit voltage ($V_{oc}$) value due to the intrinsically low energy of the conduction band of $SnO_2$ [20]. Therefore, addressing these issues is of great importance for the development of $SnO_2$ based photovoltaic (PV) cells. Moreover, although $SnO_2$ possesses higher electron mobility than $TiO_2$, further improvement in the electron transport in $SnO_2$ photoanode would be of great value to maximize the efficiency.

Due to their excellent conductivity, carbon nanotubes (CNTs) and graphene can act to improve electron transport and reduce the charge recombination which results from sluggish charge transport of semiconducting oxide based photoanodes; thus significantly enhancing the PCE of PV cells [21–26]. Over the past few years, researchers have incorporated graphene derivatives into various $TiO_2$ structures and shown remarkable efficiency enhancement [27–30]. However, until now, there has been no report on the use of graphene structures in $SnO_2$ photoanodes for DSSCs. Moreover, the kinetics of dye adsorption and performance enhancement for carbonaceous photoanodes is still unclear, with some studies sug-

* Corresponding author.
*E-mail address:* joe.shapter@flinders.edu.au (J.G. Shapter).
[1] These authors contributed equally.

http://dx.doi.org/10.1016/j.apsusc.2016.06.146
0169-4332/

gesting contrary results [21,28,29,31,32]. Therefore, exploring the effect of graphene or reduced graphene oxide (RGO) in $SnO_2$ photoanode based DSSCs would be valuable.

Herein we report a facile preparation of hybrid structures based on morphologically controllable $SnO_2$ combined with RGO for use as a photoanode in DSSCs. To the best of our knowledge, this work is the first effort involving the application of a graphene structure in $SnO_2$ photoanode based DSSCs. We found that the incorporation of RGO into the $SnO_2$ film not only enhances the electron transfer rate of the photoanode, it also increases the adsorption of dye molecules into the film, thus greatly improving DSSC performance.

## 2. Experimental

### 2.1. Materials

All chemicals were purchased from Sigma-Aldrich and used without further purification, unless otherwise stated. Tin(II) chloride dihydrate ($SnCl_2{\cdot}2H_2O$) powder (>99% purity, Merck) was used as a starting material. Flourine-doped tin oxide (FTO) coated glass electrode with a sheet resistance ($R_s$) of ~12 Ω/□ (TCO30-8), Ruthenizer 535-bisTBA (N719 dye), iodide/tri-iodide electrolyte (Iodolyte Z-50), DuPont Surlyn® (Meltonix 1170-60) and Platinum catalyst (Platisol T) were obtained from Solaronix, Switzerland.

### 2.2. Preparation of graphene oxide

Graphite oxide was prepared from natural graphite using the approach from Marcano et al. [33]. Briefly, a 9:1 (v:v) mixture of sulfuric acid (95–98% $H_2SO_4$) and phosphoric acid (85% $H_3PO_4$) (240:27 mL) was kept in the cold room (3–5 °C) until it was added to a mixture of graphite flakes (2 g) and potassium permanganate (99% $KMnO_4$) (12 g). The oxidation process of graphite was carried out by stirring the mixture at ~50 °C for 12 h. Upon completion, the reaction was cooled down to room temperature and poured onto ice (approximately 300 mL) with 30% hydrogen peroxide ($H_2O_2$) (2 mL). The mixture was then washed with distilled (DI) water, 30% hydrochloric acid (HCl) and ethanol (× 2 times). For each sequential wash, the product was centrifuged at 4400 rpm for 3 h and the supernatant decanted away. The obtained light brown sample was then vacuum-dried overnight at room temperature. Then the as-prepared graphite oxide was exfoliated in water (1 mg $mL^{-1}$) by bath ultrasonication (Elma, Germany) for 60 min to obtain homogenous graphene oxide (GO) dispersion.

### 2.3. Synthesis of $SnO_2$-RGO hybrid

The $SnO_2$-RGO hybrid was prepared using a facile microwave-assisted method [34]. In a typical process, six glass beakers containing 90 mL DI water and different GO content (0 mg, 2 mg, 4.5 mg, 7 mg, 12 mg and 50 mg) were ultrasonicated for 2 h. Meanwhile, 1.5 g of $SnCl_2{\cdot}2H_2O$ powder was added into 200 mL of 0.02 M HCl solution. Then the previously prepared GO dispersions were added into the $SnCl_2{\cdot}2H_2O$ solutions, followed by stirring for 30 min. The as-obtained mixtures were then reacted using a microwave technique (StartSYNTH Microwave Synthesis Labstation, Milestone s.r.l) for 5 min under 600 W power. The temperature was adjusted to 90 °C during the microwave treatment. After cooling to room temperature, the obtained precipitates were centrifuged at 2000 rpm for 10 min and washed several times with DI water, followed by drying overnight at 80 °C in an oven to obtain $SnO_2$-RGO powders. Finally, six samples of different RGO content (0 wt%, 0.2 wt%, 0.45 wt%, 0.7 wt%, 1.2 wt% and 4.75 wt% in the hybrid) were prepared and have been used for DSSC fabrication. It should be noted that the amount of $SnO_2$ in these samples was not changed. For the calculation of the RGO concentration in the hybrid, it was assumed that the conversion of $SnCl_2{\cdot}2H_2O$ to $SnO_2$ is 100% based on the lack of a Cl peak observed in various hybrid characterizations.

### 2.4. Device fabrication

Firstly, viscous $SnO_2$ and $SnO_2$-RGO pastes were prepared from the previously prepared six samples according to the established procedures described in the literature [35]. FTO coated glass substrates were cleaned by a detergent (Pyroneg), followed by washing with Milli-Q water, acetone and ethanol under ultrasonication for 10 min each and subsequently dried with a nitrogen gas. The cleaned FTO glass subtrates were immersed in a 40 mM $TiCl_4$ aqueous solution at 70 °C for 30 min. Then the $TiCl_4$ treated FTO electrodes were coated with the $SnO_2$ and $SnO_2$-RGO pastes by a doctor blade technique to prepare the photoanodes. All photoanode films were obtained by applying two layers of adhesive scotch tape (*Magic™ Tape, 3M*) on the FTO electrode, which gives a film thickness of ~15 μm [36]. It is well established that the photoanode thickness of 12–16 μm is the optimum condition for achieving high DSSC performance [36–38]. After the deposition of $SnO_2$ and $SnO_2$-RGO pastes onto the FTO substrates, the photoanode films were gradually heated under an air flow at 125 °C for 5 min, 325 °C for 5 min, at 375 °C for 15 min and at 450 °C for 30 min, followed by cooling to room temperature. Then the films were again soaked in 40 mM $TiCl_4$ solution at 70 °C for 30 min, followed by sintering at 450 °C for 30 min. After cooling to ~50 °C, the prepared films were immersed into 0.5 mM N719 dye in an ethanol solution for 20 h at 40 °C. Then, the dye adsorbed photoanodes were washed with ethanol to remove non-adsorbed dye from the films.

In the meantime, platinum (Pt) catalyst was coated onto FTO substrates from Pt precursor (Solaronix) by a brush-painting method to prepare the counter electrodes. The dye-adsorbed photoanodes and Pt counter electrodes were assembled into a sealed sandwich-type cell, with a 60 μm thick hot-melt sealing Surlyn between the electrodes. The electrolyte solution, Iodolyte Z-50 (Solaronix), was introduced into the cell via a vacuum-filling method through an injection hole on the counter electrode side. Finally, the hole was sealed with scotch tape.

### 2.5. Characterization

Scanning electron microscopy (SEM) images were obtained using an Inspect F50 SEM (FEI) with accelerating voltage of 10 kV. Energy dispersive X-ray spectroscopy (EDX) analysis was completed on the same system with Team EDS Octane Pro (EDAX) attachment. Elemental compositions of the samples were analyzed at binding energy ranging from 0 eV to 1200 eV using a X-ray photoelectron spectroscopy (XPS), Leybold Heraeus LHS-10 with a SPECS XR-50 dual anode source operating at 250 W. The Mg-Kα source, which has energy of 1253.6 eV, was used for the XPS analysis. X-ray diffraction (XRD) patterns were carried out on a powder X-ray diffractometer at 40 kV and 15 mA in the range of $2\theta = 3–80°$ using Cu Kα radiation (Model Miniflex 600, Rigaku, Japan). Attenuated Total Reflection-Fourier Transform Infrared Spectroscopy (ATR-FTIR) spectra were acquired over a wavenumber range of 4000–500 $cm^{-1}$ in transmission mode using a Frontier FTIR spectrometer (Perkin Elmer, USA) with a germanium crystal. Raman spectroscopy was carried out on LabRAM HR Evolution spectrometer (Horiba Jobin Yvon, Japan). Raman spectra were collected using a 532 nm laser (mpc 3000) as the excitation source. A 50× objective was used with a confocal hole size of 100 μm. Auger spectromicroscopy "PHI 710 scanning auger nanoprobe" operating at base vacuum below $1 \times 10^{-9}$ Torr was used to analyse the elemental analysis of the samples. Sputtering samples for the analysis was

performed using ultra high purity Argon. Data was collected using an electron beam of 10 kV, 10 nA.

To determine the adsorbed amount of dye molecules in the $SnO_2$ and $SnO_2$-RGO films, the dye in the films was dissolved in 0.1 M NaOH aqueous solution and then measured by a Varian Cary 50G UV–vis Spectrophotometer at wavelengths ranging from 300 to 1000 nm. Sheet resistivities were performed on the microscope slide substrate coated with $SnO_2$-only and/or $SnO_2$-RGO hybrid using a four point probe technique (KeithLink Technology Co., Ltd. Taiwan). The photocurrent–voltage ($J$–$V$) characteristics were investigated using a Keithley 2400 SMU instrument and recorded using a custom LabView Virtual Instrument program. A standard silicon test cell with NIST-traceable certification was used to calibrate the power density as 100 mW $cm^{-2}$ at the sample plane of the collimated xenon-arc light source, which was passed through an AM 1.5G filter. The active area of each device was 0.25 $cm^2$. The $J$–$V$ curves were measured in the air through reverse-scan direction from 1 V to −1 V. Incident-photon-to-current conversion efficiency (IPCE) measurements as a function of wavelength ranging from 400 nm to 800 nm were taken by passing chopped light from a Xenon source through a monochromator and onto the devices.

## 3. Results and discussion

The preparation of $SnO_2$-RGO hybrid is shown in Scheme 1. Firstly, $SnCl_2{\cdot}2H_2O$ powder (Fig. S1) was mixed with GO (Fig. 1a) in aqueous hydrochloric acid (HCl, 0.02 M) to form a homogenous solution, which was stirred and reacted using a microwave technique. During this process, GO was reduced and is termed "RGO". Then, the resulting product was centrifuged and dried to obtain a $SnO_2$-RGO hybrid. For comparison, the same process was carried out in the absence of GO to produce only $SnO_2$ [36].

The SEM image in Fig. 1b shows that the synthesized $SnO_2$ is a 1 dimensional (1D) microstructure with a rod-like shape. It is worth noting that 1D structures can provide fast electron transport pathway [39]. Fig. 1c depicts the SEM image of the $SnO_2$-RGO hybrid, which demonstrates clear differences compared to GO (Fig. 1a) and $SnO_2$-only. It can be seen that the $SnO_2$ micro-rods were well mixed and wrapped in the RGO flakes, as expected, to form the hybrid material. As shown in Fig. 1d and e, during the microwave-assisted synthesis, small $SnO_2$ nanoparticles were also formed on both $SnO_2$ rods and RGO flakes which are expected to be beneficial for dye adsorption.

Fig. 2a shows the XRD patterns of GO, $SnO_2$-only and $SnO_2$-RGO hybrid. GO displays an intense peak at around $2\theta = 10.9°$, which corresponds to the (002) reflection of the stacked GO nanosheets [40]. It can be observed that the $SnO_2$-only sample shows broad and weak peaks ((110), (101), (200), (211) and (112)), which can be indexed to a tetragonal-structured $SnO_2$ with poor crystallinity [41]. It is well known that after the reduction process, the diffraction peak of the GO shifts to around $2\theta = 24.5°$. This peak at $2\theta = 24.5°$ cannot be observed in the XRD pattern of the hybrid because this peak will be overlapped with the $SnO_2$ peak (110). Another noticeable feature in the XRD pattern of $SnO_2$-RGO is that the $SnO_2$ in the hybrid shows narrow and strong peaks, which can be assigned to a tetragonal structure (JCPDS card no. 41-1445), indicating an improved crystallinity of $SnO_2$ and larger average crystal size [42]. This improvement in the crystallinity is often observed in nanocarbon-metal oxide materials and is attributed to a heat-sink effect in which the nanocarbon facilitates crystallization via heat transfer [43].

The results of the XRD analysis were further confirmed by characterizing the samples using XPS (Fig. 2b), ATR-FTIR (Fig. 3a) and Raman spectroscopy (Fig. 3b). It can be clearly observed from the Raman spectra of the $SnO_2$-RGO hybrid (Fig. 3b) that the $I_D/I_G$ ratio of RGO increased compared to that of the GO. This increase in the $I_D/I_G$ ratio can be attributed to the defects caused during reduction of GO [27]. Moreover, it should be noted that in the XPS survey spectra, negligible Cl 2p peaks can be found in the $SnO_2$-based samples, which could be attributed to the unreacted $Cl^-$ of $SnCl_2{\cdot}2H_2O$. Additionally, Auger and EDX elemental analysis were carried out on selected area of SEM images of the $SnO_2$-RGO hybrid and reveal a small amount of chlorine remaining in the sample (see Fig. S2). These results of Auger and EDX spectroscopies were in good agreement with the XPS and may explain the sample crystallinity.

To study the influence of RGO on the efficiency of PV cells, DSSCs were fabricated using six photoanodes of different RGO content in the hybrid and were evaluated using simulated AM1.5 sunlight with an output power of 100 mW $cm^{-2}$. Notably, for the fabrication of DSSCs, the photoanodes were immersed in a $TiCl_4$ aqueous solution before they were soaked in the dye solution. This process is a commonly followed strategy to deposit a thin layer of $TiO_2$ over $SnO_2$ ($SnO_2$-RGO in our case) which can improve the $V_{oc}$ of the $SnO_2$-based DSSCs [18,44–46]. Therefore, the photoanodes were denoted as "$TiO_2$-$SnO_2$-RGO (X)", where the value of X indicates the weight concentration (wt%) of RGO in the hybrid. For example, the photoanode film prepared with 0.2 wt% RGO is denoted "$TiO_2$-$SnO_2$-RGO (0.2)".

The photocurrent density–voltage ($J$–$V$) characteristics of the DSSCs assembled with these photoanodes are shown in Fig. 4a and the corresponding PV parameters have been summarized in Table 1. The control DSSC device ($TiO_2$-$SnO_2$-RGO (0)) fabricated based on $SnO_2$ photoanode without RGO showed an average PCE ($\eta$) of 1.28 ± 0.52% with a short-circuit current ($J_{sc}$) value of 4.78 ± 0.95 mA $cm^{-2}$ and $V_{oc}$ of 0.64 ± 0.01 V which are typical values for such cells [12,18].

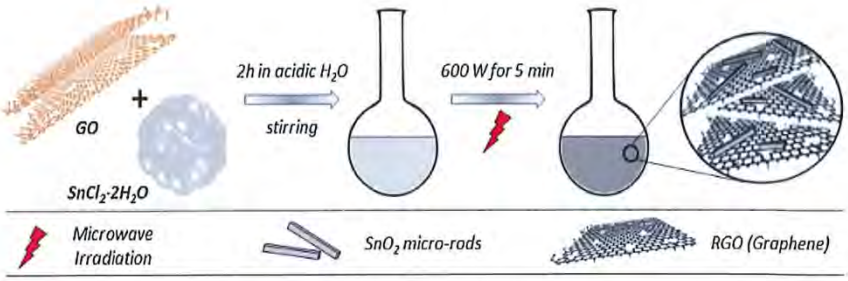


**Scheme 1.** Synthetic procedure of $SnO_2$-RGO hybrid structure.

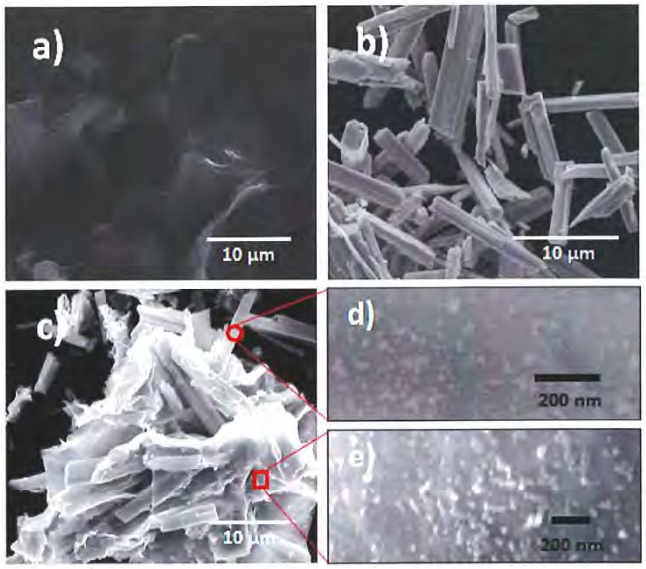


**Fig. 1.** SEM images of (a) GO, (b) $SnO_2$ micro-rod and (c) $SnO_2$-RGO hybrid. High resolution SEM images of (d) $SnO_2$ micro-rod and (e) RGO sheet in the hybrid showing that small $SnO_2$ nanoparticles are formed on $SnO_2$ and RGO surface.

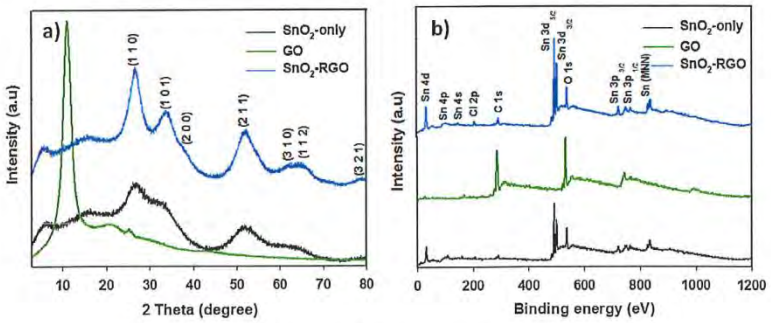


**Fig. 2.** (a) XRD patterns and (b) XPS survey spectra of the samples.

It can be seen from Table 1 that from $TiO_2$-$SnO_2$-RGO (0) to $TiO_2$-$SnO_2$-RGO (0.7) (increasing RGO content), the $J_{sc}$ value increases from $4.78 \pm 0.95$ to $10.23 \pm 0.88$ mA cm$^{-2}$. We hypothesize that this increase in the $J_{sc}$ is due to the improved dye loading into the film and enhanced electron transfer within the photoanode [22,27,28]. In order to confirm our hypothesis, we fabricated $SnO_2$ films (Fig. S3) with different RGO content and investigated the dye adsorption capability of the films. No treatment with $TiCl_4$ solution was done to allow the effect of RGO in the $SnO_2$ film on the extent of dye adsorption to be probed without any interference. As shown in Fig. S3, the films after dye adsorption and also the solutions after subsequent desorption of the dye molecules using NaOH show that the dye adsorption of the $SnO_2$ films was significantly improved by incorporating RGO. Moreover, UV–vis spectra in Fig. 4b show the absorbance of dye desorbed from the films and shows that dye adsorption increases with increasing RGO concentration in the hybrid. This improvement in the dye adsorption is most likely due to a better matching of the molecular nature of the N719 dye and the chemical nature of the hybrid. N719 has both polar groups and aromatic regions. Since our RGO was derived from GO, some functional groups (—OH, —COOH etc.) would remain on the surface of RGO due to the partial reduction and these would interact with the polar groups on N719. These functional groups may be playing an important role in the dye adsorption [21]. $SnO_2$ would also inter-

**Table 1**
PV parameters of the DSSCs fabricated based on $SnO_2$ photoanodes with different RGO content. Average values and the standard deviations of the DSSCs are shown based on at least three cells for each device. Parameters of the best cells are highlighted in **bold**.

| Device | RGO, wt% | $J_{sc}$, (mA cm$^{-2}$) | $V_{oc}$, (V) | FF | $\eta$ (%) |
|---|---|---|---|---|---|
| $TiO_2$-$SnO_2$-RGO (0) | 0 | **5.735**; 4.78 ± 0.95 | **0.64**; 0.64 ± 0.01 | **0.45**; 0.43 ± 0.04 | **1.65**; 1.28 ± 0.52 |
| $TiO_2$-$SnO_2$-RGO (0.2) | 0.2 | **8.196**; 8.20 ± 0.15 | **0.64**; 0.63 ± 0.01 | **0.45**; 0.44 ± 0.01 | **2.36**; 2.27 ± 0.07 |
| $TiO_2$-$SnO_2$-RGO (0.45) | 0.45 | **10.185**; 9.41 ± 1.00 | **0.67**; 0.67 ± 0.01 | **0.46**; 0.46 ± 0.01 | **3.16**; 2.94 ± 0.24 |
| $TiO_2$-$SnO_2$-RGO (0.7) | 0.7 | **10.954**; 10.23 ± 0.88 | **0.52**; 0.50 ± 0.02 | **0.39**; 0.41 ± 0.04 | **2.15**; 2.08 ± 0.17 |
| $TiO_2$-$SnO_2$-RGO (1.2) | 1.2 | **2.914**; 2.91 ± 0.03 | **0.52**; 0.51 ± 0.01 | **0.45**; 0.44 ± 0.01 | **0.68**; 0.66 ± 0.03 |
| $TiO_2$-$SnO_2$-RGO (4.75) | 4.75 | **1.984**; 1.74 ± 0.26 | **0.31**; 0.27 ± 0.05 | **0.46**; 0.43 ± 0.04 | **0.29**; 0.22 ± 0.08 |

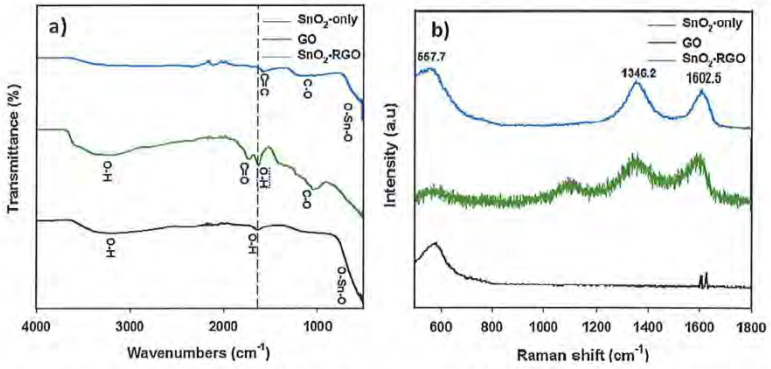


**Fig. 3.** (a) ATR-FTIR and (b) Raman spectra of $SnO_2$-only, GO and $SnO_2$-RGO hybrid materials. Long dash line in ATR-FTIR spectra proves that "—OH" is different from the "C=C" in the hybrid.

act with these polar groups. The introduction of the RGO provides some aromatic nature to the hybrid and one can speculate that this will create polar and aromatic regions in close proximity and will further enhance dye adsorption. Additionally the high-surface area of RGO may contribute to the adsorption of the dye [28]. Interestingly, the dye adsorption of the film with the highest RGO content (4.75 wt%) is starting to saturate, indicating that adding more RGO into the film would likely not lead to significant further increases in dye adsorption (see Fig. S4).

To determine the mechanism for the improved $J_{sc}$ value, the sheet resistivity ($R_s$) of the $TiCl_4$ treated $SnO_2$ film without and with 0.45 wt% RGO was measured using a four point probe. The same film thickness on a glass substrate was obtained using the doctor blade method (see experimental details). The film without RGO shows a $R_s$ of $4.51 \times 10^6$ Ω/□, while the RGO incorporated film exhibits a comparatively low $R_s$ ($1.81 \times 10^6$ Ω/□) (see Table S1). The decrease in the $R_s$ (nearly 3-fold) of the film with RGO is due to the fact that high conductivity of the RGO in the hybrid reduces the interfacial resistance between $SnO_2$. In addition, the measured series resistance ($R_{series}$) of the $TiO_2$-$SnO_2$-RGO (0.45) based DSSC was 97.9 Ω, which was ~1.7-fold lower than that of the control cell (Table S1). On the basis of these results, it is clear that the presence of RGO accelerated electron transport process within the photoanode and suppressed the charge recombination of the cells; thus significantly enhancing the $\eta$ [21,22,28].

However, although $TiO_2$-$SnO_2$-RGO (0.7) based cell showed the highest $J_{sc}$ (10.95 mA cm$^{-2}$), the measured average $\eta$ (2.08 ± 0.17%) was not the best observed, despite the films having high dye adsorption. When the RGO concentration in the hybrid further increased to 1.2 wt% and 4.75 wt%, a significant drop in the $J_{sc}$ value and $V_{oc}$ was observed for the $TiO_2$-$SnO_2$-RGO (1.2) and $TiO_2$-$SnO_2$-RGO (4.75) based DSSCs, thus resulting in very poor efficiencies. We attribute this $\eta$ decrease of the DSSCs with higher RGO loading to (i) opacity of the film (see films before dye adsorption in Fig. S3) reducing light absorption and (ii) high catalytic property of RGO, which has been shown to limit the continuous electron transfer at the photoanode [2,21,47].

It is well established that although carbon materials can facilitate electron transport in the DSSC, the catalytic activity of carbon materials toward reduction of the electrolyte causes significant charge recombination at the interface of the photoanode and electrolyte (since this reaction should only occur at the cathode) if too high concentration of carbon is used [2]. Fig. 4c shows the dark $J$–$V$ characteristics of DSSCs fabricated without and with RGO in the $SnO_2$ photoanodes. It is known that the magnitude and onset of the dark current indicates the level of charge recombination between the electrons from the dye excitation process and the $I_3^-$ ions in the electrolyte [48]. It can be seen that the dark current onset shifted to a lower potential after adding a small amount of RGO into the $SnO_2$ photoanodes. This is known to be due to the increased charge recombination rate of the DSSCs caused by the reaction between the RGO and electrolyte. Therefore, at a given voltage, the dark current increased when the RGO was added into the $SnO_2$ photoanode

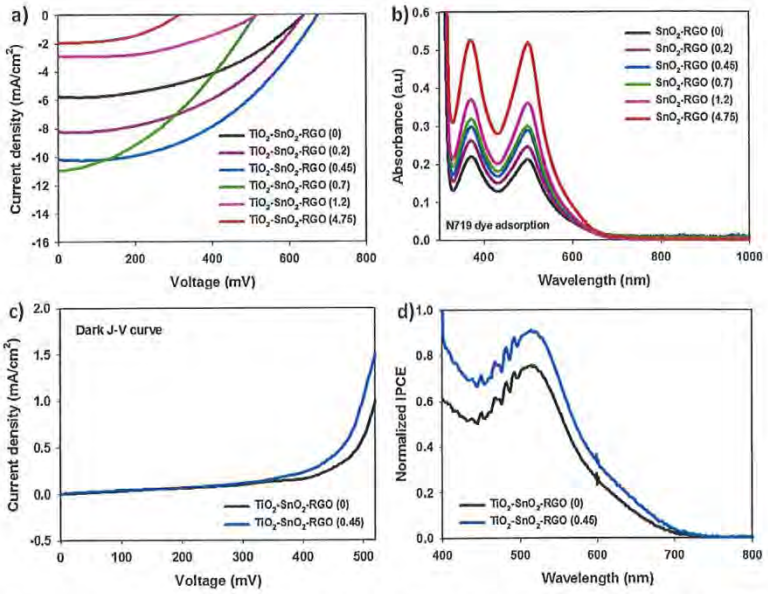


**Fig. 4.** (a) *J–V* curves of DSSCs assembled with different RGO content in the $TiO_2$-$SnO_2$ photoanode measured under AM 1.5 G illumination at 100 mW $cm^{-2}$. (b) UV–vis spectra of N719 dye molecules desorbed from $SnO_2$ films with different amount of RGO using 0.1 M NaOH solution. (c) *J–V* curves of DSSCs fabricated without and with RGO in the $SnO_2$ photoanodes measured under the dark state. (d) Normalized IPCE value of DSSCs fabricated based on $TiO_2$-$SnO_2$ photoanodes with (0.45 wt%) and without RGO.

of DSSC. Our finding is in line with similar report of adding carbon powders into $TiO_2$ photoanodes [48].

Indeed, the highest $\eta$ (3.16%) with an average $\eta$ of 2.94 ± 0.24% was achieved for the device based on $TiO_2$-$SnO_2$-RGO (0.45). In the $TiO_2$-$SnO_2$-RGO based DSSC, the $TiO_2$ can act as a barrier layer reducing the contact of RGO with the electrolyte and therefore reducing the likelihood of RGO catalyzing recombination at the photoanode. Taking into account the $TiO_2$ deposition process (dip coating) which unlikely to achieve 100% coverage, we speculate that with higher RGO content the net amount of RGO in contact with the electrolyte will increase accordingly. Moreover, we fabricated $SnO_2$ and $SnO_2$-RGO photoanodes based DSSCs without $TiCl_4$ treatment and their PV results have been plotted in Fig. S5a. The efficiencies of these DSSCs were ~2-fold lower than those of the devices fabricated with $TiCl_4$ treatment, confirming that the use of $TiCl_4$ treatment is a vital method to enhance the cell performance in $SnO_2$ photoanode DSSCs.

It can be seen from Table 1 that all parameters of DSSC fabricated with $SnO_2$ photoanodes increased after incorporating 0.45 wt% RGO. The calculated $\eta$ enhancement of $TiO_2$-$SnO_2$-RGO (0.45) photoanode based device was impressive (91.5%) as compared to the control cell especially in light of the fact that a very small amount of RGO is required to realise these large improvements in efficiency. This photoanode ($TiO_2$-$SnO_2$-RGO (0.45)) was chosen for further investigation to fully understand the role of RGO in the DSSC.

IPCE spectra offer important information on the light harvesting efficiency which is mainly determined by the absorption of light by the dye molecules at the photoanode and electron transport processes. The IPCE spectra of the DSSCs with and without RGO in the photoanode are illustrated in Fig. 4d. It should be noted that the IPCE spectra of the DSSCs were characterized after the devices were aged for approximately 10 days. The IPCE of the $TiO_2$-$SnO_2$-RGO (0.45) photoanode based device is higher than that of the control DSSC over the entire wavelength region. The lack of wavelength dependence indicates that the addition of RGO into the $SnO_2$ photoanode improves the DSSC performance without altering the internal mechanism, likely by enhancing electron transfer rate and increasing dye adsorption onto the photoanode.

As discussed earlier, RGO in the hybrid ensures rapid electron transport process (Fig. 5a) and significantly enhances the $J_{sc}$ value of the DSSC. Importantly, it can be expected that incorporation of RGO in the $SnO_2$ photoanode would improve the DSSC performance owing to presence of suitable energy levels. Fig. 5b shows an energy level diagram for the $TiCl_4$ treated $SnO_2$ photoanode with RGO. Since a thin $TiO_2$ layer was deposited on the FTO and on the $SnO_2$ or $SnO_2$-RGO layers by $TiCl_4$ treatment, it is reasonable to include the energy level of $TiO_2$ in this diagram. The red arrow in Fig. 5b represents the fact that the electron transfer from the conduction band of $SnO_2$ to that of $TiO_2$ is not possible due to their mismatching band energy levels. As the $TiO_2$ coverage on the FTO is incomplete (not 100%), both $SnO_2$ and $TiO_2$ are in contact with the FTO and hence electron transfer from both the $SnO_2$ and $TiO_2$ to the FTO is still feasible. The results from Figs. S6 and S7 show that despite the fact that the $TiO_2$ on the FTO is very thin, it does make a contribution to the current and voltage of the cell and as such is important to show. Since the energy level of RGO (−4.40 eV) lies between the conduction band of $TiO_2$ (−4.26 eV) and $SnO_2$ (−4.56 eV), the electrons can be rapidly transferred stepwise from the $TiO_2$ to the $SnO_2$ conduction band (see Fig. 5b) [18,28]. Here RGO can act as a bridge between $TiO_2$ and $SnO_2$. This effective

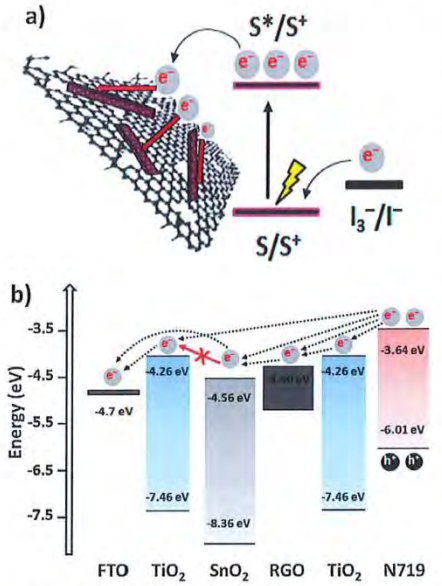


**Fig. 5.** (a) A possible mechanism for the enhanced electron transfer in $SnO_2$-RGO hybrid. (b) Energy level diagram for the $TiCl_4$ treated $SnO_2$ photoanode with RGO.

**Table 2**
PV parameters of the DSSCs fabricated based on various $SnO_2$ photoanode structures and our best performing cell ($TiO_2$-$SnO_2$-RGO (0.45).

| Structure | Ref. | $J_{sc}$, (mA cm$^{-2}$) | $V_{oc}$, (V) | FF | $\eta$ (%) |
|---|---|---|---|---|---|
| This study | – | 10.18 | 0.67 | 0.46 | 3.16 |
| $SnO_2$ nanoparticles | [49] | 7.63 | 0.35 | 0.43 | 1.14 |
| $SnO_2$ nanoparticles | [44] | 4.90 | 0.40 | 0.51 | 1.00 |
| $SnO_2$ nanoparticles | [50] | 7.90 | 0.47 | 0.55 | 2.03 |
| $SnO_2$ nanofibers | [51] | 7.04 | 0.51 | 0.38 | 1.34 |
| $SnO_2$ multiporous NFs | [12] | 10.0 | 0.44 | 0.45 | 2.00 |
| $SnO_2$ nanoflowers | [52] | 7.30 | 0.70 | 0.60 | 3.00 |
| $SnO_2$ NWs + NPs | [53] | 9.90 | 0.53 | 0.49 | 2.53 |
| $SnO_2$ spheres (hierarchical mesoporous) | [54] | 12.3 | 0.52 | 0.58 | 3.70 |

electron transfer would likely reduce the charge recombination of the cell, thus improves the performance.

Finally, the PV parameters of our best-performing cells have been compared with values reported in the literature for other DSSCs with $SnO_2$ based photoanodes. Table 2 summarizes the PV parameters such as $J_{sc}$, $V_{oc}$, $FF$ and $\eta$ of DSSC devices fabricated with various $SnO_2$ structures based photoanodes and our best performing cells. It can be observed from Table 2 that the efficiency observed for our DSSC fabricated with $SnO_2$-RGO photoanode is comparable or higher than those achieved by other 1D and 3D $SnO_2$ structured photoanode films. Therefore, this indicates that the incorporation of graphene structures into $SnO_2$ photoanode is an effective strategy to achieve high efficiency DSSCs.

## 4. Conclusion

In summary, the successful application of RGO structures in 1D $SnO_2$ micro-rod based photoanodes for DSSCs has been demonstrated. Herein we show that the application of RGO overcomes the major shortcoming of $SnO_2$ when applied as a DSSC photoanode, namely poor dye adsorption. In addition, owing to its suitable energy levels and excellent conductivity, RGO significantly improved the electron transport rate in the cells. Importantly, PCE ($\eta$) of the DSSC was significantly improved to 3.16% by incorporating a very small amount of RGO into the photoanode, demonstrating a ~91.5% enhancement in the efficiency when compared to $SnO_2$-only photoanode based DSSC (1.65%).

## Acknowledgements

The support of the Australian Research Council Discovery Program (DP130101714) is gratefully acknowledged. Munkhbayar Batmunkh acknowledges International Postgraduate Research Scholarship (IPRS) and Australian Postgraduate Award (APA) for their financial support during his study in Australia. We acknowledge the use of South Australian node of the Australian Microscopy & Microanalysis Research Facility (AMMRF) at Flinders University.

## Appendix A. Supplementary data

Supplementary data associated with this article can be found, in the online version, at http://dx.doi.org/10.1016/j.apsusc.2016.06.146.

## References

[1] G. Hashmi, K. Miettunen, T. Peltola, J. Halme, I. Asghar, K. Aitola, M. Toivola, P. Lund, Review of materials and manufacturing options for large area flexible dye solar cells, Renew. Sustain. Energy Rev. 15 (2011) 3717–3732.
[2] M. Batmunkh, M.J. Biggs, J.G. Shapter, Carbon nanotubes for dye-sensitized solar cells, Small 11 (2015) 2963–2989.
[3] F. Bella, C. Gerbaldi, C. Barolo, M. Gratzel, Aqueous dye-sensitized solar cells, Chem. Soc. Rev. 44 (2015) 3431–3473.
[4] J. Wu, Z. Lan, J. Lin, M. Huang, Y. Huang, L. Fan, G. Luo, Electrolytes in dye-sensitized solar cells, Chem. Rev. 115 (2015) 2136–2173.
[5] Y. Hao, E. Gabrielsson, P.W. Lohse, W. Yang, E.M.J. Johansson, A. Hagfeldt, L. Sun, G. Boschloo, Peripheral hole acceptor moieties on an organic dye improve dye-sensitized solar cell performance, Adv. Sci. 2 (2015) 1500174.
[6] L. Han, A. Islam, H. Chen, C. Malapaka, B. Chiranjeevi, S. Zhang, X. Yang, M. Yanagida, High-efficiency dye-sensitized solar cell with a novel co-adsorbent, Energy Environ. Sci. 5 (2012) 6057–6060.
[7] S. Mathew, A. Yella, P. Gao, R. Humphry-Baker, F.E. CurchodBasile, N. Ashari-Astani, I. Tavernelli, U. Rothlisberger, K. NazeeruddinMd, M. Grätzel, Dye-sensitized solar cells with 13% efficiency achieved through the molecular engineering of porphyrin sensitizers, Nat. Chem. 6 (2014) 242–247.
[8] S.G. Hashmi, M. Ozkan, J. Halme, K.D. Misic, S.M. Zakeeruddin, J. Paltakari, M. Grätzel, P.D. Lund, High performance dye-sensitized solar cells with inkjet printed ionic liquid electrolyte, Nano Energy 17 (2015) 206–215.
[9] A.K. Chandiran, M. Abdi-Jalebi, M.K. Nazeeruddin, M. Grätzel, Analysis of electron transfer properties of ZnO and TiO2 photoanodes for dye-sensitized solar cells, ACS Nano 8 (2014) 2261–2268.
[10] J. Fan, Z. Li, W. Zhou, Y. Miao, Y. Zhang, J. Hu, G. Shao, Dye-sensitized solar cells based on TiO2 nanoparticles/nanobelts double-layered film with improved photovoltaic performance, Appl. Surf. Sci. 319 (2014) 75–82.
[11] S. Ferrere, A. Zaban, B.A. Gregg, Dye sensitization of nanocrystalline tin oxide by perylene derivatives, J. Phys. Chem. B 101 (1997) 4490–4493.
[12] Q. Wali, A. Fakharuddin, I. Ahmed, M.H. Ab Rahim, J. Ismail, R. Jose, Multiporous nanofibers of SnO2 by electrospinning for high efficiency dye-sensitized solar cells, J. Mater. Chem. A 2 (2014) 17427–17434.
[13] Q. Wali, A. Fakharuddin, R. Jose, Tin oxide as a photoanode for dye-sensitised solar cells: current progress and future challenges, J. Power Sources 293 (2015) 1039–1052.
[14] I. Concina, A. Vomiero, Metal oxide semiconductors for dye- and quantum-dot-sensitized solar cells, Small 11 (2015) 1744–1774.
[15] E. Ramasamy, J. Lee, Ordered mesoporous SnO2-based photoanodes for high-performance dye-sensitized solar cells, J. Phys. Chem. C 114 (2010) 22032–22037.
[16] S. Gubbala, V. Chakrapani, V. Kumar, M.K. Sunkara, Band-edge engineered hybrid structures for dye-sensitized solar cells based on SnO2 nanowires, Adv. Funct. Mater. 18 (2008) 2411–2418.
[17] J. Gong, H. Qiao, S. Sigdel, H. Elbohy, N. Adhikari, Z. Zhou, K. Sumathy, Q. Wei, Q. Qiao, Characteristics of SnO2 nanofiber/TiO2 nanoparticle composite for dye-sensitized solar cells, AIP Adv. 5 (2015) 067134.

[18] A. Thapa, J. Zai, H. Elbohy, P. Poudel, N. Adhikari, X. Qian, Q. Qiao, TiO2 coated urchin-like SnO2 microspheres for efficient dye-sensitized solar cells, Nano Res. 7 (2014) 1154–1163.
[19] C.-L. Wang, J.-Y. Liao, Y. Zhao, A. Manthiram, Template-free TiO2 hollow submicrospheres embedded with SnO2 nanobeans as a versatile scattering layer for dye-sensitized solar cells, Chem. Commun. 51 (2015) 2848–2850.
[20] A. Birkel, Y.-G. Lee, D. Koll, X.V. Meerbeek, S. Frank, M.J. Choi, Y.S. Kang, K. Char, W. Tremel, Highly efficient and stable dye-sensitized solar cells based on SnO2 nanocrystals prepared by microwave-assisted synthesis, Energy Environ. Sci. 5 (2012) 5392–5400.
[21] M. Batmunkh, M.J. Biggs, J.G. Shapter, Carbonaceous dye-sensitized solar cell photoelectrodes, Adv. Sci. 2 (2015) 1400025.
[22] J.D. Roy-Mayhew, I.A. Aksay, Graphene materials and their use in dye-sensitized solar cells, Chem. Rev. 114 (2014) 6323–6348.
[23] M. Batmunkh, C.J. Shearer, M.J. Biggs, J.G. Shapter, Nanocarbons for mesoscopic perovskite solar cells, J. Mater. Chem. A 3 (2015) 9020–9031.
[24] A. Kongkanand, R. Martínez Domínguez, P.V. Kamat, Single wall carbon nanotube scaffolds for photoelectrochemical solar cells. Capture and transport of photogenerated electrons, Nano Lett. 7 (2007) 676–680.
[25] S.-B. Kim, J.-Y. Park, C.-S. Kim, K. Okuyama, S.-E. Lee, H.-D. Jang, T.-O. Kim, Effects of graphene in dye-sensitized solar cells based on nitrogen-doped TiO2 composite, J. Phys. Chem. C 119 (2015) 16552–16559.
[26] A. Sacco, S. Porro, A. Lamberti, M. Gerosa, M. Castellino, A. Chiodoni, S. Bianco, Investigation of transport and recombination properties in graphene/titanium dioxide nanocomposite for dye-sensitized solar cell photoanodes, Electrochim. Acta 131 (2014) 154–159.
[27] Z. He, G. Guai, J. Liu, C. Guo, J.S. Chye Loo, C.M. Li, T.T.Y. Tan, Nanostructure control of graphene-composited TiO2 by a one-step solvothermal approach for high performance dye-sensitized solar cells, Nanoscale 3 (2011) 4613–4616.
[28] Y.-B. Tang, C.-S. Lee, J. Xu, Z.-T. Liu, Z.-H. Chen, Z. He, Y.-L. Cao, G. Yuan, H. Song, L. Chen, L. Luo, H.-M. Cheng, W.-J. Zhang, I. Bello, S.-T. Lee, Incorporation of graphenes in nanostructured TiO2 films via molecular grafting for dye-sensitized solar cell application, ACS Nano 4 (2010) 3482–3488.
[29] T. Chen, W. Hu, J. Song, G.H. Guai, C.M. Li, Interface functionalization of photoelectrodes with graphene for high performance dye-sensitized solar cells, Adv. Funct. Mater. 22 (2012) 5245–5250.
[30] Y.H. Ng, I.V. Lightcap, K. Goodwin, M. Matsumura, P.V. Kamat, To what extent do graphene scaffolds improve the photovoltaic and photocatalytic response of TiO2 nanostructured films? J. Phys. Chem Lett. 1 (2010) 2222–2227.
[31] P. Brown, K. Takechi, P.V. Kamat, Single-walled carbon nanotube scaffolds for dye-sensitized solar cells, J. Phys. Chem. C 112 (2008) 4776–4782.
[32] K.T. Dembele, G.S. Selopal, C. Soldano, R. Nechache, J.C. Rimada, I. Concina, G. Sberveglieri, F. Rosei, A. Vomiero, Hybrid carbon nanotubes–TiO2 photoanodes for high efficiency dye-sensitized solar cells, J. Phys. Chem. C 117 (2013) 14510–14517.
[33] D.C. Marcano, D.V. Kosynkin, J.M. Berlin, A. Sinitskii, Z. Sun, A. Slesarev, L.B. Alemany, W. Lu, J.M. Tour, Improved synthesis of graphene oxide, ACS Nano 4 (2010) 4806–4814.
[34] L. Yin, D. Chen, X. Cui, L. Ge, J. Yang, L. Yu, B. Zhang, R. Zhang, G. Shao, Normal-pressure microwave rapid synthesis of hierarchical SnO2@rGO nanostructures with superhigh surface areas as high-quality gas-sensing and electrochemical active materials, Nanoscale 6 (2014) 13690–13700.
[35] Y. Xiong, D. He, Y. Jin, P.J. Cameron, K.J. Edler, Ordered mesoporous particles in titania films with hierarchical structure as scattering layers in dye-sensitized solar cells, J. Phys. Chem. C 119 (2015) 22552–22559.
[36] M. Batmunkh, M. Dadkhah, C.J. Shearer, M.J. Biggs, J.G. Shapter, Tin oxide light scattering layer for titania photoanodes in dye-sensitized solar cells, Energy Technol. 4 (2016), http://dx.doi.org/10.1002/ente.201600008.
[37] L. Yang, W.W.-F. Leung, Electrospun TiO2 nanorods with carbon nanotubes for efficient electron collection in dye-sensitized solar cells, Adv. Mater. 25 (2013) 1792–1795.
[38] S. Ito, T.N. Murakami, P. Comte, P. Liska, C. Grätzel, M.K. Nazeeruddin, M. Grätzel, Fabrication of thin film dye sensitized solar cells with solar to electric power conversion efficiency over 10%, Thin Solid Films 516 (2008) 4613–4619.
[39] P. Poudel, Q. Qiao, One dimensional nanostructure/nanoparticle composites as photoanodes for dye-sensitized solar cells, Nanoscale 4 (2012) 2826–2838.
[40] Y.-T. Xu, Y. Guo, H. Jiang, X.-B. Xie, B. Zhao, P.-L. Zhu, X.-Z. Fu, R. Sun, C.-P. Wong, Enhanced performance of lithium-ion batteries with copper oxide microspheres @ graphene oxide micro/nanocomposite electrodes, Energy Technol. 3 (2015) 488–495.
[41] M. Dadkhah, M. Salavati-Niasari, Controlled synthesis of tin dioxide nanostructures via two simple methods and the influence on dye sensitized solar cell, Electrochim. Acta 129 (2014) 62–68.
[42] A.L. Patterson, The scherrer formula for X-ray particle size determination, Phys. Rev. 56 (1939) 978–982.
[43] Z. Ren, E. Kim, S.W. Pattinson, K.S. Subrahmanyam, C.N.R. Rao, A.K. Cheetham, D. Eder, Hybridizing photoactive zeolites with graphene: a powerful strategy towards superior photocatalytic properties, Chem. Sci. 3 (2012) 209–216.
[44] J. Qian, P. Liu, Y. Xiao, Y. Jiang, Y. Cao, X. Ai, H. Yang, TiO2-coated multilayered SnO2 hollow microspheres for dye-sensitized solar cells, Adv. Mater. 21 (2009) 3663–3667.
[45] M.-S. Wu, Z.-Z. Ceng, C.-Y. Chen, Surface modification of porous TiO2 electrode through pulse oxidative hydrolysis of TiCl3 as an efficient light harvesting photoanode for dye-sensitized solar cells, Electrochim. Acta 191 (2016) 256–262.
[46] Q. Yi, S. Cong, H. Wang, Y. Wang, X. Dai, J. Zhao, Y. Sun, Y. Lou, G. Zou, High-stability Ti4+ precursor for the TiO2 compact layer of dye-sensitized solar cells, Appl. Surf. Sci. 356 (2015) 587–592.
[47] J. Chen, B. Li, J. Zheng, J. Zhao, Z. Zhu, Role of carbon nanotubes in dye-sensitized TiO2-based solar cells, J. Phys. Chem. C 116 (2012) 14848–14856.
[48] S.H. Kang, J.-Y. Kim, Y.-K. Kim, Y.-E. Sung, Effects of the incorporation of carbon powder into nanostructured TiO2 film for dye-sensitized solar cell, J. Photochem. Photobiol. A: Chem. 186 (2007) 234–241.
[49] M.-H. Kim, Y.-U. Kwon, Semiconducting divalent metal oxides as blocking layer material for SnO2-based dye-sensitized solar cells, J. Phys. Chem. C 115 (2011) 23120–23125.
[50] Y. Duan, J. Zheng, N. Fu, Y. Fang, T. Liu, Q. Zhang, X. Zhou, Y. Lin, F. Pan, Enhancing the performance of dye-sensitized solar cells: doping SnO2 photoanodes with Al to simultaneously improve conduction band and electron lifetime, J. Mater. Chem. A 3 (2015) 3066–3073.
[51] C. Gao, X. Li, X. Zhu, L. Chen, Z. Zhang, Y. Wang, Z. Zhang, H. Duan, E. Xie, Branched hierarchical photoanode of titanium dioxide nanoneedles on tin dioxide nanofiber network for high performance dye-sensitized solar cells, J. Power Sources 264 (2014) 15–21.
[52] E.N. Kumar, R. Jose, P.S. Archana, C. Vijila, M.M. Yusoff, S. Ramakrishna, High performance dye-sensitized solar cells with record open circuit voltage using tin oxide nanoflowers developed by electrospinning, Energy Environ. Sci. 5 (2012) 5401–5407.
[53] T. Krishnamoorthy, M.Z. Tang, A. Verma, A.S. Nair, D. Pliszka, S.G. Mhaisalkar, S. Ramakrishna, A facile route to vertically aligned electrospun SnO2 nanowires on a transparent conducting oxide substrate for dye-sensitized solar cells, J. Mater. Chem. 22 (2012) 2166–2172.
[54] J.T. Park, C.S. Lee, J.H. Kim, One-pot synthesis of hierarchical mesoporous SnO2 spheres using a graft copolymer: enhanced photovoltaic and photocatalytic performance, RSC Adv. 4 (2014) 31452–31461.

# Appendix C

www.solar-rrl.com ISSN 2367-198X · Sol. RRL · 1 · No. 3-4 (2017)

3-4/2017

RRL Solar

Rapid Research Letters
Full Papers · Reviews

# Sulfur-doped Graphene with Iron Pyrite ($FeS_2$) as an Efficient and Stable Electrocatalyst for the Iodine Reduction Reaction in Dye-sensitized Solar Cells

M. Batmunkh, A. Shrestha, G. Guo, L. Yu, J. Zhao, M. J. Biggs, C. J. Shearer, J. G. Shapter

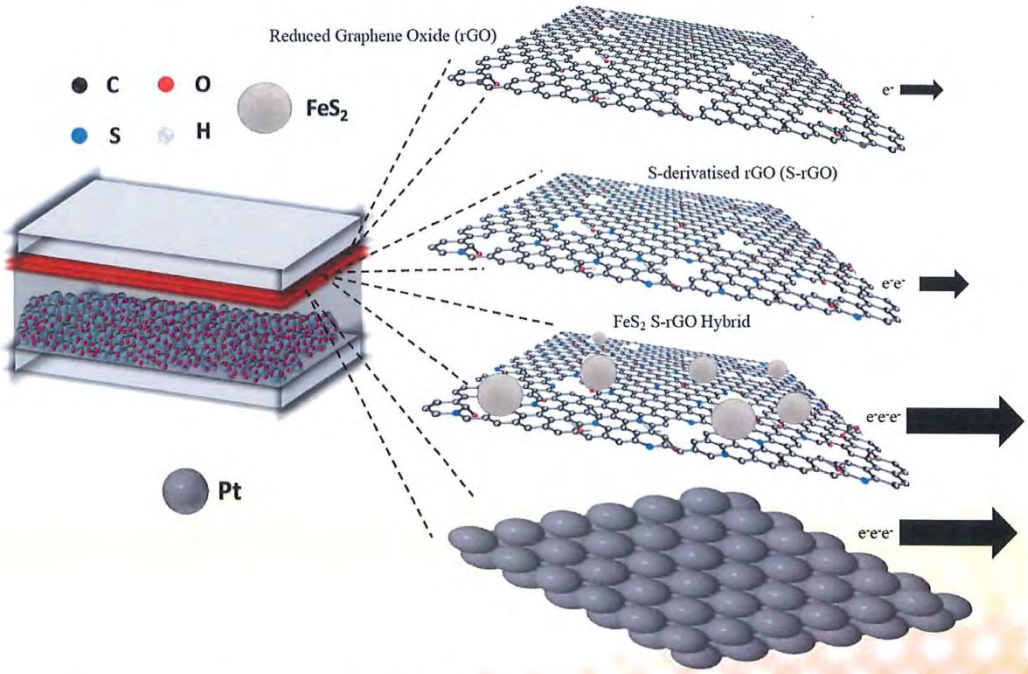


WILEY-VCH

ADVANCED SCIENCE NEWS
www.advancedsciencenews.com

Solar RRL
www.solar-rrl.com



# Sulfur-Doped Graphene with Iron Pyrite ($FeS_2$) as an Efficient and Stable Electrocatalyst for the Iodine Reduction Reaction in Dye-Sensitized Solar Cells

*Munkhbayar Batmunkh, Aabhash Shrestha, Gao Guo, Leping Yu, Jing Zhao, Mark J. Biggs, Cameron J. Shearer, and Joseph G. Shapter**

**As an alternative to platinum (Pt), hybrid electrocatalysts based on sulfur-doped graphene with $FeS_2$ microspheres (SGN-$FeS_2$) were used as a counter electrode (CE) in dye-sensitized solar cells (DSSCs). Benefiting from the high conductivity of SGN and excellent electrocatalytic activity of the $FeS_2$, the bifunctional hybrid electrocatalyst-based device displays a power conversion efficiency (PCE) of 8.1%, which is comparable to that (8.3%) of traditional Pt CE-based DSSC, while also exhibiting excellent stability in ambient conditions. These characteristics, in addition to its low-cost and facile preparation, make the SGN–$FeS_2$ hybrid an ideal CE material for DSSCs.**

Dye-sensitized solar cells (DSSCs) have attracted tremendous interest from the photovoltaic (PV) community owing to the potential they offer in terms of low manufacturing cost, high power conversion efficiency (PCE), and excellent stability.[1,2] A typical DSSC consists of organic dye-sensitizers adsorbed onto a porous $TiO_2$ photoelectrode, an iodide/triiodide ($I^-/I_3^-$) redox electrolyte, and a platinum (Pt)-coated counter electrode (CE).[3] In this device structure, the Pt-coated CE serves an essential role in reducing $I_3^-$ to $I^-$ (called the iodine reduction reaction, IRR). However, Pt is an expensive and relatively rare material, which limits its use in the large-scale commercialization of DSSCs.[4]

Over the past two decades, the development of alternative electrocatalysts that are low-cost and can exhibit higher or comparable performance to the conventional Pt has been the subject of intense research.[5,6] The ideal CE materials for DSSCs should possess not only high electrical conductivity, but also excellent catalytic activity and stability.[7] A wide range of alternative materials have been explored as electrocatalysts for IRR in DSSCs.[7–13] Graphene nanosheets doped with heteroatoms, such as sulfur (S),[14] nitrogen (N),[15] boron (B),[16] phosphorous (P),[17] show great promise as catalysts for the IRR in DSSCs owing to their high surface area and good conductivity. Among the different doping atoms, S-doped graphene (SGN) has to date yielded the most efficient electrocatalyst for IRR (also found in our preliminary investigation, see Supporting Information (SI)).[14,18] This is in part due to the sulfur "S" atoms being efficient electrocatalytic active sites for the IRR.[19] This good performance is also linked to the SGN possessing enhanced electrical conductivity and improved surface area compared to un-doped graphene,[20,21] which helps improve the charge transfer process in DSSCs. Despite these advantages, the performance of devices fabricated with SGN only based CEs are still lower than that of the Pt-based CEs cells because the electrocatalytic activity of single SGN for IRR is inferior to that of Pt.

Recently, iron pyrite ($FeS_2$), a narrow band-gap semiconductor, has been shown to be a promising candidate for use as a CE material in DSSCs owing to its abundance in nature, non-toxicity, low-cost as well as outstanding electrocatalytic activity.[22–24] Although $FeS_2$ has shown some promise as a CE material in DSSCs, its relatively low conductivity limits the further improvement of the device performances. Therefore, combining the excellent catalytic activity of $FeS_2$ with the high conductivity of SGN would be a promising strategy to produce highly efficient electrocatalyst material for DSSC.

In this work, we report the preparation of Pt-free hybrid electrocatalysts, consisting of SGN nanosheets wrapped $FeS_2$, for use as CE materials in DSSCs. The DSSC device fabricated with this hybrid electrocatalyst yields a PCE of 8.1%, which was comparable to that (8.3%) of the cell using Pt. Electrochemical measurements in combination with electrical conductivity analysis reveal that this remarkable PV performance of DSSC originates from the synergistic effect of this hybrid electrocatalyst, in which $FeS_2$ provides excellent electrocatalytic activity for the IRR, while SGN facilitates the electron-transfer process (Scheme 1).

M. Batmunkh, A. Shrestha, M. J. Biggs
School of Chemical Engineering, The University of Adelaide, Adelaide, South Australia 5005, Australia
J. G. Shapter, M. Batmunkh, L. Yu, J. Zhao, C. J. Shearer
Centre for Nanoscale Science and Technology, School of Chemical and Physical Sciences, Flinders University, Bedford Park, Adelaide, South Australia 5042, Australia
E-mail: joe.shapter@flinders.edu.au
G. Guo
Department of Instrument Science and Engineering, Institute of Nano Biomedicine and Engineering, Shanghai Engineering Research Center for Intelligent Diagnosis and Treatment Instrument, School of Electronic Information and Electrical Engineering, Shanghai Jiao Tong University, 800 Dongchuan Road, Shanghai 200240, P. R. China
M. J. Biggs
School of Science, Loughborough University, Loughborough, Leicestershire LE11 3TU, UK

DOI: 10.1002/solr.201700011

  

Solar RRL
www.solar-rrl.com



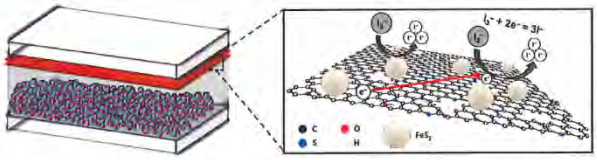


**Scheme 1.** Schematic illustration of DSSC device fabricated with SGN–$FeS_2$ electrocatalyst as a CE material. Note: $FeS_2$ spheres used in this scheme are from the scanning electron microscopy (SEM) images of the synthesized $FeS_2$.

In order to compare the doping effect of different heteroatoms on graphene in terms of their ability to catalyze the IRR in DSSC system, five individual non-metallic elements (I, P, B, N, S) were selected and species containing each element were used to prepare single atom-doped GN materials. All the doped GN materials including I-doped GN (IGN), P-doped GN (PGN), B-doped GN (BGN), N-doped GN (NGN), and S-doped GN (SGN) were prepared from graphene oxide (GO) by using different precursors under the same experimental conditions (details can be found in SI Table S1). These heteroatom-doped graphene electrocatalysts were then used as CE materials in DSSCs. For comparison, DSSCs were fabricated with GO and graphene (produced by thermal reduction of GO, see SI Table S1) based CEs. We found that due to its good electrocatalytic activity and high conductivity, the SGN nanosheets-based device showed the best PCE, as compared to DSSCs with CEs made using the other heteroatom-doped GN materials (see SI Figure S1). The successful doping of sulfur atoms onto the GN nanosheets was confirmed using X-ray photoelectron spectroscopy (XPS) (SI Figure S2a and b). The morphology of the SGN nanosheets examined by scanning electron microscopy (SEM) is depicted in SI Figure S2c. Although the SGN materials exhibited the highest electrocatalytic activity and the lowest charge-transfer resistance ($R_{ct}$) as compared the other doped GN nanosheets (see SI Table S2), the PCE of the DSSCs fabricated with this material was still unsatisfactory. Therefore, further work was needed to improve the performance of this single SGN electrolcatalyst.

Recent studies have demonstrated that $FeS_2$ is a very promising material for DSSC application because of its excellent electrocatalytic activity.[22,24] In this work, $FeS_2$ spheres (SI Figure S2d) were synthesized using a hydrothermal method (see experimental details in SI).[25] In addition to XPS (see SI Figure S2e and f for detail), X-ray diffraction (XRD) analysis was used to evaluate the composition of the prepared $FeS_2$ sample. The majority of the XRD diffraction peaks in **Figure 1**a can be readily indexed to a cubic lattice of pyrite $FeS_2$ and are in good agreement with the previously published literature.[24,26] Based on the XRD pattern, we note that some other components such as oxidized Fe ($Fe_3O_4$) and sulfur were present in the sample. The presence of $Fe_3O_4$ in the sample was further confirmed by both XPS (SI Figure S2e and f) and Raman spectroscopy (SI Figure S3). Notably, recent studies have demonstrated that the $Fe_3O_4$ possess good electrocatalytic properties and may be a promising candidate for use as CE material in DSSC,[27,28] while others have reported that sulfur powder can be used to introduce an extra S-doping in GN nanosheets and thus to improve the DSSC performance.[29] Based on these studies, we expect that the presence of these components in our sample is beneficial in achieving high efficiency of DSSCs.

The SGN–$FeS_2$ hybrid electrocatalyst was prepared by mixing and sonicating the previously prepared SGN (SI Figure S2c) and $FeS_2$ spheres (SI Figure S2d) in an ethanol dispersion. The XRD patterns of the samples are illustrated in Figure 1a. The XRD of the SGN sample shows a pronounced broad peak at around $2\theta = 26°$ and a weak peak at $\approx 2\theta = 43.2°$ corresponding to the (002) and (100) diffraction planes, respectively.[15,30] When analyzing the SGN–$FeS_2$ (40 wt.% $FeS_2$) hybrid sample, XRD diffraction peaks corresponding to both SGN and $FeS_2$ throughout the sample were observed. However, the intensity of the diffraction peaks for $FeS_2$ in the hybrid was very low. This is not unexpected as the 60:40 weight ratio of SGN/$FeS_2$ corresponds to an atomic ratio in the order of 15:1, meaning the intensity of the X-ray scattering from the carbon material, even with the lower scattering probability from the lighter element, will be much greater than the scattering from the lower amount of $FeS_2$.

The morphology of the as-prepared hybrid catalyst was examined by SEM. The SEM image in Figure 1b shows that the $FeS_2$ particles are wrapped by several layers of transparent silk-like SGN nanosheets. It can also be seen from Figure 1c that the $FeS_2$ particles are well distributed in the SGN nanosheets. Energy dispersive X-ray spectroscopy (EDX) elemental mapping was acquired to further investigate the distribution of different species in this hybrid electrocatalyst (Figure 1d). EDX elemental mapping confirmed that C, O, Fe, and S were uniformly distributed in the SGN–$FeS_2$ hybrid sample (Figure 1e).

To evaluate the electrocatalytic activity of CEs based on SGN, $FeS_2$, SGN–$FeS_2$ hybrid, and Pt for the IRR in the DSSC system, cyclic voltammetry (CV) measurements were carried out with a three-electrode system and recorded at the same scan rate of $50\,mV\,s^{-1}$. In **Figure 2**a, two pairs of oxidation and reduction peaks (Ox-A/Red-A (left) and Ox-B/Red-B (right)) are clearly observed for all samples, which can be attributed to the oxidation and reduction reactions of $I^-/I_3^-$ and $I_3^-/I_2$, respectively.[31] Since the main role of the CE in DSSCs is to catalyze the reduction of $I_3^-$ to $I^-$, which corresponds to the lower voltage pair of peaks (Ox-A and Red-A) in the CV curves, the characteristics of these peaks were the main focus of our investigation. The peak separation between the anodic and cathodic peaks ($E_{pp}$), and the peak current density are the main parameters needed to evaluate the electrocatalytic activity of CE

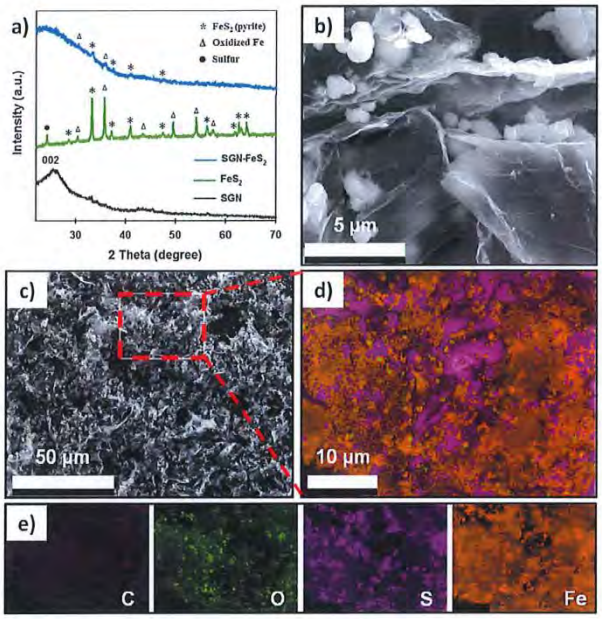


**Figure 1.** (a) XRD patterns of SGN, $FeS_2$, and SGN–$FeS_2$ (40 wt.% $FeS_2$) hybrid samples. (b) High and (c) low resolution SEM image of SGN–$FeS_2$ hybrid. The red box in the inset is the selected area for EDX elemental mapping. SEM-EDX elemental mapping of (d) overlay image and (e) elemental C, O, S, and Fe in the SGN–$FeS_2$ hybrid sample.

materials.[32] In general, an ideal material for IRR – one with the highest electrocatalytic activity – should exhibit the lowest $E_{pp}$ value, while achieving the highest peak current density. As shown in Figure 2a, the SGN–$FeS_2$ hybrid electrode displayed an $E_{pp}$ value of 0.279 V, which was lower than that of the SGN (0.285 V) and Pt (0.345 V) (**Table 1**). We note that the $E_{pp}$ value of our Pt is consistent with recent studies.[15,24,31,33,34] Interestingly, the $FeS_2$ electrode showed an $E_{pp}$ value as low as 0.161 V owing to its known excellent electrocatalytic activity,[22,24] but its current density from the CV measurement was very low. To determine

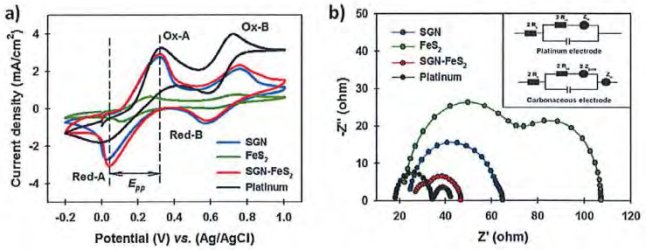


**Figure 2.** (a) Cyclic voltammograms (CVs) of SGN, $FeS_2$, SGN–$FeS_2$, hybrid and Pt electrodes in acetonitrile solution containing 10 mM LiI, 1 mM $I_2$, and 0.1 mM $LiClO_4$ at a scan rate of 50 mV $s^{-1}$. (b) Nyquist plots of symmetric sandwich cells structure fabricated with different CE materials on FTO electrodes. Inset shows the equivalent circuit diagrams for the control Pt and other electrodes for EIS analysis.

Table 1. Detailed PV parameters of the DSSC devices fabricated based on different CE materials.

| Samples | $J_{sc}$ (mA cm$^{-2}$) | $V_{oc}$ (V) | FF | PCE (%) | $E_{pp}$ (V) | $R_{ct}$ (Ω) | $R_{sheet}$ (Ω/□) |
|---|---|---|---|---|---|---|---|
| SGN | **15.96;** | **0.77;** | **0.55;** | **6.79;** | 0.285 | 22.3 | $2.37 \pm 0.54 \times 10^3$ |
| | 15.86 ± 0.33 | 0.77 ± 0.01 | 0.52 ± 0.02 | 6.36 ± 0.32 | | | |
| $FeS_2$ | **15.94;** | **0.73;** | **0.47;** | **5.51;** | 0.161 | 39.8 | $1.50 \pm 0.09 \times 10^6$ |
| | 15.86 ± 0.37 | 0.74 ± 0.01 | 0.46 ± 0.02 | 5.43 ± 0.09 | | | |
| SGN–$FeS_2$ | **16.43;** | **0.82;** | **0.60;** | **8.10;** | 0.279 | 11.2 | $4.52 \pm 0.15 \times 10^3$ |
| | 16.51 ± 0.26 | 0.80 ± 0.02 | 0.59 ± 0.02 | 7.82 ± 0.26 | | | |
| Platinum | **16.96;** | **0.81;** | **0.60;** | **8.33;** | 0.345 | 14.2 | – |
| | 16.77 ± 0.47 | 0.81 ± 0.00 | 0.60 ± 0.01 | 8.13 ± 0.21 | | | |

Average values and the error bars are calculated based on five cells and samples. Parameters of the best cells are highlighted in bold. $E_{pp}$: peak-to-peak voltage separation was calculated from the CV measurements. $R_{ct}$: charge-transfer resistances were obtained from the EIS analysis by fitting the measured EIS data to a modeled equivalent circuit diagram. $R_{sheet}$: sheet resistances were measured using a four-point probe technique.

the mechanism for this low current density value of the $FeS_2$, we explored the sheet resistance ($R_{sheet}$) of the thin films based on our samples using a four point probe and their results are summarized in Table 1. We confirm that a very high $R_{sheet}$ ($1.50 \pm 0.09 \times 10^6$ Ω/□) of the $FeS_2$ is responsible for its low current density. Because of its improved electrical conductivity (see Table 1), the SGN–$FeS_2$ hybrid electrocatalyst-based electrode exhibited a high peak current density. Higher peak current density and lower $E_{pp}$ values (see Figure 2a) suggest that the SGN–$FeS_2$ hybrid electrocatalyst possess excellent electrochemical activity for the IRR, which is even comparable and/or superior to that of Pt electrode. Moreover, it can be observed from SI Figure S4 that our SGN–$FeS_2$ hybrid is electrochemically stable in tri-iodide electrolyte.

Electrochemical impedance spectroscopy (EIS) is another important technique to understand the capacity of CE materials to catalyze the IRR in DSSCs. EIS were recorded for the dummy cells consisting of a symmetrical sandwich structure (electrode/($I^-/I_3^-$ electrolyte)/electrode) with SGN, $FeS_2$, SGN–$FeS_2$ hybrid, and Pt as electrodes. The Nyquist plots shown in Figure 2b are obtained by fitting the measured EIS data to a modeled equivalent circuit diagram. Typical modeled equivalent circuit diagrams used for Pt and carbon-based CEs are illustrated in the inset of Figure 2b. A typical Nyquist plot for CE materials for the IRR consists of two semi-circles.[32,33,35] The lower Z′ semicircle is attributed to the $R_{ct}$, which originates from the interface between CEs and electrolyte; whereas the higher Z′ semicircle is related to ionic diffusion impedance ($Z_N$) of the redox couples in the electrolyte.[33] Since $R_{ct}$ directly reflects to the performance of the electrocatalyst materials, the measured $R_{ct}$ values of the SGN, $FeS_2$, SGN–$FeS_2$ hybrid, and Pt cells are listed in Table 1. Due to the combination of excellent conductivity and high catalytic activity, the SGN–$FeS_2$ hybrid electrocatalyst exhibited the smallest $R_{ct}$ value (11.2 Ω), which was even slightly lower than that of Pt (14.2 Ω) and significantly lower than the values for SGN (22.3 Ω) and $FeS_2$ (39.8 Ω). The EIS results were in good agreement with the CV results. Overall, the electrochemical characterization (CV and EIS analysis) clearly indicates that our SGN–$FeS_2$ electrocatalyst could be used as a promising alternative CE to catalyze the IRR in DSSCs. Therefore, as compared to the Pt CE-based devices, we expected to achieve comparable or even higher PV performance for DSSCs using this hybrid electrocatalyst-based CEs.

As mentioned earlier, good CE materials should have both high catalytic activity and excellent electrical conductivity to efficiently catalyze the redox reaction and rapidly transfer the electrons in DSSCs.[7] Since our findings from the electrochemical and electrical characterization suggest that the SGN possesses excellent conductivity and $FeS_2$ has high catalytic activity, the amount (loadings) of SGN or $FeS_2$ in the hybrid would play an important role for the DSSC performance. There is clearly an optimum concentration of SGN or $FeS_2$ in the hybrid. Therefore, based on DSSC efficiencies, we optimized the concentration of the SGN or $FeS_2$ in the hybrid CEs for DSSCs and found that 60 wt.% SGN and 40 wt.% $FeS_2$ in the hybrid are the optimum loadings (see **Figure 3**a).

Furthermore, DSSC devices were fabricated using the four electrocatalysts, namely SGN, $FeS_2$, SGN–$FeS_2$, and Pt as CE materials. The photocurrent density–voltage ($J$–$V$) characteristics of the DSSCs fabricated with these CEs are illustrated in Figure 3b and the corresponding PV parameters have been summarized in Table 1. The control DSSC fabricated with the conventional Pt CE showed a PCE as high as 8.3% with a short-circuit current ($J_{sc}$) of 16.96 mA cm$^{-2}$, open-circuit voltage ($V_{oc}$) of 0.81 V and fill factor (FF) of 0.60. As expected, the PCEs of single SGN-only (6.79%) and $FeS_2$-only (5.51%) based DSSCs are significantly lower than the conventional Pt CE-based devices. The lower PCE of the DSSCs with SGN-only, as compared to the Pt-based cells, is mainly due to the lack of electrocatalytic activity, while the poor conductivity of $FeS_2$ is responsible for its poor PV efficiency. By coupling both excellent conductivity of SGN and high catalytic activity of $FeS_2$, the cell fabricated with the SGN–$FeS_2$ hybrid-based CE showed a notable enhancement in the PCE as compared to the efficiencies of single SGN-only and $FeS_2$-only based DSSCs. In particular, the measured $J_{sc}$, $V_{oc}$, and FF values for this hybrid CE-based DSSC were 16.43 mA cm$^{-2}$, 0.82 V, and 0.60, respectively, and a PCE of 8.1% was achieved. The results of PV performances were in line with our electrochemical characterization (CV and EIS). More importantly, this impressive PCE (8.1%), achieved by the SGN–$FeS_2$ hybrid electrocatalyst-based DSSC, was comparable to that (8.3%) of the expensive Pt electrocatalyst-based device.

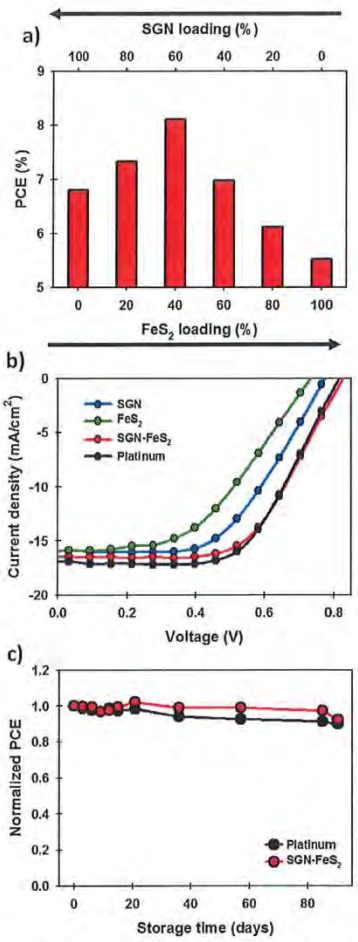


**Figure 3.** (a) Influence of SGN and $FeS_2$ loadings in the hybrid on the efficiency of the DSSCs. (b) *J–V* curves of best performing DSSCs fabricated with different CEs. (c) Normalized PCE of DSSCs fabricated with SGN–$FeS_2$ and Pt as a function of long-term storage time in ambient conditions.

The stability of PV devices is one of the most critical factors for their potential commercialization on an industrial scale. For the storage-stability test, the unencapsulated DSSC devices fabricated with SGN–$FeS_2$ and Pt CEs were kept in ambient conditions for 90 days. Normalized PCEs of these two devices are plotted in Figure 3c. It can be seen from Figure 3c that the SGN–$FeS_2$ hybrid CE-based DSSC showed excellent storage-stability (more than 90% of initial PCE after 90 days of storage was retained), comparable to the stability of the Pt-based cell. This excellent stability of our SGN–$FeS_2$ hybrid-based DSSC confirms the good electrochemical stability explored using CV measurements (see SI Figure S4) of this electrocatalyst.

In summary, in this work, a series of heteroatom (I, P, B, N, S)-doped graphene materials have been prepared and employed as CE materials to catalyze the IRR in DSSCs. We found based on the electrochemical characterization and PV analysis that the elemental S-doping on graphene is the most effective in improving the electrocatalytic activity among other types of doping atoms. Of particular note, however, is the combination of this material with $FeS_2$ yielded a CE material whose electrocatalytic activity and electrochemical stability is comparable to that of the standard Pt-based CE. The combination of high electrocatalytic activity, good electrical conductivity, outstanding electrochemical stability, and impressive device performance of the SGN–$FeS_2$ hybrid electrocatalyst makes this material an ideal candidate for highly efficient and stable DSSCs.

## Supporting Information

Additional supporting information may be found in the online version of this article at the publisher's website.

## Acknowledgements

The support of the Australian Research Council Discovery Program (DP130101714, DP150101354, and DP160101301) is gratefully acknowledged. Munkhbayar Batmunkh acknowledges International Postgraduate Research Scholarship (IPRS) and Australian Postgraduate Award (APA) for their financial support during his study in Australia. We acknowledge the use of South Australian nodes of the Australian Microscopy & Microanalysis Research Facility (AMMRF) and the Australian National Fabrication Facility (ANFF) at Flinders University. The authors would also like to thank Jade Taylor and Yanting Yin of School of Chemical and Physical Sciences at Flinders University for their help with the XPS analysis.

Received: January 19, 2017
Revised: February 21, 2017
Published online: March 9, 2017

[1] Zhang, S., Yang, X., Numata, Y., Han, L., *Energy Environ. Sci.* **2013**, *6*, 1443.
[2] Batmunkh, M., Biggs, M. J., Shapter, J. G., *Adv. Sci.* **2015**, *2*, 1400025.
[3] Ye, M., Wen, X., Wang, M., Iocozzia, J., Zhang, N., Lin, C., Lin, Z., *Mater. Today* **2015**, *18*, 155.
[4] Hwang, S., Batmunkh, M., Nine, M. J., Chung, H., Jeong, H., *ChemPhysChem* **2015**, *16*, 53.
[5] Briscoe, J., Dunn, S., *Adv. Mater.* **2016**, *28*, 3802.
[6] Janani, M., Srikrishnarka, P., Nair, S. V., Nair, A. S., *J. Mater. Chem. A* **2015**, *3*, 17914.
[7] Wang, H., Hu, Y. H., *Energy Environ. Sci.* **2012**, *5*, 8182.
[8] Thomas, S., Deepak, T. G., Anjusree, G. S., Arun, T. A., Nair, S. V., Nair, A. S., *J. Mater. Chem. A* **2014**, *2*, 4474.
[9] Batmunkh, M., Biggs, M. J., Shapter, J. G., *Small* **2015**, *11*, 2963.
[10] Yun, S., Hagfeldt, A., Ma, T., *Adv. Mater.* **2014**, *26*, 6210.

[11] Zhang, J., Yu, M., Li, S., Meng, Y., Wu, X., Liu, J., *J. Power Sources* **2016**, *334*, 44.
[12] Wang, H., Sun, K., Tao, F., Stacchiola, D. J., Hu, Y. H., *Angew. Chem. Int. Ed.* **2013**, *52*, 9210.
[13] Munkhbayar, B., Nine, M. J., Jeoun, J., Ji, M., Jeong, H., Chung, H., *J. Power Sources* **2013**, *230*, 207.
[14] Luo, Q., Hao, F., Wang, S., Shen, H., Zhao, L., Li, J., Grätzel, M., Lin, H., *J. Phys. Chem. C* **2014**, *118*, 17010.
[15] Meng, X., Yu, C., Song, X., Liu, Y., Liang, S., Liu, Z., Hao, C., Qiu, J., *Adv. Energy Mater.* **2015**, *5*, 1500180.
[16] Fang, H., Yu, C., Ma, T., Qiu, J., *Chem. Commun.* **2014**, *50*, 3328.
[17] Wang, Z., Li, P., Chen, Y., He, J., Liu, J., Zhang, W., Li, Y., *J. Power Sources* **2014**, *263*, 246.
[18] Kannan, A. G., Zhao, J., Jo, S. G., Kang, Y. S., Kim, D.-W., *J. Mater. Chem. A* **2014**, *2*, 12232.
[19] Yu, D., Nagelli, E., Du, F., Dai, L., *J. Phys. Chem. Lett.* **2010**, *1*, 2165.
[20] Yang, Z., Yao, Z., Li, G., Fang, G., Nie, H., Liu, Z., Zhou, X., Chen, X. a., Huang, S., *ACS Nano* **2012**, *6*, 205.
[21] Jiao, Y., Zheng, Y., Jaroniec, M., Qiao, S. Z., *J. Am. Chem. Soc.* **2014**, *136*, 4394.
[22] Wang, Y.-C., Wang, D.-Y., Jiang, Y.-T., Chen, H.-A., Chen, C.-C., Ho, K.-C., Chou, H.-L., Chen, C.-W., *Angew. Chem. Int. Ed.* **2013**, *52*, 6694.
[23] Huang, Q.-H., Ling, T., Qiao, S.-Z., Du, X.-W., *J. Mater. Chem. A* **2013**, *1*, 11828.
[24] Shukla, S., Loc, N. H., Boix, P. P., Koh, T. M., Prabhakar, R. R., Mulmudi, H. K., Zhang, J., Chen, S., Ng, C. F., Huan, C. H. A., Mathews, N., Sritharan, T., Xiong, Q., *ACS Nano* **2014**, *8*, 10597.
[25] Zhang, M., Chen, B., Tang, H., Tang, G., Li, C., Chen, L., Zhang, H., Zhang, Q., *RSC Adv.* **2015**, *5*, 1417.
[26] Xue, H., Yu, D. Y. W., Qing, J., Yang, X., Xu, J., Li, Z., Sun, M., Kang, W., Tang, Y., Lee, C.-S., *J. Mater. Chem. A* **2015**, *3*, 7945.
[27] Wang, L., Shi, Y., Zhang, H., Bai, X., Wang, Y., Ma, T., *J. Mater. Chem. A* **2014**, *2*, 15279.
[28] Zhou, H., Yin, J., Nie, Z., Yang, Z., Li, D., Wang, J., Liu, X., Jin, C., Zhang, X., Ma, T., *J. Mater. Chem. A* **2016**, *4*, 67.
[29] Meng, X., Yu, C., Song, X., Liu, Z., Lu, B., Hao, C., Qiu, J., *J. Mater. Chem. A* **2017**, *5*, 2280.
[30] Mei, L., Zhao, H., Lu, B., *Adv. Sci.* **2015**, *2*, 1500116.
[31] Shrestha, A., Batmunkh, M., Shearer, C. J., Yin, Y., Andersson, G. G., Shapter, J. G., Qiao, S., Dai, S., *Adv. Energy Mater.* **2017**, *7*, 1602276.
[32] Cui, X., Xiao, J., Wu, Y., Du, P., Si, R., Yang, H., Tian, H., Li, J., Zhang, W.-H., Deng, D., Bao, X., *Angew. Chem. Int. Ed.* **2016**, *55*, 6708.
[33] Bi, E., Chen, H., Yang, X., Peng, W., Gratzel, M., Han, L., *Energy Environ. Sci.* **2014**, *7*, 2637.
[34] Duan, Y., Tang, Q., Liu, J., He, B., Yu, L., *Angew. Chem. Int. Ed.* **2014**, *53*, 14569.
[35] Xue, Y., Liu, J., Chen, H., Wang, R., Li, D., Qu, J., Dai, L., *Angew. Chem. Int. Ed.* **2012**, *51*, 12124.

# Appendix D

Journal of Materials Chemistry A

PAPER

View Article Online



Cite this: J. Mater. Chem. A, 2016, 4, 2605

# Solution processed graphene structures for perovskite solar cells†

Munkhbayar Batmunkh,[ab] Cameron J. Shearer,[b] Mark J. Biggs[ac] and Joseph G. Shapter*[b]

Organometallic trihalide perovskite light absorber based solar cells have drawn increasing attention because of their recent rapid increase in power conversion efficiency (PCE). These photovoltaic cells have relied significantly on transparent conducting oxide (TCO) electrodes which are costly and brittle. Herein, solution processed transparent conductive graphene films (TCGFs) are utilized, for the first time, as an alternative to traditional TCO electrodes at the electron collecting layer in perovskite solar cells (PSCs). By investigating and optimizing the trade-off between transparency and sheet resistance ($R_s$) of the graphene films, a PCE of 0.62% is achieved. This PCE is further improved to 0.81% by incorporating graphene structures into both compact and mesoporous $TiO_2$ layers of the solar cell. We anticipate that the present study will lead to further work to develop graphene-based transparent conductive electrodes for future solar cell devices.

Received 7th November 2015
Accepted 22nd January 2016

DOI: 10.1039/c5ta08996d

www.rsc.org/MaterialsA

## Introduction

Photovoltaic (PV) cells are devices that convert sunlight directly into electrical power and have great potential to meet society's continuously increasing energy demands with negligible environmental impact.[1] The current PV market is mainly dominated by crystalline silicon (1st generation) and compound semiconductor (2nd generation) based solar cells, which can produce energy with a power conversion efficiency (PCE) that is the highest of all solar cell technologies.[2,3] These commercially available solar devices are, however, produced using complex, high-cost manufacturing processes. Recently reported solar cells based on hybrid organometallic halide perovskites are considered the most promising alternatives to the more established solar cell technologies because of their relatively high PCE, and simpler, cheaper fabrication processes.[4–7]

Organic–inorganic halide structures (such as $CH_3NH_3PbX_3$ (X = Cl, I or Br)), called perovskite materials, have been known for several decades and have recently attracted much attention from the PV community owing to some key exceptional properties.[8] These properties include the ability to absorb significant levels of incident light across a wide part of the solar spectrum, and the ability to effectively carry the photoelectrons created from the incident light away into a circuit.[9] The PCE of perovskite solar cells (PSCs) has rapidly increased from less than 4% to more than 20% in only 6 years,[10–13] making the efficiency comparable with current commercial technologies.[12,13]

A typical PSC is composed of a transparent conducting oxide (TCO) (indium-doped and/or fluorine-doped tin oxide (ITO or FTO)) electrode, a thin compact hole blocking ($TiO_2$) layer, a perovskite layer with or without a porous metal oxide scaffold layer, a hole transporting layer (HTL) and a metal contact (Au or Ag).[11,14,15] In such a device structure, the TCO electrode plays a vital role in collecting electrons from the semiconducting $TiO_2$ and transferring them to the external circuit. However, limited resources of the materials used in typical TCO electrodes and consequent high cost are major issues.[16] Additionally, their brittle nature and high structural defects are a major concern for PSC technologies where ease of transportation, handling and installation are important.[17] Therefore, the replacement of TCO electrodes with cheaper and robust alternatives is desirable.

Graphene has attracted considerable interest for potential applications in various optoelectronic devices due to its properties including excellent conductivity, low cost and high flexibility.[18,19] Moreover, compared to ITO and FTO, graphene has several advantages such as abundance, high transparency in the near-infrared region and high stability in the presence of acid or base.[16,20] These unique properties suggest graphene films could be a possible replacement for TCO electrodes. To date, two main processes have been developed for the fabrication of graphene films.[21] The first is based on chemical vapor deposition (CVD) of graphene using a metal sheet catalyst (Cu or Ni), followed by

[a]School of Chemical Engineering, The University of Adelaide, Adelaide, South Australia 5005, Australia
[b]Centre for Nanoscale Science and Technology, School of Chemical and Physical Sciences, Flinders University, Bedford Park, Adelaide, South Australia 5042, Australia. E-mail: joe.shapter@flinders.edu.au; Tel: +61 8 82012005
[c]School of Science, Loughborough University, Loughborough, Leicestershire, LE11 3TU, UK

† Electronic supplementary information (ESI) available. See DOI: 10.1039/c5ta08996d

transfer printing to target substrates. However, CVD is expensive and its operation is complicated while it also requires high temperatures (>750 °C). Alternatively, solution processed graphene has been considered a promising future electrode material because it can be deposited on large-area flexible substrates and is compatible with roll-to-roll manufacturing techniques.[22] Based on these advantages, solution processed graphene films have been used as transparent electrodes for inorganic–organic hybrid solar cells,[23,24] organic photovoltaic cells[25,26] and dye-sensitized solar cells (DSSCs).[27] In addition, CVD processed-graphene based transparent conductive films have very recently been employed as hole collecting electrodes in PSCs even though they are costly and difficult to produce.[28,29] However, until now, there has been no effort in the application of graphene based transparent and conductive films to replace traditional TCO electrodes in PSCs despite recent reviews[30,31] and a computational study[32] suggesting some promise.

In the work reported here, transparent conductive graphene films (TCGFs) prepared from low-temperature processed and chemically derived graphene (or solution processed graphene, Scheme 1) have been employed as a substitute for the electron collecting TCO electrode to test their feasibility in PSCs. Furthermore, the incorporation of graphene structures into semiconducting oxide scaffolds has been shown to be a promising strategy to enhance the efficiency in DSSCs.[33] After optimizing sheet resistance ($R_s$) and light transmittance for PSC performance, we further improved the PCE by employing graphene into both compact and mesoporous $TiO_2$ layers of the devices.

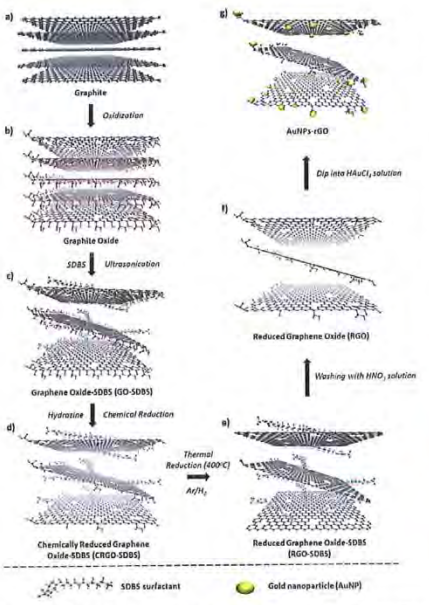


Scheme 1 Schematic of the preparation procedure of graphene films.

## Results and discussion

### Preparation and characterization of graphene films

Graphite oxide was synthesized from natural graphite by an improved Hummers method[34] followed by exfoliation to produce graphene oxide (GO) sheets (Scheme 1a–c). A detailed description of the process is given in the experimental section. The prepared GO is known to be electrically non-conductive and the removal of its functional groups is necessary to obtain conductive graphene-based materials.[17] In general, GO can be reduced by using chemical agents such as hydrazine or sodium borohydride.[35] However, the insolubility of the GO after such chemical reduction limits its further application. In order to tackle this limitation; we added sodium dodecylbenzene sulfonate (SDBS) surfactant into the graphite oxide solution before the exfoliation step (Scheme 1c).[36,37]

In a typical experiment, large-area GO with or without SDBS surfactant was produced by the exfoliation of the previously prepared graphite oxide solution (Scheme 1c). It should be noted that the prepared GO aqueous dispersion was very stable without any precipitation for several months, which is known to be due to the presence of hydrophilic groups (*e.g.*, hydroxyl, epoxy, or carboxyl) on the surface of graphene.[21] Subsequently, the chemical reduction of GO aqueous solution was carried out with hydrazine solution in the presence of SDBS. For comparison, the same procedure was also performed in the absence of SDBS. Chemically reduced graphene oxide (CRGO-only) without surfactant disperses poorly in aqueous conditions because of its hydrophobic surface after the removal of oxygen containing functional groups during the reduction process.[23] Subsequently, strong π–π interaction between CRGO flakes leads to agglomeration and poor dispersion (inset of Fig. 1a). The atomic force microscopy (AFM) image (Fig. 1a) shows that the CRGO-only flakes without SDBS are aggregated or stacked on each other and their lateral size was measured to be smaller

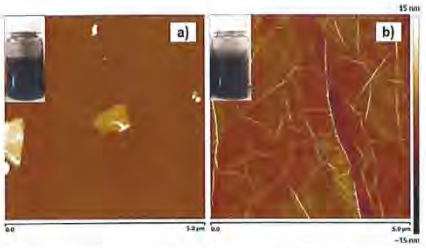


Fig. 1 AFM images (5 × 5 $\mu m^2$) of chemically reduced graphene oxide (CRGO) (a) without and (b) with SDBS. Insets show digital photographs of the corresponding samples in an aqueous 1 mg $mL^{-1}$ solution.

than 1 μm, which is consistent with the results reported in the literature.[38,39] In contrast, the SDBS supported CRGO (Scheme 1d, termed "CRGO-SDBS") showed dramatically improved dispersion in aqueous solution. As illustrated in the inset of Fig. 1b, no precipitate was observed and the solution was stable for several months. More importantly, the flake size of the CRGO-SDBS (Fig. 1b) was significantly larger than that of CRGO-only (Fig. 1a).[40] It is known that sonication and conventional chemical reduction steps of GO create many structural defects, decrease the flake size and increase the degree of $sp^3$ hybridization.[21] Interestingly, in this study, the SDBS acts to prevent CRGO from fracturing during ultrasonication resulting in large-size graphene sheets. The large-sized graphene structures should, in principle, exhibit lower $R_s$ when used in transparent conductive films because the larger flakes will have less charge scattering related to charge hopping through sheet–sheet contacts in the film.[41,42]

Structural information for these samples was obtained using Raman spectroscopy. It is well known that the intensity ratio ($I_D$/$I_G$) is usually used to determine the level of defects.[43] Raman spectra (see Fig. S1†) shows that the $I_D/I_G$ value of the CRGO–SDBS is lower than that of the CRGO without surfactant, confirming that the chemical (hydrazine) reduction of GO in the presence of SDBS creates less defects on the CRGO compared to the number produced without any surfactant present. Although the use of SDBS during the chemical reduction process has the additional advantage of preventing defect production in the CRGO and providing large graphene sheets, the presence of residual SDBS surfactant may degrade the electrical properties of the graphene films because of its highly insulating nature.[36] Therefore, removing SDBS surfactant from the prepared films is of great importance for maximizing the electrical conductivity of the films. In addition, it is well known that the chemical reduction with hydrazine alone is not sufficient to fully reduce the oxygen containing functional groups from the graphene layers.[44]

In order to improve the quality of graphene structures, the films were prepared from the CRGO-SDBS solution using a vacuum-filtration and transfer technique[44] and have been thermally annealed at a temperature of 400 °C under the protection of an Ar and $H_2$ gas flow. Interestingly, we observed that the filtration time for the CRGO-SDBS solution was relatively longer than that for the CRGO-only samples. We attribute this phenomenon to the size of the graphene sheets with the larger CRGO-SDBS sheets blocking the filter paper pores faster. After the thermal annealing of CRGO-SDBS film, the resultant product (Scheme 1e) is denoted "RGO-SDBS".

The extent of reduction of the prepared samples was studied by attenuated total reflection-Fourier transform infrared spectroscopy (ATR-FTIR) and X-ray photoelectron spectroscopy (XPS). ATR-FTIR spectra of GO, CRGO-only, CRGO-SDBS and RGO-SDBS are presented in Fig. 2a. All the observed peaks can be ascribed to O–H stretching mode, C=O carboxyl or carbonyl stretching vibration, C=C stretching, O–H deformations in the C–OH groups, C–OH stretching and C–O stretching vibrations in C–O–C in epoxide from GO.[34] After chemical reduction, the peak intensities of the oxygen containing functional groups in

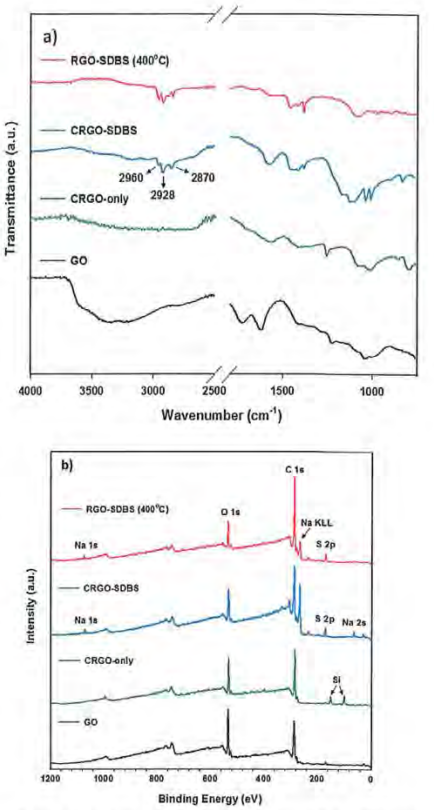


Fig. 2 (a) ATR-FTIR and (b) XPS survey spectra of GO, CRGO-only, with SDBS and thermally reduced CRGO–SDBS (RGO–SDBS).

both CRGO-only and CRGO–SDBS become very weak compared to that of GO, but not completely gone, indicating that only partial reduction of GO was obtained using hydrazine monohydrate solution (Scheme 1d). However, the CRGO–SDBS exhibits new prominent characteristic peaks at 2960 $cm^{-1}$, 2928 $cm^{-1}$ and 2870 $cm^{-1}$ which correspond to C–H vibrations in SDBS. These absorption peaks in the CRGO–SDBS sample indicates that the SDBS is adsorbed on the CRGO.[40] After thermal annealing, the majority of oxygen peaks associated with the functional groups in CRGO–SDBS became very weak, confirming the successful reduction of the GO by the combination of chemical and thermal processes (Scheme 1e, confirmed by curve fitting of C 1s peaks in XPS spectra shown in Fig. S2†). However, the absorption peaks due to the presence of SDBS remain unchanged after annealing at 400 °C for 1 h. This result

suggests that the insulating SDBS was not removed by the low-temperature thermal treatment.

XPS survey spectra of CRGO–SDBS and RGO–SDBS (Fig. 2b) show peaks (in addition to 283.5 eV (C 1s) and 530.5 eV (O 1s)) at binding energies of around 166 eV (S 2p), 262 eV (Na KLL) and 1059.5 eV (Na 1s), further illustrating that the SDBS remains on the CRGO structure after annealing at 400 °C. Nevertheless, it should be noted that the peak intensities of both ATR-FTIR and XPS for CRGO–SDBS structure decreased slightly after annealing at 400 °C. Another noticeable feature from the XPS survey spectra in Fig. 2b is that the appearance of Si 2s and Si 2p peaks at around 99.0 eV and 149.5 eV, respectively for the CRGO without SDBS. These Si peaks can be explained by the poor solubility of the CRGO solution. Due to the large aggregation of CRGO in the solvent, the CRGO sample did not completely cover the silicon substrate. Additionally, the thermal stability of SDBS was investigated using thermo-gravimetric analysis (TGA) (see Fig. S3†). Our finding from TGA analysis was in good agreement with the ATR-FTIR and XPS and suggests that the thermal annealing at 400 °C cannot remove the residual surfactants from the graphene. Therefore, further treatment is required to completely remove the SDBS.

According to previous studies,[45–48] the application of concentrated acid solution can be an effective way to completely remove the residual SDBS surfactant and other organic contaminants from the graphene films. Therefore, we used concentrated nitric acid ($HNO_3$, 68%) solution (Scheme 1f). It is widely accepted that the use of $HNO_3$ has the advantage of not only eliminating the insulating surfactant, it also enhances the electrical properties of carbon films by an oxidative doping effect.[49,50] In addition to these effects, chemical $HNO_3$ treatment can also cause some weak edge defects with oxygen containing functional groups (see Scheme 1f, termed as "RGO"),[45,51,52] which could be very useful for further treatment to maximize the film performance. In order to produce high-performance graphene films, we also introduced metallic gold nanoparticles (AuNPs) onto our RGO by dipping $HNO_3$-functionalized RGO films into $HAuCl_4$ solution (Scheme 1g, called "AuNPs–RGO"). The removal of SDBS and the deposition of AuNPs of the RGO films were characterized by using XPS, scanning electron microscopy (SEM) and energy-dispersive X-ray spectroscopy (EDX).

Fig. 3a shows that the peaks of RGO–SDBS sample at binding energy of 166 eV (S 2p), 262 eV (Na KLL) and 1059.5 eV (Na 1s) have disappeared after treatment with $HNO_3$ and $HAuCl_4$ solutions, indicating of successful removal of the surfactant from the RGO. Additionally, in Fig. 3a, the appearance of two new prominent peaks at around 83.5 eV (Au 4f) and 200 eV (Cl 2p) indicates the successful AuNPs deposition and some residual $HAuCl_x$. Moreover, the SEM image (inset of Fig. 3a) clearly shows that the AuNPs were formed on the RGO after dipping the partially functionalized RGO film (Scheme 1f) into $HAuCl_4$ solution. It is worth noting that the deposition of AuNPs on the RGO was achieved without the assistance of any reducing agents due to the $HNO_3$ post-treatment. Therefore the edge defects ($OH^-$, $COOH^-$ *etc.*) in RGO introduced by $HNO_3$ treatment play an important role in reducing $Au^{3+}$ to $Au^0$.[52,53] Moreover, the EDX elemental analysis (Fig. 3b) was carried out

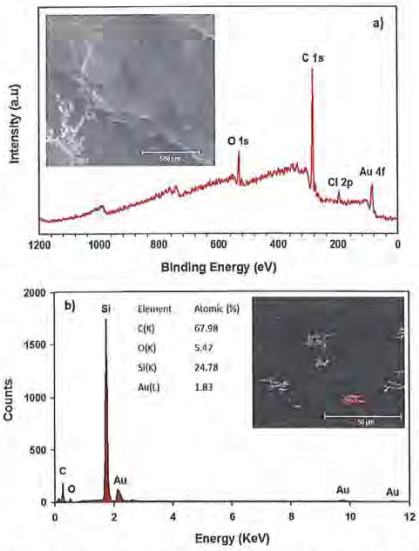


Fig. 3 (a) XPS survey spectra (inset: SEM image of AuNPs–RGO) and (b) EDX analysis (red box in the inset is the selected area for analysis) of RGO–SDBS film after $HNO_3$ and $HAuCl_4$ treatments.

on the selected area of SEM image of the prepared sample and further confirms the removal of residual SDBS from the RGO and the formation of AuNPs on the RGO films.

### Optical and electrical properties of the graphene films

An ideal PV device – one with the highest PCE – is achieved by having the lowest sheet resistance of the TCF, $R_s$, while achieving the highest transparency. Thin graphene films can exhibit high optical transparency, but they suffer from relatively high $R_s$. The $R_s$ can be reduced by making the graphene films thicker, but this leads to an increase in the film opacity. There is clearly an optimum film thickness. We sought this thickness by changing the volume of filtered CRGO–SDBS solution. Fig. 4a illustrates the $R_s$ of graphene films prepared from four different structures plotted as a function of filtration volume. These graphene structures are (a) CRGO–SDBS films (Scheme 1d), (b) RGO–SDBS films (Scheme 1e), (c) RGO films (Scheme 1f, $HNO_3$-treated), and (d) AuNPs–RGO films (Scheme 1g). Additionally, the wavelength-dependent optical transparencies of each film with different thicknesses and their corresponding $R_s$ values are shown in Fig. S4.† It can be seen from Fig. S4a† that the transparency of the films decreased with increasing filtered volume of the RGO solution. As shown in Fig. 4a, the $R_s$ of our CRGO–SDBS films were in the range from 2 MΩ $sq^{-1}$ to 12 MΩ $sq^{-1}$ depending on the thickness. Interestingly, these $R_s$ values are found to be slightly lower than that of previously reported

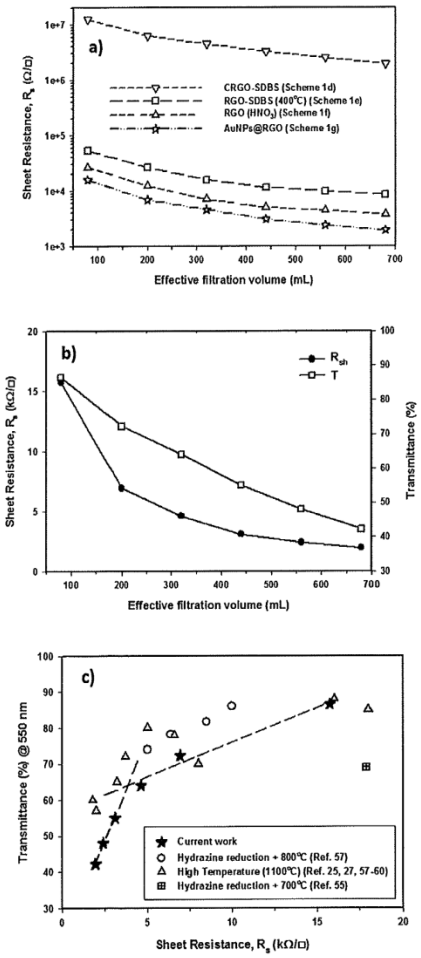


Fig. 4 (a) $R_s$ *vs.* thickness of the graphene films prepared from four different structures; (b) $R_s$ and transmittance (at $\lambda$ = 550 nm) of selected TCGFs with different thicknesses; (c) comparison of $R_s$ as a function of transmittance (at $\lambda$ = 550 nm) between our AuNPs–RGO films and other studies. Dash lines show the two regions of differing resistance for the graphene films and the threshold transmittance and corresponding $R_s$.

chemically reduced GO films,[44,54,55] despite our films containing insulating SDBS. We attribute this better performance of our CRGO–SDBS films to the production of large-size graphene sheets.[40] Although our CRGO–SDBS films showed lower $R_s$ compared to other studies, such $R_s$ values are still too high for satisfactory solar devices.

As also demonstrated in Fig. 4a, the $R_s$ of CRGO–SDBS film decreased by more than 2 orders of magnitude for a given thickness after the thermal treatment. This improvement in the electrical properties is known to be due to the better graphitization, deoxygenation and cross-linking of the graphene sheets.[27,39] However, the thermal reduction of the CRGO–SDBS film reduced the transparency by 4–5% (Fig. S4b†). The darkening of the films after thermal annealing is due to the restoration of the π-electron system in the graphene structure and some impurities from the re-deposition of carbonaceous material which desorbs during thermal treatment and then adsorbs on both sides of the substrate.[55] Although residual insulating SDBS is still present in the film after thermal treatment, we were able to achieve a $R_s$ of as low as 8.5 kΩ $sq^{-1}$ using this film such as that shown in Scheme 1e. Therefore, the removal of the SDBS surfactants with $HNO_3$ was expected to improve the performance of our films.

As expected, the $R_s$ of the RGO–SDBS films were significantly reduced (by more than 2-fold) after treating with concentrated $HNO_3$ (see Fig. 4a). This dramatic improvement in the electrical properties is most likely due to the removal of any remaining SDBS from the film. Another possible reason behind the enhanced conductivity is the chemical doping effect of $HNO_3$ on graphene films.[17,49,56] In particular, the $R_s$ value of the RGO–SDBS films was reduced from 8.5 kΩ $sq^{-1}$ to 3.74 kΩ $sq^{-1}$ at the same thickness after treating with $HNO_3$ solution. More importantly, the $HNO_3$ treatment not only enhanced the electrical conductivity of the films, it also increased the transparency by around 5% for any given thickness (Fig. S4c†). The increase in the transparency of the films after washing with $HNO_3$ could be ascribed to the removal of remaining impurities of the films, particularly on the underside of the glass.

After depositing the AuNPs on RGO films, the $R_s$ and transmittance of the dried films were measured. Fig. 4a shows that the $R_s$ of RGO films decreased by about 1.8 times after introducing AuNPs onto the films, while no degradation in transmittance was observed (Fig. S4d†) compared to the $HNO_3$-treated RGO films. The improved conductivity could be due to the fact that the AuNPs deposited on RGO created bridges between adjacent sheets, both in-plane and out-of-plane. A low electrical conductivity of graphene film mainly arises from the high inter-sheet contact resistance (deriving from charge hopping) between the edges of graphene sheets.[41] In our AuNPs deposited RGO films, the AuNPs play a vital role in conjugating adjacent graphene sheets and subsequently reducing the overall $R_s$ of the film.

The correlation of $R_s$ and transmittance at $\lambda$ = 550 nm of our AuNPs–RGO films to their volume of filtered solution is depicted in Fig. 4b. Through the systematic treatments, we obtained an $R_s$ of as low as 1.96 kΩ $sq^{-1}$ for the thick graphene film with transmittance of 42.3%. In contrast, a high optical transparency of 86.6% was achieved for the thin film, but its $R_s$ is 15.7 kΩ $sq^{-1}$. It should be noted that our $R_s$ values are comparable to previous reports of solution processed graphene films produced by using hydrazine reduction and high-temperature annealing

process (800–1100 °C) (Fig. 4c).[25,27,55,57–61] Therefore, these TCGFs exhibit great potential for use as transparent electrodes in PV devices. The films based on AuNPs–RGO structures such as that illustrated in Scheme 1g have been chosen for the fabrication of PSC devices. Moreover, we calculated a figure of merit ($\sigma_{DC}/\sigma_{OP}$) for these TCGFs (Table 1) and the film with $R_s$ = 3.08 kΩ sq$^{-1}$ at $T$ = 55% showed a high figure of merit (0.176). This $\sigma_{DC}/\sigma_{OP}$ value was higher than that of thinner films, which is expected to correlate with high performance of solar cells.

### Fabrication and characterization of PV devices

**Transparent graphene electrodes based PSCs.** To investigate the suitability of our TCGFs as transparent electrodes in PV devices, $CH_3NH_3PbI_{3-x}Cl_x$ perovskite sensitizer based solar cells were fabricated on the graphene films. The layered structure of the device is displayed in Fig. 5a. In our devices, a thin $TiO_2$ compact layer was used as blocking layer to suppress the possible charge recombination between the graphene anode and the hole transporting material (HTM). Spiro-OMeTAD (HTM) was used as electron blocking layer between the perovskite sensitizer and Au cathode. Mesoporous $TiO_2$ and $CH_3NH_3PbI_{3-x}Cl_x$ perovskite were employed as electron transporting layer and photosensitizer, respectively. In order to investigate the balance between transparency and $R_s$ of the graphene films, six PSC devices (device 1–6) were built on the TCGFs with different thicknesses (see Fig. 4b for properties). Digital photographs of the graphene films are also shown in Fig. 5a. The device number depends on the transparency and $R_s$ of the films. For example, the film with highest transparency and lowest $R_s$ based cell is denoted 'device 1' while the TCGF with lowest transparency and highest $R_s$ based PSC is denoted 'device 6'.

The photocurrent density–voltage ($J$–$V$) characteristics of the PSCs fabricated with different TCGFs are shown in Fig. 5b and the corresponding PV parameters such as open-circuit voltage ($V_{oc}$), short-circuit current density ($J_{sc}$), fill factor (FF) and PCE have been summarized in Table 1. The measured $V_{oc}$ values of all devices are essentially constant at 0.695 ± 0.05 V, indicating that the thickness of graphene films does not influence this parameter. This is reasonable since the $V_{oc}$ parameter is mainly determined by the energy level difference between the conduction band of electron transporting material and the potential energy of the HTM. In contrast, significant changes in the $J_{sc}$ and FF were observed. Because of its comparatively high $R_s$, device 1 showed the lowest $J_{sc}$ (0.56 mA cm$^{-2}$) and FF (0.25)

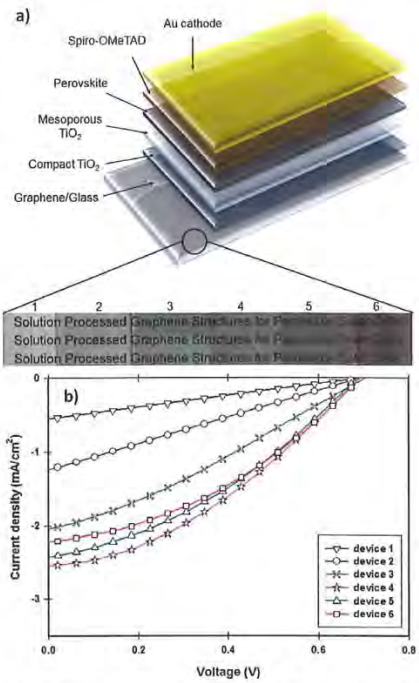


Fig. 5 (a) Device structure, (b) photocurrent density–voltage ($J$–$V$) curve of the fabricated solar cells with transparent graphene electrodes. PSC devices with 0.075 cm$^2$ active area were illuminated under AM 1.5G simulated sunlight (100 mW cm$^{-2}$).

values, despite the transparency of graphene film being quite high. Interestingly, the FF value of our PSCs continuously increased from device 1 to device 6, likely to be due to the improvement in the $R_s$ of the graphene films. Therefore the maximum FF value (0.37) was achieved for the device 6 which is made of our most-conductive graphene film with lowest transparency. However, the measured $J_{sc}$ value (2.21 mA cm$^{-2}$) of device 6 was not the highest observed. Unlike the FF parameter,

Table 1 PV parameters and PCE ($\eta$) of TCO-free PSCs with graphene films. Results for champion cells shown

| Device | $R_s$@$T$ | $\sigma_{DC}/\sigma_{OP}$ | $J_{sc}$ (mA cm$^{-2}$) | $V_{oc}$ (V) | FF | $\eta$ (%) |
|---|---|---|---|---|---|---|
| (1) (80 mL) | 15.7 kΩ sq$^{-1}$@86.6% | 0.161 | 0.56 | 0.692 | 0.25 | 0.1 |
| (2) (200 mL) | 6.93 kΩ sq$^{-1}$@72.3% | 0.154 | 1.25 | 0.695 | 0.26 | 0.23 |
| (3) (320 mL) | 4.61 kΩ sq$^{-1}$@64.1% | 0.164 | 2.02 | 0.700 | 0.29 | 0.41 |
| (4) (440 mL) | 3.08 kΩ sq$^{-1}$@55.0% | 0.176 | 2.55 | 0.690 | 0.35 | 0.62 |
| (5) (560 mL) | 2.41 kΩ sq$^{-1}$@48.0% | 0.176 | 2.43 | 0.690 | 0.36 | 0.60 |
| (6) (680 mL) | 1.96 kΩ sq$^{-1}$@42.3% | 0.177 | 2.21 | 0.694 | 0.37 | 0.57 |

no continuous increase was observed for the $J_{sc}$ value of our devices when the thickness of graphene films increases. In particular, from device 1 to device 4 (an increase in the thickness of graphene films), the $J_{sc}$ increases from 0.56 to 2.55 mA $cm^{-2}$ owing to the reduction of $R_s$. However, when the transmittance of the film drops below 55%, $J_{sc}$ of the cells decreases (device 5 & 6) despite the films having reduced $R_s$. This decrease in $J_{sc}$ is due to the absorption of incident light by the TCGF before it reaches the active perovskite layer. Indeed, the optimum PV parameters for the TCGFs-based PSC were achieved for the graphene film with 3.08 k$\Omega$ $sq^{-1}$@55.0%*T*. The observed $J_{sc}$, $V_{oc}$ and FF values for this PSC (device 4) were 2.55 mA $cm^{-2}$, 0.69 V and 0.35, respectively, yielding a power conversion efficiency of 0.62%.

For comparison, an FTO electrode based PSC device was also fabricated under the same conditions as devices 1–6 and its *J–V* curve is plotted in Fig. S5.† The FTO based device exhibited a $J_{sc}$ of 17.49 mA $cm^{-2}$, $V_{oc}$ of 0.71 V and FF of 0.63, yielding a PCE of 7.82%. It is obvious that the PCE of our graphene film-based PSCs is significantly lower to that of the control cell based on FTO. The major issues for our TCGFs based devices are relatively low $J_{sc}$ and lower FF values as compared to the cell based on FTO. This might be due to the high $R_s$ and poor optical transmittance of our graphene films. Although the PCE (0.62%) of our graphene electrode based device is far from that of the PSC fabricated with FTO, this efficiency value is higher than that achieved for previously published inorganic–organic hybrid solar cells[24] or DSSCs[37] in which graphene films act as the electron collection electrode. It should also be noted that the $V_{oc}$ value (0.71 V) and PCE achieved using our typical FTO based PSC is lower than recently reported values for standard cells using typical ITO or FTO transparent conducting electrodes.[62–64] The perovskite precursor and deposition process we have used were chosen for their simplicity in deposition and under the conditions we followed typically yield PCEs of 7–9% with low $V_{oc}$ (0.7–0.8 V)[65–67] which are consistent with our results using the standard transparent conducting electrodes. More importantly, here in this work, we demonstrate the feasibility of solution processed graphene films as alternatives to the traditional TCO electrodes in the state-of-the-art PSCs. We anticipate that significant improvement in the PCE can be made for this class of PV devices by enhancing the performance of the graphene films and/or using other solar cell architectures.

**Effect of graphene structures in the $TiO_2$ layers.** The use of carbonaceous materials in the semiconducting oxide scaffolds has previously led to great enhancement in the efficiency of DSSCs.[68,69] Therefore, in this work, we introduce this concept of incorporating graphene structures into the electron transporting $TiO_2$ layers of the mesoscopic PSCs to further improve the efficiency of our graphene electrode based device. The TCGF, which was previously used for the device 4 and gave the best PCE, was chosen for the fabrication of the graphene incorporated $TiO_2$ photoanode-based PSCs. In the fabricated device, the graphene structures were incorporated into the compact $TiO_2$ only, the mesoporous $TiO_2$ only and both the compact and mesoporous $TiO_2$ layers. The incorporated graphene was prepared by mixing GO (0.6 and 0.2% w/w in the compact layer and the mesoporous layer, respectively) with the $TiO_2$ precursors prior to deposition. The GO is then thermally reduced *in situ* when sintering the $TiO_2$ layers at 500 °C in an Ar atmosphere.

The *J–V* characteristics and device structures of the TCGFs based PSCs with and without graphene in the semiconducting oxide layers are illustrated in Fig. 6. The PV performances of these PSC devices have been summarized in Table 2. For comparison, the *J–V* curve and the corresponding energy level diagram of device 4 (TCGF based PSC without graphene in the semiconducting layer) is also plotted in Fig. 6a and a′, respectively. Since the work function of RGO is close to that of FTO, and lower than the conduction band of $TiO_2$,[25] it is reasonable to expect that the injected electrons at the $TiO_2$ conduction band can be transferred to the graphene electrode without any barrier. Changes to the work function of gold chloride doped graphene have previously been shown to be minimal after thermal annealing, as has been done in this work.[70]

On the other hand, the application of graphene in the semiconducting oxide layers should principally increase the efficiency of this class of solar cells due to enhanced charge transport.[71] However, as shown in Fig. 6b, no significant improvement in the PV parameters for the PSC was observed after incorporating graphene into the mesoporous $TiO_2$ layer only (structure 2). We hypothesize that these unchanged PV parameters are associated with the energy level alignment of $TiO_2$ and graphene. In fact, the injected electrons from the excited perovskite sensitizer and/or mesoporous $TiO_2$ into the graphene cannot be transferred to the conduction band of the compact $TiO_2$ (Fig. 6b′) which results in incomplete electron transport within the networks.

Furthermore, the addition of graphene into the compact $TiO_2$ layer of device (structure 3) exhibited some enhancement in the $J_{sc}$ and FF parameters and displayed a PCE of 0.75%, as illustrated in Fig. 6c. These increased $J_{sc}$ and FF values could be due to the suitable energy levels of graphene in the cell. The energy levels of graphene in the compact $TiO_2$ layer can be ideal for this class of PSC (structure 3) as its work function sits between the $TiO_2$ and graphene anode and so that the electrons transfer stepwise from the perovskite to the graphene anode without an energy barrier (see Fig. 6c′). Here, graphene, which was incorporated into the compact $TiO_2$ layer, acts as a bridge between $TiO_2$ and graphene anode. In the energy diagram, it is reasonable to assume that the work function of RGO (graphene anode; used as a transparent conductive film in the PSC) is higher than that of the graphene used in the semiconducting oxide layers because the extent of reduction in the electrode is relatively high.

Structure 4 showed a promising improvement in the power conversion efficiency (0.81%) (Fig. 6d). In particular, the $J_{sc}$ and FF values of structure 4 increased to 3.04 mA $cm^{-2}$ and 0.38, respectively, after incorporating graphene structures into both the compact $TiO_2$ and mesoporous $TiO_2$ layers. The improvement in these parameters ($J_{sc}$ and FF) can be ascribed to the fact that the conductive graphene in the cells enhances the charge transport rate and suppresses the charge recombination. Moreover, it is reasonable to expect that the presence of

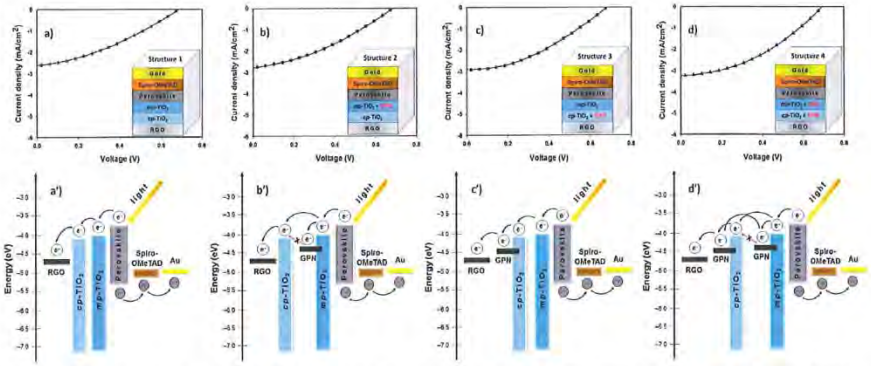


Fig. 6 *J–V* curves (top) and the corresponding energy level diagrams (bottom) of TCGF film based PSCs with and without graphene in the semiconducting oxide layers. The device structures are shown in the insets. The abbreviations are as follows: RGO – reduced graphene oxide; graphene – GPN; mp-$TiO_2$ – mesoporous $TiO_2$; cp-$TiO_2$ – compact $TiO_2$.

Table 2 Summary of the PV performance of PSCs (structure 1–4, shown in Fig. 6) with RGO incorporated in different segments. Average values and the standard deviation (at least three cells for each structure) of the PSCs are shown. Parameters of the best cells are also highlighted in bold

| Device | $J_{sc}$ (mA $cm^{-2}$) | $V_{oc}$ (V) | FF | $\eta$ (%) |
|---|---|---|---|---|
| Structure 1 | **2.55**; 2.55 ± 0.03 | **0.690**; 0.689 ± 0.001 | **0.35**; 0.35 ± 0.01 | **0.62**; 0.62 ± 0.00 |
| Structure 2 | **2.77**; 2.75 ± 0.02 | **0.684**; 0.686 ± 0.002 | **0.36**; 0.36 ± 0.00 | **0.66**; 0.65 ± 0.01 |
| Structure 3 | **2.90**; 2.85 ± 0.05 | **0.690**; 0.695 ± 0.005 | **0.38**; 0.38 ± 0.00 | **0.75**; 0.74 ± 0.01 |
| Structure 4 | **3.05**; 2.94 ± 0.11 | **0.687**; 0.689 ± 0.002 | **0.38**; 0.38 ± 0.01 | **0.81**; 0.79 ± 0.02 |

graphene in both the compact and mesoporous $TiO_2$ layers provides a thermodynamically favorable energy transfer path and potentially offers an extra graphene to graphene conduction path both of which enable successful charge collection and hence higher PCE (see Fig. 6d′). A detailed investigation on the effect of carbonaceous materials in the $TiO_2$ photoanodes of PSCs is ongoing research in our group.

The external quantum efficiency (EQE) is an important parameter for evaluating the performance of solar cells. PSC devices (structure 4 in Fig. 6) with TCGF and graphene in mesoporous and compact $TiO_2$ were chosen for EQE analysis. For comparison, the EQE characteristic of the conventional PSC fabricated on FTO electrode without graphene was also investigated. Fig. 7 compares the obtained EQE spectra. Both cells show a broad EQE peak across the visible region, typical for PSCs.[66] The cell fabricated with graphene (structure 4 in Fig. 6) shows a similar shape to the FTO-electrode based PSC (see Fig. 7 inset) but much lower EQE value, showing that the difference is wavelength independent which indicates that the use of graphene film did not alter the internal mechanism of the PSC. The lower EQE value of TCGF based cell is expected when considering the low PCE obtained, as discussed previously. Moreover, the stability of these two PSCs, namely FTO-based and TCGF-based, was investigated for 60 h and the results are plotted in Fig. S6.† The degradation rate of TCGF based cell was very similar to that of an FTO-based device.

The initial reported PCE of PSCs was relatively low but has increased rapidly in just a few years. It is anticipated that PCE of TCGF in PSCs will show a similar rapid improvement as they

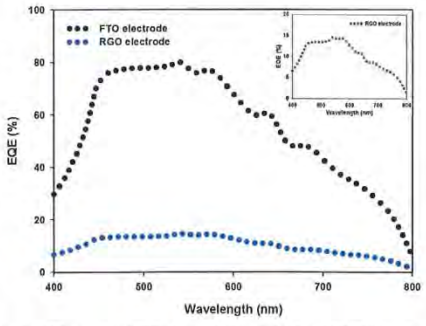


Fig. 7 EQE spectra of FTO electrode (black dots) and TCGF (blue dots, structure 4 (from Fig. 6 and Table 2)) based PSCs. Inset shows the expanded EQE spectrum of RGO electrode based PSC.

have in other solar cell architectures.[19] A promising result is that the observed $V_{oc}$ for all devices fabricated with TCGF films were similar to that of FTO electrodes based cells, indicating that the energy bands of graphene are suitable for application in PSCs, supporting theoretical predictions.[32] Therefore, our results demonstrate that the use of graphene films as the electron transporting transparent conducting electrode in the PSCs is viable. The two key areas for research are the improvement in $R_s$ with high transmittance and the creation of flexible PSCs using TCGFs. Further modification of the reduction of GO to increase flake size could produce graphene films with better performance for PSCs without increasing manufacturing cost.

## Conclusions

Herein, we demonstrate the feasibility of transparent conductive graphene films (TCGFs) formed by solution processing as alternatives to the conventional transparent conducting oxide (TCO) electrodes in PSC devices. The TCGFs were prepared by using a low-temperature annealing process as well as chemical post-treatments. By using an optimal balance of $R_s$ and transparency of the graphene films, a maximum PCE of 0.62% was obtained. By incorporating graphene structures into both compact $TiO_2$ and mesoporous $TiO_2$ layers of the PSCs, the PCE was further improved to 0.81%. Further PCE enhancement is expected in this class of solar cells by applying high-quality graphene films with improved electrical conductivity and high transparency. Finally, we anticipate that the current work will open new avenues for the development of graphene materials in perovskite based solar cells.

## Experimental

### Materials

Unless otherwise specified, all chemicals were purchased from Sigma-Aldrich and used without further purification. Methylammonium iodide ($CH_3NH_3I$), $TiO_2$ paste (18NR-T) and tris(1-(pyridin-2-yl)-1*H*-pyrazol)cobalt(III)tris(hexafluorophosphate) (FK102 Co(III) PF6) salt were purchased from Dyesol. (2,2′,7,7′-Tetrakis-(*N*,*N*-di-*p*-methoxyphenylamine)-9,9′-spirobifluorene) (Spiro-OMeTAD) was obtained from Solaronix.

### Preparation of graphene films

Graphite oxide was prepared *via* the oxidation of natural graphite according to an improved Hummers method.[34] In brief, a 9 : 1 (v/v) mixture of concentrated sulfuric acid (95–98% $H_2SO_4$) and phosphoric acid (85% $H_3PO_4$) (240 : 27 mL) was kept in the cold room (3–5 °C) until it was added to a mixture of graphite flakes (2 g) and potassium permanganate (99% $KMnO_4$) (12 g). Then the oxidation process was carried out by stirring at 50 °C for 12 h. Upon completion, the reaction was cooled down to room temperature and poured onto ice (approximately 300 mL) with 30% hydrogen peroxide ($H_2O_2$) (2 mL). The mixture was then washed with distilled (DI) water, 30% hydrochloric acid (HCl) and ethanol (2 times). For each sequential wash, the product was centrifuged at 4400 rpm for 3 h and the supernatant decanted away. The obtained light brown sample was then vacuum-dried overnight at room temperature.

The as-prepared graphite oxide was exfoliated in water (1 mg $mL^{-1}$) by bath ultrasonication (Elma, Germany) for 40 min in the presence of SDBS (1 wt% in the solution). The obtained homogenous dispersion was named "GO–SDBS solution". The GO–SDBS colloidal dispersion (10 mL) was chemically reduced by hydrazine monohydrate solution (40 μL, 64–65% $N_2H_4 \cdot H_2O$) and ammonium hydroxide solution (120 μL, 30% $NH_3 \cdot H_2O$).[44] The chemical reduction was performed in an oil bath at 100 °C overnight. The resultant solution (termed as "CRGO–SDBS") was then diluted with DI water to obtain the final concentration of CRGO–SDBS (0.16 mg $L^{-1}$). The diluted solution was further used to prepare the transparent films. For comparison, the chemical reduction of GO was performed in the absence of SDBS and the resultant solution was named CRGO-only.

The glass substrates (25 mm × 25 mm) were cleaned by detergent (Pyroneg) followed by washing with acetone, ethanol and Milli-Q water under ultrasonication for 10 min each and subsequently dried with a stream of nitrogen gas. The cleaned glass substrates were pretreated with 3-aminopropyl-triethoxysilane (APTES) (3% in toluene) to improve the surface functionalities of the substrates.[24,39,56] Transparent graphene films were prepared on mixed cellulose ester (MCE) membranes (0.45 μm HAWP, Millipore) through the vacuum filtration of CRGO–SDBS solution.[44] The transparency of the films was controlled by varying the effective filtration volume of solutions. The filtered films (CRGO–SDBS/MCE membrane) were subsequently pressed against the APTES-modified glass surface with the graphene side in contact with the substrate. The substrates where then firmly clamped in place at room temperature for 2 days to completely adhere the CRGO–SDBS film to the substrate. The MCE membranes were dissolved in an acetone bath to leave CRGO–SDBS film on the substrate. The obtained CRGO–SDBS films were then rinsed with methanol and dried by blowing nitrogen. To further improve the electrical conductivity of the films, the as-produced CRGO–SDBS films were thermally reduced in a tube furnace at low temperature (400 °C) for 1 h. The annealing and cooling processes were performed under the protection of an Ar and $H_2$ (20 : 1) atmosphere. The obtained films are named "RGO–SDBS". To remove the residual SDBS surfactant from the films, the RGO–SDBS films were then immersed in concentrated nitric acid ($HNO_3$, 68%) solution for 3 h and rinsed thoroughly with DI water, and dried at 100 °C for 1 h in a hot oven. After the application of the $HNO_3$-treatment, the samples are called "RGO films". The AuNPs were then deposited onto the RGO films by dynamic spin coating of 0.5 mM $HAuCl_4$ in nitromethane, and finally dried completely at 200 °C overnight. The prepared films are named "AuNPs–RGO films" and have been used to fabricate the PSC devices.

### Fabrication of PSC devices

PSC devices with the structure of graphene anode/compact $TiO_2$/mesoporous $TiO_2$/$CH_3NH_3PbI_{3-x}Cl_x$/Spiro-OMeTAD/Au were fabricated according to the following procedure. The fabrication process of PSCs has been reported elsewhere.[12,14] A

thin compact $TiO_2$ layer was spin-coated onto the previously prepared graphene film and/or cleaned FTO electrode (~12 Ω $sq^{-1}$, Solaronix TCO30-8) substrate at a rotation speed of 2000 rpm for 20 s using 0.2 M titanium diisopropoxide bis(acetylacetonate) (75 wt% in isopropanol, Aldrich) in 1-butanol solution, followed by heating at 125 °C for 5 min. The same process was repeated twice with the above solution, followed by drying at 125 °C for 5 min and sintering at 500 °C for 1 h. For the preparation of the graphene incorporated compact $TiO_2$ layer, GO–ethanol solution (1 mg $mL^{-1}$) was added into the titanium diisopropoxide bis(acetylacetonate) in 1-butanol solution. The concentration of the GO in the composite was calculated to be 0.6 wt%. After cooling to room temperature, a thick mesoporous $TiO_2$ layer was deposited onto the compact $TiO_2$ layer by spin coating a solution of $TiO_2$ paste (Dyesol 18NR-T) in a 2 : 7 weight ratio to ethanol at 4000 rpm for 30 s. After drying at 125 °C for 5 min, the films were sintered at 500 °C for 1 h. The mesoporous $TiO_2$ deposited films were then immersed in 40 mM aqueous $TiCl_4$ (Aldrich) solution at 70 °C for 30 min, which was again annealed at 500 °C for 30 min. Similarly, to prepare the graphene/mesoporous $TiO_2$ layer, the GO-ethanol solution was also added into the diluted $TiO_2$ paste solution and the concentration of the GO in the composite was controlled to be 0.2 wt%. The GO in the compact and/or mesoporous $TiO_2$ layers can simply be converted to graphene during the annealing processes. Moreover, during the deposition of the compact and mesoporous layers on the transparent electrodes, Parafilm® M seal was rolled onto one side of the TCGFs to protect the graphene anode contact. After the completion of all annealing processes at 500 °C, conductive adhesive tape was carefully applied onto the graphene anode to serve as electrical contact. Notably, we measured the $R_s$ of the graphene films before and after annealing at 500 °C for 1 h as this thermal annealing process was done after the deposition of $TiO_2$ layers and no significant changes in the $R_s$ were observed. Particularly, the $R_s$ of $HNO_3$ and $HAuCl_4$ treated RGO films before and after thermal treatment at 500 °C were measured to be 4.08 ± 0.04 kΩ $sq^{-1}$ and 4.21 ± 0.12 kΩ $sq^{-1}$, respectively. It should also be noted that for the fabrication of PSC devices with graphene structures, the thermal annealing processes at more than 400 °C were carried out under the protection of Ar to protect graphene from the mild oxidation.

For the preparation of $CH_3NH_3PbI_{3-x}Cl_x$ perovskite, a 1 : 3 molar ratio of $PbCl_2$ : $CH_3NH_3I$ was mixed in anhydrous *N*,*N*-dimethylformamide (DMF) (99.8% Aldrich), with a concentration of 0.73 M and 2.2 M, respectively. The mixture was stirred at room temperature for at least 6 h before spin coating (100 μL of the solution) onto the mesoporous layers at 2500 rpm for 30 s in air and then heated at 100 °C for 1 h. The deposition process of the perovskite was carried out in controlled humidity under 35%.

The HTM (120 μL of the prepared solution) was then deposited onto the perovskite layer by spin coating at 4000 rpm for 30 s in a nitrogen-filled glovebox. The HTM was prepared by dissolving 72.3 mg Spiro-OMeTAD, 28.8 μL 4-*tert*-butylpyridine (tBP), 17.5 μL of a stock solution of 520 mg $mL^{-1}$ lithium bis(trifluoromethylsulphonyl)imide (Li-TFSI) in acetonitrile and 29 μL of a stock solution of 300 mg $mL^{-1}$ FK102 Co(III) PF6 salt in acetonitrile, in 1 mL chlorobenzene. Finally, 60 nm gold electrodes were deposited on top of devices by thermal evaporation at a rate of 1 Å $s^{-1}$ under a high vacuum (~$10^{-6}$ bar) through a shadow mask.

### Measurement and characterizations

AFM images were acquired in air using a Bruker Dimension FastScan AFM with Nanoscope V controller, operating in tapping mode. Silicon cantilevers (MikroMasch) with a fundamental resonance frequency of between 300 and 400 kHz were used. Images were obtained using a scan rate of 1 Hz with the set point, amplitude, and feedback control parameters optimized manually for each sample. The images presented have been flattened using NanoScope Analysis v1.4 software. SEM images were obtained using an Inspect F50 SEM (FEI) with accelerating voltage of 20 kV. EDX analysis was completed on the same system with Team EDS Octane Pro (EDAX) attachment. ATR-FTIR spectra were acquired over a wavenumber range of 4000–650 $cm^{-1}$ in transmission mode using a Frontier FTIR spectrometer (Perkin Elmer, USA) with a germanium crystal. The elemental compositions of the samples were characterized at binding energies ranging from 0 eV to 1200 eV using a XPS, Leybold Heraeus LHS-10 with a SPECS XR-50 dual anode source operating at 250 W. A Mg-Kα source, which has energy of 1253.6 eV, was used for the XPS analysis. Curve fitting of the C 1s in XPS spectra was done using peak fitting software "Fityk".[72] High resolution XPS of the C 1s were collected with a step size of 0.1 eV and the presented spectra are an average of 5 collections. Raman spectroscopy was performed on LabRAM HR Evolution spectrometer (Horiba Jobin Yvon, Japan). Raman spectra were collected using a 532 nm laser (mpc 3000) as the excitation source. A 50× objective was used with a confocal hole size of 100 μm. Thermal decomposition of SDBS was performed using a thermal gravimetric analyser (TA Instruments TGA 2950 Thermogravimetric Analyzer, USA) under a flow of nitrogen at a rate of at 20.0 mL $min^{-1}$. The transmittances of the films on glass slides were determined using a Varian Cary 50G UV-vis spectrophotometer at wavelengths ranging from 400 to 1000 nm. Sheet resistance measurements were performed on the same films using a four point probe technique (KeithLink Technology Co., Ltd. Taiwan). The *J*–*V* curves were measured using a Keithley 2400 SMU instrument and recorded using a custom LabView Virtual Instrument program. A standard silicon test cell with NIST-traceable certification was used to calibrate the power density as 100 mW $cm^{-2}$ at the sample plane of the collimated xenon-arc light source, which was passed through an AM 1.5G filter. The active area of each device was 0.075 $cm^2$. The *J*–*V* curves were obtained in the air in reverse-scan direction from 1 V to −1 V. EQE measurements as a function of wavelength ranging from 400 nm to 800 nm were taken by passing chopped light from a xenon source through a monochromator and onto the devices.

## Acknowledgements

The support of the Australian Research Council Discovery Program (DP130101714) is gratefully acknowledged. Munkhbayar

Batmunkh acknowledges International Postgraduate Research Scholarship (IPRS) and Australian Postgraduate Award (APA) for their financial support during his study in Australia. We acknowledge the use of South Australian node of the Australian Microscopy & Microanalysis Research Facility (AMMRF) at Flinders University. The authors would also like to thank Meisam V. Kiamahalleh of School of Chemical Engineering at the University of Adelaide for graphic design.



## Notes and references

1 S. Chu and A. Majumdar, *Nature*, 2012, **488**, 294–303.
2 T. Saga, *NPG Asia Mater.*, 2010, **2**, 96–102.
3 M. Bosi and C. Pelosi, *Prog. Photovoltaics*, 2007, **15**, 51–68.
4 N.-G. Park, *J. Phys. Chem. Lett.*, 2013, **4**, 2423–2429.
5 G. Hodes, *Science*, 2013, **342**, 317–318.
6 P. Docampo, S. Guldin, T. Leijtens, N. K. Noel, U. Steiner and H. J. Snaith, *Adv. Mater.*, 2014, **26**, 4013–4030.
7 M. A. Green, A. Ho-Baillie and H. J. Snaith, *Nat. Photonics*, 2014, **8**, 506–514.
8 M. M. Lee, J. Teuscher, T. Miyasaka, T. N. Murakami and H. J. Snaith, *Science*, 2012, **338**, 643–647.
9 G. Xing, N. Mathews, S. Sun, S. S. Lim, Y. M. Lam, M. Grätzel, S. Mhaisalkar and T. C. Sum, *Science*, 2013, **342**, 344–347.
10 A. Kojima, K. Teshima, Y. Shirai and T. Miyasaka, *J. Am. Chem. Soc.*, 2009, **131**, 6050–6051.
11 J. Burschka, N. Pellet, S.-J. Moon, R. Humphry-Baker, P. Gao, M. K. Nazeeruddin and M. Gratzel, *Nature*, 2013, **499**, 316–319.
12 H. Zhou, Q. Chen, G. Li, S. Luo, T.-B. Song, H.-S. Duan, Z. Hong, J. You, Y. Liu and Y. Yang, *Science*, 2014, **345**, 542–546.
13 W. S. Yang, J. H. Noh, N. J. Jeon, Y. C. Kim, S. Ryu, J. Seo and S. I. Seok, *Science*, 2015, **348**, 1234–1237.
14 G. E. Eperon, V. M. Burlakov, P. Docampo, A. Goriely and H. J. Snaith, *Adv. Funct. Mater.*, 2014, **24**, 151–157.
15 X. Chen, S. Yang, Y. C. Zheng, Y. Chen, Y. Hou, X. H. Yang and H. G. Yang, *Adv. Sci.*, 2015, **2**, 1500105.
16 X. Huang, Z. Zeng, Z. Fan, J. Liu and H. Zhang, *Adv. Mater.*, 2012, **24**, 5979–6004.
17 D. S. Hecht, L. Hu and G. Irvin, *Adv. Mater.*, 2011, **23**, 1482–1513.
18 F. Bonaccorso, Z. Sun, T. Hasan and A. C. Ferrari, *Nat. Photonics*, 2010, **4**, 611–622.
19 Z. Yin, J. Zhu, Q. He, X. Cao, C. Tan, H. Chen, Q. Yan and H. Zhang, *Adv. Energy Mater.*, 2014, **4**, 1300574.
20 H. Chang and H. Wu, *Adv. Funct. Mater.*, 2013, **23**, 1984–1997.
21 Y. Zhu, S. Murali, W. Cai, X. Li, J. W. Suk, J. R. Potts and R. S. Ruoff, *Adv. Mater.*, 2010, **22**, 3906–3924.
22 M. Hösel, D. Angmo, R. R. Søndergaard, G. A. dos Reis Benatto, J. E. Carlé, M. Jørgensen and F. C. Krebs, *Adv. Sci.*, 2014, **1**, 1400002.
23 Q. Su, S. Pang, V. Alijani, C. Li, X. Feng and K. Müllen, *Adv. Mater.*, 2009, **21**, 3191–3195.
24 Z. Yin, S. Wu, X. Zhou, X. Huang, Q. Zhang, F. Boey and H. Zhang, *Small*, 2010, **6**, 307–312.
25 Z. Yin, S. Sun, T. Salim, S. Wu, X. Huang, Q. He, Y. M. Lam and H. Zhang, *ACS Nano*, 2010, **4**, 5263–5268.
26 E. Kymakis, K. Savva, M. M. Stylianakis, C. Fotakis and E. Stratakis, *Adv. Funct. Mater.*, 2013, **23**, 2742–2749.
27 X. Wang, L. Zhi and K. Müllen, *Nano Lett.*, 2008, **8**, 323–327.
28 P. You, Z. Liu, Q. Tai, S. Liu and F. Yan, *Adv. Mater.*, 2015, **27**, 3632–3638.
29 F. Lang, M. A. Gluba, S. Albrecht, J. Rappich, L. Korte, B. Rech and N. H. Nickel, *J. Phys. Chem. Lett.*, 2015, **6**, 2745–2750.
30 Z. Liu, S. P. Lau and F. Yan, *Chem. Soc. Rev.*, 2015, **44**, 5638–5679.
31 M. Batmunkh, C. J. Shearer, M. J. Biggs and J. G. Shapter, *J. Mater. Chem. A*, 2015, **3**, 9020–9031.
32 G. Volonakis and F. Giustino, *J. Phys. Chem. Lett.*, 2015, **6**, 2496–2502.
33 N. Yang, J. Zhai, D. Wang, Y. Chen and L. Jiang, *ACS Nano*, 2010, **4**, 887–894.
34 D. C. Marcano, D. V. Kosynkin, J. M. Berlin, A. Sinitskii, Z. Sun, A. Slesarev, L. B. Alemany, W. Lu and J. M. Tour, *ACS Nano*, 2010, **4**, 4806–4814.
35 O. C. Compton and S. T. Nguyen, *Small*, 2010, **6**, 711–723.
36 M. Lotya, Y. Hernandez, P. J. King, R. J. Smith, V. Nicolosi, L. S. Karlsson, F. M. Blighe, S. De, Z. Wang, I. T. McGovern, G. S. Duesberg and J. N. Coleman, *J. Am. Chem. Soc.*, 2009, **131**, 3611–3620.
37 H. Chang, L. Tang, Y. Wang, J. Jiang and J. Li, *Anal. Chem.*, 2010, **82**, 2341–2346.
38 M. J. Fernández-Merino, L. Guardia, J. I. Paredes, S. Villar-Rodil, P. Solís-Fernández, A. Martínez-Alonso and J. M. D. Tascón, *J. Phys. Chem. C*, 2010, **114**, 6426–6432.
39 S. J. Wang, Y. Geng, Q. Zheng and J.-K. Kim, *Carbon*, 2010, **48**, 1815–1823.
40 H. Chang, G. Wang, A. Yang, X. Tao, X. Liu, Y. Shen and Z. Zheng, *Adv. Funct. Mater.*, 2010, **20**, 2893–2902.
41 Q. Zheng, Z. Li, J. Yang and J.-K. Kim, *Prog. Mater. Sci.*, 2014, **64**, 200–247.
42 C. J. Shearer, A. Cherevan and D. Eder, *Adv. Mater.*, 2014, **26**, 2295–2318.
43 A. C. Ferrari and D. M. Basko, *Nat. Nanotechnol.*, 2013, **8**, 235–246.
44 G. Eda, G. Fanchini and M. Chhowalla, *Nat. Nanotechnol.*, 2008, **3**, 270–274.
45 M. S. Kang, K. T. Kim, J. U. Lee and W. H. Jo, *J. Mater. Chem. C*, 2013, **1**, 1870–1875.
46 H.-Z. Geng, K. K. Kim, K. P. So, Y. S. Lee, Y. Chang and Y. H. Lee, *J. Am. Chem. Soc.*, 2007, **129**, 7758–7759.
47 A. K. K. Kyaw, H. Tantang, T. Wu, L. Ke, C. Peh, Z. H. Huang, X. T. Zeng, H. V. Demir, Q. Zhang and X. W. Sun, *Appl. Phys. Lett.*, 2011, **99**, 021107.
48 S. Kim, J. Yim, X. Wang, D. D. C. Bradley, S. Lee and J. C. deMello, *Adv. Funct. Mater.*, 2010, **20**, 2310–2316.
49 A. Kasry, M. A. Kuroda, G. J. Martyna, G. S. Tulevski and A. A. Bol, *ACS Nano*, 2010, **4**, 3839–3844.
50 L. J. Larsen, C. J. Shearer, A. V. Ellis and J. G. Shapter, *RSC Adv.*, 2015, **5**, 38851–38858.

51 R. Jackson, B. Domercq, R. Jain, B. Kippelen and S. Graham, *Adv. Funct. Mater.*, 2008, **18**, 2548–2554.
52 Q. W. Li, Y. Li, X. F. Zhang, S. B. Chikkannanavar, Y. H. Zhao, A. M. Dangelewicz, L. X. Zheng, S. K. Doorn, Q. X. Jia, D. E. Peterson, P. N. Arendt and Y. T. Zhu, *Adv. Mater.*, 2007, **19**, 3358–3363.
53 B.-S. Kong, J. Geng and H.-T. Jung, *Chem. Commun.*, 2009, 2174–2176.
54 H. A. Becerril, J. Mao, Z. Liu, R. M. Stoltenberg, Z. Bao and Y. Chen, *ACS Nano*, 2008, **2**, 463–470.
55 Y. Xu, G. Long, L. Huang, Y. Huang, X. Wan, Y. Ma and Y. Chen, *Carbon*, 2010, **48**, 3308–3311.
56 Q. B. Zheng, M. M. Gudarzi, S. J. Wang, Y. Geng, Z. Li and J.-K. Kim, *Carbon*, 2011, **49**, 2905–2916.
57 J. Geng, L. Liu, S. B. Yang, S.-C. Youn, D. W. Kim, J.-S. Lee, J.-K. Choi and H.-T. Jung, *J. Phys. Chem. C*, 2010, **114**, 14433–14440.
58 L. Zhao, L. Zhao, Y. Xu, T. Qiu, L. Zhi and G. Shi, *Electrochim. Acta*, 2009, **55**, 491–497.
59 J. Wu, H. A. Becerril, Z. Bao, Z. Liu, Y. Chen and P. Peumans, *Appl. Phys. Lett.*, 2008, **92**, 263302.
60 X. Wang, L. Zhi, N. Tsao, Ž. Tomović, J. Li and K. Müllen, *Angew. Chem., Int. Ed.*, 2008, **47**, 2990–2992.
61 J. H. Noh, S. H. Im, J. H. Heo, T. N. Mandal and S. I. Seok, *Nano Lett.*, 2013, **13**, 1764–1769.
62 H.-S. Ko, J.-W. Lee and N.-G. Park, *J. Mater. Chem. A*, 2015, **3**, 8808–8815.
63 Y. Liu, Q. Chen, H.-S. Duan, H. Zhou, Y. Yang, H. Chen, S. Luo, T.-B. Song, L. Dou, Z. Hong and Y. Yang, *J. Mater. Chem. A*, 2015, **3**, 11940–11947.
64 P. Qin, M. Paulose, M. I. Dar, T. Moehl, N. Arora, P. Gao, O. K. Varghese, M. Grätzel and M. K. Nazeeruddin, *Small*, 2015, **11**, 5533–5539.
65 F. Di Giacomo, V. Zardetto, A. D'Epifanio, S. Pescetelli, F. Matteocci, S. Razza, A. Di Carlo, S. Licoccia, W. M. M. Kessels, M. Creatore and T. M. Brown, *Adv. Energy Mater.*, 2015, **5**, 1401808.
66 Y. Shi, Y. Xing, Y. Li, Q. Dong, K. Wang, Y. Du, X. Bai, S. Wang, Z. Chen and T. Ma, *J. Phys. Chem. C*, 2015, **119**, 15868–15873.
67 M. Lyu, J.-H. Yun, R. Ahmed, D. Elkington, Q. Wang, M. Zhang, H. Wang, P. Dastoor and L. Wang, *J. Colloid Interface Sci.*, 2015, **453**, 9–14.
68 M. Batmunkh, M. J. Biggs and J. G. Shapter, *Adv. Sci.*, 2015, **2**, 1400025.
69 M. Batmunkh, M. J. Biggs and J. G. Shapter, *Small*, 2015, **11**, 2963–2989.
70 K. C. Kwon, B. J. Kim, J.-L. Lee and S. Y. Kim, *J. Mater. Chem. C*, 2013, **1**, 2463–2469.
71 J. T.-W. Wang, J. M. Ball, E. M. Barea, A. Abate, J. A. Alexander-Webber, J. Huang, M. Saliba, I. Mora-Sero, J. Bisquert, H. J. Snaith and R. J. Nicholas, *Nano Lett.*, 2014, **14**, 724–730.
72 M. Wojdyr, *J. Appl. Crystallogr.*, 2010, **43**, 1126–1128.

# Appendix E

# Carbon Nanotubes in $TiO_2$ Nanofiber Photoelectrodes for High-Performance Perovskite Solar Cells

*Munkhbayar Batmunkh, Thomas J. Macdonald, Cameron J. Shearer, Munkhjargal Bat-Erdene, Yun Wang, Mark J. Biggs, Ivan P. Parkin, Thomas Nann, and Joseph G. Shapter**

**1D semiconducting oxides are unique structures that have been widely used for photovoltaic (PV) devices due to their capability to provide a direct pathway for charge transport. In addition, carbon nanotubes (CNTs) have played multifunctional roles in a range of PV cells because of their fascinating properties. Herein, the influence of CNTs on the PV performance of 1D titanium dioxide nanofiber ($TiO_2$ NF) photoelectrode perovskite solar cells (PSCs) is systematically explored. Among the different types of CNTs, single-walled CNTs (SWCNTs) incorporated in the $TiO_2$ NF photoelectrode PSCs show a significant enhancement (≈40%) in the power conversion efficiency (PCE) as compared to control cells. SWCNTs incorporated in $TiO_2$ NFs provide a fast electron transfer within the photoelectrode, resulting in an increase in the short-circuit current ($J_{sc}$) value. On the basis of our theoretical calculations, the improved open-circuit voltage ($V_{oc}$) of the cells can be attributed to a shift in energy level of the photoelectrodes after the introduction of SWCNTs. Furthermore, it is found that the incorporation of SWCNTs into $TiO_2$ NFs reduces the hysteresis effect and improves the stability of the PSC devices. In this study, the best performing PSC device constructed with SWCNT structures achieves a PCE of 14.03%.**

## 1. Introduction

High-performance photovoltaic (PV) cells that can convert the sun's energy directly into electricity through the PV effect are promising clean and renewable energy technologies and have great potential to address current energy related issues.[1] Organolead halide ($CH_3NH_3PbX_3$, X = I, Cl, or Br) implemented solar cells (known as perovskite solar cells (PSCs)) have received significant attention from both scientific and industrial communities and have become one of the most popular topics in scientific research.[2,3] This increasing popularity of PSCs is due to the unprecedented rapid progress that has been made in their power conversion efficiencies (PCEs) over a short period of time.[4,5] Since 2009, the PCEs of PSCs have increased from 3.8% to 22.1%, making them the fastest advancing PV technology.[6–10] Recent successful fabrication of flexible and large-area PSC devices shows great promise for the commercialization of this cutting-edge PV technology.[11–16]

The most commonly explored PSC architecture consists of a transparent conducting oxide (TCO) coated glass substrate, a compact titanium dioxide ($TiO_2$) layer, mesoporous nanocrystalline $TiO_2$ layer, perovskite layer, hole transporting layer, and metal contact.[5,17–21] The working principle of this class of PSCs can be expressed

M. Batmunkh, Prof. M. J. Biggs
School of Chemical Engineering
The University of Adelaide
Adelaide, South Australia 5005, Australia

M. Batmunkh, Dr. C. J. Shearer, M. Bat-Erdene, Prof. J. G. Shapter
School of Chemical and Physical Sciences
Flinders University
Bedford Park, Adelaide, South Australia 5042, Australia
E-mail: joe.shapter@flinders.edu.au

Dr. T. J. Macdonald, Prof. I. P. Parkin
Department of Chemistry
University College London
WC1H OAJ London, UK

Dr. Y. Wang
Centre for Clean Environment and Energy
Griffith School of Environment
Gold Coast Campus
Griffith University
Queensland 4222, Australia

DOI: 10.1002/advs.201600504

Prof. M. J. Biggs
School of Science
Loughborough University
Loughborough, LEC LE11 3TU, UK

Prof. T. Nann
MacDiarmid Institute for Advanced Materials and Nanotechnology
School of Chemical and Physical Sciences
Victoria University of Wellington
6140 Wellington, New Zealand

as follows: upon illumination, the perovskite is excited, producing an electron–hole pair. Then the electrons are injected into the conduction band of the *n*-type semiconducting oxide (generally $TiO_2$), while the holes are transported to the *p*-type hole transporting materials (HTMs). Finally, the electrons and holes are collected at conductive electrodes such as TCO-based anodes and metal cathodes, respectively.[22] Fast charge-transfer processes in PSCs are of particular importance to maximize the device performance. The measured values for the injection times of electrons and holes in PSCs are 0.4 and 0.6 ns, respectively.[23] However, these values are three orders of magnitude longer than the hot carrier cooling time (≈0.4 ps), which leads to carrier trapping and a significant loss of the photon energy due to thermalization.[23] Moreover, a large number of grain boundaries in the nanocrystalline films leads to rapid charge recombination, resulting in reduced device performance. These issues have led to some recent efforts focused on developing strategies to enhance the charge transport properties in PSCs.

One promising strategy is to use a 1D nanostructure as a substitute for the nanoparticles in the photoelectrode to suppress the charge recombination and provide a direct pathway along the long axis of 1D nanostructures for electron transport.[24–28] In addition, the electron transport rate in 1D nanostructures such as nanofibers, nanowires, nanocolumns, and nanorods has been considered to be several orders of magnitude faster than that of nanoparticles.[29–32] This is achieved by reducing the scattering of free electrons from the grain boundaries of the interconnected nanoparticles.[33] On the other hand, the incorporation of highly conductive carbon nanomaterials such as graphene and carbon nanotubes (CNTs) has also been proven to be an effective method to facilitate the charge transport and extend the electron lifetime, thereby enhancing the efficiency of PV devices.[22,34–37] Although graphene and its derivatives have been successfully utilized for improving the performance of PSCs,[38–43] there has been no effort in the application of CNTs for use in PSC photoelectrodes. It should be noted that due to their unique structure and outstanding properties including excellent conductivity and high optical transparency, CNTs have exhibited promising results when they are used as an HTM and cathode in PSCs.[44–49] Moreover, CNTs are promising candidates for fabricating flexible fiber-shaped PSCs.[50–53] Therefore, integrating highly conductive CNTs into 1D structured $TiO_2$ for use in the photoelectrode of PSCs is an alternative approach to provide an ultrafast electron transport pathway to enhance device performance.

In the work presented here, the influence of CNTs on the performance of PSCs fabricated with 1D $TiO_2$ nanofibers (NFs) is systematically examined. By using an optimal amount of single-walled CNTs (SWCNTs) in the $TiO_2$ NFs, a significant enhancement (≈40%) in the device performance is achieved as compared to the control cell fabricated without CNTs. Further, PCE enhancement is obtained by incorporating SWCNTs into both compact and mesoporous $TiO_2$ layers of the PSCs. Based on our experimental and theoretical analysis, we attribute the performance enhancement of PSCs obtained by employing SWCNTs to the introduction of suitable energy levels and reduced charge recombination due to the increased charge transport of the photoelectrodes. More importantly, PSCs fabricated with SWCNT-$TiO_2$ NFs exhibited reduced hysteresis and improved stability both under light and during storage under humid conditions with respect to the control devices without SWCNTs. We also demonstrate in this study that SWCNTs can be used as an efficient HTM in PSCs. While previous work has shown $TiO_2$ NF-based PSCs can achieve PCE values of up to 9.8%[25] and 13.4% for atomic layer deposited nanorods,[54] in this work, our best performing PSC achieved a PCE of 14.03%.

## 2. Results and Discussion

In order to fabricate PSCs with the device architecture displayed in **Figure 1**a, $TiO_2$ NFs were first prepared using an electrospinning method. $CH_3NH_3PbI_3$ was used as a light absorbing perovskite material. A detailed description of the synthesis process can be found in the Experimental Section. Low- and high-resolution scanning electron microscopy (SEM) images of the prepared $TiO_2$ NFs are shown in Figure 1b,c, respectively. The $TiO_2$ NFs were several micrometres in length, while their diameter varied within a few hundreds of nanometres. In addition to the relatively uniform morphology, the prepared $TiO_2$ NF films showed an excellent porous network, which can be beneficial for perovskite absorber loading (see Figure S1a–d, Supporting Information). The anatase phase of the $TiO_2$ NFs on fluorine-doped tin oxide (FTO) was confirmed by X-ray diffraction as compared to the reference values (9853-ICSD)[55] and can be seen in Figure S1e (Supporting Information). In our devices (Figure 1d), $TiO_2$ NFs were used as electron transporting layer (ETL).

The thickness of ETLs in the PSCs has a critical influence on the device performance.[10,56] To investigate the effect of the thickness of $TiO_2$ NF films on the cell efficiency, five PSC devices were fabricated based on the $TiO_2$ NF photoelectrodes with different thicknesses. The thickness of the $TiO_2$ NF layer was controlled by dilution of the $TiO_2$ NF paste. The diluted $TiO_2$ solutions were spin-coated onto the compact $TiO_2$ (cp-$TiO_2$) with identical conditions. Cross-sectional SEM images of $TiO_2$ NF films with different thicknesses (≈285 to ≈2200 nm) are depicted in Figure S2a–e (Supporting Information). For comparison, a planar PSC device was fabricated without the $TiO_2$ NF layer (Figure S2f and Figure S3, Supporting Information).

The PV characteristics of the fabricated devices were studied under an air mass (AM) 1.5 illumination at 100 mW $cm^{-2}$. The photocurrent density–voltage (*J*–*V*) characteristics of the PSCs fabricated with different $TiO_2$ NF thicknesses are displayed in **Figure 2**a and the corresponding PV parameters such as short-circuit current ($J_{sc}$), open-circuit voltage ($V_{oc}$), fill factor (FF), and PCE have been summarized in Table S1 (Supporting Information). As an optimal thickness of $TiO_2$ NFs, the PSCs fabricated with ≈400 nm $TiO_2$ NFs exhibited the highest PCE (average efficiency of 8.21 ± 0.46%). The observed $J_{sc}$, $V_{oc}$, and FF values for the best device based on ≈400 nm $TiO_2$ NF photoelectrode PSCs were 15.91 mA $cm^{-2}$, 0.87 V, and 0.62, respectively, yielding a PCE of 8.56%.

As shown in Figure 2a and Table S1 (Supporting Information), both $J_{sc}$ and $V_{oc}$ values of PSCs continuously decreased with the $TiO_2$ NF film thickness (from ≈400 to ≈2200 nm), resulting in lower cell efficiencies. Increasing the film thickness, which in turn lowers the PCE, is believed to be a result of

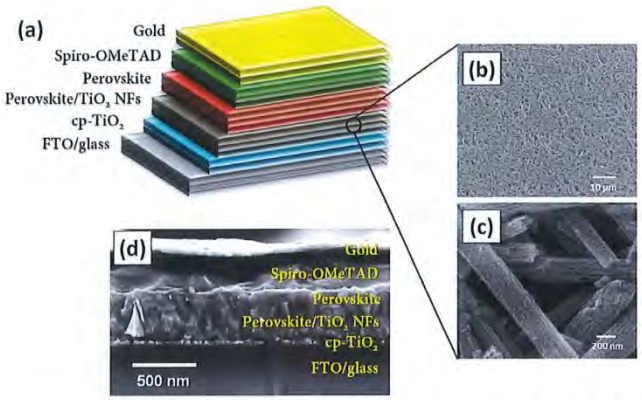


**Figure 1.** a) Schematic illustration of $TiO_2$ NF photoelectrode based PSC. b) Low- and c) high-resolution SEM image of $TiO_2$ NFs. d) Cross-sectional SEM image of representative $TiO_2$ NF (400 nm thickness) photoelectrode based PSC.

the high charge recombination rate within the $TiO_2$ NF based devices.[10,25,57] In contrast, the devices fabricated without $TiO_2$ NFs (called planar PSCs) or with thin $TiO_2$ NF layers (≈285 nm) showed high $V_{oc}$, but their PCEs were low due to the decreased $J_{sc}$ and FF values. This higher $V_{oc}$ value of planar devices can be associated with the lower probability of charge recombination as compared to the porous structured PSCs. These results are very consistent with recent studies on $CH_3NH_3PbI_3$-based planar PSC devices.[25,58,59] Considering the PCEs of the devices, the $TiO_2$ NF (≈400 nm) film was chosen for further investigations and device fabrication.

To understand the effect of CNT types on the performance of PSCs, three different types of CNTs, namely double-walled CNTs (DWCNTs), multiwalled CNTs (MWCNTs), and single-walled CNTs (SWCNTs) were incorporated into the $TiO_2$ NF photoelectrode based PSCs under the same experimental conditions. The *J–V* curves of these devices are plotted in Figure 2b. The concentration of CNTs in the $TiO_2$ NF–CNT hybrid was 0.02 wt%. The average PCEs of these PSCs were calculated based on five identical devices (see Table S2 in the Supporting Information). It can be seen from Figure 2b and Table S2 (Supporting Information) that the incorporation of CNTs, regardless of their type, increases the $J_{sc}$ value compared to the $TiO_2$ NF-only photoelectrodes, which can be associated with the high conductivity of CNTs.[36] In particular, the use of the SWCNTs in $TiO_2$ NF photoelectrodes was shown to considerably enhance the PCE of PSCs by improving the $J_{sc}$ and $V_{oc}$ values despite the fact that a very small amount of SWCNTs was added and no optimization was undertaken at this point. Indeed, the addition of SWCNTs (0.02 wt%) into the $TiO_2$ NF photoelectrodes of PSCs increased the PCE from 8.56% to 9.91%. We hypothesize that this PCE enhancement is due to the excellent conductivity and mixture of metallic and semiconducting behaviour of SWCNTs. Therefore, the SWCNTs were chosen for further optimization of the devices to maximize the cell performance.

**Figure 3**a displays the SEM image of SWCNT-incorporated $TiO_2$ NFs. SWCNTs a few nanometers in diameter (highlighted by yellow arrows in Figure 3a) are observed and wrapped

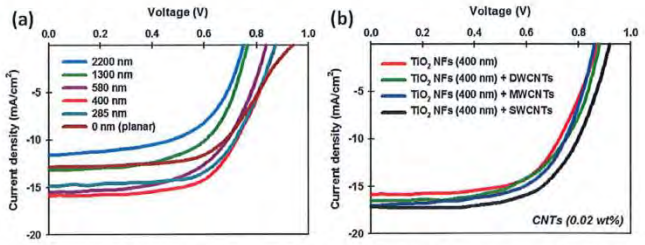


**Figure 2.** *J–V* curves of PSCs fabricated based on a) different thicknesses of $TiO_2$ NF films and b) various types of CNT-incorporated $TiO_2$ NF photoelectrodes. For the fabrication of $TiO_2$ NF–CNT photoelectrodes ≈400 nm $TiO_2$ NFs was chosen.

  

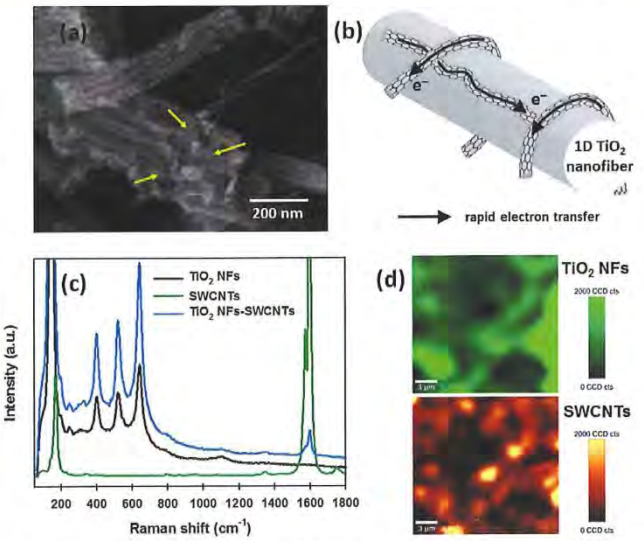


**Figure 3.** a) SEM image and b) schematic illustration of $TiO_2$ NF-SWCNT hybrid. c) Raman spectra of $TiO_2$ NFs, SWCNTs, and $TiO_2$ NFs–SWCNTs. d) Raman mapping image of $TiO_2$ NFs (top, green) and SWCNTs (bottom, orange) in the hybrid sample. In both images, the "bright" regions represent the presence of the materials.

around the $TiO_2$ NFs, indicating successful integration of the SWCNTs into the $TiO_2$ NFs. It is worth noting that 1D $TiO_2$ NFs can provide a direct electron transport pathway.[24] More importantly, in such hybrid structure ($TiO_2$ NFs-SWCNTs), the SWCNTs are expected to provide extremely fast electron transport pathway with excellent conductivity (see Figure 3b).

To further confirm the presence of SWCNTs in the hybrid, the samples were characterized using Raman microspectroscopy. Figure 3c shows the Raman spectra of $TiO_2$ NFs, SWCNTs, and their hybrid structures. For the pure $TiO_2$ NFs, four strong peaks at around 149, 397, 512, and 639 $cm^{-1}$, which correspond to the $E_{g(1)}$, $B_{1g(1)}$, $A_{1g} + B1g(2)$, and $E_{g(2)}$ modes of anatase $TiO_2$, respectively, were observed.[41] On the other hand, the SWCNTs showed two typical Raman feature peaks at around 1346 and 1587 $cm^{-1}$, which can be assigned to the "D" band (the disordered mode) and "G" band (tangential mode), in addition to the radial breathing mode peak at around 172 $cm^{-1}$.[44] For $TiO_2$ NF-SWCNT hybrid, all the Raman bands of both $TiO_2$ NFs and SWCNTs were observed, further confirming the successful incorporation of SWCNTs into the $TiO_2$ NF system. Moreover, confocal Raman spectral mapping was carried out on a selected area of the $TiO_2$ NF-SWCNT hybrid. Notably, the obtained maps in Figure 3d confirm the coexistence of $TiO_2$ NFs and SWCNTs throughout the imaged area indicating a relatively homogeneous distribution of SWCNTs within the porous film.

In order to optimize the devices, five PSCs were fabricated using different SWCNT content in the $TiO_2$ NF photoelectrodes and their performances were compared with $TiO_2$ NF-only photoelectrodes control cells. **Figure 4** shows the typical *J–V* curves of the $TiO_2$ NF-SWCNT hybrid photoelectrode based PSC devices. The corresponding PV parameters of these devices have been summarized in **Table 1**. Starting from the control devices constructed based on $TiO_2$ NF-only photoelectrodes, the $J_{sc}$ and

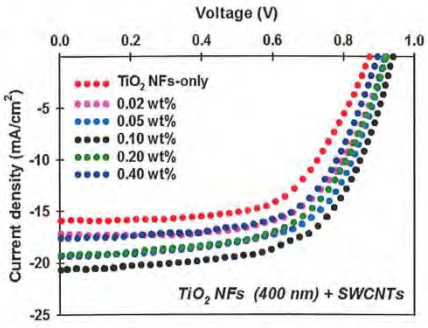


**Figure 4.** *J–V* curves of best performing PSC devices fabricated with different SWCNT content in the $TiO_2$ NF photoelectrodes. The performance of the cells was measured under AM 1.5G illumination at 100 mW $cm^{-2}$.

**Table 1.** PV parameters of best performing PSC devices fabricated based on $TiO_2$ NF photoelectrodes with different SWCNT loadings (extracted from the *J–V* characteristics reported in Figure 4). The average PCEs were calculated based on at least five devices. PV parameters of the best devices are highlighted in bold.

| Device | $J_{sc}$ [mA cm$^{-2}$] | $V_{oc}$ [V] | FF | PCE [%] |
|---|---|---|---|---|
| $TiO_2$ NF-only | **15.91;** | **0.87;** | **0.62;** | **8.56;** |
| | 15.44 ± 0.54 | 0.87 ± 0.01 | 0.61 ± 0.01 | 8.21 ± 0.46 |
| 0.02 wt% SWCNTs | **17.20;** | **0.93;** | **0.62;** | **9.91;** |
| | 17.11 ± 0.20 | 0.92 ± 0.01 | 0.61 ± 0.01 | 9.69 ± 0.23 |
| 0.05 wt% SWCNTs | **19.34;** | **0.93;** | **0.61;** | **11.05;** |
| | 19.04 ± 0.43 | 0.93 ± 0.00 | 0.61 ± 0.00 | 10.81 ± 0.34 |
| 0.10 wt% SWCNTs | **20.68;** | **0.94;** | **0.62;** | **12.03;** |
| | 20.26 ± 0.37 | 0.94 ± 0.01 | 0.62 ± 0.01 | 11.51 ± 0.40 |
| 0.20 wt% SWCNTs | **19.24;** | **0.92;** | **0.60;** | **10.54;** |
| | 19.16 ± 0.31 | 0.91 ± 0.01 | 0.59 ± 0.01 | 10.16 ± 0.32 |
| 0.40 wt% SWCNTs | **17.56;** | **0.90;** | **0.62;** | **9.80;** |
| | 17.43 ± 0.37 | 0.89 ± 0.01 | 0.60 ± 0.02 | 9.40 ± 0.39 |

$V_{oc}$ are 15.91 mA cm$^{-2}$ and 0.87 V, respectively. With increasing SWCNT loading in the $TiO_2$ NF photoelectrodes, both the $J_{sc}$ and $V_{oc}$ values of the PSCs increased up to 20.68 mA cm$^{-2}$ and 0.94 V, respectively, peaking at 0.10 wt%, followed by a decrease with further increases in SWCNTs content. We postulate that the increase in the $J_{sc}$ of the cells is due to the improved conductivity of the films (see Figure S4 in the Supporting Information) that can accelerate the electron transport process within the photoelectrode of PSCs. However, when the concentration of SWCNTs in the hybrid further increases to 0.20 and 0.40 wt%, both $J_{sc}$ and $V_{oc}$ values of the devices decreased despite the films having reduced sheet resistance ($R_s$).

A series of detailed investigations have been carried out to understand the origin of the decrease in PV performance at higher SWCNT loadings. We measured the optical transmittance of the $TiO_2$ NF films (on a glass slide) with different SWCNT loadings (Figure S5a, Supporting Information). A low optical transmittance of photoelectrode could elucidate the decreased $J_{sc}$ value of the cells due to the less light being incident upon the perovskite layer. However, not surprisingly given the small amounts of CNTs being added, the changes in the film transmittance by adding SWCNTs into the $TiO_2$ NFs were very small. For example, for the 0.20 wt% SWCNTs incorporated $TiO_2$ NF film, the reduction of the transmittance was only ≈4% as compared to that of the $TiO_2$ NF-only film. Therefore, the decreased $J_{sc}$ of the device after adding 0.20 and 0.40 wt% SWCNTs into the $TiO_2$ NF photoelectrodes cannot be explained solely by the slightly reduced transmittance of the films. As with all other work that has incorporated nanocarbons in solar cells, we observed that there is an optimal loading which gives the maximum efficiency. At loading above the optimal, it is likely that the decreased PV performance is due to the fact that the CNTs provide extra junctions or sites where recombination of charge carriers is possible. It has been found that nanocarbons including CNTs are suitable candidates to replace the conventional HTMs in PSCs and/or improving the device efficiency owing to their fascinating properties.[44–48,60] In order to confirm our hypothesis, we used SWCNTs as an HTM for the $TiO_2$ NF-only photoelectrode based PSCs. For comparison, PSC devices with and without conventional HTM (Spiro-OMeTAD) were fabricated and compared (Figure S5, Supporting Information). It is not surprising that the HTM-free device (Perovskite/Au) exhibited a very poor PCE (3.65%), while Spiro-OMeTAD (typical HTM) based PSC was able to achieve an average PCE of 8.21%. The poor performance of HTM-free PSC is known to be due to the significant charge recombination caused by direct contact between the perovskite and gold electrode.[44] Interestingly, when SWCNTs are used as an HTM in PSCs by inserting them between the perovskite and gold electrode, the fabricated device showed an improved PCE (6.01%) compared to the device without HTM, demonstrating that SWCNTs can act as an efficient HTL for PSCs. It is known that CNTs are ambipolar and can conduct both holes and electrons.[61] This ability in PSCs is confirmed in these experiments. Thus, in the $TiO_2$ NF-SWCNT-based electrode, it is very likely that the presence of larger amounts of SWCNTs will prolong the lifetime of the hole charge carriers and this will lead to increased recombination rates in the ETL. This likely explains the decreased $J_{sc}$ and $V_{oc}$ values of the PSC devices after adding high concentrations of SWCNTs into the $TiO_2$ NF photoelectrodes.

As can be seen from Figure 4 and Table 1, the PSC devices fabricated based on the 0.10 wt% SWCNTs incorporated $TiO_2$ NF photoelectrodes showed the highest PCE of 12.04% with an average efficiency of 11.51 ± 0.40%, whereas the control cells without SWCNTs displayed an average PCE of 8.21 ± 0.46%. The calculated PCE enhancement of PSCs loaded with 0.10 wt% SWCNTs (in comparison to the efficiency of the control cell) was 40.6%. In addition, the reproducibility of both control and SWCNTs incorporated devices was high and this is evident from the small standard deviation in the PV efficiency (Figure S6, Supporting Information). This result confirms that the incorporation of SWCNTs in the $TiO_2$ NF photoelectrodes does not alter the reproducibility of the devices. Indeed, the increased $J_{sc}$ and $V_{oc}$ values were the major contributions to this efficiency enhancement. Therefore, the devices loaded with 0.10 wt% SWCNTs and the control cells were chosen for further investigation to fully understand the role of SWCNTs in the PSCs.

To confirm the enhancement of the $J_{sc}$, the incident-photon-to-current conversion efficiency (IPCE) spectra of the PSCs fabricated with and without SWCNTs (0.10 wt%) in the photoelectrodes were recorded and their results are plotted in **Figure 5a**. Clearly, the IPCE value of $TiO_2$ NF photoelectrodes containing SWCNTs is higher than that of the control cell without SWCNTs. The integrated photocurrent density of the $TiO_2$ NF-only and $TiO_2$ NF-SWCNT photoelectrode based PSCs was 15.20 and 19.50 mA cm$^{-2}$, respectively, which are in agreement with the measured $J_{sc}$ from the *J–V* characteristics of the devices. The improved current is evident over the entire wavelength region, indicative of enhanced electron collection in the PSC loaded with SWCNTs.

The improved $J_{sc}$ value of the $TiO_2$ NF-SWCNT photoelectrodes was further examined using electrochemical impedance spectroscopy (EIS). EIS measurement of full PSC devices in the dark can be used to distinguish the charge transfer at the

  

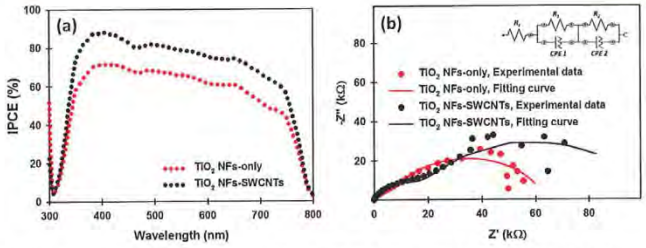


Figure 5. a) IPCE and b) EIS spectra of PSC fabricated with and without SWCNTs (0.10 wt%) in the $TiO_2$ NF photoelectrode.

perovskite/HTM/cathode interface and the charge recombination at the ETL ($TiO_2$)/perovskite interface.[62] EIS of the PSCs fabricated with and without SWCNTs in the $TiO_2$ NF photoelectrodes was measured at a bias of 0.3 V in the dark and the extracted data with a simplified circuit model are illustrated in Figure 5b. In general, the high frequency arc is associated with the diffusion of holes through the HTM, while the lower frequency arc is related to the recombination resistance, $R_{rec}$, mainly due to the charge recombination between the electron transporting material and HTM.[62,63] Clearly, the diameter of the semicircle at the lower frequency of SWCNT-incorporated $TiO_2$ NF photoelectrode based PSC is larger than that of $TiO_2$ NF-only device, indicating higher $R_{rec}$ (87.0 kΩ) for SWCNTs employed device as compared to the control device (58.3 kΩ). The high $R_{rec}$ indicates an efficient blocking for possible recombination. This result clearly demonstrates that the SWCNTs significantly reduced the charge recombination and increased the charge transfer within the cell as expected.

To further investigate the effect of SWCNTs on the charge transfer process of $TiO_2$ NF photoelectrode based PSCs, dark $J$–$V$ measurements were carried out (see Figure S7 in the Supporting Information). The dark $J$–$V$ measurement can provide important information about the recombination process in the devices.[42] From the dark $J$–$V$ measurement, an ideality factor of each device can be calculated, and notably, low values of ideality factor represent less charge recombination. The ideality factor of the $TiO_2$ NF-SWCNT photoelectrode based PSC device was 1.82, which was lower than that (2.41) of the control PSC, proving that the incorporation of SWCNTs in the $TiO_2$ NFs significantly suppresses the recombination process in the devices.

It should be noted that the previous studies have shown decreased and/or unchanged $V_{oc}$ values of PSC devices after the incorporation of various nanocarbon materials into the ETLs.[39,40,42] Interestingly, our study demonstrates that the addition of a small amount of SWCNTs into the ETL leads to a considerable enhancement in the $V_{oc}$. In order to explain why the $V_{oc}$ value increased after adding SWCNTs into the $TiO_2$ NFs, we investigated the interactions between SWCNTs and anatase $TiO_2$ (101) surface using a computational method based on the first principles density functional theory (DFT). In theory, the $V_{oc}$ of PSCs is the difference between the conduction band minimum (CBM) of the $TiO_2$ and the potential energy of the HTM. Based on the DFT results, the CBM level is 0.58 V versus standard hydrogen electrode (SHE) (see **Figure 6**a). After the adsorption of SWCNT, the analysis of density of states (DOS) demonstrates that the system changes from a semiconductor to a metallic material (see Figure 6b), which supports the improved electronic conductivity observed in EIS measurements. Moreover, the theoretical $V_{oc}$ can be calculated based on the difference between the work function of metallic SWCNT-$TiO_2$ and the potential energy of the HTM. The theoretical results reveal that the work function of SWCNT-$TiO_2$ is 0.35 V versus SHE, which is 0.23 V higher than the CBM level

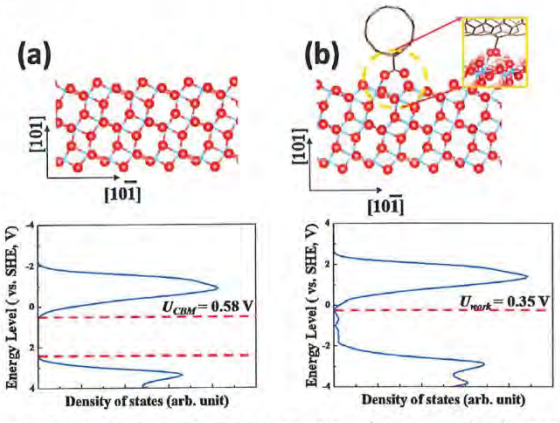


Figure 6. a) Atomic structure of pure anatase $TiO_2$ (101) surface (upper panel) and its DOS plot versus the SHE in V (lower panel). b) Atomic structure of SWCNT–anatase $TiO_2$ (101) surface (upper panel) and its DOS plot versus the SHE in V (lower panel). Inset in (b) is the atomic structure at the interface between the SWCNT and $TiO_2$ (101). Blue, Ti; red, O; brown, C; pink, H.

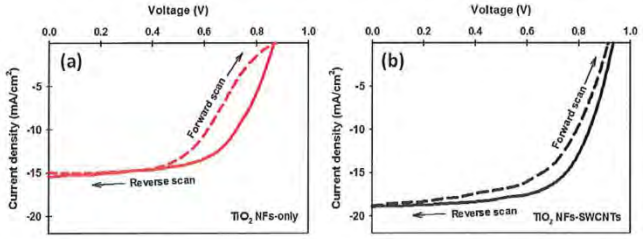


**Figure 7.** *J–V* curves measured with FS and RS for the a) $TiO_2$ NF-only and b) $TiO_2$ NF-SWCNT photoelectrode based PSCs. Detailed PV parameters are given in Table S3 (Supporting Information).

of $TiO_2$. Since the redox potential of the HTM is a constant, the theoretical $V_{oc}$ can, therefore, be enhanced by 0.23 V, which matches the experimental observations.

One of the critical challenges in PSCs is hysteretic *J–V* behaviour. In general, the hysteresis effect in PSCs is observed from the forward scan (FS, from $J_{sc}$ to $V_{oc}$) and reverse scan (RS, from $V_{oc}$ to $J_{sc}$) of *J–V* measurement.[64] Here, we studied the hysteresis behaviour of our PSCs fabricated with and without SWCNTs in the $TiO_2$ NF photoelectrodes (see **Figure 7**). As illustrated in Figure 7a, the $TiO_2$ NF-only-based device exhibited a large hysteresis and distortion in the *J–V* curves. Such hysteresis behaviour causes an underestimation of the real *J–V* curves in the FS and overestimation in the RS. Interestingly, it can be seen from Figure 7b and Table S3 (Supporting Information) that the incorporation of SWCNTs into the photoelectrodes reduces the hysteresis behaviour of the cells. The exact mechanism of hysteresis phenomenon in PSCs is not well established, however, several explanations have been suggested based on both experimental and theoretical investigations.[64] It has been suggested that an anomalous hysteresis in PSCs can be attributed to the charge recombination at the interface between perovskite and charge transporting layer.[42,65] Clearly, SWCNTs suppressed the charge recombination in the PSC photoelectrodes and this may contribute to the reduced *J–V* curve hysteresis.

The stability of PSCs is an important factor for their potential commercialization on an industrial scale. The long-term storage stability of the PSC devices fabricated with and without SWCNTs in the $TiO_2$ NF photoelectrodes was investigated over 12 d (288 h). For the long-term storage stability test, the unencapsulated cells were stored in the dark and kept in ambient conditions (normal laboratory) at a relative humidity of at least 60%. Normalized PCEs of these two devices are plotted in **Figure 8**a and detailed PV parameters ($J_{sc}$, $V_{oc}$, FF, and PCE) are also shown in Figure S8a (Supporting Information). It can be seen from Figure 8a that the PCE of the control PSC without SWCNTs in the photoelectrode dropped by ≈90% after 288 h, while the $TiO_2$ NF-SWCNT photoelectrodes exhibited ≈66% degradation after the same period. Similar phenomena were also observed in several recent reports using graphene derivatives in the $TiO_2$ photoelectrodes of PSCs.[42,43] It is now accepted that in a humid environment, water molecules cause the decomposition of perovskite and result in severe morphological changes (such as pinholes, small grains, and coarse surface).[66] Such morphological features are detrimental to the direct electron transfer between perovskite and $TiO_2$. The presence of SWCNTs in the $TiO_2$ photoelectrodes provides better connectivity with the perovskite, and hence provides extra charge carrying pathways, which may mitigate the changes in the perovskite structure. Undoubtedly, this extends the electron

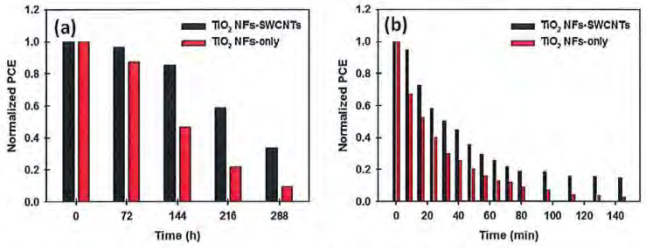


**Figure 8.** a) Normalized PCE of PSCs fabricated with and without SWCNTs in the $TiO_2$ NF photoelectrodes as a function of long-term storage time. The unencapsulated cells were kept in the dark in ambient conditions at a relative humidity of at least 60%. b) Normalized PCE of the devices with and without SWCNTs in the $TiO_2$ NF photoelectrodes as a function of time exposed to continuous light illumination (100 mW $cm^{-2}$, xenon lamp) for 144 min.

  

lifetime in the cell helping maintain efficiency over longer times.

In addition to the long-term storage stability in ambient conditions, the light stability of the PSCs with and without SWCNTs was explored. This was achieved by exposing PSCs to continuous light illumination (100 mW $cm^{-2}$, xenon lamp) for 144 min. The data were collected in the reverse scan direction every 8 min in an ambient atmosphere. Detailed PV parameters are also shown in Figure S8b (Supporting Information). It can be clearly observed from Figure 8b that the device fabricated with $TiO_2$ NF-SWCNT photoelectrodes showed relatively better stability than the control cell based on $TiO_2$ NF-only photoelectrode. This improved light stability of the device with SWCNTs in the photoelectrode may be attributed to the high thermal conductivity of SWCNTs. The highly conductive SWCNTs are expected to effectively remove the heat during cell operation (during light soaking), which will likely help stability of the devices during operation.

It has been well established that the use of nanocarbons in the compact $TiO_2$ (cp-$TiO_2$) layer of PSCs is an effective strategy to enhance the performance of PSC devices.[38,40] Therefore, in this work, we also explored the influence of SWCNTs in the cp-$TiO_2$ layer on the efficiency of $TiO_2$ NF-only photoelectrode based PSCs. As compared to the control device without any SWCNTs (Figure S9a, Supporting Information), SWCNT-incorporated cp-$TiO_2$ layer based $TiO_2$ NF photoelectrode based device exhibited a clear enhancement in the efficiency (see Figure S9b and Table S4 in the Supporting Information). We postulate that this improvement in the efficiency of PSCs is due to the enhanced electron transport rate and thermodynamically favourable energy transfer path within the photoelectrode.[40] Furthermore, in order to maximize our device performance, we fabricated PSC devices with SWCNTs in both cp-$TiO_2$ layer and $TiO_2$ NF layer. The layered structure and PV characteristics of the device are illustrated in **Figure 9**. The observed $J_{sc}$, $V_{oc}$, and FF values for this device were 21.42 mA $cm^{-2}$, 0.98 V, and 0.67, respectively, yielding a PCE of 14.03%. It should be pointed out that while this enhanced PCE is not over the 20% being reported for the best cells,[8] the considerable improvement in PCE using CNTs in combination with a 1D nanomaterial does point to a promising research direction where other materials could be used for these systems and as such the improved PCE observed is an important result.

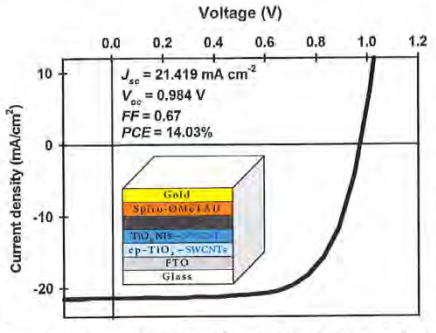


**Figure 9.** *J–V* curve of the best performing device in this study. Inset shows the device structure and detailed PV parameters.

It should be noted that the $V_{oc}$ values of our devices were slightly lower than those reported in other studies,[24,25] despite optimization. It was found that the aperture masking of the PSCs during the *J–V* analysis has some influence on the $V_{oc}$ of the devices, which leads to an underestimation and/or overestimation of cell performance.[67] We note that the aperture mask with an area of 0.081 $cm^2$ was used for all above *J–V* measurements in this work to provide an accurate comparison of PSC devices, while the active area (overlapped area of FTO electrode and gold electrode) of the devices was 0.14 $cm^2$. In order to understand the effect of the aperture mask on the PV parameters of our devices, the control device based on $TiO_2$ NF-only photoelectrodes and the best performing PSC (device structure shown in the inset of Figure 9) were fabricated and their *J–V* characteristics are analyzed with and without an aperture mask. It can be observed from Figure S10 (Supporting Information) that the $V_{oc}$ values of PSCs were increased by ≈53 mV when measurement is carried out without an aperture mask, but no changes were observed in the $J_{sc}$ and FF values. For example, the $V_{oc}$ of the $TiO_2$ NF-only PSCs (control cell) increased from 0.87 to 0.93 V when *J–V* characteristics are measured without a mask, and yielding an improved PCE (9.1%). These improved values ($V_{oc}$ and PCE) are comparable and similar to those reported in the literature,[24,25] suggesting that in our study, the $V_{oc}$ values measured with aperture mask were slightly underestimated and would be higher if no mask was applied during the *J–V* analysis.

## 3. Conclusion

In this work, we have demonstrated the successful incorporation of highly conductive CNTs into 1D $TiO_2$ NF photoelectrodes for highly efficient PSCs. We found that the use of SWCNTs is the most effective material among three different types of CNTs to obtain high PCEs from the devices. In comparison to the control device fabricated without CNTs, a significant enhancement (≈40%) in the cell efficiency is achieved by incorporating an optimized amount of SWCNTs into the $TiO_2$ NF PSCs. The improved $J_{sc}$ and $V_{oc}$ values are the main contributions to this efficiency enhancement. The increased $J_{sc}$ is due to the fact that hybrid structure of $TiO_2$ NF-SWCNT provided a fast electron transport pathway with excellent conductivity and thus suppressed the charge recombination rate in the PSCs. Our theoretical calculation revealed that the energy level of the photoelectrode is changed by introducing SWCNTs into the $TiO_2$ NFs, and resulted in an increase in the $V_{oc}$. Interestingly, we found that the use of SWCNTs in the $TiO_2$ NF photoelectrode reduced the hysteresis behaviour and improved the stability of the PSC devices both during operation under light and for long-term storage in humid conditions. Importantly, our best performing PSC device fabricated with SWCNTs in both cp-$TiO_2$ and $TiO_2$ NF layers achieved a PCE of 14.03%. Therefore, we believe that this work will open new research avenues for the development of nanocarbon and nanofiber materials in PSCs.

## 4. Experimental Section

*Materials*: Unless otherwise stated, all chemicals and reagents were purchased from Sigma-Aldrich. An FTO-coated glass electrode, methylammonium iodide ($CH_3NH_3I$), and tris(1-(pyridin-2-yl)-1*H*-pyrazol)cobalt(III)*tris*(hexafluorophosphate) (FK102 Co(III) PF6) salt were obtained from Dyesol. 2,2′,7,7′-Tetrakis-(*N*,*N*-di-*p*-methoxyphenylamine)-9,9′-spirobifluorene (Spiro-OMeTAD) was purchased from Solaronix. Arc-discharge SWCNTs (P3-SWNT) were purchased from Carbon Solution Inc., Riverside, CA, USA, while both DWCNTs (<5 nm in diameter) and MWCNTs (<10 nm in diameter) with a purity of 90% and a length of 5–15 µm were obtained from Shenzhen Nanotech Port Co., Ltd, China.

*Materials Preparation*: $TiO_2$ NFs were prepared by electrospinning a sol–gel solution consisting of titanium(IV) *n*-butoxide (TIB, 5.0 g), poly(vinyl pyrrolidone) (PVP, 1.0 g), and glacial acidic acid (1 mL) in an ethanol (10 mL). A detailed description of the $TiO_2$ NF synthesis process can be found in the literature.[37] The obtained $TiO_2$ NFs were further used to prepare a viscous paste according to the established procedure.[37] The concentration of the $TiO_2$ NFs in the paste was calculated to be ≈15.14 wt%. To optimize the thickness of the $TiO_2$ NF layer in the photoelectrodes, the prepared viscous paste was diluted with various amounts of ethanol for various times, followed by spin-coating at 2500 rpm for 30 s. Dilution ratios of $TiO_2$ NF paste and ethanol, namely 1:1, 1:2, 1:4, 1:6, and 1:8 (weight ratio), were used to prepare films with thicknesses of 2200, 1300, 580, 400, and 280 nm, respectively. On the basis of PV performance obtained using these diluted solutions, the dilution ratio of 1:6 (paste/ethanol) was chosen.

In order to prepare the stock solution of CNTs, an aqueous Triton X-100 solution with 1 vol% concentration was first prepared. Then, CNTs (10 mg) were dispersed in the previously prepared Triton X-100 solution (10 mL) using an ultrasonication (bath) for 1 h. The concentration of the CNT stock solution was 1 mg $mL^{-1}$. For the preparation of $TiO_2$ NF–CNT hybrid based solutions, the desired concentration (wt%) of CNTs in the hybrid was obtained by adding an appropriate volume of the CNT stock solution into 3.50 g of the diluted $TiO_2$ NF dispersion.

*Device Fabrication*: First, FTO-coated glass substrates were etched using 2 M HCl and Zn powder, followed by sequential cleaning with a detergent (Pyroneg) and washing with acetone, ethanol, and Milli-Q water under ultrasonication for 10 min each. After drying the cleaned FTO electrodes with a stream of nitrogen gas, a thin compact layer of $TiO_2$ was deposited onto the FTO substrate by spin-coating 0.15 and 0.25 M titanium diisopropoxide bis(acetylacetonate) (75 wt% in isopropanol, Aldrich) in 1-butanol solution. After each spin-coating, the films were dried by heating at 150 °C for 15 min in air. For the fabrication of our best performing PSC (device structure is shown in the inset of Figure 9), SWCNTs were added into the titanium diisopropoxide bis(acetylacetonate) in 1-butanol solution to prepare the precursor for the compact layer. The concentration of the SWCNTs in the composite was 0.02 wt%. Then, a thick ETL was deposited onto the compact layer to prepare the photoelectrode by spin-coating a solution of $TiO_2$ NF-only and/or $TiO_2$ NF-CNT at 2500 rpm for 30 s. The films were heated gradually under an air flow at 125 °C for 5 min, 325 °C for 5 min, 375 °C for 15 min, and 450 °C for 1 h, followed by cooling to room temperature. The photoelectrode films were immersed in $40 \times 10^{-3}$ M $TiCl_4$ aqueous solution at 70 °C for 30 min and dried with nitrogen gas, which was again annealed at 450 °C for 1 h. After cooling to ≈120 °C, the films were transferred into a nitrogen-filled glove box.

The perovskite precursor solution was prepared by dissolving a stoichiometric amount (1:1 molar ratio) of $PbI_2$ (0.507 g) and $CH_3NH_3I$ (0.175 g) in an anhydrous dimethylsulfoxide (DMSO, 1 mL). The perovskite layer was deposited onto the photoelectrode films by spin-coating as described in the literature.[68] The spin-coating recipe includes two steps, first 1000 rpm for 10 s with a ramp of 250 rpm $s^{-1}$, then 5000 rpm for 30 s with a ramp of 2000 rpm $s^{-1}$. ≈12 s before the end of the spin-coating program, anhydrous chlorobenzene (120 µL) was gently dropped on the spinning substrate. The films were then heated at 95 °C for 1 h in the glovebox.

After drying perovskite coated films completely, the HTM (70 µL) was deposited onto the perovskite layer by spin-coating at 4000 rpm for 20 s. The HTM was prepared by dissolving 28.9 mg Spiro-OMeTAD, 11.5 µL 4-*tert*-butylpyridine (tBP), 7.0 µL of a stock solution of 520 mg $mL^{-1}$ lithium bis(trifluoromethylsulphonyl)imide (Li-TFSI) in acetonitrile and 9.0 µL of a stock solution of 100 mg $mL^{-1}$ FK102 Co(III) PF6 salt in acetonitrile, in 400 µL chlorobenzene. For the fabrication of SWCNT–HTM-based device, dispersion of SWCNTs in chlorobenzene (1 mg $mL^{-1}$) was spin-coated onto the perovskite layer at 4000 rpm for 20 s. After the HTMs deposition, the films were stored overnight in a dry air desiccator. Finally, 50 nm gold electrodes were thermally evaporated at a rate of 1 Å $s^{-1}$ under a high vacuum through a shadow mask.

*Characterization*: Top-view and cross-sectional SEM images were obtained using an Inspect F50 SEM (FEI) with accelerating voltage of 20 kV. X-ray diffraction (XRD) of $TiO_2$ NF films on FTO was carried out using a Bruker D8 diffractometer with Cu K$\alpha$ source and parallel beam optics equipped with a PSD LynxEye silicon strip detector. The incident beam was kept at an angle of 1° and the angular range of diffraction patterns was collected at $10° < 2\theta < 66°$ with a step size of 0.05° at 2 s per step. The anatase phase of $TiO_2$ was confirmed by comparing the patterns from the Inorganic Crystal Structure Database (ICSD). Raman confocal spectroscopy and spectral mapping were completed using a Witec Alpha 300RS with a 40× objective and 532 nm laser excitation. Raman single spectra were acquired with integration times of 5 s and three accumulations. The Raman spectral image was obtained by collecting a series of 100 × 100 single spectra (0.2 s integration per spectrum) over an area of 20 × 20 µm. The optical transmittances of the films on glass slides were analyzed using a Varian Cary 50G UV–vis spectrophotometer at wavelengths ranging from 400 to 1000 nm. Sheet resistance measurements were performed on the same films using a four point probe technique (KeithLink Technology Co., Ltd, Taiwan). The electrochemical impedance spectroscopy was measured with an Autolab PGSTAT128N on the photoelectrodes using a half cell configuration in 0.1 M NaCl. Analysis was completed in the dark with 0 V bias with 10 mV modulation over the frequency range of 100 000–0.1 Hz.

The photocurrent–voltage (*J*–*V*) characteristics were analyzed using a Keithley 2400 SMU instrument and recorded using a custom LabView Virtual Instrument program. A standard silicon test cell with NIST-traceable certification was used to calibrate the power density as 100 mW $cm^{-2}$ at the sample plane of the collimated a 150W xenon-arc light source (Newport), which was passed through an AM 1.5G filter. The scan rate and delay time are 200 mV $s^{-1}$ and 30 ms, respectively. The active area of the fabricated devices was 0.14 $cm^2$. The devices were masked with an aperture mask (with an area of 0.081 $cm^2$) and tested in air atmosphere without encapsulation. No device preconditioning, such as prolonged light soaking or forward voltage bias, and no equilibration time was used. The IPCE spectra as a function of wavelength ranging from 300 to 800 nm were taken by passing chopped light from a xenon source through a monochromator and onto the devices. The light intensity of the illumination source was adjusted using a photodiode detector (silicon calibrated detector, Newport).

*Computational Detail*: All DFT computations were performed with the Vienna ab initio simulation package (VASP, version 5.4.1) using the projector-augmented wave (PAW) method.[69,70] Electron–ion interactions were described using standard PAW potentials with valence configurations of $3s^23p^64s^23d^2$ for Ti (Ti_sv_GW), $2s^22p^2$ for C (C_GW_new), $2s^22p^4$ for O (O_GW_new), and $1s^1$ for H (H_GW). A plane-wave basis set was employed to expand the smooth part of wave functions with a cutoff kinetic energy of 520 eV. The electron–electron exchange and correlation interactions were parameterized by Perdew–Burke–Ernzerhhof (PBE),[71] a form of the general gradient approximation (GGA), was used throughout.

To simulate the interaction between the SWCNT and anatase $TiO_2$, the anatase $TiO_2$ (101) surface was employed since it is the most stable.[72] For structural relaxations of the anatase (101) surfaces, a 12-layer slab for the (2 × 2) surface cell with 144 atoms was enclosed in a supercell with sufficiently large vacuum regions of 15 Å to ensure the periodic images to be well separated. During the geometry optimizations, all

  

atoms were allowed to relax until the Hellmann–Feynman forces were smaller than 0.001 eV Å$^{-1}$. The convergence criterion for the electronic self-consistent loop was set to $10^{-5}$ eV. Brillouin-zone integrations were performed using a gamma-centered ($1 \times 3 \times 1$) *k*-point grid. The corresponding *k*-mesh densities and the cutoff kinetic energy have been justified in our previous studies.[73,74] Since P3-SWCNT used in this study has 3%–6% carboxylic acid groups, the adsorption of SWCNT was investigated through the interaction between carboxylic acid group with the Ti and O atoms in the (101) surface. The detailed atomic structure at the interface of SWCNT and $TiO_2$ can be found in Figure 6b. The energy level versus the SHE is calculated according to the Equation

$$U(\text{vs SHE,V}) = (E_{vac} - E_b - E_{SHE})/e$$

where $E_{vac}$, $E_b$, and $E_{SHE}$ are vacuum energy, the energy of electronic bands, and the absolute energy of SHE (which is 4.44 eV), respectively. And "*e*" represents the electron charge here.

## Supporting Information

Supporting Information is available from the Wiley Online Library or from the author.

## Acknowledgements

Munkhbayar Batmunkh acknowledges International Postgraduate Research Scholarship (IPRS) and Australian Postgraduate Award (APA) for their financial support during his study in Australia. Dr. Thomas J. Macdonald and Prof. Ivan P. Parkin acknowledge the Engineering and Physical Sciences Research Council (EPSRC) for their financial support (EP/L015862/1). The authors acknowledge the use of South Australian nodes of the Australian Microscopy & Microanalysis Research Facility (AMMRF) and the Australian National Fabrication Facility (ANFF) at Flinders University. All theoretical research was undertaken on the supercomputer of National Computational Infrastructure (NCI) in Canberra, Australia, which is supported by the Australian Commonwealth Government. The support of the Australian Research Council Discovery Program (DP130101714, DP150101354, and DP160101301) is gratefully acknowledged.

Received: December 9, 2016
Published online:

[1] A. Polman, M. Knight, E. C. Garnett, B. Ehrler, W. C. Sinke, *Science* **2016**, *352*, 307.
[2] Science's Top 10 Breakthroughs of 2013, http://www.sciencemag.org/news/2013/12/sciences-top-10-breakthroughs-2013 (accessed December 2016).
[3] 365 Days: Nature's 10, http://www.nature.com/news/365-days-nature-s-10-1.14367 (accessed December 2016).
[4] X. Tong, F. Lin, J. Wu, Z. M. Wang, *Adv. Sci.* **2016**, *3*, 1500201.
[5] T. Salim, S. Sun, Y. Abe, A. Krishna, A. C. Grimsdale, Y. M. Lam, *J. Mater. Chem. A* **2015**, *3*, 8943.
[6] A. Kojima, K. Teshima, Y. Shirai, T. Miyasaka, *J. Am. Chem. Soc.* **2009**, *131*, 6050.
[7] M. M. Lee, J. Teuscher, T. Miyasaka, T. N. Murakami, H. J. Snaith, *Science* **2012**, *338*, 643.
[8] M. Saliba, S. Orlandi, T. Matsui, S. Aghazada, M. Cavazzini, J.-P. Correa-Baena, P. Gao, R. Scopelliti, E. Mosconi, K.-H. Dahmen, F. De Angelis, A. Abate, A. Hagfeldt, G. Pozzi, M. Graetzel, M. K. Nazeeruddin, *Nat. Energy* **2016**, *1*, 15017.
[9] Best Research-Cell Efficiencies (NREL), http://www.nrel.gov/ncpv/images/efficiency_chart.jpg (accessed: June, 2016).
[10] H.-S. Kim, C.-R. Lee, J.-H. Im, K.-B. Lee, T. Moehl, A. Marchioro, S.-J. Moon, R. Humphry-Baker, J.-H. Yum, J. E. Moser, M. Grätzel, N.-G. Park, *Sci. Rep.* **2012**, *2*, 591.
[11] F. Di Giacomo, V. Zardetto, A. D'Epifanio, S. Pescetelli, F. Matteocci, S. Razza, A. Di Carlo, S. Licoccia, W. M. M. Kessels, M. Creatore, T. M. Brown, *Adv. Energy Mater.* **2015**, *5*, 1401808.
[12] F. Matteocci, L. Cinà, F. Di Giacomo, S. Razza, A. L. Palma, A. Guidobaldi, A. D'Epifanio, S. Licoccia, T. M. Brown, A. Reale, A. Di Carlo, *Prog. Photovoltaics: Res. Appl.* **2016**, *24*, 436.
[13] S. Razza, F. Di Giacomo, F. Matteocci, L. Cinà, A. L. Palma, S. Casaluci, P. Cameron, A. D'Epifanio, S. Licoccia, A. Reale, T. M. Brown, A. Di Carlo, *J. Power Sources* **2015**, *277*, 286.
[14] B. J. Kim, D. H. Kim, Y.-Y. Lee, H.-W. Shin, G. S. Han, J. S. Hong, K. Mahmood, T. K. Ahn, Y.-C. Joo, K. S. Hong, N.-G. Park, S. Lee, H. S. Jung, *Energy Environ. Sci.* **2015**, *8*, 916.
[15] A. Fakharuddin, F. Di Giacomo, A. L. Palma, F. Matteocci, I. Ahmed, S. Razza, A. D'Epifanio, S. Licoccia, J. Ismail, A. Di Carlo, T. M. Brown, R. Jose, *ACS Nano* **2015**, *9*, 8420.
[16] K. Hwang, Y.-S. Jung, Y.-J. Heo, F. H. Scholes, S. E. Watkins, J. Subbiah, D. J. Jones, D.-Y. Kim, D. Vak, *Adv. Mater.* **2015**, *27*, 1241.
[17] P. P. Boix, K. Nonomura, N. Mathews, S. G. Mhaisalkar, *Mater. Today* **2014**, *17*, 16.
[18] M. A. Green, A. Ho-Baillie, H. J. Snaith, *Nat. Photonics* **2014**, *8*, 506.
[19] H. S. Jung, N.-G. Park, *Small* **2015**, *11*, 10.
[20] S. D. Sung, D. P. Ojha, J. S. You, J. Lee, J. Kim, W. I. Lee, *Nanoscale* **2015**, *7*, 8898.
[21] C. Yi, X. Li, J. Luo, S. M. Zakeeruddin, M. Grätzel, *Adv. Mater.* **2016**, *28*, 2964.
[22] M. Batmunkh, C. J. Shearer, M. J. Biggs, J. G. Shapter, *J. Mater. Chem. A* **2015**, *3*, 9020.
[23] G. Xing, N. Mathews, S. Sun, S. S. Lim, Y. M. Lam, M. Grätzel, S. Mhaisalkar, T. C. Sum, *Science* **2013**, *342*, 344.
[24] H.-S. Kim, J.-W. Lee, N. Yantara, P. P. Boix, S. A. Kulkarni, S. Mhaisalkar, M. Grätzel, N.-G. Park, *Nano Lett.* **2013**, *13*, 2412.
[25] S. Dharani, H. K. Mulmudi, N. Yantara, P. T. Thu Trang, N. G. Park, M. Graetzel, S. Mhaisalkar, N. Mathews, P. P. Boix, *Nanoscale* **2014**, *6*, 1675.
[26] O. A. Jaramillo-Quintero, M. Solis de la Fuente, R. S. Sanchez, I. B. Recalde, E. J. Juarez-Perez, M. E. Rincon, I. Mora-Sero, *Nanoscale* **2016**, *8*, 6271.
[27] H. Sun, J. Deng, L. Qiu, X. Fang, H. Peng, *Energy Environ. Sci.* **2015**, *8*, 1139.
[28] T. Macdonald, J. Xu, S. Elmas, Y. Mange, W. Skinner, H. Xu, T. Nann, *Nanomaterials* **2014**, *4*, 256.
[29] L. Yang, W. W.-F. Leung, *Adv. Mater.* **2011**, *23*, 4559.
[30] F. J. Ramos, M. Oliva-Ramirez, M. K. Nazeeruddin, M. Gratzel, A. R. Gonzalez-Elipe, S. Ahmad, *J. Mater. Chem. A* **2015**, *3*, 13291.
[31] L. Yang, W. W.-F. Leung, *Adv. Mater.* **2013**, *25*, 1792.
[32] G. S. Han, H. S. Chung, D. H. Kim, B. J. Kim, J.-W. Lee, N.-G. Park, I. S. Cho, J.-K. Lee, S. Lee, H. S. Jung, *Nanoscale* **2015**, *7*, 15284.
[33] G. K. Mor, K. Shankar, M. Paulose, O. K. Varghese, C. A. Grimes, *Nano Lett.* **2006**, *6*, 215.
[34] A. Abrusci, S. D. Stranks, P. Docampo, H.-L. Yip, A. K. Y. Jen, H. J. Snaith, *Nano Lett.* **2013**, *13*, 3124.
[35] M. Batmunkh, M. J. Biggs, J. G. Shapter, *Adv. Sci.* **2015**, *2*, 1400025.
[36] M. Batmunkh, M. J. Biggs, J. G. Shapter, *Small* **2015**, *11*, 2963.
[37] T. J. Macdonald, D. D. Tune, M. R. Dewi, C. T. Gibson, J. G. Shapter, T. Nann, *ChemSusChem* **2015**, *8*, 3396.
[38] J. T.-W. Wang, J. M. Ball, E. M. Barea, A. Abate, J. A. Alexander-Webber, J. Huang, M. Saliba, I. Mora-Sero, J. Bisquert, H. J. Snaith, R. J. Nicholas, *Nano Lett.* **2014**, *14*, 724.
[39] Z. Zhu, J. Ma, Z. Wang, C. Mu, Z. Fan, L. Du, Y. Bai, L. Fan, H. Yan, D. L. Phillips, S. Yang, *J. Am. Chem. Soc.* **2014**, *136*, 3760.

[40] M. Batmunkh, C. J. Shearer, M. J. Biggs, J. G. Shapter, *J. Mater. Chem. A* **2016**, *4*, 2605.
[41] G. S. Han, Y. H. Song, Y. U. Jin, J.-W. Lee, N.-G. Park, B. K. Kang, J.-K. Lee, I. S. Cho, D. H. Yoon, H. S. Jung, *ACS Appl. Mater. Interfaces* **2015**, *7*, 23521.
[42] A. Agresti, S. Pescetelli, L. Cinà, D. Konios, G. Kakavelakis, E. Kymakis, A. D. Carlo, *Adv. Funct. Mater.* **2016**, *26*, 2686.
[43] M. M. Tavakoli, R. Tavakoli, Z. Nourbakhsh, A. Waleed, U. S. Virk, Z. Fan, *Adv. Mater. Interfaces* **2016**, *3*, 1500790.
[44] K. Aitola, K. Sveinbjornsson, J.-P. Correa-Baena, A. Kaskela, A. Abate, Y. Tian, E. M. J. Johansson, M. Gratzel, E. I. Kauppinen, A. Hagfeldt, G. Boschloo, *Energy Environ. Sci.* **2016**, *9*, 461.
[45] Z. Li, P. P. Boix, G. Xing, K. Fu, S. A. Kulkarni, S. K. Batabyal, W. Xu, A. Cao, T. C. Sum, N. Mathews, L. H. Wong, *Nanoscale* **2016**, *8*, 6352.
[46] X. Wang, Z. Li, W. Xu, S. A. Kulkarni, S. K. Batabyal, S. Zhang, A. Cao, L. H. Wong, *Nano Energy* **2015**, *11*, 728.
[47] S. N. Habisreutinger, T. Leijtens, G. E. Eperon, S. D. Stranks, R. J. Nicholas, H. J. Snaith, *Nano Lett.* **2014**, *14*, 5561.
[48] Z. Li, S. A. Kulkarni, P. P. Boix, E. Shi, A. Cao, K. Fu, S. K. Batabyal, J. Zhang, Q. Xiong, L. H. Wong, N. Mathews, S. G. Mhaisalkar, *ACS Nano* **2014**, *8*, 6797.
[49] R. Ihly, A.-M. Dowgiallo, M. Yang, P. Schulz, N. J. Stanton, O. G. Reid, A. J. Ferguson, K. Zhu, J. J. Berry, J. L. Blackburn, *Energy Environ. Sci.* **2016**, *9*, 1439.
[50] L. Qiu, J. Deng, X. Lu, Z. Yang, H. Peng, *Angew. Chem., Int. Ed.* **2014**, *53*, 10425.
[51] S. He, L. Qiu, X. Fang, G. Guan, P. Chen, Z. Zhang, H. Peng, *J. Mater. Chem. A* **2015**, *3*, 9406.
[52] J. Deng, L. Qiu, X. Lu, Z. Yang, G. Guan, Z. Zhang, H. Peng, *J. Mater. Chem. A* **2015**, *3*, 21070.
[53] L. Qiu, S. He, J. Yang, J. Deng, H. Peng, *Small* **2016**, *12*, 2419.
[54] S. S. Mali, C. S. Shim, H. K. Park, J. Heo, P. S. Patil, C. K. Hong, *Chem. Mater.* **2015**, *27*, 1541.
[55] M. Horn, C. F. Schwerdtfeger, E. P. Meagher, *Zeitschrift für Kristallographie* **2010**, *136*, 273.
[56] H.-S. Kim, N.-G. Park, *J. Phys. Chem. Lett.* **2014**, *5*, 2927.
[57] J. H. Heo, S. H. Im, J. H. Noh, T. N. Mandal, C.-S. Lim, J. A. Chang, Y. H. Lee, H.-J. Kim, A. Sarkar, K. Nazeeruddin, M. Gratzel, S. I. Seok, *Nat. Photonics* **2013**, *7*, 486.
[58] Y. H. Lee, J. Luo, M.-K. Son, P. Gao, K. T. Cho, J. Seo, S. M. Zakeeruddin, M. Grätzel, M. K. Nazeeruddin, *Adv. Mater.* **2016**, *28*, 3966.
[59] Y. Shi, Y. Xing, Y. Li, Q. Dong, K. Wang, Y. Du, X. Bai, S. Wang, Z. Chen, T. Ma, *J. Phys. Chem. C* **2015**, *119*, 15868.
[60] M. Cai, V. T. Tiong, T. Hreid, J. Bell, H. Wang, *J. Mater. Chem. A* **2015**, *3*, 2784.
[61] R. Martel, V. Derycke, C. Lavoie, J. Appenzeller, K. K. Chan, J. Tersoff, P. Avouris, *Phys. Rev. Lett.* **2001**, *87*, 256805.
[62] D. S. Lee, W. Kim, B. G. Cha, J. Kwon, S. J. Kim, M. Kim, J. Kim, D. H. Wang, J. H. Park, *ACS Appl. Mater. Interfaces* **2016**, *8*, 449.
[63] G. Niu, W. Li, F. Meng, L. Wang, H. Dong, Y. Qiu, *J. Mater. Chem. A* **2014**, *2*, 705.
[64] B. Chen, M. Yang, S. Priya, K. Zhu, *J. Phys. Chem. Lett.* **2016**, *7*, 905.
[65] S. van Reenen, M. Kemerink, H. J. Snaith, *J. Phys. Chem. Lett.* **2015**, *6*, 3808.
[66] W. Huang, J. S. Manser, P. V. Kamat, S. Ptasinska, *Chem. Mater.* **2016**, *28*, 303.
[67] X. Xu, J. Shi, H. Wu, Y. Yang, J. Xiao, Y. Luo, D. Li, Q. Meng, *J. Renewable Sustainable Energy* **2015**, *7*, 043104.
[68] K. Rakstys, A. Abate, M. I. Dar, P. Gao, V. Jankauskas, G. Jacopin, E. Kamarauskas, S. Kazim, S. Ahmad, M. Grätzel, M. K. Nazeeruddin, *J. Am. Chem. Soc.* **2015**, *137*, 16172.
[69] G. Kresse, D. Joubert, *Phys. Rev. B* **1999**, *59*, 1758.
[70] G. Kresse, J. Furthmüller, *Comput. Mater. Sci.* **1996**, *6*, 15.
[71] J. P. Perdew, K. Burke, M. Ernzerhof, *Phys. Rev. Lett.* **1996**, *77*, 3865.
[72] Y. Wang, H. Zhang, Y. Han, P. Liu, X. Yao, H. Zhao, *Chem. Commun.* **2011**, *47*, 2829.
[73] P. Liu, Y. Wang, H. Zhang, T. An, H. Yang, Z. Tang, W. Cai, H. Zhao, *Small* **2012**, *8*, 3664.
[74] Y. Wang, T. Sun, D. Yang, H. Liu, H. Zhang, X. Yao, H. Zhao, *Phys. Chem. Chem. Phys.* **2012**, *14*, 2333.

  